

# Fabrication of CZTS Solar Cells Using Electrodeposition Techniques

---

Alexander Riches

Prof. Trystan Watson

Swansea University 2021

Thesis submitted to Swansea University in fulfilment of  
the requirements for the Degree of Doctor of Engineering

Materials Research Centre, College of Engineering

## DECLARATION

This work has not previously been accepted in substance for any degree and is not being concurrently submitted in candidature for any degree.

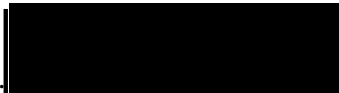
Signed ..  ..... (candidate)

Date ...**20/05/2021**.....

## STATEMENT 1

This thesis is the result of my own investigations, except where otherwise stated. Where correction services have been used, the extent and nature of the correction is clearly marked in a footnote(s).

Other sources are acknowledged by footnotes giving explicit references. A bibliography is appended.

Signed ..  ..... (candidate)

Date ...**20/05/2021**.....

## STATEMENT 2

I hereby give consent for my thesis, if accepted, to be available for photocopying and for inter-library loan, and for the title and summary to be made available to outside organisations.

Signed ..  ..... (candidate)

Date ...**20/05/2021**.....

## Abstract

Copper zinc tin sulphide (CZTS) is a p-type semiconductor that can be used as the light absorbing layer in thin-film heterojunction solar cells, with the specific advantage of being comprised only of non-toxic, earth abundant elements. There are many methods through which CZTS can be synthesised, one of which is electrodeposition, which is an industrially scalable process used extensively in the steel industry.

This thesis details a study of the electrodeposition of stacked elemental layers and their subsequent sulphurisation in the manufacture of CZTS. A range of electrodeposition parameters are tested for each elemental layer, each of which is characterised through a range of techniques, including scanning electron microscopy (SEM) and energy dispersive spectroscopy (EDS), which enables the development of optimised conditions. It was found that the deposition of copper favoured potentiostatic deposition, with a smooth granular structure being deposited onto molybdenum at -0.98V vs Hg|HgO from a sodium hydroxide based electrolyte, while tin required galvanostatic deposition from a methanesulfonic acid electrolyte in order to return consistent results. This was optimised to an initial high current density period of  $-20 \text{ mA cm}^{-2}$  for 1.2 s to nucleate grains, falling to  $-5 \text{ mA cm}^{-2}$  to minimise hydrogen evolution thereafter. Trial of numerous electrolyte formulae found that an acid-sulphate electrolyte gave the most promising results, with galvanostatic deposition at  $-50 \text{ mA cm}^{-2}$  being found to be suitable. Optimised stacked elemental layer precursors are then progressed to the annealing and sulphurisation stage for conversion into CZTS. One key area of study is the inclusion of a pre-alloying annealing step prior to sulphurisation, and its effect on the morphology of the CZTS films and subsequent solar cell device performance.

Pre-alloyed metallic films are extensively characterised by means of X-ray photoelectron spectroscopy (XPS) depth profiling, X-ray diffractometry (XRD) and EDS elemental mapping as part of an optimisation process, and Raman spectroscopy is used in conjunction with XRD and EDS in the analysis of CZTS films sulphurised in a rapid thermal processing (RTP) furnace. A pre-alloying step at 300 °C for 10 minutes was found to be sufficient for the deposited elements to fully intermix. It was discovered that not only does the inclusion of an optimised pre-alloying step improve the morphology of the CZTS films and the subsequent solar cell performance, but the integration of a pre-alloying stage with the sulphurisation in a single furnace operation does not lead to any evidence of disadvantage when compared with pre-alloying and sulphurisation processes conducted separately. In fact, 8 out of 45 cells with an integrated pre-alloying process achieved 0.1% efficiency or greater, compared to 5 out of 45 for those that underwent a separate pre-alloying process, and 0 out of 45 for those that received no pre-alloying process. This positive result for the integration of the pre-alloy offers simplification of the manufacturing process for a potential future scaled-up CZTS solar cell device.

## Acknowledgements

First and foremost, I would like to thank my academic supervisor, Prof. Trystan Watson for his encouragement and support during the course of this project, for providing me with the opportunity to study for this doctorate, and for putting up with me for far longer than I deserve! I would also like to express my sincerest gratitude to my disability support tutor, Dr. Margaret Meehan, not only for her sound academic advice, but also for patiently listening me to air the contents of my head at times when my head was not in a good place.

I would like to express thanks to the many people who have assisted with the work carried out in this project. I would like to thank Dr. Zhengfei Wei for his assistance with many aspects, particularly training on the RTP furnace and the solar simulator, and for the help given in depositing the buffer and window layers on completed solar cell devices. I would like to thank Dr. James McGettrick and the Advanced Imaging of Materials (AIM) centre for carrying out the XPS depth profiles, and for allowing access to the XRD and JEOL FEG-SEM. I would like to thank Ian Matthews and Dr. Rhys Charles for their assistance with the MP-AES experiments, Michael Newman and Harry Lakhiani for assistance with Raman spectroscopy, Dr. Ricardo Bouwer and Dr. Jon Elvins for their input as industrial supervisors, Dr. Matt Burton and Dr. Raman Subramanian (“Subbu”) for their advice on electrochemistry, and Dr. Katherine Hooper for being an excellent go-to lab oracle.

I would like also to acknowledge the research groups that I have been part of and the benefit this has brought. These groups include the SPECIFIC Research Centre and the PV group within it, Materials and Manufacturing Academy (M2A), Steel Training and Research Innovation Partnership (STRIP), and the PV Technology from Earth Abundant Materials (PVTEAM) collaboration with Bristol, Bath, Northumbria and Loughborough Universities. I would particularly like to mention Dr. Gabriela Kissling and Prof. Laurie Peter from PVTEAM for their helpful advice on electrodeposition for CZTS, and all the staff on the M2A project for their hard work and support.

I would like to express my thanks and gratitude to my friends and family for the kindness, encouragement and support that they have shown me over the time I have been studying for this project, I could not have got this far without them. Last, but by no means least, I would like to thank my housemate, Ben Thorpe. We have shared many of life’s ups and downs over the last few years, and I could not ask for a more loyal friend.

I would like to respectfully dedicate this thesis to the memory of my Grandfather, John Harry Fagg, who sadly passed away during the course of my studies, and to whose gentleness, patience and generosity I can only aspire.

*This project was made possible through funding from the Engineering and Physical Sciences Research Council (EPSRC), European Social Fund (ESF) via the Welsh European Funding Office (WEFO), and sponsorship by TATA Steel.*



## List of Contributions

### Conferences

- Sêr Solar Printed PV Conference (Swansea), April 2015: **Poster**
- European Kesterite Conference (Northumbria University, Newcastle), November 2015: **Poster**
- Next Generation Materials for Solar Photovoltaics (Royal Society of Chemistry, London), January 2016: **Poster**
- HOPV Conference (Swansea University), June 2016: **Poster**
- Sêr Solar Symposium (Swansea University), November 2016: **Poster**
- TATA Postgraduates' Conference (Swansea), July 2017: **Poster**
- Sêr Solar Symposium (Swansea University), November 2017: **Poster**
- M2A Annual Conference 2017 (Swansea University), April 2017: **Presentation (1<sup>st</sup> Prize Award)**

# Contents

<b>1</b>	<b>Introduction</b>	<b>1</b>
<b>1.1</b>	<b>Background</b>	<b>1</b>
1.1.1	The Need for Sustainable Energy and the Potential of Photovoltaics	1
1.1.2	Different Types of Currently Available Solar Cells	2
1.1.3	The Potential of Copper Zinc Tin Sulphide	13
<b>1.2</b>	<b>The Functions of a Solar Cell</b>	<b>15</b>
1.2.1	Inorganic Semiconductors – The Silicon Example	15
1.2.2	The p-Type Properties of CZTS	17
1.2.3	The p-n Junction	18
<b>1.3</b>	<b>The Functions of the Different Layers in a CZTS Solar Cell</b>	<b>19</b>
1.3.1	The Substrate	19
1.3.2	The Bottom Contact	20
1.3.3	The n-Type Buffer Layer	21
1.3.4	The n-Type Window Layer	22
1.3.5	The Transparent Conducting Oxide	23
<b>1.4</b>	<b>Material Properties and Deposition of CZTS</b>	<b>24</b>
1.4.1	Stoichiometry and Phase Formation	24
1.4.2	Deposition Techniques	27
<b>1.5</b>	<b>Electrodeposition</b>	<b>31</b>
1.5.1	Electrolytes for the Electrodeposition of Copper	32
1.5.2	Electrolytes for the Electrodeposition of Tin	33
1.5.3	Electrolytes for the Electrodeposition of Zinc	34
1.5.4	Electrodeposition Parameters	36
<b>1.6</b>	<b>Sulphurisation and Annealing</b>	<b>37</b>
1.6.1	Pre-Alloying and Sulphurisation of Sequentially Electrodeposited Stacks	39

1.6.2	Rapid Thermal Processing	40
<b>1.7</b>	<b>Summary</b>	<b>42</b>
<b>1.8</b>	<b>References</b>	<b>43</b>
<b>2</b>	<b>Experimental Techniques</b>	<b>68</b>
<b>2.1</b>	<b>Electrodeposition</b>	<b>68</b>
2.1.1	Electrodeposition of Metals	68
2.1.2	The Functions of a Potentiostat/Galvanostat	68
2.1.3	Cyclic Voltammetry	70
2.1.4	The Electrochemical Series	72
2.1.5	Electrodeposition of Copper	74
2.1.6	The Rotating Disc Electrode	75
2.1.7	Substrate Preparation	78
2.1.8	Electrodeposition of Tin	81
2.1.9	Electrodeposition of Zinc	82
2.1.10	Film Thickness Control	87
<b>2.2</b>	<b>Annealing and Sulphurisation</b>	<b>90</b>
2.2.1	Hot-Dip Simulator	90
2.2.2	Rapid Thermal Processing	92
<b>2.3</b>	<b>Photovoltaic Device Fabrication and Measurement</b>	<b>94</b>
2.3.1	Cadmium Sulphide Deposition	95
2.3.2	Four-Point Probe Measurements	96
2.3.3	Transparent Conducting Oxide Deposition	97
2.3.4	Solar Cell Measurement	97
<b>2.4</b>	<b>Analytical Techniques</b>	<b>100</b>
2.4.1	Microwave Plasma – Atomic Emission Spectrometry	100
2.4.2	X-Ray Diffractometry	103
2.4.3	Raman Spectroscopy	105
2.4.4	X-Ray Photoelectron Spectroscopy	106
2.4.5	Scanning Electron Microscopy and Energy Dispersive Spectroscopy	107

2.4.6	Profilometry	108
2.4.7	Sigma Scan™	109
2.4.8	Visual Inspection	109
<b>2.5</b>	<b>References</b>	<b>110</b>
<b>3</b>	<b>Electrodeposition of Copper and Tin</b>	<b>115</b>
<b>3.1</b>	<b>Introduction</b>	<b>115</b>
<b>3.2</b>	<b>Experimental Methods</b>	<b>116</b>
3.2.1	Sample Preparation	116
3.2.2	Sample Analysis	117
<b>3.3</b>	<b>Results and Discussion</b>	<b>119</b>
3.3.1	Deposition of Copper onto FTO using a Static Working Electrode	119
3.3.2	Deposition of Copper onto FTO using a Rotating Disc Electrode	127
3.3.3	Deposition of Copper onto Molybdenum Coated Glass	134
3.3.4	Electrodeposition of Tin onto Copper	139
3.3.5	Deposition Efficiency	150
3.3.6	Electrodeposition of Copper onto Tin	154
<b>3.4</b>	<b>Conclusions</b>	<b>165</b>
<b>3.5</b>	<b>References</b>	<b>166</b>
<b>4</b>	<b>Electrodeposition of Zinc</b>	<b>169</b>
<b>4.1</b>	<b>Introduction</b>	<b>169</b>
<b>4.2</b>	<b>Experimental Methods</b>	<b>170</b>
4.2.1	Sample Preparation	170
4.2.2	Sample Analysis	170
<b>4.3</b>	<b>Results and Discussion</b>	<b>172</b>
4.3.1	Deposition of Zinc from a pH3 Electrolyte	172
4.3.2	Experimentation Varying the pH of the Electrolyte	179
4.3.3	Deposition from an Acid-Chloride Electrolyte	183
4.3.4	Sample Analysis using XPS Depth Profiling	187

4.3.5	Further Adjustments to the Electrolyte Composition	194
4.3.6	Comparison of Four Diverse Electrolyte Compositions	198
4.3.7	Final Word on Deposition Efficiency	218
<b>4.4</b>	<b>Conclusions</b>	<b>229</b>
<b>4.5</b>	<b>References</b>	<b>230</b>
<b>5</b>	<b>Annealing and Sulphurisation</b>	<b>233</b>
<b>5.1</b>	<b>Introduction</b>	<b>233</b>
<b>5.2</b>	<b>Experimental Methods</b>	<b>234</b>
5.2.1	Sample Preparation	234
5.2.2	Sample Analysis	237
<b>5.3</b>	<b>Results and Discussion</b>	<b>239</b>
5.3.1	Elemental Alloying Prior to Sulphurisation	239
5.3.2	Reducing Blistering and Optimising Pressure During Sulphurisation	265
5.3.3	Optimisation of Sulphur Concentration for Sulphurisation	276
5.3.4	Combining the Elemental Alloying and Sulphurisation Processes	284
<b>5.4</b>	<b>Conclusions</b>	<b>294</b>
<b>5.5</b>	<b>References</b>	<b>296</b>
<b>6</b>	<b>Photovoltaic Device Fabrication and Measurement</b>	<b>300</b>
<b>6.1</b>	<b>Introduction</b>	<b>300</b>
<b>6.2</b>	<b>Experimental Methods</b>	<b>301</b>
<b>6.3</b>	<b>Results and Discussion</b>	<b>302</b>
<b>6.4</b>	<b>Conclusions</b>	<b>312</b>
<b>6.5</b>	<b>References</b>	<b>312</b>
<b>7</b>	<b>Conclusions and Further Work</b>	<b>314</b>
<b>7.1</b>	<b>Conclusions</b>	<b>314</b>
<b>7.2</b>	<b>Further Work</b>	<b>316</b>

# **1 Introduction**

## **1.1 Background**

### **1.1.1 The Need for Sustainable Energy and the Potential of Photovoltaics**

In December 2015, the United Nations Framework Convention on Climate Change (UNFCCC) reached an agreement to act to mitigate climate change. The agreement stipulates that global average temperatures at the end of the century must be kept well below a 2 °C increase when compared to pre-industrial temperatures, with a target maximum of 1.5 °C. By November 2016, 55 countries that produce at least 55% of the world's greenhouse gases had ratified the agreement, including the UK, with this figure having risen to 125 countries in early 2017 [1]. Furthermore, the UK government has made its own commitment to reduce greenhouse gas emissions to net zero by the year 2050 [2].

Electricity production is a significant contributor to greenhouse gas emissions as a substantial portion of electricity is still generated through the combustion of fossil fuels. In 2018, roughly half of the electricity consumed in the UK was generated in this manner, with a third coming from renewable sources, and the majority of the remaining sixth being generated by nuclear power plants. Of the electricity generated from renewable sources, 31.57% came from biomass [3]. Although biomass has the potential to be carbon neutral, this relies on at least as many trees being planted as are being cut down for fuel, and when a shortfall occurs, this leads to deforestation and net CO<sub>2</sub> emissions. There are further disadvantages in the use of biomass as large areas of land are required to grow the required trees, and sufficient water must also be available (which is a scarce resource in some parts of the world) [4].

The sum of the surface areas of all commercial buildings in the UK is estimated at 250,000 hectares [5], which, if fitted with PV devices, is sufficient to generate approximately 50% of the total electricity required in the UK [6]. Yet despite this, only 11.69% (12.9 terawatt hours [7]) of the electricity generated from renewables (equivalent to ~4% of total electricity production) in the UK in 2018 was sourced

from solar PV [3]. This suggests that PV is an underexploited resource, and represents a significant opportunity for the expansion of PV to play a part in meeting targets for net zero greenhouse gas emissions and mitigating climate change.

For the mass deployment of PV across commercial buildings to be viable, it must be possible to manufacture the PV devices using easily available materials that are not likely to run into supply issues. It would also be advantageous to utilise manufacturing techniques that are already well established in UK industry, so that large scale production of the required PV modules could be accomplished without the need for high-cost investments in newly designed manufacturing equipment or techniques. Ideally, the option to integrate the PV modules into the building materials during the manufacturing process should be available, so that the need to retrofit PV to new buildings, and buildings undergoing the refitting of roofing or panelling, is eliminated.

### **1.1.2 Different Types of Currently Available Solar Cells**

#### ***1.1.2.1 Silicon***

Much of the PV seen in use in the UK is silicon-based. The first Si PV device was made by Russell Ohl of Bell Laboratories Inc. in 1941, by the careful cutting segments from ingots of recrystallized silicon melts [8] and achieved an efficiency of less than 1% [9]. This efficiency was greatly improved upon by Pearson, Fuller and Chappin (also of Bell Laboratories Inc.) in 1954 [10], achieving efficiencies of 4.5% through lithium diffusion, and 6% through boron diffusion [9]. Since then, polycrystalline Si has become well established as a material for the manufacture of PV and has achieved efficiencies of up to 26.7% when manufactured with an amorphous silicon/crystalline silicon junction [11, 12, 13]. It is a relatively abundant material, with a crustal abundance of 282,000 parts per million [14] (equivalent to ~28% of the mass of the earth's crust [15]), compared to indium, for example (another element used extensively in electronics), which has a crustal abundance of just 0.052 parts per million [16]. This is an advantage of using silicon, as there are no concerns about ongoing supply issues, and this contributes to the relatively low cost

of the technology at approximately £80 per megawatt hour (compared to coal with carbon capture and storage, for example, at approximately £134 per megawatt hour) [17]. The power conversion efficiency of an industrial scale Si PV module can be expected to be approximately 16% [18], and the company Foresight Solar Fund Ltd reported that in the 6 months ending 30<sup>th</sup> June 2017, they generated a total of 223.5 gigawatt hours of electricity across their 18 UK solar farms, averaging 12.4 GW hrs per site [19]. Industrial Silicon PV has also been successfully integrated into building design through PV roof tiles, or to provide partial shading in glass roof panelling [20]. However, the scope for building integration of the most common form of silicon PV, crystalline Si, is limited due to its rigid and brittle nature, which prevents it from being applied to a curved surface or flexible substrate. As many large industrial buildings, such as factories, are constructed using curved or corrugated steel panelling, this limits the ability of crystalline Si PV to be incorporated. One potential solution to this problem is to use amorphous rather than crystalline silicon, as this can be flexible. Unfortunately, amorphous silicon (a-Si) lags behind crystalline silicon (c-Si) in terms of its efficiency, with a typical commercial module expected to achieve ~7% [21]. It can also suffer from degradation over time, and can lose 15-30% of its initial efficiency over the first 1000 hours of light exposure, although the efficiency would normally stabilise from this point for hydrolysed a-Si (a-Si:H) [22]. In addition to these disadvantages, a-Si solar cells require the use of silane gas in their manufacturing process, which is both highly toxic and explosive [23, 24]. Several alternatives to silicon PV have been developed over the course of time in order to attempt to eliminate some of the disadvantages of Si PV. One of these alternatives is Copper Indium Gallium Selenide/Sulphide (CIGS).

#### *1.1.2.2 Copper Indium Gallium Selenide/Sulphide*

CIGS is a type of thin-film PV technology that has a relatively high light absorption coefficient, which is in the range of  $2.7 \times 10^3$  and  $>3 \times 10^5 \text{ cm}^{-1}$  for the 1400 nm to 400 nm wavelength interval [25]. By comparison, the absorption coefficient of n-type Si is  $\sim 1 \times 10^4 \text{ cm}^{-1}$  across the same interval, whereas it ranges from  $<1$  to  $\sim 1 \times 10^5 \text{ cm}^{-1}$  for p-type c-Si for typical doping densities [26]. This lower absorption



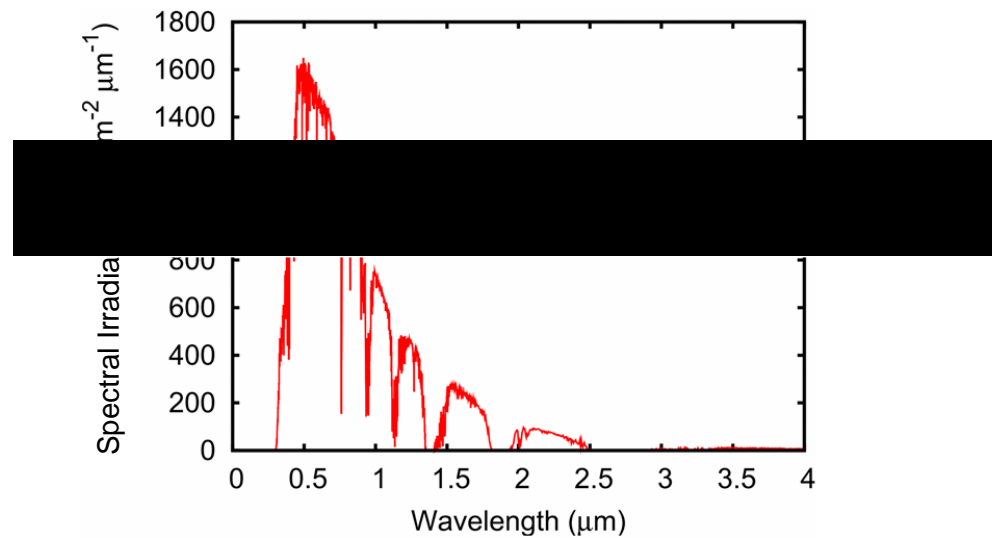


**Figure 1-1 – The AM1.5 solar spectrum showing power per unit area of the incident radiation plotted against wavelength (taken from [28]).**

coefficient for c-Si is related to the fact that it has an indirect band gap of 1.17 eV and a direct band gap of 3 eV [27]. This means that photons of a wavelength greater than  $\sim 400$  nm would require a coincidental change in the momentum of an electron, for that electron to transition from the valence to conduction band and the photon to be absorbed. By contrast, CIGS has a tuneable direct bandgap between 1.04 eV and 1.68 eV, depending on the controllable ratio of indium and gallium, with a greater ratio of gallium to indium giving a larger bandgap [25]. This enables the incident sunlight to be fully absorbed over a short depth, which in turn enables relatively high efficiencies to be achieved with a much thinner absorber layer, facilitating the manufacture of a flexible PV device. The AM1.5 solar spectrum can be seen in Figure 1-1 [28], which demonstrates that the majority of incident light in outdoor conditions falls within the 400 nm to 1400 nm wavelength range, and Figure 1-2 [25] demonstrates the difference in thickness of material required for c-Si and CIGS to fully absorb photons in the AM1.5 spectrum. It can be seen that a full absorption occurs for CIGS from a thickness of  $\sim 1$   $\mu\text{m}$  and greater, whereas Si requires a thickness of  $\sim 1000$   $\mu\text{m}$ . In a typical CIGS solar cell, the light absorbing layer is approximately 2 – 2.5  $\mu\text{m}$  thick [29], with the total thickness of a CIGS PV device being approximately 3 – 4.5  $\mu\text{m}$  (excluding the substrate) [25]. Unlike silicon, CIGS

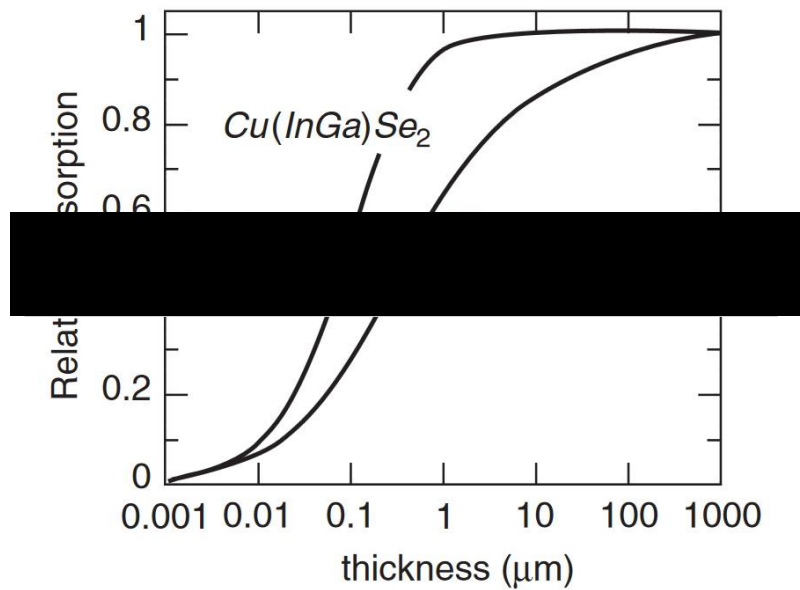


**Figure 1-2 – The proportion of incident radiation absorbed (of energy greater than the band gap), plotted against film thickness, for CIGS and c-Si (taken from [25]). Please note the logarithmic scale on the horizontal axis.**

is a heterojunction solar cell, meaning that the p-n junction is formed between two different materials rather than differently doped sections of the same material (a homojunction). In the case of CIGS cells, the light absorbing CIGS layer is a p-type material, with the n-type properties being present in the immediately adjacent buffer layer and subsequent window layer (the functions of these layers are detailed further in section 1.2.3). Typically the window layer would be intrinsic zinc oxide, whereas the buffer layer would be cadmium sulphide. This is a cause for concern due to the toxicity of cadmium, however, it is possible for the cadmium sulphide buffer layer to be replaced with a cadmium-free alternative – Solar Frontier are commercial manufacturers of cadmium-free CIGS solar cells and published an efficiency of 15.5% for a lab-scale cell with a zinc-based buffer layer in 2016 [30]. They also broke the CIGS world record with a 23.35% efficient cadmium-free solar cell in January 2019 [31, 32]. Cadmium-free CIGS modules that are flexible and can be integrated into wall and roof panels are manufactured in South Wales by BIPVco [33], and are in use on permanent buildings at Swansea University at the time of writing.

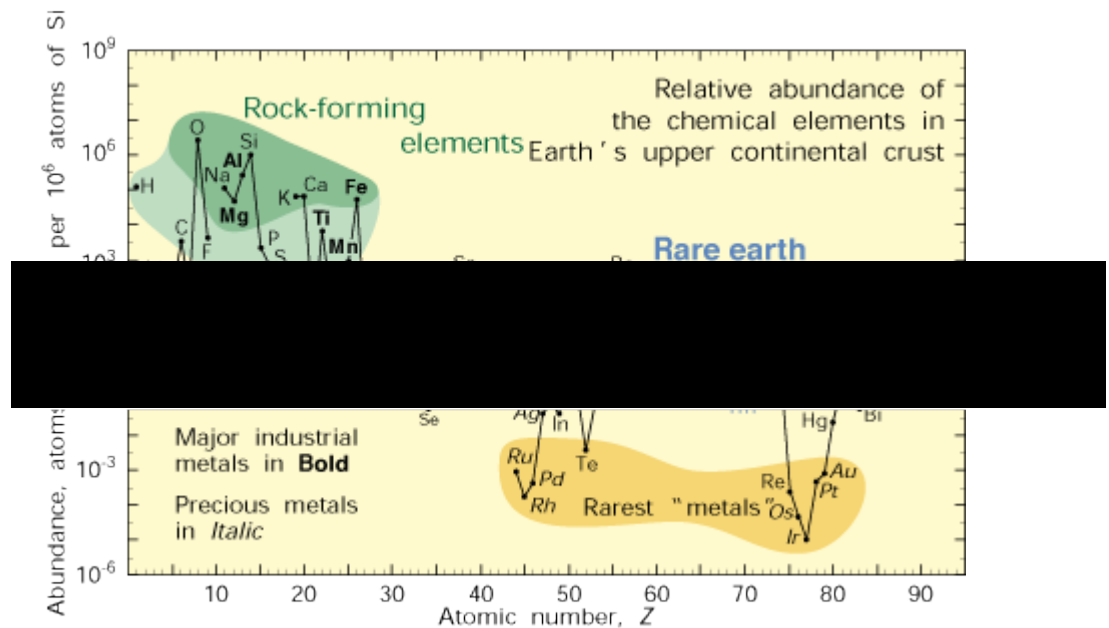


**Figure 1-3 - Abundance of chemical elements in the earth's upper continental crust, relative to that of silicon, plotted as a function of atomic number (taken from [35]). Please note the logarithmic scale on the vertical axis.**

Although CIGS has a number of advantages over silicon for the manufacture of solar cells (as discussed above), it does have one very significant limitation – it is reliant upon the rare and expensive elements, indium and gallium. It is worth noting at this stage that, according to the European Chemical Society, the world's supply of indium is likely to become exhausted in approximately 20 years' time if the current rate of consumption continues [34]. Figure 1-3 (taken from [35]) indicates the relative abundance of a range of elements in the earth's upper continental crust, with oxygen being the most abundant and iridium being the least abundant of those featured. It is possible to see that all of the elements contained in CIGS are less abundant than silicon, with indium being particularly scarce. However, it is curious to note that gallium is in fact more prevalent than tin, which is a relatively low cost material. There several reasons for gallium being referred to as scarce – it does not naturally exist in a pure form, and it has not been selectively concentrated into minerals by any geological process. This means that it is relatively dispersed, and not particularly accessible [36]. Gallium is typically produced as a by-product from

bauxite and sulphidic zinc ores rather than as a primary product in its own right [37], making it a scarce and relatively costly metal in practical terms. Furthermore, there are additional factors that contribute to the cost of manufacturing CIGS solar cells, particularly that a two-stage manufacturing process is often needed in order to incorporate the selenium and form the quaternary CIGS. A thermal co-evaporation technique can be used to deposit all four elements concurrently [25, 29], however this is a vacuum-based process and is more difficult to up-scale than many of the techniques that require a separate selenisation stage [38]. In contrast, cadmium telluride (CdTe) is a binary rather than quaternary compound, and can be used in the manufacture of solar cells at a lower cost than that of CIGS [38].

#### *1.1.2.3 Cadmium Telluride*

Cadmium telluride has a number of properties in common with CIGS and shares many of its advantages. It is used as a p-type light absorbing layer for thin film photovoltaic devices, including on flexible substrates. With a direct band gap of 1.45 eV [39], it can effectively absorb incident light of wavelengths  $< \sim 850$  nm, and with a high absorption coefficient of  $> 5 \times 10^5 \text{ cm}^{-1}$  for photons of energy greater than the band gap [40], it efficiently absorbs the most powerful part of the AM1.5 solar spectrum. The band gap is also very close to the theoretical ideal (1.5 eV) for maximum solar cell performance [40]. This means that 99% of incident photons of energy greater than 1.45 eV (wavelength  $< \sim 850$  nm) are absorbed within 2  $\mu\text{m}$  of the CdTe surface [40], aiding the manufacture of an efficient thin film, flexible device. The record efficiency for a CdTe device is 22.1%, achieved by First Solar in the year 2016 [12, 41]. At the time of writing, First Solar were marketing 2.47m<sup>2</sup> commercially available modules of up to 18.2% efficiency [42]. One advantage that CdTe holds over CIGS is the lower cost of production, despite the rarity of tellurium. This is partly due to the fact that, unlike CIGS, it does not require a selenisation/sulphurisation or annealing step to be added into the manufacturing process [38]. Cadmium telluride also has a negative enthalpy of formation when compared to its constituent elements, meaning that its formation is exothermic and gives a stable product, which reduces the energy consumption of the synthesis

process [40]. Unfortunately, CdTe is afflicted by some significant disadvantages. Firstly, with tellurium being such a rare element, there is the risk of ongoing supply issues and future cost increases expected in the future [38]. Secondly, the toxicity of cadmium simply cannot be overlooked. Not only is cadmium contained in the absorber layer, but it is contained in the CdS buffer layer as well. This leads to environmental concerns relating to the utilisation of the technology, and concerns regarding the health and exposure of workers to the accumulatively toxic and carcinogenic cadmium at CdTe solar cell manufacturing plants. Cadmium has officially been banned in electronic goods under EU legislation, and, although photovoltaic cells have been granted exemption from this [43], it is an indicator of the need for an alternative, safer material to be made available for future large-scale PV production.

#### *1.1.2.4 Organic Photovoltaics*

One relatively new PV technology is organic PV (OPV). These solar cells are based on organic compounds such as phenyl-C61-butyric acid methyl ester (PCBM) and poly(3-hexylthiophene-2,5-diyl) (P3HT), which do not exhibit the toxicity of CdTe. OPV has the further advantage that it can be manufactured using solution based processing and deposition, eliminating the need for costly vacuum-based techniques. The record efficiency for a laboratory fabricated OPV device is 18.2% and was achieved using a modified material based on dithieno[3',2':3,4;2'',3'':5,6]benzo[1,2-c][1,2,5]thiadiazole (DTBT). It was deposited from a chloroform solution via spin coating [44]. Spin coating is not a scalable technique, however, devices of 15.5% efficiency have been manufactured using blade-coating of a blend of BTP-4Cl-12 (a non-fullerene electron acceptor) and PBDB-TF (an electron donor) [45]. Blade coating is a scalable technique, however the devices reported were only 0.81cm<sup>2</sup> in area. The highest recorded efficiency of an OPV module is 12.6%, which was achieved with an area of 26cm<sup>2</sup> [46]. OPV is not as well established as other (inorganic) forms of PV, with efficiencies still lagging behind those of CIGS and CdTe. However, this disadvantage may be negated by the reduced cost of manufacture, in turn leading to a faster payback time. Furthermore, there are not the

expected future supply limitations on materials required to manufacture OPV that there are for CIGS and CdTe. Unlike CdTe and CIGS, OPV encompasses a very broad group of compounds rather than focussing on variations of a single one. This leads to a more diverse range of properties within the group. One of the properties that can vary is the long-term stability of the organic compound. For example, if a solar cell is intended to be used on a product with a short lifespan, it may be more important that the material used leads to a high efficiency than good long-term stability, whereas PV installed on a building would require long-term stability. OPV typically has a 'burn in' period during which there is rapid exponential decay in its efficiency when first placed under solar illumination, which is followed by relatively slow ongoing linear decay. Rapid decay during the 'burn in' period does not necessarily lead to the subsequent linear decay being rapid, therefore OPV life times can be quoted either as the time taken to lose 20% of their initial efficiency (T80) or the time take to lose 20% of their post 'burn in' efficiency (Ts80). Ts80 is more commonly used when discussing life-times under solar illumination. Reference [47] collates data on OPV lifetimes from a number of different sources, and by way of example, it can be seen that an OPV cell with a PTB7-Th: PC<sub>70</sub>BM active layer had an initial efficiency of 10.5% and a lifetime under constant irradiance of >600 hours, and a PCDTBT: PC<sub>70</sub>BM cell had an initial efficiency of 5.5% and a lifetime of ~18,000 hours under constant irradiance. P3HT: PCBM devices are known to have relatively high levels of intrinsic stability (estimated 2.5 – 3.8 years), but effective encapsulation is needed to achieve this in outdoor conditions and encapsulation typically accounts for approximately 60% of the cost of an OPV device. Furthermore, P3HT: PCBM devices tend to achieve relatively low efficiencies of ~3-6% [48], dropping to ~2-4% for modules [49]. When compared to other forms of PV, such as Si (which has a typical module efficiency of 16% [18]), OPV performance is relatively poor, therefore it is currently only suitable for niche applications (for example, a short-lived electronic device to be used in indoor conditions). Another aspect to take into account when considering the suitability of OVP for large-scale production is the toxicity of the solvents required in their manufacture. Examples of

the solvents used include chlorobenzene, chloroform [50], tetrahydrofuran [51], and o-xylene [49], all of which are known to be hazardous to human health and the environment. This limits the potential for large-scale production of OPV. An efficient, flexible, low-cost and environmentally friendly alternative is still needed.

#### *1.1.2.5 Dye-Sensitised Solar Cells*

One potential alternative is the dye-sensitised solar cell (DSSC). In these solar cells, the light is absorbed by a layer of porous metal oxide (typically nanoporous anatase titanium dioxide [52]) that has been ‘sensitised’ with a dye that absorbs well in the solar spectrum [53]. The band gap of anatase  $\text{TiO}_2$  is 3.2 eV, which absorbs effectively in the UV part of the spectrum but not the visible part [54], hence the need for a dye to overcome that issue. Some of the most effective dyes used are ruthenium based and can absorb effectively in the wide visible and near infrared (NIR) region across wavelengths from 400 to 800 nm [53]. One of the most commonly used dyes is referred to as N-719 [55] and has an energy gap of 2.33 eV [56]. Dye cells have not achieved as high efficiencies as silicon, CdTe or CIGS, with the maximum published efficiency for a lab scale device being 11.9% [12], while PV modules have reached up to 8.8% with a surface area of 399  $\text{cm}^2$  [12]. Despite their lower power conversion efficiencies, dye cells offer several advantages. For example, they can be manufactured to work on flexible substrates [57], they can be manufactured using rapid thermal processing techniques [58], and they can be engineered to be semi-transparent in a range of colours and incorporated into aesthetically pleasing window designs [59, 60]. Unfortunately, the disadvantages of dye cells do not end with their limited efficiencies. Many dye cell designs incorporate a liquid electrolyte, which is vulnerable to leaking out over time [61]. In addition to this, they can also suffer stability issues and lose efficiency over time [62]. For a PV cell to be viable for large-scale deployment and building integration, it needs to be durable and maintain its power conversion efficiency in long term use, therefore the scope for dye cells to fulfil this purpose is limited.

#### *1.1.2.6 Perovskite Solar Cells*

A further development of DSSC technology is the perovskite based solar cell. Despite its known problems with degradation [63], perovskites present a number of advantages. They can be manufactured at relatively low cost – the materials required in their manufacture are inexpensive [64], and, as relatively thin active layers are required to make a working perovskite solar cell, only small quantities of the raw materials are required. The deposition process can be carried out using relatively simple printing techniques, such as screen printing, and it is possible to adapt existing textile printing equipment for such purposes [65]. This means that there is the potential to set up a manufacturing plant with relatively low up-front costs. They can be manufactured using roll-to roll printing techniques onto flexible substrates [66]. Further advantages include their superior power conversion efficiencies when compared to dye cells (up to 25.2% PCE has been achieved) [12], accompanied by a steep upward trajectory in the recorded maximum efficiencies, as can be seen in the NREL Best Research-Cell Efficiencies chart (displayed in Figure 1-4) [67], positioning them as a promising technology for the future. In addition to this, unlike silicon solar cells, perovskites can maintain respectable efficiencies in low light conditions [68, 69], making them ideal for use in indoor settings, as well as in climates that experience frequent overcast skies, such as the UK. The thin layers of active material required also make perovskite cells suitable for light weight applications [66].

As mentioned previously, the stability of perovskite cells poses a challenge. Unfortunately, they are susceptible to photodegradation [70], and also suffer from sensitivities to oxygen [71] and water [70, 72]. This means that they are also very sensitive to their processing conditions, with the oxygen levels, humidity and cleanliness of their manufacturing environment all having substantial effects on the efficiency and stability of the cells and must be carefully controlled [72]. This adds to their manufacturing costs, as does the required encapsulation to keep water and oxygen out of the manufactured cells. They also have the disadvantage of toxicity. Perovskite cells contain lead based salts, which are both poisonous and water



1



achieved by perovskite solar cells.

soluble, and can damage ecosystems as well as being easily absorbed into the human body [73]. Furthermore, some of the solvents used in their manufacture, for example, dimethylformamide (DMF), are also toxic and can easily be absorbed through human skin, carrying toxic lead salts into the body [74]. These factors are of significant concern when considering the suitability of a technology for large scale industrial production, which ideally would be manufactured using only non-toxic substances and would exhibit robust chemical and performance stability.

### **1.1.3 The Potential of Copper Zinc Tin Sulphide**

Copper zinc tin sulphide ( $\text{Cu}_2\text{ZnSnS}_4$  – CZTS) is a stable [75], non-toxic compound comprising of earth abundant elements [76]. It is structurally analogous to CIGS [77], with the indium and gallium atoms effectively exchanged for zinc and tin atoms, eliminating the expected future availability challenges and cost increases associated with CIGS. It has strong potential to become a low-cost alternative to more established technologies, as, not only are the materials used in its manufacture relatively cheap [78], it can be deposited via a wide range of scalable processes, including non-vacuum techniques, such as screen printing [79]. It has also been demonstrated that CZTS can be deposited onto flexible substrates [80]. In common with CIGS, CZTS is a direct band gap p-type semiconductor [81, 82]. It also has a relatively high optical absorption coefficient of approximately  $10^4 \text{ cm}^{-1}$  for visible light [83]. It is possible to incorporate selenium into the lattice structure in partial substitution for sulphur, to create  $\text{Cu}_2\text{ZnSnS}_x\text{Se}_{4-x}$  (CZTSSe), or to manufacture copper zinc tin selenide ( $\text{Cu}_2\text{ZnSnSe}_4$  – CZTSe) [84]. In doing this, it is possible to tune the bandgap from 0.95 eV for pure selenide CZTSe, to 1.5 eV for pure sulphide CZTS [84]. Although the band gap of 1.5 eV is a closer match for visible optical wavelengths, incorporating Se has been shown to lead to higher efficiencies [85]. This is likely due to the fact that a type-inverted n-type phase can exist at the surface of the absorber material which facilitates the separation of photogenerated charge carriers, and this forms more readily for selenium-rich CZTSSe or CZTSe than it does for pure sulphide CZTS [85]. However, the manufacture of CZTS(Se) is not without its challenges. The improved efficiencies achieved through selenium

incorporation come at the price of increased toxicity [86] and higher materials costs [87], and, although the materials and device efficiencies are stable, the maximum efficiency achieved to date is just 12.6% [12, 75], significantly lower than its CIGS counterparts. Also, this record efficiency was achieved using hydrazine [88] (a toxic and explosive compound [89]) in its manufacture process. Thankfully, comparable efficiencies (up to 11.8%) have been achieved without the use of hydrazine [90], however, the most commonly used material for the buffer layer in a CZTS cell is cadmium sulphide, which poses a toxicity risk [91]. It is possible to manufacture CZTS with a cadmium-free buffer layer, such as zinc tin oxide [92], but, in contrast to the situation with CIGS, cadmium-free devices have yet to achieve the efficiency levels of their cadmium containing counterparts. The most efficient Cd-free CZTS cell reported in literature achieved 9.7% [92], although this was achieved using a pure-sulphide absorber layer, the record efficiency for pure sulphide CZTS being 11.0% [93]. Yet despite these limitations, there is still potential for CZTS to be utilised in large scale PV applications as a low cost of manufacturing and a lack of risk to the environment could offset the disadvantage of reduced efficiency, particularly as there is scope for CZTS to be applied directly to large area building materials, such as sheet steel [94]. If the relatively high efficiencies that have reportedly been achieved using non-scalable methods thus far could be achieved via a scalable, low cost route without toxic components, then CZTS would be an ideal candidate for large scale, affordable, building integrated PV. The aim of this project is to address the challenge of depositing CZTS using a technique that is suitable for large scale deposition onto sheet steel, while attempting to optimise the power conversion efficiency. However, before exploring the possible methods for the deposition of CZTS, it would be useful to consider the function performed by each of the component layers in a solar cell.

## **1.2 The Functions of a Solar Cell**

### **1.2.1 Inorganic Semiconductors – The Silicon Example**

In order to understand how a solar cell works, it is important to consider the electronic properties of the materials from which it is comprised. CZTS is an inorganic semiconductor, therefore the focus needs to be on the properties of inorganic semiconductors. Silicon can be considered initially as an example – the majority of solar cells are silicon based [95].

In elemental form, silicon has four electrons on its outer shell, which has a total capacity for eight electrons [96]. In a silicon crystal, silicon atoms will bond covalently with four neighbouring atoms in a lattice structure [97]. This enables the effective filling of the outer shells, while, at lower temperatures, the electrons remain localised as they are being used in covalent bonding [98]. In this instance, the electrons are in the valence band and are not available for conduction [99]. In order for the electrons to become available for conduction, they must acquire sufficient energy to become delocalised from the covalent bonds. If this occurs, they become mobile and move within the conduction band. The energy required to make this transition is equal to the bandgap,  $E_g$  [98]. In intrinsic silicon, the bandgap is approximately 1.1 eV at room temperature [100], however, this is an indirect bandgap, meaning that an electron would need to undergo a coincidental change in momentum as well as energy for the transition to take place (the band energy state depends on both the potential energy and the kinetic energy of the electron) [99]. This would require the concurrent creation or annihilation of a phonon (lattice vibration) [101]. For an electron to transition from the valence band to the conduction band in silicon without this change in momentum (a direct transition), the additional potential energy required would be approximately 3.5eV [99, 102], as can be seen in Figure 1-5, which shows the conduction and valence band structures for gallium arsenide (which has a direct bandgap) and silicon. When an electron becomes excited and delocalised from a covalent bond in this way, it creates a hole, which is the mobile absence of an electronic bond – electrons in neighbouring bonds

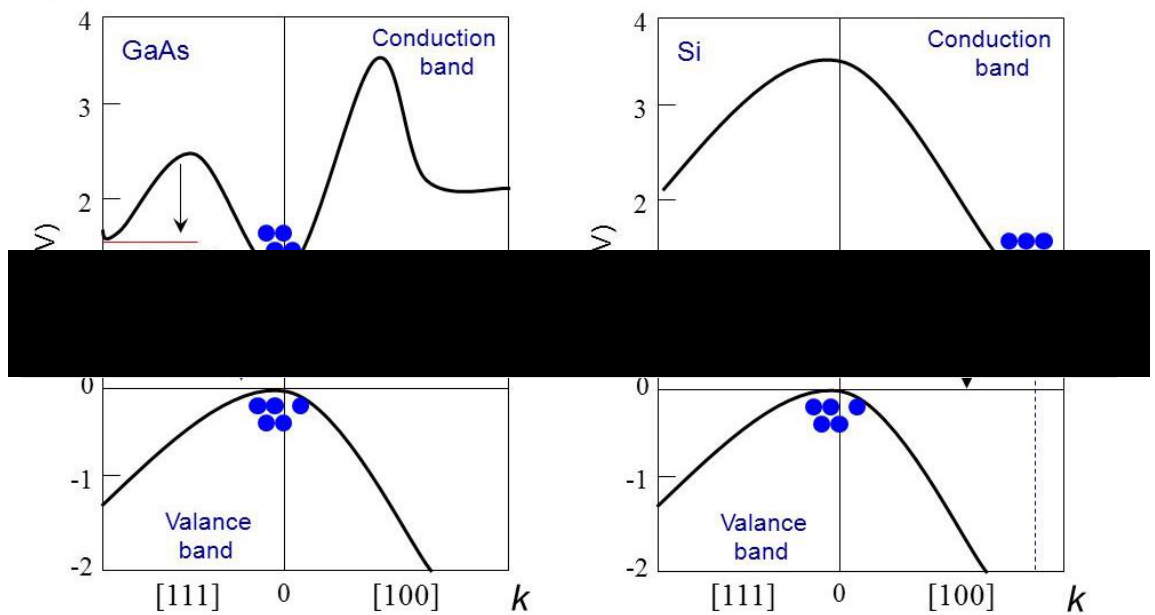


**Figure 1-5 - The energy band structures of gallium arsenide (left), which has a direct bandgap, and silicon (right), which has an indirect bandgap. It can be seen that for an electron to make a direct transition from the valence band to the conduction band without a corresponding change in momentum in silicon, it would need to be excited by approximately 3.5 eV. Diagram taken from [102], a similar example can be seen in [99].**

will transition to replace the bond, but will break their previous bonds when doing so [98, 99]. A hole effectively behaves as a positively charged particle and can participate in conduction [98, 99].

It is possible for silicon (and other semiconductors) to be doped with impurities to alter their electrical characteristics. If silicon is infused with atoms that have five electrons in their outer shells, for example, phosphorous, then one electron on each of these atoms will not be used for bonding and can participate in conduction [103]. The phosphorous atoms would be referred to as donors as they donate electrons to the conduction band [99]. Silicon doped in such a way is an n-type semiconductor due to the additional negative charge carriers [99]. Conversely, it is possible to dope silicon with impurity atoms that have only three electrons in their outer shells, for example, boron [100]. In this instance, an electron will be taken, or accepted, from a bond of a neighbouring silicon atom so that four covalent bonds form around the

boron atom. This creates a hole that is mobile in the valence band [99]. The boron atoms can be referred to as acceptors, and silicon doped in such a way would be p-type due to the additional positive charge carriers [99].

### 1.2.2 The p-Type Properties of CZTS

In the case of CZTS, p-type doping does not require the introduction of impurity atoms. In CZTS, the copper vacancy,  $V_{Cu}$  (the absence of an atom at a point in the lattice where a copper atom would be normally be sited), forms readily, as does the antisite defect,  $Cu_{Zn}$  (the substitution of a copper atom in a position normally occupied by zinc) [104]. Both of these defects can act as electron acceptors and have lower formation energies than the 11 other intrinsic point defects that are possible in CZTS [104]. The formation of these acceptors gives rise to the p-type nature of CZTS [104, 105]. However, the  $Cu_{Zn}$  antisite defect has a relatively large activation energy - it is a relatively deep acceptor level [105]. Both shallow acceptors and deep acceptors create energy states that lie between the valance and conduction bands, however, the deep acceptor energy states are further from the valence band than those of the shallow acceptors. This means that it is possible for a deep acceptor to act as a recombination point for electrons from the conduction band and holes from the valance band. This offers an explanation for the fact that copper poor stoichiometry tends to lead to better performing solar cells as it encourages the preferential formation of the  $V_{Cu}$  (which is shallow – estimated at 0.02 eV above the valence band maximum) rather than the  $Cu_{Zn}$  defect, which is estimated at 0.1 eV above the valence band maximum [104]. The deep acceptor defect that is considered likely to be the most active recombination point is the  $Cu_{Sn}$  antisite defect as it sits near the middle of the bandgap, estimated at 0.6 eV above the valence band maximum, however, it has a much higher energy of formation than the  $V_{Cu}$  and  $Cu_{Zn}$  defects and is therefore less common [104].

It is common for a CZTS solar cell to have cadmium sulphide (CdS) positioned as the next layer above CZTS, and zinc oxide (ZnO) above the cadmium sulphide (more details on CZTS device architecture are given in section 1.3). Cadmium sulphide and

zinc oxide are both naturally n-type semiconductors, and, in common with CZTS, do not require the addition of impurities. The n-type nature in ZnO arises due to oxygen vacancies ( $V_O$ ) and zinc interstitial ( $Zn_i$ ) defects [106]. Cadmium sulphide has a number of defects that include both acceptors and donors, however, the most dominant are sulphur vacancies ( $V_S$ ) and cadmium interstitials ( $Cd_i$ ), which act as donors [107]. Sulphur vacancies are particularly important as they are the majorly active point defect and act as double donors [108]. One of the reasons that CdS is deposited on to CZTS is because its n-type nature enables the formation of a p-n junction with the surface of the p-type CZTS, and the electrical properties arising from the p-n junction are crucial to the function of a CZTS solar cell.

### 1.2.3 The p-n Junction

In an n-type semiconductor, the concentration of free electrons is significantly greater than that in a p-type semiconductor, and the concentration of free holes in a p-type semiconductor would be significantly greater than that in an n-type semiconductor [100]. Also, in isolation and without the application of an external electric field, each semiconductor would be electrically neutral. If these two pieces of semiconducting material were to be brought together to form a p-n junction, the high concentration of free holes in the p-type semiconductor would result in some of them diffusing into the n-type semiconductor. Conversely, some electrons would diffuse from the n-type to the p-type side. This would cause a charge imbalance between the two sides, with the p-type layer being *negatively* charged and the n-type layer being *positively* charged. In addition to this, some of these diffused charge carriers will recombine with their ‘native’ opposite charges, leaving some ionised donors without the charge carriers of the opposite charge to counteract them [100]. This creates a region either side of the junction in which the charges of the ionised donors and acceptors are not compensated by the oppositely charged electrons or holes. The electric field that results from this will repel any further charges that diffuse into the region, with electrons being driven towards the n-type side and holes being driven towards the p-type side. This region is referred to as the depletion region, as, at equilibrium, there are no mobile charge carriers present [109]. The p-n junction acts

as a diode, which exhibits rectifying behaviour, i.e. an applied electric current can only flow in one direction, unless a potential difference is applied that is sufficient to overcome the potential barrier (this is referred to as the breakdown voltage) [109].

In a p-n junction solar cell, charge carriers are generated when electrons become excited through the absorption of light (in the case of a CZTS cell, this occurs in the p-type absorber material at the junction interface [110]). The electron is promoted to the conduction band and a hole is created in the valence band. The electric field at the junction (described in the paragraph above) acts to separate the charge carriers, creating a potential difference across the solar cell that can drive an electric current when connected to an external circuit [111, 112]. The electron passes through the n-type layer and enters the circuit via the negative terminal, whereas the hole passes through the p-type layer and recombines with an electron that is entering the cell at the positive terminal. In the case of CZTS, the positive terminal is typically the bottom contact of the device. For a solar cell to be effective, it is important to minimise the probability of the generated free charges becoming trapped and recombining with their opposites. This can occur, for example, at material grain boundaries and defect points [113, 114]. Another undesirable effect that can occur in a PV device is shunting. This is when there is a route for charges to effectively bypass the light absorbing layer, and this can occur if there are pinholes, cracks, or other gaps at grain boundaries [115], and one of the challenges of producing a good quality absorber layer is to avoid the formation of these shunting paths.

## **1.3 The Functions of the Different Layers in a CZTS Solar Cell**

### **1.3.1 The Substrate**

Although the quality of the CZTS absorber layer is important in a CZTS solar cell, it is not the only layer that requires consideration when manufacturing a device. A diagram of a typical CZTS device structure (which is similar to that of CIGS) can be seen in Figure 1-6. The substrate is most commonly soda-lime glass. This is not



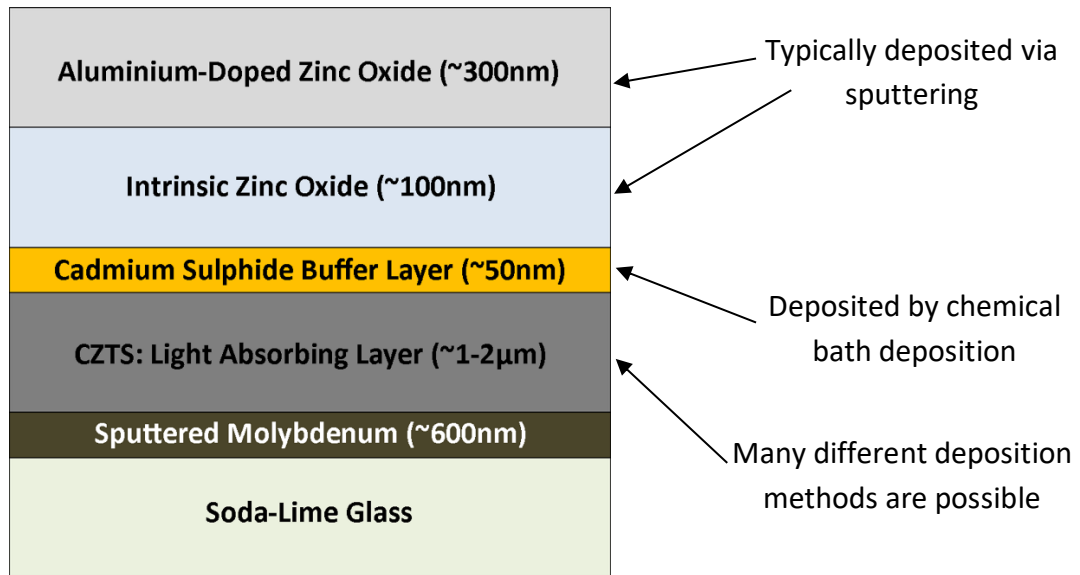


**Figure 1-6 - A diagram (not to scale) indicating a commonly used configuration of layers in CZTS solar cell devices.**

because the substrate needs to be transparent – it does not, as the light would enter from the top of a device with this architecture. Other substrates can be used [80, 94], however, the diffusion of sodium from the glass into the CZTS absorber has been found to enhance performance [116]. Sodium doping of CZTS causes the formation of  $\text{Na}_{\text{Zn}}$  shallow acceptor antisite defects, which increases the hole concentration in the material [117]. Furthermore, as this defect has a lower energy of formation than the  $\text{Sn}_{\text{Zn}}$  antisite defect, which is a deep acceptor defect and increases charge carrier recombination, it can form preferentially and increase charge carrier concentration by suppressing the formation of the  $\text{Sn}_{\text{Zn}}$  defect [117]. When a steel substrate is used, it is useful to introduce the sodium via other means, and also to deposit a layer of titanium to block iron diffusion into the CZTS [94] (iron and other trace elements have been found to be detrimental [118]).

### 1.3.2 The Bottom Contact

The most common material used for the bottom contact in a CZTS cell is molybdenum [119]. It can be sputtered on to the soda-lime glass substrate and is typically approximately 600nm thick. The usage of molybdenum for this purpose has largely been carried over from a typical CIGS cell architecture [119], however, a thin

layer of molybdenum sulphide/selenide forms upon the annealing of CZTS and works well as an ohmic contact between the two layers [120]. Theoretical studies on the work function of a number of potential candidates for the back contact have found that there are other metals, such as gold, that would be expected to create a lower potential barrier height for charges passing into the CZTS absorber layer and therefore improve cell performance [121]. It has also been found experimentally that gold can work effectively as a back contact for CZTS [122], although the publication reporting this did not draw a direct comparison with results obtained using molybdenum and did not suggest that gold was superior. The record efficiencies for CZTS devices have been achieved using molybdenum back contacts, and molybdenum has the advantage of having a high melting point of 2610 °C [123] (compared to 1062 °C for gold [124]), making it able to withstand a range of high-temperature annealing treatments.

### **1.3.3 The n-Type Buffer Layer**

Above the CZTS light absorbing layer lies the n-type buffer layer. As mentioned previously, this is typically cadmium sulphide, in common with the typical CIGS architecture, and the best CZTS cell efficiencies have been achieved by devices with CdS buffer layers [75, 92]. This CdS layer is commonly deposited via chemical bath deposition [125], although it is possible to deposit it via other methods, such as sputtering [126]. One of the purposes of the buffer layer is to facilitate the transition of charges between the light absorbing layer and the adjacent n-type window layer [127]. In order to achieve this, it is necessary for the conduction and valence bands to sit at energy levels that are between that of CZTS and that of the window layer (typically zinc oxide), thus reducing the height of potential barriers experienced by the charge carriers [127]. As can be seen in Figure 1-7, this is the case with CdS [128]. Ideally, a buffer layer should be transparent in the visible range, allowing light to pass through it to reach the absorber layer. With a band gap of ~2.4 eV [128], CdS absorbs some visible light in the blue and violet regions, and is known to be yellow in colour. This means that it is necessary to limit the thickness of the CdS layer, with a thickness of ~50nm being typical [128]. Other than favourable band alignment,

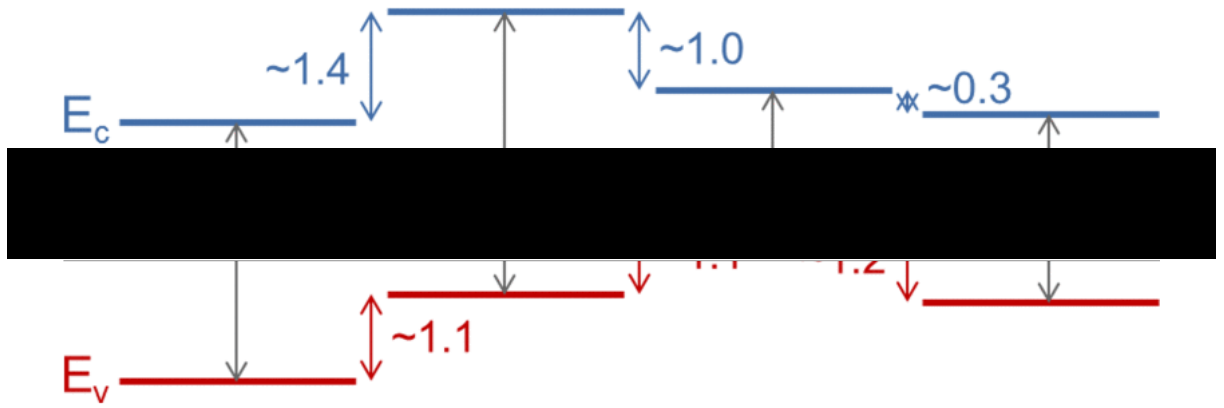


**Figure 1-7 - A diagram indicating the approximate relative band alignments of CZTS, cadmium sulphide (the most commonly used buffer layer), zinc oxide (a commonly used window layer), and zinc sulphide (trialled by some as an alternative buffer layer, but with limited results [128]). Diagram taken from [128].**

another potential reason for the favourable efficiencies obtained with CdS could be due to its ability to passivate point defects at the interface between the absorber and buffer layers [129]. Cadmium atoms from the CdS are able to occupy copper vacancies on the surface of the absorber layer, which has the effect of reducing charge carrier trapping and recombination [129].

### 1.3.4 The n-Type Window Layer

Above the buffer layer sits the window layer. As mentioned in the previous paragraph, this is most commonly zinc oxide in a CZTS solar cell, which is most frequently deposited via sputtering [130]. Solution processing deposition methods exist, but they are less common [131]. Together, the CdS and ZnO form the n-type layer of the CZTS solar cell. The ZnO assists in the separation of the charge carriers as its valence band energy sits lower than that of both CZTS and CdS (as can be seen in Figure 1-7) [128], resisting the flow of holes towards the negative terminal of the device. The ZnO layer is typically ~100 nm thick – much thinner than that of the CZTS absorber (which is ~1-2  $\mu\text{m}$  thick). This is to reduce the chance of charge carrier recombination as electrons transition towards the negative terminal. With a band gap of ~3.3 eV [128], ZnO has the advantage of having a wider bandgap than CdS, making it colourless and transparent to visible light [132]. This allows more of

the incident light to reach the p-n junction interface between CZTS and CdS. It is possible to manufacture a CZTS solar cell where ZnO is deposited directly on to the CZTS absorber and CdS is omitted, however, cells that have been made in this way have fallen significantly short of the efficiencies achieved when a CdS buffer layer has been included [91, 133].

### **1.3.5 The Transparent Conducting Oxide**

On top of the ZnO window layer, a transparent conducting oxide (TCO) is deposited. This is typically deposited via sputtering [134, 135, 131] and is approximately 300 nm thick [134, 136, 135] (see Figure 1-6). Other, non-vacuum techniques have been trialled, including electrodeposition [137, 138] and solution processing [139, 140] techniques, although these are not common methods for depositing TCOs on CZTS cells. The TCO used can vary, although indium tin oxide (ITO) and aluminium-doped zinc oxide (AZO) are popular choices [136]. ITO has the disadvantage of containing indium, which, as explained previously, is a relatively scarce and costly material. The purpose of the TCO layer is to aid the transition of electrons to the metal top contact [141] (which is not shown in the diagram in Figure 1-6): The metal top contact is a fine metal grid, usually aluminium or nickel-aluminium deposited via thermal or electron beam evaporation [142, 143, 144, 145], and can only contact a relatively small surface area due to its opacity and the associated shadowing of the layers beneath it. As undoped zinc oxide is a relatively resistive material [141], depositing the metal grid directly onto the window layer would limit the amount of charge that could transition to the top contact. Including a TCO as an intermediary helps to alleviate that problem as it can collect charges across the entire top surface area of the ZnO layer, which can be conducted into the metal grid with relative ease.

In some instances, an anti-reflection layer is also deposited, which increases the amount of light that reaches the absorber layer and therefore increases the device efficiency. The layer is ~100 nm thick [146, 147] and magnesium fluoride ( $\text{MgF}_2$ ), aluminium oxide ( $\text{Al}_2\text{O}_3$ ) and cerium fluoride ( $\text{CeF}_3$ ), for example, can be used

[148]. One method of deposition is via electron beam evaporation [146, 147], although non-vacuum methods have also been reported in studies on the potential to use ZnS or ZnO nanorods for anti-reflection coatings [149, 150].

Having considered the functions of different layers in a CZTS solar cell, it is important to also look in detail at the material properties of CZTS itself, including how it is deposited. The factors that affect the quality of the CZTS light absorbing layer and challenges faced in achieving high quality production also need to be considered.

## **1.4 Material Properties and Deposition of CZTS**

It has already been established that CZTS possesses favourable properties with regard to having a suitable direct band gap of up to  $\sim 1.5$  eV [84] and an optical absorption coefficient of  $\sim 10^4$  cm<sup>-1</sup> for visible light [83] (see section 1.1.3). This section will focus more on the physical properties of the material and how these translate to the performance of the absorber layer and solar cell.

### **1.4.1 Stoichiometry and Phase Formation**

One of the main challenges in manufacturing CZTS is accurately controlling the stoichiometry during the manufacturing process. A ternary phase diagram including the three metallic elements in CZTS can be seen in Figure 1-8 [151]. This diagram assumes that the sulphur content is not an independent variable (that it is directly linked to the quantities of the metallic elements present), and projects the compounds formed as the ratios of the three metallic elements are changed. The ratios are read off the axes along the gridlines at 120° around any vertex inside the triangle, with the total of the ratios summing to 1. The point at which stoichiometric CZTS (a quaternary compound) should theoretically form is marked with an asterisk, and it can be seen that deviation from these ratios will result in the formation of other compounds, which can include both individual compounds and mixtures. Some of these are quaternaries, but there are also binaries and ternaries. When these unwanted phases are formed alongside CZTS, they can be referred to as secondary phases. A

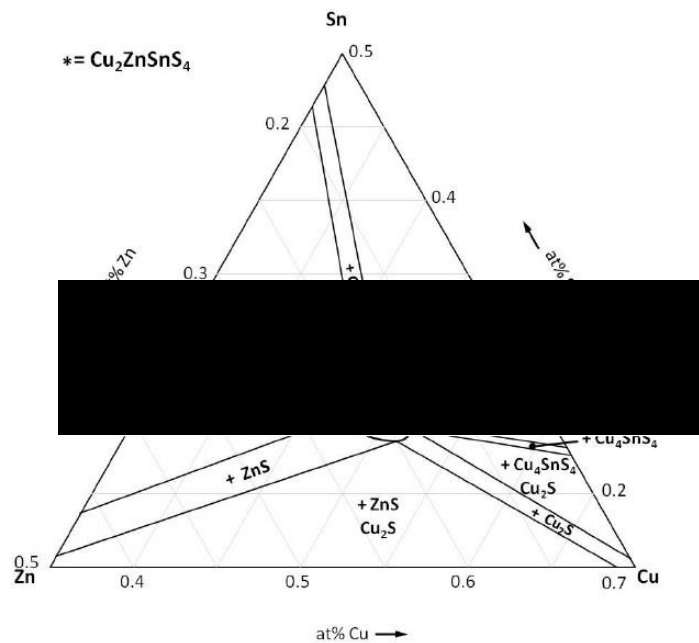
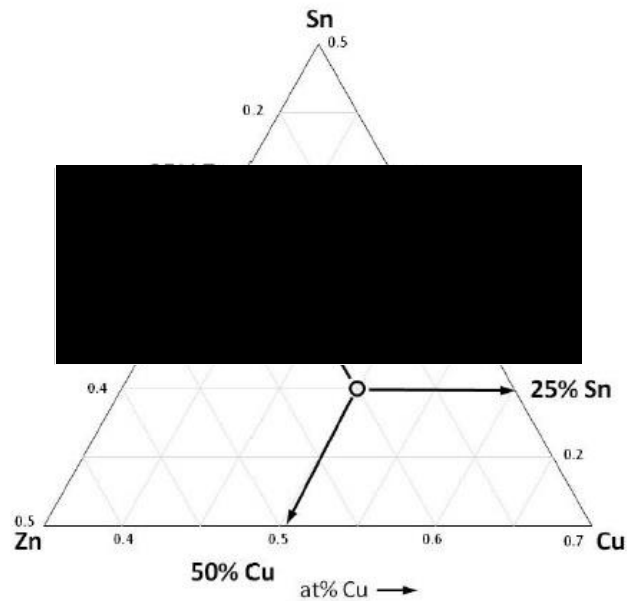


**Figure 1-8 – Phase diagrams to help predict the phases that will form when different proportions of copper, zinc and tin are used in the CZTS manufacturing process. The diagram labelled with phases assumes a temperature of 400 °C. The diagrams have been taken from reference [151].**

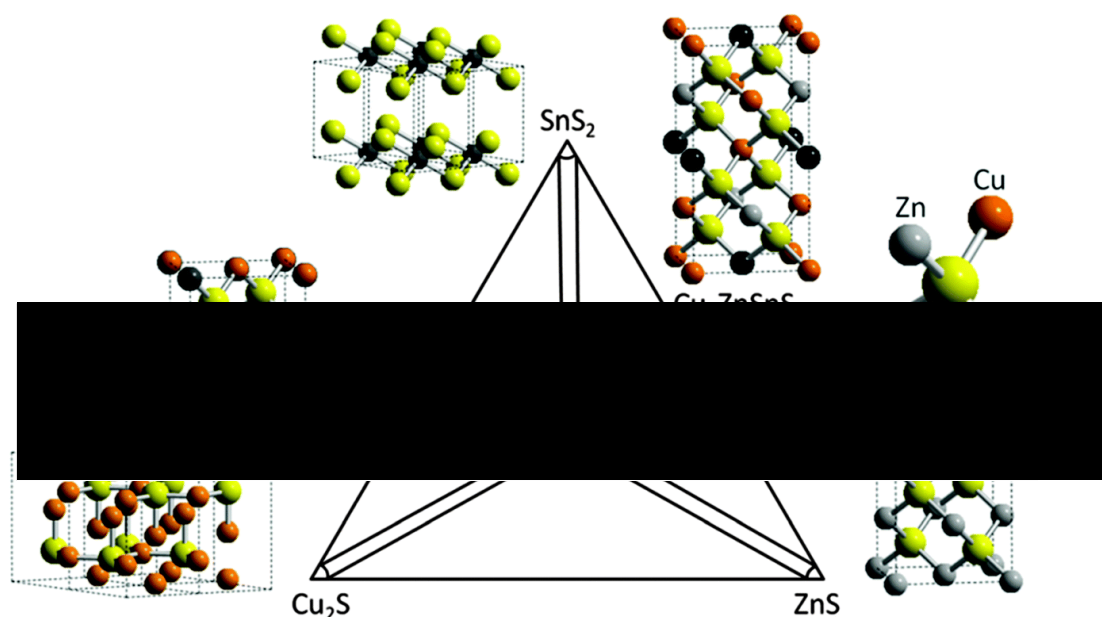


**Figure 1-9 – A simplified phase diagram indicating the crystal structures of kesterite CZTS and the common secondary phases that can form. Image taken from [152].**

simplified phase diagram showing the crystal structures of kesterite CZTS and the common secondary phases that can form is presented in Figure 1-9 (taken from [152]). Secondary phase formation is detrimental to the performance of a CZTS solar cell as charges can become trapped at the boundaries between different phases [153]. In reality, a slightly off-stoichiometric CZTS composition has been found to lead to increased efficiency, particularly copper-poor zinc-rich stoichiometry [152], and for the defects to form that give CZTS its p-type nature (see section 1.2.2), a copper-poor stoichiometry is considered preferential [154]. This does add an additional degree of complexity, as not only are there challenges in avoiding the formation of secondary phases, but there is an additional challenge in producing CZTS with a stoichiometry that gives optimal electronic properties. One of the factors that can affect the stoichiometry of the finished film is the material losses during the manufacturing processes, particularly heating processes [155]. By way of example, it is known that tin is lost in a greater proportion than that of the other elements during sulphurisation, due to the volatility of tin sulphide [155]. Therefore, the deposition

techniques chosen, and the parameters used can strongly affect the results obtained, and even very small changes can have great effects.

#### **1.4.2 Deposition Techniques**

There are many methods by which CZTS can be manufactured. The most suitable deposition technique can differ depending on the resources available, the intended application of the CZTS device and the aims and objectives of those carrying out the manufacturing. For example, those who have access to existing PV printing equipment may take a different route to synthesis and deposition to those who have access to a sputtering lab, or those who are starting without specific equipment assets. Similarly, if the main objective is to demonstrate the highest possible efficiency, a different route may be chosen than if the main objective is to deposit on the largest surface area at the lowest cost. In this section, examples of different deposition techniques will be given, and their advantages and disadvantages will be discussed in relation to particular applications of CZTS, including key results that can be found in literature.

There are multiple ways in which different deposition techniques can be categorised. One way of categorising techniques is to separate them as being either vacuum-based or non-vacuum based. A non-vacuum technique is often considered preferential to a vacuum-based technique – pre-existing printing and coating equipment can be repurposed at relatively low cost and without the expense of vacuum pumps and systems. Non-vacuum techniques can also be simpler to deploy at large scale. However, this does not necessarily mean that vacuum-based techniques cannot be a cost effective method of depositing CZTS on a large scale, particularly if the end product has a high power conversion efficiency. Another method of broadly separating deposition techniques is to consider those which involve the synthesis of CZTS as a separate process prior to deposition, and those in which only precursors are deposited onto the substrate and undergo subsequent treatments to convert them to CZTS. Manufacturing CZTS separately prior to deposition can simplify the deposition process, and allows for a range of deposition techniques to be used. Such



techniques can include spray coating [156], screen printing [157], doctor blade coating [158], slot-die coating [159], roller coating [160] (if flexible substrates are used), and, for lab-scale PV devices, spin-coating [161]. The pre-prepared CZTS that is deposited can come in the form of a nanocrystal ink or paste. Techniques such as spray coating and spin coating would require a low viscosity ink, whereas other techniques, such as doctor blading and screen printing require higher viscosity pastes. This can add to the complexity of the manufacturing process as the nanocrystal suspension and the solvents used must be engineered to suit the deposition process, and drying stages added to remove the solvents and plasticisers. It is common for a carbon rich layer to form at the bottom of the CZTS layer close to the back contact when these types of inks and techniques are used [162], which can be detrimental to cell performance [163].

#### *1.4.2.1 The Manufacture of Nanocrystal Inks*

Nanocrystal inks can be manufactured using multiple different methods. One such method is the “hot injection” method that uses a Schlenk line. This involves the dissolution of organic compounds, such as acetylacetonates, of copper zinc and tin, in an organic solvent, such as oleylamine at a temperature of ~200 – 250 °C in a round-bottomed flask under inert gas. A sulphur solution is then injected into the mixture for the reaction to take place [164]. Once cooled, the CZTS nanocrystals are extracted using a centrifuge, and washed and re-suspended in an organic solvent [164]. Alternative methods of manufacturing CZTS inks include using a spray pyrolysis method, where the dissolved metallic compounds are sprayed through a tube furnace [156], a microwave solution heating method [158, 165], and the solid state reaction of copper, zinc, tin and sulphur powders in a furnace followed by ball milling and re-suspension in a solvent [166]. CZTS deposited from inks and pastes still requires sulphurisation or selenisation in order to facilitate grain growth, and selenised films have achieved efficiencies of up to 9.0% [167].

#### *1.4.2.2 Other Solution Processing Methods*

As mentioned previously, another approach to solution processing is to deposit precursors that contain the constituents of CZTS, but require subsequent treatments for CZTS to form. The method that has achieved the highest efficiency (12.6% [88]) involves dissolving metallic elements and/or their sulphides in hydrazine, and the subsequent spin coating of the solution onto a substrate, followed by a heat treatment at up to 500 °C. Due to the instability of hydrazine (which, as mentioned previously, is toxic and explosive), this must all be carried out in a nitrogen glovebox [168]. An alternative route is to use less toxic solvents, such as dimethyl sulphoxide (DMSO), in which metal chlorides and thiourea are dissolved and spin coated onto substrates, and subsequently heated at ~540 °C. Once selenised, this method can achieve efficiencies of approximately 10% if doped with lithium, and nearly 8% if not, however, this still involves preparation in a nitrogen glove box [90]. One technique that can be used without the requirement of an inert atmosphere is spray pyrolysis. One of the ways this differs from spray coating is that the substrate is heated during the deposition process. Metallic compounds, such as chlorides of copper zinc and tin, along with a sulphur source, such as thiourea, are dissolved and sprayed onto substrates that are heated to ~300 – 400 °C [169, 170]. A range of different solvents can be used, including ethanol and water [169, 170]. Spray pyrolysis has the advantage of being a scalable, non-vacuum technique, however, cell efficiencies lag behind those of other techniques at around 6% [169, 170]. In common with other techniques, a sulphurisation/selenisation step in a furnace is still required.

#### *1.4.2.3 Sputtering*

A common vacuum-based technique for the deposition of CZTS precursors is sputtering. Metallic elements, or their sulphides, can be sputtered, along with sulphur, either through co-sputtering or sequential sputtering. Precursor films can be subsequently converted into CZTS through annealing and sulphurisation processes. The record efficiency for a cadmium-free CZTS solar cell is 9.7% and it was manufactured via sputtering [92]. Solar cells with cadmium-based buffer layers have also been manufactured with respectable efficiencies via sputtering: Pure sulphide

CZTS cells have achieved 8.8% when manufactured via both sequential and co-sputtering techniques [171], pure selenide films have achieved 9.7% [172], and the selenisation of sulphur containing precursors to form  $\text{Cu}_2\text{ZnSn}(\text{S},\text{Se})_4$  has led to an efficiency of 10% [173]. Although sputtering is a vacuum-based technique, it has been used for industrial scale film deposition in the semiconductor electronics industry for over 30 years [174]. It does, however, have the disadvantage of very high up-front costs when compared to other deposition techniques as the equipment is very expensive.

#### *1.4.2.4 The Potential of Electrodeposition*

An example of a deposition technique with much lower overhead costs is electrodeposition. Electrodeposition involves the deposition of metallic precursors from electrolytic solutions containing salts of the elements to be deposited. Metal ions in the solution are reduced to become metal atoms as current is passed through, and these atoms deposit as a film on the conductive substrate which acts as an electrode in the circuit. This process is described in detail in section 2.1 of this thesis. Electrodeposition has the advantage that, other than the sulphurisation and annealing process, which all CZTS deposition techniques benefit from, all steps can be carried out in ambient conditions without the need for a vacuum or inert atmosphere. It also does not require any toxic or volatile solvents as the electrolytes are typically aqueous. Pure sulphide CZTS cells of up to 8.7% efficiency have been achieved using this technique [175], and it has been evidenced that it can be used to deposit CZTS onto flexible substrates [145]. Electrodeposition (or electroplating) is already established as a large scale commercial process and is used extensively in the steel industry [176]. Electrodeposition therefore offers strong potential for deployment in the manufacture of efficient, cost effective CZTS solar cells on large-scale, flexible substrates such as sheet steel.

## 1.5 Electrodeposition

There are two main approaches to the electrodeposition of precursor films for CZTS. These are sequential deposition and co-deposition. Sequential deposition requires three separate electrolytes to deposit copper, tin and zinc, whereas with co-deposition, all three metallic elements are deposited simultaneously from one electrolyte (alloy co-deposition), and sulphur may be included as well (quaternary/chalcogenide co-deposition) [177]. Co-deposition techniques have the advantage that the deposition process is carried out in a single step with a single electrolyte. If used industrially, this would reduce the complexity of the production line, save space, and reduce waste. Co-deposition was used to make the record electrodeposited CZTS device [175], and although it may seem an attractive method, it does have its drawbacks. Finding deposition parameters, including an electrolyte composition, that enable the deposition of all elements in the required proportions at the desired rate is an extremely challenging process – each element has its own optimum set of deposition parameters, and adjusting the electrolyte and/or deposition settings to improve deposition of one element would likely cause detriment to that of another [178]. The more complicated electrolyte compositions required would also increase the probability of unwanted chemical reactions occurring and also decrease the stability and lifetime of the electrolyte [178]. On the other hand, these problems can be avoided if a sequential deposition approach is used. With sequential deposition, attention must be paid to the order in which the elements are deposited, as well as the pH and other properties of the electrolyte [178], and this is discussed in further detail in chapters 2, 3 and 4. This is not an insurmountable problem, and sequential deposition has led to respectable efficiencies, including an 8% pure sulphide film [179], which is on par with the efficiency of co-deposited pure selenide CZTSe [180]. Another factor that requires consideration when electrodepositing for CZTS is whether to deposit galvanostatically (constant current) or potentiostatically (constant electric potential). Galvanostatic deposition is the method used in industrial electroplating processes as it leads to a more consistent rate of deposition, however, potentiostatic deposition has its advantages as it provides greater control of the

morphology and purity of the films deposited, as well more control over whether unwanted reactions are occurring (these factors are discussed further in chapters 2, 3 and 4). Despite this, it has been demonstrated that galvanostatic sequential deposition can be used to manufacture efficient CZTSe cells on relatively large area ( $15\text{ cm} \times 15\text{ cm}$ ) substrates, with 8.2% having been achieved [181]. This is further evidence of the potential for electrodeposition to be used for large scale manufacture of CZTS solar cells.

### **1.5.1 Electrolytes for the Electrodeposition of Copper**

Copper is most commonly the first of the three elements to be deposited when carrying out sequential deposition for CZTS [177], the reasons for this being related to the standard reduction potentials of the metals and their positions in the electrochemical series (see section 2.1.4 for more information). It is common for an acidic solution containing copper sulphate to be used, and it is known that the addition of sulphuric acid leads to a better quality electrodeposit [177]. However, the addition of sulphuric acid can also lead to the problem of surface oxidation and passivation of the molybdenum substrate, causing poor adhesion of the deposited copper [177, 182]. One potential solution to this problem is to deposit an intermediary palladium layer [183], however, this adds to the time, complexity and cost of the film manufacturing process. An alternative approach is to use sodium citrate and tartaric acid in the electrolytes [182]. These form chelate complexes with the molybdenum and prevent further oxidation [177, 182]. It is also possible to use citric acid rather than sulphuric acid in the electrolyte [179]. Another method to prevent the issue from occurring is to use an alkaline electrolyte, typically containing sodium hydroxide, which is perhaps the simplest solution and has been demonstrated to return good quality electrodeposits that adhere well to their substrates [177, 184, 185]. The concentration of copper salt varies a great deal between publications, and relatively high solar cell efficiencies have been achieved while depositing from both relatively low concentrations of 0.05 M  $\text{CuSO}_4$  (8% cell efficiency) [179] and relatively high concentrations of 0.46 M  $\text{CuSO}_4$  (7.3% efficiency) [146].

### 1.5.2 Electrolytes for the Electrodeposition of Tin

Tin is most commonly the second metallic layer to be deposited, in common with the reasons stated previously (see section 2.1.4 for more information). The two most commonly reported electrolytes for the electrodeposition of tin for CZTS are alkaline (sodium hydroxide) based electrolytes containing tin(II) chloride as the tin salt [182, 186, 187], and methanesulfonic acid based electrolytes containing tin(II) methanesulfonate as the tin salt [181, 184, 185]. The hydroxide based electrolytes are more commonly reported in earlier publications and tend to be associated with lower solar cell efficiencies (<1%) [187] or no completed solar cell device [182, 186]. This is most likely linked to issues occurring with lack of coverage of the copper film beneath, with tin depositing in islands rather than a continuous film. This can be seen in Figure 1-10 taken from [188]. This leads to the formation of regions that are tin rich and regions that are tin poor in the sulphurised film, increasing the presence of unwanted secondary phases. In contrast, the methanesulfonic acid based electrolytes lead to the deposition of continuous films with close-packed tin grains, as can be seen in image (a) in Figure 1-11, which has been taken from [189]. Similar results were also obtained by Vauche et. al. using a sulphuric acid based electrolyte with tin sulphate as the zinc salt and some unspecified organic additives [181] (image (b) in Figure 1-11). Tin salt concentrations tend to be in the 0.05 – 0.1 M range [177].

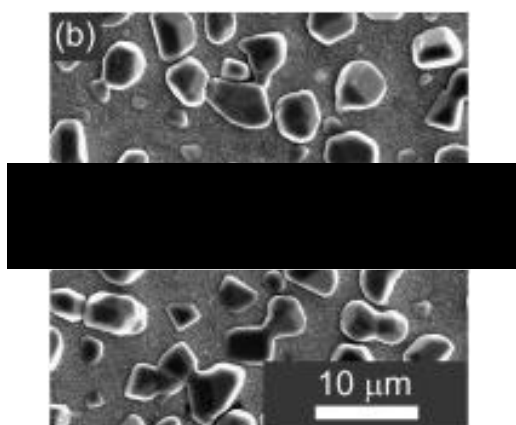


**Figure 1-10 – An SEM image of tin deposited onto copper from a sodium hydroxide based electrolyte (taken from [188]), in which it can be seen that tin islands have formed rather than a continuous film.**

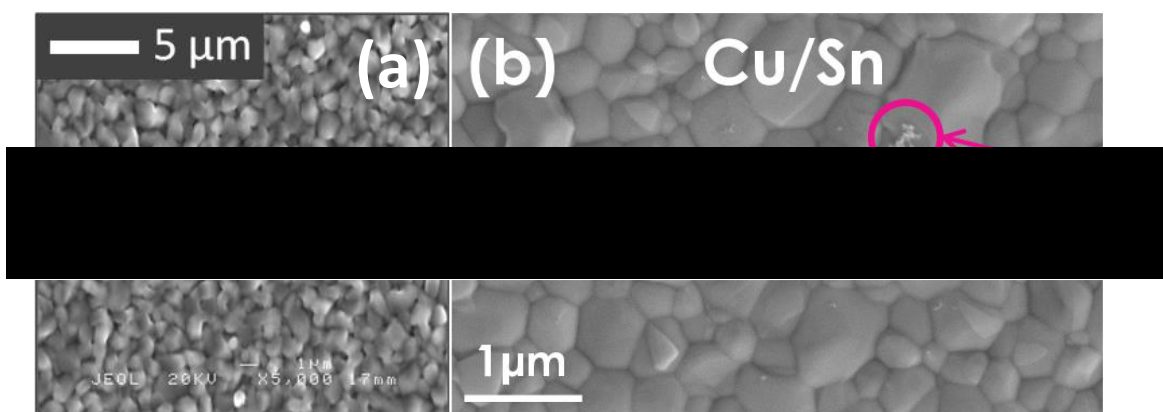


**Figure 1-11 – SEM images of (a) tin deposited onto copper from a methanesulfonic acid based electrolyte (taken from [189]), and (b) tin deposited onto copper from a sulphuric acid based electrolyte (taken from [181]). Both images display a continuous granular tin film, in contrast to that seen in Figure 1-10. Please note that the highlighted blemish in (b) can be ignored for the purposes of this review.**

An alternative approach to aqueous electrolytes is to use ionic liquid electrolytes. The deposition of tin from a choline chloride based ionic, using 0.1 M tin(II) chloride as a tin salt, is reported by Bhattacharya in [190]. Although no specific commentary is given on the quality of the tin layer, a solar cell of 3.6% efficiency is manufactured. Bhattacharya and Kim also report a CZTS cell manufactured through the electrodeposition of all three metallic layers from choline chloride based electrolytes, however, this cell only achieved an efficiency of 1.7% [191].

### 1.5.3 Electrolytes for the Electrodeposition of Zinc

Zinc is most commonly the third and final metallic element to be electrodeposited, in common with the reasons stated previously (see section 2.1.4 for more information). There are two zinc salts commonly used in the deposition of zinc for CZTS and these are zinc sulphate and zinc chloride [177]. It is common for an acidic solution to be used, and a pH 3 Hydrion™ buffer has been used successfully by multiple research groups [179, 184, 185, 187]. During zinc deposition, the pH of the solution can change as  $H^+$  ions are consumed by hydrogen evolution, and the purpose of the pH buffer is to mitigate this [177]. Some of the other electrolytes reported are based on methanesulfonic acid [146], and sodium citrate with tartaric acid [182]. Alkaline

electrolytes can also be used – it is reported in that a sodium hydroxide electrolyte with zinc hydroxide as the zinc salt (and some unspecified organic additives) gave a zinc deposit with high levels of uniformity. The sequentially electrodeposited CZTS solar cells with the highest efficiencies had zinc deposited from a variety of electrolytes, making it difficult to discern if any particular formula is likely to return superior results. These electrolytes were: 0.1 M zinc sulphate with 0.5 M potassium sulphate and Hydrion™ pH 3 buffer (8% PV device efficiency) [179]; 0.2 M zinc sulphate with 0.5 M methanesulfonic acid, the solution being adjusted to pH 2 (7.3% PV device efficiency) [146]; and zinc hydroxide with sodium hydroxide and organic additives, all of unspecified concentrations [181].

#### *1.5.3.1 The Relevance of Throwing Power*

Zinc is commonly electroplated as a corrosion inhibitor onto other metals, particularly steel, and a wide variety of electrolyte formulations exist in addition to those included in the paragraph above. When depositing zinc onto tin, the negativity of the potential required can lead to competition with hydrogen evolution [177]. This can cause issues with the quality of the zinc deposits, exacerbated by the fact that zinc does not alloy with tin [192], leading to incomplete coverage and poor film adhesion. It is worth, therefore, to give consideration to the throwing power of the electrolyte. Throwing power is the ability to deposit at the same rate in low current density areas as high current density areas [193], and a high throwing power can help achieve superior coverage at sites where the zinc plating current is competing with current associated with hydrogen reduction. The throwing power of an electrolyte relates to its polarisation characteristics [194], which relate to how ions in the solution respond to an applied potential. This can be affected by factors such as the conductivity of the electrolyte [195, 196], or the viscosity of the solution [197]. The choice and concentration of zinc salt, solution pH, temperature, and any additional salts and additives can all have an influence on the throwing power [193, 196, 198]. Organic compounds containing nitrogen or sulphur, such as amines, sulfonates, etc., can improve throwing power, due to the interaction of these polarisable charged groups [196]. Some surfactants, e.g. sodium dodecylbenzenesulfonate, can improve



throwing power by selectively adsorbing onto active zinc ion reduction sites, inhibiting further zinc reduction at the site and encouraging the formation of nuclei elsewhere on the substrate [196]. Discussion around expectations of the throwing power of various electrolyte formulae can be found in section 2.1.9, section 4.3.3 and section 4.3.6.

#### **1.5.4 Electrodeposition Parameters**

There are a number of parameters, in addition to the electrolyte formulation, that can be adjusted for electrodeposition. These include (but are not limited to) the electrolyte temperature, whether or not the solution is agitated, and whether potentiostatic (constant potential) or galvanostatic (constant current) deposition is used. Electrodeposition from ionic liquids for CZTS has been reported at a temperature of 53 °C [190, 191], and it is not unusual to heat a zinc electrolyte for industrial deposition purposes [193], however, successful deposition of copper, tin and zinc from aqueous electrolytes for CZTS has been predominantly carried out at room temperature [181, 182]; [184] - [188]. As mentioned previously, galvanostatic deposition is generally favoured for industrial processes [199], meaning that it may be considered advantageous to deposit galvanostatically when considering the future commercialisation of CZTS. Although potentiostatic deposition offers superior control when attempting to avoid parasitic processes, and high efficiency electrodeposited cells have been achieved through potentiostatic electrodeposition [179], it has also been shown that it is possible to achieve similar efficiencies using galvanostatic deposition [146, 181, 200]. Fluid agitation can assist in controlling the rate of deposition, as without it, the rate of chemical reduction, and therefore the deposition rate, becomes diffusion limited [178]. Some publications report the use of fluid agitation during the deposition process, for example, through the use of a rotating disc electrode [184, 185], or a paddle cell [146, 200]. Although these publications report respectable solar cell efficiencies (5.5 – 7.3%), higher efficiencies (8 – 8.2%) are reported in [179] and [181], which do not report the use of fluid agitation. This suggests that, although fluid agitation can help with the speed of the deposition, it does not necessarily improve the quality of the electrodeposit.

In summary, electrodeposition can be used to manufacture stacked elemental layer precursors for further processing into CZTS cells of respectable efficiencies of up to ~8% both galvanostatically and potentiostatically. Copper deposits of good quality can be achieved by depositing from alkaline electrolytes, or acid electrolytes with chelate forming complexing agents. The morphology of tin deposits improve when a methanesulfonic acid based electrolyte is used rather than an alkaline one, and zinc can be deposited successfully from a variety of electrolyte compositions, although it is of benefit to pay consideration to the throwing power of the electrolyte formulation.

It is clear that it is necessary to ensure that the stacked elemental precursors are of sufficient quality in order to achieve respectable solar cell efficiencies. However, it is also important to consider the sulphurisation and annealing processes, and their advantages and disadvantages, as numerous different methods are available. These factors will be discussed in the next section.

## **1.6 Sulphurisation and Annealing**

Although it is possible for CZTS to be manufactured in a single-step process through co-evaporation of all four elements onto a heated substrate, it is more common that a precursor is deposited, followed by a reactive anneal in a sulphur-rich environment [201]. The reactive anneal would typically be in the temperature range of ~ 450 – 600 °C [202]. It has been shown that, although some techniques can be used to manufacture CZTS without a subsequent annealing process, such as the growth of CZTS monograins, the resulting solar cell efficiencies are relatively low and their performance is significantly enhanced by the inclusion of a reactive anneal [201]. When precursors are deposited via electrodeposition, it is essential that they undergo a reactive annealing (sulphurisation) process in order for CZTS to form. Different types of furnaces can be used to perform this reactive anneal, such as rapid thermal processing/annealing (RTP/RTA) furnaces [203], tube furnaces [145], or standard convection furnaces (in which the annealed sample would be placed inside a quartz

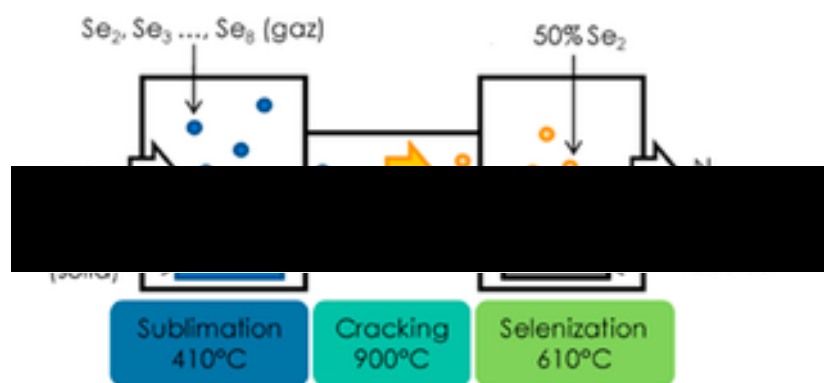


**Figure 1-12 – An example of a three-zoned furnace under gas flow, in which the selenium is vaporised at the lowest temperature on the left, the vapours are “cracked” into smaller molecules at the highest temperature in the centre and flow to react with the metallic precursor at 610 °C on the right. Image taken from [203].**

ampoule [200]). In addition to the type of furnace, there are other variables that can be adjusted, such as the type of inert gas used (typically nitrogen [204] or argon [205]), the background pressure (if using a closed system) [206], the gas flow rate (if using a gas flow system) [207], whether a source of tin is included to reduce tin evaporation [201], the source and quantity [206] of sulphur/selenium (which can be elemental sulphur/selenium [206] or hydrogen sulphide gas [204, 205]), and the temperature-time profile [208]. It is also possible to use a zoned furnace, in which the sulphur/selenium source is held at a lower temperature to the precursor sample [209]. This avoids all of the sulphur/selenium being evaporated and lost in the early stages of the annealing process and provides a continuous supply of vapours. It is also possible to have third temperature zone that the sulphur/selenium vapours pass through to reach the precursor sample [203]. This can be set to a higher temperature than the precursor sample in order to act as a “cracking” zone, in which the vapour particles break up into individual molecules. An example of such a setup can be seen in Figure 1-12, which has been taken from [203]. In addition to the reactive anneal, many publications also report a pre-anneal, sometimes referred to as a soft anneal or a pre-alloying step, in which the precursor is annealed without the presence of sulphur or selenium in order to encourage the intermixing of the metallic elements [146, 179, 210, 211]. This is particularly the case when the precursors are

sequentially deposited stacked elemental layers rather than co-deposited elements. As there are such a large number of possible variables relating to the annealing processes, the following discussion will initially focus on published results relating to stacked elemental layer precursors.

### **1.6.1 Pre-Alloying and Sulphurisation of Sequentially Electrodeposited Stacks**

In the publication by Ahmed et. al. [146] relating to the annealing of electrodeposited stacked elemental layer precursors, an investigation is reported in which precursors were annealed (sulphurised) in a quartz ampoule under  $N_2$  with 2-5 mg of sulphur for 5-15 minutes at 540-590 °C. The precursors had also undergone a pre-alloying treatment at 210-350 °C. The investigation finds that sulphurisation annealing at temperatures in excess of 580 °C led to the elimination of secondary phases being detected by Raman spectroscopy, and suggests that this is due to  $Cu_2SnS_3$  and ZnS reacting with each other to form CZTS at these higher temperatures. An optimum sulphurisation anneal at 585 °C for 12 minutes is presented as having achieved a solar cell efficiency of 7.3%, which was one of the highest for an electrodeposited CZTS cell at the time. What was not clear from the publication, however, was the optimum conditions for the pre-alloying process, although 350 °C is offered in the publication as an example in an SEM image.

Since the publication of the aforementioned article by Ahmed et. al. [146], attempts have been made by others to optimise the pre-alloying process. Lin et. al. [212] processed electroplated stack precursors by sulphurising them in a quartz ampoule at 580 °C with 5 mg sulphur for 10 minutes, the precursor samples having undergone either a 40 minute, a 20 minute, or no pre-alloy at 350 °C. It was found that the inclusion of a 20 minute pre-alloy reduced issues with film delamination and void formation, as well as eliminating the formation of  $Cu_2SnS_3$ , resulting in a cell efficiency increase from 0.43% to 5.6%. However, when the pre-alloy was extended to 40 minutes, it was found that void formation reoccurred and the cell efficiency fell to 2.6%, although the voids were smaller than those on the sample that received no pre-alloy, and no  $Cu_2SnS_3$  was detected.

In contrast, Jiang et. al. reported that extending the pre-alloy time led to improved results [179, 211]. In [211], a 10 minute sulphurisation at 590 °C with 5-10 mg sulphur in a quartz ampoule is used, with pre-alloy times ranging from 20 to 200 minutes, all carried out at 310 °C. The control sample, which received no pre-alloy, returned the lowest cell efficiency of 2.0%, while this increased to 3.7% after 20 minutes of pre-alloying. The best results were obtained after 200 minutes of pre-alloying, which achieved 8.1% efficiency. It is suggested that 200 minutes is required to fully alloy the tin with the copper. It is reported that the grain size of the sulphurised CZTS relates to the duration of the preceding pre-alloy, with larger grain sizes resulting from longer pre-alloying times. The improvement in performance is attributed to the larger grains leading to a reduction in charge carrier recombination at CZTS-CdS interface due to reduced surface area.

Although Lin et. al. [212] and Jiang et. al. [179, 211] present contrasting results with regard to the duration of the pre-alloying period, they are in agreement with each other and with Ahmed et. al. [146] in that the inclusion of a pre-alloying step is beneficial to the overall results. These results are amongst the best reported for sequentially electrodeposited CZTS cells, however, the annealing method of using a quartz ampoule is not easily scalable, and would not be suitable for commercial production. As mentioned previously, Vauche et. al. report an 8.2% efficient cell in [181]. This was annealed and selenised using a tube furnace, with the sample being placed inside a graphite box. Although this is a step towards scalability in that a quartz ampoule is no longer used, the annealing times required are relatively long at 45 minutes (30 minutes at 400 °C followed by 15 minutes at 550 °C), and the ramp rates relatively low at 20 °C min<sup>-1</sup>, meaning that the annealing process would last over an hour.

### **1.6.2 Rapid Thermal Processing**

An alternative to a tube furnace is an RTP furnace. An RTP uses infrared heat lamps rather than the resistive heating elements of conventional furnaces, enabling very fast ramp rates of up to 10 °C s<sup>-1</sup> [213] and rapid heat transfer to the sample. A more

detailed description of an RTP system is provided in section 2.2.2. RTP is a more feasible annealing system for scale-up than the use of a conventional furnace [213]. It has been reported for the successful annealing of stacked elemental layers prepared via sputtering, leading to a respectable cell efficiency of 6.6% [214], and a multiple-zoned RTP system was used to selenise electrodeposited elemental stacks in [203] which achieved efficiencies of over 5%. Vauche et. al. report the use of an RTP system for the sulphurisation of electrodeposited stacked elemental layers in [213]. The system was a closed system, with argon as the inert gas. The background pressure was varied from 7 mbar to 500 mbar while the sulphur mass was 100 mg. It is reported that higher background pressures prevented the sulphurisation of the centre of the sample (which was relatively large at  $15 \times 15 \text{ cm}^2$ ), and, although this problem was minimised at the lowest pressures, material losses became a problem. This resulted in blisters, as well as causing difficulty in predicting the elemental ratios of the sulphurised CZTS due to differing proportions of each metal being lost. Changing from a very fast anneal of 3 minutes with a ramp rate of  $10 \text{ }^\circ\text{C s}^{-1}$  to a slower anneal of 9 minutes with a ramp rate of  $2 \text{ }^\circ\text{C s}^{-1}$  enabled the manufacture of a functioning device of 1.8% efficiency. This was further enhanced to 2.4% when a pre-anneal (with sulphur present) of 2 minutes at 350-450  $^\circ\text{C}$  was included (the device area was  $0.435 \text{ cm}^2$ ). This indicates that there are substantial challenges in using RTP for the annealing processes for electrodeposited stacks, however, optimisation steps have been shown to increase device efficiencies, and the potential for rapid processing of samples in a scaled-up production scenario would make a comprehensive optimisation worthwhile.

In summary, the inclusion of a pre-alloying or pre-annealing phase has been established in literature as leading to increased device efficiencies for sequentially electrodeposited elemental stacks. The most efficient sequentially electrodeposited CZTS solar cells were sulphurised/selenised using either a quartz ampoule in a convection furnace or a graphite box in a tube furnace, with different heating profiles required for different furnace types. The use of an RTP system would be favourable in terms of manufacture scale-up, however, it still requires extensive optimisation

before it can be used to make high-efficiency sequentially electrodeposited solar cells.

## **1.7 Summary**

CZTS has potential to become a viable low-cost alternative to CIGS while avoiding the use of scarce or toxic elements. This is particularly the case now that cells manufactured with cadmium-free buffer layers are able to achieve efficiencies not far short of their CdS containing counterparts. It is possible to achieve respectable efficiencies of over 8% using electrodeposition techniques, which is a non-vacuum technique that can be deployed for industrial scale manufacturing, although some challenges still occur in the deposition of zinc onto tin and it is beneficial to consider how the zinc electrolyte can be formulated to increase throwing power. The inclusion of a pre-alloying step assists in reaching higher efficiencies. However, there are still substantial hurdles to overcome in the avoidance of detrimental secondary phase formation in the manufacture of CZTS. The published best cell efficiencies have plateaued for a number of years, and still fall substantially short of those for CIGS. Furthermore, with reference specifically to electrodeposited CZTS, the best cell efficiencies have been achieved using non-scalable sulphurisation methods, with efficiencies for cells manufactured using RTP annealing routes falling behind. This leaves significant challenges to be overcome before CZTS can become a commercial product and play its part in providing affordable renewable energy. This necessitates research to further optimise the manufacture of CZTS through scalable methods, and this thesis aims, at least in part, to address this.

## 1.8 References

- [1] United Nations Framework Convention on Climate Change, “What is the Paris Agreement? | UNFCCC,” 2019. [Online]. Available: <https://unfccc.int/process-and-meetings/the-paris-agreement/what-is-the-paris-agreement>. [Accessed 29 December 2019].
- [2] Committee on Climate Change, “UK regulations: the Climate Change Act - Committee on Climate Change,” 2019. [Online]. Available: <https://www.theccc.org.uk/what-is-climate-change/the-legal-landscape/the-climate-change-act/>. [Accessed 29 December 2019].
- [3] Energy Saving Trust, “Buying green electricity | Energy Saving Trust,” 2019. [Online]. Available: <https://energysavingtrust.org.uk/home-energy-efficiency/switching-utilities/buying-green-electricity>. [Accessed 29 December 2019].
- [4] Renewable Resources Coalition, “Biomass Energy Advantages & Disadvantages | Renewable Resources Co,” 9 December 2016. [Online]. Available: <https://www.renewableresourcescoalition.org/biomass-energy-advantages-disadvantages/>. [Accessed 30 December 2019].
- [5] Department of Energy & Climate Change, “UK Solar PV Strategy Part 2: Delivering a Brighter Future,” UK Government, London, 2014.
- [6] K. Arora, S. Diu, J. Roper and G. Hartnell, “Solar PV on Commercial Buildings: A Guide for Owners and Developers,” BRE National Solar Centre, St Blazey, Cornwall, 2016.
- [7] W. Spry and B. Lucking, “Section 6 – UK Renewables 2019 and October to December 2019,” UK Government - Department for Business, Energy & Industrial Strategy, London, 2020.
- [8] M. A. Green, “Crystalline- and Polycrystalline-Silicon Solar Cells,” in *Renewable Energy*, T. B. Johansson, H. Kelly, A. K. N. Reddy, R. H. Williams and L. Burnham, Eds., Washington D.C., Island Press, 1993, pp. 337-360.
- [9] S. R. Wenham and M. A. Green, “Silicon Solar Cells,” *Progress in Photovoltaics: Research and Applications*, vol. 4, no. 1, pp. 3-33, 1996.



- [10] J. Nelson, "Chapter 1 - Introduction," in *The Physics of Solar Cells*, London, Imperial College Press, 2004, pp. 1-16.
- [11] J. Dréon, Q. Jeangros, J. Cattin, J. Haschke, L. Antognini, C. Ballif and M. Boccard, "23.5%-efficient silicon heterojunction silicon solar cell using molybdenum oxide as hole-selective contact," *Nano Energy*, vol. 70, p. 104495, 2020.
- [12] M. A. Green, E. D. Dunlop, J. Hohl-Ebinger, M. Yoshita, N. Kopidakis and A. W. Ho-Baillie, "Solar cell efficiency tables (Version 55)," *Progress in Photovoltaics: Research and Applications*, vol. 28, no. 1, pp. 3-15, 20 December 2019.
- [13] K. Yoshikawa, H. Kawasaki, W. Yoshida, T. Irie, K. Konishi, K. Nakano, T. Uto, D. Adachi, M. Kanematsu, H. Uzu and K. Yamamoto, "Silicon heterojunction solar cell with interdigitated back contacts for a photoconversion efficiency over 26%," *Nature Energy*, vol. 2, p. 17032, 20 March 2017.
- [14] Royal Society of Chemistry, "Silicon - Element information, properties and uses | Periodic Table," [Online]. Available: <https://www.rsc.org/periodic-table/element/14/silicon>. [Accessed 27 May 2020].
- [15] Royal Society of Chemistry, "Minerals, elements and the Earth's crust," 20 November 2003. [Online]. Available: <https://www.rsc.org/education/teachers/resources/jesei/minerals/students.htm>. [Accessed 27 May 2020].
- [16] Royal Society of Chemistry, "Indium - Element information, properties and uses | Periodic Table," [Online]. Available: <https://www.rsc.org/periodic-table/element/49/indium>. [Accessed 27 May 2020].
- [17] Department for Business, Energy & Industrial Strategy, "Electricity Generation Costs," UK Government, London, 2016.
- [18] E. O'Shaughnessy and R. Margolis, "Using Residential Solar PV Quote Data to Analyze the Relationship between Installer Pricing and Firm Size," National Renewable Energy Laboratory, Golden, US, 2017.

- [19] Foresight Solar Fund Limited, “Unaudited Consolidated Interim Report and Financial Statements for the Period 1 January 2017 to 30 June 2017,” Foresight Group LLP, London, 2017.
- [20] P. Heinstein, C. Ballif and L.-E. Perret-Aebi, “Building Integrated Photovoltaics (BIPV): Review, Potentials, Barriers and Myths,” *Green*, vol. 3, no. 2, pp. 125-156, 2013.
- [21] A. Shah, “Chapter IC-1: Thin Film Solar Cells, Section 1.1: Tandem and Multijunction Solar Cells,” in *Practical Handbook of Photovoltaics: Fundamentals and Applications*, 2 ed., A. McEvoy, T. Markvart and L. Castaner, Eds., London, Elsevier AP, 2012, pp. 214-215.
- [22] E. A. Schiff, S. Hegedus and X. Deng, “Amorphous Silicon-based Solar Cells,” in *Handbook of Photovoltaic Science and Engineering*, 2 ed., A. Luque and S. Hegedus, Eds., Chichester, United Kingdom, John Wiley & Sons, 2011, pp. 487-545.
- [23] A. Shah, “Chapter IC-1: Thin Film Solar Cells, Section 1: Introduction,” in *Practical Handbook of Photovoltaics: Fundamentals and Applications*, 2 ed., A. McEvoy, T. Markvart and L. Castaner, Eds., London, Elsevier AP, 2012, pp. 214-215.
- [24] National Library of Medicine (US), “Silane | SiH<sub>4</sub> - PubChem,” U.S. National Center for Biotechnology Information, [Online]. Available: <https://pubchem.ncbi.nlm.nih.gov/compound/Silane>. [Accessed 28 May 2020].
- [25] W. N. Shafarman, S. Siebentritt and L. Stolt, “Cu(InGa)Se<sub>2</sub> Solar Cells,” in *Handbook of Photovoltaic Science and Engineering*, 2 ed., Chichester, United Kingdom, John Wiley & Sons, 2011, pp. 546-599.
- [26] R. Santbergen and R. J. C. van Zolingen, “The absorption factor of crystalline silicon PV cells: A numerical and experimental study,” *Solar Energy Materials and Solar Cells*, vol. 92, no. 4, pp. 432-444, 2008.
- [27] I. Tobias, C. del Canizo and J. Alonso, “Crystalline Silicon Solar Cells and Modules,” in *Handbook of Photovoltaic Science and Engineering*, 2 ed., Chichester, United Kingdom, John Wiley & Sons, 2011, pp. 265-313.

- [28] O. Kurniawan and E. P. Li, "Study of a single coaxial silicon nanowire for on-chip integrated photovoltaic application," in *Proceedings of the 2009 12th International Symposium on Integrated Circuits*, Singapore, 2009.
- [29] G. Rajan, K. Aryal, S. Karki, P. Aryal, R. W. Collins and S. Marsillac, "Characterization and Analysis of Ultrathin CIGS Films and Solar Cells Deposited by 3-Stage Process," *Journal of Spectroscopy*, p. 8527491, 2 May 2018.
- [30] H. Hiroi, Y. Iwata, H. Sugimoto and A. Yamada, "High Efficiency Pure-Sulfide Cu(In,Ga)S<sub>2</sub> Solar Cells with Cd-free Buffer Layer," in *EMRS Spring Meeting 2016*, Lille, France, 2016.
- [31] Solar Frontier, *Solar Frontier Achieves World Record Thin-Film Solar Cell Efficiency of 23.35%*, S. Yoshida, Ed., Tokyo, Japan: PR Team, Corporate Administration Department, Solar Frontier, 2019.
- [32] Solar Frontier, "Ecology," 2019. [Online]. Available: <http://www.solar-frontier.com/eng/technology/Ecology/index.html>. [Accessed 26 January 2020].
- [33] BiPVco, "Products - BiPVco -The Building Integrated Photovoltaic Company," 2019. [Online]. Available: <https://bipvco.com/products/>. [Accessed 2 January 2020].
- [34] B. Spektor, *Europe's 'New' Periodic Table Predicts Which Elements Will Disappear in the Next 100 Years*, New York: Future US, Inc., 2019.
- [35] G. B. Haxel, J. B. Hedrick and G. J. Orris, *Rare Earth Elements—Critical Resources for High Technology*, P. H. Stauffer and J. W. I. Hendley, Eds., Washington D.C.: U.S. Geological Survey, 2002.
- [36] Lenntech Water Treatment Solutions, "Gallium (Ga) - Chemical Properties, Health and Environmental Effects," 2020. [Online]. Available: <https://www.lenntech.com/periodic/elements/ga.htm>. [Accessed 12 March 2020].
- [37] M. Frenzel, M. P. Ketris, T. Seifert and J. Gutzmer, "On the current and future availability of gallium," *Resources Policy*, vol. 47, pp. 38-50, 2016.

- [38] C. Candelise, M. Winkler and R. Gross, "Implications for CdTe and CIGS technologies production costs of indium and tellurium scarcity," *Progress in Photovoltaics: Research and Applications*, vol. 20, no. 6, pp. 816-831, 2012.
- [39] A. M. Ali, K. S. Rahman, L. M. Ali, M. Akhtaruzzaman, K. Sopian, S. Radiman and N. Amin, "A computational study on the energy bandgap engineering in performance enhancement of CdTe thin film solar cells," *Results in Physics*, vol. 7, pp. 1066-1072, 2017.
- [40] B. E. McCandless and J. R. Sites, "Cadmium Telluride Solar Cells," in *Handbook of Photovoltaic Science and Engineering*, 2 ed., A. Luque and S. Hegedus, Eds., Chichester, United Kingdom, John Wiley & Sons, 2011, pp. 600-635.
- [41] First Solar, *First Solar Achieves Yet Another Cell Conversion Efficiency World Record*, S. Krum, Ed., First Solar Media, 2016.
- [42] First Solar, *First Solar Series 6(TM) Module Datasheet*, First Solar Inc., 2020.
- [43] I. Wissenbach, A. Palmen and C. Steitz, *First Solar wins reprieve in EU toxic substance ban*, J. Gleave, Ed., Duesseldorf: Thomson Reuters, 2010.
- [44] Q. Liu, Y. Jiang, K. Jin, J. Qin, J. Xu, W. Li, J. Xiong, J. Liu, Z. Xiao, K. Sun, S. Yang, X. Zhang and L. Ding, "18% Efficiency organic solar cells," *Science Bulletin*, vol. 65, no. 4, pp. 272-275, 2020.
- [45] Y. Cui, H. Yao, L. Hong, T. Zhang, Y. Tang, B. Lin, K. Xian, B. Gao, C. An, P. Bi, W. Ma and J. Hou, "17% efficiency organic photovoltaic cell with superior processability," *National Science Review*, 5 December 2019.
- [46] ZAE Bayern and Energie Campus Nürnberg, *New World Record Efficiency for Organic Solar Modules*, H. Egelhaaf, Ed., Nuremberg: ZAE Bayern and Energie Campus Nürnberg, 2019.
- [47] Y. Zhang, I. D. W. Samuel, T. Wang and D. G. Lidzey, "Current Status of Outdoor Lifetime Testing of Organic Photovoltaics," *Advanced Science*, vol. 5, no. 8, p. 1800434, 2018.

- [48] C. Sartorio, V. Campisciano, C. Chiappara, S. Cataldo, M. Scopelliti, M. F. Gruttadauria and B. Pignataro, "Enhanced power-conversion efficiency in organic solar cells incorporating copolymeric phase-separation modulators," *Journal of Materials Chemistry A*, vol. 6, no. 9, pp. 3884-3894, 2018.
- [49] S. Strohm, F. Machui, S. Langner, P. Kubis, N. Gasparini, M. Salvador, I. McCulloch, H. J. Egelhaaf and C. J. Brabec, "P3HT: non-fullerene acceptor based large area, semi-transparent PV modules with power conversion efficiencies of 5%, processed by industrially scalable methods," *Energy & Environmental Science*, vol. 11, no. 8, pp. 2225-2234, 2018.
- [50] X. Xu, G. Zhang, L. Yu, R. Li and Q. Peng, "P3HT-Based Polymer Solar Cells with 8.25% Efficiency Enabled by a Matched Molecular Acceptor and Smart Green-Solvent Processing Technology," *Advanced Materials*, vol. 31, no. 52, p. e1906045, 2019.
- [51] Y. S. Zimmermann, A. Schaffer, C. Hugli, K. Fent, P. F. Corvini and M. Lenz, "Organic photovoltaics: potential fate and effects in the environment," *Environment International*, vol. 49, pp. 128-140, 15 November 2012.
- [52] N.-G. Park, J. van de Lagemaat and A. J. Frank, "Comparison of Dye-Sensitized Rutile- and Anatase-Based TiO<sub>2</sub> Solar Cells," *Journal of Physical Chemistry B*, vol. 104, no. 38, pp. 8989-8994, 2000.
- [53] K. Hara and S. Mori, "Dye-sensitized Solar Cells," in *Handbook of Photovoltaic Science and Engineering*, 2 ed., A. Luque and S. Hegedus, Eds., Chichester, United Kingdom, John Wiley & Sons, 2011, pp. 642-674.
- [54] C. Dette, M. A. Pérez-Osorio, C. S. Kley, P. Punke, C. E. Patrick, P. Jacobson, F. Giustino, S. J. Jung and K. Kern, "TiO<sub>2</sub> Anatase With a Bandgap in the Visible Region," *Nano Letters*, vol. 14, no. 11, pp. 6533-6538, 2014.
- [55] C. Lai, S. Lee and Y. Chao, "Efficient Dye-Sensitized Solar Cells Based on Ru (II) Complex Black Dye Sensitizers," in *Proceedings of ISES World Congress 2007 (Vol. I – Vol. V)*, Berlin, 2008.
- [56] J. Zhang, C. Yu, L. Wang, Y. Li, Y. Ren and K. Shum, "Energy barrier at the N719-dye/CsSnI<sub>3</sub> interface for photogenerated holes in dye-sensitized solar cells," *Scientific Reports*, vol. 4, p. 6954, 2015.

- [57] Y. Lin, Y. Wu, H. You, P. Chen, Y. Tsai and B. Lai, “Ultra-low Temperature Flexible Dye-Sensitized Solar Cell,” in *2014 International Symposium on Computer, Consumer and Control*, Taichung, Taiwan, 2014.
- [58] K. Hooper, M. Carnie, C. Charbonneau and T. Watson, “Near Infrared Radiation as a Rapid Heating Technique for TiO<sub>2</sub> Films on Glass Mounted Dye-Sensitized Solar Cells,” *International Journal of Photoenergy*, p. 953623, 2014.
- [59] Romande Energie / Mediacom, *EPFL's campus has the world's first solar window*, Lausanne: École Polytechnique Fédérale de Lausanne (EPFL), 2013.
- [60] A. Roy, A. Ghosh, S. Bhandari, P. Selvaraj, S. Sundaram and T. K. Mallick, “Color Comfort Evaluation of Dye-Sensitized Solar Cell (DSSC) Based Building-Integrated Photovoltaic (BIPV) Glazing after 2 Years of Ambient Exposure,” *The Journal of Physical Chemistry C*, vol. 123, no. 39, p. 23834–23837, 2019.
- [61] H. Iftikhar, G. G. Sonai, S. G. Hashmi, A. F. Nogueira and P. D. Lund, “Progress on Electrolytes Development in Dye-Sensitized Solar Cells,” *Materials (Basel)*, vol. 12, no. 12, p. 1998, 2019.
- [62] C.-F. Lin, W.-G. Huang, P.-H. Chen and J.-H. Kung, “Lifetime study of Dye sensitized solar cells,” in *2015 22nd International Workshop on Active-Matrix Flatpanel Displays and Devices (AM-FPD)*, Kyoto, 2015.
- [63] R. Wang, M. Mujahid, Y. Duan, Z.-K. Wang, J. Xue and Y. Yang, “A Review of Perovskites Solar Cell Stability,” *Advanced Functional Materials*, vol. 29, no. 47, p. 1808843, 2019.
- [64] F. Zhang, Z. Wang, H. Zhu, N. Pellet, J. Luo, C. Yi, X. Liu, H. Liu, S. Wang, X. Li, Y. Xiao, S. M. Zakeeruddin, D. Bi and M. Grätzel, “Over 20% PCE perovskite solar cells with superior stability achieved by novel and low-cost hole-transporting materials,” *Nano Energy*, vol. 41, pp. 469-475, 2017.
- [65] D. Pourjafari, D. Peralta, R. Escalante, G. Oskam, J. Baker, S. Meroni, A. Yasin, C. Charbonneau and T. Watson, “Feasibility Study of Economics, Facilities and Skills for Production of Printed Photovoltaics Utilising Resources Available in Merida Mexico,” in *15th Photovoltaic Science, Applications & Technology Conference (PV-SAT 15)*, Warwick, 2019.

- [66] N. L. Chang, A. W. Y. Ho-Baillie, D. Vak, M. Gao, M. A. Green and R. J. Egan, "Manufacturing cost and market potential analysis of demonstrated roll-to-roll perovskite photovoltaic cell processes," *Solar Energy Materials and Solar Cells*, vol. 174, pp. 314-324, 2018.
- [67] National Renewable Energy Laboratory (NREL), US Department of Energy, "Best Research-Cell Efficiency Chart - best-research-cell-efficiencies.20200708.pdf," 8 July 2020. [Online]. Available: <https://www.nrel.gov/pv/cell-efficiency.html>. [Accessed 30 July 2020].
- [68] S. S.-Y. Juang, P.-Y. Lin, Y.-C. Lin, Y.-S. Chen, P.-S. Shen, Y.-L. Guo, Y.-C. Wu and P. Chen, "Energy Harvesting Under Dim-Light Condition With Dye-Sensitized and Perovskite Solar Cells," *Frontiers in Chemistry*, vol. 7, p. 209, 2019.
- [69] H. K. H. Lee, J. Barbé, S. Meroni, T. Du, C.-T. Lin, A. Pockett, J. Troughton, S. M. Jain, F. De Rossi, J. Baker, M. J. Carnie, M. A. McLachlan, T. Watson, J. R. Durrant and W. C. Tsoi, "Outstanding Indoor Performance of Perovskite Photovoltaic Cells – Effect of Device Architectures and Interlayers," *Solar Rapid Research Letters*, vol. 3, p. 1800207, 2019.
- [70] J. S. Manser, M. I. Saidaminov, J. A. Christians, O. M. Bakr and P. V. Kamat, "Making and Breaking of Lead Halide Perovskites," *Accounts of Chemical Research*, vol. 49, no. 2, pp. 330-338, 2016.
- [71] T. Leijtens, G. E. Eperon, N. K. Noel, S. N. Habisreutinger, A. Petrozza and H. J. Snaith, "Stability of Metal Halide Perovskite Solar Cells," *Advanced Energy Materials*, vol. 5, no. 20, p. 1500963, 2015.
- [72] J. A. Christians, P. A. Miranda Herrera and P. V. Kamat, "Transformation of the Excited State and Photovoltaic Efficiency of CH<sub>3</sub>NH<sub>3</sub>PbI<sub>3</sub> Perovskite upon Controlled Exposure to Humidified Air," *Journal of the American Chemical Society*, vol. 137, no. 4, pp. 1530-1538, 2015.
- [73] J.-A. Alberola-Borràs, J. A. Baker, F. De Rossi, R. Vidal, D. Beynon, K. E. Hooper, T. M. Watson and I. Mora-Seró, "Perovskite Photovoltaic Modules: Life Cycle Assessment of Pre-industrial Production Process," *iScience*, vol. 9, pp. 542-551, 2018.

- [74] E. Greul, P. Docampo and T. Bein, "Synthesis of Hybrid Tin Halide Perovskite Solar Cells with Less Hazardous Solvents: Methanol and 1,4-Dioxane," *Zeitschrift für anorganische und allgemeine Chemie*, vol. 643, pp. 1704-1711, 2017.
- [75] A. S. Nazligul, M. Wang and K. L. Choy, "Recent Development in Earth-Abundant Kesterite Materials and Their Applications," *Sustainability*, vol. 12, p. 5138, 2020.
- [76] W. Ki and H. W. Hillhouse, "Earth-Abundant Element Photovoltaics Directly from Soluble Precursors with High Yield Using a Non-Toxic Solvent," *Advanced Energy Materials*, vol. 1, no. 5, pp. 732-735, 2011.
- [77] X.-T. Lu, Z.-B. Zhuang, Q. Peng and Y.-D. Li, "Wurtzite Cu<sub>2</sub>ZnSnS<sub>4</sub> nanocrystals. A novel quaternary semiconductor," *Chemical Communications*, vol. 47, no. 11, pp. 3141-3143, 2011.
- [78] D. Hodges, C. Sana, S. Shahriar, J. Galindo, D. Kava, E. C. R. Castro, D. Buck and L. Echegoyen, "Earth abundant and nontoxic absorber material for low cost, thin film solar cells," in *2015 IEEE Conference on Technologies for Sustainability (SusTech)*, Ogden UT, USA, 2015.
- [79] D. Tang, Q. Wang, F. Liu, L. Zhao, Z. Han, K. Sun, Y. Lai, J. Li and Y. Liu, "An alternative route towards low-cost Cu<sub>2</sub>ZnSnS<sub>4</sub> thin film solar cells," *Surface and Coatings Technology*, vol. 232, pp. 53-59, 2013.
- [80] Q. Tian, X. Xu, L. Han, M. Tang, R. Zou, Z. Chen, M. Yu, J. Yang and J. Hu, "Hydrophilic Cu<sub>2</sub>ZnSnS<sub>4</sub> nanocrystals for printing flexible, low-cost and environmentally friendly solar cells," *CrystEngComm*, vol. 14, no. 11, pp. 3847-3850, 2012.
- [81] A. G. Kannan, T. E. Manjulavalli and J. Chandrasekaran, "Influence of solvent on the properties of CZTS nanoparticles," in *MRS 8th International Conference on Materials for Advanced Technologies Symposia Poceedings*, Singapore, 2016.
- [82] A. G. Kannan, T. E. Manjulavalli and J. Chandrasekaran, "Influence of solvent on the properties of CZTS nanoparticles," *Procedia Engineering*, vol. 141, pp. 15-22, 2016.



- [83] H. Ferhati and F. Djeflal, "Graded band-gap engineering for increased efficiency in CZTS solar cells," *Optical Materials*, vol. 76, pp. 393-399, 2018.
- [84] S. Mohammadnejad and A. B. Parashkouh, "CZTSSe solar cell efficiency improvement using a new band-gap grading model in absorber layer," *Applied Physics A*, vol. 123, p. 758, 2017.
- [85] S. Chen, A. Walsh, J.-H. Yang, X. G. Gong, L. Sun, P.-X. Yang, J.-H. Chu and S.-H. Wei, "Compositional dependence of structural and electronic properties of  $\text{Cu}_2\text{ZnSn}(\text{S},\text{Se})_4$  alloys for thin film solar cells," *Physical Review B*, vol. 83, no. 12, p. 125201, 2011.
- [86] F. A. Jhuma, M. Z. Shaily and M. J. Rashid, "Towards high-efficiency CZTS solar cell through buffer layer optimization," *Materials for Renewable and Sustainable Energy*, vol. 8, p. 6, 2019.
- [87] X. Song, X. Ji, M. Li, W. Lin, X. Luo and H. Zhang, "A Review on Development Prospect of CZTS Based Thin Film Solar Cells," *International Journal of Photoenergy*, p. 619179, 2014.
- [88] W. Wang, M. T. Winkler, O. Gunawan, T. Gokmen, T. K. Todorov, Y. Zhu and D. B. Mitzi, "Device Characteristics of CZTSSe Thin-Film Solar Cells with 12.6% Efficiency," *Advanced Energy Materials*, vol. 4, no. 7, p. 1301465, 2014.
- [89] R. Fletcher-Wood, "Magnificent Molecules - Hydrazine," Royal Society of Chemistry (RSC Education), 3 August 2016. [Online]. Available: <https://edu.rsc.org/magnificent-molecules/hydrazine/2000023.article>. [Accessed 28 July 2020].
- [90] H. Xin, S. M. Vorpahl, A. D. Collord, I. L. Braly, A. R. Uhl, B. W. Kreuger, D. S. Ginger and H. W. Hillhouse, "Lithium-doping inverts the nanoscale electric field at the grain boundaries in  $\text{Cu}_2\text{ZnSn}(\text{S},\text{Se})_4$  and increases photovoltaic efficiency," *Physical Chemistry Chemical Physics*, vol. 17, no. 37, pp. 23859-23866, 2015.
- [91] M. T. Htay, Y. Hashimoto, N. Momose, K. Sasaki, H. Ishiguchi, S. Igarashi, K. Sakurai and K. Ito, "A Cadmium-Free  $\text{Cu}_2\text{ZnSnS}_4/\text{ZnO}$  Heterojunction Solar Cell Prepared by Practicable Processes," *Japanese Journal of Applied Physics*, vol. 50, no. 3R, p. 032301, 2011.

- [92] J. K. Larsen, F. Larsson, T. Törndahl, N. Saini, L. Riekehr, Y. Ren, A. Biswal, D. Hauschild, L. Weinhardt, C. Heske and C. Platzer-Björkman, “Cadmium Free  $\text{Cu}_2\text{ZnSnS}_4$  Solar Cells with 9.7% Efficiency,” *Advanced Energy Materials*, vol. 9, no. 21, p. 1900439, 2019.
- [93] C. Yan, J. Huang, K. Sun, S. Johnston, Y. Zhang, H. Sun, A. Pu, M. He, F. Liu, K. Eder, L. Yang, J. M. Caaney, N. Ekins-Daukes, Z. Hameiri, J. A. Stride, S. Chen, M. A. Green and X. Hao, “ $\text{Cu}_2\text{ZnSnS}_4$  solar cells with over 10% power conversion efficiency enabled by heterojunction heat treatment,” *Nature Energy*, vol. 3, no. 9, pp. 764-772, 2018.
- [94] K. Sun, F. Liu, J. Huang, C. S. N. Yan, H. Sun, C. Xue, Y. Zhang, A. Pu, Y. Shen, J. A. Stride, M. Green and X. Hao, “Flexible kesterite  $\text{Cu}_2\text{ZnSnS}_4$  solar cells with sodium-doped molybdenum back contacts on stainless steel substrates,” *Solar Energy Materials and Solar Cells*, vol. 182, pp. 14-20, 2018.
- [95] S. Almosni, A. Delamarre, Z. Jehl, D. Suchet, L. Cojocar, M. Giteau, B. Behaghel, A. Julian, C. Ibrahim, L. Taty, H. Wang, T. Kubo, S. Uchida, H. Segawa, N. Miyashita, R. Tamaki, Y. Shoji, K. Yoshida, N. Ahsan, K. Watanabe, T. Inoue, M. Sugiyama, Y. Nakano, T. Hamamura, T. Toupance, C. Olivier, S. Chambon, L. Vignau, C. Geffroy, E. Cloutet, G. Hadziioannou, N. Cavassilas, P. Rale, A. Cattoni, S. Collin, F. Gibelli, M. Paire, L. Lombez, D. Aureau, M. Bouttemy, A. Etcheberry, Y. Okada and J. F. Guillemoles, “Material challenges for solar cells in the twenty-first century: directions in emerging technologies,” *Science and Technology of Advanced Materials*, vol. 19, no. 1, pp. 336-369, 2018.
- [96] C. Honsberg and S. Bowden, “Semiconductor Structure | PVEducation,” PVEducation, 2019. [Online]. Available: <https://www.pveducation.org/pvcdrom/pn-junctions/semiconductor-structure>. [Accessed 10 August 2020].
- [97] S. Guccione, M. M. Swamy and A. Stankovic, “Chapter 4 - Rectifiers,” in *The Power Electronics Handbook*, T. L. Skvarenina, Ed., Boca Raton, Florida, CRC Press, 2018, pp. 4.1 - 5.1.
- [98] C. Honsberg and S. Bowden, “Conduction in Semiconductors | PVEducation,” PVEducation, 2019. [Online]. Available: <https://www.pveducation.org/pvcdrom/conduction-in-semiconductors>. [Accessed 11 August 2020].

- [99] S. M. Sze, “Chapter 1 - Energy Bands and Carrier Concentration,” in *Semiconductor Devices: Physics and Technology*, New York, John Wiley and Sons Inc., 1985, pp. 1-29.
- [100] P. Hofmann, “Chapter 7 - Semiconductors,” in *Solid State Physics: An Introduction*, Weinheim, Germany, Wiley-VCH, 2008, pp. 113-135.
- [101] B. Van Zeghbroeck, “Section 4.6 - Optoelectronic Devices,” in *Principles of Semiconductor Devices*, Boulder, U.S., University of Colorado, 2011. [Online]. Available: <http://ecee.colorado.edu/~bart/book/>. [Accessed 11 August 2020].
- [102] B. Gönül, *Chapter 2 - Energy Bands and Effective Mass*, Ganziantep, Turkey: Ganziantep University, [Online]. Available: <https://pdfslide.net/documents/chapter-2-energy-bands-and-effective-mass-prof-dr-besire-goenuel-prof-dr.html>. [Accessed 11 August 2020].
- [103] J. Ogborn and M. Whitehouse, “Section 5.4 - Controlling Conductivity,” in *Advancing Physics AS*, Bristol, Institute of Physics Publishing, 2000, pp. 122-128.
- [104] S. Das, K. C. Mandal and R. N. Bhattacharya, “Chapter 2 - Earth-Abundant  $\text{Cu}_2\text{ZnSn}(\text{S},\text{Se})_4$  (CZTSSe) Solar Cells,” in *Semiconductor Materials for Solar Photovoltaic Cells*, M. P. Paranthaman, W. Wong-Ng and R. N. Bhattacharya, Eds., Cham, Switzerland, Springer, 2015, pp. 25-74.
- [105] S. Chen, J.-H. Yang, X. G. Gong, A. Walsh and S.-H. Wei, “Intrinsic point defects and complexes in the quaternary kesterite semiconductor,” *Physical Review B*, vol. 81, no. 24, p. 245204, 2010.
- [106] M. Sahal, M. Mollar and B. Marí, “p- and n-type doping of zinc oxide through electrochemical methods,” in *2016 International Renewable and Sustainable Energy Conference (IRSEC)*, Marrakech, 2016.
- [107] J.-C. Wu, J. Zheng, P. Wu and R. Xu, “Study of Native Defects and Transition-Metal (Mn, Fe, Co, and Ni) Doping in a Zinc-Blende CdS Photocatalyst by DFT and Hybrid DFT Calculations,” *The Journal of Physical Chemistry C*, vol. 115, no. 13, pp. 5675-5682, 2011.

- [108] V. Kumar and F. A. Kröger, “Self-diffusion and the defect structure of cadmium sulfide,” *Journal of Solid State Chemistry*, vol. 3, no. 3, pp. 387-400, 1971.
- [109] S. M. Sze, “Chapter 3 - p-n Junction,” in *Semiconductor Devices: Physics and Technology*, New York, John Wiley and Sons, Inc., 1985, pp. 70-108.
- [110] S. Rondiya, Y. Jadhav, M. Nasane, S. Jadkar and N. Y. Dzade, “Interface Structure and Band Alignment of CZTS/CdS Heterojunction: An Experimental and First-Principles DFT Investigation,” *Materials*, vol. 24, no. 12, p. 4040, 2019.
- [111] J. Nelson, “Chapter 2 - Photons In, Electrons Out: Basic Principles of PV,” in *The Physics of Solar Cells*, London, Imperial College Press, 2004, pp. 17-40.
- [112] J. Nelson, “Chapter 6 - Analysis of the p-n Junction,” in *The Physics of Solar Cells*, London, Imperial College Press, 2004, pp. 145-176.
- [113] K. Kaur, N. Kumar and M. Kumar, “Strategic review of interface carrier recombination in earth abundant Cu–Zn–Sn–S–Se solar cells: current challenges and future prospects,” *Journal of Materials Chemistry A*, vol. 5, no. 7, pp. 3069-3090, 2017.
- [114] S. Kim, J.-S. Park, S. N. Hood and A. Walsh, “Lone-pair effect on carrier capture in Cu<sub>2</sub>ZnSnS<sub>4</sub> solar cells,” *Journal of Materials Chemistry A*, vol. 7, no. 6, pp. 2686-2693, 2019.
- [115] C. Leidholm, C. Hotz, A. Breeze, C. Sunderland, W. Ki and D. Zehnder, “Final Report: Sintered CZTS Nanoparticle Solar Cells on Metal Foil,” National Renewable Energy Laboratory (U.S. Department of Energy), Golden, Colorado, 2012.
- [116] T. Prabhakar and N. Jampana, “Effect of sodium diffusion on the structural and electrical properties of Cu<sub>2</sub>ZnSnS<sub>4</sub> thin films,” *Solar Energy Materials and Solar Cells*, vol. 95, no. 3, pp. 1001-1004, 2011.
- [117] B. Liu, J. Gou, R. Hao, L. Wang, K. Gu, S. Sun and A. Aierken, “Effect of Na doping on the performance and the band alignment of CZTS/CdS thin film solar cell,” *Solar Energy*, vol. 201, pp. 219-266, 2020.

- [118] F. Pianezzi, A. Chirilă, S. Nishiwaki, S. Buecheler and A. N. Tiwari, “Influence of impurities on the performance of CIGS thin film solar cells,” EMPA - Swiss Federal Laboratories for Materials Testing and Research, Dübendorf, Zürich, Switzerland, 2012.
- [119] N. Dhar, P. Chelvanathan and M. S. K. A. N. Zaman, “An Investigation on Structural and Electrical Properties of RF-Sputtered Molybdenum Thin Film Deposited on Different Substrates,” *Energy Procedia*, no. 33, pp. 186-197, 2013.
- [120] P. Chelvanathan, M. I. Hossain, J. Husna, M. Alghoul, K. Sopian and N. Amin, “Effects of Transition Metal Dichalcogenide Molybdenum Disulfide Layer Formation in Copper–Zinc–Tin–Sulfur Solar Cells from Numerical Analysis,” *Japanese Journal of Applied Physics*, no. 51, p. 10NC32, 2012.
- [121] F. Z. Boutebakh, M. L. Zeggar, N. Attaf and M. S. Aida, “Electrical properties and back contact study of CZTS/ZnS heterojunction,” *Optik*, no. 144, pp. 180-190, 2017.
- [122] M. Patel and A. Ray, “Enhancement of output performance of Cu<sub>2</sub>ZnSnS<sub>4</sub> thin film solar cells — A numerical simulation approach and comparison to experiments,” *Physica B: Condensed Matter*, vol. 407, no. 21, p. 4391–4397, 2012.
- [123] Lenntech Water Treatment Solutions, “Molybdenum (Mo) - Chemical properties, Health and Environmental effects,” 2020. [Online]. Available: <https://www.lenntech.com/periodic/elements/mo.htm>. [Accessed 29 October 2020].
- [124] Lenntech Water Treatment Solutions, “Gold (Au) - Chemical properties, Health and Environmental effects,” 2020. [Online]. Available: <https://www.lenntech.com/periodic/elements/au.htm>. [Accessed 29 October 2020].
- [125] C. W. Hong, S. W. Shin, M. P. Suryawanshi, M. G. Gang, J. Heo and J. H. Kim, “Chemically Deposited CdS Buffer/Kesterite Cu<sub>2</sub>ZnSnS<sub>4</sub> Solar Cells: Relationship between CdS Thickness and Device Performance,” *ACS Applied Materials and Interfaces*, vol. 9, no. 42, p. 36733–36744, 2017.

- [126] J. Tao, K. Zhang, C. Zhang, L. Chen, H. Cao, J. Liu, J. Jiang, L. Sun, P. Yang and J. Chu, "A sputtered CdS buffer layer for co-electrodeposited Cu<sub>2</sub>ZnSnS<sub>4</sub> solar cells with 6.6% efficiency," *Chemical Communications*, vol. 51, no. 51, pp. 10337-10340, 2015.
- [127] M. Sokolich, "What is a buffer layer in a solar cell, and what is its significance? - Quora," University of California, Los Angeles, 26 August 2018. [Online]. Available: <https://www.quora.com/What-is-a-buffer-layer-in-a-solar-cell-and-what-is-its-significance>. [Accessed 25 November 2020].
- [128] T. Ericson, J. J. Scragg, A. Hultqvist, J. T. Wätjen, P. Szaniawski, T. Törndahl and C. Platzer-Björkman, "Zn(O, S) Buffer Layers and Thickness Variations of CdS Buffer for Cu<sub>2</sub>ZnSnS<sub>4</sub> Solar Cells," *IEEE Journal of Photovoltaics*, vol. 4, no. 1, pp. 465-469, 2014.
- [129] A. Le Donne, S. Marchionna, P. Garattini, R. Mereu, M. Acciarri and S. Binetti, "Effects of CdS Buffer Layers on Photoluminescence Properties of Cu<sub>2</sub>ZnSnS<sub>4</sub> Solar Cells," *International Journal of Photoenergy*, p. 583058, 2015.
- [130] M. Jiang and X. Yan, "Chapter 5 - Cu<sub>2</sub>ZnSnS<sub>4</sub> Thin Film Solar Cells: Present Status and Future Prospects," in *Solar Cells: Research and Application Perspectives*, A. Morales-Acevedo, Ed., London, IntechOpen Limited, 2013.
- [131] E. Della Gaspera, J. van Embden, A. S. R. Chesman, N. W. Duffy and J. J. Jasieniak, "Mimicry of Sputtered i-ZnO Thin Films Using Chemical Bath Deposition for Solution-Processed Solar Cells," *ACS Applied Materials and Interfaces*, vol. 6, no. 24, pp. 22519-22526, 2014.
- [132] E. Fortunati, D. Puglia, I. V. A. Armentano, M. Ramos, N. Juárez, M. C. Garrigós and J. M. Kenny, "Chapter 8 - Multifunctional antimicrobial nanocomposites for food packaging applications," in *Food Preservation*, A. Mihai Grumezescu, Ed., Amsterdam, Academic Press, 2017, pp. 265-303.
- [133] M. Neuschitzer, K. Lienau, M. Guc, L. C. Barrio, S. Haass, J. Marquez Prieto, Y. Sanchez, M. Espindola-Rodriguez, Y. Romanyuk, A. Perez-Rodriguez, V. Izquierdo-Roca and E. Saucedo, "Towards high performance Cd-free CZTSe solar cells with a ZnS(O,OH) buffer layer: the influence of thiourea concentration on chemical bath deposition," *Journal of Physics D: Applied Physics*, vol. 49, no. 12, p. 125602, 2016.

- [134] Y. Lu, S. Wang, M. Yang, X. Xu and Q. Li, “Comparative study of AZO and ITO thin film sputtered at different temperatures and their application in Cu<sub>2</sub>ZnSnS<sub>4</sub> solar cells,” *Journal of Materials Science: Materials in Electronics*, vol. 29, no. 20, pp. 17525-17532, 2018.
- [135] J.-S. Kim, J.-K. Kang and D.-K. Hwang, “High efficiency bifacial Cu<sub>2</sub>ZnSnSe<sub>4</sub> thin-film solar cells on transparent conducting oxide glass substrates,” *APL Materials*, vol. 4, no. 9, p. 096101, 2016.
- [136] T. P. Dhakal, C. Peng, R. R. Tobias, R. Dasharathy and C. R. Westgate, “Characterization of a CZTS thin film solar cell grown by sputtering method,” *Solar Energy*, vol. 100, pp. 23-30, 2014.
- [137] E. M. Mkawi, K. Ibrahim, M. K. M. Ali, M. A. Farrukh and A. S. Mohamed, “The effect of dopant concentration on properties of transparent conducting Al-doped ZnO thin films for efficient Cu<sub>2</sub>ZnSnS<sub>4</sub> thin-film solar cells prepared by electrodeposition method,” *Applied Nanoscience*, vol. 5, no. 8, pp. 993-1001, 2015.
- [138] F. Tsin, A. Venerosy, J. Vidal, S. Collin, J. Clatot, L. Lombez, M. Paire, S. Borensztajn, C. Broussillou, P. P. Grand, S. Jaime, D. Lincot and J. Rousset, “Electrodeposition of ZnO window layer for an all-atmospheric fabrication process of chalcogenide solar cell,” *Scientific Reports*, vol. 5, p. 8961, 2015.
- [139] H. Hagendorfer, K. Lienau, S. Nishiwaki, C. M. Fella, L. Kranz, A. R. Uhl, D. Jaeger, L. Luo, C. Gretener, S. Buecheler, Y. E. Romanyuk and A. N. Tiwari, “Highly Transparent and Conductive ZnO: Al Thin Films from a Low Temperature Aqueous Solution Approach,” *Advanced Materials*, vol. 26, no. 4, pp. 632-636, 2014.
- [140] T. Aizawa, K. Tanaka, K. Tagami and H. Uchiki, “Investigation of ZnO:Al window layer of Cu<sub>2</sub>ZnSnS<sub>4</sub> thin film solar cells prepared by non-vacuum processing,” *Physica Status Solidi C*, vol. 10, no. 7-8, pp. 1050-1054, 2013.
- [141] C. Platzer-Björkman, N. Barreau, M. Bär, L. Choubrac, L. Grenet, J. Heo, T. Kubart, A. Mittiga, Y. Sanchez and J. Scragg, “Back and front contacts in kesterite solar cells: state-of-the-art and open questions,” *Journal of Physics: Energy*, vol. 1, no. 4, p. 0440055, 2019.

- [142] P. A. Fernandes, P. M. P. Salomé, A. F. da Cunha and B.-A. Schubert, "Cu<sub>2</sub>ZnSnS<sub>4</sub> solar cells prepared with sulphurized dc-sputtered stacked metallic precursors," *Thin Solid Films*, vol. 519, no. 21, pp. 7382-7385, 2011.
- [143] F. Biccari, R. Chierchia, M. Valentini, P. Mangiapane, E. Salza, C. Malerba, C. L. A. Ricardo, L. Mannarino, P. Scardi and A. Mittiga, "Fabrication of Cu<sub>2</sub>ZnSnS<sub>4</sub> solar cells by sulfurization of evaporated precursors," *Energy Procedia*, vol. 10, pp. 187-191, 2011.
- [144] N. Muhunthan, O. P. Singh, M. K. Thakur, P. Karthikeyan, D. Singh, M. Saravanan and V. N. Singh, "Interfacial Properties of CZTS Thin Film Solar Cell," *Journal of Solar Energy*, vol. 2014, p. ID 476123, 2014.
- [145] M. I. Khalil, R. Bernasconi, A. Lucotti, A. Le Donne, R. A. Mereu, S. Binetti, J. L. Hart, M. L. Taheri, L. Nobili and L. Magagnin, "CZTS thin film solar cells on flexible Molybdenum foil by electrodeposition-annealing route," *Journal of Applied Electrochemistry*, vol. 51, no. 2, p. 209–218, 2021.
- [146] S. Ahmed, K. B. Reuter, O. Gunawan, L. Guo, L. T. Romankiw and H. Deligianni, "A High Efficiency Electrodeposited Cu<sub>2</sub>ZnSnS<sub>4</sub> Solar Cell," *Advanced Energy Materials*, vol. 2, no. 2, pp. 253-259, 2012.
- [147] G. Rajan, S. Karki, R. W. Collins, N. J. Podraza and S. Marsillac, "Real-Time Optimization of Anti-Reflective Coatings for CIGS Solar Cells," *Materials*, vol. 13, no. 19, p. 4259, 2020.
- [148] O. K. Simya, K. Balachander, D. Dhanalakshmi and A. M. Ashok, "Performance of different anti-reflection coating and TCO layers for kesteritebased thin film photovoltaic devices using Essential Macleod simulation program," *Superlattices and Microstructures*, vol. 145, p. 106579, 2020.
- [149] M. I. Fathima, A. Arulanantham and K. J. Wilson, "Effect of ZnS nanowire ARC on CZTS/CdS thin film solar cell by Nebulizer Spray Pyrolysis Technique," *Materials Research Express*, vol. 7, no. 1, p. 015510, 2020.
- [150] F.-I. Lai, J.-F. Yang, W.-X. Liao and S.-Y. Kuo, "Enhanced omnidirectional and weatherability of Cu<sub>2</sub>ZnSnSe<sub>4</sub> solar cells with ZnO functional nanorod arrays," *Scientific Reports*, no. 7, p. 14927, 2017.



- [151] G. Altamura, *Développement de cellules solaires à base de films minces Cu<sub>2</sub>ZnSn(S,Se)<sub>4</sub>*, Grenoble, France: Université de Grenoble, 2014.
- [152] M. Kumar, A. Dubey, N. Adhikari, S. Venkatesan and Q. Qiao, “Strategic review of secondary phases, defects and defect-complexes in kesterite CZTS–Se solar cells,” *Energy & Environmental Science*, vol. 8, no. 11, pp. 3134–3159, 2015.
- [153] Y. Gong, Y. Zhang, Q. Zhu, Y. Zhou, R. Qiu, C. Niu, W. Yan, W. Huang and X. Hao, “Identifying the origin of the Voc deficit of kesterite solar cells from the two grain growth mechanisms induced by Sn<sup>2+</sup> and Sn<sup>4+</sup> precursors in DMSO solution,” *Energy and Environmental Science*, Online Publication, 15 February 2021.
- [154] L. L. Baranowski, P. Zawadzki, S. Lany, E. S. Toberer and A. Zakutayev, “A review of defects and disorder in multinary tetrahedrally bonded semiconductors,” *Semiconductor Science and Technology*, vol. 31, no. 12, p. 123004, 2016.
- [155] M. A. Olgar, “Optimization of sulfurization time and temperature for fabrication of Cu<sub>2</sub>ZnSnS<sub>4</sub> (CZTS) thin films,” *Superlattices and Microstructures*, vol. 126, pp. 32–41, 2019.
- [156] S. Exarhos, E. Palmes, R. Xu and L. Mangolini, “Oxide-induced grain growth in CZTS nanoparticle coatings,” *RSC Advances*, vol. 7, no. 41, pp. 25575–25581, 2017.
- [157] Y. Wang, Y. Huang, A. Y. Lee, C. F. Wang and H. Gong, “Influence of sintering temperature on screen printed Cu<sub>2</sub>ZnSnS<sub>4</sub> (CZTS) films,” *Journal of Alloys and Compounds*, vol. 539, pp. 237–241, 2012.
- [158] P. R. Ghediya and T. K. Chaudhuri, “Doctor-blade printing of Cu<sub>2</sub>ZnSnS<sub>4</sub> films from microwave-processed ink,” *Journal of Materials Science: Materials in Electronics*, vol. 26, no. 3, pp. 1908–1912, 2015.
- [159] M. Mokhtarimehr, *Sustainable photovoltaics –Cu<sub>2</sub>ZnSnS<sub>4</sub> thin films produced by the conversion of mechano-chemical synthesised precursors*, Newcastle Upon Tyne: Northumbria University, 2018.

- [160] Y. Cao, J. V. Caspar, M. S. Denny (Jr.), L. K. Johnson, M. Lu and D. R. Radu, "CZTS/Se precursor inks and methods for preparing CZTS/Se thin films and CZTS/Se-based photovoltaic cells". U.S. Patent 9105796, 11 August 2015.
- [161] X. Zhang, E. Fu, Y. Wang and C. Zhang, "Fabrication of Cu<sub>2</sub>ZnSnS<sub>4</sub> (CZTS) Nanoparticle Inks for Growth of CZTS Films for Solar Cells," *Nanomaterials*, vol. 9, no. 3, p. 336, 2019.
- [162] Y. Qu, G. Zoppi and N. S. Beattie, "The role of nanoparticle inks in determining the performance of solution processed Cu<sub>2</sub>ZnSn(S,Se)<sub>4</sub> thin film solar cells," *Progress in Photovoltaics: Research and Applications*, vol. 24, no. 6, pp. 836-845, 2016.
- [163] T. Todorov, H. Hillhouse, S. Aazou, Z. Sekkat, O. Vigil-Galán, S. Deshmukh, R. Agrawal, S. Bourdais, M. Valdés, P. Arnou, D. Mitzi and P. Dale, "Solution-based synthesis of kesterite thinfilm semiconductors," *Journal of Physics: Energy*, vol. 2, no. 1, p. 012003, 2020.
- [164] N. J. Carter, W.-C. Yang, C. K. Miskin, C. J. Hages, E. A. Stach and R. Agrawal, "Cu<sub>2</sub>ZnSn(S,Se)<sub>4</sub> solar cells from inks of heterogeneous Cu–Zn–Sn–S nanocrystals," *Solar Energy Materials & Solar Cells*, vol. 124, pp. 189-196, 2014.
- [165] A. Krishnan, G. Vishnu and P. Kannan, "Rapid microwave synthesis of Cu<sub>2</sub>ZnSnS<sub>4</sub> nanocrystals for photovoltaic junctions," *International Journal of Energy Research*, vol. 43, no. 1, pp. 589-595, 2019.
- [166] T. M. Ng, *Synthesis and characterisation of copper zinc tin sulphide photovoltaic materials in bulk and single crystal forms*, Bath: University of Bath, 2018.
- [167] C. K. Miskin, W.-C. Yang, C. J. Hages, N. J. Carter, C. S. Joglecar, E. A. Stach and R. Agrawal, "9.0% efficient Cu<sub>2</sub>ZnSn(S,Se)<sub>4</sub> solar cells from selenized nanoparticle inks," *Progress in Photovoltaics: Research and Applications*, vol. 23, no. 5, pp. 654-659, 2015.
- [168] D. B. Mitzi, Y. Min, W. Liu, A. J. Kellock, S. Jay Chey, L. Gignac and A. G. Schrott, "Hydrazine-based deposition route for device-quality CIGS films," *Thin Solid Films*, vol. 517, no. 7, pp. 2158-2162, 2009.

- [169] T. H. Nguyen, W. Septina, S. Fujikawa, F. Jiang, T. Harada and S. Ikeda, "Cu<sub>2</sub>ZnSnS<sub>4</sub> thin film solar cells with 5.8% conversion efficiency obtained by a facile spray pyrolysis technique," *RSC Advances*, vol. 5, no. 95, pp. 77565-77571, 2015.
- [170] S. Cisse, M. Covei, D. Jean Jude and A. Duta, "Thin-Film FTO-ZnO-CZTS Solar Cells Fully Deposited by Spray Pyrolysis," *American Journal of Materials Synthesis and Processing*, vol. 4, no. 1, pp. 1-8, 2019.
- [171] S. Zhuk, A. Kushwaha, T. K. Wong, S. Masudy-Panah, A. Smirnov and G. K. Dalapati, "Critical review on sputter-deposited Cu<sub>2</sub>ZnSnS<sub>4</sub> (CZTS) based thin film photovoltaic technology focusing on device architecture and absorber quality on the solar cells performance," *Solar Energy Materials and Solar Cells*, vol. 171, pp. 239-252, 2017.
- [172] G. Brammertz, M. Buffière, S. Oueslati, H. El Anzeery, K. Ben Messaoud, S. Sahayaraj, C. Köble, M. Meuris and J. Poortmans, "Characterization of defects in 9.7% efficient Cu<sub>2</sub>ZnSnSe<sub>4</sub>-CdS-ZnO solar cells," *Applied Physics Letters*, vol. 103, no. 16, p. 163904, 2013.
- [173] J. Li, H. Wang, M. Luo, J. Tang, C. Chen, W. Liu, F. Liu, Y. Sun, J. Han and Y. Zhang, "10% Efficiency Cu<sub>2</sub>ZnSn(S,Se)<sub>4</sub> thin film solar cells fabricated by magnetron sputtering with enlarged depletion region width," *Solar Energy Materials and Solar Cells*, vol. 149, pp. 242-249, 2016.
- [174] R. Kukla, "Magnetron sputtering on large scale substrates: an overview on the state of the art," *Surface and Coatings Technology*, vol. 93, no. 1, pp. 1-6, 1997.
- [175] C. Zhang, J. Tao and J. Chu, "An 8.7% efficiency co-electrodeposited Cu<sub>2</sub>ZnSnS<sub>4</sub> photovoltaic device fabricated via a pressurized post-sulfurization process," *Journal of Materials Chemistry C*, vol. 6, no. 4, pp. 13275-13282, 2018.
- [176] TATA Steel, "Tata Steel Plating | Tata Steel in Europe," 2021. [Online]. Available: <https://www.tatasteeleurope.com/ts/about-us/sites-and-facilities/plating>. [Accessed 15 February 2021].

- [177] D. Colombara, A. Crossay, L. Vauche, S. Jaime, M. Arasimowicz, P. Grand and P. J. Dale, "Electrodeposition of kesterite thin films for photovoltaic applications: Quo vadis?," *Physica Status Solidi A*, vol. 212, no. 1, pp. 88-102, 2015.
- [178] J. J. Scragg, "Section 2.2 - Electrodeposition of Metallic Precursors: Experimental Approaches for Cu<sub>2</sub>ZnSnS<sub>4</sub> Precursor Production," in *Copper Zinc Tin Sulfide Thin Films for Photovoltaics: Synthesis and Characterisation by Electrochemical Methods*, Berlin, Springer-Verlag, 2011, pp. 19-23.
- [179] F. Jiang, S. Ikeda, T. Harada and M. Matsumura, "Pure Sulfide Cu<sub>2</sub>ZnSnS<sub>4</sub> Thin Film Solar Cells Fabricated by Preheating an Electrodeposited Metallic Stack," *Advanced Energy Materials*, vol. 4, no. 7, p. 1301381, 2014.
- [180] J.-O. Jeon, K. D. Lee, L. S. Oh, S.-W. Seo, D.-K. Lee, H. Kim, J.-h. Jeong, M. J. Ko, B. S. Kim, H. J. Son and J. Y. Kim, "Highly Efficient Copper–Zinc–Tin–Selenide (CZTSe) Solar Cells by Electrodeposition," *ChemSusChem*, vol. 7, no. 4, pp. 1073-1077, 2014.
- [181] L. Vauche, L. Risch, Y. Sánchez, M. Dimitrievska, M. Pasquinelli, T. Goislard de Monsabert, P. Philippe Grand, S. J. Ferrer and E. Saucedo, "8.2% pure selenide kesterite thin-film solar cells from large-area electrodeposited precursors," vol. 24, no. 1, pp. 38-51, 2016.
- [182] X. He, H. Shen, J. Pi, C. Zhang and Y. Hao, "Synthesis of Cu<sub>2</sub>ZnSnS<sub>4</sub> films from sequentially electrodeposited," *Journal of Materials Science: Materials in Electronics*, vol. 24, no. 11, pp. 4578-4584, 2013.
- [183] H. Araki, Y. Kubo, A. Mikaduki, K. Jimbo, W. S. Maw, H. Katagiri, M. Yamazaki, K. Oishi and A. Takeuchi, "Preparation of Cu<sub>2</sub>ZnSnS<sub>4</sub> thin films by sulfurizing electroplated precursors," *Solar Energy Materials and Solar Cells*, vol. 93, no. 6-7, pp. 996-999, 2009.
- [184] R. Djemour, M. Mousel, A. Redinger, L. Gütay, A. Crossay, D. Colombara and P. J. S. S. Dale, "Detecting ZnSe secondary phase in Cu<sub>2</sub>ZnSnSe<sub>4</sub> by room temperature photoluminescence," *Applied Physics Letters*, vol. 102, no. 22, p. 222108, 2013.

- [185] D. Colombara, E. Victoria, C. Robert, A. Crossay, A. Taylor, M. Guennou, M. Arasimowicz, J. C. B. Malaquias, R. Djemour and P. J. Dale, "Quantification of surface ZnSe in Cu<sub>2</sub>ZnSnS<sub>4</sub>-based solar cells by analysis of the spectral response," *Solar Energy Materials and Solar Cells*, vol. 123, pp. 220-227, 2014.
- [186] J. J. Scragg, P. J. Dale and L. M. Peter, "Synthesis and characterization of Cu<sub>2</sub>ZnSnS<sub>4</sub> absorber layers by an electrodeposition-annealing route," *Thin Solid Films*, vol. 517, no. 7, p. 2481–2484, 2009.
- [187] J. J. Scragg, P. J. Dale, L. M. Peter, G. Zoppi and I. Forbes, "New routes to sustainable photovoltaics: evaluation of Cu<sub>2</sub>ZnSnS<sub>4</sub> as an alternative absorber material," *Physica Status Solidi B*, vol. 245, no. 9, pp. 1772-1778, 2008.
- [188] J. J. Scragg, P. J. Dale and L. M. Peter, "Towards sustainable materials for solar energy conversion: Preparation and photoelectrochemical characterization of Cu<sub>2</sub>ZnSnS<sub>4</sub>," *Electrochemistry Communications*, vol. 10, no. 4, p. 639–642, 2008.
- [189] J. J. Scragg, "Section 2.7 - Electrodeposition of Metallic Precursors: Electrodeposition of Sn: The Methane Sulfonic Acid Electrolyte," in *Copper Zinc Tin Sulfide Thin Films for Photovoltaics: Synthesis and Characterisation by Electrochemical Methods*, Berlin, Springer-Verlag, 2011, pp. 33-36.
- [190] R. N. Bhattacharya, "3.6%-CZTSS Device Fabricated From Ionic Liquid Electrodeposited Sn Layer," *The Open Surface Science Journal*, vol. 5, pp. 21-24, 2013.
- [191] R. N. Bhattacharya and J. Y. Kim, "Cu-Zn-Sn-S Thin Films from Electrodeposited Metallic Precursor Layers," *The Open Surface Science Journal*, vol. 4, pp. 19-24, 2012.
- [192] J. J. Scragg, "Section 2.8 - Electrodeposition of Metallic Precursors: Electrodeposition of Zn from an Acid Chloride Electrolyte," in *Copper Zinc Tin Sulfide Thin Films for Photovoltaics: Synthesis and Characterisation by Electrochemical Methods*, Berlin, Springer-Verlag, 2011, pp. 42-47.
- [193] Y. D. Gamburg and G. Zangari, "Technologies for the Electrodeposition of Metals and Alloys: Electrolytes and Processes," in *Theory and Practise of Metal Electrodeposition*, New York, Springer, 2011, pp. 265-316.

- [194] T. Pearson, J. K. Dennis, J. F. Houlston and M. Dorey, "The Effect of Pulsed Reversed Current on the "Hole Throwing Power" of Acid Copper Electrolytes containing Organic Additives," *Transactions of the IMF*, vol. 69, no. 1, pp. 9-14, 1991.
- [195] R. J. Kee, A. M. Colclasure and H. Zhu, "FUEL CELLS – SOLID OXIDE FUEL CELLS | Cells and Stacks," in *Encyclopedia of Electrochemical Power Sources*, J. Garche, Ed., Amsterdam, Elsevier, 2009, pp. 51-62.
- [196] M. A. M. Ibrahim, "Improving the Throwing Power of Acidic Zinc Sulfate Electroplating Baths," *Journal of Chemical Technology and Biotechnology*, vol. 75, no. 8, pp. 745-755, 2000.
- [197] K. K. Maniam and S. Paul, "A Review on the Electrodeposition of Aluminum and Aluminum Alloys in Ionic Liquids," *Coatings*, vol. 11, no. 1, p. 80, 2021.
- [198] H. Hayashida and R. Nakahara, "Studies of Throwing Power in Various Non-Cyanide Zinc Plating Baths," *Journal of the Metal Finishing Society of Japan*, vol. 22, no. 7, pp. 326-334, 1971.
- [199] M. Wadowska, T. Frade, D. Siopa, K. Lobato and A. Gomes, "ZnO Nanostructured Films Electrodeposited at Room Temperature," *ECS Electrochemistry Letters*, vol. 2, no. 7, p. D40, 2013.
- [200] L. Guo, Y. Zhu, O. Gunawan, T. Gokmen, V. R. Deline, S. Ahmed, L. T. Romankiw and H. Deligianni, "Electrodeposited Cu<sub>2</sub>ZnSnSe<sub>4</sub> Thin Film Solar Cell with 7% Power Conversion Efficiency," *Progress in Photovoltaics: Research and Applications*, vol. 22, no. 1, pp. 58-68, January 2014.
- [201] T. Ratz, G. Brammertz, R. Caballero, M. León, S. Canulescu, J. Schou, L. Gütay, D. Pareek, T. Taskesen, D.-H. Kim, J.-K. Kang, C. Malerba, A. Redinger, E. Saucedo, B. Shin, H. Tampo, K. Timmo, N. D. Nguyen and B. Vermang, "Physical routes for the synthesis of kesterite," *Journal of Physics: Energy*, vol. 1, no. 4, p. 042003, 2019.
- [202] Y. Ren, "Annealing of Cu<sub>2</sub>ZnSn(S,Se)<sub>4</sub> Thin Films," Uppsala Universitet, Uppsala, Sweden, 2017.

- [203] L. Vauche, J. Dubois, A. Laparre, F. Mollica, R. Bodeux, S. Delbos, C. M. Ruiz, M. Pasquinelli, F. Bahi, T. G. de Monsabert, S. Jaime, S. Bodnar and P.-P. Grand, “Cu<sub>2</sub>ZnSnSe<sub>4</sub> thin film solar cells above 5% conversion efficiency from electrodeposited Cu Sn Zn precursors,” *Physica Status Solidi A*, vol. 211, no. 9, pp. 2082-2085, 2014.
- [204] A. Ziti, B. Hartiti, H. Labrim, S. Fadili, A. Batan, A. Ridah and P. Thevenin, “Growth and Characterization of CZTS Thin Films Synthetized by Electrodeposition Method for Photovoltaic Applications,” *IOP Conference Series: Materials Science and Engineering*, vol. 948, p. 012025, 2020.
- [205] H. Borate, A. Bhorde, A. Waghmare, S. Nair, S. Pandharkar, A. Punde, P. Shinde, P. Vairale, V. Jadkar, R. Waykar, S. Rondiya, Y. Hase, R. Aher, N. Patil, M. Prasad and S. Jadkar, “Single-step Electrochemical Deposition of CZTS Thin Films with Enhanced Photoactivity,” *ES Materials and Manufacturing*, vol. 11, pp. 30-39, 2021.
- [206] J. K. Larsen, J. J. Scragg, N. Ross and P.-B. C., “Band Tails and Cu–Zn Disorder in Cu<sub>2</sub>ZnSnS<sub>4</sub> Solar Cells,” *ACS Applied Energy Materials*, vol. 3, no. 8, pp. 7520-7526, 2020.
- [207] M. A. Olgar, A. Altuntepe, S. Erkan and R. Zan, “Fabrication of Cu-rich CZTS thin films by two-stage process: Effect of gas flow-rate in sulfurization process,” *Journal of Molecular Structure*, vol. 1230, p. 129922, 2021.
- [208] G. K. Gupta, A. Garg and A. Dixit, “Electrical and impedance spectroscopy analysis of sol-gel derived spin coated Cu<sub>2</sub>ZnSnS<sub>4</sub> solar cell,” *Journal of Applied Physics*, vol. 123, no. 1, p. 013101, 2018.
- [209] M. Valdés, Y. Di Iorio, K. Castañeda, R. E. Marotti and M. Vázquez, “Cu<sub>2</sub>ZnSnS<sub>4</sub> thin films prepared by sulfurization of co-electrodeposited metallic precursors,” *Journal of Applied Electrochemistry*, vol. 47, no. 6, pp. 755-765, 2017.
- [210] V. V. Rakitin, M. V. Gapanovich, A. M. Kolesnikova, D. M. Sedlovets, S. A. Bashkurov, V. S. Hekkel, Y. V. Osakovich, V. F. Gremenok and G. F. Novikov, “The influence of high-temperature annealing of electrochemically deposited Cu-Zn-Sn layers on the composition and structure of kesterite films — absorbing layers of solar cells,” *Russian Chemical Bulletin (International Edition)*, vol. 68, no. 6, pp. 1171-1177, 2019.

- [211] F. Jiang, S. Ikeda, Z. Tang, T. Minemoto, W. Septina, T. Harada and M. Matsumura, "Impact of alloying duration of an electrodeposited Cu/Sn/Zn metallic stack on properties of Cu<sub>2</sub>ZnSnS<sub>4</sub> absorbers for thin-film solar cells," *Progress in Photovoltaics: Research and Applications*, vol. 23, no. 12, pp. 1884-1895, 2015.
- [212] Y. Lin, S. Ikeda, W. Septina, Y. Kawasaki, T. Harada and M. Matsumura, "Mechanistic aspects of preheating effects of electrodeposited metallic precursors on structural and photovoltaic properties of Cu<sub>2</sub>ZnSnS<sub>4</sub> thin films," *Solar Energy Materials & Solar Cells*, vol. 120, no. A, pp. 218-225, 2014.
- [213] L. Vauche, J. Dubois, A. Laparre, M. Pasquinelli, S. Bodnar, P.-P. Grand and S. Jaime, "Rapid thermal processing annealing challenges for large scale Cu<sub>2</sub>ZnSnS<sub>4</sub> thin films," *Physica Status Solidi A*, vol. 212, no. 1, pp. 103-108, 2015.
- [214] R. Lechner, S. Jost, J. Palm, M. Gowtham, F. Sorin, B. Louis, H. Yoo, R. A. Wibowo and R. Hock, "Cu<sub>2</sub>ZnSn(S,Se)<sub>4</sub> solar cells processed by rapid thermal processing of stacked elemental layer precursors," *Thin Solid Films*, vol. 535, pp. 5-9, 2013.



## **2 Experimental Techniques**

### **2.1 Electrodeposition**

#### **2.1.1 Electrodeposition of Metals**

The electrodeposition of metals, sometimes referred to as electroplating, is the passage of electric current through an electrolytic solution such that positive metal ions in the solution are reduced to form metal atoms at the surface of one of the electrodes. This would normally plate-out to form a film, the thickness of which would be dependent upon the total electric charge passed per unit area and the oxidation state of the metal ion in the solution during the electroplating process for a given electrolyte and electric potential. Electroplating can be carried out using some very simple apparatus, for example a 1.5 volt battery connected to two electrodes, the electrodes being immersed in an electrolyte containing the desired metal salt. The coating of a ten pence coin with copper from a copper sulphate solution is a well-known experiment [1]. This rudimentary setup, however, offers very little control over the thickness or morphology of the film, and accurate control is crucial when attempting to manufacture a compound that is very sensitive to the ratios and uniform distribution of its constituent elements. For this reason, all electrodeposition experiments for this project were carried out using a potentiostat/galvanostat, which enabled precise control of current and voltage conditions within a structured time frame.

#### **2.1.2 The Functions of a Potentiostat/Galvanostat**

The main purpose of a potentiostat/galvanostat is to accurately control either the current or electric potential while measuring the other. The parameter being controlled can be fixed for the duration of the experiment, but it is also common for it to follow a sequence prescribed by the user, which could include a continuous sweep, a sinusoidal wave, a series of fixed values, or many other functions depending on the nature of the experiment being performed. For all of the experiments described in this project, aqueous electrolytes were used, and the potentiostat/galvanostat was set up as a three electrode cell. A three electrode cell

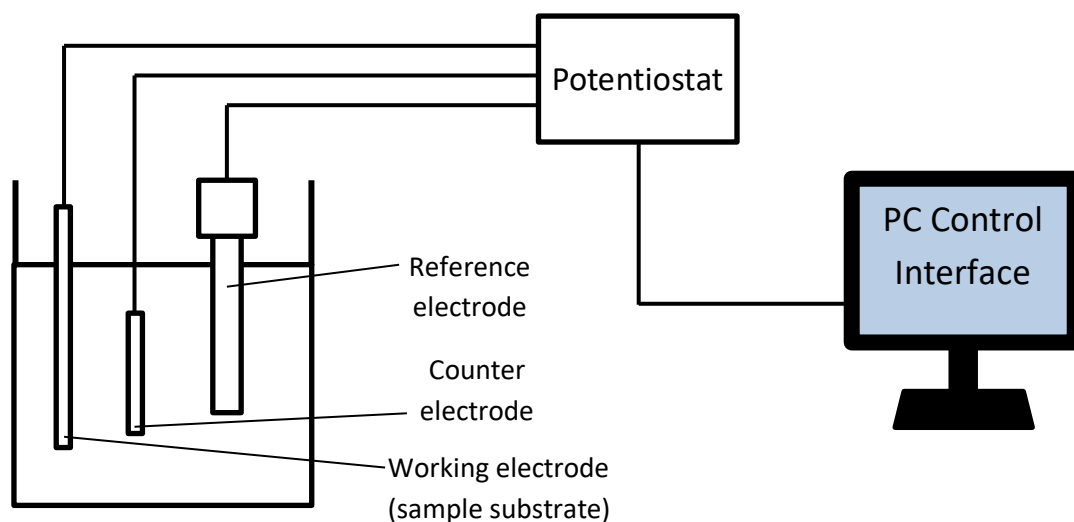


**Figure 2-1 - A simple schematic of a potentiostat/galvanostat with a three electrode setup.**

comprises of a working electrode, a counter electrode and a reference electrode (see Figure 2-1). The current flowing during the experiment is between the working electrode and the counter electrode, but the electric potential is measured between the working electrode and the reference electrode. In the context of using an aqueous electrolyte containing a metallic salt, the reference electrode would normally be a small, self-contained vessel that contains a metal – metal salt compound with its own reduction-oxidation (redox) potential. This reference electrode is electrically connected to the potentiostat/galvanostat via a high resistance terminal and to the electrolyte via a porous membrane; hence the current flowing through the reference electrode is negligible. It is important that the reference electrode is positioned as close to the working electrode as possible in order to minimise the amount of potential dropped across the resistance of the electrolyte between the two electrodes.

For the electrodeposition experiments described here, the setup was such that the sample substrate acted as the working electrode at which metal ions were reduced to form metal atoms. The counter electrode chosen was a platinum gauze as this is a largely inert material and did not react with any of the solutions during the course of the experiments. Being a gauze, it also allowed the diffusion of electrolyte through the electrode also provides a large surface area, minimising the restriction to the rate of reaction. The reference electrode chosen varied depending on the composition of

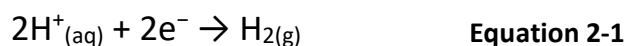
the electrolyte, but for the majority of experiments, a silver – silver chloride (Ag|AgCl) electrode in 3 M potassium chloride was used for acidic solutions and a mercury – mercuric oxide (Hg|HgO) electrode in 5 M potassium hydroxide was used for alkaline solutions.

Advice had been provided by an experienced electrochemist that using fixed potential (potentiostatic) deposition would provide superior control of the purity and morphology of the deposited films, therefore many of the deposition experiments were carried out potentiostatically. In order to establish a suitable potential for deposition, cyclic voltammetry was carried out as part of the preliminary experimentation.

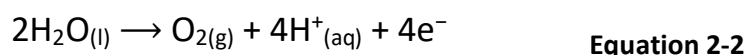
### **2.1.3 Cyclic Voltammetry**

Cyclic voltammetry is a controlled sweep through a range of electric potentials. The potentiostat/galvanostat will normally end at the potential with which it starts. In preparation for electrodeposition experiments, it is useful to carry out cyclic voltammetry where the initial potential will be set at a voltage where no reactions are expected to occur. The potential can then be swept firstly in a negative direction until it reaches a set limit, at which point the scan direction will reverse and sweep the potential in a positive direction. The potential will then reach another set limit, usually more positive than the starting potential, at which it will reverse direction again and sweep in a negative direction until it returns to the starting potential. The current flowing throughout the process will be measured and plotted against the voltage, and the resulting curve is called a voltammogram. The purpose of obtaining a voltammogram is to acquire information about the reactions taking place at different potentials based on the electric current data. A negative current represents electrons flowing from the potentiostat/galvanostat to the working electrode and into the sample. This can occur as positively charged metal ions in an electrolyte are reduced to metal atoms at the surface of the sample. This process will usually concur with a peak in the negative current seen on the voltammogram, referred to as a deposition peak [2]. The position of the deposition peak relates to the standard reduction potential of the metal being deposited, but is also affected by other factors, including the electrolyte ingredients, electrolyte acidity and substrate material [3, 4].

In electrodeposition, it is normally desirable for the metal ions to adhere to their substrate and form a metallic film (in some conditions, a poorly adhering powder-like deposit can form [5, 6]). A negative current can also occur as hydrogen ions ( $H^+$ ) receive electrons at the surface of the sample to make hydrogen gas ( $H_2$ ). This is referred to as hydrogen evolution and is an unwanted, parasitic reaction. As well as reducing the deposition efficiency, hydrogen evolution can cause damage to the deposited films in the form blisters, and pitting can also be seen as it blocks the deposition of metal at the sites at which it evolves. The chemical reaction equation for hydrogen evolution is as follows [6]:



The flow of electric current in the negative direction would require the extraction of electrons from the electrolyte via a reaction at the counter electrode, for example the breakdown of water through an oxidation reaction [7]:



When the current is registering as positive, the electrons are flowing out of the sample through the working electrode connection and into the potentiostat/galvanostat. This can occur as a metal film on the sample is stripped and dissolves into the electrolyte. In this case, the metal atoms are losing electrons as they are oxidised. This will usually concur with a peak in the positive current on the voltammogram and is referred to as a stripping peak [2]. A positive current can also occur if oxygen is evolving at the working electrode. A positive current would also require electrons to re-enter the electrolyte via a reaction at the counter electrode, such as the breakdown of water via a reduction reaction [8]:



This would be observed as hydrogen evolution at the counter electrode. An example of a voltammogram can be seen in Figure 2-2. As the surface of the sample can undergo some changes due to the chemical processes occurring during cyclic voltammetry, the current at the end of the cycle may not exactly match that at the start, giving an apparent hysteresis. In addition to this, the current characteristics are

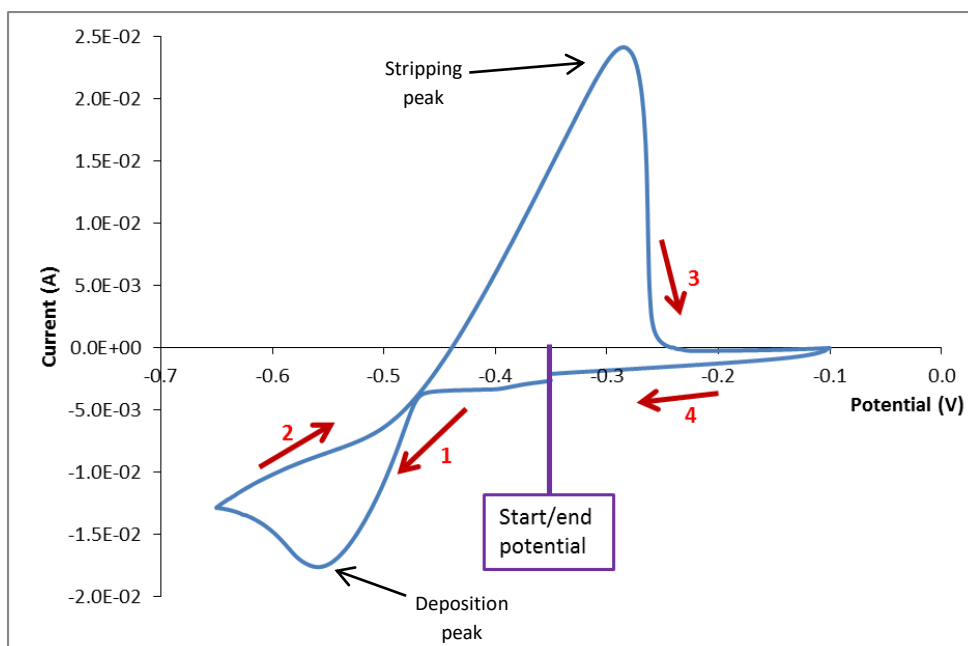


**Figure 2-2 - An example of a voltammogram showing deposition and stripping peaks. The voltammogram was obtained by performing cyclic voltammetry using a methanesulfonic acid based electrolyte for the deposition of tin on a 1 cm<sup>2</sup> copper surface. An Ag|AgCl in 3 M potassium chloride reference electrode was used. The red arrows indicate the direction of sweep in potential for different stages of the voltammetric cycle.**

sensitive to the surface concentration of species being reduced/oxidised at the electrodes [4], meaning that a deposition peak is often only visible when scanning in a negative direction. Despite this, the position of the deposition peak from a single voltammetric sweep can be used to inform the selection of the deposition potential as it is representative of a sample that has not undergone any pre-treatment, in common with samples that undergo deposition. For the experiments carried out in this project, the potential limits were selected using reference [9] as an initial guide, and then adjusted using trial and error processes, depending upon whether clear deposition and stripping peaks were observed and their relative positions.

#### **2.1.4 The Electrochemical Series**

The electrochemical series is a list which ranks elements based on their ability to act as an oxidising (or reducing) agent. Typically, the electrochemical potential associated with each element is its redox potential measured with respect to that of hydrogen [10]. The more positive the potential, the stronger the element is as an

oxidising agent. The more negative the potential, the stronger the element is as a reducing agent. When layers of different elements are being electrodeposited sequentially, it is possible that a pre-existing electrodeposit can become oxidised and dissolved during the electrodeposition of a subsequent element, if the element being deposited is a stronger oxidising agent. This means that it is important to consider the ranking of the elements in the electrochemical series prior to attempting their deposition, particularly when depositing a multi-layered stack. An example of the electrochemical series can be seen in Figure 2-3. It can be noted that the standard redox potentials of copper(II), zinc(II) and tin(II) are +0.344, -0.762 and -0.136 volts respectively. This would suggest that the preferred order of deposition would be

<i>Metal</i>	<i>Valency of ion</i>	<i>Normal electrode potential (volts)</i>	<i>Metal</i>	<i>Valency of ion</i>	<i>Normal electrode potential (volts)</i>
Gold	1	+ 1.68	Indium	1	— 0.3
„	3	+ 1.4	Thallium	1	— 0.336
Chlorine	1	+ 1.3594	Indium	3	— 0.34
Platinum	2	+ 1.2	Cadmium	2	— 0.402
Bromine	1	+ 1.0659	Iron	2	— 0.440
Iridium	3	+ 1.0	Cellium	2	— 0.5
Ruthenium	2	+ 0.45	Vanadium	2	— 1.5
Oxygen	2	+ 0.3976	Aluminium	3	— 1.67
Copper	2	+ 0.344	Beryllium	2	— 1.70
Bismuth	3	+ 0.20	Titanium	2	— 1.75
Antimony	3	+ 0.1	Magnesium	2	— 2.38
Tungsten	3	+ <0.05	Sodium	1	— 2.71
Hydrogen	1	± 0.000	Calcium	2	— 2.8
Iron	3	— 0.04	Strontium	2	— 2.89
Lead	2	— 0.126	Barium	2	— 2.90
Tin	2	— 0.136	Potassium	1	— 2.92
Molybdenum	3	— 0.2	Rubidium	1	— 2.93
Nickel	2	— 0.25	Lithium	1	— 3.0
Cobalt	2	— 0.28			

**Figure 2-3 – An example of a table of elements listed in order of their redox potential with respect to hydrogen (referred to here as the Normal Electrode Potential), the order of the electrochemical series. This table is taken from [10].**

copper first, followed by tin, and then finally zinc, in order to avoid the oxidation and therefore dissolution of any of the deposited layers (assuming that the metal ions in each of the deposition electrolytes are in a 2<sup>+</sup> oxidation state).

### 2.1.5 Electrodeposition of Copper

For all of the copper deposition experiments, an aqueous alkaline electrolyte containing copper(II) sulphate was used and had the following composition:

3 M Sodium hydroxide

0.1 – 0.2 M Copper sulphate pentahydrate

0.2 – 0.4 M D-Sorbitol

0.025 vol. % Empigen BB<sup>TM</sup> surfactant

This composition is based on that reported in [11], where the purpose of the sorbitol is to act as a complexing agent and the purpose of the Empigen BB<sup>TM</sup> surfactant is to act as a levelling agent. A surfactant can affect the morphology of a deposit due to its concentration dependent activity during electrodeposition [12]. It acts as a levelling agent by selectively adsorbing onto surface sites on projecting regions, inhibiting the addition of further material to those sites [9]. A complexing agent forms complex ions with the metal ions in the electrolyte, which affect their transport characteristics in the solution. Complexing agents are added to improve the smoothness and grain structure of the deposited films [13]. The components were added sequentially to distilled water, the sodium hydroxide being first, then the sorbitol, followed by copper sulphate, and finally the surfactant. The solution required heating to approximately 50 °C on a hotplate for approximately 10 minutes in order for the copper sulphate to fully dissolve, and was allowed to cool to room temperature before being used for electrodeposition. All copper deposition experiments were carried out potentiostatically, using a three electrode cell, with a mercury – mercuric oxide (Hg|HgO) reference electrode. This is sometimes referred to as chronoamperometry if there is a step in the potential during the deposition process. The chemical equation for the reduction of copper from a 2+ oxidation state (as would be the case with the selected electrolyte, see above) is as follows [14]:



Copper was predominantly deposited as the first of the three required metallic elements. The substrates used were glass coated with either fluorine-doped tin oxide (FTO, purchased from Solaronix Ltd.) or sputtered molybdenum (supplied by M-Solv Ltd.), with the FTO having a sheet resistance of either  $\sim 7 \Omega/\square$  (TEC 7) or  $\sim 15 \Omega/\square$  (TEC 15). Some of the copper films were deposited onto tin, and required differing deposition conditions to that deposited onto FTO or molybdenum (more details of which are given in chapter 3). The depositions onto FTO followed a two-step process in which the initial potential was selected such that no current expected to be flowing. This is partly to allow the system to equilibrate prior to deposition, but also in order to create a useful point of reference in any current-time graphs that may be generated. These potentials were chosen based on the results of cyclic voltammetry and were refined through trial and error. Rather than repeating cyclic voltammetry experiments with a molybdenum substrate, which would have risked damaging the molybdenum, the deposition potentials were, at first, the same as the optimised conditions for FTO, and were refined through a process of trial and error (more details in chapter 3).

Copper was always deposited at room temperature, the electrolyte having been left to cool for at least an hour between being prepared and the deposition taking place, and was deposited predominantly using a stagnant electrolyte. In order to try and suppress the effect of deposition rate limitation due to the diffusion speed of the metal ions in the solution, trials were also conducted with a stirred electrolyte, and with the use of a rotating disc electrode (RDE). The RDE was used to place the substrate horizontally into the electrolyte and spin it at a finely controlled rate (see section 2.1.6).

### **2.1.6 The Rotating Disc Electrode**

A rotating disc electrode (RDE) can rotate a sample at a controlled frequency while maintaining electrical contact with the working electrode terminal of a potentiostat/galvanostat. The centrifugal force on the solution in contact with the spinning sample causes it to flow outwards away from the sample, drawing fresh electrolyte from beneath to replace it. In electrodeposition experiments, the purpose of this is to create a laminar flow of electrolyte towards the sample surface in order



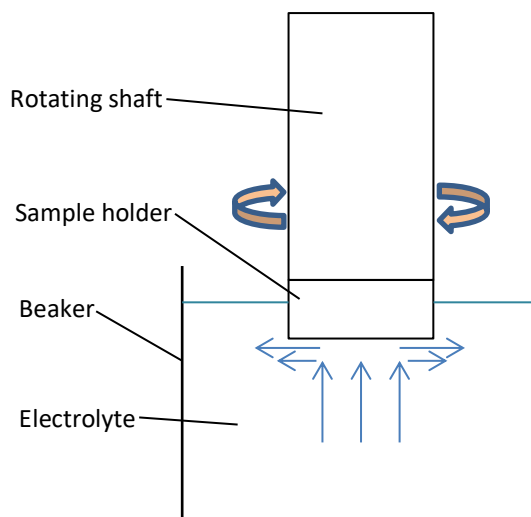


**Figure 2-4 - A diagram (not to scale) showing how the RDE is assembled and positioned when in use. The blue arrows give an indication of how the electrolyte is expected to flow when the RDE is rotating.**

that the concentration of ions in the solution in immediate proximity to the sample surface remains constant with time (see Figure 2-4 to aid understanding). This eliminates the problem of the deposition rate becoming limited by diffusion, without introducing problems (such as uneven thickness and coverage) that are associated with the turbulent flow that occurs when a magnetic stirrer is used. This controlled flow of the electrolyte to the substrate is sometimes referred to as mass transport

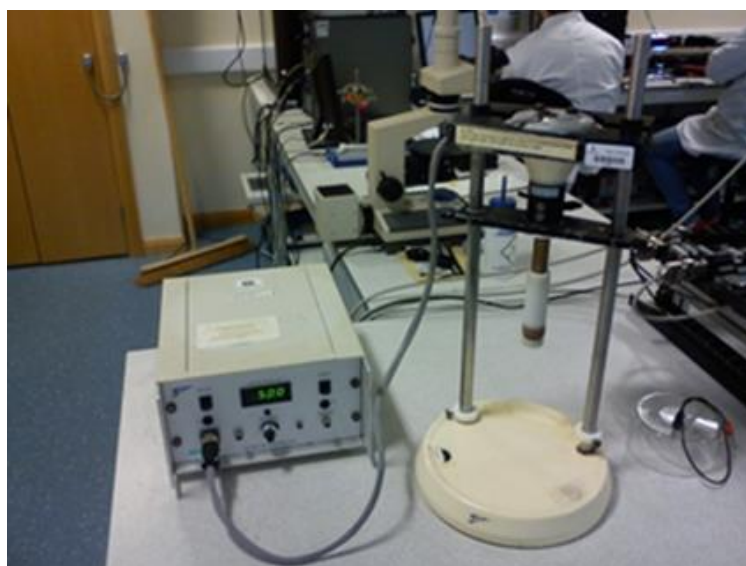


**Figure 2-5 - The rotating disc electrode used in the experiments, which is mounted on an adjustable stand and connected to a control unit.**

control. An RDE also eliminates the problem of diffusion currents causing thicker films at the bottom of a vertical substrate in stagnant solution. This phenomenon occurs as the electrolyte is denser when it has a higher content of metal ions, with less concentrated solution moving in an upward direction. The RDE used for the experiments in this project consisted of a rotating shaft attached below a motor unit that was mounted on a height adjustable stand. The motor unit was powered by a separate control unit with a digital display indicating the rotation rate, with the rate being adjustable in the 1 – 100 Hz range at increments of 0.05 Hz. All experiments involving the RDE were carried out using a rotation rate of 5 Hz as this was reported to lead to even film thicknesses in reference [15] (see Figure 2-5 for a photograph of the equipment). Connectors for the working electrode and working electrode sense terminals for the potentiostat/galvanostat were mounted in a static position, just above the rotating shaft. The sample was placed in a collar-type holder (with an internal diameter of 24 mm) that screwed on to the bottom of the rotating shaft.

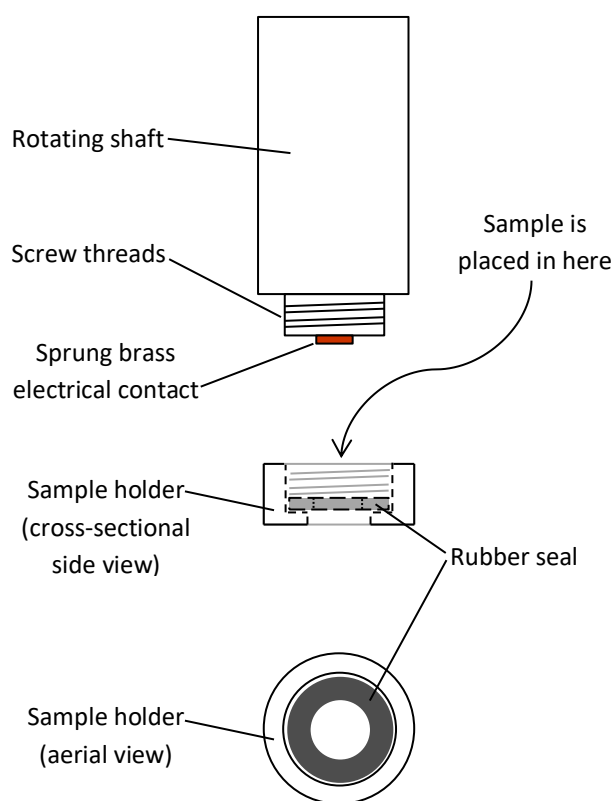


**Figure 2-6 - A diagram (not to scale) showing the design of various components of the Rotating Disc Electrode.**

Electrical connectivity was made with the back of each sample via a sprung brass contact. This brass contact was in turn connected via a cable inside the shaft of the RDE to a sealed ring of mercury around the axle of the RDE, linking to the working electrode and working electrode sense connection terminals for the potentiostat/galvanostat. The sealed mercury ring allowed the shaft to rotate with minimal friction, yet maintained electrical connectivity between the sprung brass contact for the sample and the connection terminals for the potentiostat/galvanostat. A circular rubber seal prevented electrolyte ingress into the sample holder. The rubber seal had an inner diameter of 13 mm, which was the limiting factor for the deposition area. A detailed diagram showing the key components of the RDE can be seen in Figure 2-6.

### **2.1.7 Substrate Preparation**

All substrates were cleaned by treatment in an ultrasonic bath while submerged in acetone for 10 minutes, followed by either ethanol or isopropanol for a further 10 minutes. The substrates were then rinsed and dried. The majority of substrates were dried using a clean, dry nitrogen jet or compressed air; however, for some experiments later in the project, samples were spin dried using a spin coater at 4500 RPM for 40 seconds. This was due to persistent contamination of substrates which was found to be originating from the gas lines. When molybdenum substrates were first used in the project, they were subjected to a further cleaning stage in which they were submerged in 28% ammonium hydroxide for 10 minutes in order to etch off any molybdenum oxides that might be present on the surface. It was found that when this step was omitted, no detriment to the electrodeposited film coverage, morphology or deposition rate were observed and it was therefore discontinued.

In addition to cleanliness, it is also important that the surface area of deposition is a known quantity so that current density can be calculated and a comparison can be made between the electric current data for different samples. In order to achieve this, substrates were masked with either PTFE or Kapton tape leaving an exposed area for deposition of a known surface area. Copper tape was also applied to part of the substrate to improve electrical contact between the FTO or molybdenum and the

connecting clip for the potentiostat/galvanostat. For most electrodeposition trials, the exposed area was 1 cm<sup>2</sup> (utilising 1 cm wide substrates), which simplified calculations for the current density. A schematic diagram of this taping arrangement can be seen in Figure 2-7. Experiments later in the project required larger films to facilitate analysis through X-Ray Diffraction (XRD), and these were most commonly 4 cm<sup>2</sup> and utilised 2 cm wide substrates. In many cases, it was useful to have an area of uncoated substrate at opposing edges of the deposited film so that the thickness of the film could be gauged on both sides by using profilometry. In this instance, a slight modification to the taping arrangement was made and can also be seen in Figure 2-7. When using the RDE, a different shape of substrate and a different taping arrangement was required. The samples used were FTO coated glass cut into 16 mm × 16 mm squares, as this was the largest square that would fit in the RDE sample holder. As the electrical contact to the samples on the RDE contacts the back of the substrates, copper tape was applied around the perimeter of the front of the substrate and wrapped around to the back. Copper tape on the front and edges of the substrate was masked by PTFE tape to prevent contact with the electrolyte, and to leave a 1 cm<sup>2</sup> square of FTO exposed for copper electrodeposition. Initially, this taping arrangement was performed using four separate pieces each of copper tape and PTFE

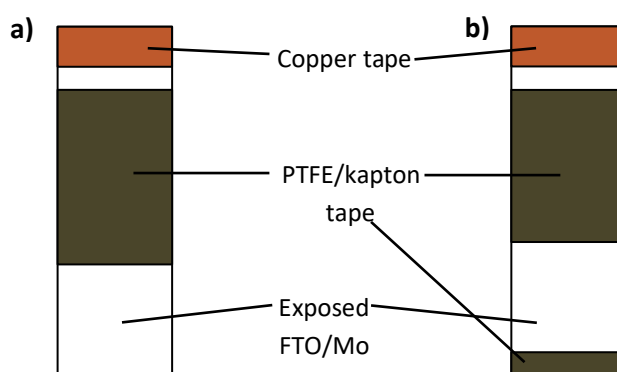


**Figure 2-7 - Diagrams showing how substrates were masked and copper tape was applied to expose only the required deposition area and provide good electrical contact. Substrate a) (left) shows the simplest taping arrangement, whereas substrate b) (right) shows how some of the substrate was masked either side of the deposition area so that profilometry could be performed on two opposing edges of the film.**

tape, but this was difficult to carry out without touching, and therefore contaminating, the exposed FTO. For this reason, the tape was subsequently applied using one piece each of copper tape and PTFE tape, and removing tape from the required areas by scoring it out with a scalpel. While there was initial concern that this could damage the FTO and reduce its conductivity, a quick check using a digital multimeter (in which one probe was placed on the FTO at the front and another on the copper tape at the rear to test for low resistance electrical connectivity) did not detect any problems. A diagram of this taping arrangement is shown in Figure 2-8. This taping arrangement was further modified due to difficulty in removing the tape at the end of deposition, the amount of glue left on the substrate and incidences of accidental contamination, however, it was found that electrolyte ingress around the rubber seal on the RDE was minimal and therefore acted as a suitable mask for the substrate. The new taping arrangement consisted of a thin piece of copper tape applied only to one corner of the conductive side of the substrate and wrapped around to the non-conducting side to make electrical contact with the RDE. The copper tape was covered with a piece of PTFE tape only slightly larger than the

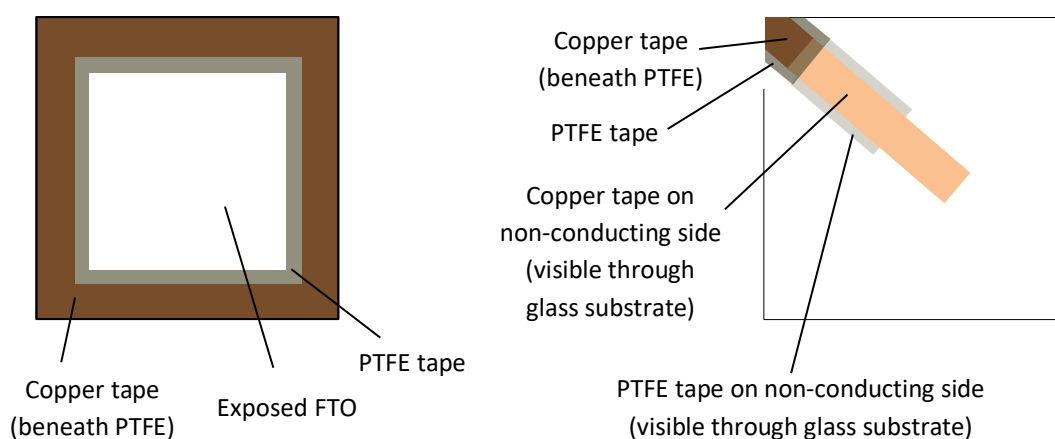
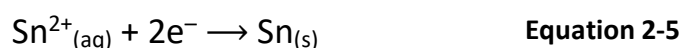


**Figure 2-8 - Diagrams showing how substrates were masked and copper tape was applied for use in the RDE. The diagram on the left shows the earlier taping arrangement, in which copper tape was wrapped over all four edges of the substrate and covered the back surface. The diagram on the right shows the modified arrangement, in which only a small strip of copper tape is applied to one front corner and wrapped to the back to make electrical contact with the RDE terminal. In this case, the rubber seal of the RDE acted as a mask and circular film deposits of 13 mm diameter were formed.**

copper tape. A diagram of this can also be seen in Figure 2-8. In this case, the electrodeposited films were circular and had a diameter of 13 mm. Thickness measurements with a profilometer were still possible as scans were taken diagonally from an uncoated corner onto the electrodeposited film.

### 2.1.8 Electrodeposition of Tin

Tin was the second element to be deposited and was deposited potentiostatically from aqueous electrolytes at room temperature. The electrolytes were un-stirred (stagnant) and a static electrode was used. The deposition potentials were determined using cyclic voltammetry, and the reference electrodes were silver – silver chloride for the acidic electrolyte and mercury – mercuric oxide for the alkaline electrolyte. The silver – silver chloride electrode was not recommended for use in strong alkaline solutions due to risk of damage to the electrode, and similarly the mercury – mercuric oxide electrode was not recommended for use in acidic solutions. The substrates already had copper films deposited onto either FTO coated glass or molybdenum coated glass, and any masking tapes that were used for the deposition of the copper films were left in place. All samples were thoroughly rinsed with deionised water at the end of each electrodeposition process to avoid any cross contamination between deposition stages and electrolytes. The chemical equation for the reduction of tin from a 2+ oxidation state (as would be the case with the selected electrolytes, see below) is as follows [14]:



Some consideration was given to the choice of electrolyte composition - an acidic electrolyte had reportedly produced smooth films with good coverage in [11], however, this involved diluting a concentrated (100%) liquid acid, and there was a desire to avoid handling this for safety reasons. Sodium hydroxide based electrolytes had been used in [16] and [17], but it was reported that this tended to result in islands of tin being deposited onto the copper rather than a continuous homogeneous film. Sodium hydroxide had been used in the deposition of copper in this project and came in the form of pellets that were easy and relatively safe to handle. Further reading on the subject led to reference [18], in which it is reported that, when depositing tin onto

platinum, the coverage and uniformity increased when the concentration of sorbitol was increased. The decision was taken to trial a sodium hydroxide based electrolyte, with the main difference when compared to that reported in [16] and [17] being the large excess of sorbitol. The composition trialled was as follows:

3.0 M Sodium hydroxide

0.1 M Tin(II) chloride pentahydrate

1.0 M D-Sorbitol

For the first round of experiments, there was also the inclusion of 0.1 vol. % Empigen BB<sup>TM</sup> surfactant in an attempt to further improve the smoothness of the deposits.

In later experiments, after having conducted a thorough risk assessment, the acidic electrolyte reported in [11] was used. It had the following composition:

1 M Methanesulfonic acid

50 mM Sn(II) methanesulfonate

0.1 vol. % Empigen BB surfactant

The tin electrolytes were prepared at room temperature under continuous stirring, with the acid or base being added first, followed by the complexing agent (if included), then the tin containing compound, and finally the surfactant (if included). The acidic electrolyte comprised entirely of liquid components and these were added to the water using Eppendorf automated pipettes. In order to prevent tin oxide precipitation in the electrolyte, it was kept refrigerated at 3 – 6 °C and was useable for up to seven days after preparation.

### **2.1.9 Electrodeposition of Zinc**

For the majority of zinc deposition experiments, zinc formed the third layer in the elemental stack, with the deposition taking place onto an electrodeposited tin film, with copper beneath, and molybdenum coated glass as the substrate. Some zinc deposition was carried out onto copper, and in these circumstances the zinc was forming the fourth layer, with there being two copper layers with a tin layer in

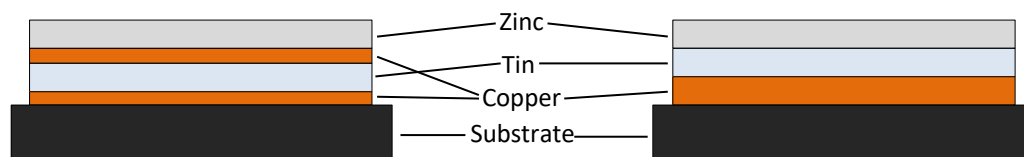


**Figure 2-9 - A schematic diagram showing zinc as the top layer on a four-layer stack (left) and a three layer stack (right).**

between (see Figure 2-9 for a schematic representation). Zinc deposition was carried out at room temperature using aqueous electrolytes and both galvanostatic (chronopotentiometry) and potentiostatic deposition was utilised in different experiments. The chemical equation for the reduction of zinc is as follows [14]:



Seven different electrolyte compositions were trialled in attempts to optimise the uniformity of the zinc films. This was partially due to hydrogen evolution causing damage in the zinc deposition process, but also partially due to issues relating to the zinc grain growth during deposition.

The first batch of zinc deposition experiments were carried out using the zinc electrolyte composition used in [17] and [19]. This had the following formula:

#### **Electrolyte Zn 1.**

Hydrion™ pH 3 buffer solution

2 M Potassium chloride

50 mM Zinc chloride

0.2 wt.% Polyquaternium-2

Hydrion™ pH 3 buffer is a proprietary branded product that is supplied in the form of powder contained in sachets, along with a separate liquid preservative contained in a dropper bottle that can be added optionally. The pH 3 buffer solution was made up according to the manufacturer's instructions (each sachet of powder made 500 mL of buffer solution), including the addition of the preservative, which contained a coloured pH indicator. All other components of this electrolyte were dissolved into the pH 3 buffer solution.



Deposition with this electrolyte was carried out using a range of different deposition potentials. The initial deposition potential was obtained through cyclic voltammetry; however a sequence of less negative potentials were trialled in attempts to limit the amount of hydrogen evolved in the deposition process and minimise the associated effects. In addition to this, modifications to the pH of the electrolyte by using different pH buffers were made for comparative studies, which included deposition – stripping experiments (efficiency testing) and cyclic voltammetry with the zinc component omitted to gauge the contribution of hydrogen evolution to the current flowing. This was to generate voltammograms that could be referred to in order to compare the relative quantity of hydrogen being generated across a range of potentials in electrolytes of differing pH, assuming that all negative current flowing in the absence of a zinc salt component was involved in the generation of hydrogen. For clarity, this process did not involve the physical collection of the hydrogen gas. Although no specific value was selected as a “cut off” point in terms of the acceptability of the quantity of hydrogen evolved, an electrolyte formula that leads to less current being attributed to hydrogen evolution would be considered preferable to any formula that leads to a greater current being attributed to hydrogen evolution.

Deposition experiments were also carried out using the following electrolyte composition, which was taken from [20]:

**Electrolyte Zn 2.**

Zinc chloride – 30 g L<sup>-1</sup>

Ammonium chloride – 120 g L<sup>-1</sup>

Boric acid – 5 g L<sup>-1</sup>

The deposition experiments using this electrolyte were carried out using potentiostatic electrodeposition. In attempts to increase film smoothness, trials were carried out where an organic surfactant (polyquaternium-2) was added to this electrolyte at concentrations of 0.2 wt.% to 0.8 wt.%. It is worth noting here, that literature that referred to electrodeposition for PV applications quoted molar concentrations in the electrolyte formulae [17, 19, 21, 22], whereas literature referring to industrial electroplating quoted concentrations in g L<sup>-1</sup> [5, 10, 20, 23].

When it was desired to compare the concentrations directly during day-to-day laboratory work, simple calculations were performed using the molar masses of the constituent compounds.

The third zinc electrolyte to be trialled was a methanesulfonic acid based electrolyte. All of the deposition experiments involving this electrolyte were galvanostatic. This electrolyte formula was chosen because it was reportedly used in the deposition of zinc for the manufacture of CZTS in [21], in which a significant increase in efficiency for CZTS devices manufactured through electroplating was reported. This had the following composition:

**Electrolyte Zn 3.**

0.5 M Methanesulfonic acid

0.2 M Zinc sulphate heptahydrate

Sodium hydroxide for pH adjustment

The pH of the electrolyte was adjusted to pH 2 by slowly adding 3 M sodium hydroxide using a dropper while carefully monitoring the solution with a pH meter. This required ~30 mL sodium hydroxide solution, bringing the total solution volume to ~180 mL.

Further improvements to the deposition efficiency, as well as the smoothness and uniformity of the films was sought, therefore a further four electrolyte compositions were tested. These were all tested using galvanostatic deposition, with the current density optimised through trial and error processes.

The compositions trialled were as follows:

**Electrolyte Zn 4.**

Zinc sulphate heptahydrate – 30 g L<sup>-1</sup>

Sodium hydroxide – 120 g L<sup>-1</sup>

Cetyltrimethylammonium bromide (CTAB) – 6 g L<sup>-1</sup>

Ethylenediaminetetraacetic acid (EDTA) – 20 g L<sup>-1</sup>

Salicylaldehyde – 1.6 mL L<sup>-1</sup>

This was an alkaline solution and the composition formula was acquired from [5]. An alkaline solution was desired in particular to study the effect it may have on hydrogen evolution and therefore deposition efficiency. This particular composition does not contain cyanide, which is highly toxic and has been used extensively in alkaline baths for industrial zinc electroplating historically [6]. Alkaline zinc electroplating baths are also known, in general, to have a higher throwing power than acidic zinc electroplating baths (throwing power is the ability to deposit at the same rate in low current density areas as high current density areas) [20]. Although throwing power is less important when dealing with a flat 2-dimensional substrate than it is when dealing with a 3-dimensional object, a higher throwing power could help to reduce thickness variation across the film, particularly at the edges with respect to the centre. See section 1.5.3.1 for more information.

#### **Electrolyte Zn 5.**

Zinc chloride – 60 g L<sup>-1</sup>

Potassium chloride – 150 g L<sup>-1</sup>

Boric acid – 20 g L<sup>-1</sup>

2.5 vol. % Zylite™ brightener

This composition formula was that recommended in a car restoration video available through YouTube [23]. It was chosen due to its inclusion of a commercially available brightener, with the desire existing for a study of its effects on the grain size and structure.

#### **Electrolyte Zn 6.**

Zinc sulphate heptahydrate – 300 g L<sup>-1</sup>

Sodium chloride – 12.5 g L<sup>-1</sup>

Boric acid – 19 g L<sup>-1</sup>

Aluminium sulphate – 19 g L<sup>-1</sup>

Dextrin (yellow) – 10 g L<sup>-1</sup>

This electrolyte bath is suggested as being suitable for electroplating zinc onto sheet steel in [10]. Although it is expected to have a low throwing power due to its use of an acid-sulphate bath [24] [25] (potentially alleviated to an extent by the high

concentration of zinc salt [25]), it was considered of interest due to its explicit inclusion of dextrin as a levelling agent, with the expectation that this could improve the smoothness of the deposited films. The high concentration of zinc was also expected to have the effect of being able to generate a relatively high current density (and therefore a rapid film deposition) at potentials that were not sufficiently negative to lead to large amounts of hydrogen evolution.

### **Electrolyte Zn 7.**

30 mM Zinc sulphate

20 mM Potassium tartrate

100 mM Trisodium citrate

This electrolyte was formulated for the co-deposition of copper, tin and zinc for the manufacture of CZTS, and also included 20mM tin sulphate and 10mM copper sulphate in [22]. This electrolyte was included in the experiments because there was a desire to test a composition that had been specifically formulated for the manufacture of CZTS, other than that used by Scragg et. al. in [17] and [19], which had already been tested.

The resulting zinc films and the elemental stacks as a whole were initially examined through visual inspection to check for obvious imperfections, such as blisters. Further analyses were carried out by means of SEM, and XRD and XPS depth profiling were carried out on a selection of samples.

#### **2.1.10 Film Thickness Control**

It is possible to calculate the theoretical thickness of an electrodeposited film if the following parameters are known: Deposition efficiency, surface area, density of the metal, oxidation state of the metal atoms in the electrolyte, and the total amount of charge passed in the deposition process. Deposition efficiency relates to the proportion of electric charge that reduces metal ions in the solution causing them to form part of the deposited film. As mentioned in section 2.1.3, unwanted parasitic reactions can occur, hydrogen evolution being a common example, which are driven by the passage of electric charge causing some of it to be effectively wasted. Work

carried out to try to quantify and maximise the deposition efficiency is discussed in chapters 3 and 4.

If the deposition efficiency is assumed to be 100%, the following equation can be used to calculate the number of atoms deposited:

$$N_{\text{at}} = \frac{Q}{nq}$$

**Equation 2-7**

Where  $N_{\text{at}}$  is the number of atoms deposited,  $Q$  is the total charge passed in the deposition experiment,  $n$  is the oxidation state of the metal ions in the electrolyte and  $q$  is the charge of one electron ( $1.60 \times 10^{-19}$  C). To obtain the total mass ( $m$ ) of the deposited film, the following equation can be used:

$$m = \frac{N_{\text{at}} A_r}{A_v}$$

**Equation 2-8**

Where  $A_r$  is the relative atomic (molar) mass of the element and  $A_v$  is Avogadro's number ( $6.022 \times 10^{23}$ ). The spatial volume occupied by the film ( $V_f$ ) can be expressed by dividing Equation 2-8 by the density of the material,  $\rho_m$ , which gives:

$$V_f = \frac{N_{\text{at}} A_r}{A_v \rho_m}$$

**Equation 2-9**

To obtain the average film thickness ( $T_f$ ), the film volume can simply be divided by the deposition area ( $a$ ):

$$T_f = \frac{N_{\text{at}} A_r}{A_v \rho_m a}$$

**Equation 2-10**

Finally, combining Equation 2-7 with Equation 2-10 provides a useful expression for the theoretical average film thickness:

$$T_f = \frac{Q A_r}{n q A_v \rho_m a} \quad \text{Equation 2-11}$$

If the deposition efficiency is known, it can be factored into Equation 2-11 simply by multiplication to yield a more accurate value for the film thickness. If a specific film thickness is required, the simplest way to obtain this is by using a potentiostat/galvanostat with current integration software that can be set to automatically terminate the deposition process once the required value for the charge passed has been met (this is sometimes referred to as chronocoulometry). This feature was used for nearly all potentiostatic deposition experiments in this project, with the exception being some early-stage copper deposition experiments that were carried out using a potentiostat/galvanostat without this feature. When galvanostatic deposition was carried out, the charge passed is directly proportional to the time passed and this feature becomes superfluous. The target total thickness for the electrodeposited metallic stack in this project was 670 nm, and the target elemental ratios were Cu/Sn = 1.83, Zn/Sn = 1.35, and Cu/(Zn+Sn) = 0.78. These values were chosen to match those in [21], as the publication reported an efficiency of 7.3% for an electroplated CZTS cell, which was one of the most efficient at the time. A copper-poor, zinc-rich stoichiometry such as this would be expected to lead to higher cell efficiencies [26]. In this project, the density values for copper (8.96 g cm<sup>-3</sup> [27]), tin (7.287 g cm<sup>-3</sup> [28]) and zinc (7.134 g cm<sup>-3</sup> [29]) were used to calculate corresponding charge passed density values of 572 mC cm<sup>-2</sup>, 312 mC cm<sup>-2</sup> and 420 mC cm<sup>-2</sup> respectively, in order to achieve the target thickness and elemental ratios, assuming 100% deposition efficiency.

Several techniques for gauging deposition efficiency were utilised in this project, and arguably any quantitative elemental analysis technique is relevant (for example,

Energy Dispersive Spectroscopy (EDS) or X-Ray Photoelectron Spectroscopy (XPS)), however, there were two techniques that were deployed to quantify the deposition efficiency directly. These were Microwave Plasma – Atomic Emission Spectroscopy (MP-AES), which is discussed in more detail in section 2.4.1, and the deposition followed by the immediate stripping of the deposited film. A value for the most effective potential for stripping a film can be obtained by observing the stripping peak on a voltammogram, with the stripping process expected to be highly efficient (provided that there is no oxidation of water occurring) [9]. Therefore, by integrating the current with respect to time (current – time data being logged by the potentiostat/galvanostat software) for both the deposition and stripping processes to obtain the charge passed, it is theoretically possible to calculate the deposition efficiency by dividing the charge passed during stripping by the charge passed during deposition.

## **2.2 Annealing and Sulphurisation**

Once the electrodeposited elemental layers have been prepared, it is necessary for the samples to undergo annealing processes. In order for CZTS to form, a sulphurisation process is required in which the precursors are heated to 550 °C in an oxygen free, sulphur rich environment. In some of the experiments, a pre-alloying process was carried out in which the electroplated stacks were annealed without sulphur at temperatures between 285 °C and 350 °C. This was in order to cause the intermixing and alloying of the deposited metals, which is reported in literature to benefit the performance of solar cells when carried out prior to sulphurisation [21].

### **2.2.1 Hot-Dip Simulator**

The Hot-Dip Simulator (HDS) is designed to simulate the hot-dip galvanisation process in order to apply a layer of zinc to metals on a smaller scale than an industrial scale zinc bath. The HDS is designed such that samples are placed in a clamp above a vertically mounted quartz tube, the tube being surrounded by infra-red heat lamps. There is also the option of being able to fill the tube with an inert gas. When the HDS is in operation, the sample is lowered into the tube to simulate the

hot-dipping process. The temperature, temperature ramp rate and duration are programmed via a touch screen, and the temperature is monitored and fed-back into the system from a thermocouple that is attached to the sample. Although the HDS is designed for the application of zinc to metal substrates, it was not used for such a purpose in this project and was used purely for its heating capabilities. The HDS used in this project was a Surtec Iwatani Rhesca, capable of heating to in excess of 700 °C. It is programmable to the nearest 5 °C and accurate to  $\pm 2$  °C.

The HDS was trialled in some experiments for the pre-alloying (sometimes referred to as soft annealing) stage in the sample processing, in which the electroplated stack is heated in an inert environment without any sulphur present to encourage intermixing of the metallic layers prior to the sulphurisation stage. Prior to starting the heating cycle, the quartz tube was evacuated down to a pressure of 0.3 Torr and purged with nitrogen twice. During the heating cycle, the nitrogen was set to continuous flow at a rate of 40 litres per minute. It was not possible to attach the thermocouple to the glass substrate or hold the glass substrate in the clamp above the quartz tube. For this reason, the sample was placed in a custom made basket, which was made from a piece of stainless steel with an array of holes of approximately 5

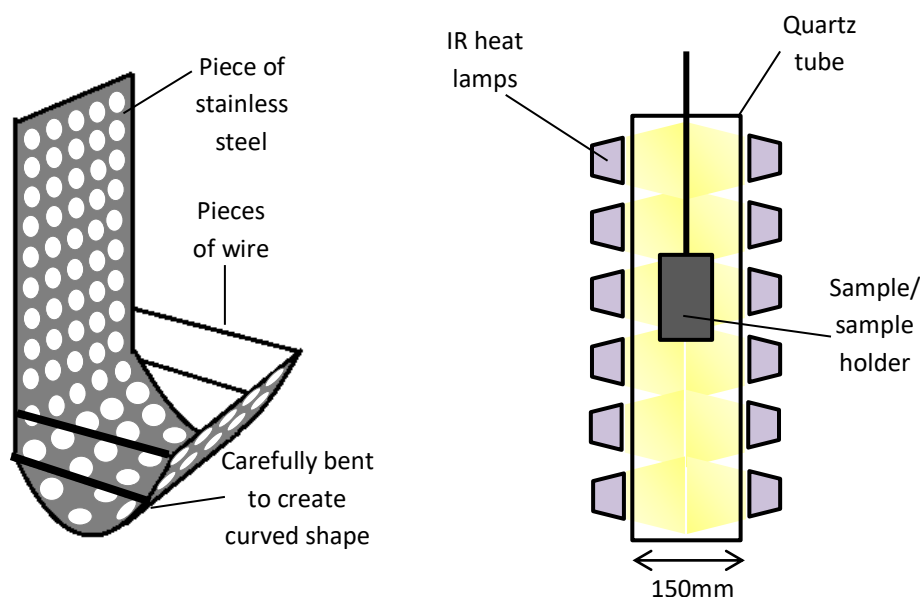


**Figure 2-10 - A drawing of the sample basket used in the HDS (left) and a schematic diagram of the HDS setup (right).**



mm diameter. The basket was approximately 7 cm wide. A small piece of steel was placed in the basket alongside the sample and the thermocouple was attached to the piece of steel. The basket was held in the clamp. A diagram of the basket and the HDS setup can be seen in Figure 2-10 to aid understanding.

The HDS is similar in some respects to a Rapid Thermal Processing Furnace (RTP Furnace) in that the heat transfer process is carried out through IR radiation rather than convection. RTP was also used in this project and was effective in both the alloying and sulphurisation of samples.

### 2.2.2 Rapid Thermal Processing

Rapid Thermal Processing (RTP) uses an infrared heat lamp to heat a shallow graphite box in which the sample is placed. The box is heated from above and a thermocouple is placed in contact with the bottom of the box. The samples, along with any sulphur pieces, sit flat on the floor of the box, which is expected to lead to an even distribution of heat across the sample and accurate control of its temperature. Once the sample and sulphur (if required) have been placed inside the box, they are loaded into the furnace via a drawer mechanism prior to the commencement of the heating cycle. The RTP furnace used in this project was an MTI Corporation OTF-1200X-4-RTP, capable of heating up to 1100 °C, programmable to the nearest 1 °C and accurate to  $\pm 1$  °C. The pressure was measured using an InstruTech Stinger EQ-CVM-211-P-LD Pirani gauge, capable of measuring in the range between 1000 Torr and 0.1 mTorr. The basics of the RTP furnace setup can be seen in Figure 2-11.

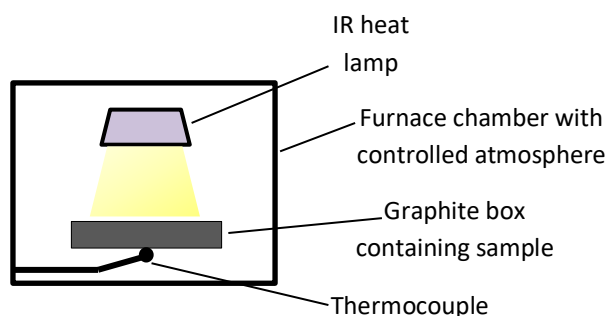


**Figure 2-11 - A schematic diagram indicating the basics of the RTP furnace setup.**

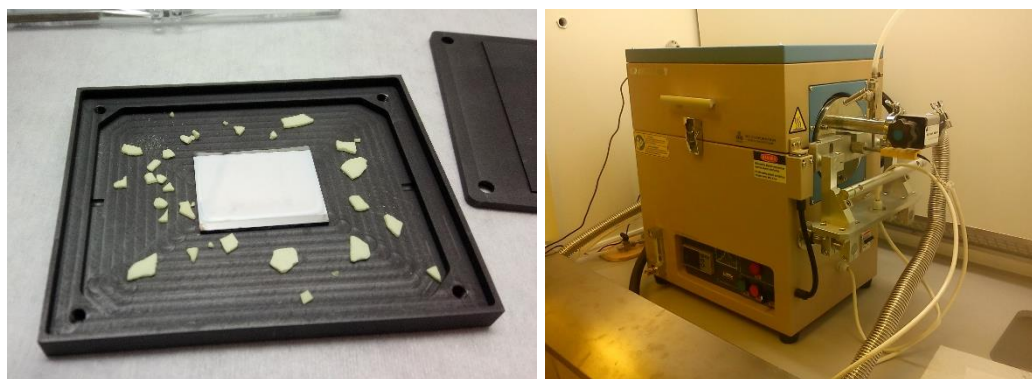


**Figure 2-12 - Photographs of the graphite box used in the RTP experiments containing a sample and sulphur flakes (left), and of the RTP furnace (right).**

The graphite box used in this project had internal dimensions of  $5 \times 7 \times 0.2 \text{ cm}^3$ , and external dimensions of  $6 \times 8 \times 0.5 \text{ cm}^3$ . There are two small holes ( $\sim <1 \text{ mm}$  diameter), one at either end of the box to provide for the optional insertion of a thermocouple, although this feature was not used in this project as the high concentration of sulphur vapour within the box could lead to excessive corrosion of the thermocouple. The lid was placed on without any means for holding it in place other than gravity; therefore excess internal pressure could escape without hindrance. The sulphur used in this project was in the form a flakes and was sourced from Sigma-Aldrich, with a purity of 99.998% (trace metals basis). Photographs of The graphite box and the RTP furnace can be seen in Figure 2-12.

Prior to the commencement of the heating cycle, the furnace was evacuated to a pressure of 20 mTorr or less, followed by refilling with nitrogen to a pressure of 450 Torr. This process was repeated twice. Finally, the furnace was filled with nitrogen to the desired pressure before starting the heating process. The heating sequence was programmed via a Proportional Integral Derivative (PID) controller, which made it possible to enter a detailed sequence of accurately controlled temperature ramping periods and hold times. As its name would suggest, the RTP furnace was capable of very fast ramping rates, and was able to increase temperature by hundreds of degrees in a matter of seconds. Although the furnace was cooled by the circulation of water from a chiller, the cooling rate was approximately  $8 \text{ }^\circ\text{C}$  per minute, so it was not possible to “quench” the samples from a high temperature.

## 2.3 Photovoltaic Device Fabrication and Measurement

There are multiple configurations that can be used for a CZTS solar cell structure, however, for this project, the most common arrangement was adhered to and this is presented in Figure 2-13. As mentioned in section 2.1.5, the molybdenum was sputtered onto the soda-lime glass by the supplier, M-Solv Ltd. Molybdenum is used as a back contact as it has a particularly high melting point (2622 °C [30]) making it resistant to the annealing processes that are used in the manufacture of CZTS. It also forms a thin layer of MoS<sub>2</sub> in the sulphurisation process, which acts as an ohmic back contact for a CZTS device [31].

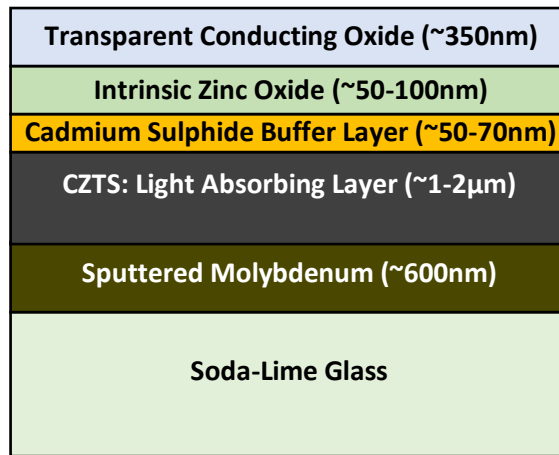


**Figure 2-13 - Diagram giving details of a typical CZTS device structure.**

CZTS is the light absorbing layer and forms the p-type layer of the heterojunction device [32], while the cadmium sulphide and intrinsic zinc oxide are n-type. The cadmium sulphide acts as a buffer layer. The purpose of a buffer layer is to ease the flow of electrons by reducing the conduction band offset at the p-n junction – the conduction band of the buffer layer will be between that of the p-type absorbing layer beneath it and the n-type window layer above it [33]. The top layer is a doped Transparent Conducting Oxide (TCO). This has a higher electrical conductivity than the intrinsic zinc oxide beneath it and can act as a top electrical contact (although sometimes a metal grid, such as nickel-aluminium, is also evaporated on top to further improve the conductivity [34]). Typically, the TCO used is either aluminium-doped zinc oxide (AZO) or tin-doped indium oxide (ITO). Aluminium and zinc are more earth abundant than indium, therefore AZO was used as the top layer for the

solar cells manufactured as part of this project. Although an evaporated metallic grid could have been added as a top contact to improve lateral photocurrent collection, it was decided to omit this as it would have become damaged in the grid scoring as part of the solar cell measurement process (see section 2.3.4). The main purpose of the manufactured solar cells was that the efficiencies would be compared to each other in order to compare the processes that they had undergone.

### 2.3.1 Cadmium Sulphide Deposition

Cadmium sulphide was deposited to a thickness of ~70 nm by means of chemical bath deposition. The deposition beaker used was a 400 mL tall form beaker, which was placed into a warm water bath inside a jacketed circulated hot water cylinder. The water temperature of the cylinder was maintained at a constant 70 °C throughout the deposition process by a thermostatic hot water circulator, which was pre-heated

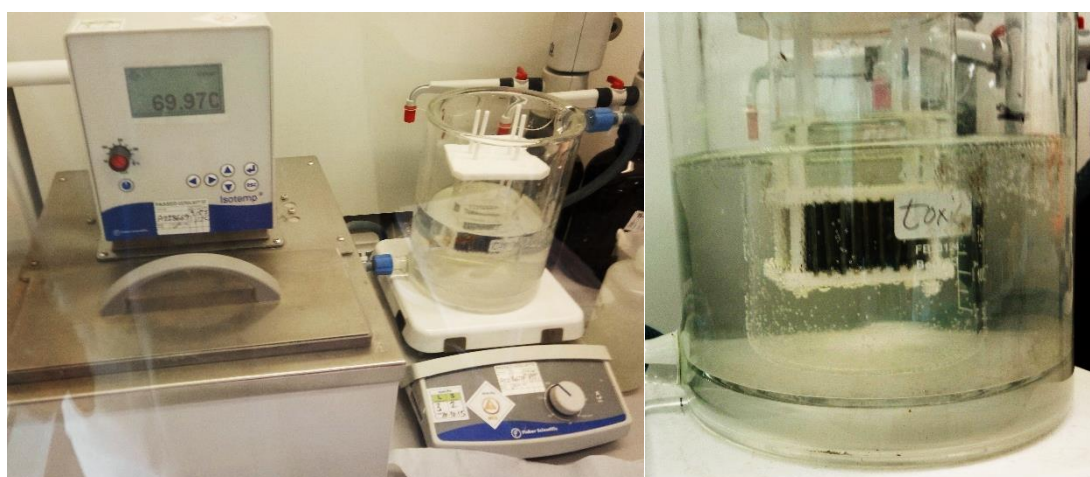


**Figure 2-14 – The chemical bath deposition setup, with the hot water circulator and jacketed cylinder visible in the left image. The samples, sample holder and deposition beaker can be seen placed in the warm water bath in the image on the right.**

for approximately 30 minutes. The samples were placed in a specially designed sample holder that enabled deposition to occur on up to ten samples simultaneously by suspending them in an upright position approximately 2.5 cm above the base of the deposition beaker, allowing for the stirring of the deposition solution by the placing of a magnetic flea while maintaining full submersion in the deposition solution throughout the deposition process. The photographs in Figure 2-14 have

been included in order to aid understanding. All of the deposition procedure was carried out inside a fume cupboard.

The deposition procedure was as follows:

Firstly, the samples were etched in 3% ammonium hydroxide solution in a separate beaker for 5 minutes in order to assist the activation of the CZTS surface, followed by rinsing in deionised water. Secondly, 185 mL of deionised water was added to the deposition beaker, followed by 15 mL of 0.03 M cadmium acetate (Sigma-Aldrich) dispensed using a calibrated automated dispenser. Next, 35 mL of 28-30% ammonium hydroxide (Fisher Scientific) was dispensed into the beaker using a measuring cylinder, with the final component being 15 mL of 0.38 M thiourea (Sigma-Aldrich), which would start the chemical reaction (also dispensed using a calibrated automated dispenser). The samples were then swiftly transferred into the deposition beaker, which was then placed into the aforementioned 70 °C warm water bath. The magnetic stirrer was set to 300 rpm (although the actual rotation speed of the magnetic flea was visibly less than this). The deposition process was terminated after 25 minutes, at which point the samples were removed and rinsed in deionised water, followed by drying under a low pressure nitrogen jet (a low pressure jet was used in order to avoid film damage). Once dried, the undersides of the samples were wiped with tissue paper moistened with 10% hydrochloric acid in order to remove the unwanted area of cadmium sulphide. The samples were then then carefully placed in Perspex sample boxes and vacuum sealed ready for the following stage in the cell fabrication process, which was the deposition of the TCO layers. Finally, all glassware and utensils were cleaned by submersion in 10% hydrochloric acid.

### **2.3.2 Four-Point Probe Measurements**

Sheet resistivity measurements were carried out on some FTO substrates for comparative and identification purposes. A four-point probe consists of four metallic probes arranged in a straight line with equal spacing between each one (typically ~0.5cm). A fixed current is passed between the two outer probes and the resulting voltage is measured across the two inner probes, enabling the sheet resistivity to be calculated [35]. These measurements were taken using a Jandel 3000 four-point probe.

### 2.3.3 Transparent Conducting Oxide Deposition

The intrinsic zinc oxide (iZnO) window layer was deposited via sputtering using a Kurt J. Lesker PVD 75. An 86 W DC power source was used, and the iZnO was RF sputtered using a pressure control mode with an argon-oxygen mix that generated a working pressure of  $5 \times 10^{-3}$  mbar, with the base pressure being maintained at  $1.5 \times 10^{-7}$  mbar. The total thickness of the deposited film was 50 nm. The aluminium-doped zinc oxide (AZO) was also RF sputtered with the same apparatus using a 95 W power source under a gas flow of 3 sccm argon to generate a working pressure of  $2 \times 10^{-3}$  mbar, with the base pressure being maintained at  $1.5 \times 10^{-7}$  mbar. The thickness of the AZO layer was 500 nm. The sheet resistance of the deposited iZnO/AZO bilayer was approximately  $20 \Omega/\square$ .

### 2.3.4 Solar Cell Measurement

Prior to carrying out electrical measurements on the samples, further preparations were necessary. Firstly, the area of the substrates either side of the CZTS films were scraped with a scalpel in order to remove the TCOs and CdS from these regions, leaving two strips of exposed molybdenum. Secondly, silver paint was applied to one of the Mo strips in order to improve electrical contact – this is where an electrical probe was placed to connect the solar simulator to the back contact of the devices. Finally, the samples were scored with a scalpel to create an array of  $4 \times 4$  mm<sup>2</sup> individual solar cells on each sample. It was possible to create a  $3 \times 5$  grid on each

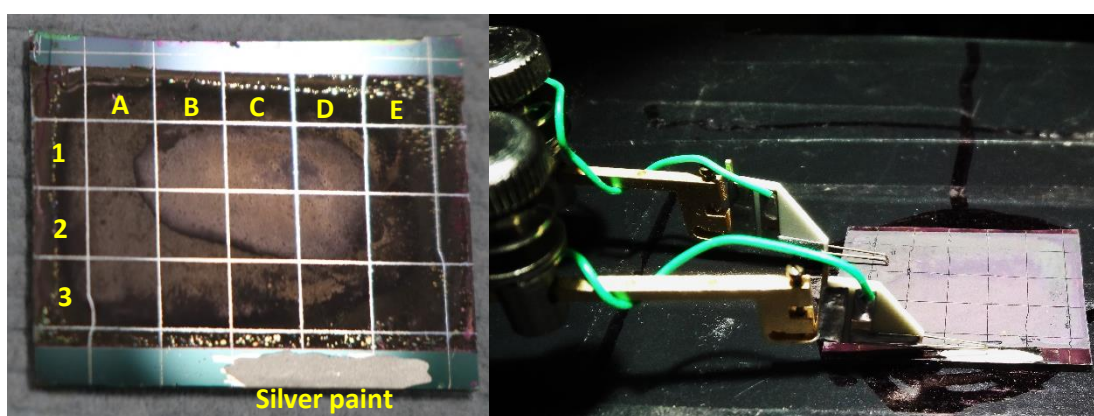


**Figure 2-15 - A photograph showing how the samples were scored into  $4 \times 4$  mm<sup>2</sup> cells and the grid referencing system used (left), and a photograph showing a device under test with a solar simulator, one probe being placed on top of the cell being tested and the other on the silver paint (right).**



sample, and a reference system using the letters A – E and the numbers 1 – 3 were used to identify the individual cells. It was possible to measure the cells individually by placing one of the two solar simulator probes on the silver paint back contact and the other on top of the cell under test, where the AZO would act as a top contact. Photographs of a sample under electrical measurement and of a scored sample indicating the grid referencing system can be seen in Figure 2-15 to aid understanding.

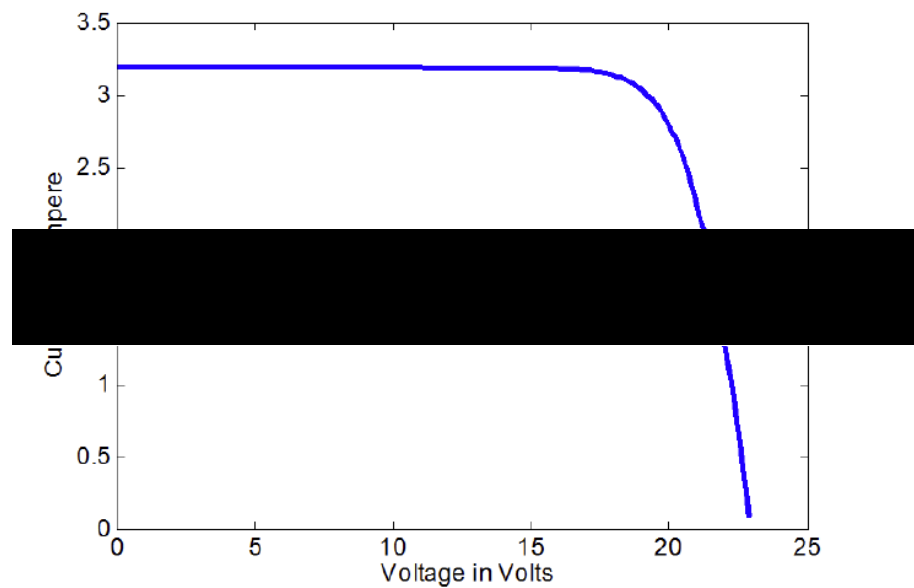


**Figure 2-16 – A graph showing the typical shape of a J-V curve of a solar cell, taken from [37].**

The completed solar cells were measured using the AM1.5 Global spectrum (which has an incident irradiance of  $1 \text{ kW m}^{-2}$ , or,  $100 \text{ mW cm}^{-2}$  [36]) with a Newport Oriel Sol3A solar simulator. Prior to the cell measurements commencing, the instrument was calibrated using a Newport Oriel 51150V monocrystalline silicon reference cell, which is NREL certified. The applied voltage was swept across the range  $-0.2 \text{ V}$  to  $+0.6 \text{ V}$  with  $0.01 \text{ V}$  increments, while the resulting current density was measured. This made it possible to plot current density–voltage (J-V) curves (an example of the shape of a typical J-V curve of a solar cell is given in Figure 2-16 [37]) and calculate the device efficiencies using the following equation [38]:

$$\eta = \frac{FF J_{sc} V_{oc}}{I_0}$$

**Equation 2-12**

Where  $\eta$  is the power conversion efficiency of the device, FF is the fill factor,  $J_{sc}$  is the short-circuit current density (the current density when the voltage is equal to zero),  $V_{oc}$  is the open circuit voltage (the voltage when the current density is equal to zero) and  $I_0$  is the incident irradiance. The fill factor is defined by the following equation [38]:

$$FF = \frac{J_{MPO} V_{MPO}}{J_{sc} V_{oc}} \quad \text{Equation 2-13}$$

Where  $J_{MPO}$  and  $V_{MPO}$  are the respective current density and voltage at the point of maximum power output. An annotated example of a J-V curve obtained during this project is presented in Figure 2-17 to aid understanding. In the device measuring experiments carried out in this project, each of the relevant variables were automatically calculated using the solar simulator software.

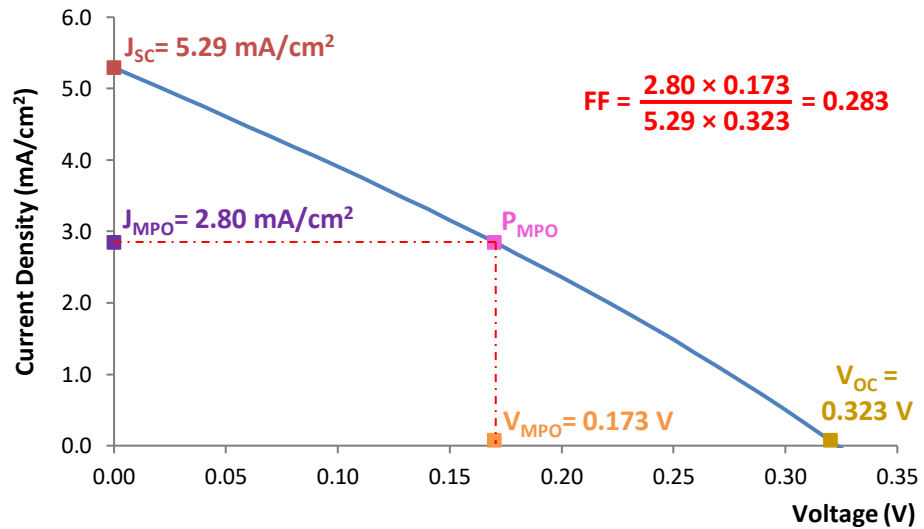


**Figure 2-17 - An example of a J-V curve showing how the fill factor (FF) is calculated.  $P_{MPO}$  denotes the point of maximum power output.**



## 2.4 Analytical Techniques

### 2.4.1 Microwave Plasma – Atomic Emission Spectrometry

A Microwave Plasma – Atomic Emission Spectrometry (MP-AES) is used to accurately measure the concentration of specified metallic elements in an aqueous solution, and is capable of detecting and quantifying very low concentrations ( $0 - 10 \text{ mg L}^{-1}$ ). In this project, electrodeposited metal stacks were dissolved in known volumes of aqueous acids, which in turn were analysed using an MP-AES system. By knowing the concentration of each metal and the volume of the solutions, it was possible to calculate the total mass of each metal deposited on the analysed samples and therefore calculate the deposition efficiency using the deposition current data.

#### 2.4.1.1 The Function of a Microwave Plasma – Atomic Emission Spectrometer

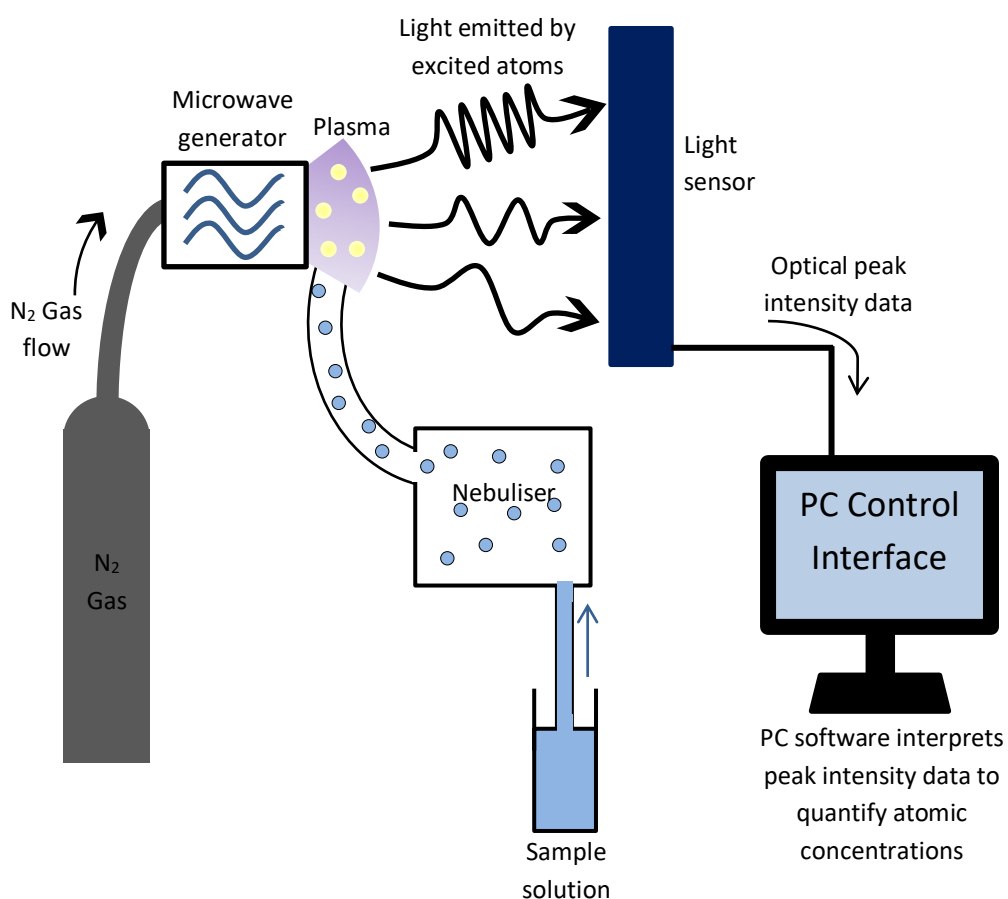


**Figure 2-18 - A schematic diagram showing the basic functions of an MP-AES system.**

A Microwave Plasma – Atomic Emission Spectrometry (MP-AES) system works by exciting the atoms of a sample using a plasma, and analysing the intensity of particular wavelengths in the resulting optical spectrum. The plasma is a microwave generated nitrogen plasma, with a typical temperature of around 5000 K [39]. The sample is presented in liquid form and is passed through a nebuliser before being injected into the plasma. Each element in the sample will have a distinctive emission spectrum containing peaks corresponding to the differences between the energy levels of its electronic excitation states. This emission occurs as electrons, excited by the plasma, relax back into lower energy states. The emission peaks are detected by a light sensor that feeds the information back to a computer, which is able to quantify the concentration of specific elements in the sample from the intensity of their associated emission peaks. A schematic diagram of the system setup can be seen in Figure 2-18 to aid understanding. In order for the computer software to accurately produce concentration data, a set of standards with known concentrations of the elements under analysis must be run at the start of each experiment in order to calibrate the system.

#### ***2.4.1.2 Calibration Standard and Sample Preparation***

It is necessary to calibrate the MP-AES system prior to running the samples under test and therefore it is essential to create a set of five calibration standards to be fed into the system at the start of any analysis procedure. These calibration standards are created using a commercially available concentrated ( $1000 \text{ mg L}^{-1}$ ) standard and diluting it into five different concentrations in the  $0 - 10 \text{ mg L}^{-1}$  range (this is the range in which the system can produce accurate results). Although multi-element standards exist, there are none available that include both tin and copper. The reason for this is that the commercially available standards normally use either nitric acid or hydrochloric acid as a solvent as these are safe to use in the system at relatively low concentrations ( $\sim 10 \text{ wt.}\%$  or less). Copper does not dissolve easily in hydrochloric acid, but does dissolve in nitric acid. Tin, on the other hand, will dissolve easily in hydrochloric acid, but tends to form a powder-like tin oxide precipitate when dissolved in nitric acid. Zinc can fully dissolve in either hydrochloric or nitric acid and was included, along with copper, in the VWR Multi-Element Standard (21

element standard in dilute nitric acid) used in this project. A separate standard containing tin in dilute hydrochloric acid was purchased from Sigma-Aldrich.

To digest (dissolve) the deposited films, the samples were first placed in a 50 mL beaker with 20-30 mL of 10 wt.% hydrochloric acid at room temperature. After 24 hours, the sample was removed from the beaker and carefully rinsed with fresh 10 wt.% hydrochloric acid into the same beaker. The sample was then transferred into another beaker (150 mL) containing 40-50 mL of 10 wt.% nitric acid. The hydrochloric acid solution was then passed through filter paper using a Buchner funnel placed in a side-armed flask connected to a vacuum pump. The filter paper was then removed from the funnel and transferred into the beaker containing the 10 wt.% nitric acid and the sample. The digest in the side-armed flask was decanted into a 250 mL volumetric flask and topped-up to the 250 mL line.

After a further 24 - 48 hours, once all of the sample material had dissolved, the nitric acid digest was filtered using a similar method as that described for the hydrochloric acid digest.

#### ***2.4.1.3 Experimental Procedure***

Each sample digest solution was analysed for all three elements – copper, zinc and tin. This meant that the samples had to be analysed in two phases. Firstly, the MP-AES system software was instructed to analyse for copper and tin, and the five copper and zinc standards were presented sequentially. The concentration of each standard was entered into the software to enable a calibration curve to be generated. The software generated this curve automatically and indicated when to present the samples (sequentially). The software automatically calculated the concentration of copper and zinc in each sample. Finally, two calibration standards were presented for a second time ( $4 \text{ mg L}^{-1}$  and  $10 \text{ mg L}^{-1}$ ) to check for any drift in the calibration of the system. Once the cycle for quantifying copper and zinc was complete, the second phase, in which the tin concentrations were quantified, was carried out. This followed the same pattern as described above, but the system was instructed to quantify tin, and the set of tin calibration standards were presented.

### 2.4.2 X-Ray Diffractometry

X-Ray Diffractometry (XRD) is able to provide information on both the crystallinity and the lattice spacing of the material under analysis. In XRD, an X-ray beam is projected onto a sample while the X-ray source and X-ray detector are scanned through a range of angles, with the sample at the vertex between them (see Figure 2-19). This generates a diffraction pattern as the X-ray intensity at the detector is plotted against the diffraction angle. The lattice spacing can be calculated by reading the angles at which the X-ray intensity at the detector peaks (these correspond with constructive interference as X-rays enter the detector in phase with each other) [40]. The equation used for this is:

$$n\lambda = 2d \sin\theta$$

**Equation 2-14**

Where  $n$  is an integer,  $\lambda$  is the wavelength of the X-rays,  $\theta$  is the diffraction angle and  $d$  is the spacing between the crystallographic planes [40]. The diffraction pattern seen for a material is dependent upon its lattice spacing and therefore its crystal packing, and different diffraction patterns will be obtained as a result of this. It is possible to identify many different compounds by their diffraction pattern. In practise, the software used to operate the XRD can scan a database of diffraction patterns and give percentage similarities against a list of materials, in comparison to

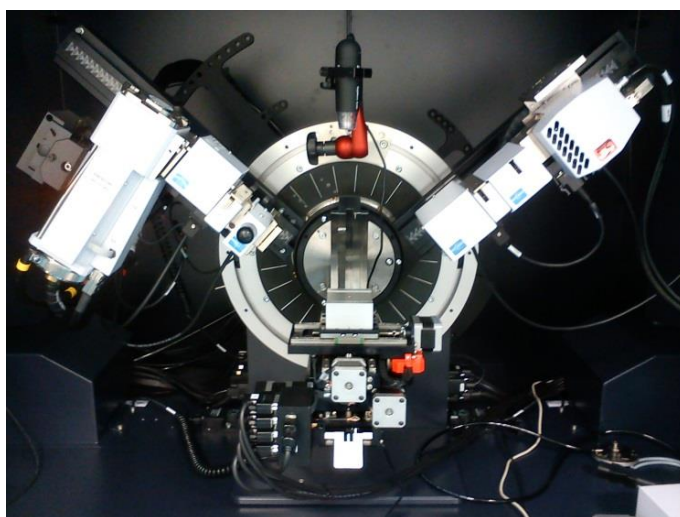


**Figure 2-19 - A Photograph of the arms of the XRD, with the X-Ray source on the left and the detector on the right, the sample stage being at the vertex of the angle.**

the diffraction pattern obtained in a given experiment. The crystallinity of a sample is associated with the breadth of the diffraction peaks – very sharp peaks are indicative of a material comprising of large crystals, whereas a material comprising of smaller crystals would return broad peaks. No peaks would be visible when analysing an amorphous material.

The XRD used in this project was a Bruker™ D8 Discover and the associated software matched diffraction patterns using the Crystallography Open Database (COD). XRD was carried out on electroplated stacks before and after annealing as an alloy between two metals can give rise to diffraction peaks that are not seen in either of the two metals individually, giving information on the level of intermixing between the metals. XRD was also used to analyse sulphurised CZTS films. This work is presented in chapter 5, in which more experimental detail on the use of XRD is stated. An example of an XRD pattern for CZTS is provided in Figure 2-20. Although an XRD pattern can give an indication of whether CZTS may be present, many of the diffraction peaks of CZTS are shared with copper tin sulphide (CTS), zinc sulphide (ZnS) and other phases, therefore it is not possible to rule out the presence of these unwanted compounds through XRD alone [41]. This being the case, it is useful to complement XRD with an additional technique. Although Raman Spectroscopy does not examine a CZTS film to as great a depth as XRD, the peaks

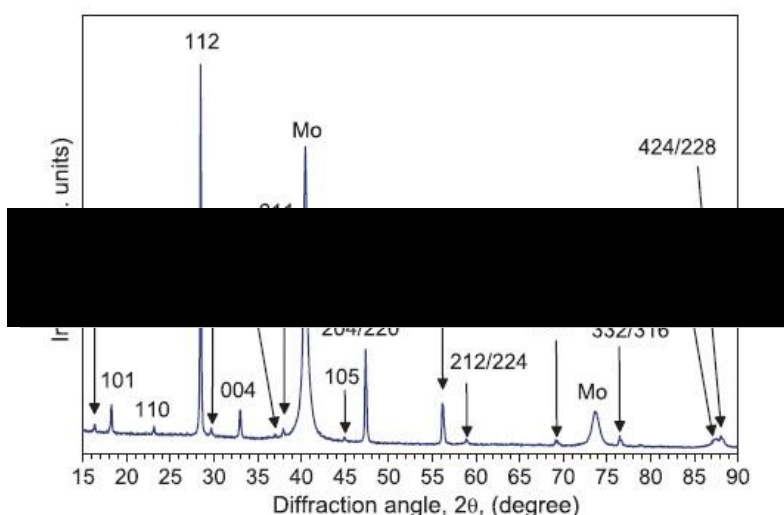


**Figure 2-20 – An example of an XRD pattern for CZTS, taken from [41]. Crystallographic orientation planes are included in the peak labelling.**

associated with CZTS in a Raman Spectrum are more distinct than those associated with unwanted phases. Furthermore, the standard slit size on the XRD would lead to the analysis of a surface area of  $0.6 \times 20 \text{ mm}^2$ . Analysing a smaller area would require the fitment of a collimator and would significantly reduce the strength of the signal, meaning that longer scans of several hours duration would be required. In contrast, the Raman spectrometer analyses a spot diameter of  $3 \text{ }\mu\text{m}$  at 20x objectification and takes less than one minute to gather the required data. This made it possible to analyse the composition at multiple specific points on sulphurised films quickly and with ease.

### **2.4.3 Raman Spectroscopy**

A Raman Spectrometer functions on the principle of Raman scattering, in which light undergoes a shift in wavelength when scattered off a material [42]. Materials that cause such a shift in wavelength are referred to as Raman active materials, and CZTS is one of them [41]. Raman scattering occurs when an incident photon leads to the creation or annihilation of a lattice vibration, or phonon, and the degree of wavelength shift is related to the resonant vibrational frequencies of the molecular bonds in the material [42]. The resonant vibrational frequencies of the molecular bonds are dependent upon the precise chemistry of the compounds. A Raman Spectrometer is equipped with a monochromatic laser, which is directed at the sample being analysed, and is capable of detecting the spectral intensity of the scattered light. The optical intensity is then plotted against the Raman shift (which is the inverse of the change in wavelength) to create a Raman spectrum. The spectrum can then be used to identify the Raman active compounds present. An example of a Raman spectrum for CZTS is provided in Figure 2-21. In the case of CZTS, many of the unwanted secondary phases that are likely to be present can be distinguished from CZTS by the differences in their Raman spectra [41], however, when using a 532 nm laser (as was the case with this project), it can be difficult to absolutely rule out the presence of CTS or ZnS. In order to confidently distinguish all of the unwanted phases, it would be necessary to carry out analyses with a range of laser wavelengths, however, that facility was not available during the course of this project. Nonetheless, Raman spectroscopy proved useful and led to the identification

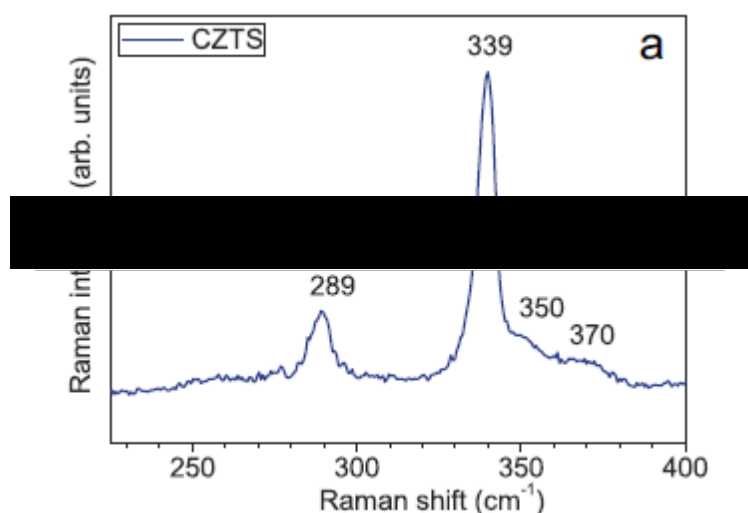


**Figure 2-21 - The Raman spectrum for CZTS when using a laser with a wavelength of 488 nm, as presented in [41].**

of phases that would not have been detected through the use of XRD alone. The technique was used during the course of the experiments discussed in chapter 5, in which experimental detail is given.

#### **2.4.4 X-Ray Photoelectron Spectroscopy**

An X-Ray Photoelectron Spectrometer (XPS) can identify and quantify the abundance of nearly all elements (except hydrogen and helium) in a sample. It works on the principle of calculating the binding energy of the electrons by measuring the kinetic energy of electrons ejected from a sample undergoing X-ray bombardment. This leads to the detection of energy peaks, which are effectively fingerprints of the specific chemical elements present. [43].

X-Ray Photoelectron Spectroscopy (also commonly abbreviated to XPS) is a surface technique and is typically analysing to a depth of 2 – 5 nm [43], however, a depth profile of a sample can be generated where the XPS is fitted with an argon ion etching gun. This allows the sample to be analysed at regular intervals as the ion beam gradually etches further into the film. This technique proved useful for measuring the changes that occurred during the pre-alloying annealing stage. Samples that were electroplated under identical conditions were subjected to annealing under different conditions (or no annealing) prior to examination through

XPS depth profiling. This led to information on the degree of alloying, intermixing and elemental losses that occur through annealing at a range of temperatures and durations. This work is presented in chapter 5. XPS depth profiling was also used in the analysis of multi-layered electroplated stacks, which is discussed in chapter 4.

#### **2.4.5 Scanning Electron Microscopy and Energy Dispersive Spectroscopy**

Scanning Electron Microscopy (SEM) is a useful technique for obtaining high resolution images of sample surfaces. It functions based on de Broglie's theory that moving particles exhibit some of the properties of a wave, and that a particle's associated wavelength ( $\lambda$ ) can be calculated using the following equation:

$$\lambda = h/(mv) \quad \text{Equation 2-15}$$

Where  $h$  is Planck's constant ( $6.63 \times 10^{-34}$  Js), and  $m$  and  $v$  are the mass and the velocity of the particle respectively [44]. SEM uses high acceleration voltages ( $\sim 5 - 30$  kV) to enable electrons to achieve velocities that result in a de Broglie wavelength in the order of  $10^{-11}$  m [45], which is many orders of magnitude smaller than the wavelength of visible light ( $\sim 10^{-7}$  m). This makes it possible to achieve very high resolution images using SEM as the limits of resolution are dependent upon wavelength [46]. The main disadvantage of using SEM is the requirement for samples to be conductive, although this did not present as a major problem for the samples requiring analysis as part of this project. During the earlier stages of this project, SEM images were obtained using a Hitachi Desktop SEM, and during the latter stages, a JEOL 7800 FEG-SEM was used. These will be distinguished where images are presented, with higher resolution images being achievable using the Field Effect Gun (FEG) SEM.

Energy Dispersive Spectroscopy (EDS) is an additional function of an SEM for the purpose of elemental analysis. Samples are bombarded with electrons, causing the atoms to emit X-rays [47]. The energy of the emitted X-rays are detected and related to the elemental composition of the sample material, including atomic abundancies [48]. The data generated by EDS is quantitative only if the system is frequently calibrated [49], and this was by no-means a given when using the systems that were available for use during this project. It was, however, a useful tool for comparative



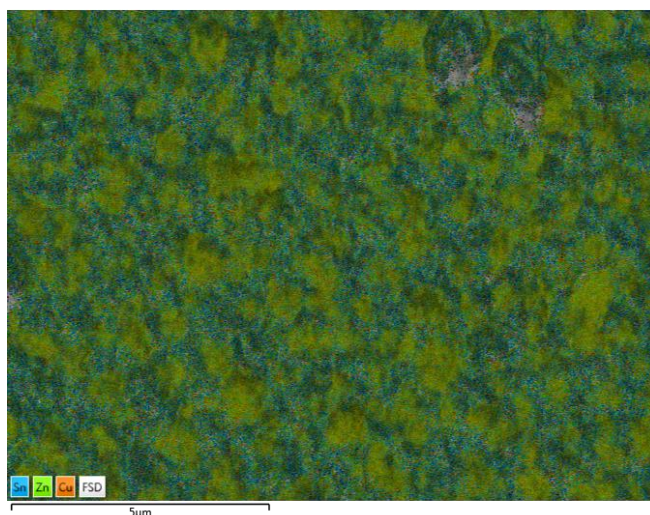


**Figure 2-22 - An example of an EDS colour map image, indicating a raised concentration of zinc in the green coloured regions.**

purposes, such that samples could be ranked in order of their abundance of a particular element, which in turn could be correlated, for example, with the duration of an annealing process. Furthermore, as EDS is used in conjunction with SEM imaging, it can be used to generate a coloured map indicating the relative abundances of selected elements across a specified area. By way of example, it could indicate that blisters on a sample coincide with a deficiency of a particular element, as the colour assigned to that element (which can be specified using the system software) would be fainter around the blisters. An example of an EDS coloured map can be seen in Figure 2-22.

#### **2.4.6 Profilometry**

Profilometry was carried out on electrodeposited metallic films to measure thicknesses and obtain average surface roughness (Ra) values. This was carried out using Veeco Dektak™ profilometers. These were contact stylus profilometers, therefore the stylus exerts a small force on the film. Due to the granular nature of CZTS and the weak bonding between its grains, as well as limited adhesion to the substrate, it was not possible to perform profilometry on sulphurised CZTS as the stylus would damage the delicate films. The scan resolution is dependent upon stylus force, physical scan length and scan duration, and these settings are stated where relevant.

### **2.4.7 Sigma Scan™**

Sigma Scan™ is a piece of software that can be used to calculate the surface area of a flat object without straight edges. It can do so by processing an image of the object, alongside an appropriate scale, and calculate the area that is covered by a particular colour. This proved useful for calculating the current density for the electrodeposition of zinc where a precise value for the deposition surface area was required. In order to carry out the surface area calculation, samples were photographed using a stereo microscope alongside a ruler with a 0.5 mm scale. The perimeter of deposition area was then marked out manually through the Sigma Scan™ software and flood-filled with a fixed colour. The ruler scale was also entered. The software was then able to calculate the deposition area.

### **2.4.8 Visual Inspection**

#### ***2.4.8.1 Inspection Using the Naked Eye***

Many of the desired film properties, such as absence of blisters and pits, and good macroscopic coverage, can be screened for by simple visual inspection. In this instance, many of the samples were photographed using a digital camera to enable future comparison and record keeping. The use of a light box was trialled in an attempt to ensure consistency, but this led to some features becoming indistinguishable due to the square angle at which the photographs were taken. Photographing samples from multiple angles, with and without the use of a flash, proved more useful.

#### ***2.4.8.2 Optical Microscopy***

In some instances, it was only possible to partially distinguish some features with the naked eye. When this was the case, optical microscopy provided a useful intermediate level of detail, without the need to expend the time required for SEM. Magnification levels of up to 200x were available on one particular microscope, but for the majority of samples it was found that 50x magnification was sufficient. It was also possible to obtain photographs of the magnified samples using integrated cameras and the appropriate computer software.

## 2.5 References

- [1] Science Project, “The Chemistry of Copper Plating. – Science Projects,” [Online]. Available: <https://www.scienceprojects.org/the-chemistry-of-copper-plating/>. [Accessed 21 02 2021].
- [2] C. Ponce de Leon and F. C. Walsh, “Research and Development Techniques 1: Potentiodynamic Studies of Copper Metal Deposition,” *Transactions of the IMF*, vol. 81, no. 5, pp. B95-B100, 2003.
- [3] K. J. Aoki and J. Chen, “Tips of Voltammetry,” in *Voltammetry*, N. W. Maxakato, S. S. Gwebu and G. H. Mhlongo, Eds., London, IntechOpen, 2018.
- [4] N. Elgreshi, K. J. Rountree, B. D. McCarthy, E. S. Rountree, T. T. Eisenhart and J. L. Dempsey, “A Practical Beginner’s Guide to Cyclic Voltammetry,” *Journal of Chemical Education*, vol. 95, no. 2, pp. 197-206, 2018.
- [5] Y. A. Naik and T. V. Venkatesha, “A New Brightener for Zinc Plating from Non-Cyanide Alkaline Bath,” *Indian Journal of Engineering and Materials Sciences*, vol. 10, pp. 318-323, 2003.
- [6] R. Winand, “Electrodeposition of Zinc and Zinc Alloys,” in *Modern Electroplating*, 5th ed., Hoboken, New Jersey: John Wiley and Sons, 2010, pp. 285-308.
- [7] J. D. Blakemore, R. H. Crabtree and G. W. Brudvig, “Molecular Catalysts for Water Oxidation,” *Chemical Reviews*, vol. 115, no. 23, p. 12974–13005, 2015.
- [8] J. O. G. Posada and P. J. Hall, “Controlling hydrogen evolution on iron electrodes,” *International Journal of Hydrogen Energy*, vol. 41, no. 45, pp. 20807-20817, 2016.
- [9] J. J. Scragg, “Section 2.1 - Electrodeposition of Metallic Precursors: Electrochemical Deposition (Electrodeposition),” in *Copper Zinc Tin Sulfide Thin Films for Photovoltaics: Synthesis and Characterisation by Electrochemical Methods*, Berlin, Springer-Verlag, 2011, pp. 9-19.
- [10] E. A. Ollard, *Introductory Electroplating*, Teddington: Robert Draper Publishing, 1969.

- [11] J. J. Scragg, D. M. Berg and P. J. Dale, “A 3.2% efficient Kesterite device from electrodeposited stacked elemental layers,” *Journal of Electroanalytical Chemistry*, vol. 646, no. 1-2, p. 52–59, 2010.
- [12] D. P. Dubal, W. B. Kim and C. D. Lokhande, “Surfactant assisted electrodeposition of MnO<sub>2</sub> thin films: Improved supercapacitive properties,” *Journal of Alloys and Compounds*, vol. 509, no. 41, pp. 10050-10054, 2011.
- [13] P. Sivasakthi, R. Sekar and G. N. K. Ramesh Babu, “Electrodeposition and characterisation of copper deposited from cyanide-free alkaline glycerol complex bath,” *Transactions of the IMF*, vol. 93, no. 1, pp. 32-37, 2015.
- [14] Chemistry Dictionary, “Electrochemical Series | Explanation Applications & Table,” 22 October 2019. [Online]. Available: <https://chemdictionary.org/electrochemical-series/>. [Accessed 12 April 2021].
- [15] J. J. Scragg, “Section 2.10 - Electrodeposition of Metallic Precursors: Electrodeposition at the Rotating Disc Electrode,” in *Copper Zinc Tin Sulfide Thin Films for Photovoltaics: Synthesis and Characterisation by Electrochemical Methods*, Berlin, Springer-Verlag, 2011, pp. 42-45.
- [16] J. J. Scragg, P. J. Dale and L. M. Peter, “Towards sustainable materials for solar energy conversion: Preparation and photoelectrochemical characterization of Cu<sub>2</sub>ZnSnS<sub>4</sub>,” *Electrochemistry Communications*, vol. 10, no. 4, p. 639–642, 2008.
- [17] J. J. Scragg, P. J. Dale and L. M. Peter, “Synthesis and characterization of Cu<sub>2</sub>ZnSnS<sub>4</sub> absorber layers by an electrodeposition-annealing route,” *Thin Solid Films*, vol. 517, no. 7, p. 2481–2484, 2009.
- [18] R. L. Broggi, G. M. De Oliveira, L. L. Barbosa, E. M. J. A. Pallone and I. A. Carlos, “Study of an alkaline bath for tin deposition in the presence of sorbitol and physical and morphological characterization of tin film,” *Journal of Applied Electrochemistry*, vol. 36, no. 4, pp. 403-409, 2006.
- [19] J. J. Scragg, “Section 2.4 - Electrodeposition of Metallic Precursors: Description of Electrodeposition Methodology,” in *Copper Zinc Tin Sulfide Thin Films for Photovoltaics: Synthesis and Characterisation by Electrochemical Methods*, Berlin, Springer-Verlag, 2011, pp. 25-28.

- [20] Y. D. Gamburg and G. Zangari, "Technologies for the Electrodeposition of Metals and Alloys: Electrolytes and Processes," in *Theory and Practise of Metal Electrodeposition*, New York, Springer, 2011, pp. 265-316.
- [21] S. Ahmed, K. B. Reuter, O. Gunawan, L. Guo, L. T. Romankiw and H. Deligianni, "A High Efficiency Electrodeposited  $\text{Cu}_2\text{ZnSnS}_4$  Solar Cell," *Advanced Energy Materials*, vol. 2, no. 2, pp. 253-259, 2012.
- [22] S. Shin, C. Park, C. Kim, Y. Kim, S. Park and J.-H. Lee, "Cyclic Voltammetry Studies of Copper, Tin and Zinc Electrodeposition in a Citrate Complex System for CZTS Solar Cell Application," *Current Applied Physics*, vol. 16, no. 2, pp. 207-210, 2016.
- [23] "Restoring Yellow Passivated Zinc Parts by DIY Electroplating - YouTube," The Lotus Elan M100 Restoration Series, 21 March 2016. [Online]. Available: <https://www.youtube.com/watch?v=PoU7UHU71Ww>. [Accessed 31 May 2018].
- [24] H. Hayashida and R. Nakahara, "Studies of Throwing Power in Various Non-Cyanide Zinc Plating Baths," *Journal of the Metal Finishing Society of Japan*, vol. 22, no. 7, pp. 326-334, 1971.
- [25] M. A. M. Ibrahim, "Improving the Throwing Power of Acidic Zinc Sulfate Electroplating Baths," *Journal of Chemical Technology and Biotechnology*, vol. 75, no. 8, pp. 745-755, 2000.
- [26] M. Kumar, A. Dubey, N. Adhikari, S. Venkatesan and Q. Qiao, "Strategic review of secondary phases, defects and defect-complexes in kesterite CZTS–Se solar cells," *Energy & Environmental Science*, vol. 8, no. 11, pp. 3134-3159, 2015.
- [27] Royal Society of Chemistry, "Copper - Element Information, Properties and Uses | Periodic Table," 2019. [Online]. Available: <http://www.rsc.org/periodic-table/element/29/Copper>. [Accessed 23rd April 2019].
- [28] Royal Society of Chemistry, "Tin - Element Information, Properties and Uses | Periodic Table," 2019. [Online]. Available: <http://www.rsc.org/periodic-table/element/50/tin>. [Accessed 23rd April 2019].
- [29] Royal Society of Chemistry, "Zinc - Element Information, Properties and Uses | Periodic Table," 2019. [Online]. Available: <http://www.rsc.org/periodic-table/element/30/zinc>. [Accessed 23rd April 2019].

- [30] Royal Society of Chemistry, “Molybdenum - Element Information, Properties and Uses | Periodic Table,” 2019. [Online]. Available: <http://www.rsc.org/periodic-table/element/42/Molybdenum>. [Accessed 21st May 2019].
- [31] P. Chelvanathan, M. I. Hossain, J. Husna, M. Alghoul, K. Sopian and N. Amin, “Effects of Transition Metal Dichalcogenide Molybdenum Disulfide Layer Formation in Copper–Zinc–Tin–Sulfur Solar Cells from Numerical Analysis,” *Japanese Journal of Applied Physics*, vol. 51, no. 10S, 2012.
- [32] D. A. R. Barkhouse, R. Haight, N. Sakai, H. Hiroi, H. Sugimoto and D. B. Mitzi, “Cd-free Buffer Layer Materials on  $\text{Cu}_2\text{ZnSn}(\text{SxSe1-x})_4$ : Band Alignments with ZnO, ZnS, and  $\text{In}_2\text{S}_3$ ,” *Applied Physics Letters*, vol. 100, no. 19, 2012.
- [33] M. Sokolich, “What is a buffer layer in a solar cell, and what is its significance? - Quora,” 26th August 2018. [Online]. Available: <https://www.quora.com/What-is-a-buffer-layer-in-a-solar-cell-and-what-is-its-significance>. [Accessed 21st May 2019].
- [34] Z. Wei, C. M. Fung, A. Pockett, T. O. Dunlop, J. D. McGettrick, P. J. Heard, O. J. Guy, M. J. Carnie, J. H. Sullivan and T. M. Watson, “Engineering of a Mo/SiNx Diffusion Barrier to Reduce the Formation of  $\text{MoS}_2$  in  $\text{Cu}_2\text{ZnSnS}_4$  Thin Film Solar Cells,” *ACS Applied Energy Materials*, vol. 1, no. 6, pp. 2749-2757, 2018.
- [35] C. Honsberg and S. Bowden, “Four Point Probe Resistivity Measurements | PVEducation,” PVEducation, 2018. [Online]. Available: <https://www.pveducation.org/pvcdrom/characterisation/four-point-probe-resistivity-measurements>. [Accessed 11 June 2018].
- [36] C. Honsberg and S. Bowden, “Standard Solar Spectra | PVEducation,” 2019. [Online]. Available: [www.pveducation.org/pvcdrom/appendices/standard-solar-spectra](http://www.pveducation.org/pvcdrom/appendices/standard-solar-spectra). [Accessed 21st May 2019].
- [37] R. S. AbdelHady, “Detecting the Parameters of Solar Cells Using Efficient Curve Fitting Techniques,” *International Journal of Engineering Research and Technology*, vol. 7, no. 3, pp. 185-199, 2014.
- [38] S. M. Sze, “Section 7.5 - Photonic Devices: Solar Cell,” in *Semiconductor Devices: Physics and Technology*, New York, John Wiley and Sons Inc., 1985, pp. 287-299.

- [39] L. H. J. Lajunen and P. Perämäki, "Chapter 5 - Plasma Atomic Emission Spectrometry," in *Spectrochemical Analysis by Atomic Absorption and Emission*, 2nd ed., Cambridge, The Royal Society of Chemistry, 2004, pp. 202-255.
- [40] K. Krane, "The Particlelike Properties of Electromagnetic Radiation," in *Modern Physics*, New York, John Wiley and Sons, 1983, pp. 54-82.
- [41] P. A. Fernandes, P. M. P. Salome and A. F. da Cunha, "Growth and Raman Scattering Characterization of Cu<sub>2</sub>ZnSnS<sub>4</sub> Thin Films," *Thin Solid Films*, vol. 517, no. 7, pp. 2519-2523, 2009.
- [42] E. Smith and G. Dent, *Modern Raman Spectroscopy - A Practical Approach*, Chichester: John Wiley and Sons, 2005.
- [43] Los Alamos National Laboratory, "How XPS Works," *Actinide Research Quarterly*, no. 2, 2004.
- [44] K. Krane, "The Wavelike Properties of Particles," in *Modern Physics*, New York, John Wiley and Sons, 1983, pp. 83-113.
- [45] H. Adaniya, M. Cheung, C. Cassidy, M. Yamashita and T. Shintake, "Development of a SEM-Based Low-Energy In-Line Electron Holography Microscope for Individual Particle Imaging," *Ultramicroscopy*, vol. 188, pp. 31-40, 2018.
- [46] E. Hecht, *Optics*, 2 ed., Reading, Massachusetts: Addison-Wesley, 1987.
- [47] J. I. Goldstein, D. E. Newbury, P. Echlin, D. C. Joy, C. Fiori and E. Lifshin, "Electron-Beam - Specimen Interactions," in *Scanning Electron Microscopy and X-Ray Microanalysis: A Text for Biologists, Materials Scientists and Geologists*, New York, Plenum Press, 1981, pp. 53-122.
- [48] J. I. Goldstein, D. E. Newbury, P. Echlin, D. C. Joy, C. Fiori and E. Lifshin, "X-Ray Spectral Measurement: WDS and EDS," in *Scanning Electron Microscopy and X-Ray Microanalysis: A Text for Biologists, Materials Scientists and Geologists*, New York, Plenum Press, 1981, pp. 205-274.
- [49] D. E. Newbury and N. W. M. Ritchie, "Is Scanning Electron Microscopy/Energy Dispersive X-Ray Spectrometry (SEM/EDS) Quantitative?," *Scanning*, vol. 35, no. 3, pp. 141-168, 2013.

### **3 Electrodeposition of Copper and Tin**

#### **3.1 Introduction**

The aim of this investigation was to establish reliable methods by which the required metallic elements for CZTS can be deposited using electrochemical techniques. In order to ensure consistency in the resultant sulphurised CZTS films, one of the key aims was to maintain a fixed elemental ratio across the entire surface area of the substrate. In order to achieve this, each electrodeposited layer was required to be as homogeneous, pure, uniform and smooth as possible. It was also important to control the quantity of each metal deposited and therefore the thickness of each film.

This chapter seeks to describe how each of these factors were addressed via a range of techniques. It starts by presenting some simple studies in which copper was deposited onto FTO and analysed using profilometry and EDS. EDS was also used to gauge relative thickness variation of copper and tin deposits across a sample surface. The chapter considers different electrodeposition techniques for copper, including the use of a rotating disc electrode (RDE). It must be emphasised that the only reason for experimenting with FTO was that a supply of molybdenum coated glass was not available during the early stages of the project. There was no expectation that FTO would return results that were as good as those obtained when using molybdenum coated glass. Progression from an FTO substrate to molybdenum coated glass when it became available is also considered in this chapter, and deposition efficiency is addressed through the use of both electrochemical stripping tests and through an MP-AES system.

This chapter also shows the development of appropriate conditions for the deposition of tin onto copper using different electrochemical parameters and different electrolytes, and carrying out analysis through microscopy, profilometry and SEM. Finally, there is a discussion regarding the challenges involved in depositing a second copper layer onto the tin layer, and how this was eventually achieved.



## 3.2 Experimental Methods

### 3.2.1 Sample Preparation

Prior to electrodeposition of copper taking place, samples were cut, cleaned and masked in order that only the desired deposition area came in contact with the electrolyte. This process is described in section 2.1.7. Cyclic voltammetry was used frequently in the experiments described in this chapter, a description of which can be found in section 2.1.3. For experiments involving the electrodeposition of tin, tin was always deposited onto an existing electrodeposited copper films. In these cases, copper was deposited using a static electrode in stagnant alkaline electrolyte, the electrolyte formula being available in section 2.1.5. The main reason for this relates to the relative positions of copper, tin and zinc in the electrochemical series, where attempting to deposit copper onto tin or zinc can damage the underlying layer due to the ordering of their oxidation/reduction potentials. It was also found that, when using a Mo-SLG substrate, tin would not form an adherent film when attempts were made to deposit directly onto it. When an FTO substrate was used, copper was deposited at  $-1.20\text{ V vs Hg|HgO}$  and when a Mo-SLG substrate was used, the deposition potential chosen was  $-0.98\text{ V vs Hg|HgO}$ . The charge-passed density for these copper films was typically  $572\text{ mC cm}^{-2}$ , although it was found that for the purposes of experimenting with the deposition of tin, using a thinner copper deposit of roughly  $300\text{ mC cm}^{-2}$  did not impact upon the results.

#### 3.2.1.1 Sample Preparation for the RDE

Four pieces of TEC 7 and three pieces of TEC 15 were cut and prepared using the methods described in section 2.1.7. Once they had been taped, each of the cut pieces underwent profilometry (see section 3.2.2.1) in order to compare the roughness of the FTO with the subsequently deposited copper films. Substrates were then rinsed in distilled water and blown dry under nitrogen to remove any dust that may have settled, prior to being treated in an oxygen plasma cleaner for approximately 15 minutes. The plasma treatment was being trialled as it was intended to increase the surface energy and strengthen the adherence of the deposited film to the substrate, but was found to have made no noticeable difference and therefore the treatment was not applied to other substrates. One of the pieces of TEC 7 was set aside as a spare and the remaining substrates underwent copper deposition for either 50, 100 or 150

seconds (one each of TEC 7 and TEC 15 for each duration). A deposition potential of -1.20 V was used as this had proved successful while using a static working electrode. Each sample was labelled with a number and a letter to indicate its FTO type and its copper deposition time. The number (7 or 15) corresponds to TEC 7 and TEC 15 and the letters A, B and C correspond to deposition times of 50, 100 and 150 seconds respectively. An RDE rotation frequency of 5.0 Hz was chosen as this is the rate reported for copper deposition by Scragg [1].

### 3.2.2 Sample Analysis

#### 3.2.2.1 Profilometry

A brief description of profilometry is given in section 2.4.7. Profilometry experiments are referred to frequently in this chapter for the measurement of the thickness and roughness of electrodeposited films. For all such experiments, a stylus with a 12.5  $\mu\text{m}$  radius was used, a stylus force of 3 mg, and a scan resolution of 0.093  $\mu\text{m}$ . For the measurement of film thicknesses any masking tape on the substrate had to be removed, and an example of the setup is given in Figure 3-1.

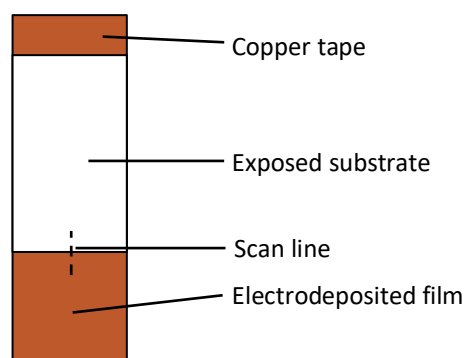


**Figure 3-1 - Diagram to show the position of the scan line during film thickness measurements, indicated by the dotted line.**

When operating the profilometer, moveable cursors on the output graph were used to select the section being analysed, making it possible to carry out roughness measurements on a deposited film and its substrate in a single scan. The intervals were chosen to avoid tall spikes in the profilometer graph where possible, as spikes are often caused by dust particles and can skew the measurements. Figure 3-2 has been provided as an example.

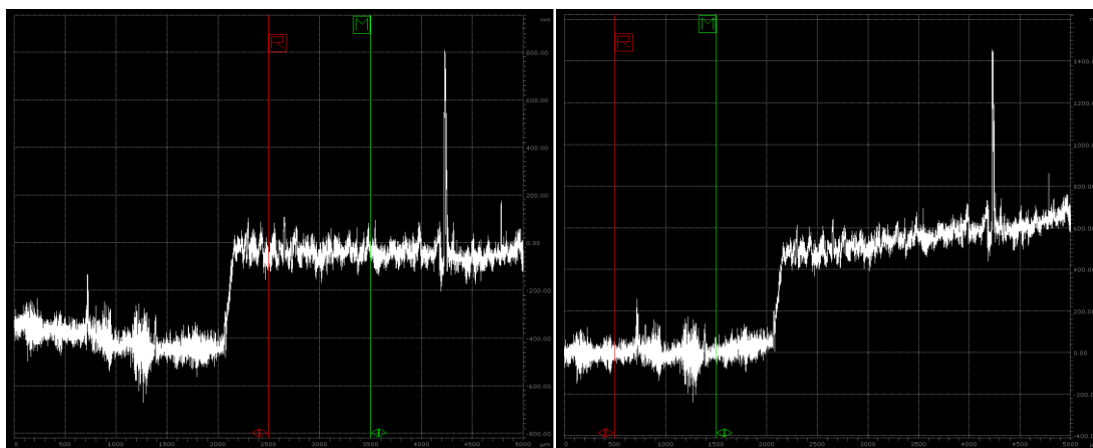


**Figure 3-2 - Examples of profilometer graphs. The intervals over which roughness measurements were taken are indicated by the red and green vertical lines. The graph on the right indicates a roughness measurement on FTO and the graph on the left indicates a roughness measurement on a copper deposit for the same sample. The gridlines represent 500  $\mu\text{m}$  intervals and the cursors are positioned 1000  $\mu\text{m}$  on each graph.**

#### ***3.2.2.2 UV-Vis-NIR Spectrophotometry***

This technique is used in this chapter to analyse the reflectivity spectra of a selection of copper electrodeposits. The settings used in these experiments are stated as the results are presented and discussed.

#### ***3.2.2.3 Scanning Electron Microscopy and Energy Dispersive Spectroscopy***

In this chapter, the EDS measurements presented were obtained using a Hitachi Desktop SEM (at an acceleration voltage of 15 kV). SEM images were obtained either using a Hitachi Desktop SEM or a JEOL 7800 FEG-SEM, and this is clarified where relevant. See section 2.4.5 for more information.

#### ***3.2.2.4 Microwave Plasma – Atomic Emission Spectrometry***

Electrodeposited films were dissolved in acidic solutions and the concentrations of the dissolved metallic elements were quantified using MP-AES. This was in order to calculate the efficiency of copper and tin deposition, and the results of these experiments are presented in section 3.3.5.2. A full description of how the samples were digested in acid and analysed using the MP-AES is given in section 2.4.1.

### 3.3 Results and Discussion

#### 3.3.1 Deposition of Copper onto FTO using a Static Working Electrode

##### 3.3.1.1 Establishing an Appropriate Deposition Potential

Cyclic voltammetry (as described in section 2.1.3) was carried out using TEC 7 FTO substrates with a 1 cm<sup>2</sup> deposition area, having been masked using the methods described in section 2.1.7. The parameters for the scan limits were chosen using reference [2] as a guide, being mindful of the fact that the substrate being experimented on in this case was FTO rather than the platinum working electrode described in reference [2]. The first cyclic voltammetry experiment used scan limits of 0.0 V and -1.70 V with -0.70 V as a starting potential. This did not return the required information, with no clear deposition or stripping peaks. The scan limits were extended to +0.80 V and -2.80 V, returning the voltammogram in Figure 3-3. A deposition peak became visible at approximately -1.70 V, which was subsequently

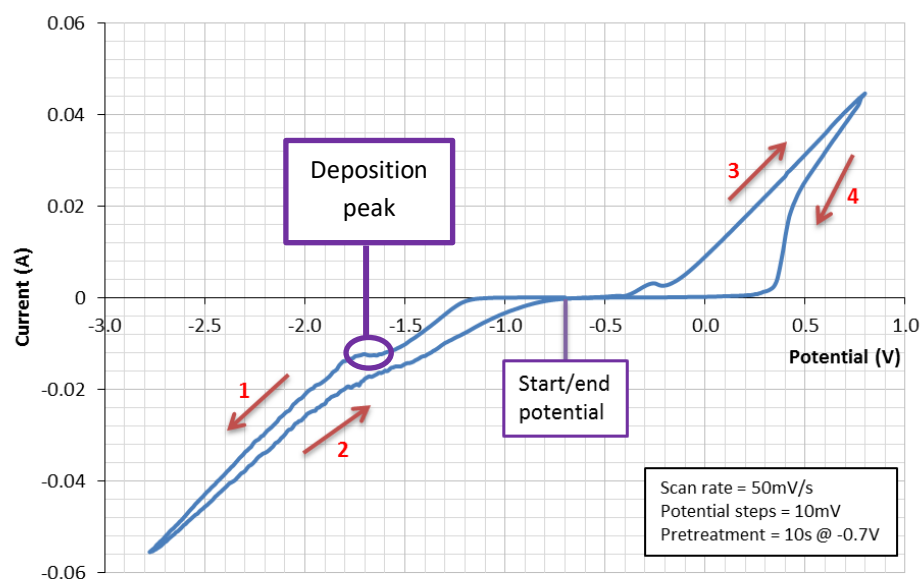


**Figure 3-3 – A cyclic voltammogram indicating a copper deposition peak in the region of -1.70V. A TEC 7 FTO substrate was used.**

used as the deposition potential in the initial copper electrodeposition experiments. The long “tail” on the negative end of the scan is caused by current flowing as a result of hydrogen evolution. This deposition potential returned films that were darker in appearance than expected. Most of the deposited films, although copper-like in their hue, were darker than other copper objects, for example the copper tape

used as an electrical contact on the substrates; however, some of the films had a blue tint, which was a cause for concern that compounds or elements other than copper may have been deposited. For comparative purposes, further deposition trials were carried out using a deposition potential of -1.20 V, which concurs with the onset of negative current flow in the first scan stage of the cyclic voltammogram in Figure 3-3. These were lighter in colour and more similar in their shade to other copper items. This is evident in the three electrodeposited copper films that can be seen in Figure 3-4, where the sample on the left and the sample in the centre have films that were deposited at -1.70 V, and the film on the sample on the right was deposited at -1.20 V.



**Figure 3-4 - Three copper films of differing colour deposited at -1.70 V (left and centre) and -1.20 V (right). The deposition time for the film on the left was 12 s, whereas the other two films had a deposition time of 150 s.**

In order to establish the differences in the elemental composition between the samples, chemical analysis was carried out using a Hitachi desktop EDS system using an acceleration voltage of 5 kV (see sections 2.4.5 and 3.2.2.3). Deposition and analysis parameters are laid out for four samples in Table 3-1. Sulphur was included when analysing sample F to find out whether the blue colour in the deposited film had been caused by contamination with copper(II) sulphate from the electrolyte. Carbon was omitted when analysing sample O due to human error, however, the results were considered useful nonetheless. One of the samples was deposited using a stirred solution – this was expected to lead to a thicker film deposited as the deposition rate would no longer be diffusion limited. This would result in a reduction

**Table 3-1 - Table showing deposition and EDS analysis settings for four samples. Samples deposited at -1.70 V have longer deposition times due to the reduced current when compared to -1.20 V depositions.**

Sample label	Deposition potential (V vs Hg HgO)	Deposition time (s)	Solution stirred?	Analysed for
F	-1.70	12	No	Cu, Sn, O, C, S
O	-1.20	150	No	Cu, Sn, O
P	-1.20	150	Yes	Cu, Sn, O, C
S	-1.20	150	No	Cu, Sn, O, C

of the tin signal and an increase in the copper signal. Tin was included to aid comparison between samples – tin is a component of FTO and the quantity was expected to remain consistent between samples (although as a percentage it was expected to vary dependent on the quantity of other elements present). Oxygen and carbon were included as elements that were considered the most likely contaminants, for example from the surfactant in the electrolyte or deposition of copper oxide. In a similar way to tin, as oxygen is present in the FTO, it can be expected to be present in all samples.

The EDS data is presented in Figure 3-5. It must be stressed that these results are not strictly quantitative; however, they are suitable for comparing the variation between samples. Although sample F was analysed for sulphur content, it returned an atomic abundance of 0%, hence sulphur content is not included in the chart. This absence of

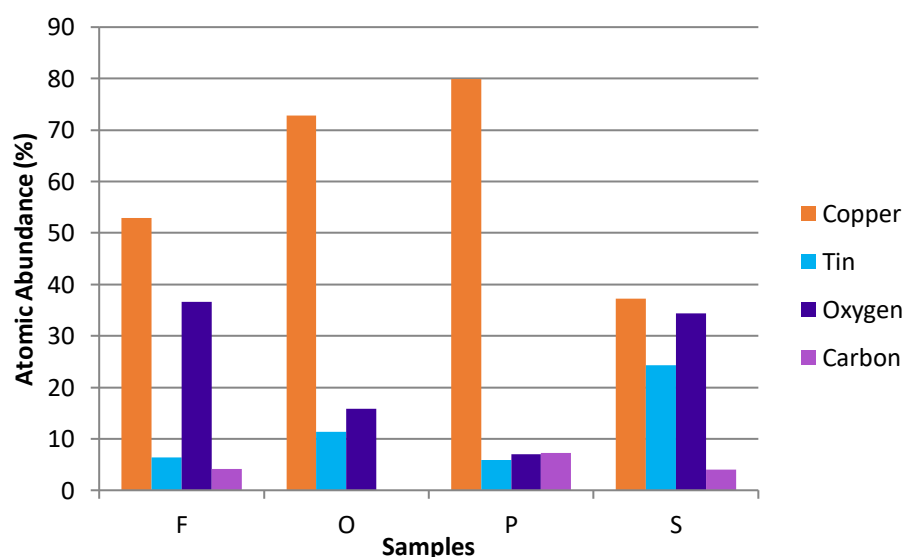


**Figure 3-5 - EDS data on the four samples described in Table 3-1.**

sulphur would suggest that the blue colour to the film was not as a result of the presence of copper(II) sulphate. The next observation to make is that sample P appears to have the greatest proportion of copper – this was expected, and will be discussed further in section 3.3.1.1. What is of particular interest, is that the ratio between the oxygen content and the tin content is similar for samples O, P and S, and the oxygen to tin ratio is much greater for sample F. This suggests that it may be the case that the oxygen in samples O, P and S is present mainly in the FTO and not the copper deposit, whereas sample F may have a significant quantity of oxygen present in the electrodeposited film. Although this could be an explanation for the difference in the film appearance, it contradicts the expectation that a more negative deposition potential would create a more reducing environment. Despite this apparent contradiction and the lack of certainty in the implications of these results, a decision had to be taken on the information available at the time. It was therefore decided that -1.20 V would be a suitable potential for depositing copper onto FTO thereafter.

### ***3.3.1.2 Film Growth and Film Morphology***

The mass of metal deposited in an electrodeposition process, and therefore the thickness of the film, is directly proportional to the charge passed in that process, as expressed by Equation 2-7 through to Equation 2-11 in section 2.1.10. In order to accurately control the mass of metal deposited in the electrodeposition process, the potentiostat/galvanostat used for the deposition needs have a current integration function that is able to terminate the process once a specified amount of electric charge has passed. Fortunately, a potentiostat/galvanostat with this function was obtained for the deposition of films that were progressed for further processing later in this project, however, a basic potentiostat/galvanostat with more limited functionality could still be used in experiments looking at the rate of film growth and the film morphology at earlier stages in the project.

During the electrodeposition process, positive copper ions are reduced at the working electrode to form atomic copper (see Equation 2-4 in section 2.1.5). Without fluid agitation, ions near the working electrode will be replaced by the diffusion of ions from the rest of the solution (“diffusion limited”), which is a relatively slow process and will not replace the ions as quickly as they are consumed, meaning that the deposition rate slows with time. Eventually, the deposition rate will become limited

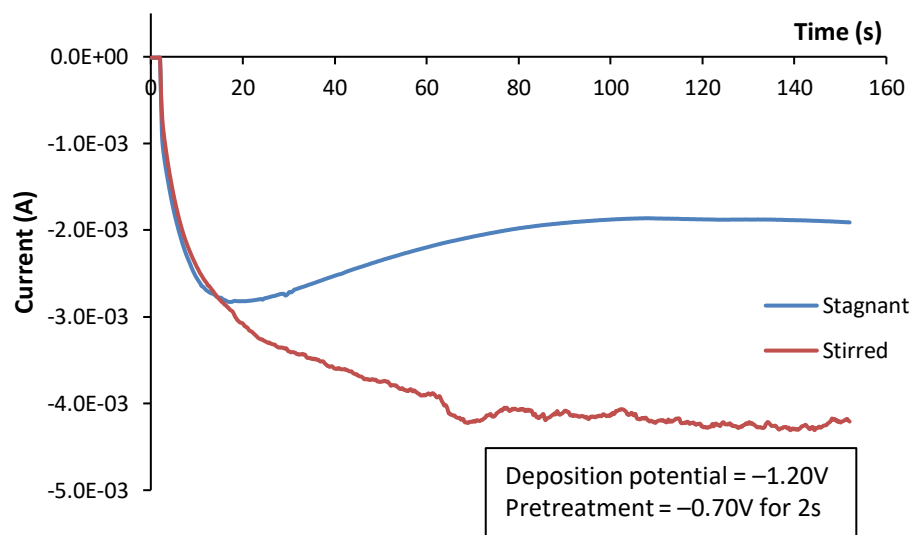


**Figure 3-6 - Current vs time for electrodeposition of copper for a stagnant electrolyte and a stirred electrolyte on 1 cm<sup>2</sup> TEC 7 FTO substrates. It is possible to see that the current magnitude declines for the stagnant electrolyte until a constant rate is reached at ~100 s, as it is diffusion limited, in contrast to that of the stirred electrolyte.**

by the diffusion rate and will settle to a constant. If the electrolyte is agitated (using a magnetic stirrer, for example), then the deposition rate is limited by the rate of the electrochemical reaction, including the supply of electrons involved in reducing the copper ions. An example in which current is plotted against time for the deposition of copper from both stirred and stagnant electrolytes can demonstrate this, which is presented in Figure 3-6. Copper deposition onto FTO using stirred and stagnant electrolytes were carried out many times during the course of this project, and the shape of the plot lines seen in Figure 3-6 are typical. It can be seen that, for the stagnant electrolyte, the current flow decreases in magnitude between 10 s and 100 s into the deposition, after which it settles at a constant rate from 100 s onwards. For the stirred electrolyte, the current flow increases in magnitude until roughly 100 s, after which the current is roughly constant and approximately twice that of the stagnant electrolyte. The precise reason for the increase in current magnitude up to 100 s was not established, but there is a possibility that it is because it takes time for copper grains to nucleate across the entire surface of the FTO until a saturation point is reached, the rate of current flow increasing with the number of nucleated grains. Although no information with regard to this specifically related to the electrodeposition of copper was found in literature, information was found relating to



the electrodeposition of a Sn-O-C composite onto nickel. It was reported that a stirred electrolyte favoured the nucleation and slow growth of many, smaller grains, whereas a stagnant electrolyte favoured the growth of fewer nuclei into larger grains [3]. This supports the hypothesis regarding copper electrodeposition stated above. Similar shapes for current-time plots relating to stirred and stagnant electrolytes were also reported [3]. The grain nucleation and growth characteristics of electrodeposited copper could be studied with the aid of a high powered FEG-SEM. This facility was not available at this stage in the project, but it could be an opportunity for further work in a future project.

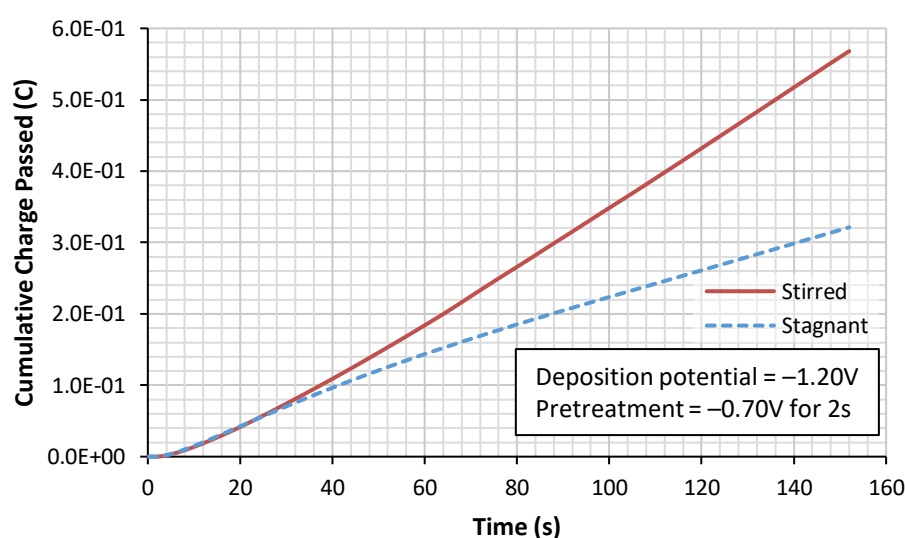


**Figure 3-7 - Cumulative charge passed plotted against time in order to compare how the charge passed, and therefore the film thickness, grows with time for stirred and stagnant electrolytes. More rapid growth is seen for the stirred electrolyte than the stagnant electrolyte from ~25 s onwards in this example.**

As stated previously, the thickness of the film is directly proportional to the charge passed in the electrodeposition process, therefore, the rate of film growth during electrodeposition is proportional to the current at any given time. In order to compare how the thickness of the deposited film grows with time for stirred and stagnant electrolytes, Figure 3-7 has been plotted, which shows the cumulative charge passed plotted against time for the same samples as Figure 3-6. It is possible to see that there is a steeper gradient, and therefore a more rapid film growth rate, for the stirred solution from approximately 25 s onwards. This would enable a shorter deposition time for films of a fixed thickness, which would be considered advantageous.

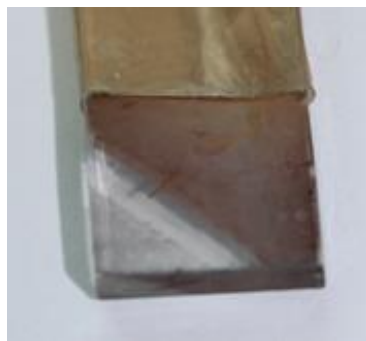


**Figure 3-8 - A 1 cm<sup>2</sup> sample deposited using a stirred electrolyte for 50 s showing poor and non-uniform film coverage. Please note that, although it appears that the PTFE masking tape became partially delaminated when the sample was dried with a nitrogen gas jet after the deposition and the subsequent rinsing (which can be seen near the top of the image), this had no effect on the copper deposit obtained.**

Unfortunately, there were concerns regarding the uniformity of deposits obtained using stirred electrolytes, particularly for shorter deposition times, with the turbulent flow around the substrates appearing to cause uneven deposits. An example of this can be seen in Figure 3-8, where patches of poor deposition can be seen, despite the fact that the substrate was cleaned and prepared in the same way as those that returned good results. Uniformity was considered to be more important than speed, therefore deposition from stagnant electrolytes was considered preferable to stirred electrolytes when samples were progressed for the deposition of subsequent layers at a later stage in the project.

Another factor of consideration was the roughness of the deposited film. It was desired that the film was as uniform as possible, not just in terms of its macroscopic visual properties, but also on a microscopic scale. A rough film can be indicative of non-uniformity, or the formation of granular clusters or “islands”. It was useful to test how rough the deposited films were in comparison to their substrates – a continuous, uniform, conformal film would have a similar roughness to its substrate, whereas a discontinuous, microscopically non-uniform film would be expected to be rougher than its substrate. Seven samples where copper had been deposited onto TEC 7 FTO with deposition times of 50-200 s were analysed using profilometry. The roughness of the FTO and the copper films were measured over 1000  $\mu\text{m}$  intervals (scan settings are given in section 3.2.2.1). The roughness of each copper film was plotted against the roughness of its substrate, the results of which are presented in

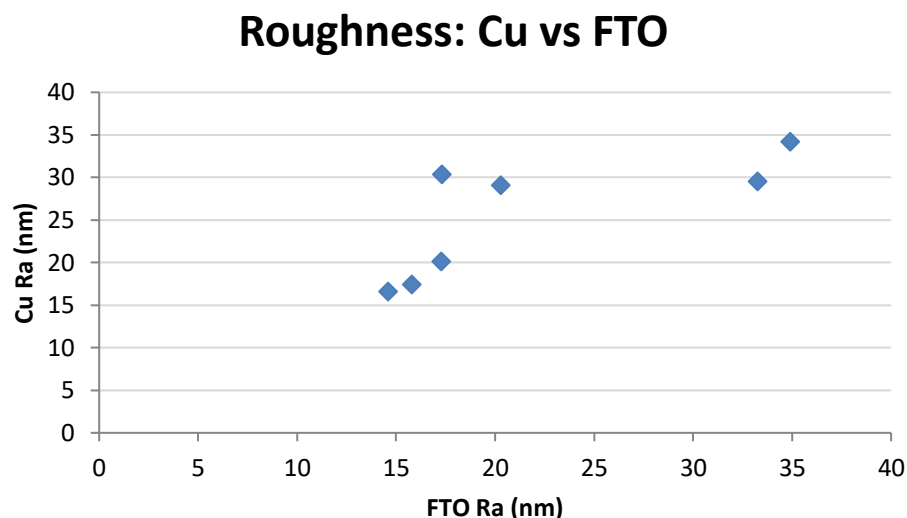


**Figure 3-9 - The roughness of each copper film plotted against the roughness of its FTO substrate. Roughness measurements were taken over 1000  $\mu\text{m}$  intervals. A correlation between the roughness of the substrate and the roughness of the copper film can be seen.**

Figure 3-9. It can be seen that the roughness of the copper is in the order of the roughness of its substrate and that there is appears to be a significant correlation between the two values, suggesting that the copper has formed continuous conformal films. This is further supported by the fact that, when a small piece of a smooth grade of TEC 15 was found, a trial deposition of copper was carried out and analysed with profilometry – the roughness of the FTO and the copper were found to be 12.83 nm and 11.08 nm respectively when measured over 3000  $\mu\text{m}$  intervals. For reference, an image of this specularly reflective copper film can be seen in Figure 3-10. This confirms that the electrolyte composition and deposition potential chosen were able to deliver smooth copper deposits provided that a smooth substrate was used.

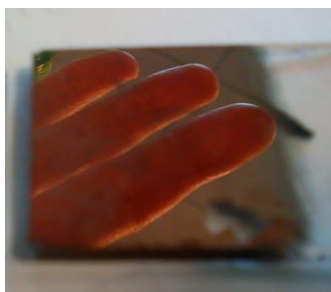


**Figure 3-10 – A specularly reflective copper film in which a reflection of three fingers can be seen. The FTO and the copper were found to have Ra values of 12.83 nm and 11.08 nm respectively. This supports the suggestion that the copper films were continuous and conformal to their substrates, and that a smooth copper film could be obtained provided that the substrate was smooth.**

### 3.3.2 Deposition of Copper onto FTO using a Rotating Disc Electrode (RDE)

The RDE was trialled for several reasons. There was a desire to test whether the more rapid deposition achieved with a stirred electrolyte was also possible with an RDE, and whether the morphological issues experienced with a stirred electrolyte due to turbulent flow could be eliminated by the laminar flow generated by an RDE (see section 2.1.6). In addition to this, as Mo-SLG was still not available at this stage in the project, there was a desire to test whether the RDE had any effect on the roughness of the deposited films.

#### 3.3.2.1 Current-Time Characteristics

In order to compare the current-time characteristics with those of a static electrode in a stirred solution, current was plotted against time for three samples, each deposited for 150 s. A deposition potential of -1.20 V was used as this had been established as being suitable with a static working electrode and it had been assumed that using an RDE would not affect the deposition potential. Both TEC 7 and TEC 15 were trialled in the RDE in order to compare their current-time characteristics, and also to later examine whether there were any differences in the surface roughness. The current-time plot is presented in Figure 3-11. It can be seen that, in common with the stirred solution, samples deposited using the RDE exhibit a gradual increase in current up until approximately 70 s and then settle to a near-constant value thereafter. It is also of note that more current flow is indicated for the TEC 7 sample than the TEC 15

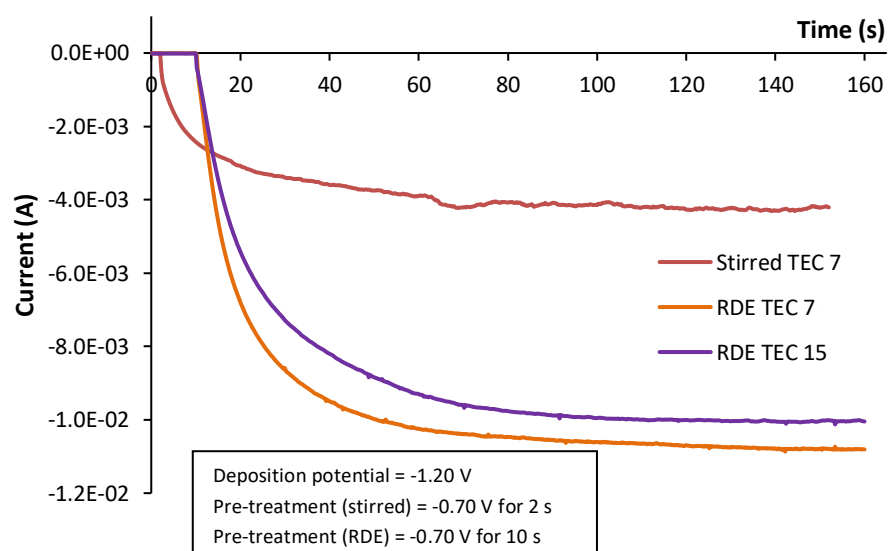


**Figure 3-11 – Current-time characteristics of RDE and stirred samples for 150 s depositions.**

sample – this was expected due to the lower sheet resistance of TEC 7. Another obvious feature is that the current for the RDE samples is more than twice that for the stirred deposition. This was a factor that required further investigation and is discussed in section 3.3.2.3.

### **3.3.2.2 Film Morphology and Appearance**

All of the films had a dark copper-like colour, similar to that seen on samples deposited at -1.70 V with a static electrode. Many of the films also had a circular line of deposit that was of a lighter colour than the rest of the film, as can be seen in Figure 3-12, although none of the films had the degree of non-uniformity seen on some of the samples produced using a static electrode in a stirred electrolyte (Figure 3-8). In addition to the profilometry carried out to measure the roughness of the

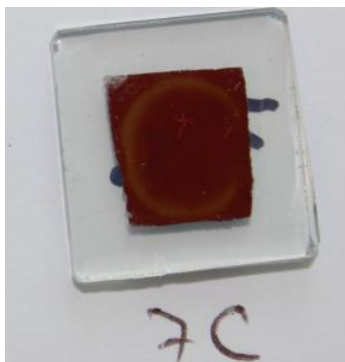


**Figure 3-12 – A 1 cm<sup>2</sup> copper film deposited using an RDE at -1.20 V for 150 s onto TEC 7 FTO. It is possible to see that the film is mostly dark in colour with a lighter coloured circular ring towards the edges.**

substrates and deposits (see below), some of the films underwent full-width profilometry scans in order to find out if the lighter coloured rings were associated with thickness variations in the film, and to check the consistency of the film thickness across the substrate (scan settings are given in section 3.2.2.1. An example of one of the scan outputs can be seen in Figure 3-13. The film appears to be of consistent thickness across the full width of the sample, with the exception of a tall spike on the very edge of the right hand side, which is most likely caused by a grain of dust.

In order to compare the roughness of TEC 7 and TEC 15 FTO, and consider which may be a smoother substrate that could be used until the Mo-SLG was available,

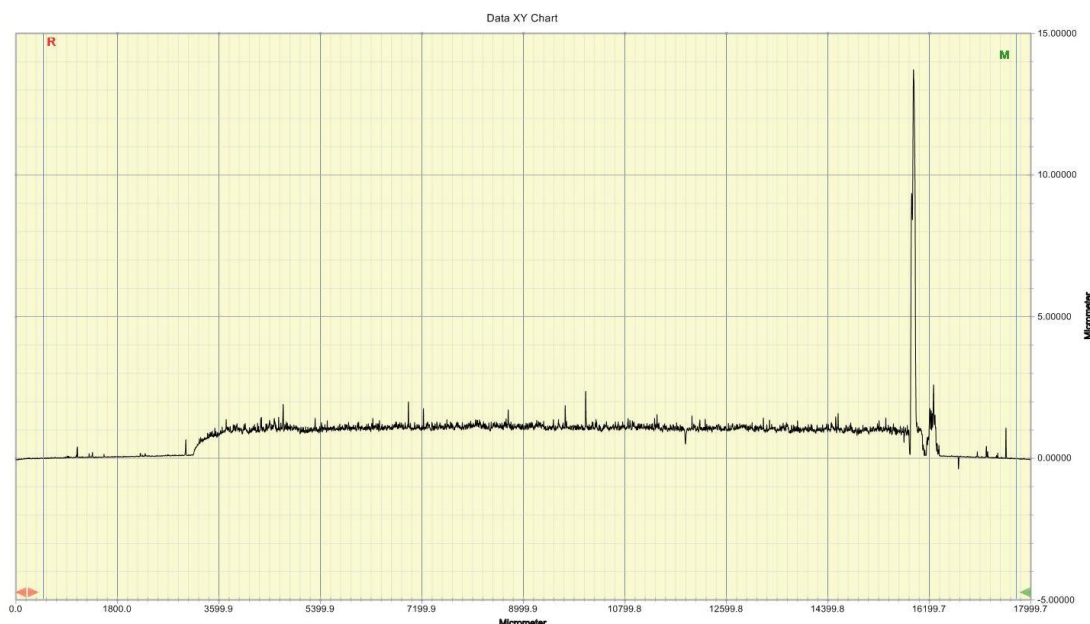


**Figure 3-13 – A full-width profilometry scan across a sample deposited with copper at -1.20 V for 150 s onto TEC 7 FTO using an RDE. It is possible to see that the film is of a consistent thickness across the full width of the sample, except for the spike on the right hand edge, most likely caused by a grain of dust. The horizontal axis is numbered at 1800  $\mu\text{m}$  intervals, while the vertical axis is numbered at 5  $\mu\text{m}$  intervals.**

profilometry was carried out on each substrate using the same scan settings as described in section 3.2.2.1 prior to copper deposition. The scan line was as near to the centre of the sample as could possibly be discerned with the naked eye. The scan results obtained are presented in Table 3-2, the  $R_a$  values having been measured across a 3000  $\mu\text{m}$  interval. It appears that the roughness of TEC 7 and TEC 15 FTO is similar, with no significant difference being discernible from this data. After film

**Table 3-2 - FTO surface roughness ( $R_a$ ) values in nm measured prior to copper deposition.**

<b><u>FTO Surface Roughness (<math>R_a/\text{nm}</math>)</u></b>		
	TEC 7	TEC 15
A	17.02	23.57
B	20.12	14.16
C	25.00	20.87
Spare	26.36	-----
Average	22.13	19.53

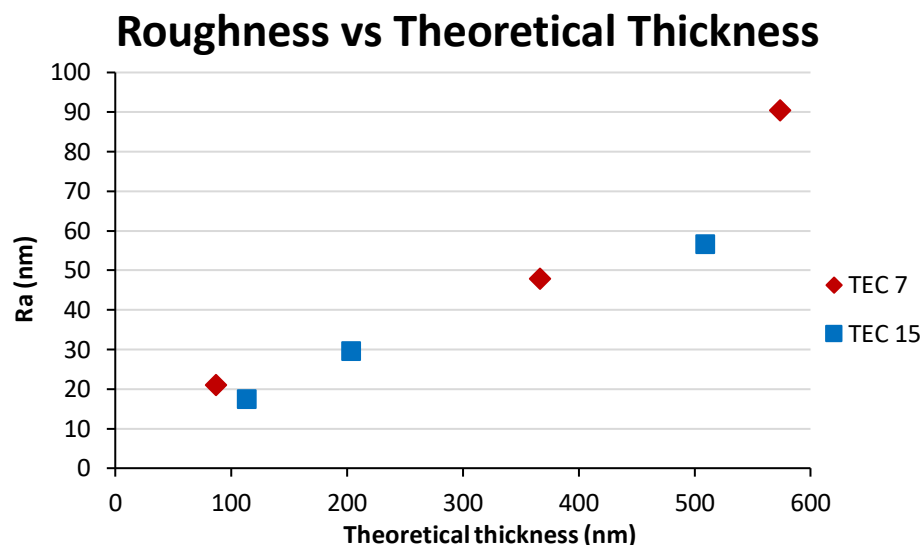


**Figure 3-14 - Copper film surface roughness plotted against theoretical film thicknesses for films deposited onto TEC 7 and TEC 15 FTO using the RDE.**

deposition, profilometry was repeated on all but the spare sample, with the scan line again being as near as possible to the sample centre. In order to investigate whether there was a correlation between the roughness of the copper deposits and their thicknesses, the measured film roughness values were plotted against theoretical film thickness (calculated from the electric charge passed) and can be seen in Figure 3-14. The trend evident on this graph would suggest that, when using an RDE, the roughness of the deposited film does tend to increase with film thickness and is less dependent on the roughness of the substrate. However, when the results in Figure 3-14 are compared to those in section 3.3.1.2, there is no evidence that using an RDE leads to smoother films overall when compared those deposited using a static electrode.

### ***3.3.2.3 Equipment Condition and its Effect on Results***

Concerns remained as to why the films deposited using the RDE at -1.20 V were noticeably darker and deposited more rapidly than those deposited at the same potential using a static electrode in stirred electrolyte. It had previously been assumed that the use of an RDE would not have an effect on the optimum deposition potential, however, experimental observations suggested that this may have been a poor assumption. For this reason, cyclic voltammetry was carried out using the RDE on TEC 7 FTO and the resulting voltammogram can be seen in Figure 3-15. When compared to the voltammogram for a static electrode (see Figure 3-3 in section

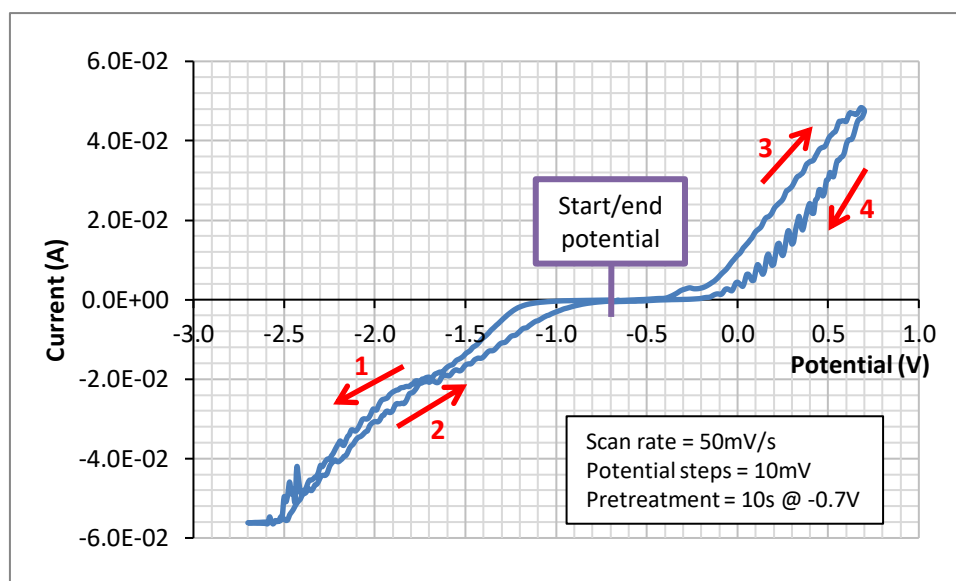


**Figure 3-15 - Voltammogram obtained for copper deposition on a TEC 7 FTO substrate using the RDE rotating at 5 Hz.**

3.3.1.1), the current obtained with the RDE is generally similar in magnitude, however, there are more fluctuations in the current towards the extremities of the potential and the onset of negative current occurs at a less negative potential. This positive shift in the deposition potential is of particular interest.

Two trial depositions were carried out on TEC 7 FTO at -1.05 V for 150 s and 900 s duration respectively. A potential of -1.05 V was chosen as this is the point of onset of negative current follow in the voltammogram in Figure 3-15. Please note that at this stage, a new taping arrangement was in use due to concerns regarding contamination of the substrate surface in the previous, more complex taping arrangement (hence the circular deposit of 13 mm – see section 2.1.7). The colour of

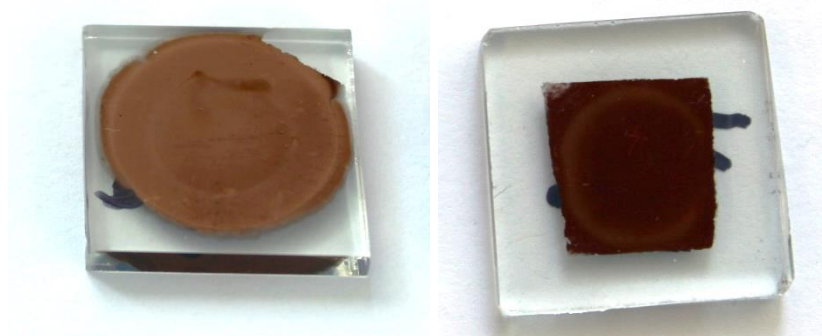


**Figure 3-16 - A paler copper film deposited at -1.05 V (left) and a darker one deposited at -1.20 V (right). Please note that there was a difference in taping method between the two samples.**



the film was visibly paler than those deposited at -1.20 V, as can be seen in Figure 3-16, which shows one copper film deposited at -1.05 V and one at -1.20 V for comparison.

A plot of current against time for the 900 s deposition is presented in Figure 3-17. Initially, the current gradually increases for approximately 370 s before settling to a near-constant magnitude of approximately 3 mA. When compared to the data for deposition at -1.20 V (see Figure 3-11 in section 3.3.2.1), this is roughly five times the time taken to settle and approximately one third of the current. If this initial period of increasing current occurs as a result of the time taken for grains to nucleate

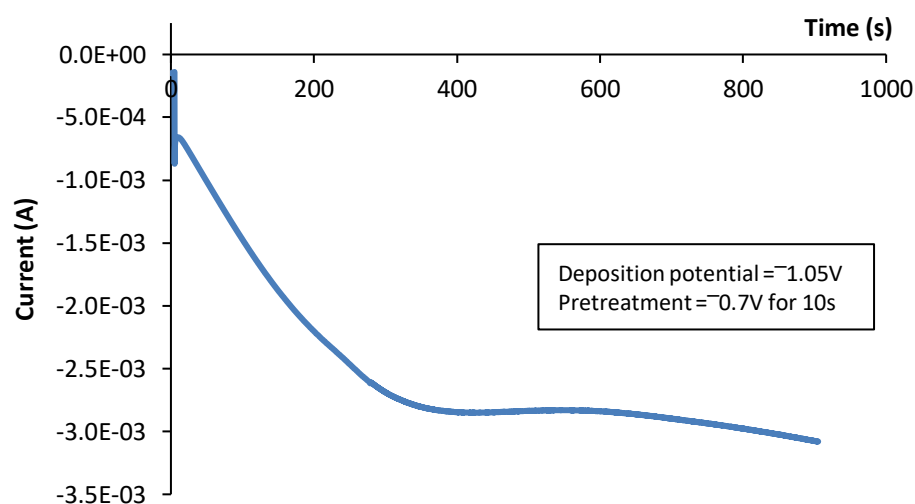


**Figure 3-17 - A current-time plot for copper deposited at -1.05 V using the RDE for 900 s.**

and grow across the entire surface area of the substrate (as hypothesised previously in section 3.3.1.2), then the rate of nucleation and growth may have an effect on the microstructure of the film, which in turn could affect the reflectivity of the film. For example, a dendritic structure may lead to more light trapping and therefore more light absorption by the film compared to a close-packed granular structure, which would lead to a darker appearance. This may provide an explanation for the difference in colour shade between films deposited at different potentials, and is supported by the findings in section 3.3.3.1 and section 4.3.6, where a FEG-SEM was available and was used to take high-magnification images of electrodeposited films.

The question remained as to why the RDE appeared to require a different deposition potential compared to a static electrode setup using a stirred solution. When using the RDE, the working electrode and working electrode sense terminals are connected in different places and this became a point for consideration (the working electrode sense connector is the point through which the electric potential is fed back into the potentiostat/galvanostat). Carrying out a simple experiment with a multimeter, in which the multimeter was set to read resistance while its probes were placed in electrical contact with different contact points on the RDE, revealed that the RDE had significant internal resistances between the terminals. These are detailed in Figure 3-18. Concerns arose as to whether this was affecting the deposition potential and the data. In order to test this, two further depositions were carried out. Each of these was on TEC 7 FTO at -1.20 V for 150 s. For one of the samples, the working electrode and sense connections were transposed and for the other, the working electrode and sense connections from the potentiostat/galvanostat were both connected to the working electrode terminal on the RDE. Both of the resultant films were significantly paler than those previously produced at -1.20 V. Furthermore, the deposition current was smaller in magnitude – for the deposition with transposed terminals it was roughly half that of the previous deposits and for the other deposition it was roughly a quarter. These results suggest that the high internal resistances of the RDE (which are probably caused by internal corrosion) were having an effect on the deposition potential and the data. In addition to this issue, the long term aim of this project was to find a scalable deposition technique and the RDE

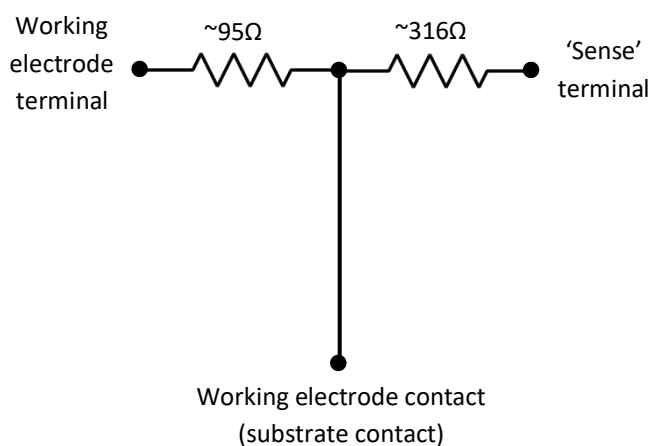


**Figure 3-18 – A schematic diagram indicating the internal resistances measured between the electrical contact points on the RDE.**

is not easily scalable. For these reasons, further experimentation with the RDE was suspended while further experimentation using static electrodes was pursued.

### **3.3.3 Deposition of Copper onto Molybdenum Coated Glass**

The most common substrate for CZTS reported in literature is Molybdenum Coated Soda-Lime Glass (Mo-SLG). There are four main reasons for this. Firstly, molybdenum has a high melting point (2622 °C) [4], which enables it to withstand the annealing processes required in the manufacture of CZTS without detrimental levels of diffusion. Secondly, when samples are sulphurised (or selenised), a layer of molybdenum sulphide (or selenide) is formed between the remaining molybdenum and the CZTS, which acts as a useful ohmic contact [5]. Thirdly, unlike some metallic elements, molybdenum does not poison the CZTS [6]. Fourthly, it allows some sodium from the soda-lime glass to diffuse into the CZTS in the annealing processes and act as a dopant, which can enhance the performance of CZTS solar cells [7]. The earlier experiments in this project were carried out using FTO due to the lack of availability of Mo-SLG, however, once a supply of sputtered Mo-SLG was sourced, this was used for subsequent electrodeposition experiments. For a brief initial period, the Mo-SLG was supplied by Loughborough University. However, this was found to be of poor quality, with scratches being visible and frequent problems with delamination presenting. A supply of high quality Mo-SLG was subsequently established with M-Solv Ltd. The samples in images, and/or data presented in Figure 3-19 through to Figure 3-22 is relating to Mo-SLG from Loughborough University, whereas all other images and data referring to Mo-SLG is relating to M-Solv products.

#### ***3.3.3.1 Establishing an Appropriate Deposition Potential***

Electrodeposition was carried out using a static working electrode in stagnant electrolyte. Samples were prepared using the methods described in section 2.1.7 and had a 1 cm<sup>2</sup> deposition area unless otherwise stated. The availability of a new potentiostat/galvanostat with a current integrator made it possible to set the experiment to terminate once a fixed amount of charge had passed. At this stage in the project, the aim was to deposit a four-layer elemental stack including two copper layers. A charge limit of 286 mC was chosen as this would lead to half the copper required for the desired elemental ratios to be obtained (with a view to the future deposition of four-layer Cu-Sn-Cu-Zn stacks. The first depositions of copper onto



**Figure 3-19 - Copper deposited onto Mo-SLG at -1.20V onto a 1 cm<sup>2</sup> area. Some pitting of the film can be seen, which likely occurred due to hydrogen evolution. The scratch marks were pre-existing on the substrate.**

Mo-SLG were carried out at -1.20 V as this had been found to be a suitable potential for deposition onto a static FTO electrode. When trialled with Mo-SLG, this returned films that were dark and pitted, with a significant amount of hydrogen evolution being observed in the form of fizzing at the working electrode surface. An example of one of these films can be seen in Figure 3-19. This dark film and hydrogen evolution suggests that the change in substrate may have caused a positive shift in the deposition potential.

The decision was taken to perform cyclic voltammetry. A cautious approach had been taken owing to the fact that molybdenum sits below copper in the electrochemical series (see Figure 2-3 in section 2.1.4), meaning that dissolution of molybdenum is to be expected during the voltammetric sweep, which could affect the data. A voltammetric sweep was carried out using -0.30 V as a start/end potential, with the first vertex set to -1.20 V and the second at +0.50 V. This produced a voltammogram with a very large stripping current, most likely due to the dissolution of molybdenum. A section of this voltammogram showing only the current in the interval between -0.40 V and -1.20 V is presented in Figure 3-20 in order to identify a deposition peak. It can be seen that there is a deposition peak evident at -1.08 V, which was chosen as the starting point for a series of samples that were deposited at incrementally more positive potentials as part of a trial and error process. It can also be noted that the voltammogram plot crosses the horizontal axis at -0.56 V, which was chosen to use as a pre-treatment for 5 s. Two samples were deposited at -1.08 V, one at -1.06 V and one at -1.05 V. The samples deposited at -1.08 V and -1.06 V returned dark films with some hydrogen evolution being evident with bubbles

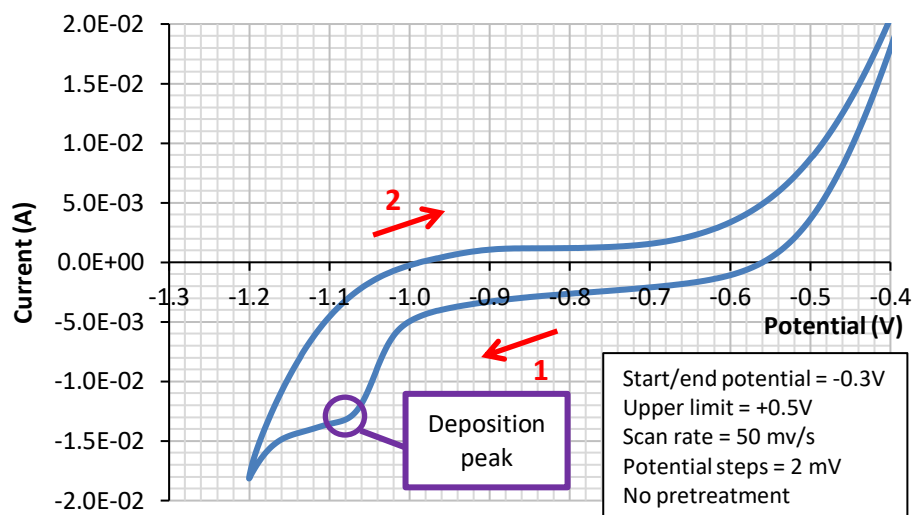


**Figure 3-20 - A section of a voltammogram for copper deposition onto Mo-SLG indicating a possible deposition peak at -1.08 V.**

adhering to the surface of the samples as they were removed from the electrolyte after deposition. There was some marking left on the film where the bubbles had been after the samples were rinsed. The sample deposited at -1.05 V returned a film much lighter in colour, similar to that of the copper tape used to aid electrical contact. This film also had a more diffusely reflective surface, similar in look to the copper films deposited at -1.20 V onto FTO. These four films are presented in Figure 3-21.

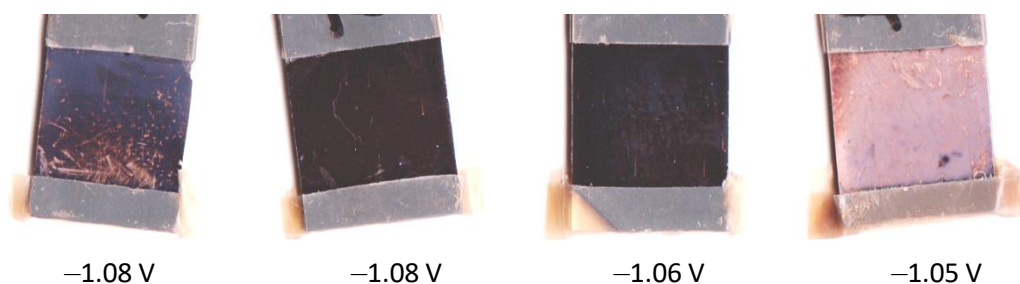


**Figure 3-21 - Copper deposited onto Mo-SLG across a small range of potentials, which are indicated beneath the image of each sample. Two samples were deposited at -1.08 V, one at -1.06 V and one at -1.05 V. Some scratch marks were pre-existing due to an initial poor quality supply of Mo-SLG, but the pitting was not and was due to hydrogen evolution.**

Further to the visual observations, the reflectivity spectra of these samples were obtained in the 200-1000 nm wavelength range using a UV-Vis-NIR Spectrophotometer and are presented in Figure 3-22. These spectra indicate that,

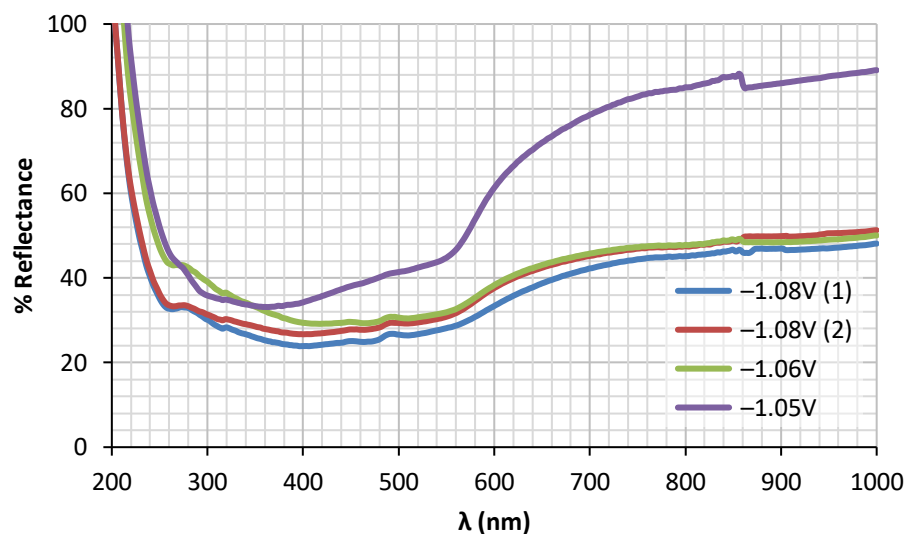


**Figure 3-22 - Reflectivity spectra in the 200-1000 nm wavelength range for four samples deposited at potentials between -1.08 V and -1.05 V.**

despite its more diffusely reflective appearance, the copper film deposited at -1.05 V is more reflective of light with a wavelength greater than 350 nm than the films deposited at -1.08 V or -1.06 V. These results were in accordance with expectation, given the significantly lighter appearance of the film. Based on these findings, -1.05 V was adopted as the deposition potential, however this was only temporarily. Further depositions at -1.05 V returned films very similar to those deposited at -1.08 V or -1.06 V. Inspection of the current-time data for the original deposition at -1.05 V revealed that there were fluctuations in the deposition current, akin to there being a loose or poor electrical connection. This prompted further experimentation where a series of samples were deposited at incrementally more positive potentials, starting with -1.03 V. It was found that films deposited at potentials more negative than -0.98 V tended to have a darker colour shade and to show evidence of hydrogen evolution, such as bubbles being visible on the substrate surface after deposition and pitting visible on the film. Films deposited at potentials positive of -0.98 V tended to be pale in colour and more diffusely reflective, as did films that were affected by poor electrical connections. Films deposited at -0.98 V with good electrical contact were generally specularly reflective, with minimal or no visible hydrogen evolution, and exhibited a light colour shade similar to that of the copper tape used in the sample preparation. Given this, -0.98 V was then chosen as the most appropriate potential for depositing copper onto molybdenum going forward.



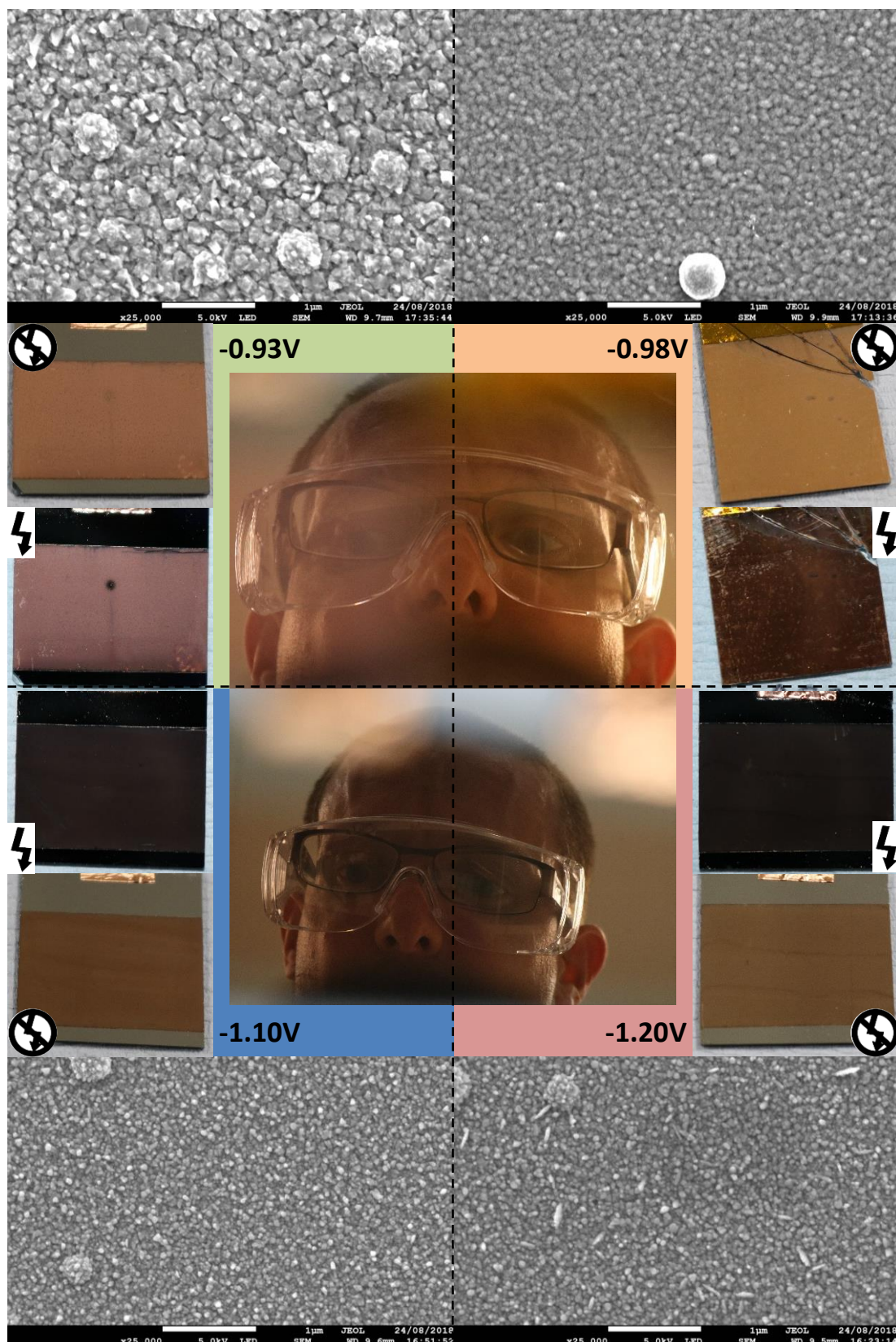


**Figure 3-23 - Photographs of samples deposited at different potentials, along with SEM images. The SEM images were taken at 25000X magnification on a FEG-SEM and the scale bars represent 1  $\mu\text{m}$ . The figure has been divided into quarters, each quarter relating to a different deposition potential. The photographs around the centre were taken without a flash and at a different focal length to those on the far left and far right. Differences in the colour tone and specular reflectivity seen in the photographs can be compared with the microstructures seen in the SEM images.**

At a later stage in the project, a high-powered FEG-SEM became available. Figure 3-23 details images of copper films deposited with a 4 cm<sup>2</sup> deposition area at -1.20 V, -1.10 V, -0.98 V and -0.93 V, and relates their visual properties to their microstructure. It can be seen that the films deposited at -1.20 V and -1.10 V are darker than the other two samples, and have little difference in their colour shade or degree of specular reflectivity when compared to each other. The SEM images show that they also have similarly sized small grains, approximately 50 nm in diameter, and there are also signs of dendrite formation on the film deposited at -1.20 V. Similar levels of specular reflectivity are observed from the film deposited at -0.98 V, which is lighter in colour. This may be a result of the larger, more closely packed grains, which are approximately 75 nm in diameter according to the SEM image. The film deposited at -0.93 V is the lightest in colour, the most diffusely reflective and has the largest grains (approximately 150 nm in diameter). The more diffuse reflectivity can be observed when comparing the clarity around the eyes of the photographer in the reflected images. These results suggest that the differing visual appearances of the films that result from changes to the deposition potential, are related to the microscopic grain form of the films, rather than the oxygen content. The information gained through the experiments in this section made it possible to deposit copper films of a reproducible high quality, meaning that the project was now in a good position to progress onto the deposition of the second metallic layer, which was tin.

### **3.3.4 Electrodeposition of Tin onto Copper**

#### ***3.3.4.1 Deposition Using an Alkaline Electrolyte***

As discussed in section 2.1.8, initial experiments for the electrodeposition of tin onto copper were carried out using a sodium hydroxide based electrolyte due to safety concerns relating to the use of methanesulfonic acid, which was reported as delivering homogeneous films by Scragg in [8]. Depositions from an alkaline electrolyte were carried out onto 1 cm<sup>2</sup> copper films that had been deposited onto TEC 7 FTO at -1.20 V using a static working electrode and a stagnant solution. The reason for using an FTO substrate was that, at this stage, Mo-SLG was only available in limited quantities until a reliable supplier was later established. The potentiostat/galvanostat was equipped with a current integrator and had been set to



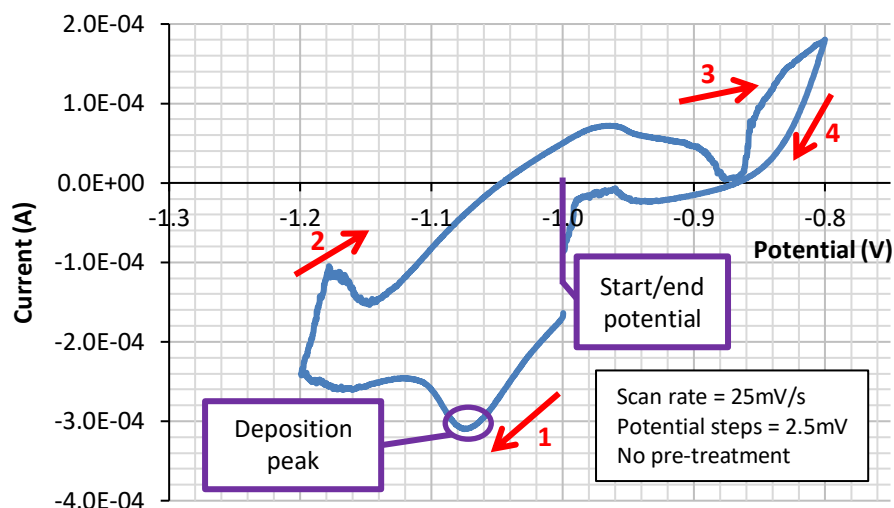


**Figure 3-24 - A voltammogram for the deposition of tin onto copper using an alkaline electrolyte. A deposition peak is indicated at -1.075 V. Other peaks are visible at -1.15 V and -0.8 V and are likely due to hydrogen evolution occurring at the working electrode and the counter electrode respectively.**

terminate after 286 mC of charge had passed during copper deposition. The composition of the copper electrolyte is given in section 2.1.5.

In order to establish an appropriate deposition potential, cyclic voltammetry was carried out using the alkaline electrolyte with the composition stated in section 2.1.8 including the surfactant. The lower limit of the voltammetric sweep was -1.20 V (vs Hg|HgO) and the upper limit was -0.80 V, with a start/end potential of -1.00 V. These parameters were taken from [9]. This voltammogram is presented in Figure 3-24 and a deposition peak is indicated at -1.075 V. It is worth noting that the current flowing is significantly less than that observed in voltammograms for copper deposition (for example in Figure 3-3 and Figure 3-20), leading to the expectation that a significantly longer deposition time would be required to reach the desired amount of charge passed. It is also worth noting that the current peaks at -1.15 V (negative current) and -0.8 V (positive current) are likely due to hydrogen evolution occurring at the working electrode and counter electrode respectively. A trial deposition was carried out at -1.075 V, with the charge limit set to 312 mC as this would lead to the mass of tin required for the desired elemental ratios to be obtained. During deposition, the current ranged from between -0.04 mA and -0.13 mA, and the experiment was terminated manually after 1002 s when only 73.5 mC of charge had passed. The reason for this premature termination was that there was no visible tin

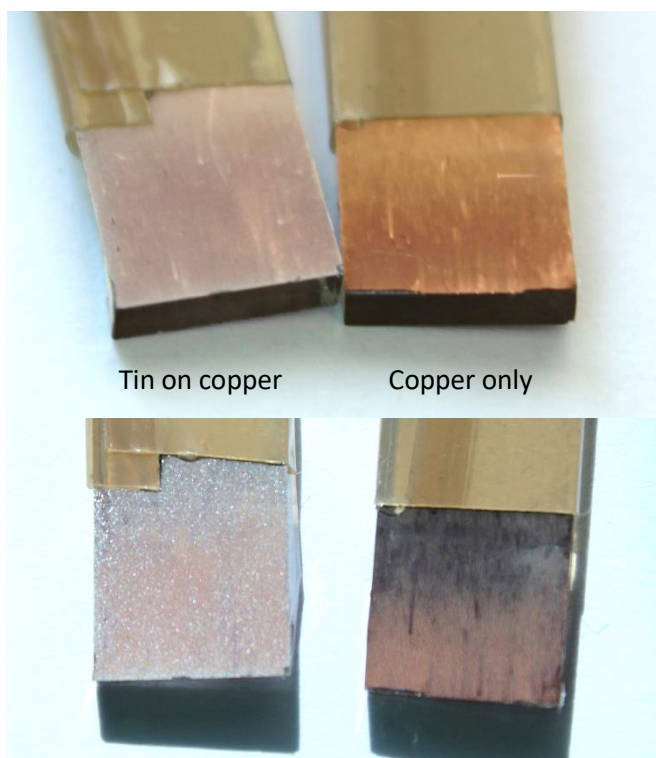


**Figure 3-25 - Photographs of tin deposited onto copper from an alkaline electrolyte (left) next to a copper film for comparison (right).**

film forming on the copper, and the copper film had become visibly damaged in the form of a slit of approximately 7 mm length running vertically near the centre of the film. When this sample was removed from the electrolyte, it was possible to see through the FTO that there had been a colour change to the underside of the copper film – it had become more silver in its colour, as if the tin had penetrated beneath the copper film. When the sample was dried under a nitrogen jet, the film delaminated and was lost, suggesting that the process of the attempted film deposition had negatively affected the adhesion of the copper film to its substrate. It is suspected that the surfactant had blocked the adhesion of tin to the outer surface of the copper film, yet some tin electrolyte had permeated the copper film and deposited on its underside, forcing it to delaminate from the FTO substrate as the tin film formed.

The experiment was repeated twice using the same deposition settings as previously and using an electrolyte with the same composition, with the exception of the surfactant being omitted (no surfactant was reported in the work described in [9]). The deposition currents were between -0.35 mA and -0.5 mA, and the depositions took 892 s and 694 s respectively to reach the required 312 mC of charge passed. One of the resulting films can be seen in Figure 3-25, where it is photographed

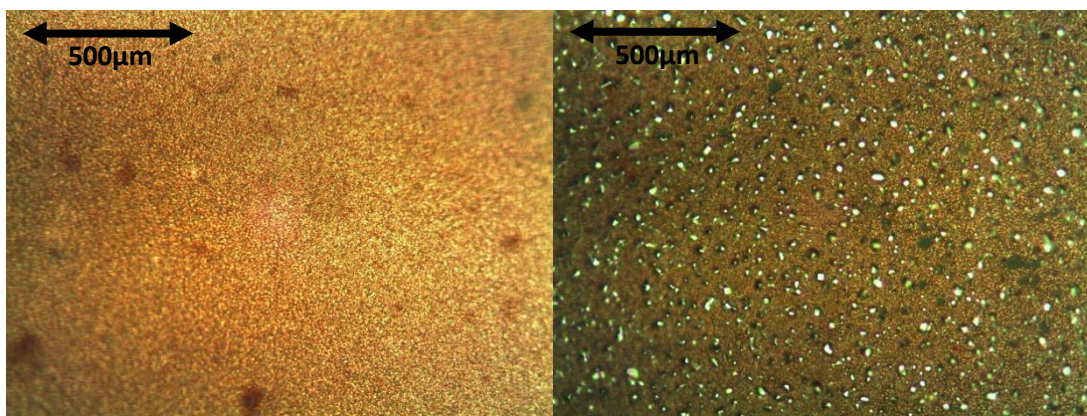


**Figure 3-26 - Microscope images (50x magnification) of copper (left) and tin deposited onto copper from an alkaline electrolyte (right), showing tin island formation.**

alongside a copper film from two different angles for comparison. It can be seen that the sample that underwent tin deposition is lighter in colour and appears to have a “glitter effect”. Although there is an obvious difference between the visual properties of the films, the sample with tin present does still present a colour tone that is akin to copper. Further examination of the films was carried out using an optical microscope and a profilometer.

Images of the tin depositions (and a copper film for comparison) were obtained using an optical microscope. Figure 3-26 presents an image of a copper film and an image of copper with tin deposited on top at 50x magnification. It can be seen that, rather than forming the desired continuous film, the tin deposited in “islands” that leave much of the copper film exposed. These islands were approximately 1-5  $\mu\text{m}$  across with spacing of approximately 1-10  $\mu\text{m}$  between them. Analysis through profilometry revealed that the average roughness ( $R_a$ ) values of the tin deposits were 817 nm and 414 nm respectively when measured across a 3000  $\mu\text{m}$  interval, compared to 17 nm for the copper film. A zoomed-in image of the profilometer graph generated by scanning one of the tin deposits is presented in Figure 3-27. It can be seen in this image that the tin crystals were typically 0.3-2.0  $\mu\text{m}$  in height. This means that the tin is effectively concentrated in patches across the deposition area and would likely lead to tin rich regions surrounded by tin poor regions upon annealing. This in turn would favour the formation of binary and ternary phases, with the associated charge trapping and recombination [10], rather than the desired homogeneous CZTS film. Therefore, the decision was taken to pursue a different electrolyte composition for tin deposition.

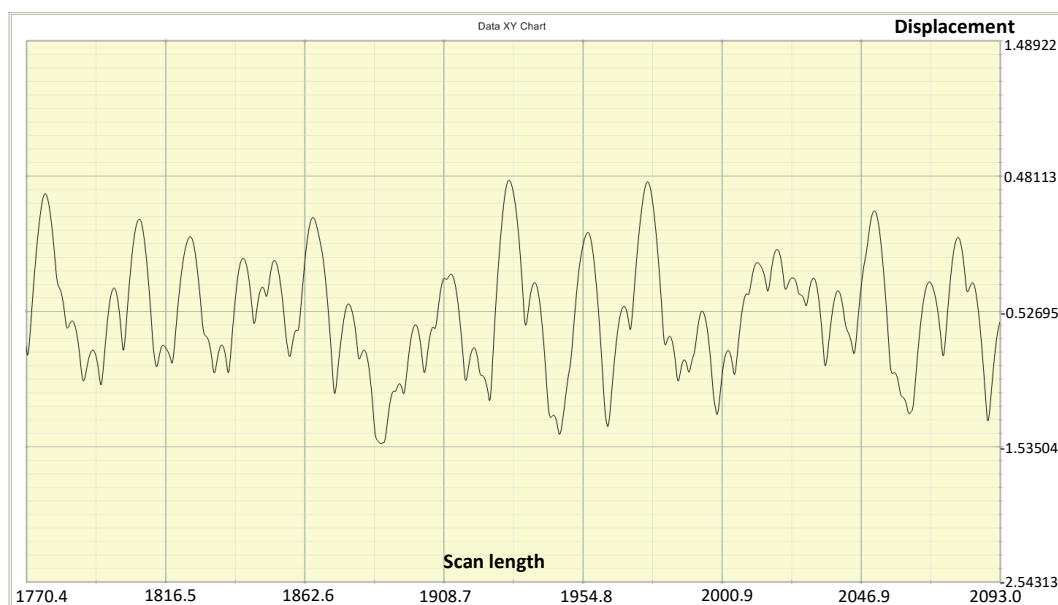


**Figure 3-27 - A zoomed-in profilometer scan of tin deposited onto copper using an alkaline electrolyte.**

### 3.3.4.2 Deposition Using a Methanesulfonic Acid Electrolyte

Having conducted a detailed risk assessment, the decision was taken to experiment with a methanesulfonic acid based electrolyte for the deposition of tin, as this is reported to have delivered favourable results by Scragg in [8]. The composition of this electrolyte is stated in section 2.1.8. Tin was deposited onto 1 cm<sup>2</sup> copper films, the copper films having been deposited potentiostatically onto Mo-SLG at -0.98 V (vs Hg|HgO) to a charge limited to 286 mC.

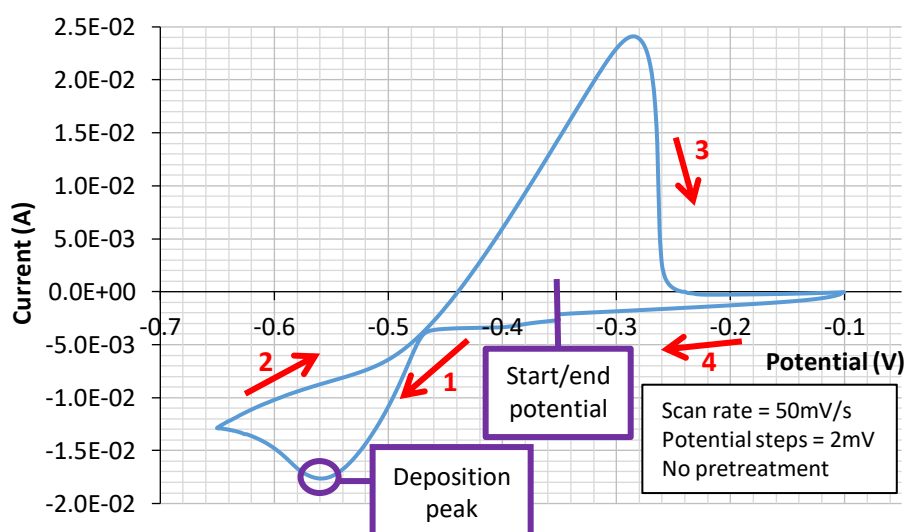


**Figure 3-28 - A voltammogram for the deposition of tin onto copper using a methanesulfonic acid electrolyte. A deposition peak is indicated at -0.56 V.**

Cyclic voltammetry was performed using a start/end potential of -0.35 V (vs Ag|AgCl), with the first scan limit set to -0.65 V and the second to -0.10 V (based on results reported by Scragg in [11]). The resulting voltammogram is presented in Figure 3-28, with a deposition peak clearly visible at -0.56 V. Trial depositions were carried out at three different potentials for comparison, in order to study whether the deposition peak was the most suitable potential, or if, as with copper, more desirable results could be achieved at a different potential.

Tin was deposited onto 1 cm<sup>2</sup> copper films on three samples, one each at -0.45 V, -0.56 V and -0.98 V. The charge limit was set to 312 mC (the calculated charge required to obtain the desired elemental ratios) except for the sample deposited at -0.98 V, which was terminated after 286 mC of charge had passed. During deposition, some hydrogen evolution was visible on the sample deposited at -0.98 V, but not the other two samples. A photograph of the three samples is presented in Figure 3-29. It can be observed that deposition at -0.98 V caused some streaking of the film, while deposition at -0.45 V led to a film that was much whiter in colour. This film was also diffusely reflective, and had a slight copper-like tint to its colour. The most specularly reflective film was that deposited at -0.56 V, which was also the most homogeneous in its appearance.

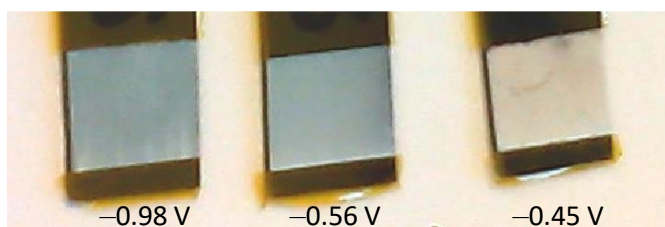


**Figure 3-29 - Tin deposited onto copper at three different potentials from a methanesulfonic acid electrolyte. Mo-SLG was used as a substrate.**

The deposition current was noticeably different for each sample, which is evident in Figure 3-30, which is a plot of current vs time for all three samples. The features that are of particular note are the large initial spike in current for the -0.56 V deposition, the slightly jagged plot line for the -0.98 V deposition (likely caused by hydrogen evolution – the current fluctuates as bubbles nucleate, grow and depart), and the fact that the deposition carried out at -0.45 V is lower in magnitude than that for the other two samples throughout the deposition process.

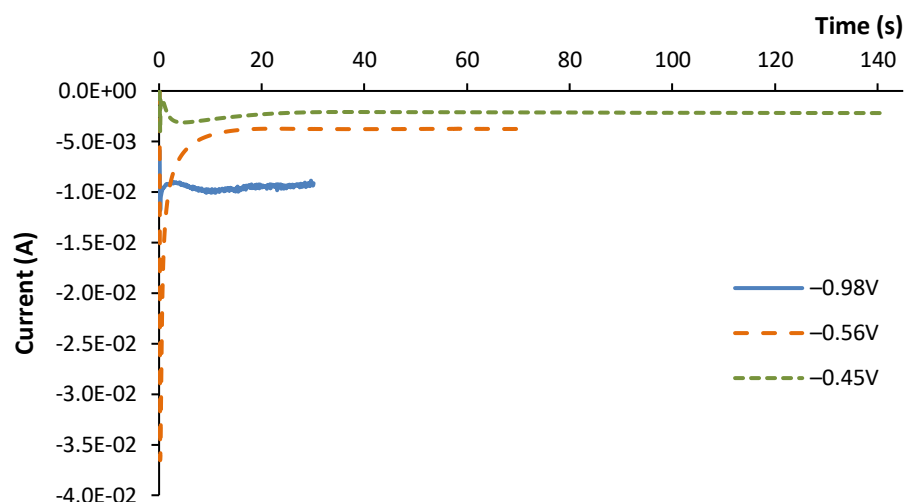


**Figure 3-30 - Current-time characteristics for tin deposited onto copper from a methanesulfonic acid electrolyte at three different deposition potentials.**

Profilometry scans were carried out on each sample using the methods described in section 3.2.2.1. The thickness of each copper-tin stack was measured at the top and bottom edges (“top” and “bottom” are a reference to the orientation of the sample when undergoing deposition) in order to ascertain whether there was a significant or consistent difference in film thickness across the deposition areas. The stylus force used was 3 mg and the scan resolution was 0.093  $\mu\text{m}$ . Roughness values were measured across 2000  $\mu\text{m}$  intervals and are presented in Table 3-3, along with film

**Table 3-3 - Film thickness and surface roughness measurements taken on copper-tin stacks for different tin deposition potentials.**

Deposition potential (V)	Film thickness ( $\mu\text{m}$ )		Surface roughness/Ra (nm)	
	Top	Bottom	Top	Bottom
-0.45	0.57	0.77	100.33	76.85
-0.56	0.30	0.63	17.38	22.59
-0.98	0.24	0.40	53.69	73.28

thickness results. In addition to profilometry measurements, images were taken using an optical microscope at 50x magnification and are presented in Figure 3-31. With reference to the profilometry results, there appears to be a significant difference in thickness between the top and bottom edges of the films, which, although undesired, is in accordance with expectations for a stagnant electrolyte and static working electrode (as explained in section 2.1.6). The least thick film was that deposited at



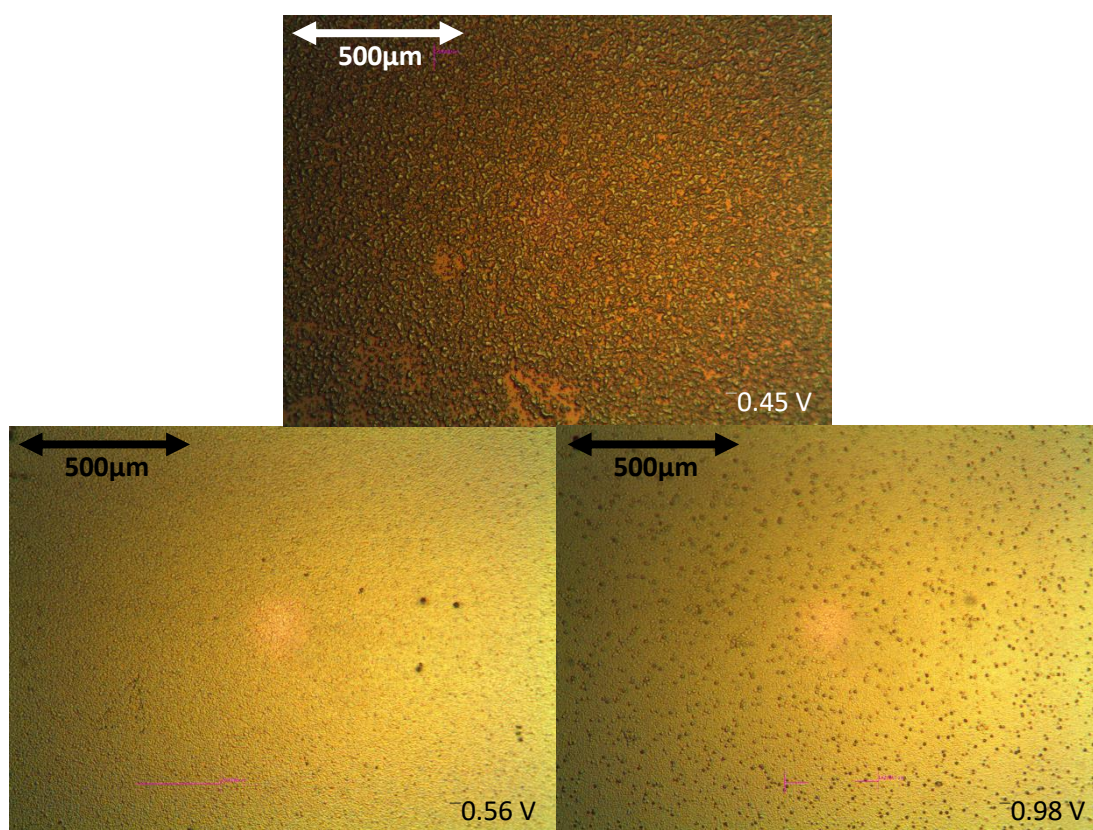


**Figure 3-31 - Microscope images taken at 50x magnification for tin deposited onto copper from a methanesulfonic acid electrolyte at different potentials.**

-0.98 V, which is also in accordance with expectations as the least charge was passed during its deposition and some of the charge was wasted due to hydrogen evolution. The thickest film was also the roughest film, which was the sample deposited at -0.45 V. The apparent thickness may be as a result of the roughness, as the additional and taller peaks would lead to this impression. The smoothest film was that deposited at -0.56 V. The microscope images also give some visual indication of the roughness of each film. The sample deposited at -0.45 V appears to have incomplete tin coverage, with the tin having deposited as small interconnected islands ( $\sim 10\ \mu\text{m}$  across) leaving much of the copper exposed, although not to the extent of films deposited from an alkaline electrolyte. The sample deposited at -0.98 V also has some roughness visible on the tin surface in the form of small raised points ( $\sim 10\ \mu\text{m}$  across, with  $\sim 100\ \mu\text{m}$  between them), which are most likely small blisters formed during the process of hydrogen evolution. There does, however, appear to be complete coverage of the copper film beneath. The film deposited at -0.56 V also displays complete coverage and has the least evidence of raised points and apparently the most homogeneous film.

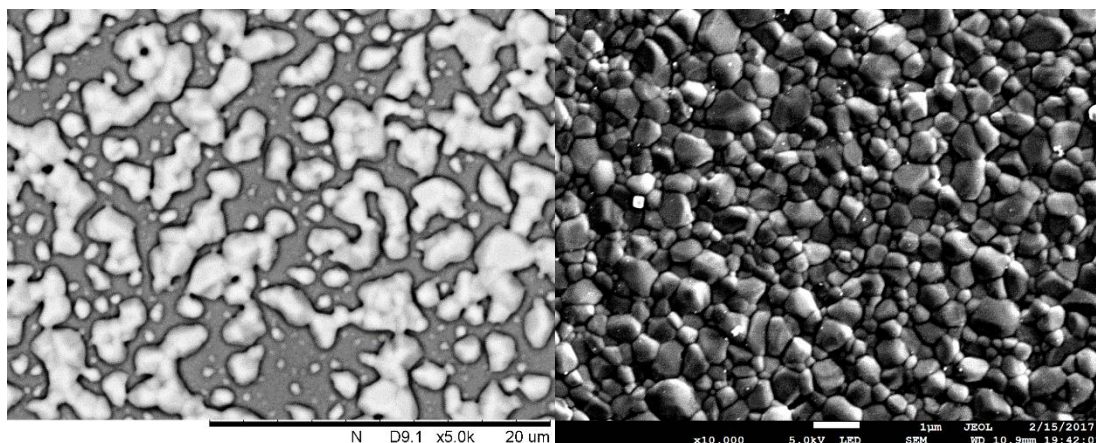


**Figure 3-32 - SEM images of tin deposited onto copper from a methanesulfonic acid electrolyte at -0.45 V (left) and -0.56 V (right). The image on the left was taken on a desktop SEM and is 5,000x magnification, while the image on the right was taken on a FEG-SEM and is 10,000x magnification (the white scale bar represents 1  $\mu\text{m}$ ).**

An SEM image of tin deposited at -0.45 V is presented in Figure 3-32, alongside an SEM image of tin deposited at -0.56 V. The image of the film deposited at -0.45 V was taken using a desktop SEM. Unfortunately, this SEM was unable to focus on the tin films deposited at -0.56 V and -0.98 V, therefore the other image included in Figure 3-32 was taken using a FEG-SEM at a later stage in the project when the instrument became available. The film deposited at -0.56 V shows a close-packed granular structure, with grains of up to 1  $\mu\text{m}$  across and full coverage of the underlying copper film, whereas image of the film deposited at -0.45 V confirms the observations drawn from the microscope image, i.e. the tin grains are relatively large, interconnected islands leaving an estimated 60% of the copper film uncoated.

The film properties observed using profilometry, microscopy and SEM can be related to the current-time characteristics seen in Figure 3-30. The large peak in initial current seen for the sample deposited at -0.56 V indicates the rapid nucleation of grains across a large surface area of the copper film, which leads to the smaller, closer packed grain structure and complete film coverage. The smallest peak in initial current followed by the continued lowest current magnitude for the sample deposited at -0.45 V relates to the initial nucleation of fewer tin grains followed by their slow growth. This, in turn, leads to the larger grains that are fewer in number and do not completely cover the underlying copper, and hence the roughness of this film was also found to be greater than that of the other two films. The film deposited at -0.98 V has initial current great enough to provide good coverage of grain nucleation, but



the continued short fluctuations and relatively large current relate to the generation of hydrogen, leading to a substantially thinner film due to current wastage and an increase in roughness due to the formation of the small blisters, which were observed in the microscope image.

The sample upon which tin was deposited at -0.56 V was analysed using EDS with a Hitachi Desktop SEM. The atomic abundance ratios relative to molybdenum in multiple different positions on the substrate are presented in Figure 3-33. The ascending numbers relate to positions on the substrate moving from bottom to top on

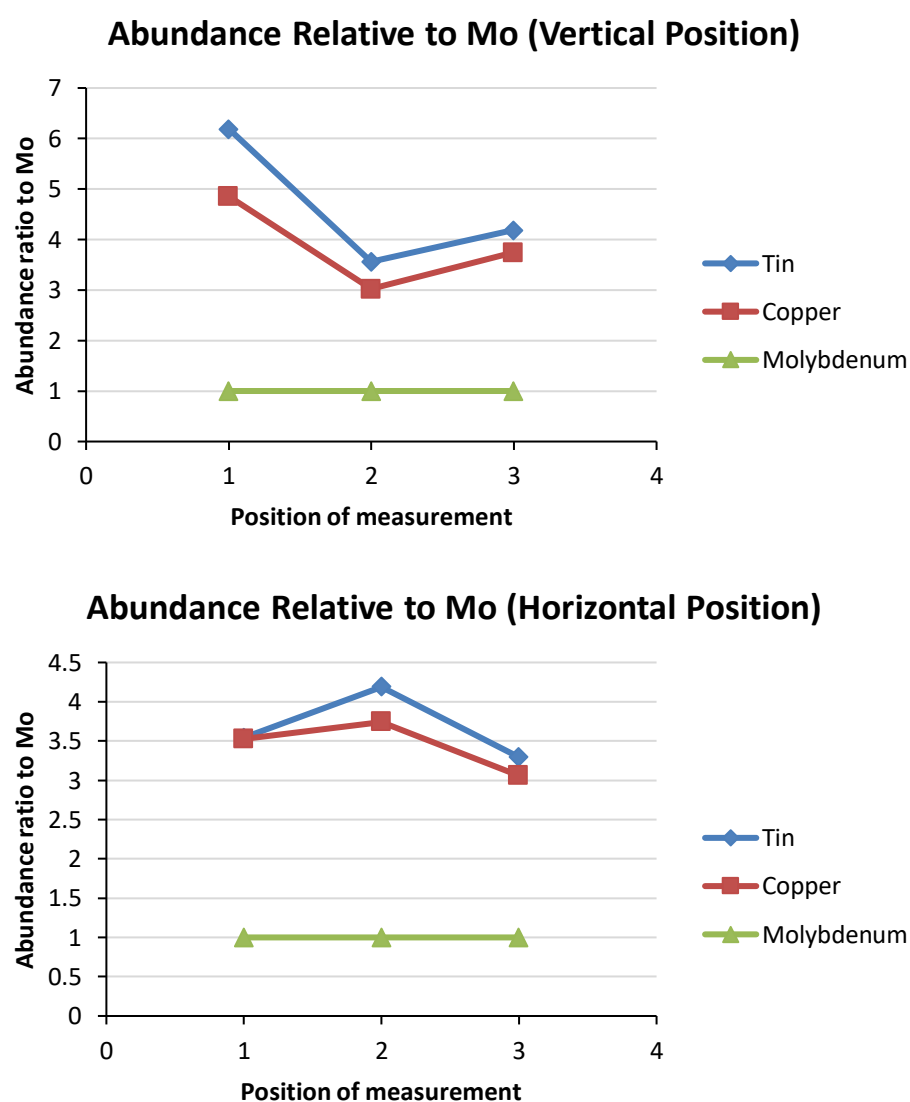


**Figure 3-33 - Atomic abundance ratios for copper and tin relative to Mo measured using EDS at points from bottom to top (upper graph), and from left to right at the top of the deposition area (lower graph) for a sample where tin was deposited at -0.56 V.**

a central line in the case of the vertical position graph, and from left to right on a line near the top of the sample area in the case of the horizontal position graph. The percentage abundancies of copper and tin were divided by that of molybdenum to provide relative thickness figures for copper and tin based on the assumption that the molybdenum was of a constant thickness across the area of the sample. As these values are ratios, they are unit less. Unfortunately, it was not possible to score the deposited films without damaging the substrate, therefore it was only possible to carry out thickness measurements via profilometry on the edges of the films. These EDS results are a useful indicator of the thickness variation in the copper and tin films across the substrate. These graphs indicate that the deposited films are thickest at the bottom, which is in agreement with profilometry results. However, they also suggest that the central point and the top left and right corners are thinner than the centre top. This suggests that there could be a ring shaped near-circular band of thicker film near the perimeter of the deposition area. There is a similar degree of variation for both copper and tin, suggesting that it is possible to control the stoichiometry of the deposited elements without necessarily having eliminated variations in the thickness.

#### ***3.3.4.3 Deposition onto a 4 cm<sup>2</sup> Substrate***

In order to aid subsequent analysis of sulphurised samples using XRD, electrodeposition was scaled-up such that the deposition area was 4 cm<sup>2</sup> on each substrate. Copper deposition continued using the same electrolyte composition and deposition settings without need for adjustment, however, tin deposits became inconsistent in their properties. Some samples were exhibiting incomplete coverage, akin to that of a less negative deposition potential, with lower magnitude deposition currents and the absence of the initial current spike associated with the rapid nucleation and coverage of grains. Initially, it was considered that this could be due to a change in the effective deposition potential due to the change in resistance between the working electrode and the other two electrodes that results from a change in the working electrode surface area. This change in potential is sometimes referred to as 'IR drop' [12]. Cyclic voltammetry was carried out on multiple different copper films, each deposited under the same conditions and with a surface area of 4 cm<sup>2</sup>, but the deposition peaks were inconsistent and appeared at potentials both positive and negative of the previously established -0.56 V (generally between

-0.50 V and -1.00 V). It was not possible to ascertain the cause of this within the time constraints of this project, however it was possible to find a suitable, if not fully optimised sequence for the galvanostatic deposition of tin.

If the graph of current vs time for tin deposited at three different potentials in Figure 3-30 is revisited, it can be seen that for -0.56 V, the current settles to  $\sim 5$  mA from  $\sim 17$  s onwards, after an initial sharp spike of  $\sim 37$  mA and an exponential decay (this was performed using a  $1\text{ cm}^2$  substrate). Unfortunately, the potentiostat/galvanostat software did not allow the exponential decay to be replicated in chronopotentiometry mode, therefore it was necessary to select a relatively large magnitude current for a short fixed period to nucleate grain growth and then switch to a lower magnitude current for the remainder of the deposition time in order to avoid film damage from hydrogen evolution. An initial test was carried out in which  $-80$  mA (i.e.  $-20\text{ mA cm}^{-2}$  as this was a  $4\text{ cm}^2$  substrate) was applied for  $1.5$  s, followed by  $-20$  mA ( $-5\text{ mA cm}^{-2}$ ) for the remaining time. This led to good coverage, but some small blisters were observed as a result of hydrogen evolution. Adjusting the second stage current from  $-20$  mA ( $-5\text{ mA cm}^{-2}$ ) to  $-16$  mA ( $-4\text{ mA cm}^{-2}$ ) did not yield any improvement, however, reducing the time of the first ( $-20\text{ mA cm}^{-2}$ ) stage from  $1.5$  s to  $1.2$  s limited the hydrogen evolution such that bubbles were observed but not sufficient to cause visible damage to the film. Therefore,  $-80$  mA ( $-20\text{ mA cm}^{-2}$ ) for  $1.2$  s followed by  $-20$  mA ( $-5\text{ mA cm}^{-2}$ ) for  $57.6$  s, delivering a total charge of  $1248\text{ mC}$  ( $312\text{ mC cm}^{-2}$ ), was chosen as a suitable galvanostatic sequence for the deposition of tin onto a  $4\text{ cm}^2$  substrate.

### 3.3.5 Deposition Efficiency

In order to maximise the probability of obtaining CZTS once the sample has been annealed, it is necessary to finely control the quantity of each element deposited in the first instance. In order for this control to be possible, it is essential to know the deposition efficiency of each electroplating process. Two different methods were used for the calibration of electrodeposition efficiency. Firstly, there were deposition-stripping experiments. In these experiments, the element is first deposited at the chosen deposition potential for a fixed period of time, after which the potential switches to that of the stripping potential (ascertained through the study of the relevant cyclic voltammogram) until the current diminishes (indicating that all of the deposited element has been removed). The stripping process can be assumed to be

100% efficient [2], therefore by plotting the current against time for both processes, integrating the area under each curve to quantify the charge passed and comparing the two values, it is possible to calculate the efficiency of the deposition process (i.e. the proportion of the charge passed that contributed to the deposition of the desired element). Secondly, there were MP-AES experiments, details of which are described in section 2.4.1. From the concentration values, the mass of each metal deposited can be calculated. The expected mass can also be calculated from the electrodeposition charge data using Equation 2-7 and Equation 2-8 in section 2.1.10, which assume a deposition efficiency of 100%. The two mass values can then be used to calculate the deposition efficiency.

### 3.3.5.1 Deposition-Stripping Tests

Due to the position of molybdenum relative to the position of copper in the electrochemical series (see Figure 2-3 in section 2.1.4), it was not possible to perform deposition-stripping tests on copper deposited onto an Mo-SLG substrate as this would also strip the molybdenum as well as the copper. It was, however, possible to carry out deposition-stripping tests for copper deposited onto FTO substrates, which was established by testing a piece of TEC 7 FTO at 0.0 V (vs Hg|HgO) and finding that no current was flowing. Figure 3-34 shows a current-time plot for a deposition-stripping experiment for copper on TEC 7 FTO. A spreadsheet was used to integrate the area under each curve, and dividing the area under the

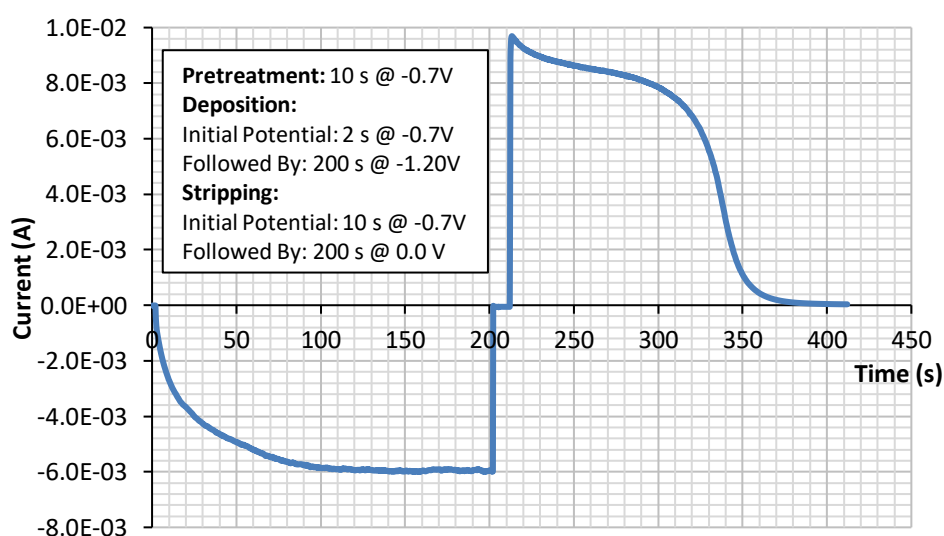


**Figure 3-34 - A current-time plot for the deposition and stripping of copper on FTO.**

stripping curve by the area under the deposition curve gave a value of 0.9841 implying a deposition efficiency of 98.4%. When a similar experiment was performed for calculating the potentiostatic deposition efficiency of tin onto copper using a methanesulfonic acid electrolyte, a deposition efficiency figure of 107.5% was returned. This indicates that for this particular circumstance, the assumption that the stripping process is 100% efficient does not hold and that the deposition process was more efficient than the stripping process. One possible cause of this could be the evolution of hydrogen at the platinum counter electrode during the stripping process.

### 3.3.5.2 MP-AES Experiments

The MP-AES experiments involved dissolving electrodeposited metals in acid and measuring the concentration of each metallic element by passing the acid through a Microwave Plasma – Atomic Emission Spectrometer. This process is described in section 2.4.1. Three samples were analysed using MP-AES, each with a deposition area of 4 cm<sup>2</sup>, with copper and tin deposited using the methods described previously in this chapter (tin was deposited potentiostatically using a methanesulfonic acid electrolyte). The mass of each dissolved film was calculated from the concentration data, and these values were compared to the expected mass based on the charge passed in deposition assuming 100% efficiency. These values are presented in Table 3-4, along with the concentration values of the 4 mg L<sup>-1</sup> and 10 mg L<sup>-1</sup> standards that were presented for a second time at the end of the sample analysis to check for calibration drift. The measured mass values were divided by the expected mass values and converted into percentages and are presented in Table 3-5. Two mean percentage efficiency values are also included for each element – one value that

**Table 3-4 - Masses measured for copper and tin films using the MP-AES system, along with drift measurements on two of the calibration standards for each copper and tin.**

Sample	Masses (mg)	
	Copper	Tin
1	0.7925	1.0075
2	0.7325	0.8125
3	0.7300	0.8675
Expected mass	0.7545	0.7688
Drift 4 mg L <sup>-1</sup> (mg L <sup>-1</sup> )	4.10	3.67
Drift 10 mg L <sup>-1</sup> (mg L <sup>-1</sup> )	10.33	9.58

**Table 3-5 - Calculated deposition efficiencies for each analysed film, including averages that factor in possible calibration drift and averages that do not.**

Sample	Deposition efficiency (%)	
	Copper	Tin
1	105.0	131.0
2	97.1	105.7
3	96.8	112.8
Ave inc. drift	96.4	127.0
Ave excl. drift	99.6	116.5

ignores the possibility of any calibration drift, and one that factors in the largest proportional drift by dividing the efficiency by the obtained concentration of the calibration standard and multiplying the outcome by the official concentration. It can be observed that all of the mass values obtained for the tin films exceed the expected value, leading to deposition efficiency values in excess of 100% for all three samples. Although this could suggest that the deposition procedure is highly efficient, it is likely that there is a source of error that has caused this. This could be due to inaccuracies in the concentrations of the calibration standards, however, given the level of care taken in their preparation, it was assumed that this was not the case. Another possible source of error could be interference from other elements present that could have similar emission lines to the elements being analysed. If this was the case, they could have originated from the Mo-SLG substrate, or be present as trace elements in the reagents used in the experiments. Ideally, a Mo-SLG substrate would have been analysed without the presence of deposited copper or tin in order to test whether any traces of copper or tin were present in the substrate. Unfortunately, this was not considered until after the results had been analysed and time constraints made it impossible to make further use of the MP-AES equipment. There may also be another source of uncertainty that is inherent to the MP-AES equipment, for example that relates to the photodetective electronics or the optics of the system. This may also explain some of the inconsistencies between samples, for example, the copper film on sample 1 was apparently deposited with greater than 100% efficiency and those on samples 2 and 3 were below 100% efficiency. A more extensive study with many samples and many repeat readings would be required in order to ascertain

the cause of the errors and accurately quantify the uncertainty in the efficiency values.

### **3.3.6 Electrodeposition of Copper onto Tin**

The original purpose of including a second copper layer, which would be situated between the tin layer and the zinc layer, was to aid the deposition of zinc. The deposition of zinc onto a copper film is aided by the favourable formation of a copper-zinc alloy in the initial stage of deposition, which encourages the rapid formation of a thin zinc film giving complete coverage of the copper film [13]. This does not happen when depositing zinc onto a tin film as tin and zinc do not alloy with each other, meaning that hydrogen evolution from the tin surface becomes a problem at the relatively negative potentials required to deposit zinc [13]. Some consideration was given to whether an alternative approach to suppressing hydrogen evolution should be taken due to information in literature explaining how a second copper layer can lead to the formation of a tin rich layer and a zinc rich layer, along with the associated secondary phases, upon sulphurisation [14]. It was decided that an alternative approach to suppressing hydrogen evolution should be taken, however, the deposition of a second copper layer was required for experiments relating to the evaporation of tin during sulphurisation at a later stage in the project (as discussed in chapter 5). For this reason, experimentation for the deposition of copper onto tin was continued until successful.

#### ***3.3.6.1 Potentiostatic Deposition of Copper onto Tin***

The relative positions of tin and copper in the electrochemical series (see Figure 2-3 in section 2.1.4) present a challenge for the electrodeposition of copper onto tin – deposition potentials suitable for copper can lead to the oxidation and dissolution of tin. According to Scragg, an effective approach was to use a relatively negative deposition potential of -1.45 V (vs Hg|HgO) for 2 s at the start of the deposition, followed by -1.10 V until completion [13]. The sample was also pre-polarised (i.e. the deposition potential started to be applied prior to the immersion of the substrate in electrolyte). The purpose of this was to rapidly deposit copper early in the deposition process giving complete coverage and therefore protecting the tin before dissolution could start to occur at the less negative deposition potential [13]. Deposition at a potential as negative as -1.45 V risks damaging the electrodeposits through hydrogen evolution, therefore it is preferable to keep its time to a minimum.

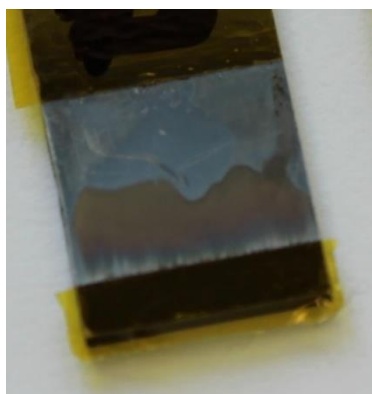


**Figure 3-35 - An attempt to deposit copper onto tin at -1.45 V for 3.8 s followed by -0.98 V for 237 s, the sample being pre-polarised at -1.45 V for 1.2 s prior to immersion.**

It was reported by Scragg that -1.08 V was a suitable potential for depositing copper onto Mo-SLG [1], however, -0.98 V was found to give the most favourable results in this project. Based on this information, the decision was taken to trial a deposition at -1.45 V followed by -0.98 V (rather than the -1.45 V followed by -1.10 V reported by Scragg). The potentiostat/galvanostats available to this project did not have the facility to trigger a timing process by immersing a pre-polarised substrate into electrolyte – the timing process would start from the moment the potential was applied. If -1.45 V had only been applied for 2 s, then the time taken to safely lower the sample into the solution would take up a large proportion of that time, making it difficult to replicate accurately between samples should the deposition be successful. Therefore, the time selected for the -1.45 V step was 5 s. In practice, it took 1.2 s to lower the substrate into the electrolyte, meaning that the length of the step was effectively 3.8 s. The experiment was terminated manually after 241 s. Once the

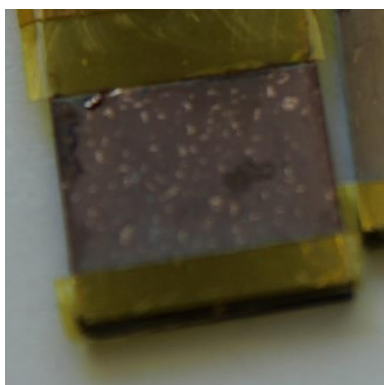


**Figure 3-36 - Sample deposited with copper onto tin at -1.45 V for 2 s followed by -1.10 V until 286 mC of charge passed. No pre-polarisation was applied. Damage in the form of blistering and delamination is evident.**



potential switched to -0.98 V, the current flowing was registering as positive, which is associated with the oxidation of the substrate. The sample can be seen in Figure 3-35. The deposition attempt was not successful, and a lot of the tin dissolved, exposing the first copper layer beneath. The decision was then taken to trial depositing at -1.45 V for 2 s followed by -1.10 V until 286 mC charge passed, but without pre-polarising the sample for the aforementioned reasons. This sample can be seen in Figure 3-36. Although a dark copper film was deposited, significant hydrogen damage can be seen in the form of blisters and also some delamination. The decision was then taken to perform two cyclic voltammetry tests prior to any further deposition experiments.

In the first test, cyclic voltammetry was performed on a tin deposit using the same copper electrolyte composition as that used for deposition. The start/end potential was -1.20 V, with the first scan limit set to -2.00 V and the second set to -0.56 V. The resulting voltammogram can be seen in Figure 3-37. A significant amount of hydrogen evolution was visible during the CV scan and the sample films were severely blistered and damaged. Two deposition peaks are indicated in the voltammogram. The first peak occurred at approximately -1.28 V, which is likely to relate to the deposition of copper onto tin. The second peak occurred at -1.14 V. This occurrence is after the passage through the stripping regime, meaning that a lot of the

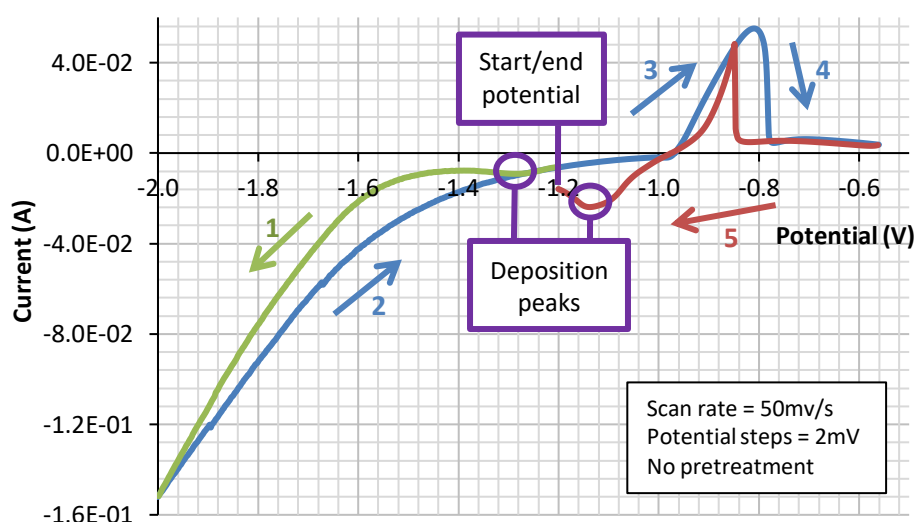


**Figure 3-37 - A voltammogram for the deposition of copper onto tin. Two deposition peaks are indicated. The deposition peak at -1.28 V was considered more useful as it occurred at a time at which less damage had been done to the tin film.**

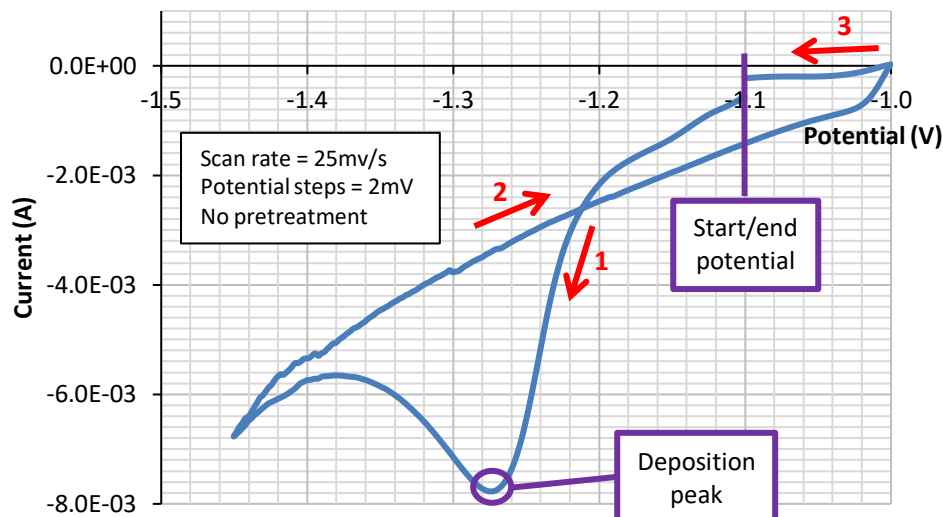


**Figure 3-38 - A voltammogram for the deposition of copper onto tin over a reduced potential range. This confirms a deposition peak at -1.275 V.**

tin film had been lost by this point (confirmed by visual observation of the sample as the experiment was progressing). This means that this deposition peak is not a useful guide for the deposition of copper onto tin. In light of this, the second CV test was performed over a smaller potential range with the intention of confirming the first deposition peak at -1.28 V. The start/end potential was -1.10 V, the first scan limit was -1.45 V and the second scan limit was -1.00 V. The resulting voltammogram can be seen in Figure 3-38, and a deposition peak is clearly visible at -1.275 V. The chemical processes that gave rise to the features that are no longer visible in this voltammogram occurred outside of this narrower potential range, making it possible to observe a more detailed representation of the deposition peak of interest.

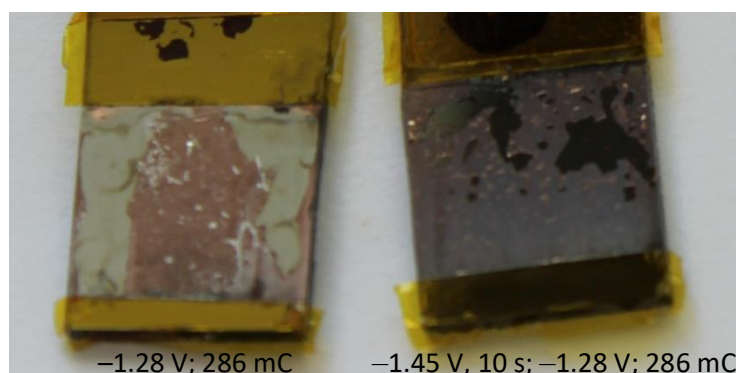


**Figure 3-39 - Copper deposited onto tin on two samples at -1.28 V with a 286 mC total charge limit (left), and -1.45 V for 10 s followed by -1.28 V with a 286 mC total charge limit (right). Both samples exhibit similar levels of extensive hydrogen damage.**

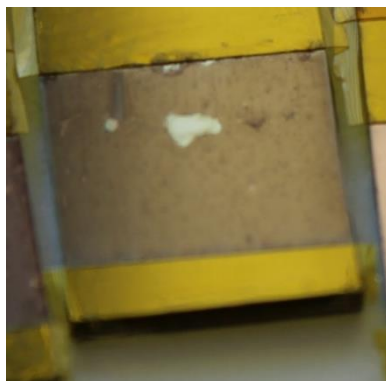


**Figure 3-40 - Film deposited with copper at -1.45 V for 3 s showing blistering and film delamination caused by hydrogen evolution.**

Based on this result, two deposition experiments were carried out. One tin film was simply deposited with copper at -1.28 V with no pre-polarisation until 286 mC charge passed, the other had an initial phase of 10 s at -1.45 V, again without pre-polarisation and with a charge limit of 286 mC. The results are presented in Figure 3-39. There are similar levels of film damage to both samples. Although it appears that copper has been deposited on each (the current was negative throughout each deposition, suggesting that tin dissolution was not occurring), hydrogen damage can be seen in the form of blisters and the delamination of the underlying films, leaving an estimated 30-50% of the molybdenum in the deposition area exposed.

Before any further deposition experiments were conducted, two experiments were carried out in order to gauge the extent of hydrogen evolution at particular deposition potentials. The first of these was to simply deposit copper onto tin at -1.45 V for 3 s. This was to gauge if any damage was caused at this deposition potential within a short period of time. The second experiment was to perform cyclic voltammetry with only the background electrolyte, i.e. the electrolyte composition used for depositing copper but without any copper compound included. This was to gauge the relative extent of hydrogen evolution across a range of potentials and also to attempt to ascertain a threshold potential for the dissolution of tin. The start/end potential was -1.00 V, with the first scan limit being -1.45 V and the second being -0.60 V.

The sample that underwent copper deposition for 3 s at -1.45 V can be seen in Figure 3-40. It was found that just 3 s is sufficient time to damage the sample, with film delamination and small blisters being evident. This suggests that potentials as negative as -1.45 V are not suitable for use in the deposition of copper onto tin, even

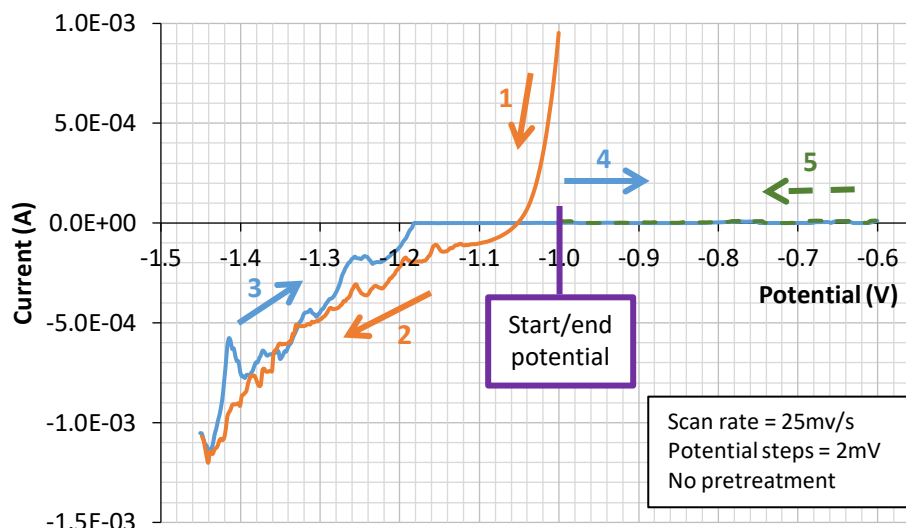


**Figure 3-41 - A voltammogram obtained performing cyclic voltammetry on a tin deposit using only the background electrolyte for copper deposition.**

for a very short time period. The voltammogram for the CV performed using the background electrolyte can be seen in Figure 3-41. In the negative direction scan, the current registers as positive for potentials positive of -1.05 V. This positive current is most likely as a result of tin dissolution. The magnitude of the negative current, which is associated with hydrogen evolution, increases substantially from ~0.1 mA at -1.10 V to ~1.2 mA at -1.45 V, with the current magnitude at -1.28 V being ~0.35 mA. It can also be noted that no positive current flows during the positive direction scan, with current plateauing at near zero from -1.18 V. Although the reasons for this are uncertain, the lack of positive current may have resulted from the level of destruction caused by hydrogen evolution, leaving little of the tin film left to

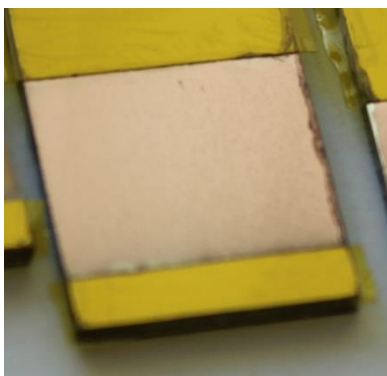


**Figure 3-42 - Copper deposited onto tin at -1.27 V for 2 s followed by -1.07 V, with a total charge limit of 286 mC. The film exhibits good coverage, with no visible hydrogen damage or tin dissolution.**

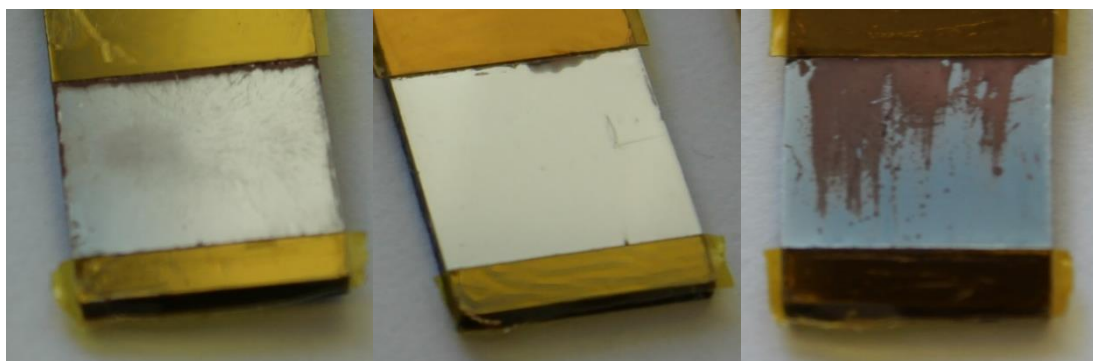


**Figure 3-43 - Repeat attempts to deposit copper onto tin at -1.27 V for 2 s followed by -1.07 V, with a total charge limit of 286 mC. These depositions were considered unsuccessful, with very poor copper coverage.**

dissolve. Using the information from these two experiments and from the previous cyclic voltammetry, the decision was taken to attempt deposition at -1.27 V for 2 s followed by -1.07 V, with a total charge limit of 286 mC. This led to the deposition of the copper film presented in Figure 3-42. The copper deposit gave complete coverage of the underlying tin, with no visible damage – there was no evidence of hydrogen evolution or tin dissolution.

This deposition experiment was repeated with the same settings five times in attempts to replicate the deposition, including replenishing the electrolyte twice. None of these attempts were successful, and three examples are presented in Figure 3-43. Although there was no damage to the tin film visible to the naked eye, there was also incomplete copper coverage on all samples, including two samples with copper deposited only at the very edges of the film. This indicated that these deposition settings do not give reproducible results. The decision was taken to seek an alternative approach and conduct trials using galvanostatic deposition.

### ***3.3.6.2 Galvanostatic Deposition of Copper onto Tin***

In order to attempt to replicate the successful deposition of copper onto tin, the current-time characteristics of the successful deposition were plotted. The intention was to then replicate the current-time sequence as accurately as permitted using a galvanostatic sequence in the potentiostat/galvanostat software. The successful deposition was one carried out at -1.27 V for 2 s followed by -1.07 V, with a total charge limit of 286 mC on a 1 cm<sup>2</sup> substrate. The current-time characteristics are plotted in Figure 3-44. It can be seen that the initial current density peaks in the first instant to approximately -5.8 mA cm<sup>-2</sup>, dropping rapidly in the first 2 s and settling to

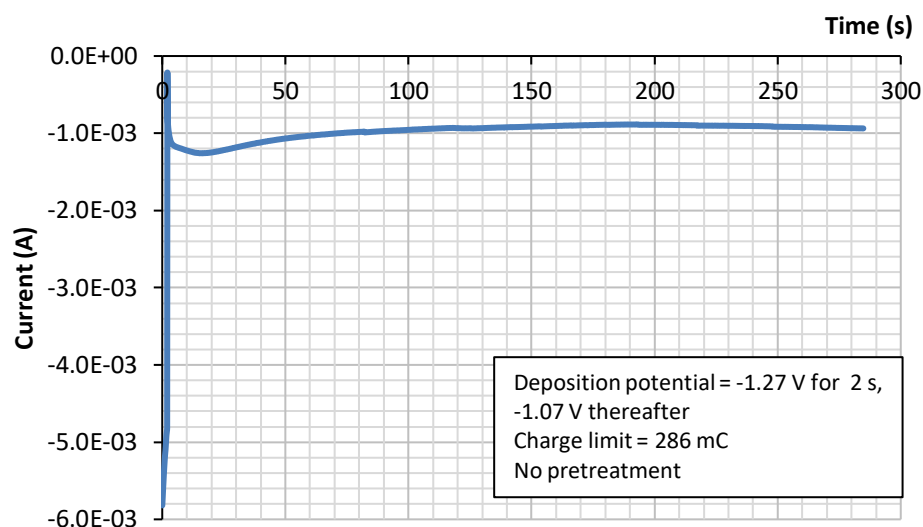


**Figure 3-44 - Current-time characteristics for the successful deposition of copper onto tin using a two-step potentiostatic process.**

-1.2 – -0.8 mA cm<sup>-2</sup> thereafter. This informed the decision to carry out a galvanostatic deposition at -5 mA cm<sup>-2</sup> for 2 s followed by -0.9 mA cm<sup>-2</sup> for 307 s. The results of this are presented in Figure 3-45, from which it can be observed that some hydrogen blistering occurred, as well as incomplete copper coverage.

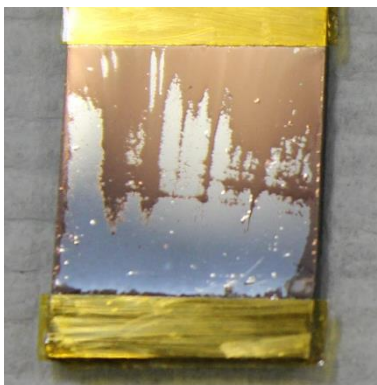


**Figure 3-45 - Copper deposited onto tin galvanostatically at -5 mA cm<sup>-2</sup> for 2 s followed by -0.9 mA cm<sup>-2</sup> for 307 s. The sample displays visible signs of blistering due to hydrogen evolution.**

For subsequent depositions, the decision was taken to reduce the magnitude of the current density in the first (high current) step in an attempt to eliminate hydrogen damage, but prolong its duration in an attempt to increase copper coverage and avoid tin dissolution. Adjustments were also made to the second (low current) step in attempts to prevent tin dissolution. A set of five depositions were carried out on 1cm<sup>2</sup> substrates, the deposition settings are set out in Table 3-6.

**Table 3-6 - Galvanostatic deposition settings for the five samples presented in Figure 3-46.**

Sample	Step 1		Step 2	
	Current Density (mA cm <sup>-2</sup> )	Time (s)	Current Density (mA cm <sup>-2</sup> )	Time (s)
1	-4	3	-1	274
2	-4	10	-1	246
3	-4	10	-2	123
4	-4	10	-3	82
5	-4	72	N/A	N/A

Images of the five aforementioned copper deposits are presented in Figure 3-46. The trend observed is, that increasing the time of the first (-4 mA cm<sup>-2</sup>) step, or increasing the current density in the second step, increases film coverage while at the same time increases damage caused by hydrogen evolution. None of the samples returned the required combination of both acceptable coverage and sufficiently undamaged films. This led to the conclusion that the most appropriate course of action would be to conduct experiments using a modified electrolyte composition.

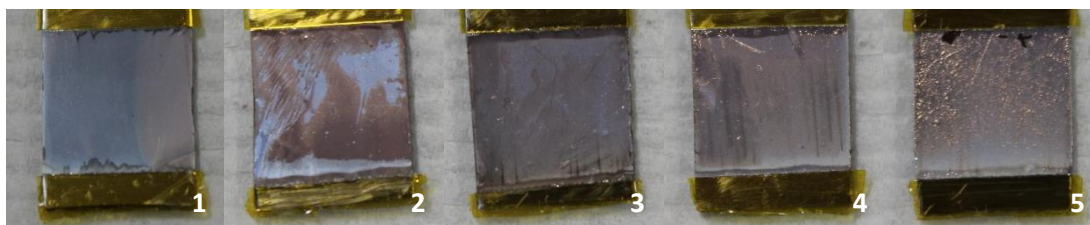


**Figure 3-46 - Five samples deposited with copper onto tin galvanostatically using the settings set out in Table 3-6. Moving from left to right, it can be seen that copper coverage increases, as well as hydrogen damage.**

### ***3.3.6.3 Deposition of Copper onto Tin from a Double-Strength Electrolyte***

The results presented in section 3.3.6.2 suggest that -4 mA cm<sup>-2</sup> could be a suitable current density for the deposition of copper onto tin, however, the issue lies with the extent of the negativity of the potential required to achieve it, i.e. the potential coincides with hydrogen evolution. Up until this point in the project, copper deposition experiments had been carried out using the composition stated in section 2.1.5, with the copper sulphate pentahydrate concentration being 0.1 mol dm<sup>-3</sup> and the D-sorbitol concentration being 0.2 mol dm<sup>-3</sup>. In order to attempt to generate the



**Table 3-7 - Deposition settings for four samples deposited with copper using a double-strength electrolyte.**

Sample	Deposition type	Step 1		Step 2	
		Setting	Limit	Setting	Limit
1	Galvanostatic	-4 mA cm <sup>-2</sup>	72 s	N/A	N/A
2	Galvanostatic	-8 mA cm <sup>-2</sup>	4 s	-4 mA cm <sup>-2</sup>	64 s
3	Potentiostatic	-1.20 V	286 mC	N/A	N/A
4	Potentiostatic, Pre-polarised	-1.20 V	286 mC	N/A	N/A

required current for copper deposition with a less negative potential, the concentration of the copper sulphate pentahydrate, and the complexing agent, D-sorbitol, were doubled. Although some consideration was given to adjusting the temperature of the electrolyte, there was concern that this could also adversely affect issues regarding the dissolution of the underlying tin and also hydrogen evolution. It was felt that increasing the copper salt and complexing agent concentration would be less likely to exacerbate other problems while enabling the deposition of copper at a less negative potential. Experiments were then conducted using the settings given in Table 3-7. The potential observed during the -4 mA cm<sup>-2</sup> galvanostatic stages informed the choice of potential for the potentiostatic depositions. The experiments described in section 3.3.6.2 using a less concentrated electrolyte gave potentials between -1.25 V and -1.39 V during the -4 mA cm<sup>-2</sup> stages, leading to film damage from hydrogen evolution. The experiments described here, using the double-strength electrolyte, gave potentials between -1.13 V and -1.21 V during the -4 mA cm<sup>-2</sup> stages of deposition. This led to a reduction in the amount of hydrogen generated, in turn reducing the associated damage, as can be seen in Figure 3-47, where the resulting electrodeposits are presented. It is also evident that the galvanostatic depositions did not lead to the required levels of coverage, suggesting that increasing the concentration of copper sulphate may have had the unwanted effect of reducing the throwing power of the electrolyte. The lowest quality film is that deposited potentiostatically without pre-polarisation as this exhibits both poor copper coverage and signs of hydrogen damage. The pre-polarised sample, however, delivered the best results, exhibiting good copper coverage and no visible hydrogen damage, despite a small amount of hydrogen evolution being observed during the deposition process. Repeat experiments confirmed that this successful result was reproducible, however,



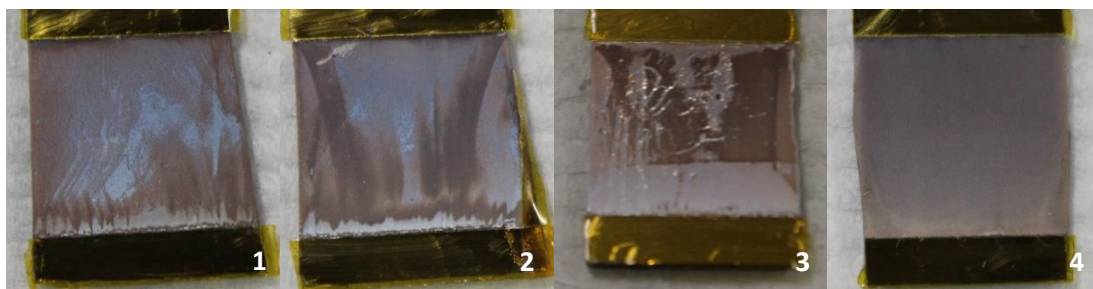


**Figure 3-47 - Copper deposited using the settings given in Table 3-7. Sample 4 demonstrates the benefits of using pre-polarisation in potentiostatic deposition.**

some films did exhibit small areas where hydrogen damage had occurred. For this reason, the deposition parameters were adjusted such that the first 20 s was set at -1.18 V, changing to -1.14 V thereafter. The substrates were immersed after approximately 5 s, meaning that the -1.18 V stage was in effect approximately 15 s. This remedied the issue of hydrogen damage.

Further repeat experiments revealed that, although the desired results were reproducible, there was a high level of sensitivity to the concentration of copper sulphate in the electrolyte. This was particularly the case when deposition was scaled-up to a 4 cm<sup>2</sup> substrate. Although the same deposition parameters as used for 1 cm<sup>2</sup> substrates could achieve the desired results, electrolytes that had been used for many depositions, typically ten or more, would produce films with insufficient coverage. An example is given in Figure 3-48, in which a 4 cm<sup>2</sup> film exhibiting insufficient coverage is presented alongside a 4 cm<sup>2</sup> film of acceptable quality for comparison. This meant that frequent replenishment of the copper electrolyte became necessary. One way that this could be alleviated is by using a piece pure

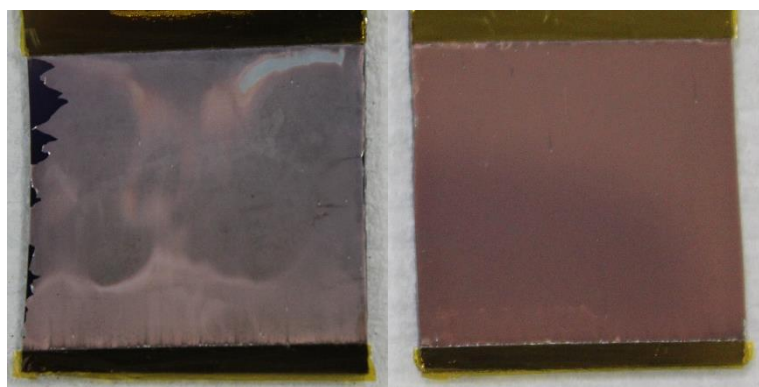


**Figure 3-48 - Copper deposited from a partially depleted electrolyte (left) and a fresh electrolyte (right).**

copper in place of the platinum counter electrode, which would dissolve into the electrolyte and hence replenish the copper content as copper deposits at the working electrode.

### **3.4 Conclusions**

Efficient and reproducible methods were established for the deposition of copper and tin using a static working electrode. It was found that the morphology of the first copper layer is sensitive to the precise potential chosen, with changes in the macroscopic properties of the films being related to changes in the microscopic grain structure on varying the potential. The desired close-packed granular structure was achieved at  $-0.98$  V. On the other hand, it was found that galvanostatic deposition was required in order to produce consistent results in the deposition of tin, indicating that grain size, film coverage and surface roughness is mostly dependent upon the current rather than the precise potential. Although efforts were made to predict charge passed (and hence film thickness) from the deposition time for potentiostatic experiments, it proved necessary to use a current integrator to ensure the required accuracy.

Other than adjusting settings related to the deposition current and potential, several other experimental parameters were trialled, including different substrates and deposition apparatus for the first copper layer, and different electrolytes for tin deposition. A static working electrode in stagnant electrolyte was found to be preferable to the use of an RDE or a stirred solution as this minimised the extraneous effects while maintaining a method that could be scaled-up in future work. Although the stagnant setup did cause variations in film thickness across the substrate, EDS data indicated that the copper to tin ratios had a degree of consistency across the substrate and therefore the ability to produce CZTS from a completed stack should not be negatively impacted. The smoothness and film coverage of tin was successfully improved by changing from an alkaline electrolyte to one based on methanesulfonic acid, with substantial improvements being indicated in the profilometry data, as well as in SEM and microscope images that showed a compact granular structure when methanesulfonic acid was used.

One issue that became particularly apparent with deposition of copper onto tin and to an extent with tin onto copper, was that there is a trade off in the competition between avoiding hydrogen evolution and obtaining the required film coverage or grain characteristics. Depositing tin onto copper with close-packed grains and good film coverage could be achieved by forcing the rapid nucleation of grains across the sample by choosing a higher current density of  $-20 \text{ mA cm}^{-2}$  for the first 1.2 s, and then reducing it four fold for the remaining time (until  $312 \text{ mC cm}^{-2}$  was reached) in order to limit damage caused by hydrogen evolution. This approach was not sufficient to prevent hydrogen damage when depositing copper onto tin, therefore it was necessary to increase the copper concentration in the electrolyte from 0.1 to 0.2  $\text{mol dm}^{-3}$  and perform potentiostatic deposition with a pre-polarised working electrode at -1.18 V for the first 15-20 s and -1.14 V thereafter in order to obtain the desired results. The optimisation carried out in this chapter was considered to be sufficient to produce films of such a quality that were suitable for further processing through the deposition of zinc, subsequent sulphurisation, and ultimately into working solar cell devices. These films met the requirements that they were conformal, with a close-packed granular structure on a microscopic scale, yet were homogeneous without pitting or blistering due to hydrogen evolution on a macroscopic scale, with full coverage of the film upon which they were deposited.

### 3.5 References

- [1] J. J. Scragg, "Section 2.11 - Electrodeposition of Metallic Precursors: Finalised Deposition Conditions for Precursor Stacks," in *Copper Zinc Tin Sulfide Thin Films for Photovoltaics: Synthesis and Characterisation by Electrochemical Methods*, Berlin, Springer-Verlag, 2011, pp. 45-53.
- [2] J. J. Scragg, "Section 2.1 - Electrodeposition of Metallic Precursors: Electrochemical Deposition (Electrodeposition)," in *Copper Zinc Tin Sulfide Thin Films for Photovoltaics: Synthesis and Characterisation by Electrochemical Methods*, Berlin, Springer-Verlag, 2011, pp. 9-19.

- [3] M. Jeong, T. Yokoshima, H. Nara, T. Momma and T. Osaka, "Influence of the diffusion-layer thickness during electrodeposition on the synthesis of nano core/shell Sn–O–C composite as an anode of lithium secondary batteries," *RSC Advances*, vol. 4, no. 51, pp. 26872-26880, 2014.
- [4] Royal Society of Chemistry, "Molybdenum - Element information, properties and uses | Periodic Table," 2021. [Online]. Available: <https://www.rsc.org/periodic-table/element/42/molybdenum>. [Accessed 18 April 2021].
- [5] F. Biccari, R. Chierchia, M. Valentini, P. Mangiapane, E. Salza, C. Malerba, C. L. A. Ricardo, L. Mannarino, P. Scardi and A. Mittiga, "Fabrication of Cu<sub>2</sub>ZnSnS<sub>4</sub> solar cells by sulfurization of evaporated precursors," *Energy Procedia*, vol. 10, pp. 187-191, 2011.
- [6] F. Pianezzi, A. Chirilă, S. Nishiwaki, S. Buecheler and A. N. Tiwari, "Influence of impurities on the performance of CIGS thin film solar cells," EMPA - Swiss Federal Laboratories for Materials Testing and Research, Dübendorf, Zürich, Switzerland, 2012.
- [7] T. Prabhakar and N. Jampana, "Effect of sodium diffusion on the structural and electrical properties of Cu<sub>2</sub>ZnSnS<sub>4</sub> thin films," *Solar Energy Materials and Solar Cells*, vol. 95, no. 3, pp. 1001-1004, 2011.
- [8] J. J. Scragg, D. M. Berg and P. J. Dale, "A 3.2% efficient Kesterite device from electrodeposited stacked elemental layers," *Journal of Electroanalytical Chemistry*, vol. 646, no. 1-2, p. 52–59, 2010.
- [9] R. L. Broggi, G. M. De Oliveira, L. L. Barbosa, E. M. J. A. Pallone and I. A. Carlos, "Study of an alkaline bath for tin deposition in the presence of sorbitol and physical and morphological characterization of tin film," *Journal of Applied Electrochemistry*, vol. 36, no. 4, pp. 403-409, 2006.
- [10] M. Kumar, A. Dubey, N. Adhikari, S. Venkatesan and Q. Qiao, "Strategic review of secondary phases, defects and defect-complexes in kesterite CZTS–Se solar cells," *Energy & Environmental Science*, vol. 8, no. 11, pp. 3134-3159, 2015.
- [11] J. J. Scragg, "Section 2.7 - Electrodeposition of Metallic Precursors: Electrodeposition of Sn: The Methane Sulfonic Acid Electrolyte," in *Copper Zinc Tin Sulfide Thin Films for Photovoltaics: Synthesis and Characterisation by Electrochemical Methods*, Berlin, Springer-Verlag, 2011, pp. 33-36.

- [12] W. Oelßner, F. Berthold and U. Guth, “The  $iR$  drop – well-known but often underestimated in electrochemical polarization measurements and corrosion testing,” *Materials and Corrosion*, vol. 57, no. 6, pp. 455-466, 2006.
- [13] J. J. Scragg, “Section 2.8 - Electrodeposition of Metallic Precursors: Electrodeposition of Zn from an Acid Chloride Electrolyte,” in *Copper Zinc Tin Sulfide Thin Films for Photovoltaics: Synthesis and Characterisation by Electrochemical Methods*, Berlin, Springer-Verlag, 2011, pp. 42-47.
- [14] M. Arasimowicz, M. Thevenin and P. Dale, “The Effect of Soft Pre-Annealing of Differently Stacked Cu-Sn-Zn Precursors on the Quality of  $Cu_2ZnSnSe_4$  Absorbers,” in *Materials Research Society Symposium C – Compound Semiconductors: Thin-Film Photovoltaics, LEDs and Smart Energy Controls*, 2013.

## 4 Electrodeposition of Zinc

### 4.1 Introduction

Having established methods to create smooth and reproducible copper and tin films, the task remained to deposit zinc to the same standards. Zinc forms the top layer of the electroplated stack and presents considerable challenges in that the potentials required in its deposition are negative to the extent that hydrogen evolution becomes a persistent problem. Although the deposition of a second copper layer eases the subsequent deposition of zinc, it is reported in literature that it can lead to the formation of two distinct layers upon annealing – one zinc-rich, and one tin rich, which was found to lead to an increase in the formation of unwanted phases [1]. A three-layer stack was therefore seen as advantageous, requiring the electrodeposition of zinc onto tin. As stated in section 3.3.6, tin and zinc do not alloy with each other, there is no rapid nucleation of zinc across the surface of the tin and hydrogen evolution from the tin surface remains a problem throughout the deposition process [2]. This not only prevents zinc from depositing at hydrogen nucleation sites, but limits the efficiency of the deposition process as some of the current is wasted as hydrogen ions in the solution are reduced.

Much of the experimentation presented in this chapter was dedicated to minimising the effects of hydrogen evolution and obtaining full and even coverage of the underlying tin. This chapter presents a series of experiments designed to optimise the electrodeposition of zinc onto tin. It starts by describing a set of experiments in which tin is deposited sequentially across a range of potentials, followed by a study on the effect of the pH of the electrolyte on the deposition efficiency. Further modifications were made in the adjustment of the electrolyte composition, including trials with the use of organic additives as levelling agents. Further experimentation was carried out in which the performance of four different electrolyte compositions designed for a variety of purposes were compared and films were studied using a FEG-SEM, and further optimisation was carried out by trialling a range of galvanostatic current densities. Finally, a discussion is included regarding the accuracy of four different methods to measure the quantity of deposited zinc, including deposition-stripping tests, XPS depth profiling, EDS and MP-AES.

## 4.2 Experimental Methods

### 4.2.1 Sample Preparation

In the majority of experiments presented in this chapter, zinc was deposited onto tin, although in some instances it was deposited onto copper. When depositing onto a tin surface, it was first necessary to prepare copper-tin stacks of good quality (attempts to deposit tin directly onto molybdenum were not successful, as described in section 3.2.1). These were deposited onto Mo-SLG under optimised conditions, as discussed in chapter 3. To re-emphasise these, a brief description follows. Static electrodes and stagnant electrolytes were used for all deposits. Copper was deposited potentiostatically at a potential of -0.98 V vs Hg|HgO from an alkaline electrolyte (formula given in section 2.1.5), and tin was deposited from a methanesulfonic acid electrolyte (formula given in section 2.1.8) either potentiostatically at -0.56 V vs Ag|AgCl, or galvanostatically at -20 mA cm<sup>-2</sup> for 1.2 s followed by -5 mA cm<sup>-2</sup> for 57.6 s, with a total charge-passed density of 312 mC cm<sup>-2</sup> in either case. When a second copper layer was deposited (when a copper-tin-copper stack was required for the deposition of zinc onto a copper surface), potentiostatic deposition at -1.18 V for 15 s followed by -1.14 V (vs Hg|HgO) until the required charge-passed density was reached. Generally speaking, for both copper-tin and copper-tin-copper stacks, the total charge-passed density for copper was 572 mC cm<sup>-2</sup>. In the case of the copper-tin-copper stacks, this was split equally between the two copper layers. There is one instance in this chapter where zinc is deposited directly onto a single copper layer on Mo-SLG, and that is when a citrate based electrolyte (Electrolyte Zn 7) is used (section 4.3.6.5).

For some zinc deposition experiments, cyclic voltammetry was first required. Details of the cyclic voltammetry are expressed where appropriate, however, an overview of this technique and its use in this project can be found in section 2.1.3.

### 4.2.2 Sample Analysis

#### 4.2.2.1 Profilometry

A brief overview of profilometry and its use in this project is given in section 2.4.6. In this chapter, zinc films deposited from Electrolyte Zn 1 and Electrolyte Zn 2 were scanned with a total scan length of 5000 μm for 180 s, giving a scan resolution of

0.093  $\mu\text{m}$ . The stylus force was 3mg and stylus radius 12.5  $\mu\text{m}$  (section 4.3.3.1). Zinc films deposited from Electrolyte Zn 6 was scanned with a total scan length of 5000  $\mu\text{m}$  for 60 s, giving a scan resolution of 0.278  $\mu\text{m}$ . The stylus force and radius were also 3 mg and 12.5  $\mu\text{m}$  respectively (section 4.3.6.4).

#### ***4.2.2.2 X-Ray Photoelectron Spectroscopy Depth Profiling***

An overview of XPS depth profiling and its use in this project is given in section 2.4.4. The instrument used was a Kratos Axis Supra with a monochromated Al-K $\alpha$  X-ray source giving a 15 mA emission current and power of 225 W. The analysis area was an oval of  $300 \times 700 \mu\text{m}^2$ . Etching for depth profiling was carried out using an Kratos Minibeam 6 argon ion etch gun and the base pressure inside the instrument was approximately  $5 \times 10^{-9}$  Torr. Elemental quantification analysis was carried out using CasaXPS software, version 2.3.17dev6.4k. For the majority of samples, XPS data was acquired every 300 s during etching unless otherwise stated.

XPS data was used to calculate the total atomic abundances of each electrodeposited element on some samples. These calculations were performed by integrating the total electron signal counts for each element with respect to time for the duration of the etching, using a spreadsheet. The total counts for copper, tin and zinc were each divided by the combined total counts for the three elements to give a percentage abundance. This method was considered preferable to simply integrating the plots in depth profile graphs as it avoids distortion of the values by the presence of carbon and oxygen at the beginning of the depth profiles, which would have disproportionately affected the values for zinc and tin, which were nearer to the top surface of the samples than copper.

#### ***4.2.2.3 Scanning Electron Microscopy and Energy Dispersive Spectroscopy***

An overview of the SEM-EDS equipment and its general usage in this project is given in section 2.4.5. All SEM images presented in this chapter were obtained using a JEOL 7800 FEG-SEM. The acceleration voltage used for imaging was either 5 kV or 20 kV, depending on which was capable of generating the clearest image of the features under examination. For EDS measurements and mapping, an acceleration voltage of 20 kV was used.



#### 4.2.2.4 Microwave Plasma – Atomic Emission Spectrometry

Experiments were carried out in which deposited electroplated stacks were dissolved in acidic solutions and the concentrations of the dissolved metallic elements were quantified as the solution was analysed using MP-AES. This was used as part of the experimentation to calculate the efficiency of zinc deposition, and the results of these experiments are presented in section 4.3.7.2. A full description of how the samples were digested in acid and analysed using the MP-AES is given in section 2.4.1.

### 4.3 Results and Discussion

#### 4.3.1 Deposition of Zinc from a pH 3 Electrolyte

The electrolyte used in the first round of zinc deposition experiments used a pH 3 buffer, and its composition is given in section 2.1.9. It is the same composition as that used by Scragg in [3] and [4]. Mo-SLG substrates were cut, cleaned and masked using the methods described in section 2.1.7 and copper and tin were deposited onto 1 cm<sup>2</sup> areas under optimised conditions and parameters (as discussed in chapter 3) in order to obtain uniform and smooth films (see section 4.2.1). In order to identify a deposition peak, cyclic voltammetry was performed using [2] as a guide, initially with -0.8 V (vs Ag|AgCl) as the start/end potential, -1.15 V as the first scan limit and

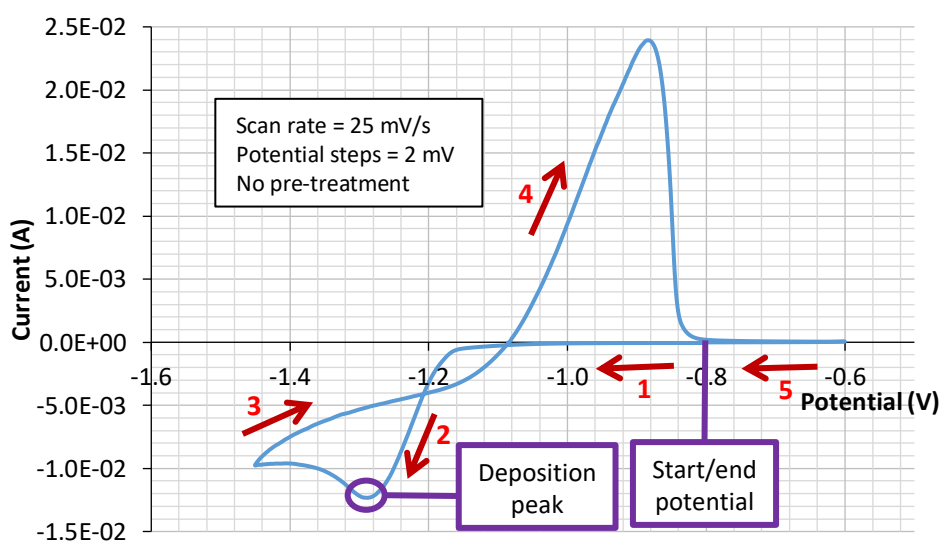


**Figure 4-1 - A cyclic voltammogram for a pH 3 zinc electrolyte using electrodeposited tin as a substrate. A deposition peak is indicated at -1.29 V.**

-0.6 V as the second scan limit. This did not return an identifiable deposition peak, therefore the first scan limit was extended to -1.45 V and the resulting voltammogram is presented in Figure 4-1 and indicates a deposition peak at -1.29 V. Hydrogen was clearly visible during the course of the scan, but was less severe at less negative potentials. In order to establish whether it was possible to deposit zinc at a potential at which hydrogen evolution was negligible, a series of six zinc depositions were carried out at incrementally less negative potentials. Five depositions were carried out from -1.29 V to -1.21 V, with a difference of 0.02 V between each, and finally one deposition was carried out at -1.18 V. The charge limit was set to 300 mC for all samples – although to some extent this was an arbitrary value, it was chosen with the expectation that it would produce a visible film, based on experience depositing copper and tin. In addition to carrying out visual observations, current was plotted against time in order to investigate whether current-time characteristics, deposition potential and the visual properties of the film could be correlated.

A current-time plot for all six samples can be seen in Figure 4-2. The plots for the samples deposited at -1.25 V, -1.23 V and -1.21 V exhibit current fluctuations that are akin to having a loose electrical connection, therefore any observations of these

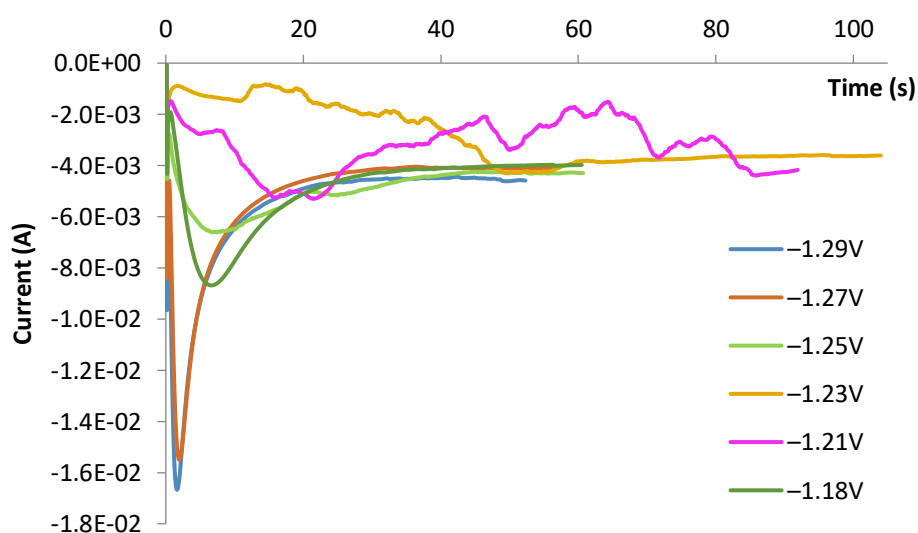


**Figure 4-2 - Current-time plots for zinc deposited onto 1 cm<sup>2</sup> tin films from a pH 3 electrolyte at incrementally less negative potentials. The jagged plot lines for -1.25 V, -1.23 V and -1.21 V are indicative of poor electrical contact.**

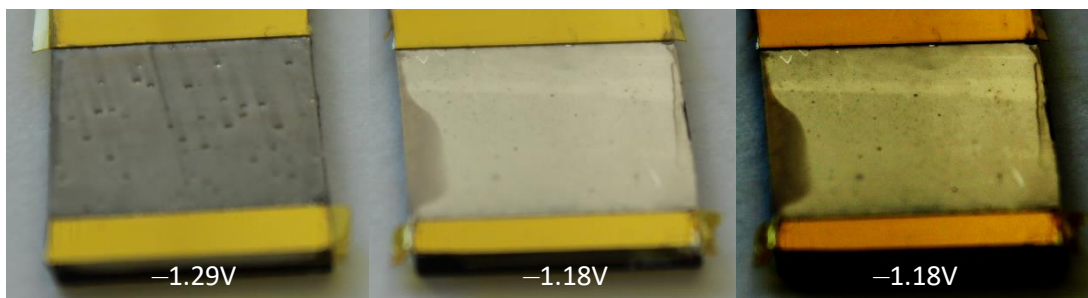


**Figure 4-3 - Zinc films deposited onto 1 cm<sup>2</sup> tin films from a pH 3 electrolyte at -1.29 V and -1.18 V. A high contrast image of the film deposited at -1.18 V has been included on the right to increase the visibility of the film surface features.**

samples may not lead to reliable conclusions. Hydrogen evolution occurred during deposition on all of the samples and this was more severe for more negative deposition potentials, as expected. This was reflected in the visual properties of the films, with those deposited at -1.29 V and -1.27 V having larger, more easily visible pits in the films where hydrogen bubbles had been present when compared to that deposited at -1.18 V. This can be seen in Figure 4-3, in which a film deposited at -1.29 V is presented alongside one deposited at -1.18 V. A high contrast image of the sample deposited at -1.18 V is also included to improve the visibility of its features. What is also visible, is the difference in colour between the two deposits, with the more negative potential leading to a darker film. The film deposited at -1.27 V was similar in appearance to that deposited at -1.29 V. If results for the samples with suspected poor electrical contact are ignored, the current-time plots indicate a strong peak within the first ten seconds of deposition, with the current diminishing to a near-constant rate from approximately 25 s. The peaks are greater in magnitude for more negative deposition potentials (ranging from ~9 mA to ~17 mA), however, the currents all settle to ~4 mA. This suggests that the properties of the films are dictated by the peak in current during the first 10 s of deposition. The results obtained from the deposition of tin in section 3.3.4.2 would suggest that a larger peak magnitude would lead to more rapid nucleation of grains across the surface of the film, leading to smaller grains. The results obtained from the deposition of copper in section 3.3.3.1 would suggest that smaller grains lead to a darker film.

One unexpected occurrence was a slight colour change in the electrolyte. The Hydrion™ pH 3 buffer contains a pH colour indicator, and during the course of the experiments, the colour changed from orange-pink (for pH 3) to orange, indicating a

slight pH increase. On being left to stand overnight, the colour changed further to yellow, suggesting that the pH had increased further to pH 5. This is contrary to expectations as the purpose of a pH buffer is to compensate for changes in pH, not amplify them. An explanation for the initial change in pH could be related to hydrogen evolution – as  $H^+$  ions are reduced and subsequently leave the solution in the form of hydrogen gas, the  $H^+$  concentration, and hence the acidity of the electrolyte will decrease.

The decision was taken to make a fresh batch of electrolyte with the same composition and carry out further deposition experiments across a series of potentials. This was partly to ascertain whether this electrolyte was suitable for obtaining reproducible results, and partly because there was an intention to perform profilometry in which the thickness of only the zinc film was measured (although this profilometry was not carried out due to technical difficulties). Cyclic voltammetry was performed on one of the partially masked tin films, which had an exposed area of approximately  $0.65\text{ cm}^2$ . The resulting voltammogram can be seen in Figure 4-4, in which a deposition peak is indicated at  $-1.26\text{ V}$  – this is a slight positive shift in potential from that seen in Figure 4-1 ( $-1.29\text{ V}$ ). A series of depositions were subsequently undertaken starting with  $-1.14\text{ V}$ , becoming incrementally more negative by  $0.02\text{ V}$  with each deposition until a final deposition

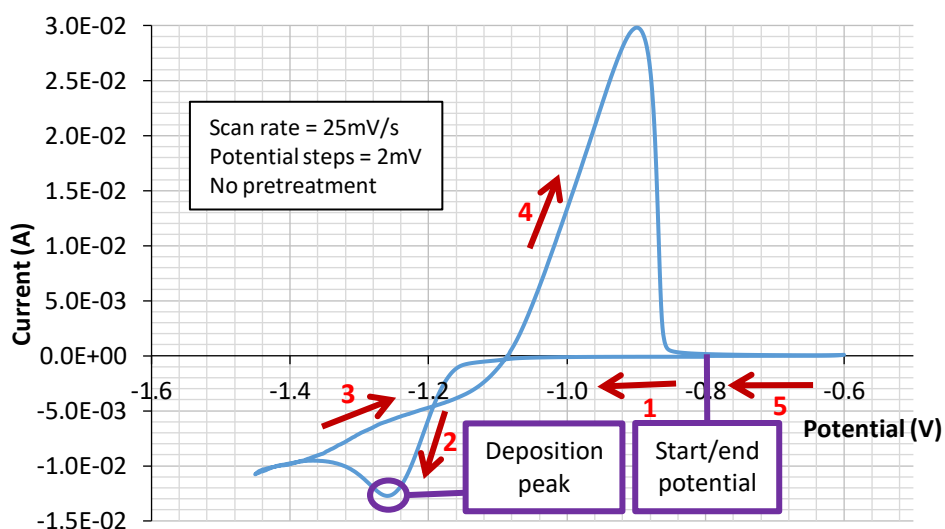


**Figure 4-4 - A voltammogram for cyclic voltammetry performed on a  $0.65\text{ cm}^2$  area of tin film. A deposition peak is indicated at  $-1.26\text{ V}$ .**

was carried out at -1.26 V. This approach was taken as the previous set of experiments were conducted in the order of most to least negative, and with the possibility of the pH of the electrolyte changing during the course of the experiments, the desire existed to reverse this order such that the majority of the hydrogen is evolved in the later experiments leaving the pH largely unaffected for the depositions at less negative potentials. The slight positive shift in deposition peak compared to the previous cyclic voltammogram (-1.26 V compared to -1.29 V) is reflected in the slightly more positive range of potentials chosen compared to the previous deposition sequence.

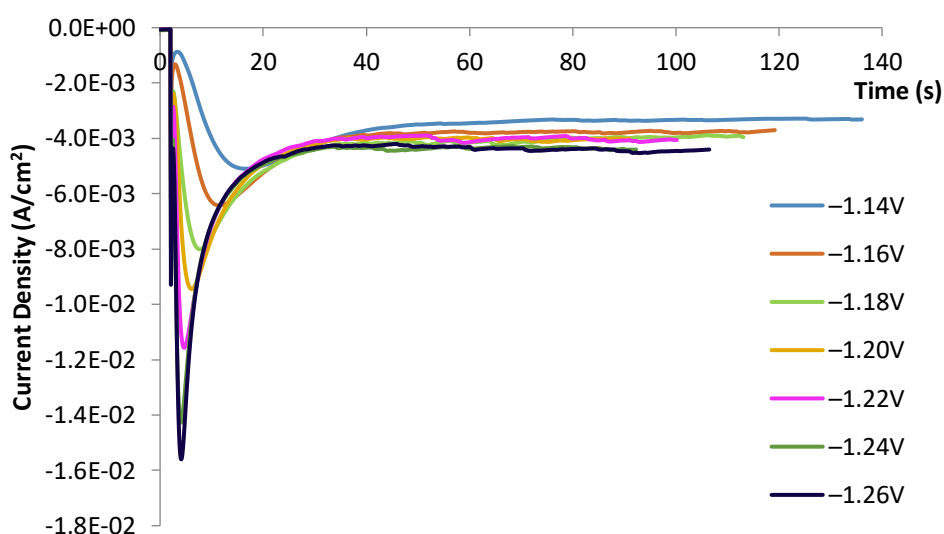


**Figure 4-5 - Current density plotted against time for zinc deposited onto 0.65 cm<sup>2</sup> tin films at incrementally more negative potentials. The large peak in current is greater in amplitude and occurs sooner for more negative potentials.**

The deposition area of each individual sample was calculated using Sigma Scan™ software as described in section 2.4.7, and these values combined with current-time data were used to plot current density against time, as seen in Figure 4-5. Accurate values for the current densities enable a clearer comparison of data between samples. This graph shows that none of the depositions in this series suffered from poor electrical contact, and confirms the previous trend of an increase in magnitude of the main initial peak correlating with an increase in the negativity of the potential. In common with the previous deposition series, all depositions settled to a similar current density magnitude (~3.5-4.5 mA in this case), however, the current peaks shifted to the right and occurred later for less negative deposition potentials. This

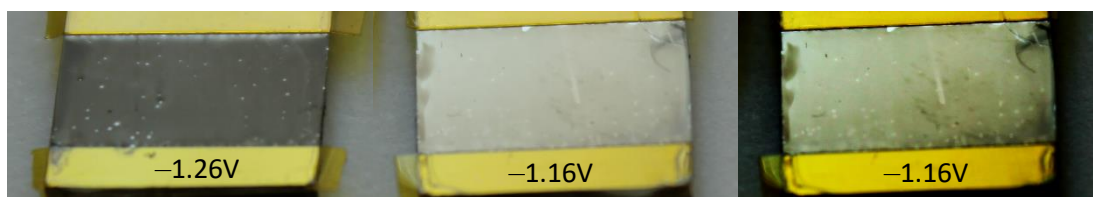


**Figure 4-6 - Zinc films deposited onto 0.65 cm<sup>2</sup> tin films at -1.26 V and -1.16 V. A high contrast image of the film deposited at -1.16 V has been included on the right. Hydrogen evolution occurred across the full range of potentials in this series and its effects are evident on both films seen here.**

suggests that the peak rate occurs once all of the zinc grains have nucleated, with the current diminishing as it becomes diffusion limited. A similar trend to the previous series was also repeated in terms of film colour and hydrogen evolution – darker films with more obvious pits from hydrogen bubbles were obtained with more negative deposition potentials, however, hydrogen evolution posed a problem for all samples in the series. Examples of two of the zinc films are presented in Figure 4-6, which are photographs of films deposited at -1.26 V and -1.16 V respectively, with a high contrast image of the film deposited at -1.16 V in order to enhance the visibility of its features.

Previous experience with tin deposition revealed that more rapid nucleation of grains led to increased film coverage. Based on that information, one may expect hydrogen evolution to be less problematic when depositing zinc at the more negative potentials trialled here, as more of the underlying tin film, from which the hydrogen is evolving, would become covered in the early stages of deposition. Evidence suggests that this is not the case, given the prevalence of hydrogen when depositing at more negative potentials. A possible explanation for this could be that, with tin acting as a catalyst for hydrogen evolution, hydrogen is becoming adsorbed onto the surface of the tin [5]. This enables the more rapid nucleation of hydrogen evolution, allowing it to become established early on in the deposition process. With this in mind, the

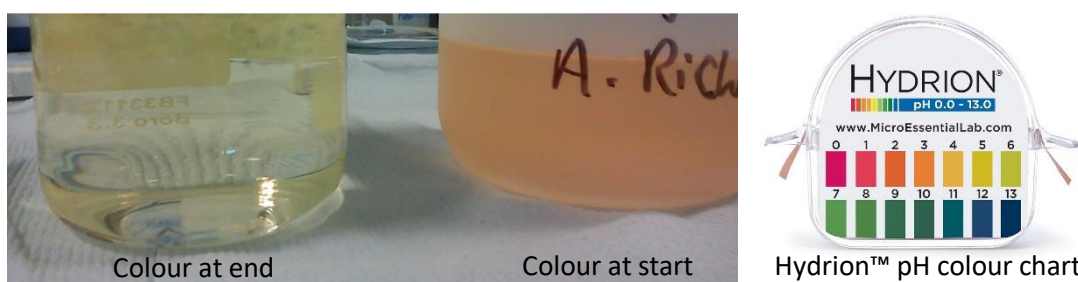


**Figure 4-7 - A photograph showing some used and unused electrolyte and the associated colour change. The accompanying pH colour chart confirms a shift from pH 3 to pH 5.**

decision was taken to try depositing zinc galvanostatically (at a constant current). Galvanostatic deposition is used in the industrial electroplating of zinc onto steel. In this case, a film was deposited at -0.65 mA for 300 s, leading to a current density magnitude of  $\sim 1 \text{ mA cm}^{-2}$ , smaller than that obtained for any of the potentiostatic zinc deposition thus far in the experimentation. This was to test if controlling and reducing the current density led to the positive effect of reducing hydrogen evolution. It was found that this sample returned the overall palest zinc deposit with the least hydrogen evolution. Despite this, there was a darker region of zinc on the sample, similar to that seen on the left edge of the sample deposited at -1.18 V in Figure 4-3, but covering a greater proportion of the sample area. This suggests that there was some inhomogeneity in the deposited film, which could diminish the ability to obtain CZTS during the sulphurisation stage.

Having carried out the depositions from -1.14 V to -1.26 V and a galvanostatic deposition, it was once again evident that the pH of the electrolyte had changed from pH 3 to pH 5, as can be ascertained by the colour change seen in Figure 4-7. To investigate whether this has an effect on the potential at which the deposition peak occurs, cyclic voltammetry was repeated with this electrolyte with an extended potential range. The start/end potential was -0.8 V, -1.65 V was the first scan limit and -0.6 V was the second scan limit. The resulting voltammogram can be seen in Figure 4-8, in which it is superimposed with the voltammogram obtained before the

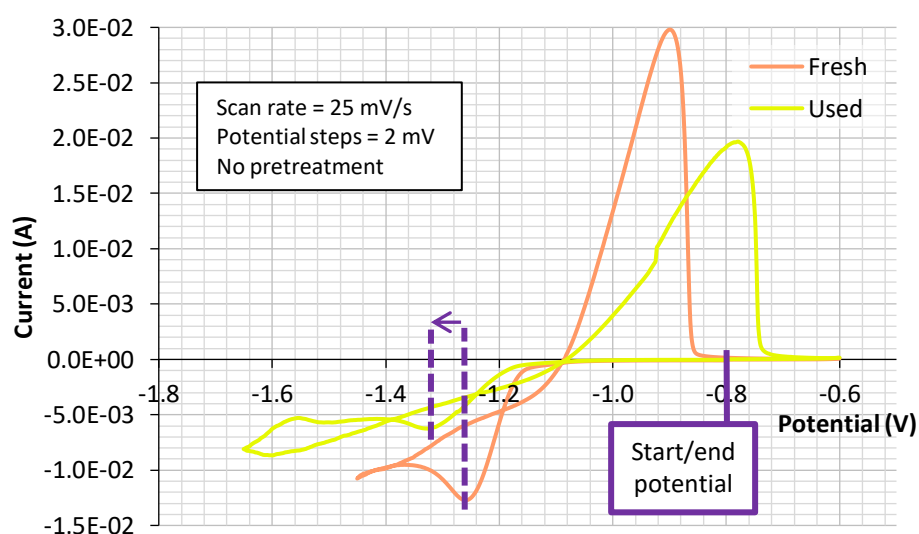


**Figure 4-8 - Cyclic voltammetry showing the deposition peak shift between the unused and used electrolyte.**



deposition experiments were carried out. This demonstrates a shift in the deposition peak from -1.26 V to -1.33 V. In order to establish a reproducible set of deposition parameters, it is necessary to use an electrolyte that will remain consistent in its properties across multiple film depositions, preferably at least ten. It appears that the phenomenon of hydrogen evolution does not only generate issues in terms of the quality of individual film deposits, but also the consistency of the potential at which particular results can be expected to be obtained. In order to attempt to tackle the problem of hydrogen evolution, the decision was taken to try and adjust the  $H^+$  concentration (vary the pH) and test the effect it has on both the potential of the deposition peak and the severity of the hydrogen evolution.

#### 4.3.2 Experimentation Varying the pH of the Electrolyte

An experiment was devised in which four electrolytes were made up using a similar composition to that used thus far for the deposition of zinc, however, each electrolyte contained a different pH buffer and no zinc salt. This was in order that no current would be flowing as a result of the reduction of zinc ions, making the current flowing due to hydrogen evolution more apparent. The composition of each electrolyte was therefore 2M potassium chloride, 0.2 wt.% polyquaternium-2 and a pH buffer. The pH buffers used were pH 3 powder sachets, (Hydrion™ brand), and pH 4, pH 7 and pH 9.2 tablets (Sigma-Aldrich brand). The pH 3 sachets were used in the same manner as that described previously (see section 2.1.9), and one pH buffer tablet each was used to make 100 mL of electrolyte. All of the electrolytes contained a pH colour indicator, as can be seen in Figure 4-9. Cyclic voltammetry was performed using each of the four background electrolytes on 1 cm<sup>2</sup> tin films – a fresh tin film

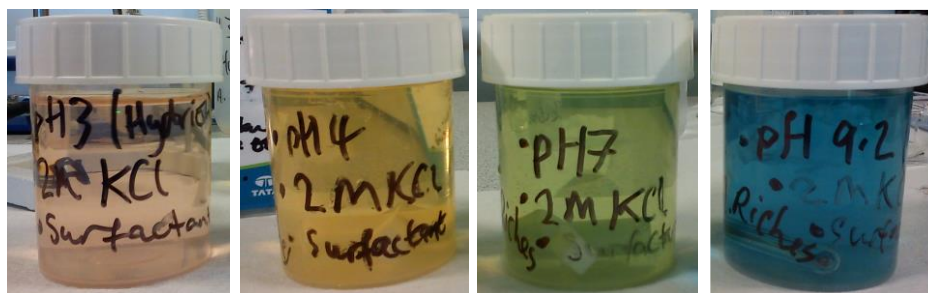


**Figure 4-9 - Four background electrolytes containing different pH buffers, each displaying a different colour due to the inclusion of pH indicator.**



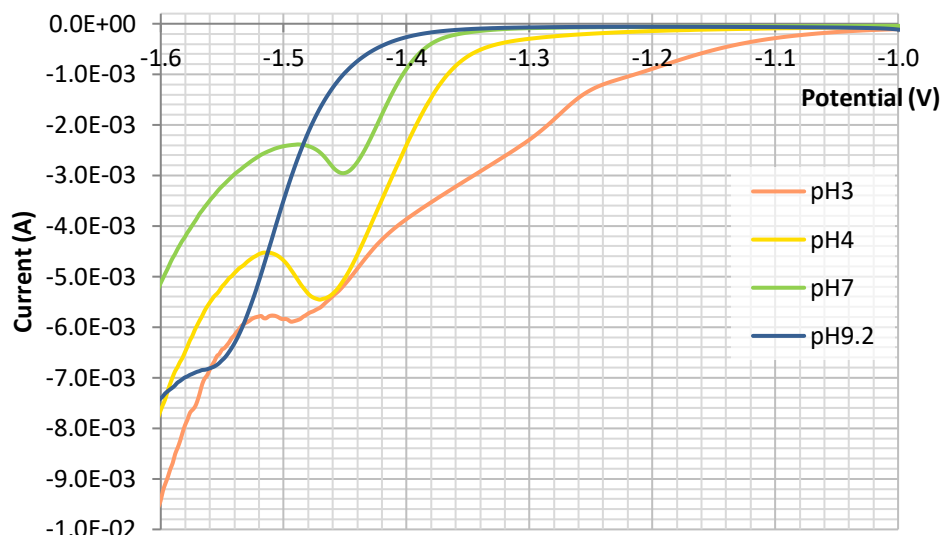


**Figure 4-10 - A section of the voltammograms obtained using four background electrolytes of pH 3 – pH 9.2, showing features of interest on the negative direction scan.**

was used for each experiment to avoid the possibility of hydrogen damage affecting results. The same parameters were used for each electrolyte, which were -0.80 V as the start/end potential, -1.80 V as the first scan limit and -0.60 V as the second scan limit. This relatively broad range of values was chosen in order to cover a range of potentials at which deposition peaks may occur if a zinc salt were added to the electrolyte. The cyclic voltammetry was first performed on each electrolyte in order to gauge the extent of hydrogen evolution across the range of chosen potentials – without any zinc being deposited, the current would almost entirely be as a result of hydrogen evolution. The resulting voltammograms have been trimmed to a potential range over which the current characteristics are displaying features of interest and are presented in Figure 4-10. This graph was to be used as a reference system where the current is read at the chosen deposition potential from the plot line for each corresponding pH. The magnitude of the current would give information on how much hydrogen was expected during the deposition process. Before this graph could be used, it was necessary to perform cyclic voltammetry with the zinc chloride present in the electrolytes in order to ascertain the deposition potential that would be used.

Zinc chloride was added to each of the four electrolytes to a concentration of 50 mM in order to repeat the cyclic voltammetry and ascertain a suitable deposition potential. Unfortunately, upon adding zinc chloride to the pH 7 and pH 9.2 solutions, a precipitate formed and a colour change was observed. This can be seen in Figure 4-11, with the colour change suggesting a shift to greater acidity. The probable situation is that the precipitate is zinc hydroxide ( $\text{Zn}(\text{OH})_2$ ) in both cases, and the removal of  $\text{OH}^-$  ions from the solution has caused a reduction in the alkalinity and therefore an increase in the acidity. This means that these two electrolytes were considered unsuitable for any experiments involving zinc deposition, however, experiments continued with the two remaining acidic electrolytes.



**Figure 4-11 - Images showing the change to a more acidic pH and the precipitate formed when zinc chloride was added to the non-acidic solutions. It is suspected that the precipitate was zinc hydroxide.**

Cyclic voltammograms for the pH 3 and pH 4 electrolytes can be seen in Figure 4-12, showing deposition peaks at -1.26 V and -1.41 V respectively. When these values are referenced against their corresponding plot lines in Figure 4-10, it can be seen that a current due to hydrogen evolution of -1.5 mA is expected for the pH 3 electrolyte, and -3.0 mA for the pH 4 electrolyte. This would suggest that use of the pH 4 electrolyte would lead to a less efficient deposition process with more hydrogen evolution occurring. In order to test this, deposition-stripping tests were carried out. As explained in section 3.3.5, deposition-stripping tests are a simple method to check how much of the charge passed in the deposition process actually contributes to the deposition of the desired metallic element, based on the assumption that the stripping process is highly efficient [6]. Any excess charge passed in the deposition process is likely to be as a result of hydrogen evolution. Current-time plots for deposition-stripping tests involving the pH 3 and the pH 4 electrolytes are shown in Figure 4-13.

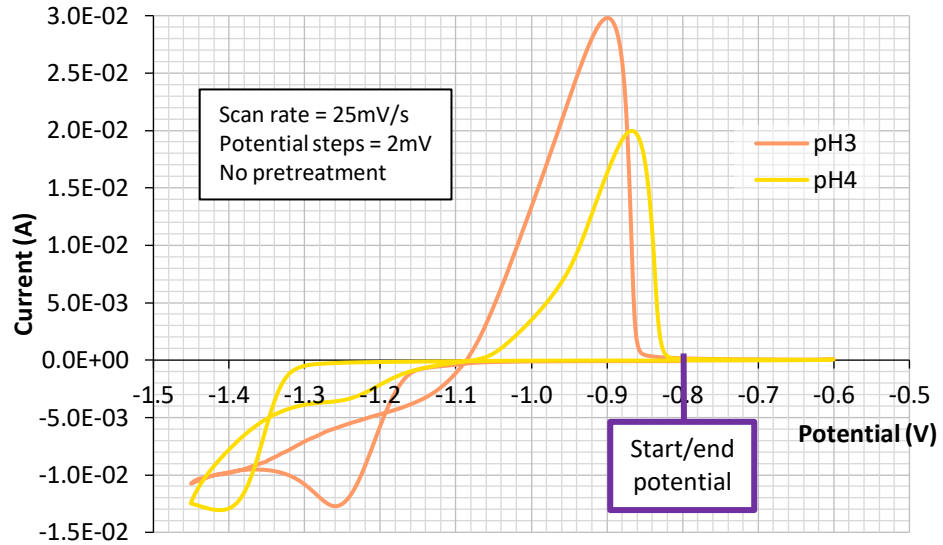


**Figure 4-12 - Cyclic voltammograms for pH 3 and pH 4 zinc electrolytes. Deposition peaks are visible at -1.26 V and -1.41 V respectively.**

The stripping potentials of -0.92 V for pH 3 and -0.87 V for pH 4 were chosen to concur with the stripping peaks seen in the voltammograms in Figure 4-12. Integrating the areas enclosed between the current-time plot lines and the x-axis enabled the calculation of the charge passed in the respective deposition and stripping processes. This yielded the results that the pH4 electrolyte gave a less efficient deposition process at just 29%, compared to 84% for the pH3 electrolyte. This was in the line with the predictions expressed previously, and suggests that a

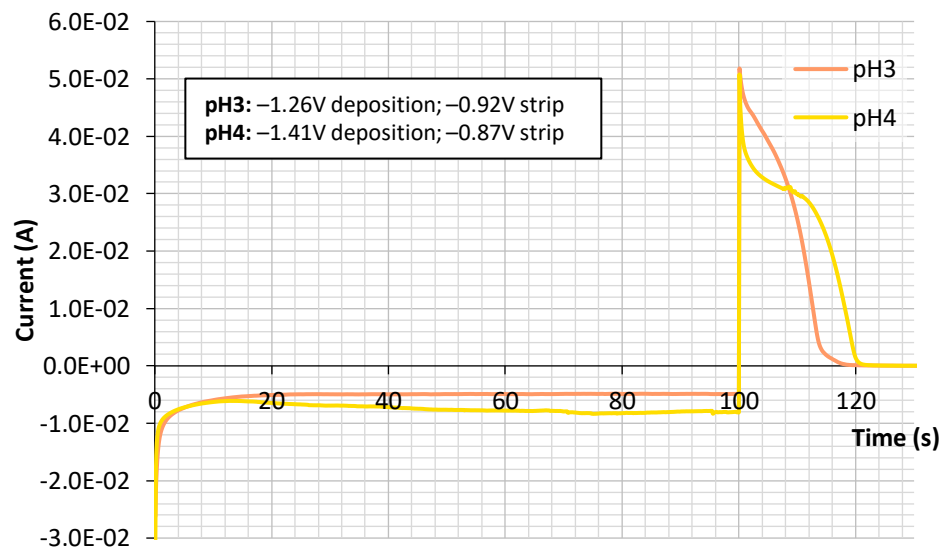


**Figure 4-13 - Current-time plots for zinc deposition-stripping experiments carried out using pH 3 and pH 4 electrolytes.**

more acidic electrolyte may help improve the deposition efficiency. The lowest pH buffer in the laboratory stocks at the time was pH 3, therefore, rather than continuing to use acidity buffers in the composition of the zinc electrolyte, the decision was taken to find an alternative electrolyte formula based on an acidic solution.

At this point in the experimentation, advice was provided by an experienced electrochemist to give consideration to other properties of the electrolyte that could improve film quality, and not simply the pH of the electrolyte. It was considered important that the next electrolyte composition should have an improved throwing power (the ability to deposit at the same rate in low current density areas as high current density areas [7]). Increased throwing power should, in theory, give a more consistent electrodeposit across the surface of the sample and the intention was to test whether this would alleviate the pitting that occurred as a result of hydrogen evolution.

#### **4.3.3 Deposition from an Acid-Chloride Electrolyte**

There are multiple factors that affect the throwing power of an electrolyte. A discussion regarding how the chemical composition of an electrolyte affects the throwing power is provided in section 1.5.3.1. It was important to consider which chemical compositions were likely to increase the throwing power while remaining suitable for use in the laboratory. Alkaline cyanide electrolytes are known to have a high throwing power [8, 9] and have been used extensively in industrial zinc plating applications historically [10], however, they are also known to be highly toxic and would not be suitable for laboratory experimentation due to safety concerns. Furthermore, part of the purpose of this project was to develop techniques that could be scaled-up to pilot production and a cyanide electrolyte would not be considered for this application due to its toxicity and the high associated costs of safe disposal. An alternative to a cyanide based electrolyte was found in the form of an acid-chloride electrolyte. It is reported in [9] that the throwing power of an acid-chloride zinc plating electrolyte was found to increase with the concentration of ammonium chloride and decrease with the concentration of  $\text{Zn}^{2+}$  ions. It also reports that, when the concentration of zinc chloride was  $30 \text{ g L}^{-1}$  or less, the throwing power exceeded that of a cyanide electrolyte [9]. This information led to the selection of Electrolyte Zn 2 (as shown in section 2.1.9), which was found in [8], for the next stage of

experimentation. It was chosen due to its relatively high concentration of ammonium chloride ( $120 \text{ g L}^{-1}$ ) and zinc chloride concentration of  $30 \text{ g L}^{-1}$ . This zinc chloride concentration equates to  $220 \text{ mM}$ , which is  $4.4\times$  that used in the electrolyte for the previous set of experiments ( $50 \text{ mM}$ ). This may appear counterproductive given that the throwing power was expected to be inversely proportional to the concentration of zinc, however, an increase in the zinc concentration could bring some advantages – a higher concentration of zinc would mean that the proportion of the current flowing due to zinc deposition would increase relative to that due to hydrogen evolution. This would mean that less hydrogen would evolve in the time required to deposit the desired quantity of zinc. This electrolyte was chosen as the high concentration of ammonium chloride was expected to lead to high throwing power; the concentration of zinc chloride was low enough to give a higher throwing power than a cyanide based electrolyte, yet strong enough for deposition to out compete the hydrogen evolution reaction.

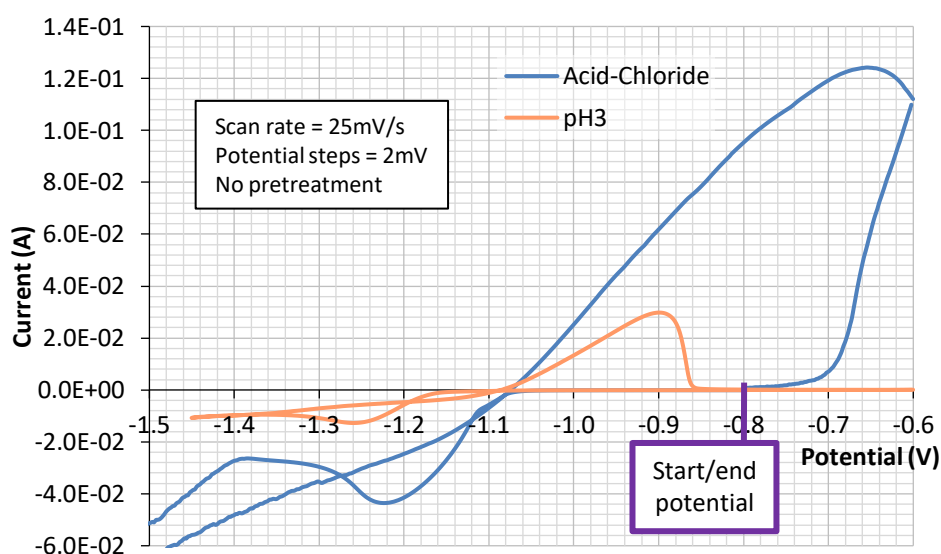


**Figure 4-14 - A cyclic voltammogram for the acid-chloride electrolyte presented alongside a voltammogram for the pH 3 electrolyte for comparison.**

Cyclic voltammetry was performed on  $1 \text{ cm}^2$  tin films using  $-0.80 \text{ V}$  as a start/end potential,  $-1.65 \text{ V}$  as the first scan limit and  $-0.60 \text{ V}$  as the second scan limit. The resulting voltammogram is presented in Figure 4-14, alongside that for the pH 3 electrolyte used previously. It can be seen that the deposition peak for the boric acid based electrolyte occurs at  $-1.22 \text{ V}$ , slightly positive of that for the pH 3 electrolyte.

It is also evident that the magnitude of the current at the deposition peak and at the stripping peak is approximately four times that of the pH 3 electrolyte, possibly due to the higher concentration of zinc in the solution. The tall stripping peak is particularly encouraging as it suggests that substantially more zinc was deposited.

Zinc was deposited at -1.22 V with a charge limit of 300 mC. This took just 9.6 s to reach including a 2 s pre-treatment at -0.8 V – this is notably quicker than any of the previous (pH 3) zinc depositions, the most rapid having been 53 s to deposit 300 mC at -1.29 V (as seen in Figure 4-2). These two films are presented alongside each other in Figure 4-15 for comparison. The deposition from the boric acid electrolyte can be seen on the left and displays a more even and consistent deposition in its appearance, with no visible pitting or variations in colour. This initial visual check would suggest that the boric acid electrolyte produces favourable results, however, it was necessary to perform further analysis to test its suitability for use in the preparation of films for further processing in to PV devices.

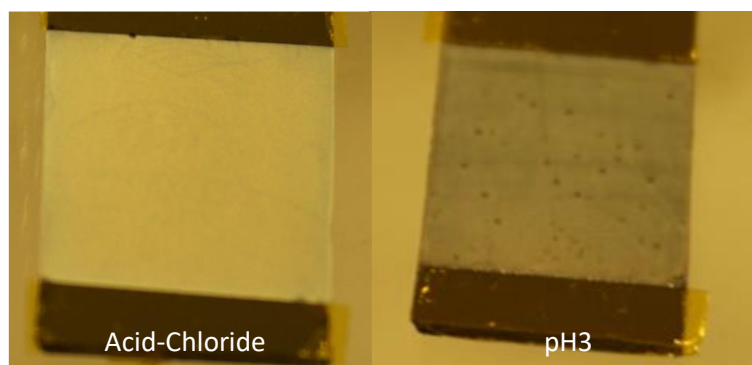


**Figure 4-15 - Zinc deposited onto tin from the acid-chloride electrolyte (left), presented alongside zinc deposited from the pH 3 electrolyte (right).**

#### ***4.3.3.1 Analysis using Profilometry and Deposition-Stripping Tests***

Profilometry was performed using the settings outlined in section 4.2.2.1 across a 5000  $\mu\text{m}$  length on both samples. This revealed that the sample deposited from the boric acid electrolyte was rougher overall, with an  $R_a$  value (measured across 2500  $\mu\text{m}$ ) of 41.3 nm, compared to 28.3 nm (measured across 1870  $\mu\text{m}$ ) for the sample deposited from a pH 3 electrolyte. This is evident from the surface profiles presented

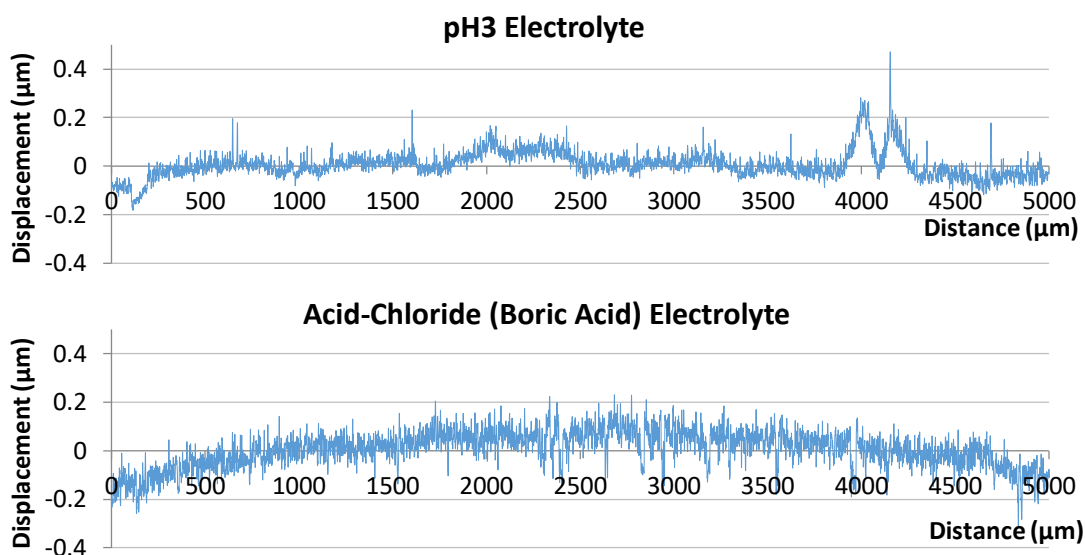


**Figure 4-16 - Surface profiles of zinc deposited from the pH 3 and the acid-chloride electrolytes.**

in Figure 4-16, in which the visible displacement of the plot line is generally greater for the boric acid sample. Conversely, there is the notable absence of the larger bumps and pit that are clearly visible positioned near 4000  $\mu\text{m}$  into the pH 3 sample scan. This is most likely caused by a “crater” around a point at which a hydrogen bubble formed and grew during the deposition process. If a sample were to be processed further for the manufacture of CZTS, some diffusion of the metallic films would occur during the heating processes. Therefore, it is preferable to use a film with a rougher overall profile but with consistent coverage than a film that contains “craters” that cause a significant localised variation in film thickness. On this basis, the boric acid sample would be considered preferable. The absence of obvious “craters” on the boric acid sample corresponds with the observations made during the deposition process – no hydrogen bubbles were visible on the sample surface or in the surrounding electrolyte. In order to verify this, a deposition-stripping test was carried out to gauge deposition efficiency.

The deposition-stripping process was carried out three times on separate substrates and deposition timescale chosen for this was relatively short – just 10 s – which was due to the higher magnitude of deposition current witnessed when using this electrolyte when compared to those used previously, which is evident in the current-time plot presented in Figure 4-17. In the three experiments carried out, the 10 s

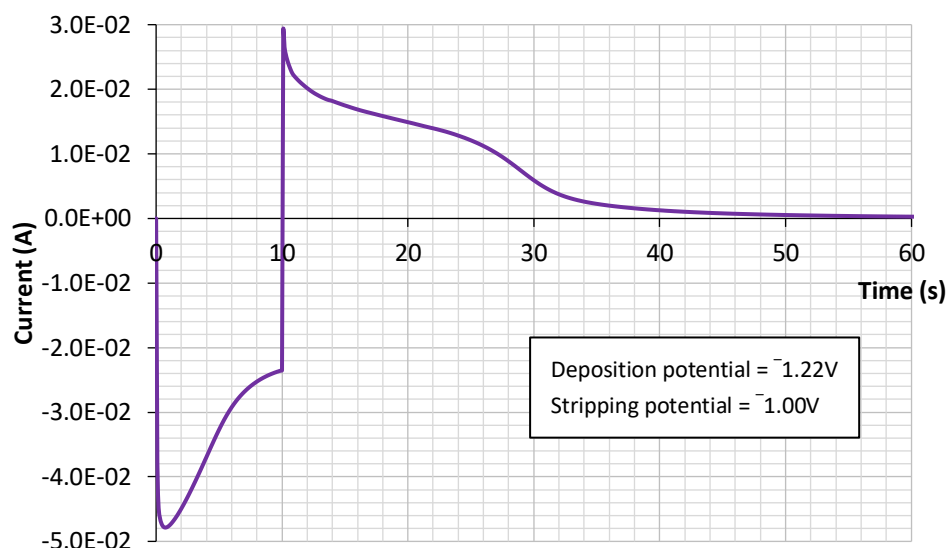


**Figure 4-17 - A current-time plot for a deposition-stripping experiment using an acid-chloride zinc electrolyte.**

deposition time was sufficient to pass 286 mC, 350 mC and 342 mC of charge respectively. During the experiment represented in Figure 4-17, 342 mC of charge was passed during deposition and 339 mC during stripping, leading to a deposition efficiency of 99%. The two other experiments each returned an efficiency of 96%. This is a substantial improvement on the 84% efficiency calculated for the pH 3 electrolyte and suggests that the boric acid electrolyte may be a suitable candidate for use in samples that are processed further for making CZTS. Prior to making a final decision as to whether to use this electrolyte for such purposes, the decision was taken to study the electroplated stacks further using XPS depth profiling. This was partly to observe the degree of intermixing between layers and to test for oxygen and carbon contamination inside the deposited films, but it was also to verify the abundance of each deposited element.

#### **4.3.4 Sample Analysis using XPS Depth Profiling**

XPS depth profiling was performed on three samples. All three samples had been deposited with copper and tin using the methods described in section 4.2.1 on substrates with a deposition area of 1 cm<sup>2</sup>. Zinc layers were deposited using three different methods. These were:



1. Potentiostatically using a pH 3 electrolyte (Electrolyte Zn 1 in section 2.1.9) at -1.24 V with charge passed density of 452 mC cm<sup>-2</sup> (expected deposition efficiency of ~84%).
2. Galvanostatically using a pH 3 electrolyte (electrolyte Electrolyte Zn 1 in section 2.1.9) at -1 mA cm<sup>-2</sup> with charge passed density of 300 mC cm<sup>-2</sup> (expected deposition efficiency of >84%).
3. Potentiostatically using an acid-chloride electrolyte (Electrolyte Zn 2 in section 2.1.9) at -1.22 V with a charge passed density of 500 mC cm<sup>-2</sup> (expected deposition efficiency of ~97%).

Total XPS etching times for the three samples were 15,000 s for samples prepared using methods 1 and 2, and 12,600 s for the sample prepared using method 3. This was sufficient to etch through all of the electrodeposited layers and reach the underlying molybdenum in all cases. Elemental abundance measurements were taken every 300 s, the measurements were in the form of electrons of specific energies corresponding to energy peaks that are characteristic of particular elements (see section 2.4.4). The percentage abundancies were calculated from the electron counts corresponding to each element, and these have been plotted against time and presented in Figure 4-18. Three separate graphs were constructed, one for each sample analysed. The most obvious feature to comment on is that, unlike copper and tin, zinc does not appear as a discrete layer on any of the samples, rather it appears to have inter-diffused between the other two layers. This was contrary to expectations given that the elemental films were deposited sequentially and no annealing had taken place prior to this analysis. Further analysis of electrodeposited stacks later in this project cast significant doubt on whether this apparent inter-diffusion was in fact taking place (see section 4.3.7.1), however, the data to evidence this had not yet been acquired at this stage.

Although the only SEM available at this stage in the project was incapable of obtaining images of the required resolution, there was some suspicion that the zinc deposited was not forming a close-packed granular structure and was leaving some of the underlying tin exposed. This is partly due to the high degree of roughness measured on the zinc deposits (Ra values of 41.3 nm and 28.3 nm on respective zinc deposits, compared to 17.4 nm and 22.6 nm on tin deposited at -0.56 V), but also

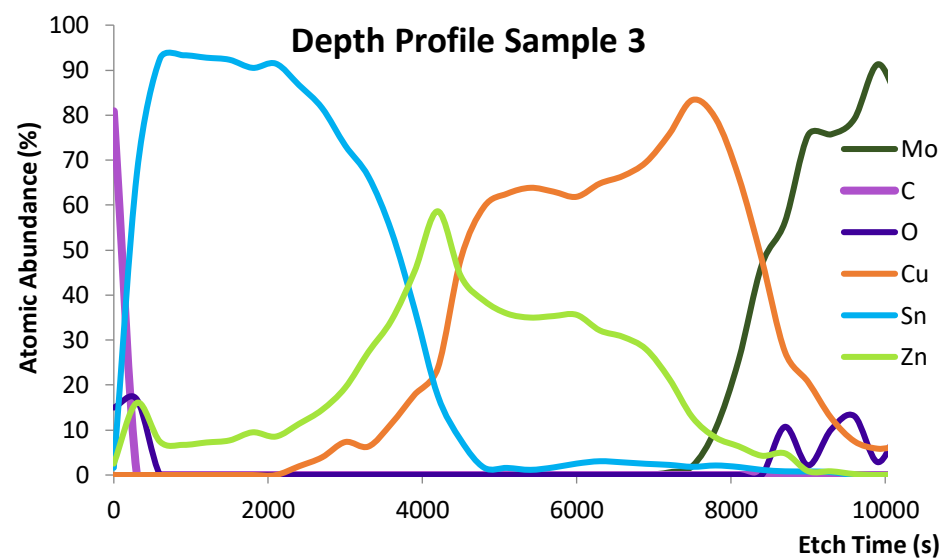
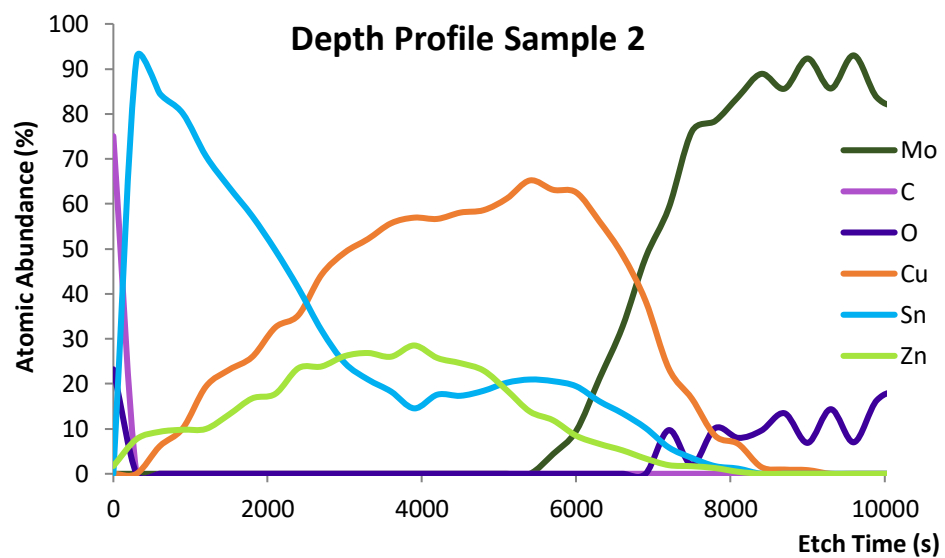
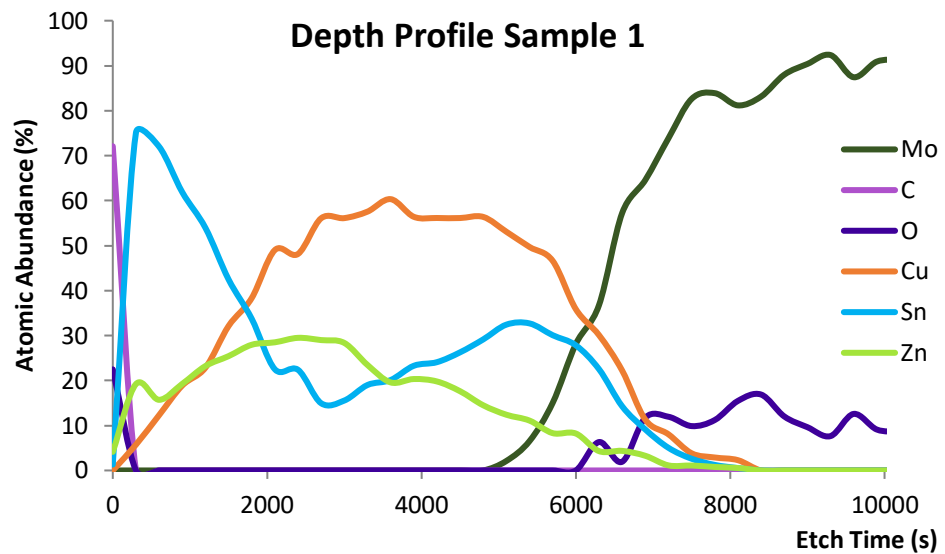


**Figure 4-18 - XPS depth profiles showing atomic abundancies for three Cu-Sn-Zn stacks. The headings ‘Sample 1’, ‘Sample 2’ and ‘Sample 3’ refer to samples with zinc deposited using methods 1, 2 and 3 respectively.**

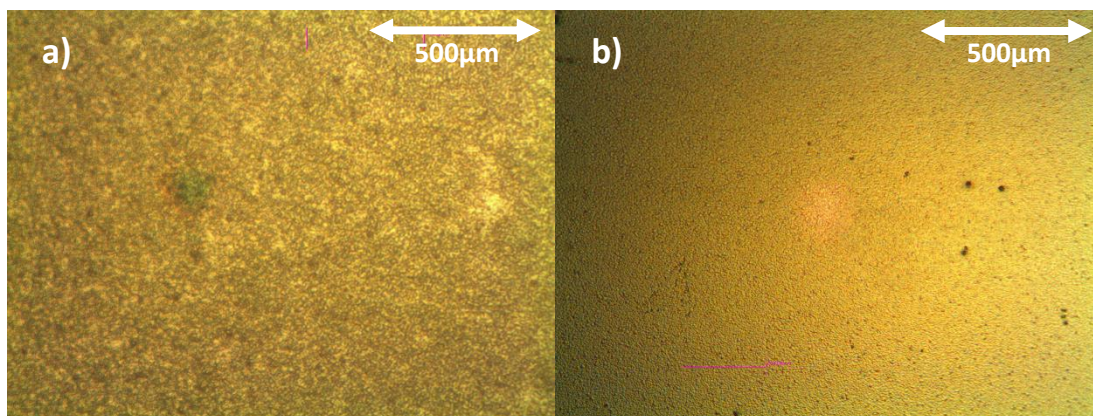


**Figure 4-19 - Microscope images (50x magnification) of a) zinc deposited from an acid-chloride electrolyte, and b) tin. The images are presented alongside each other for comparison. The zinc appears less uniform and may have left some uncoated tin between zinc deposits.**

because of the appearance of the films under an optical microscope. A film deposited using the acid-chloride (boric acid – method 3) electrolyte is shown in Figure 4-19 alongside a good quality tin deposit (as seen previously in section 3.3.4.2). When compared to the tin deposit, the surface of the zinc appears to be comprised of more pronounced grains with irregular spacing between them – it has a similar appearance to that of sandpaper. This morphology could offer some explanation as to why the zinc layer does not appear discrete in the XPS analysis. The XPS analyses a surface area enclosed by an oval of  $0.3 \times 0.7 \text{ mm}^2$ , which, judging by the microscope image in Figure 4-19, is more than sufficient to detect both the deposited zinc and exposed areas of tin. As the sample is etched, this would generate a profile through the tin and zinc simultaneously, giving the impression that the two elements had intermixed as seen in Figure 4-18. In addition to this, if zinc is deposited such that the surface is undulating, then it will be more concentrated and therefore thicker at the surface peaks, meaning that it may take more time to etch away all of the zinc deposit than the more uniform tin beneath. This could offer an explanation as to why there appears to be some zinc still present even when the majority of the tin has been removed and the etching process has started penetrating into the copper. This would not, however, explain the strong peak in zinc abundance at 4200 s of etching on the sample prepared using method 3, at which the zinc content is approximately 60% and coincides with an apparent interface between the tin and the copper. This suggests that there has in fact been some diffusion of zinc through the tin film on this sample,

although it is not clear whether this happened as part of the deposition process or whether zinc diffusion occurred in the time period between sample preparation and sample analysis, which was a matter of weeks. It is also noteworthy that the copper and tin layers do not appear as discrete layers on the samples where zinc has been deposited using methods 1 and 2. It is particularly noticeable that the copper layers are being detected by the XPS earlier in the etching process. The reason for this is unknown as copper and tin were deposited using the same methods, materials and settings on all three samples. It is, however, worth acknowledging that the graphs in Figure 4-18 are indicative of percentage abundance, not total counts associated with each element, and that the drop in counts for one element will cause the percentage abundance to increase for other elements if their count rates remain constant. The delay in detection of copper on the third (zinc deposited using acid-chloride electrolyte) sample will also have made the peak in zinc abundance more apparent.

It is evident in Figure 4-18 that contamination of the electrodeposits with oxygen and carbon is very low. There is a high proportion of carbon and some oxygen present on the surface of all three samples, which is to be expected of any sample that has been stored in ambient conditions, but the percentage abundance of carbon falls to zero after the first etching period of 300 s on all samples. Oxygen is similarly not present inside the electrodeposited films – it has fallen to zero after the first etching period on the samples where zinc has been deposited from a pH 3 electrolyte (methods 1 and 2), and by the end of the second etching period on the sample where zinc was deposited from an acid-chloride electrolyte (method 3). This is still a relatively low level of oxygen compared to other elements and would likely have only been present due to residual fragments of the top surface having not fully dispersed at the end of the first etching period. Oxygen is then no longer detected by the XPS system until the molybdenum layer has been penetrated. This is a positive result as it indicates that the organic additives used in the copper and tin deposition have not been incorporated into the films, nor have any other organic contaminants that may have been present, such as the solvents used to clean the substrates and the glassware, for example. It also suggests that no oxide layers were formed and “trapped” as each elemental layer was completed and subsequent layers were deposited on top. Oxygen inclusion in the electrodeposits could have caused difficulties in the formation of

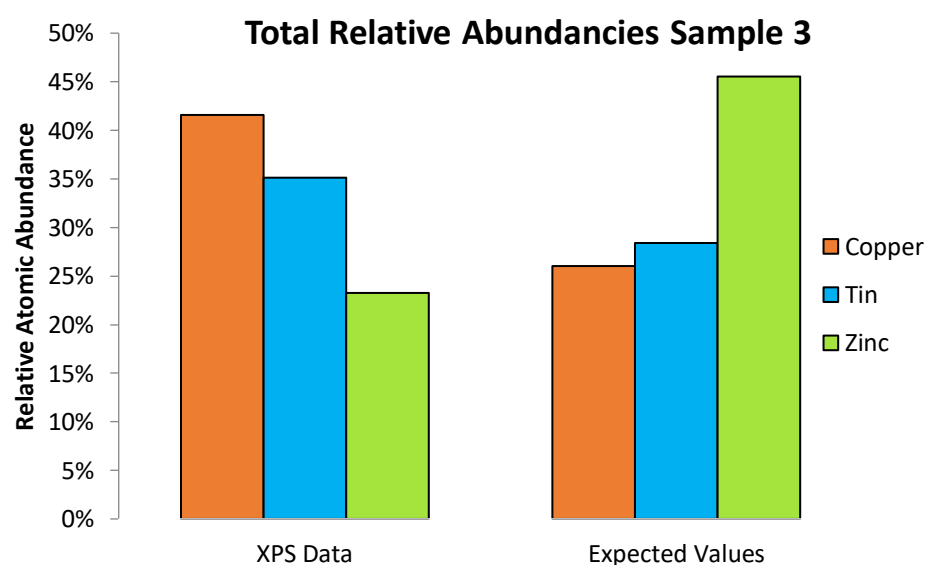
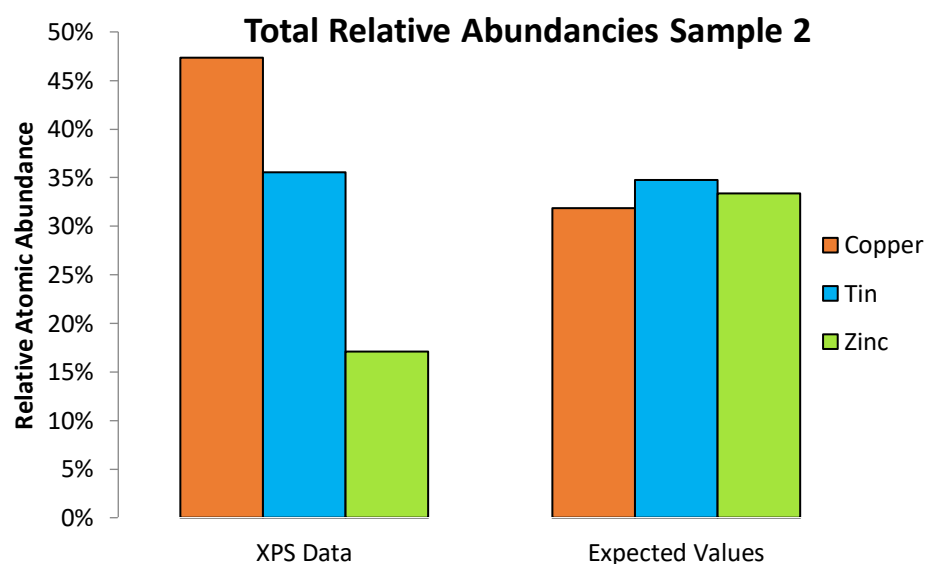
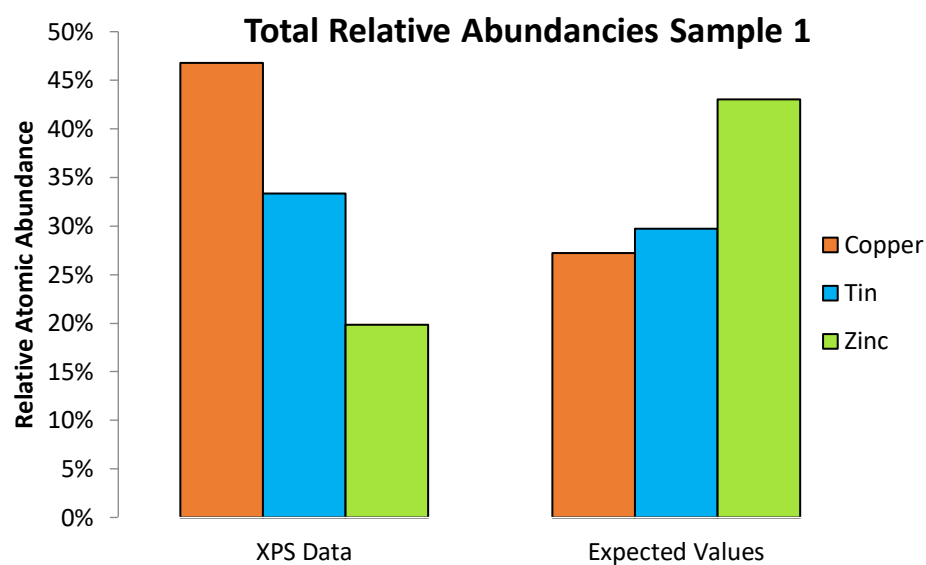


**Figure 4-20 - Bar charts showing the atomic abundancies integrated across the depth of the XPS profiles compared to expected abundancies based on electrochemical parameters for three samples. ‘Sample 1’, ‘Sample 2’ and ‘Sample 3’ refer to samples where zinc has been deposited using methods 1, 2 and 3 respectively.**

CZTS as it could lead to the preferential formation of tin oxide upon annealing and the subsequent formation of other unwanted secondary phases [11].

The total atomic abundancies of each electrodeposited element for each of the three samples were calculated using the methods described in section 4.2.2.2. These are presented alongside the expected atomic abundance values, which are based on charge passed density, in Figure 4-20 in the form of bar charts. Previously obtained deposition efficiency has not been factored in to these charts, therefore a discrepancy was predicted to occur between the expected and XPS data for the zinc abundancies on samples deposited from the pH 3 electrolyte (i.e. samples 1 and 2) but not for that deposited from the acid-chloride electrolyte (sample 3). The results obtained are contrary to that prediction, with discrepancies apparent for both copper and zinc on all samples. The zinc abundancies are all approximately half of that expected, whereas the copper abundancies are all 15 – 20 % greater than expected. The tin abundancies show the least discrepancy, with the greatest being 7% on sample 3. Unfortunately, this data does not indicate the high deposition efficiency for the acid-chloride zinc electrolyte that was expected, and suggests that the deposition efficiency of zinc could be lower than predicted for all electrolytes. However, the discrepancy in the copper abundancies calls the accuracy of all of the XPS data into question. If there were moderate discrepancies for both copper and tin, then one could argue that a higher than expected percentage of copper and tin is a result of a lower than expected quantity of zinc being present rather than a raised quantity of copper and tin, however, as the tin abundancies are in broad agreement with the expected values, then this argument does not hold. One possible explanation for these results could be differences in etch rates between the three elements, with zinc requiring the fastest etch rate and copper the slowest in order to return the obtained abundancy results. If this were the case, one may expect the zinc signal to drop very rapidly compared to those of other elements, yet this characteristic was not observed as is evident from the graphs in Figure 4-18.

Given the inconclusive nature on the quantity of deposited zinc, the decision was taken to continue to experiment by altering the composition of the electrolyte used for zinc deposition, with view to attempt to verify the deposition efficiency at a later date using MP-AES. The initial adjustments to the zinc electrolyte composition were

focussed on improving the surface morphology using the previously described acid-chloride electrolyte with varying quantities of an additional organic additive. Experiments then progressed to trials involving an electrolyte composition taken from literature in which the successful manufacture of a relatively efficient CZTS device is reported.

### **4.3.5 Further Adjustments to the Electrolyte Composition**

#### ***4.3.5.1 Experimentation through the Addition of an Organic Surfactant***

Polyquaternium-2 was present as a surfactant in the (pH 3) zinc electrolyte composition used by Scragg [4], which was trialled as the first zinc electrolyte in this project as described previously. The acid-chloride electrolyte, which returned favourable results in terms of minimised hydrogen evolution, did not contain any surfactant. The lack of surfactant may be the cause for the increased surface roughness (reported in section 4.3.3.1) when compared to zinc deposited from the pH 3 electrolyte. Therefore, a series of zinc depositions were performed with gradually increasing quantities of Polyquaternium-2 added to the acid-chloride electrolyte, its composition remaining otherwise unchanged (composition given in section 2.1.9 as Electrolyte Zn 2). Concentrations ranged from 0.2 wt.%, which was the concentration used in the pH 3 electrolyte, to 0.8 wt.%, in increments of 0.2 wt.%. The zinc was deposited onto 1 cm<sup>2</sup> copper-tin stacks on Mo-SLG, which were prepared using the methods described in section 4.2.1. The zinc deposition potential was -1.22 V as this was used successfully with this electrolyte previously, and the charge limit was set to 840 mC. This charge limit was chosen as it would lead to twice the zinc required for the desired elemental ratios to be obtained assuming a 100% deposition efficiency (these ratios were copper/tin = 1.83 and a zinc/tin = 1.35 and were taken from a publication reporting a high device efficiency [12]). Due to the fact that the XPS results (presented in section 4.3.4) suggested that the zinc deposition process was only ~50% efficient, the decision was taken to double the charge limit.

The four resulting zinc films are presented in Figure 4-21, alongside an image of zinc deposited from the acid chloride electrolyte without surfactant added (as seen previously in Figure 4-15). No specific trend correlating to the surfactant

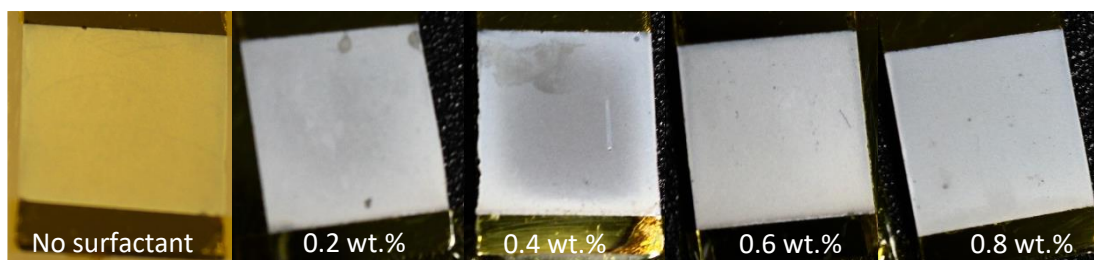


**Figure 4-21 - Zinc deposited from an acid-chloride electrolyte with varying concentrations of surfactant. The addition of the surfactant did not produce favourable results.**

concentration was observed in terms of their visual appearance, however, the zinc deposits appeared weak and of a poor quality. All of the films exhibit “spots” and regions of discolouration (including the 0.6 wt.% and 0.8 wt.% samples, although this may not be obvious in the photographs), suggesting that there was some contamination of the deposited film. There was also a “ring effect”, where the film appears to have been deposited preferentially around the perimeter of the deposition area, on the sample deposited from a surfactant concentration of 0.4 wt.% in the electrolyte. It was noted that during the deposition process for the 0.2 – 0.6 wt.% samples, they initially darkened in colour, but became lighter again after approximately 2 s, as if much of the deposited material had been removed. This effect did not occur as strongly with the 0.8 wt.% sample, which took significantly longer (53 s c.f. ~30 s) to reach the charge limit of 840 mC, suggesting that a threshold was reached at which point the surfactant starts to impede the current flow through the electrolyte. Although some previous samples were examined using XPS, there was very limited time availability on the equipment, and with the etching process for the depth profiling being very time consuming, these films were not considered to be of a high enough quality to warrant this. The decision was taken based on the visual observations to progress experimentation onto a fully revised zinc electrolyte composition.

#### ***4.3.5.2 Zinc Deposition from a Methanesulfonic Acid Electrolyte***

One of the key publications in the year 2012 with reference to electrodeposition for CZTS was [12], in which a significant increase in efficiency for CZTS devices manufactured through electroplating was reported. The decision was taken to conduct zinc electrodeposition trials using the electrolyte composition reported in



[12]. This composition is given as Electrolyte Zn 3 in section 2.1.9. There was a desire to shift away from potentiostatic to galvanostatic deposition as this is the method used in industrial plating processes, and one of the aims of this project was to establish an industrially scalable deposition method. One of the potential advantages of the zinc electrolyte composition reported in [12] was that it was used to deposit zinc galvanostatically at a current density magnitude of  $20 \text{ mA cm}^{-2}$  in the successful manufacture of CZTS devices. With this in mind, four  $1 \text{ cm}^2$  samples (copper-tin stacks on Mo-SLG – see section 4.2.1 for preparation methods) were electrodeposited with zinc using the settings given in Table 4-1. The first deposition current density magnitude of  $20 \text{ mA cm}^{-2}$  was chosen to match that reported in [12], however, this reference reported that the fluid was agitated during the deposition process, which was not repeated in the experiments presented here (a preliminary test with a stirred electrolyte led to a reduction in deposition uniformity, similar to that witnessed with copper as seen in Figure 3-8 in section 3.3.1.2). It was found in previous experiments for the deposition of copper (see section 3.3.1.2) that fluid agitation caused an increase in the current magnitude for a fixed potential. Therefore, if a fixed current is maintained, then one may expect the potential to be more negative for a stagnant solution than for an agitated solution. Based on this reasoning, attempts to improve subsequent deposits were focussed on reducing the current density magnitude and lessening any effects that are associated with hydrogen evolution. The current density magnitude for all samples was at least  $10 \text{ mA cm}^{-2}$  for at least the first 10 s in order to attempt to rapidly nucleate a zinc film across the entire surface of the tin early on in the deposition process. Deposition times were chosen such that the total charge passed would come to 412 mC, near to the  $420 \text{ mC cm}^{-2}$  that would be required if it were to be made into a CZTS film.

**Table 4-1 - Deposition settings for zinc deposited on four different samples from a methanesulfonic acid electrolyte.**

Sample	Step 1		Step 2	
	Current Density ( $\text{mA cm}^{-2}$ )	Time (s)	Current Density ( $\text{mA cm}^{-2}$ )	Time (s)
1	-20.0	20.6	N/A	N/A
2	-10.0	41.2	N/A	N/A
3	-10.0	10	-5.0	80.4
4	-10.0	10	-2.5	160.8

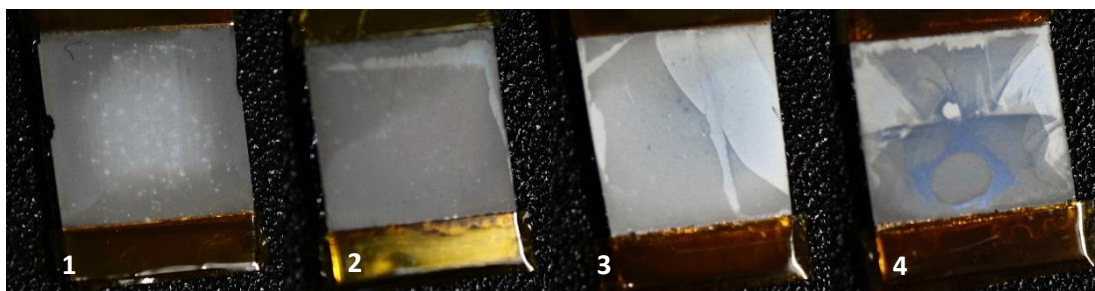


**Figure 4-22 - Zinc deposited from a methanesulfonic acid electrolyte using the four different settings given in Table 4-1. None of the deposited films are of an acceptable quality.**

The films obtained are presented in Figure 4-22. All samples exhibit inhomogeneity, with the most inhomogeneous being sample 4, with areas of uncoated tin clearly visible. Hydrogen evolution has also led to some pitting in samples 1 and 2, sample 1 being most affected, which was not unexpected given that it was deposited using the greatest current density magnitude. Although the pitting appears less severe on sample 2 in the photograph, it was still of such a degree that was considered unacceptable. It also appears that sample 1 suffered from preferential deposition of zinc around its perimeter. These symptoms suggest that the throwing power of this electrolyte is particularly low, and does not appear to offer any advantages over the acid-chloride electrolyte that was tested previously. The IBM research group that carried out the work in [12] used a more complex electroplating setup. This included the employment of a co-planar deflector electrode, which served the purpose of correcting the current and thickness distribution of the electrodeposit on the substrate [13]. This may explain, at least in part, why the positive results reported in [12] were not reproducible using this electrolyte. At this stage in the project, the desire was to remain focussed on finding the most suitable electrolyte composition for the task of electrodepositing zinc onto tin, and it was considered preferential to maintain a simple electroplating setup for the purposes of scalability. The next stage of experimentation involved the comparison of results obtained using four entirely different electrolyte compositions. These electrolytes were chosen for their diversity in the purposes for which they were formulated and therefore in their chemical make-up, the intention being that this could increase the probability of finding a suitable composition for electroplating onto tin when compared to the previous approach of making small adjustments with similar electrolyte compositions.

### 4.3.6 Comparison of Four Diverse Electrolyte Compositions

#### 4.3.6.1 Introductory Discussion on Electrolyte Compositions

The electrolyte compositions trialled in this set of experiments are electrolytes Zn 4 – Zn 7 as detailed in section 2.1.9. Electrolyte Zn 4 is an alkaline non-cyanide electrolyte that was reported in [14], a publication that details the trial of salicylaldehyde as a new brightener for the electrodeposition of zinc onto steel from an alkaline electrolyte. This electrolyte was included in the experiments in this project for several reasons. There was a desire to trial an alkaline electrolyte due to the expectation that it would have a higher throwing power than an acidic electrolyte [8], and to test the effect on hydrogen evolution given the lack of alkaline electrolyte included in the pH-based experiments described in section 4.3.2. It was also considered of interest due to the inclusion of a brightener, which could alter the grain structure of the electrodeposited film.

A brightener was also included in the composition of Electrolyte Zn 5, in this case a commercially branded one, with the electrolyte having been formulated to be used in the zinc plating stage during the restoration of classic car components. As with the electrolyte used in the experiments described in section 4.3.3, this was an acid-chloride electrolyte, although in this instance both the acid and zinc chloride were more concentrated (60 g L<sup>-1</sup> c.f. 30 g L<sup>-1</sup> of zinc chloride and 20 g L<sup>-1</sup> c.f. 5 g L<sup>-1</sup> of boric acid). This could facilitate the use of higher current densities, and therefore more rapid deposition rates, without an increased risk of hydrogen evolution.

Electrolyte Zn 6 also uses a high concentration of zinc in its formulation. This is an acid-sulphate electrolyte designed for the plating of zinc onto sheet steel, which was considered potentially promising, given that the substrates used in this project were essentially flat sheets on a relatively small scale. This is in contrast to Electrolyte Zn 5, which was formulated for plating three-dimensional shapes, such as car door hinges and sections of exhaust pipe, for example. There was particular interest in comparing the results from these two electrolytes for this reason. As mentioned in section 2.1.9, this electrolyte was not expected to have a high throwing power [9] [15], however, given the two-dimensional nature of the substrates, and minimal expected hydrogen evolution owing to the high zinc concentration, it was considered that this may not lead to significant disadvantage. Also mentioned in section 2.1.9 is

the inclusion of dextrin as a levelling agent in this electrolyte, and consideration was given to whether a levelling agent, which in theory would lead to smoother film deposits, would also have the advantageous effect of increasing coverage of the underlying tin.

As mentioned in section 2.1.9, the main reason for choosing to experiment with Electrolyte Zn 7 was that, unlike the other three electrolytes used in this set of experiments, it was specifically formulated for electroplating metals in the manufacture of CZTS solar cells, albeit via the codeposition route. It is distinctive in its low concentration of zinc (30 mM), in stark contrast to Electrolyte Zn 6 (300 g L<sup>-1</sup> zinc sulphate heptahydrate is the equivalent of 1.04 M), and it is also distinctive in that it is neither a strongly alkaline or acid solution (although the pH of this electrolyte was not specifically ascertained).

#### **4.3.6.2 Alkaline Non-Cyanide Electrolyte (Electrolyte Zn 4)**

Attempts were made to deposit zinc onto 4 cm<sup>2</sup> tin films (copper-tin stacks on Mo-SLG prepared as described in section 4.2.1) using four different galvanostatic current densities. These were -0.125 mA cm<sup>-2</sup>, -0.75 mA cm<sup>-2</sup>, -1.5 mA cm<sup>-2</sup> and -3.0 mA cm<sup>-2</sup>. Substantial hydrogen evolution was evident in every case, causing severe blistering and film damage, as can be seen in the images in Figure 4-23. Contrary to expectations, film damage appeared to increase as the current density magnitude was decreased. This suggests that the scale of the damage is more closely related to the length of time the sample is subjected to the deposition process rather than the current density used during the process. One attempt at deposition was carried out onto a copper film on a 4 cm<sup>2</sup> deposition area, with a current density of

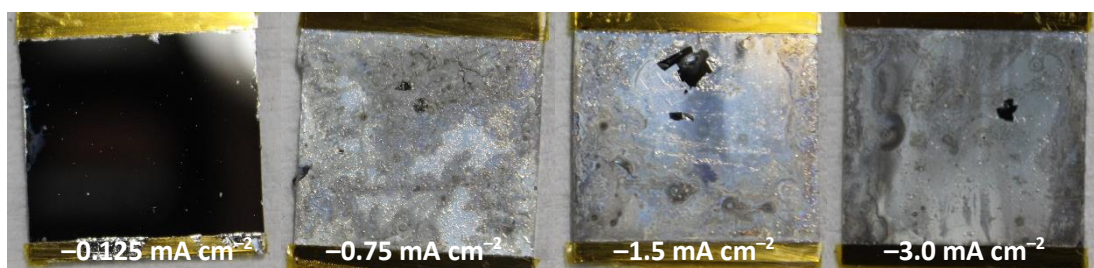


**Figure 4-23 - Zinc deposited onto tin from an alkaline non-cyanide electrolyte. Hydrogen damage was extensive on all samples, but particularly those deposited at current densities of a lower magnitude.**

-2.5 mA cm<sup>-2</sup> for 84 s. This did not yield a visible zinc deposit, with hydrogen evolution being clearly apparent during the attempted deposition process. The films deposited onto tin were so delicate that the decision was taken not to analyse them any further, and this electrolyte was deemed unsuitable for any further experimentation having produced no promising or satisfactory results.

#### 4.3.6.3 Car Restoration Acid-Chloride Electrolyte (Electrolyte Zn 5)

Trials were carried out in which zinc was deposited onto both copper films and tin films (copper-tin stacks and copper films on Mo-SLG were prepared as described in section 4.2.1). As this electrolyte contained a relatively high concentration of zinc (60 g L<sup>-1</sup> zinc chloride is equivalent to 0.44 M), current densities of up to 50 mA cm<sup>-2</sup> in magnitude were used. Zinc was deposited onto tin on six substrates using the settings given in Table 4-2, with the charge density passed in each deposition totalling 420 mC cm<sup>-2</sup>. Deposition at -25 mA cm<sup>-2</sup> was repeated (sample 3 and sample 4) as good results were returned in the first instance and there was the desire to attempt to reproduce them. The final deposition (sample 6) was the only one to utilise a two-step process in this set, with the high initial magnitude being used with the intention of rapidly nucleating many small grains across the tin surface, and the grain growth continuing at a lower current density thereafter with the expectation that it may return superior surface morphology.

**Table 4-2 - Deposition settings for zinc deposited on six different samples from an acid-chloride electrolyte designed for car restoration.**

Sample	Step 1		Step 2	
	Current Density (mA cm <sup>-2</sup> )	Time (s)	Current Density (mA cm <sup>-2</sup> )	Time (s)
1	-5.0	84.0	N/A	N/A
2	-12.5	32.8	N/A	N/A
3	-25.0	16.4	N/A	N/A
4	-25.0	16.4	N/A	N/A
5	-50.0	8.4	N/A	N/A
6	-50.0	2	-12.5	25.6

Photographs of the electrodeposits are presented in Figure 4-24 with two images of each sample taken with and without the use of a camera flash in order to bring different visual properties to prominence. The first feature that stands out, and which

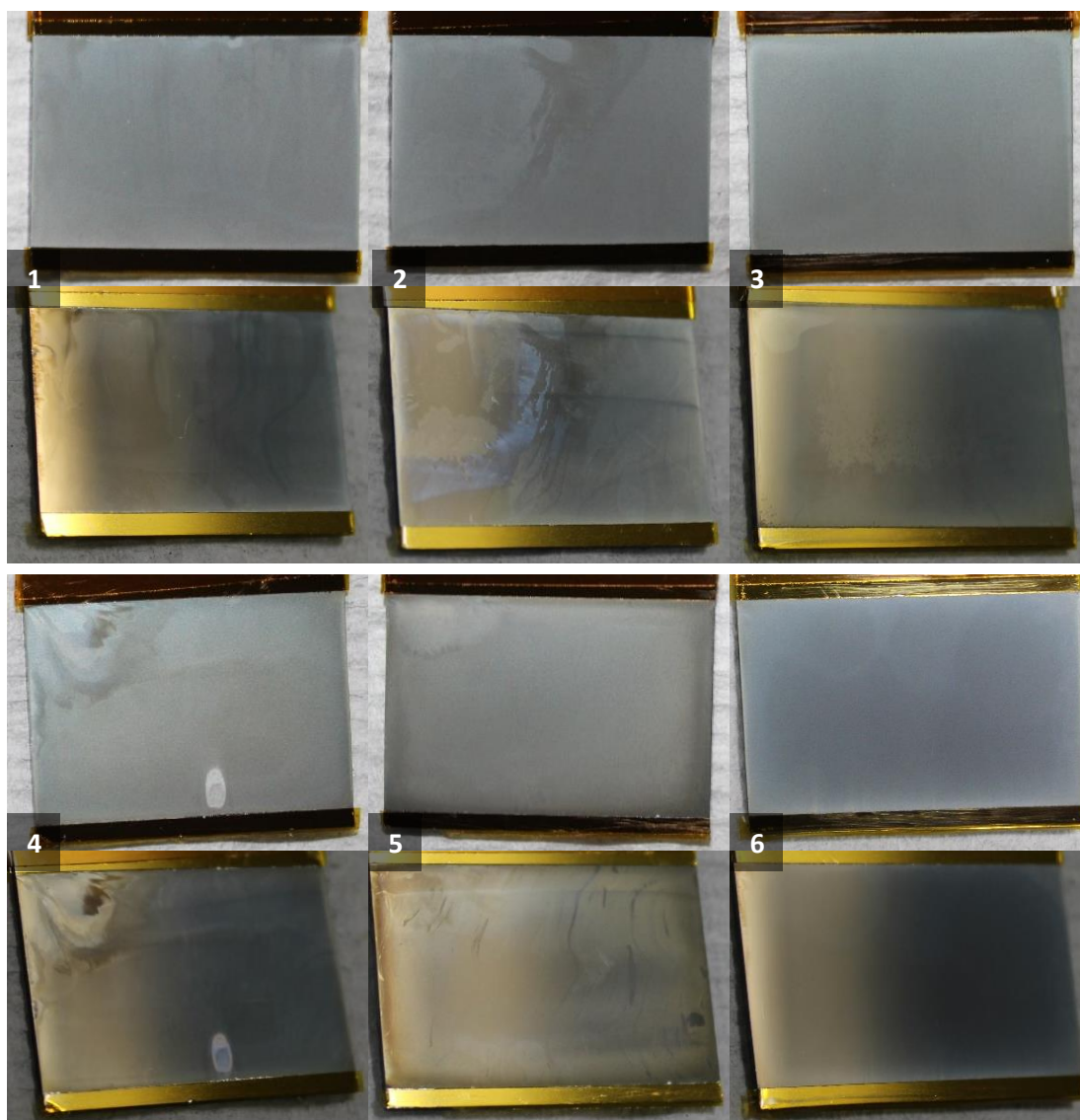


**Figure 4-24 - Zinc deposited onto tin using an acid-chloride electrolyte for car restoration. The films have been photographed with and without the use of a flash, and a particularly dark colour tone is apparent. The numbers 1 - 6 relate to the deposition settings given in Table 4-2.**

is common to all of the films, is that the colour tone is notably darker than that achieved with previous zinc electrolytes, which suggests that the grain structure may be dendritic. There was also no obvious evidence of hydrogen evolution during the deposition process. There does not appear to be any correlation between colour tone and current density, suggesting that the grain structure for all samples may be similar, however it will be necessary to examine SEM images of the films before coming to this conclusion. Despite this dark colour, the films appeared to present a greater level of specular reflectivity than those obtained using the previous zinc

electrolytes, however, there is visible inhomogeneity in the majority of the samples, particularly samples 1, 2 and 4. Furthermore, there does not appear to be any correlation between the degree of homogeneity achieved across the sample surface with the current density. This is emphasised by the fact that sample 4 returned a poor result in terms of apparent consistency across the substrate, despite being a duplicate of sample 3, which returned a more favourable result. The inhomogeneity observed on the samples may be due to surface contamination on the tin prior to the deposition of zinc. The samples each underwent the same cleaning procedure and variation in residue from previous treatment is not expected to be great. The variations in the degree of homogeneity may be indicative of a particularly high degree of sensitivity to the cleanliness of the deposition surface. Although every effort should, and was, taken to ensure a high degree of cleanliness, the necessity to operate in an ultra-clean environment would add expense and complication to the manufacturing process, and if this could be avoided by choosing a different electrolyte, then that would be considered favourable. The high level of sensitivity apparently exhibited by this electrolyte may be indicative of a particularly low throwing power, as small variations in the current density across the deposition surface may lead to localised variation in the deposition efficiency, exacerbating variations in the film thickness. The good results seen on samples 3 and 6 need to be consistently achievable and this was not possible with this electrolyte without the use of expensive clean room facilities.

Two attempts were made at depositing zinc onto copper using this electrolyte. These were carried out at a current density of  $-25 \text{ mA cm}^{-2}$  for 16.4 s and 50 s respectively, giving total charge passed densities of  $420 \text{ mC cm}^{-2}$  (sample 7) and  $1250 \text{ mC cm}^{-2}$

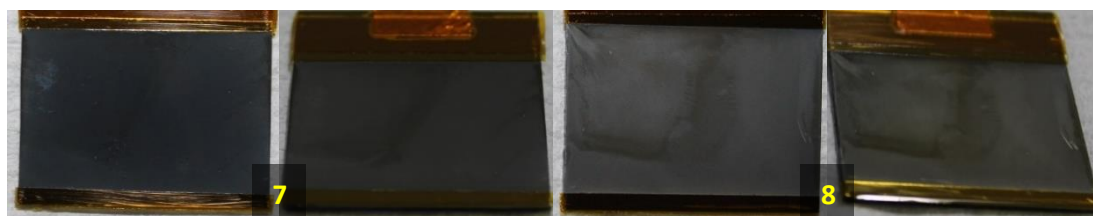


**Figure 4-25 - Zinc deposited onto tin using an acid-chloride electrolyte for car restoration. The charge passed during deposition for sample 7 was  $420 \text{ mC cm}^{-2}$  and for sample 8 it was  $1250 \text{ mC cm}^{-2}$ . The zinc films were yet darker in colour than those deposited onto tin from the same electrolyte.**



(sample 8). The larger charge passed density was chosen for the second deposit for two reasons. Firstly, as can be seen in Figure 4-25, the electrodeposits were particularly dark in colour tone, leading to a suspicion that the zinc electrodeposit was partially transparent, and that the copper surface beneath was absorbing some of the light. A thicker film was deposited to observe whether a different colour tone was obtained. Secondly, the thicker film was deposited to examine whether a more consistent and homogeneous film was obtained, the theory being that surface

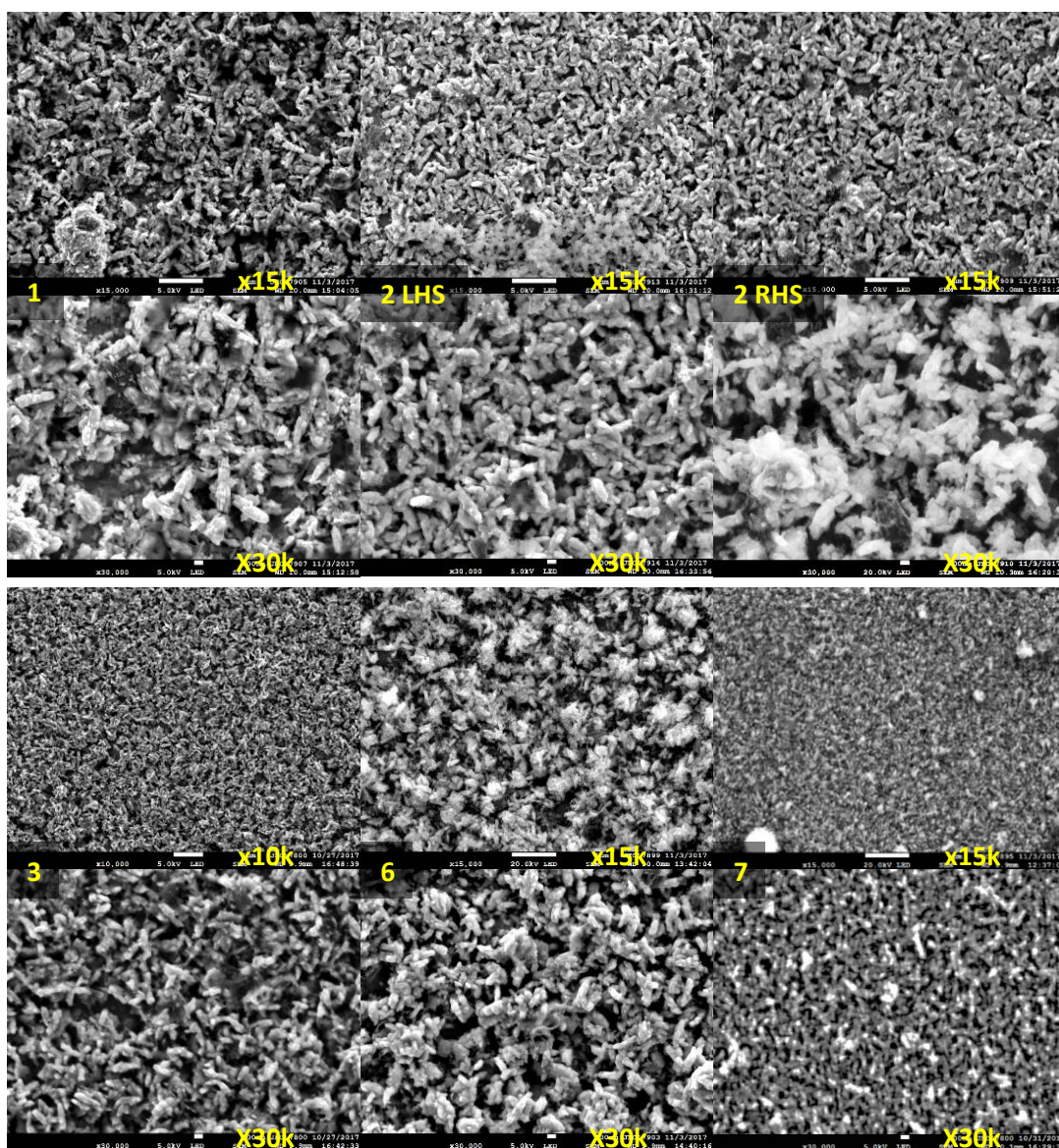


**Figure 4-26 - SEM images of zinc deposited onto tin (samples 1 - 6) and copper (sample 7) using an acid-chloride electrolyte for car restoration. The letters "LHS" and "RHS" refer to the left hand side and right hand side of sample 2 respectively. Higher and lower magnification images have 100 nm and 1  $\mu$ m scale bars respectively.**



imperfections could be “covered up” by a thicker layer, or conversely, localised differences in plating efficiency could become more apparent for a longer deposition time. Given the greater level of visual inhomogeneity presented by the thicker film in Figure 4-25, it appears that it may be more the latter than the former that is true.

SEM images were taken of the zinc deposits on samples 1 – 3, 6 and 7 using a JEOL FEG-SEM, and these images are presented in Figure 4-26. All of the electrodeposits exhibit a dendritic grain structure, with lower current densities leading to slightly longer dendrites than higher current densities. Dendrite formation was not an unexpected result as this is a common feature when using acid-chloride electrolytes [8]. The dendrite lengths range from approximately 1 – 2  $\mu\text{m}$  on sample 1 to approximately 0.2 – 0.4  $\mu\text{m}$  on sample 4. The dendrites are generally grouped together in roughly spherical clusters, and this feature is particularly prominent on sample 6, which was deposited using a two-step process. For sample 2, images were obtained on both the lighter coloured area on the left and the darker coloured area on the right, and it is possible to see that the dendrites in the darker area are grouped together in more tightly packed clusters that are less regular in their shape, and have larger spaces between them. For sample 7 where the zinc is deposited onto copper, the dendrites appear thinner and shorter, and are not grouped together in clusters like

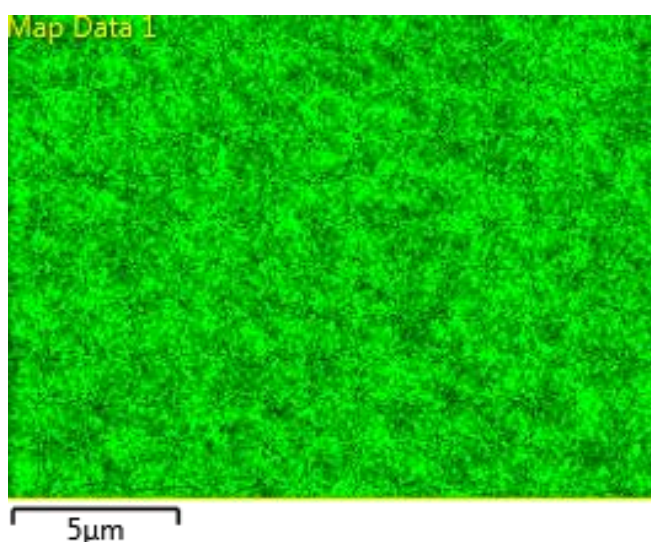


**Figure 4-27 - An EDS image of sample 6 in which zinc is coloured green. This indicates full coverage as there are no uncovered (black) spaces left on the image, despite the sharp focus (the dendritic grains can be seen under careful observation).**

those seen in films deposited onto tin. Overall coverage of the tin layer beneath appears to be good in all of the images with no obvious tin grains visible beneath the zinc, which is a promising result. For sample 6, this is confirmed in the coloured EDS image seen in Figure 4-27.

#### 4.3.6.4 Acid-Sulphate Electrolyte (Electrolyte Zn 6)

In the first set of experiments with this electrolyte, zinc was deposited onto tin on seven substrates with a  $1 \text{ cm}^2$  deposition area (copper-tin stacks were prepared as described in section 4.2.1). As the zinc concentration in this electrolyte was particularly high ( $300 \text{ g L}^{-1}$  zinc sulphate heptahydrate is the equivalent of  $1.04 \text{ M}$ ), current density magnitudes of up to  $50 \text{ mA cm}^{-2}$  were used in this set. The settings used in each deposition are stated in Table 4-3, five of which utilise a two-step process and two of which utilise a single-step process. The first six depositions were limited to a charged passed density of  $420 \text{ mC cm}^{-2}$  and the purpose of these was to ascertain the effect, if any, of the duration of the initial grain nucleation step, and whether there is a significant difference in the results obtained between depositions at high and low current density magnitudes. Sample 4 was effectively a duplicate of sample 3, as sample 3 was considered to have returned favourable results in the initial first visual inspection. A significantly greater charge passed density was chosen ( $2290 \text{ mC cm}^{-2}$ ) for the seventh deposition in order to examine whether a thicker film led to a greater level of homogeneity and improved consistency across the deposition area.

**Table 4-3 - Deposition settings for the first set of experiments utilising an acid-sulphate electrolyte to deposit zinc onto tin. A  $1 \text{ cm}^2$  deposition area was used.**

Sample	Step 1		Step 2	
	Current Density ( $\text{mA cm}^{-2}$ )	Time (s)	Current Density ( $\text{mA cm}^{-2}$ )	Time (s)
1	-50	0.2	-10	41
2	-50	0.4	-10	40
3	-50	1.0	-10	37
4	-50	1.0	-10	37
5	-10	420	N/A	N/A
6	-50	8.4	N/A	N/A
7	-50	25	-10	84

Photographs of samples 1 – 7 are presented in Figure 4-28, in which it is possible to see that there is a difference in the appearance of the deposited zinc between the centre and the edge of the film, to some extent, on all samples. When this set of experiments was first initiated, there was some speculation as to whether one current density may plate preferentially near to the substrate edges, and the other plating preferentially near the centre; and that a short high current density magnitude period at the start of the deposition might nucleate grains across the entire surface area, leading to improved coverage. However, there do not appear to be any trends relating to the current density. Sample 7, upon which the greatest quantity of zinc was deposited, returned the most consistent and homogeneous film. Although some difference in colour can be seen close to the edges of the deposition area, there is an area of approximately  $8.5 \times 8.5 \text{ mm}^2$  in which the film appears consistent and homogeneous. Some contrast can be drawn here with the acid-chloride electrolyte for car restoration, for which a thicker deposit did not improve the film homogeneity. In general, the homogeneity of the acid-sulphate electrolyte appears better – the most visible variation is between the centre and the edges of the deposition areas rather than across the substrates in general. One favourable observation that was made while using both electrolytes was that no hydrogen evolution was visible during

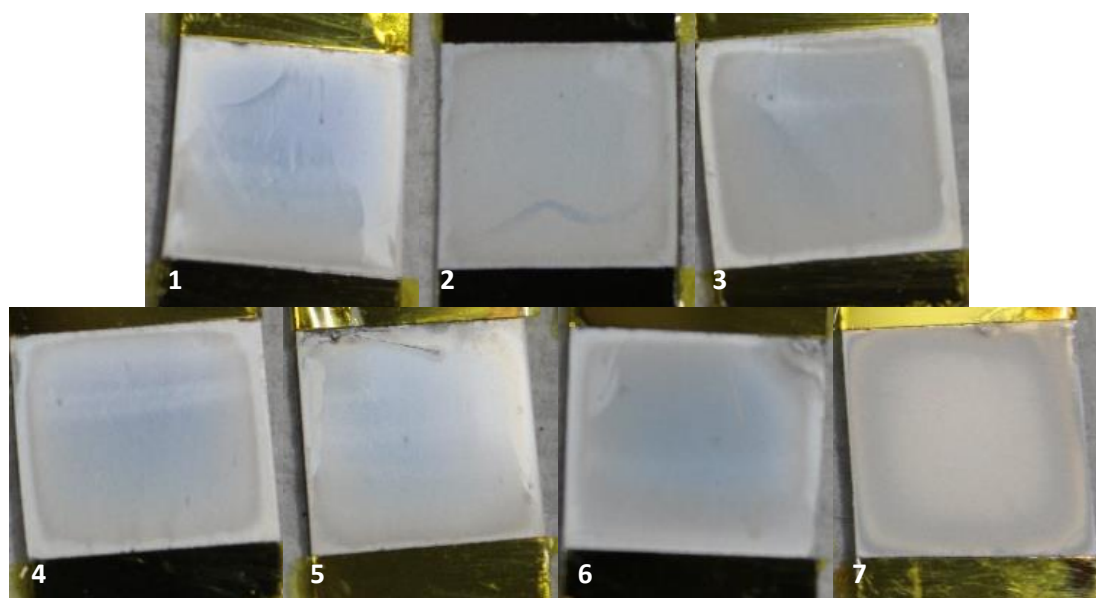


**Figure 4-28 - Zinc deposited onto tin using an acid-sulphate electrolyte. The sample numbers relate to the conditions given in Table 4-3. None of the samples experienced hydrogen damage, although there are differences in the appearance of the films between the centres and edges.**

deposition and no evidence of hydrogen damage is visible on the zinc deposits. The reflectivity of the zinc films deposited using the acid-sulphate electrolyte was less specular, which, considering that dextrin had been included in the composition as a levelling agent, was contrary to expectations. To study the grain structure of the electrodeposits, samples 3 and 7 were examined using SEM.

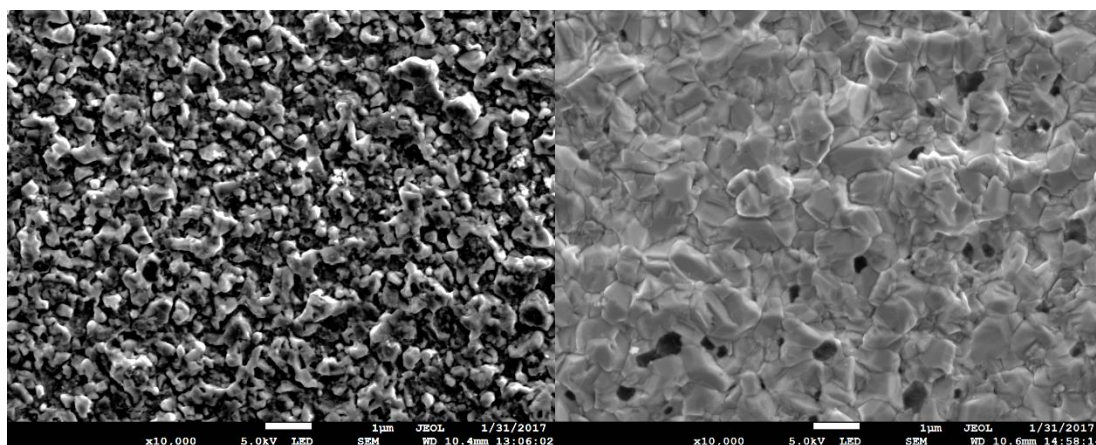


**Figure 4-29 – 10,000x magnification SEM images of zinc deposited on sample 3 (left) and sample 7 (right). It can be seen that both electrodeposits are non-dendritic, and the thicker film on sample 7 exhibits a compact granular structure.**

Images of samples 3 and 7 were taken using a JEOL FEG-SEM and are presented in Figure 4-29. Referring first to sample 3, it appears that the zinc had deposited discontinuously in relatively large irregularly shaped non-dendritic grains, generally approximately 1  $\mu\text{m}$  across, and does not give full coverage of the underlying tin. This would give some explanation as to why the colour of the underlying tin could be seen on some samples when inspected visually. It could also give some explanation for the relatively diffuse reflectivity. Referring to the SEM image of sample 7, it is possible to see that the deposited zinc grains have formed a compact granular structure giving near complete coverage of the underlying tin. The grain diameters are similar to those seen on sample 3 ( $\sim 1 \mu\text{m}$ ), suggesting that as the deposition time is extended, new grains are nucleated across the tin film rather than existing grains growing. This could be considered a favourable result as this leads to greater homogeneity and more complete coverage on a microscopic scale. In order to gain greater clarity on the characteristics of the deposit on sample 3, it was also analysed

using EDS, a colour map of which can be seen in Figure 4-30. The green coloured areas indicating zinc deposits confirm that the thinner deposit is comprised of grains deposited in islands, however these islands are more dispersed with smaller spacing ( $\sim 1\ \mu\text{m}$ ) between them than some of the previous metallic electrodeposits seen in this project, particularly the unfavourable deposits of tin on to copper that are presented in Figure 3-32 and Figure 3-26. The microscopic coverage obtained using this electrolyte is estimated to be approximately 50% on sample 3, and may be sufficient such that it is suitable for use in the manufacture of CZTS solar cells, particularly if a pre-alloy/soft annealing step is included prior to sulphurisation.

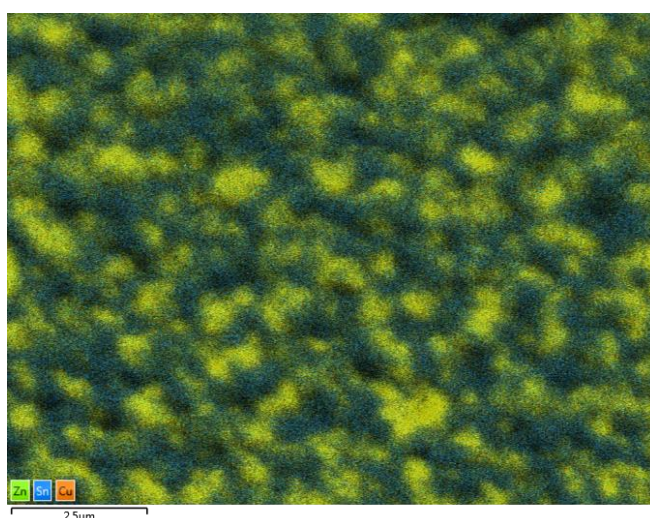


**Figure 4-30 - An EDS colour map of sample 3 in which zinc grains (green) of approximately  $1\ \mu\text{m}$  in width are seen deposited onto a tin (blue) background, with an estimated coverage of approximately 50%.**

Given the improved homogeneity and coverage seen when depositing thicker films using this electrolyte, the decision was taken to trial a set of electrodeposits on  $4\ \text{cm}^2$  substrates using relatively high deposition current magnitudes ( $30 - 70\ \text{mA cm}^{-2}$ ) and a fixed single-step deposition time of 25 s for five of the six samples. One sample (sample 8) was deposited using the same two-step current density settings as sample 7 in Table 4-3. This was in order to attempt to reproduce the favourable result seen on sample 7 (a  $1\ \text{cm}^2$  substrate) on a larger  $4\ \text{cm}^2$  substrate, and to compare this two-step processed film with other relatively thick films deposited with a single-step process, and ascertain whether a two-step process was beneficial.



**Table 4-4 - Deposition settings for the second set of experiments utilising an acid-sulphate electrolyte to deposit zinc onto tin. A 4 cm<sup>2</sup> deposition area was used.**

Sample	Step 1		Step 2	
	Current Density (mA cm <sup>-2</sup> )	Time (s)	Current Density (mA cm <sup>-2</sup> )	Time (s)
8	-50	25	-10	84
9	-30	25	N/A	N/A
10	-40	25	N/A	N/A
11	-50	25	N/A	N/A
12	-60	25	N/A	N/A
13	-70	25	N/A	N/A

Six 4 cm<sup>2</sup> copper-tin stacks on Mo-SLG were prepared as described in section 4.2.1. Zinc was deposited onto each sample using the settings given in Table 4-4. All samples underwent visual inspection and samples 8 – 10 and sample 13 were photographed and can be seen in Figure 4-31. Unfortunately, there had been some temporary unavailability of the FEG-SEM and the images in Figure 4-29 and Figure 4-30 had to be obtained retrospectively. Samples 11 and 12 were not included in the photographs as they were selected to be used in sulphurisation trials which took place prior to the photography. Observing firstly samples 9 and 10, there is some inhomogeneity visible on both films by means of horizontal bands in which there is

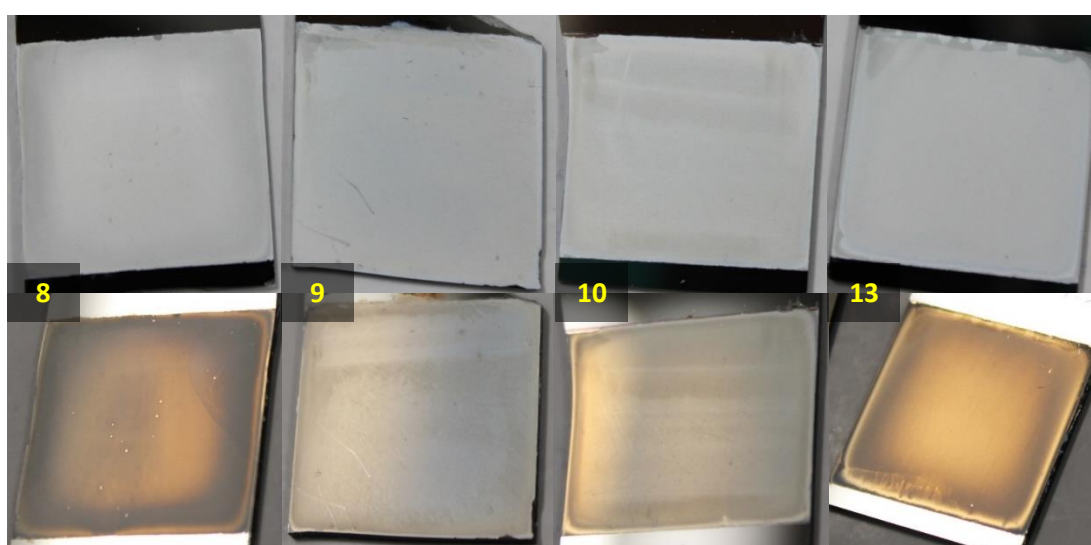


**Figure 4-31 - Zinc deposited onto tin from an acid-sulphate electrolyte using a range of current densities. Samples 9 - 13 each used a single-step process of 25 s.**

some variation in the colour tone. This may have resulted from imperfections in the underlying tin, which only became visible once the zinc was deposited, but could also be indicative of localised variations in the morphology. These two samples exhibited less of the coloured ring effect that can be seen around the film edges particularly on sample 8, but to some extent on sample 13. Both sample 8 and sample 13 display some evidence of hydrogen evolution in the form of small pits (estimated less than  $\sim 0.4$  mm across) in the film. There are approximately twenty of these across the surface of sample 8 and approximately five on sample 13. Some hydrogen evolution was observed during the deposition on sample 13, most likely due to the relatively negative potential required to drive such a high current density magnitude, however this phenomenon was not recorded in the laboratory note book entry for sample 8. The pitting seen on sample 8 may have been caused by slow and gradual evolution of hydrogen occurring over the relatively prolonged deposition process, which may have been less obvious when carrying out the experiment. From observing the laboratory note book entries for samples 11 and 12, these returned zinc deposits that were considered superior as the coloured ring effect around the film edges was less prominent than on samples 8 and 13, yet no other inhomogeneity was observed in these zinc films, with the exception of a very slight variation in colour in a band across sample 11 that was recorded as being as a result of a variation observed in the original copper deposit. For these reasons, a single-step deposition process with a current density of  $-50 \text{ mA cm}^{-2}$  was adopted for depositing zinc onto tin when using this electrolyte in future experiments.

At this point in the experiments, an optimum deposition time had not been established due to questions that remained about the deposition efficiency, which will be discussed in section 4.3.7. For the sake of information completeness, photographs were taken of a zinc deposition carried out for 25 s and a zinc deposition carried out for 8.4 s, each on a  $4 \text{ cm}^2$  substrate at  $-50 \text{ mA cm}^{-2}$  giving charge passed densities of  $1250 \text{ mC cm}^{-2}$  and  $420 \text{ mC cm}^{-2}$  respectively, and are presented in Figure 4-32. These samples had been prepared as part of a different set of experiments for sulphurisation in a furnace. It is possible to see, in common with previous results, that both samples exhibit a “ring effect”, where there is a slightly different colour tone in the zinc deposit near the edges of the sample, and that there is still a slightly

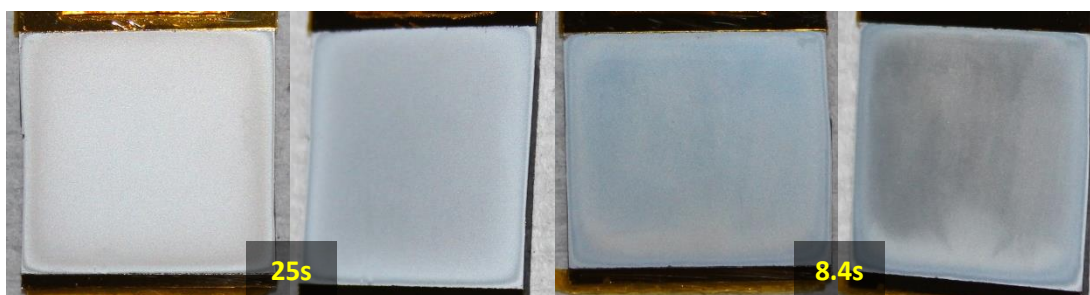


**Figure 4-32 - Zinc deposited onto tin from an acid-sulphate electrolyte at  $-50 \text{ mA cm}^{-2}$  for 25 s (left) and 8.4 s (right) onto  $4 \text{ cm}^2$  substrates. Both films exhibit relatively high levels of homogeneity.**

blue shade of grey visible on the sample with a shorter deposition time. The film deposited for 25 s appears to have given full coverage of the tin, and both films exhibit a standard of visual homogeneity that was considered acceptable for use in further processing in the manufacture of CZTS films. No hydrogen evolution was evident in either deposition.

Trials were also carried out to deposit zinc onto copper using the acid-sulphate electrolyte on  $4 \text{ cm}^2$  deposition areas. Copper-tin-copper stacks were deposited onto Mo-SLG as described in section 4.2.1. Zinc was deposited using a current density of  $-50 \text{ mA cm}^{-2}$  as this proved effective during the trials depositing onto tin. Two deposition times were used – these were 8.4 s and 25 s, in common with those for films deposited onto tin for sulphurisation. Two samples deposited using each deposition time are presented in Figure 4-33. Those deposited for 8.4 s have a very similar appearance to tin deposited onto copper from a methanesulfonic acid electrolyte, and exhibit relatively specular reflectivity, suggesting that these films are smoother than those deposited directly onto tin. Although some inhomogeneity is

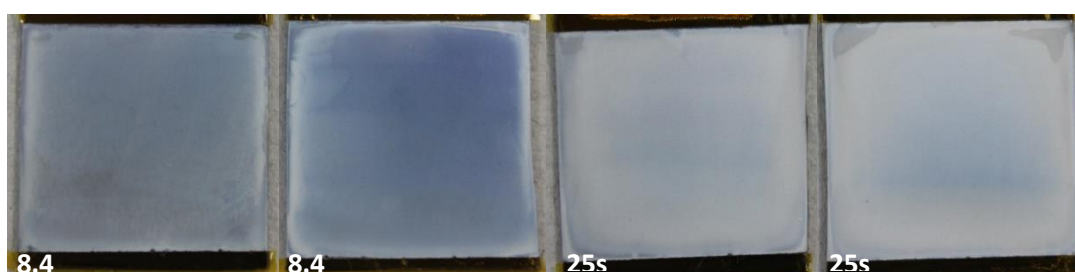


**Figure 4-33 - Zinc deposited onto copper from an acid-sulphate electrolyte at  $-50 \text{ mA cm}^{-2}$  for 8.4 s on two substrates (left), and 25 s on a further two substrates (right). Deposition areas of  $4 \text{ cm}^2$  were used.**



visible, it is mostly near to the edges of the deposit. There is no hint of the colour of copper, suggesting that full coverage of the underlying copper film had been achieved. Samples deposited for 25 s are less specular in their reflectivity, and also exhibit a slightly different colour tone near the edges when compared to the centres of the deposits. Again, this is indicative of some inhomogeneity, however, the films were considered to be of an acceptable standard for use in sulphurisation experiments, particularly when the lack of hydrogen evolution is also taken into account.

One of the zinc films deposited onto copper for 25 s was analysed further using SEM, and images were obtained at 10,000x and 25,000x magnification. These images are presented in Figure 4-34. Studying the 10,000x magnification image, it appears that the zinc deposit formed a relatively compact layer with full coverage of the underlying copper. The surface appears to have some irregular undulations, without any clear grain boundaries. When the 25,000x magnification image is observed, some grain boundaries become apparent. The grains are irregularly shaped, and approximately 0.3 – 0.5  $\mu\text{m}$  across. This is in contrast to those seen on the right of Figure 4-29 in an image of zinc deposited onto tin under the same conditions, in which the grains are larger ( $\sim 1\ \mu\text{m}$ ) and have clearer boundaries. Additionally, there are very small (less than 100 nm wide) features that are visible on the zinc deposited

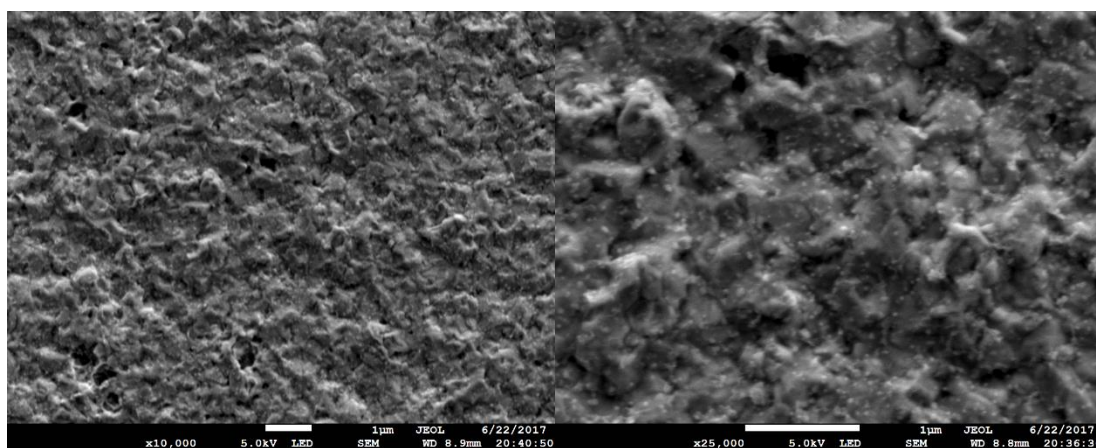


**Figure 4-34 - SEM images at 10,000x magnification (left) and 25,000x magnification (right) of zinc deposited for 25 s onto copper from an acid-sulphate electrolyte at  $-50\ \text{mA cm}^{-2}$ . Grains are smaller with less distinct boundaries when compared to those of zinc deposited onto tin under the same conditions.**

onto copper, approximately five on each grain, that are not seen on other deposits, although the cause and identity of these features remains unknown. In order to gain more information on the surface topology, zinc films deposited for 25 s at  $-50 \text{ mA cm}^{-2}$  onto copper and tin were examined using profilometry.

Profilometry scans were carried out as described in section 4.2.2.1 and the resulting graphs are presented in Figure 4-35. Simply by observing these graphs, it is possible to see that the zinc deposited onto tin is substantially rougher than that deposited onto copper. This is confirmed by the  $R_a$  surface roughness values, which were recorded as 185.8 nm and 37.9 nm for zinc deposited onto tin and copper respectively. This corroborates with the more diffuse reflectivity observed for zinc deposited onto tin and also the finer grain structure observed in SEM images of zinc deposited onto copper. This result was expected in accordance with the theory stated previously in section 3.3.6, that the deposition of zinc onto copper is aided by the favourable formation of a copper-zinc alloy in the initial stage of deposition, which encourages the rapid formation of a thin zinc film giving complete coverage of the copper film [2]. This would require the formation of many smaller grains rather than fewer larger grains in the early stages of deposition, which in turn could lead to a finer grain structure and smoother surface.

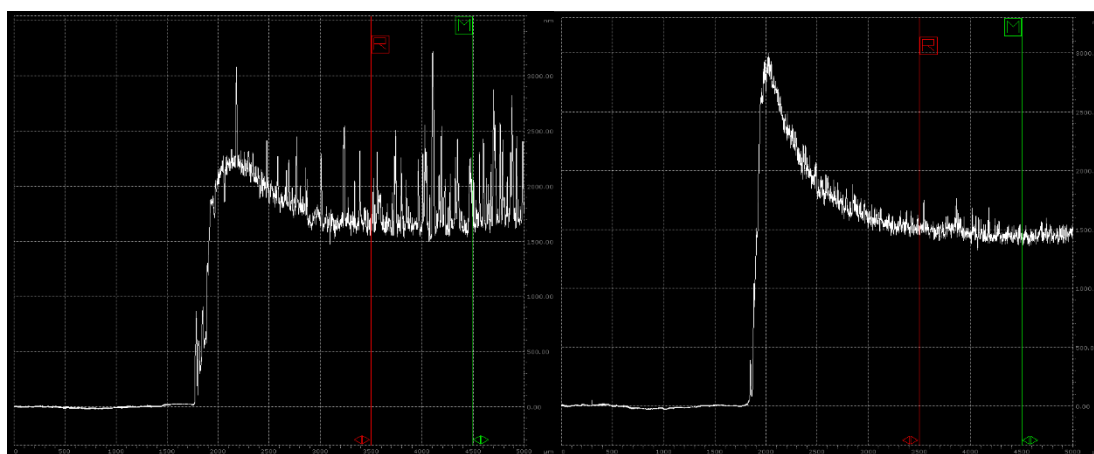


**Figure 4-35 - Surface profiles of zinc deposited onto tin (left) and onto copper (right) under the same conditions. Each grid square represents  $500 \times 500 \mu\text{m}^2$ , and it is apparent that the zinc deposited onto tin is rougher than that deposited onto copper.**

At this point in the experimentation, this electrolyte was considered potentially suitable for use in electroplating zinc on samples for further processing into CZTS. It was demonstrated that it can produce films that are relatively homogeneous and can give full coverage of the underlying tin with a compact grain structure for sufficiently thick films. However, it was considered potentially beneficial to continue the experimentation with other electrolytes, with the hope that further improvements could be made. In addition to this, the efficiency of this electrolyte remained unconfirmed, and some concerns remained regarding the consistency of the thickness, given the “ring effect” that was observed around the edges of the deposits. These two factors will be discussed in section 4.3.7.

#### 4.3.6.5 Citrate-Based Electrolyte (Electrolyte Zn 7)

Zinc was deposited onto tin on five samples, each with a deposition area of  $1\text{ cm}^2$ , as well as onto copper on two samples with a deposition area of  $4\text{ cm}^2$  (copper-tin stacks and copper films on Mo-SLG were prepared as described in section 4.2.1). This electrolyte contained only a relatively low concentration of zinc (30 mM zinc sulphate), therefore the greatest current density magnitude tested was  $5\text{ mA cm}^{-2}$  during a grain nucleation step and  $1\text{ mA cm}^{-2}$  during a main deposition step. This was in attempt to avoid the deposition potential becoming sufficiently negative to cause hydrogen evolution.

Zinc was deposited onto tin on five substrates using the settings given in Table 4-5, with the charge density passed in each deposition totalling  $420\text{ mC cm}^{-2}$ . The first deposition was the only one to utilise a two-step process, with the higher initial

**Table 4-5 - Deposition settings for zinc deposited on five different samples from a citrate-based electrolyte designed for codeposition in the manufacture of CZTS.**

Sample	Step 1		Step 2	
	Current Density ( $\text{mA cm}^{-2}$ )	Time (s)	Current Density ( $\text{mA cm}^{-2}$ )	Time (s)
1	-5.0	5	-1.0	395
2	-1.0	420	N/A	N/A
3	-0.75	560	N/A	N/A
4	-0.5	840	N/A	N/A
5	-0.25	1680	N/A	N/A

current being chosen to encourage rapid grain nucleation, however, hydrogen evolution was of such a severity that the film partially delaminated during the drying process (a nitrogen jet was used for drying in this set of experiments). Partial film delamination also occurred, to a lesser extent, on sample 2. This can be seen in Figure 4-36, as can the other samples referred to in Table 4-5. The films obtained were relatively pale in colour when compared to those deposited from other zinc electrolytes, particularly the acid-chloride electrolyte for car restoration (Electrolyte Zn 5). They were also relatively diffusely reflective, similar to that of films deposited from the acid-sulphate electrolyte (Electrolyte Zn 6), and visual inspection suggested that there was acceptable coverage of the tin beneath on a macroscopic scale (the slightly more blue shade of grey exhibited by tin was not visible). These observations could be considered favourable, however, some unfavourable observations were also made – hydrogen evolution occurred during every deposition. Rather than the more rapid “fizzing” of small bubbles observed in some previous cases, this was a slow and gradual process in which larger bubbles formed. Rather than the pitting observed with some previous electrolytes, blisters of up to approximately 1.5 mm appeared to form beneath the films. All of the films suffered from some degree of blistering, the most severe being sample 1, which suffered subsequent partial delamination as commented on previously. Of the intact films, blistering is most clearly visible on sample 3. Due to this blistering, the decision was taken that this electrolyte would not be suitable for the deposition of zinc onto tin going forward.

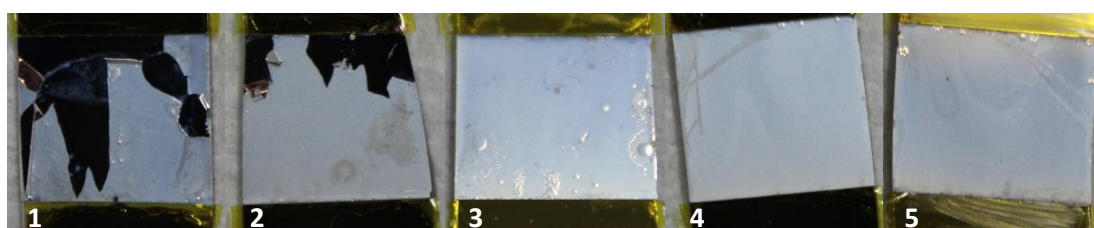


**Figure 4-36 - Zinc deposited onto tin using a citrate-based electrolyte. The sample numbers relate to the conditions given in Table 4-5. All samples suffered some degree of blistering due to hydrogen evolution, although this was more severe when higher current densities were used.**

Zinc was deposited onto copper on two 4 cm<sup>2</sup> substrates, firstly, one with a single-step process and secondly, one with a two-step process. The single-step process used a current density of -1 mA cm<sup>-2</sup> for 420 s (sample 6); the two-step process used a

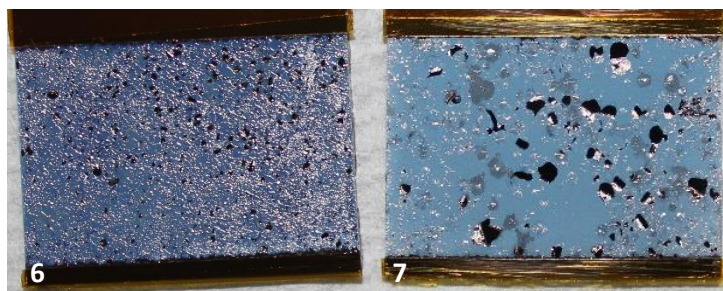


**Figure 4-37 - Zinc deposited onto copper from a citrate-based electrolyte using a single-step process (left) and a two-step process (right). A significant amount of damage occurred due to hydrogen evolution on both samples.**

current density of  $-1 \text{ mA cm}^{-2}$  for 40 s for step 1 and  $-0.25 \text{ mA cm}^{-2}$  for 1520 s for step 2 (sample 7). The decision to select the settings used in the two-step process was based on the results of the first – hydrogen evolution was slow but significant and caused the formation of many small blisters, each of which were up to approximately 1mm in diameter, with the number density being estimated to be in the order of hundreds per square centimetre. These blisters can be seen in the image presented in Figure 4-37. As the hydrogen bubbles were relatively slow to form, the first step in the two-step process was selected as 40 s, the intention being that this would be sufficient time for zinc grains to nucleate across the copper surface with the relatively modest current density of  $-1 \text{ mA cm}^{-2}$  without hydrogen damage occurring. The second step was selected to have a low current density of just  $-0.25 \text{ mA cm}^{-2}$  in order to minimise the amount of hydrogen evolved. As can be seen from the right hand side of Figure 4-37, hydrogen damage did occur and although the blisters were fewer in number (up to approximately 100 per square centimetre), they were larger in diameter (up to approximately 2 mm). Visual observations also revealed that these films exhibited a greater level of specular reflectivity than those deposited onto tin. Due to the amount of hydrogen damage observed, this electrolyte was deemed unsuitable for the deposition of zinc onto both copper and tin.

#### **4.3.6.6 Summary**

As mentioned previously, the alkaline non-cyanide electrolyte (Electrolyte Zn 4) did not yield any useful results, therefore it was deemed unsuitable for further experimentation. This left the citrate-based electrolyte (Electrolyte Zn 7), the acid-sulphate electrolyte (Electrolyte Zn 6) and the car restoration acid-chloride electrolyte (Electrolyte Zn 5) for consideration. The extent of hydrogen evolution

when depositing from the citrate-based electrolyte made it also unsuitable due to the presence of blistering even at the lowest current density ( $-0.25 \text{ mA cm}^{-3}$ ). This occurred when depositing onto both tin and copper. The citrate-based electrolyte was therefore also deemed unsuitable for further experimentation. When comparing the acid-chloride electrolyte to the acid-sulphate electrolyte, the acid-chloride electrolyte appears to lead to superior microscopic coverage of tin films (see Figure 4-26, Figure 4-27, Figure 4-29 and Figure 4-30). Despite this, concerns about the macroscopic film homogeneity remained as it appeared inconsistent on numerous samples (see Figure 4-24 and Figure 4-25). In addition to this, the effects of using a dendritic film in the sulphurisation stage of the processing were unknown. Conversely, the acid-sulphate electrolyte delivered improved macroscopic homogeneity, and some reassurance was felt on finding that both the microscopic coverage and macroscopic homogeneity improved with thicker films, an effect not seen on the homogeneity when using the acid-chloride electrolyte. Some concerns remained about thickness variation near the edge of films deposited using the acid-sulphate electrolyte due to the “ring effect” observed, and this will be addressed in section 4.3.7. When depositing onto copper, the acid-sulphate electrolyte was considered advantageous as the macroscopic homogeneity was superior (see Figure 4-25 and Figure 4-33) and the microscopic coverage was also good (see Figure 4-34), although only a relatively thick film was examined using an SEM.

As commented on previously, the macroscopic inhomogeneity witnessed on films deposited from the acid-chloride electrolyte may be symptomatic of a lack of throwing power. The “ring effect” seen when using the acid-sulphate electrolyte may also be attributed to limitations of the throwing power, however, the symptoms observed appear to differ between the two electrolytes. The answer to this may lie in the purposes for which the electrolytes were designed – the acid-sulphate electrolyte was formulated for depositing onto large sheets of steel, therefore the unwanted variations are seen towards the extremities of the sample, where a flat sheet ceases to be a sheet. This may be related to variations in the strength of the electric field in these regions – as a potential is applied by the potentiostat, this generates an electric field at the surface of the working electrode which attracts ions in the electrolytic solution. The electric field lines are roughly parallel near the centre of a flat plate, but

will curve outwards at the edges as the field is weaker there [16]. The acid-chloride electrolyte on the other hand, appears to suffer from unwanted variations across the general deposition area, where the substrate is effectively a flat sheet. This electrolyte was designed for electroplating onto three-dimensional car parts, and may be more sensitive to the microscopic properties of the substrate surface rather than macroscopic variations in the substrate shape. It could be speculated that the fine dendritic grain structures seen in films deposited using the acid-chloride electrolyte are more inclined to “amplify” the effects of imperfections of the underlying surface as they grow, whereas the larger more compact grains produced by the acid-sulphate electrolyte are more inclined to cover them. For experimentation going forward, the decision was taken that the acid-sulphate electrolyte would be used due to the superior reproducibility observed, and the belief that it could produce more reliable results while still maintaining an acceptable level of coverage on a microscopic scale.

#### **4.3.7 Final Word on Deposition Efficiency**

##### ***4.3.7.1 Further XPS Depth Profiling Experiments***

As commented on previously, the chosen (acid-sulphate) zinc electrolyte led to films that exhibited a “ring effect”, where the appearance of the film near the edges of the sample had some differences when compared to that of the centre. This led to the suspicion that there was a difference in film thickness between the centre and the regions near the edge, in addition to the normal castellation where the very edges exhibit a spike in height (as can be seen in the profilometry graphs in Figure 4-35). In order to study this, three XPS depth profiles were carried out on the same sample on three different positions – that was in the very centre, approximately 3mm from the

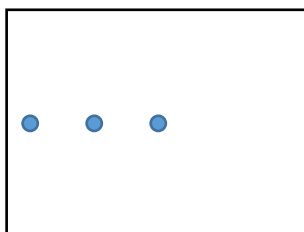


**Figure 4-38 - Three dots indicating the relative positions on which XPS depth profiling was performed on a single copper-tin-zinc stack. Please note that this diagram is not to scale.**

left hand edge (half way between the top and the bottom), and half way between the two aforementioned points. A diagram has been included in Figure 4-38 in order to provide a visual representation of this. The sample had been deposited with  $572 \text{ mC cm}^{-2}$  copper,  $312 \text{ mC cm}^{-2}$  tin and  $1250 \text{ mC cm}^{-2}$  zinc respectively, and XPS depth profiling was performed as described in section 4.2.2.2, although elemental abundance measurements were only taken every 600 s on the edge and mid-point profiles, as opposed to every 300 s on the centre profile. This decision was taken by the XPS operator, not the author of this thesis. The precise reasoning was not communicated, however, it was expressed that the duration of the depth profiling exceeded the expected time frame and it was therefore assumed that the sampling frequency was reduced in order to minimise the disruption to the equipment bookings timetable. The total etching time for these profiles was set to 12,000 s to give sufficient time to etch through all of the electrodeposited films.

The resulting XPS depth profile graphs are presented in Figure 4-39. The graphs having been cropped to 10,000 s as all features of interest occur prior to this time. Unfortunately, the depth profile on the centre position was terminated early, the exact cause of this being unknown, however there is still sufficient data to draw comparisons between the graphs. When these graphs are compared to each other, aside from the incomplete profile of the centre position, there appears to be little difference between the profiles. Although this does not give any indication of the cause of the “ring effect”, it does suggest that the thickness distribution of the film is consistent, which can be considered to be a favourable result. It is worth noting that, in common with previous XPS depth profiles seen in Figure 4-18, the impression is given that tin is sited on top of zinc, despite the substantially thicker zinc film and the expectation of full coverage (as seen in the SEM image in Figure 4-29).

In addition to producing depth profile graphs, total atomic abundancies of each electrodeposited element were calculated using the depth profile data for the mid-point. These calculations were performed by integrating the total electron signal counts for each element with respect to time for the duration of the etching, using a spreadsheet (as discussed previously in section 4.3.4). The results are presented in the form of a bar chart in Figure 4-40, alongside the expected abundancies based on the charge passed during the deposition process (assuming a 100% deposition



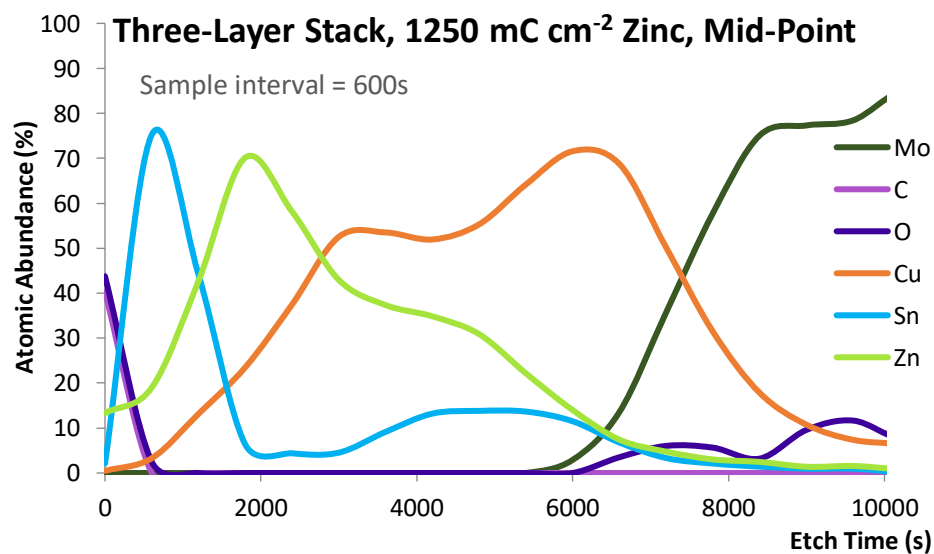
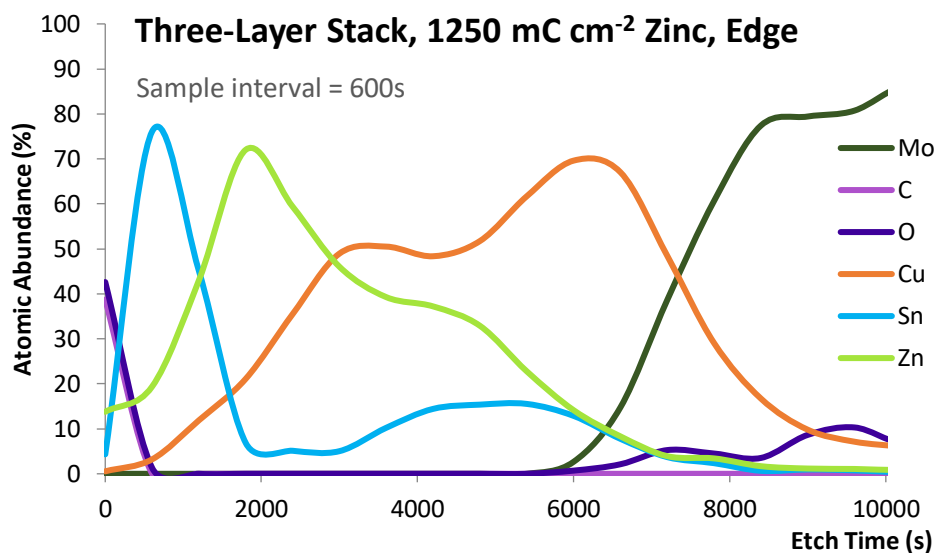
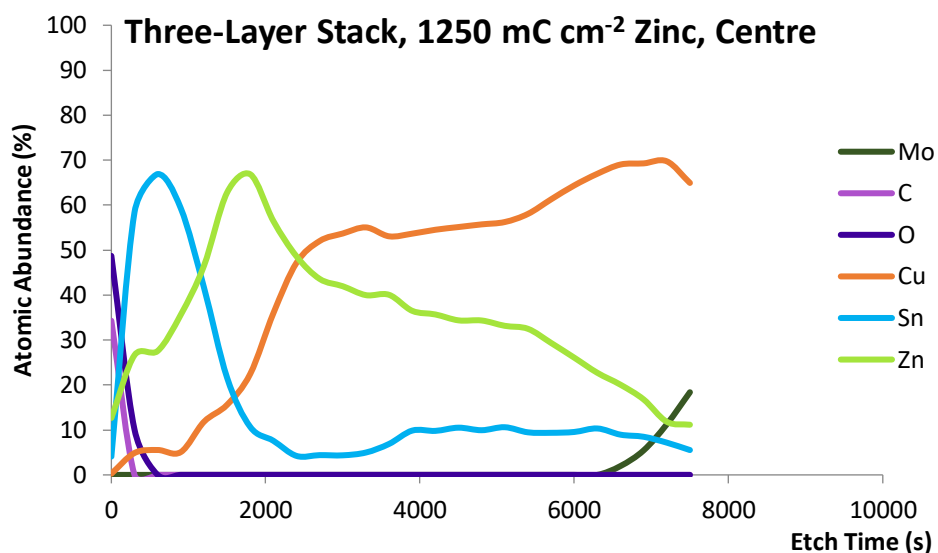


**Figure 4-39 - XPS depth profiles on three different positions on the same sample. The three graphs display little variation between the profiles of each position.**

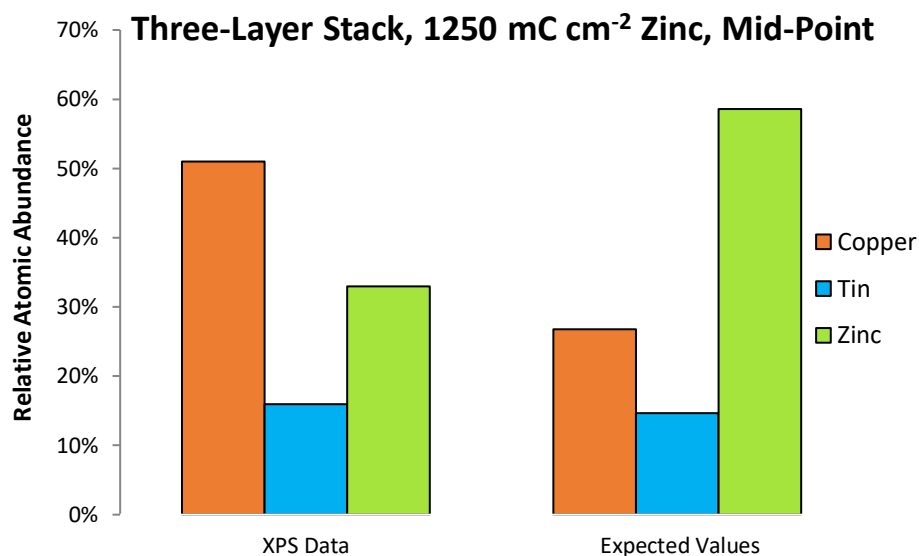


**Figure 4-40 - The total relative abundances calculated by integrating the signal for each element with respect to time for the full duration of the depth profile. This graph relates to a depth profile carried out on the sample with a thicker zinc deposit.**

efficiency). For comparative purposes, a depth profile was carried out on the centre of a sample that had been deposited with 420 mC cm<sup>-2</sup> zinc from the acid-sulphate electrolyte (other parameters remaining the same), and the total atomic abundances were calculated also. An etch time of 10,500 s was found to be sufficient in this instance owing to the thinner layer of deposited zinc. The profile can be seen in

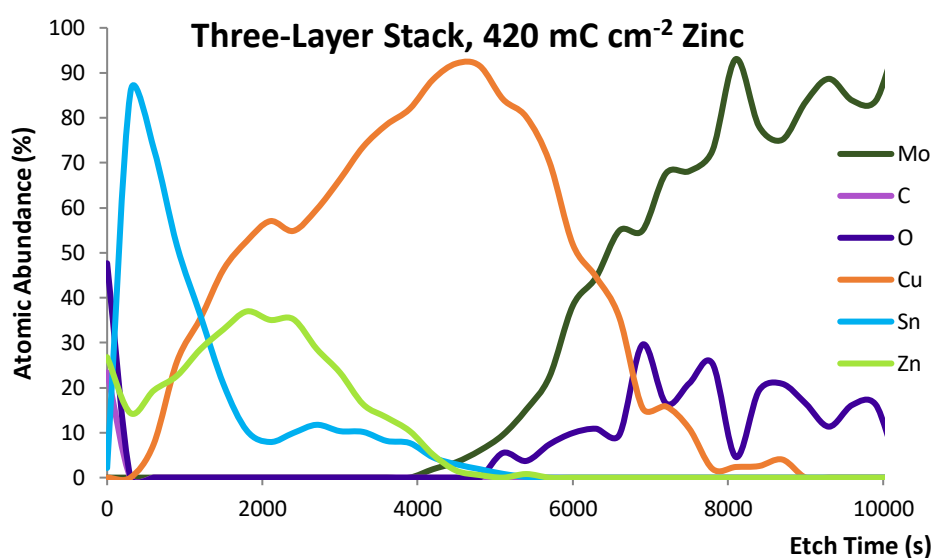


**Figure 4-41 - An XPS depth profile on a sample with a thinner zinc deposit.**

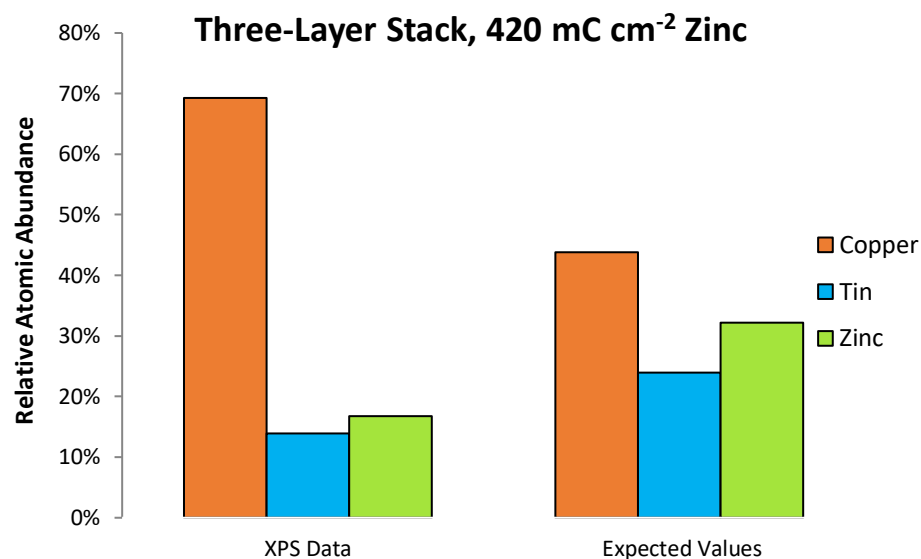


**Figure 4-42 - Total relative abundancies for a sample with a thinner zinc deposit. In contrast to the sample with the thicker zinc deposit, the abundance of tin was indicated as being lower than expected.**

Figure 4-41 and the atomic abundancies can be seen in Figure 4-42. Comparing firstly the depth profiles, the profile for the sample with the thinner zinc deposit again has a peak in tin abundance prior to that of zinc. The peak in zinc abundance is less strong than those seen for the thicker zinc deposits, and it fades more rapidly, which would be expected for a thinner film. What was not expected, however, is the more rapid fading of the tin abundance, and also the reduced overall tin abundance seen when Figure 4-42 is compared to Figure 4-40. The molybdenum layer is encountered sooner on the sample with the thinner zinc deposit, which was expected, as a thinner zinc deposit causes the thickness of the overall stack to be reduced. Observing the elemental abundance bar chart for the sample with the thicker zinc deposit, it can be seen that it has features in common with the previous XPS depth profiles (Figure 4-20, section 4.3.4) in that the abundance of copper is substantially greater than expected, the abundance of zinc is substantially less than expected, and the tin abundance returned is similar to the expected value. These phenomena are also observed for the copper and the zinc on the thinner zinc sample, but not the tin, which appeared to be less abundant than expected. In an attempt to gain further clarity, plots of the signal intensity against time for the three deposited elements were generated for both the sample with a thinner zinc deposit and the mid-point of the sample with a thicker zinc deposit. These graph plots are presented in Figure 4-43

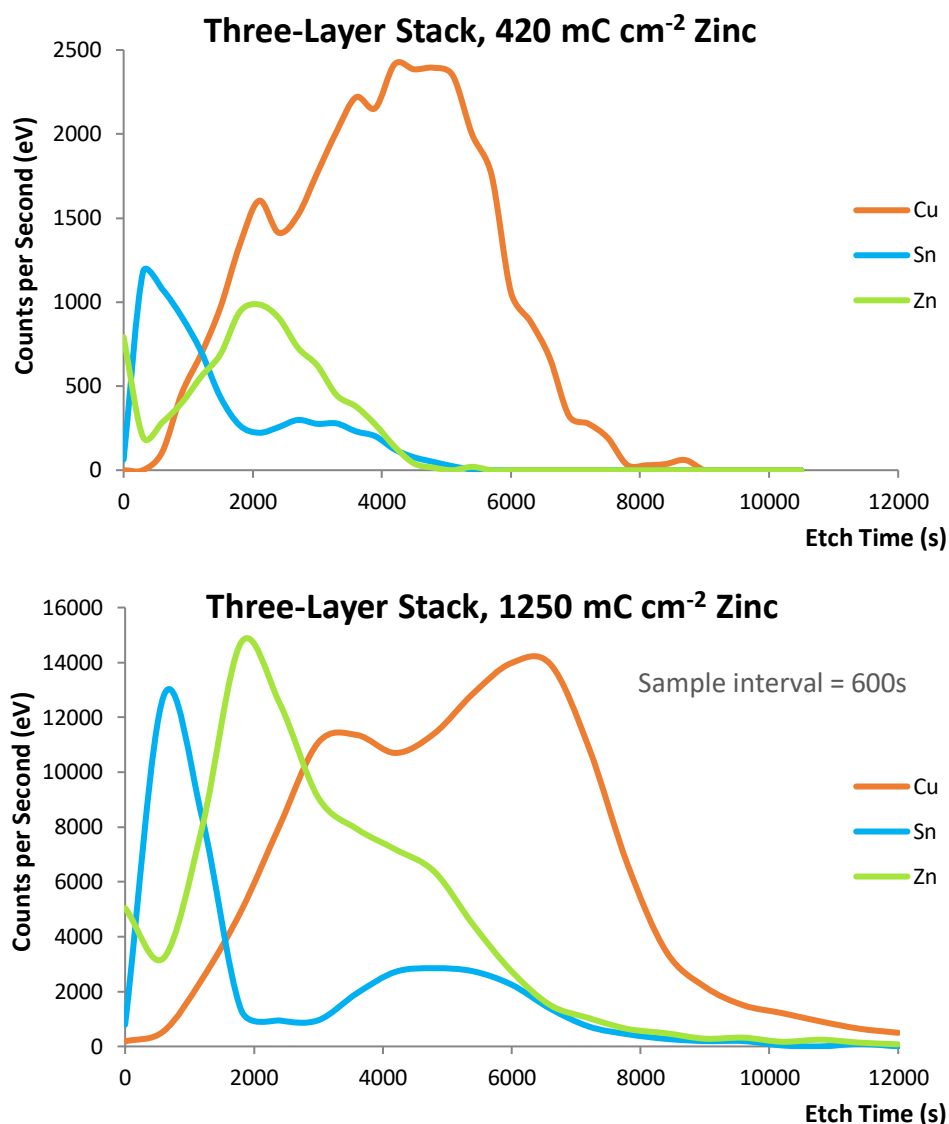


**Figure 4-43 - Signal intensity plotted against etch time for copper, tin and zinc on the sample with a thinner zinc layer (top) and the sample with a thicker zinc layer (bottom).**

and provide a useful means of comparison between the three elements and the two profiles – the characteristics are easier to see without the inclusion of plot lines for other elements, and, as each plot line is based on the signal intensity for the corresponding element rather than its percentage abundance, an increase or decrease in the signal from one element does not skew the plot lines for the others. A clear feature that is common to both of these graphs is that at zero etch time, zinc is producing the strongest signal and that a relatively small tin signal is also present. There is then an initial decrease in the zinc count coinciding with a surge in the tin count, followed by an increase in the zinc count while the tin count decreases. A

copper signal is also detected after a relatively short etch time on both samples, despite being at the bottom of the deposited stack. An explanation for the initial drop and subsequent increase in the zinc signal is difficult to find, however, the early detection of copper and tin may relate to the excitation depth of the incident x-rays, the multi-layered elemental structure of the stack, and the granular properties of the deposited films. During XPS, the incident x-rays can excite electrons to a depth of up to 2 mm [17], however, the majority of these electrons will lose their kinetic energy before reaching the surface of the sample and are not ejected, therefore they do not contribute to the detected signal [18]. The detected electrons are ejected from a depth of approximately 2-5 nm [19]. It could be speculated that in a multi-layered granular structure with film layer thicknesses substantially less than the possible 2 mm penetration depth, that excited electrons may be able to escape from an underlying layer through the grain boundaries of the layers above it, without the need to pass through any bulk material and thus maintaining their kinetic energy. Furthermore, it could be speculated that if the argon ion etching beam were to etch away preferentially at the grain boundaries of the zinc, then tin could initially become rapidly exposed. However, if prolonged etching caused the zinc grains to then fragment, this could lead to some dispersion of zinc across the underlying tin, reducing the exposed surface area of the tin, which would in turn suppress the tin signal while increasing the zinc surface area and increasing the zinc signal. As the material is etched further, zinc would be removed from the surface and therefore exposing more of the tin. It is worth noting that both samples exhibit an increase in the tin signal coinciding with a reduction in the zinc signal from approximately 2000 s etch time. This would also offer some explanation as to reason for a lower detected tin abundance on the sample with a thinner zinc deposit (that electrons are being ejected from the tin and detected prior to the tin becoming exposed). If it is taking a longer time to etch away at the zinc because it is thicker, and the tin signal is being detected for this whole duration, then that would lead to greater value of the integrated signal when integrated with respect to time. These are highly speculative hypotheses, but it may be possible to test them by running a set of depth profiles on identical samples using a range of total etching times and carefully examining the etched surfaces using a high-powered FEG-SEM and EDS. If this hypothesis were to hold true, it would suggest that the accuracy of the data produced using XPS depth

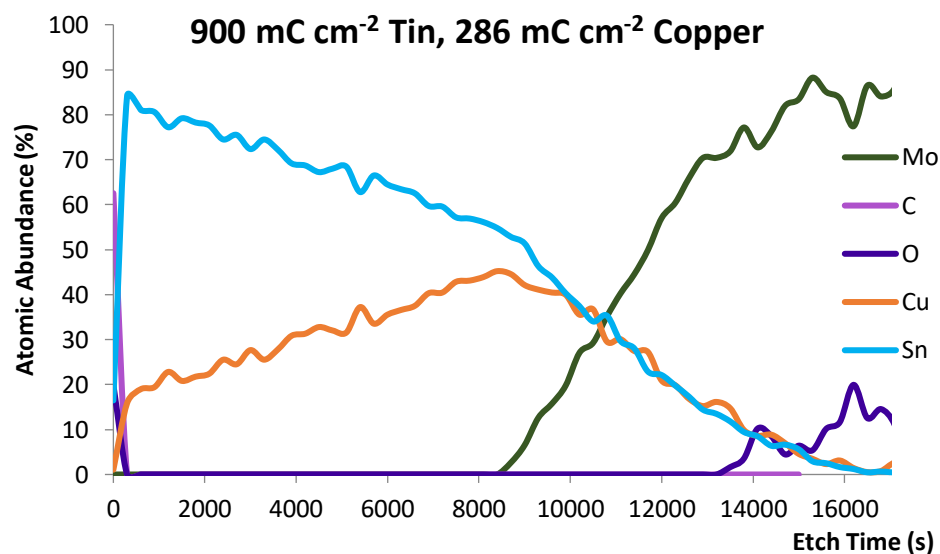


**Figure 4-44 - An XPS depth profile carried out on a sample with a relatively thick tin layer, a relatively thin copper layer and no zinc layer.**

profile analysis on a multi-layered stack may be somewhat limited, particularly if it is used to calculate an overall atomic abundance for each element. Although the test using multiple etch times described above was not performed, a more simple test where a relatively thick tin layer ( $900 \text{ mC cm}^{-2}$ ) was deposited onto a relatively thin copper layer ( $286 \text{ mC cm}^{-2}$ ) and XPS depth profiling performed. The percentage elemental abundance plotted against etch time is presented in Figure 4-44 and the overall elemental abundance (calculated by integrating the respective signals) is presented in Figure 4-45. It can be seen when observing Figure 4-44 that a copper signal is detected even at zero etch time, and increases rapidly in the first 300 s. This is despite the relatively thick tin layer, and the fact that a method for depositing tin with full coverage of the copper and a close-packed granular structure had been established (see Figure 3-32, section 3.3.4.2). The overall abundancies displayed in Figure 4-45 show tin, the upper layer, to be less abundant than expected, and copper, the lower layer, to be more abundant than expected. It could be argued that these findings partially support the hypotheses set out above, and do not contradict them. Multiple depth profiling techniques exist, one of which is secondary ion mass spectrometry (SIMS). Had this technique been available, it may have been able to produce a more accurate depth profile of a multi-layered stack – the technique works by detecting the ions that are ejected from the surface as it is etched away [20]. It performs measurements on material as it is removed, rather than on material that is

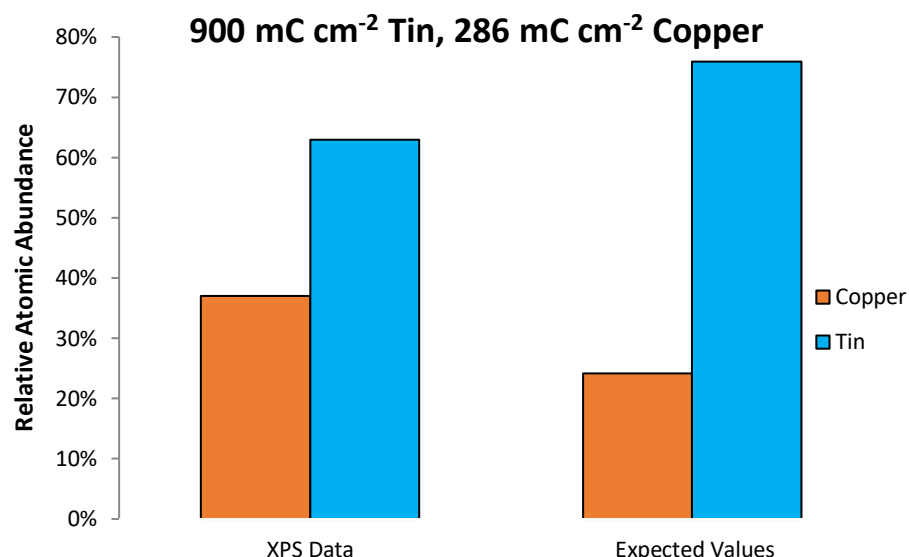


**Figure 4-45 - Total relative atomic abundancies calculated for the sample with a thick tin layer, thin copper layer and no zinc layer. The higher than expected abundance of copper and lower than expected abundance of tin supports the hypothesis that excited electrons from a lower layer can escape between the grains of another layer above it.**

remaining on the sample. However, SIMS also has limits to its resolution, caused by factors such as differing etch rates between materials, and variations in the signal for one element being caused by the presence of another (chemical effect), amongst others [20]. Without attempting this technique, it is not possible to know whether it would be more suitable for the applications in this project, however it is a potential alternative to XPS.

Given the uncertainty presented by the XPS data, the decision was taken to attempt to gauge the quantity of deposited zinc through an alternative method. As with copper and tin, MP-AES experiments were performed in which zinc was analysed in order to attempt to quantify the deposition efficiency of the chosen (acid-sulphate) electrolyte.

#### **4.3.7.2 Efficiency Calculations using MP-AES**

The MP-AES experiments involved dissolving electrodeposited films in acid and measuring the concentration of each metallic element by passing the acid through a Microwave Plasma – Atomic Emission Spectrometer. This process is described in section 2.4.1. Three electroplated stacks were analysed using MP-AES, each with a

**Table 4-6 - Masses measured for zinc films using the MP-AES system, including the drift indicated by two calibration standards, as well as the calculated deposition efficiencies.**

Sample	Mass (mg)	Deposition Efficiency (%)
1	1.8475	108.0
2	1.8400	107.6
3	1.9800	115.8
Expected mass	1.7102	N/A
Drift 4 mg L <sup>-1</sup> (mg L <sup>-1</sup> )	4.03	N/A
Drift 10 mg L <sup>-1</sup> (mg L <sup>-1</sup> )	9.72	N/A
Ave inc. drift	N/A	113.7
Ave excl. drift	N/A	110.5

deposition area of 4 cm<sup>2</sup>, with zinc having been deposited at -50 mA cm<sup>-2</sup> for 8.4 s (giving a charge passed density of 420 mC cm<sup>-2</sup>) on each of the three samples. The mass of the dissolved zinc was calculated from the concentration data for each sample, and these values were compared to the expected mass based on the charge passed in deposition assuming 100% efficiency. The measured mass values were divided by the expected mass values and converted into percentages in order to calculate the deposition efficiency, which is presented in Table 4-6, alongside the obtained film mass values. The deposition efficiency values are all slightly in excess of 100%, suggesting that there is some source of error in these measurements. The possible causes of this error have been discussed in section 3.3.5.2. Despite the suspected inaccuracy in the results, the values obtained offer some reassurance as they are similar to those obtained for copper and tin (see Table 3-4, section 3.3.5.2). This suggests that the deposition efficiency is no less than that of copper or tin, and that all three elements in fact have similar deposition efficiencies, which supports the hypothesis that the XPS results are inaccurate. Similar deposition efficiencies between all three elements are advantageous, even if they are less than 100%, as the ratios between the charges passed in deposition will be similar to the ratios between the atomic abundancies of the deposited films. This is a key factor that needs to be controlled.



#### 4.3.7.3 *Summary*

Tests carried out using XPS depth profiling demonstrated that this form of analysis can be useful in certain circumstances, however, it may not be suitable for gaining an accurate profile of the elemental distribution across the thickness of multiple different types of electrodeposited film, particularly if the purpose is to calculate the relative abundancy of each deposited element. This limits its use when attempting to obtain the efficiency of the electrodeposition processes. XPS can, however, be useful for some comparative processes, although care must be taken in how the data is interpreted. When multiple positions are profiled on the same sample, the differences between the data can give an indication of variations across the sample area. This was useful in showing that the observed “ring effect” was not indicative of substantial variations in the film thickness across the sample. There is the expectation that XPS depth profiling could be used to study the differences in elemental intermixing in heat-treated samples, as the films would no longer comprise of separate elemental layers, and the data would be used for comparative, qualitative purposes. For calculating electrodeposition efficiencies, XPS must be complemented with other techniques in order to discover the required information.

Other techniques that could be used with relation to deposition efficiency include EDS, deposition-stripping tests and MP-AES. As stated in section 2.4.5, the EDS systems used in this project could not be relied upon to return accurate quantitative data, although it could still prove useful as a guide if studying elemental ratios in a relatively homogeneous film, and was useful for elemental colour mapping the inhomogeneous surfaces of electrodeposited stacks. EDS was not used for examining elemental ratios on stacks with more than two electrodeposited layers, as the number of incident electrons reaching the bottom (copper) layer could be insufficient to yield any useful data, which would in turn skew the ratios of the overlying layers. Some useful data was obtained using deposition-stripping tests, however these could only be performed easily when the potentiostat/galvanostat was in potentiostatic mode. Executing such a test on a galvanostatically deposited zinc layer would have been a more complex process and was not attempted. Furthermore, results from earlier deposition-stripping tests conflicted with those obtained using XPS, resulting in a loss of confidence in the deposition-stripping test results. Had more XPS data been

available and fully analysed earlier in the project, greater confidence may have been awarded to the deposition-stripping data and efforts may have been made to perform such tests on the galvanostatically deposited films.

For the purposes of obtaining absolute values for the deposition efficiency of each electroplating process, MP-AES may not provide sufficiently accurate data, however, it did provide some assurance that the deposition efficiencies of each element were similar to each other, facilitating the control of the elemental ratios across the stack. Once the limitations of the XPS depth profile data was accounted for, and the results of previous deposition-stripping tests on copper and tin were considered (see section 3.3.5.1), the general indicators were that the galvanostatic deposition of zinc from the chosen acid-sulphate electrolyte was an efficient process, but a specific value for that efficiency was not obtained. Despite this, it was considered that sufficient data was available to facilitate the progression of experiments onto the annealing stage.

#### **4.4 Conclusions**

The electrodeposition of zinc onto tin proved to be the most challenging of the elemental deposition processes. This was due to two main factors – hydrogen evolution and the incomplete coverage of the tin surface. Despite these challenges, films with sufficient consistency, grain coverage and homogeneity were obtained in order to progress the experimentation to the annealing and sulphurisation stages. These results were achieved by trialling a wide range of electrolyte compositions and electrodeposition settings, and it was found that an acid-sulphate electrolyte composition formulated for the electroplating of zinc onto sheet steel returned the most favourable results, with a relatively high current density of  $-50 \text{ mA cm}^{-2}$  being found to be suitable. This was promising, as it could facilitate the scale-up of the electrodeposition process if the project were to be continued in the future. Although a precise value for the deposition efficiency from this electrolyte was not established, it would appear likely from the MP-AES data that it is an efficient process, therefore the shorter deposition time of 8.4 s was considered sufficient to deposit the required quantity of zinc to maintain the desired elemental ratios.

Although films were obtained that were deemed adequate for experimental progression, they did not meet the standards that were seen with copper and tin, where full coverage of the underlying layer was achieved on a microscopic scale. In order to attempt to achieve this, further experimentation would need to be pursued.

One aspect to experimental analysis that has become particularly apparent through the work carried out on zinc electrodeposition is the need to employ a portfolio of analysis techniques, as the inaccuracies presented by one technique may not be apparent without the verification provided by another. Had MP-AES been deployed earlier in the experimental timeline, there may have been less confusion resulting from the XPS data, however, understanding and learning how data generated by different analytical equipment can be interpreted and utilised has been an important part of the journey of this project. Despite the concerns expressed regarding the XPS data in this chapter, the results were still of value and the utilisation of XPS depth profiling continued to be deployed in the analysis of annealed samples in the subsequent experimental stage of this project.

## 4.5 References

- [1] M. Arasimowicz, M. Thevenin and P. Dale, “The Effect of Soft Pre-Annealing of Differently Stacked Cu-Sn-Zn Precursors on the Quality of Cu<sub>2</sub>ZnSnSe<sub>4</sub> Absorbers,” in *Materials Research Society Symposium C – Compound Semiconductors: Thin-Film Photovoltaics, LEDs and Smart Energy Controls*, 2013.
- [2] J. J. Scragg, “Section 2.8 - Electrodeposition of Zn from an Acid Chloride Electrolyte,” in *Copper Zinc Tin Sulfide Thin Films for Photovoltaics: Synthesis and Characterisation by Electrochemical Methods*, Berlin, Springer-Verlag, 2011, pp. 42-47.
- [3] J. J. Scragg, P. J. Dale and L. M. Peter, “Synthesis and characterization of Cu<sub>2</sub>ZnSnS<sub>4</sub> absorber layers by an electrodeposition-annealing route,” *Thin Solid Films*, vol. 517, no. 7, p. 2481–2484, 2009.

- [4] J. J. Scragg, "Section 2.4 - Electrodeposition of Metallic Precursors: Description of Electrodeposition Methodology," in *Copper Zinc Tin Sulfide Thin Films for Photovoltaics: Synthesis and Characterisation by Electrochemical Methods*, Berlin, Springer-Verlag, 2011, pp. 25-28.
- [5] O. Ola, Y. Chen, K. Thummavichai and Y. Zhu, "In situ fabrication of dendritic tin-based carbon nanostructures for hydrogen evolution reaction," *Sustainable Energy Fuels*, vol. 4, no. 10, pp. 5223-5228, 2020.
- [6] J. J. Scragg, "Section 2.1 - Electrodeposition of Metallic Precursors: Electrochemical Deposition (Electrodeposition)," in *Copper Zinc Tin Sulfide Thin Films for Photovoltaics: Synthesis and Characterisation by Electrochemical Methods*, Berlin, Springer-Verlag, 2011, pp. 9-19.
- [7] Plating Resources, Inc., "Poor Throwing Power and Coverage," 18th June 2012. [Online]. Available: <http://www.plating.com/platingtechnical/poorthrowingpower.htm>. [Accessed 12th March 2019].
- [8] Y. D. Gamburg and G. Zangari, "Technologies for the Electrodeposition of Metals and Alloys: Electrolytes and Processes," in *Theory and Practise of Metal Electrodeposition*, New York, Springer, 2011, pp. 265-316.
- [9] H. Hayashida and R. Nakahara, "Studies of Throwing Power in Various Non-Cyanide Zinc Plating Baths," *Journal of the Metal Finishing Society of Japan*, vol. 22, no. 7, pp. 326-334, 1971.
- [10] R. Winand, "Electrodeposition of Zinc and Zinc Alloys," in *Modern Electroplating*, 5th ed., Hoboken, New Jersey: John Wiley and Sons, 2010, pp. 285-308.
- [11] E. A. Pogue, A. Sutrisno, N. E. Johnson, D. P. Shoemaker and A. A. Rockett, "Oxygen-Induced Ordering in Bulk Polycrystalline  $\text{Cu}_2\text{ZnSnS}_4$  by Sn Removal," *Inorganic Chemistry*, vol. 56, no. 20, pp. 12328-12336, 16 October 2017.
- [12] S. Ahmed, K. B. Reuter, O. Gunawan, L. Guo, L. T. Romankiw and H. Deligianni, "A High Efficiency Electrodeposited  $\text{Cu}_2\text{ZnSnS}_4$  Solar Cell," *Advanced Energy Materials*, vol. 2, no. 2, pp. 253-259, February 2012.

- [13] L. Guo, Y. Zhu, O. Gunawan, T. Gokmen, V. R. Deline, S. Ahmed, L. T. Romankiw and H. Deligianni, "Electrodeposited Cu<sub>2</sub>ZnSnSe<sub>4</sub> Thin Film Solar Cell with 7% Power Conversion Efficiency," *Progress in Photovoltaics: Research and Applications*, vol. 22, no. 1, pp. 58-68, January 2014.
- [14] Y. A. Naik and T. V. Venkatesha, "A New Brightener for Zinc Plating from Non-Cyanide Alkaline Bath," *Indian Journal of Engineering and Materials Sciences*, vol. 10, pp. 318-323, 2003.
- [15] M. A. M. Ibrahim, "Improving the Throwing Power of Acidic Zinc Sulfate Electroplating Baths," *Journal of Chemical Technology and Biotechnology*, vol. 75, no. 8, pp. 745-755, 2000.
- [16] W. J. Duffin, *Electricity and Magnetism*, 3rd ed., London: McGraw-Hill, 1980.
- [17] M. Nagoshi, T. Kawano, N. Makiishi, Y. Baba and K. Kobayashi, "High-Energy Total Reflection X-Ray Photoelectron Spectroscopy for Polished Iron Surface," *Surface and Interface Analysis*, vol. 40, no. 3-4, pp. 738-740, March-April 2008.
- [18] J. Kawai, H. Adachi, Y. Kitajima, K. Maeda, S. Hayakawa and Y. Gohshi, "Inelastic Mean Free Path of Photoelectrons in Ag Determined by Total Reflection X-Ray Photoelectron Spectroscopy," *Analytical Sciences*, vol. 13, no. 5, pp. 797-801, 10 October 1997.
- [19] Los Alamos National Laboratory, "How XPS Works," *Actinide Research Quarterly*, no. 2, 2004.
- [20] E. Zinner, "Depth Profiling by Secondary Ion Mass Spectrometry," *Scanning*, vol. 3, no. 2, pp. 57-78, 1980.

## 5 Annealing and Sulphurisation

### 5.1 Introduction

Once electroplated films for CZTS have been prepared, it is necessary for them to undergo a sulphurisation treatment in order to convert the metallic precursors into CZTS. Typically, this would involve the high temperature annealing of the samples (generally in the 450°C – 600°C range [1]) in an oxygen free, sulphur rich environment. Temperatures below this tend to lead to a mixture of unwanted binary and ternary phases forming, such as  $\text{Cu}_2\text{SnS}_3$ ,  $\text{ZnS}$ ,  $\text{Cu}_{2-x}\text{S}$  and  $\text{SnS}_2$ , as the temperature is insufficient for the phases to react and form CZTS [2]. The precise temperature required is affected by the exact furnace setup used in the sulphurisation process, for example the type of furnace used (tube furnace, RTP, etc.), whether a graphite box or quartz ampoule are used, the type of inert gas, or whether the gas is stagnant or flowing. In addition to the temperature, there are numerous other adjustable parameters that can affect the results, including the background pressure, heating profile (temperature ramp rates, holding times, etc.), and sulphur concentration. In this project, a Rapid Thermal Processing (RTP) furnace with a graphite annealing box was used for the sulphurisation experiments (see chapter 2, section 2.2.2) and the optimisation experiments focussed on the background gas pressure and the sulphur concentration (a heating profile had already been developed by a research colleague, although this was for spin-coated CZTS precursors).

A pre-alloying stage, in which the samples are heated without sulphur, was also studied in this project as it is reported in literature that it can improve the quality of the obtained CZTS films [3, 4]. This stage of the processing also needed to be optimised, and hence a substantial section of this chapter is dedicated to optimising the temperature and duration of the pre-alloying process. In addition to the optimisation of the pre-alloying process using an RTP, a brief investigation was conducted as to whether the process could be carried out using a Hot-Dip Simulator (HDS).

This chapter presents a simple analysis of samples pre-alloyed using an HDS, through the use of optical microscopy, SEM and EDS. This is followed by detailed analyses of the optimisation of pre-alloying in an RTP furnace, by means of EDS

colour mapping, SEM imaging, XRD and XPS depth profiling, including a discussion on the how the ratios between the elements affect the alloying achieved. Analysis through EDS colour mapping, SEM imaging and XRD are also discussed in the following section on the optimisation of the sulphurisation conditions, as is Raman spectroscopy. The final section is dedicated to comparing sulphurised samples that have received pre-alloying treatments with those that have not, and explores the possibility of incorporating the pre-alloying treatment into the same annealing process as the sulphurisation.

## 5.2 Experimental Methods

### 5.2.1 Sample Preparation

#### 5.2.1.1 *Electrodeposition of Multi-Layered Stack Precursors*

All electrodeposition was carried out onto Mo-SLG substrates using static electrodes and stagnant electrolytes. The copper was deposited using an alkaline electrolyte and the tin was deposited using a methanesulfonic acid electrolyte, the formulae for which are stated in sections 2.1.5 and 2.1.8 respectively. These were deposited under optimised conditions as discussed in chapter 3. With the exception of samples processed in the Hot-Dip Simulator, zinc was deposited under optimised conditions as discussed in chapter 4 using Electrolyte Zn 6, which is an acid-sulphate electrolyte, the formula for which is stated in section 2.1.9.

Two samples were pre-alloyed using a hot-dip simulator, which were three-layer stacks of copper, tin and zinc with a 2 cm<sup>2</sup> surface area. The zinc was deposited prior to completion of the optimisation experiments. The electrolyte used was Electrolyte Zn 2 (see section 2.1.9 for composition details) at a potential of -1.22 V vs Ag|AgCl. The charge-passed densities for Cu/Sn/Zn were 520/433/477 mC cm<sup>-2</sup> for the first sample and 572/312/420 mC cm<sup>-2</sup> for the second sample. The reasoning for the differing elemental ratios between the two samples is explained as the results are presented and discussed.

For the samples pre-alloyed using a rapid thermal processing furnace, all electrodeposits had a surface area of 4 cm<sup>2</sup>, and copper and tin were deposited to charge-passed densities of 572 mC cm<sup>-2</sup> and 312 mC cm<sup>-2</sup> respectively. For the

temperature optimisation experiments, thicker zinc layers were deposited to a charge-passed density of  $1250 \text{ mC cm}^{-2}$ , whereas thinner zinc layers were deposited to a charge-passed density of  $420 \text{ mC cm}^{-2}$  on samples used in the duration optimisation experiments. This was due to more information being available on the zinc deposition efficiency by the time the duration optimisation experiments were carried out.

All of the samples used in sulphurisation experiments were deposited with films of  $4 \text{ cm}^2$  surface area. Only one of the films used for sulphurisation was deposited with a four-layer Cu-Sn-Cu-Zn stack, with all other samples being three layer Cu-Sn-Zn stacks. Each of these three-layer stacks were deposited with copper and tin to charge-passed densities of  $572 \text{ mC cm}^{-2}$  and  $312 \text{ mC cm}^{-2}$  respectively. For the four-layer stack, the first copper layer was deposited at a potential of  $-0.98 \text{ V}$  vs Hg|HgO to a charge-passed density of  $143 \text{ mC cm}^{-2}$ , the tin layer was deposited at  $-0.525 \text{ V}$  vs Ag|AgCl to a charge-passed density of  $312 \text{ mC cm}^{-2}$ , and the second copper layer was deposited at  $-1.18 \text{ V}$  for  $15 \text{ s}$  followed by  $-1.14 \text{ V}$  (vs Hg|HgO) to a total charge-passed density of  $429 \text{ mC cm}^{-2}$ . The electrodes were pre-polarised on submersion of the sample in electrolyte for the deposition of the second copper layer (see section 3.3.6.3 for a discussion regarding this). The zinc layer was deposited to a charge-passed density of  $1250 \text{ mC cm}^{-2}$ . For the first sulphurised sample, a three-layer stack was used with a zinc layer deposited to a charge-passed density of  $1250 \text{ mC cm}^{-2}$ . The samples used for background pressure optimisation experiments also had zinc deposited to a charge-passed density of  $1250 \text{ mC cm}^{-2}$ . The samples used for experiments to optimise the sulphur concentration, and experiments regarding the efficacy and combining of the pre-alloying process into the sulphurisation process were deposited with zinc to a charge-passed density of  $420 \text{ mC cm}^{-2}$ .

#### **5.2.1.2 Pre-Alloying and Sulphurisation Processes**

Two samples underwent pre-alloying using a hot-dip simulator and all other pre-alloying experiments were conducted using a rapid thermal processing furnace. All sulphurisation experiments were carried out using the RTP furnace. Descriptions of the HDS and RTP furnace, as well as details on how the equipment was purged with inert gas at the beginning of each experiment can be found in section 2.2.1 and section 2.2.2 respectively.



### **HDS – Pre-Alloying**

For the experiments conducted using the HDS, two samples were annealed at 350 °C under a nitrogen atmosphere for 30 minutes in accordance with that reported in [3]. In order to test the ability of the samples to withstand rapid increases in temperature, the ramp rate was set to the maximum permitted by the furnace controls, which equated to 16 °C s<sup>-1</sup>. At the end of the annealing cycle, samples were removed once the furnace had cooled to a temperature of 60 °C or less, which took approximately five minutes.

Some technical difficulties were experienced during the annealing of sample 1, where the furnace stalled after 14 minutes due to the automatic overriding of the input time setting by the default maximum time setting. The furnace was restarted within 20 s, with the minimum temperature reached in that time period being 310 °C. No technical issues were experienced during the annealing of sample 2.

### **RTP – Pre-Alloying**

The RTP furnace was used for two sets of pre-alloying experiments – one in which the heating duration was kept constant and the temperature varied between each sample, and one in which the temperature was kept constant and the heating duration was varied between each sample. For both sets of experiments, the background pressure used was 150 mTorr. The reason such a low pressure was chosen was that the long term intention was to incorporate the pre-alloy and the sulphurisation stages into one process, and that the preliminary analysis of data relating to sulphurised samples at the time suggested that very low pressures may be advantageous (see section 5.3.2). With regards to the choice of temperature and duration range for these experiments, it is stated by Scragg in [5] that 250-270 °C for 3-5 minutes was found to be sufficient to intermix the elements and that temperatures and durations greater than this caused dewetting of the films. This is in contrast to that reported in [4] and [3], where 30 minutes at 360 °C and 350 °C respectively were reported to be successful. It is also noteworthy that no dewetting was observed in the experiments using the HDS at 350 °C for 30 minutes (described in section 5.3.1.1). The decision was taken to examine the “middle ground” where one set of samples were annealed for 20 minutes at 285-340 °C, and the other set were annealed for 5-40 minutes at 300 °C (this choice of temperature was decided upon based on the results of the

temperature varied experiments). A ramp rate of  $2.5\text{ }^{\circ}\text{C s}^{-1}$  was used because this had been used for the successful sulphurisation of CZTS precursor films prepared via a spin coating technique by a colleague. It was also considered a reasonable compromise between the potentially very fast ramping rates that the RTP furnace was capable of and the much lower rates used by Scragg for similar alloying experiments ( $1.7\text{ }^{\circ}\text{C s}^{-1}$  up to  $180\text{ }^{\circ}\text{C}$ ,  $0.17^{\circ}\text{C s}^{-1}$  thereafter) [5].

### **RTP – Sulphurisation**

Sulphurisation experiments to optimise the pressure and to optimise the sulphur mass used the same heating profile, which is given in Table 5-1. Other than for some initial experiments for which the sulphur mass and background pressures are given as part of the discussion (along with reasons for choosing those values), the range of background pressures tested were 150 mTorr to 30.0 Torr with 250 mg of sulphur, and the range of sulphur masses tested were 75 mg to 750 mg at 3.75 Torr. The reasons behind these choices are dependent upon results obtained in this chapter and are given as part of the discussion as the results are presented.

**Table 5-1 - RTP furnace settings used for the majority of sulphurisation experiments described in this section.**

<b>Heating Stage</b>	<b>Ramp Rate (<math>^{\circ}\text{C s}^{-1}</math>)</b>	<b>Ramp Time (s)</b>	<b>Temperature (<math>^{\circ}\text{C}</math>)</b>	<b>Hold Time (s)</b>
1	2.5	160	400	600
2	1.5	100	550	1200

## **5.2.2 Sample Analysis**

### ***5.2.2.1 Scanning Electron Microscopy and Energy Dispersive Spectroscopy***

An overview of the SEM-EDS equipment and its general usage in this project is given in section 2.4.5. The acceleration voltage used in SEM imaging is indicated where appropriate. For the analysis of samples in experiments involving the HDS, a Hitachi Desktop SEM was used to obtain images and for EDS analysis. An acceleration of 15 kV was used for the EDS experiments. For analysis of samples in experiments involving the RTP (which were undertaken at a later stage of the project), a JEOL 7800 FEG-SEM was used for its superior image resolution. The

EDS experiments performed with this instrument used an acceleration voltage of 20 kV.

#### **5.2.2.2 X-Ray Diffractometry**

An overview of the XRD equipment and its general usage in this project is given in section 2.4.2. The instrument was a Bruker™ D8 Discover with a Cu-K $\alpha$  X-ray source generating a beam with a wavelength of 0.15418 nm. The associated Bruker™ proprietary software matched diffraction patterns using the Crystallography Open Database (COD). All of the XRD experiments used the same specific settings, which were as follows:

The beam acceleration and current were 40 kV and 40 mA respectively. The scans were standard coupled  $2\theta/\theta$  scans carried out across a range of  $10^\circ - 60^\circ$ , with  $0.02^\circ$  and a step time of 0.5 s. The scan range was chosen with sulphurised films in mind, but was also found to be appropriate for examining un-annealed and pre-alloyed metallic precursors.

#### **5.2.2.3 X-Ray Photoelectron Spectroscopy Depth Profiles**

An overview of XPS depth profiling and its use in this project is given in section 2.4.4. The instrument used was a Kratos Axis Supra with a monochromated Al-K $\alpha$  X-ray source giving a 15 mA emission current and power of 225 W. The analysis area was an oval of  $300 \times 700 \mu\text{m}^2$ . Etching for depth profiling was carried out using an Kratos Minibeam 6 argon ion etch gun and the base pressure inside the instrument was approximately  $5 \times 10^{-9}$  Torr. Elemental quantification analysis was carried out using CasaXPS software, version 2.3.17dev6.4k. For the majority of samples, XPS data was acquired every 300 s during etching unless otherwise stated.

#### **5.2.2.4 Raman Spectroscopy**

An overview of the use of Raman spectroscopy in the analysis of sulphurised films in this project can be found in section 2.4.3. The apparatus used was a Renishaw inVia Raman microscope fitted with a 60 mW laser with a wavelength of 532 nm. For all experiments, analysis was carried out at 20x objectification, leading to a spot analysis of  $3 \mu\text{m}$  diameter. The acquisition time was set to 25 s and the laser power was attenuated to 0.05%. Although the manufacturer's specifications state that the

total laser power is 60 mW, lab calibration experiments found it to be closer to 30 mW, meaning that the actual power at 0.05% is approximately 0.015 mW.

## **5.3 Results and Discussion**

### **5.3.1 Elemental Alloying Prior to Sulphurisation**

It is reported in literature in [4] and [3] that the inclusion of a pre-alloying (soft annealing) stage led to higher cell efficiencies. A pre-alloying step was also included by Scragg in [5]. In a pre-alloying process, the electrodeposited stack is heated in an inert atmosphere with no sulphur added at a temperature below that required for sulphurisation in order to encourage the elemental layers to intermix and form alloys. Two types of heating apparatus were used for this process – firstly a Hot Dip Simulator (HDS), which is described in section 2.2.1, and a Rapid Thermal Processing (RTP) furnace, which is described in section 2.2.2. The HDS was used only relatively briefly in this project, mainly due to a change of location, however, useful information was obtained and is hence included in this thesis.

#### ***5.3.1.1 Pre-Alloying Using a Hot-Dip Simulator***

Two samples were processed using the HDS, both of which were three-layer copper-tin-zinc stacks on Mo-SLG, however the stacks differed in their elemental ratios. They had a surface area of approximately 2 cm<sup>2</sup> and were prepared as described in section 5.2.1.1. The first sample had a copper/tin ratio of 1.2 and a zinc/tin ratio of 1.1; the second sample had a copper/tin ratio of 1.83 and a zinc/tin ratio of 1.35. These ratios were calculated using electrochemical data (charged passed during the deposition of each film) assuming 100% deposition efficiency. The ratios were chosen such that the elemental ratios of sample 1 matched those of samples prepared by our collaborators at Northumbria University (who were using a sputtering technique), and those of sample 2 matched those reported in [3] (which reported an efficiency of ~7% - one of the highest for an electrodeposited CZTS cell at that time). The samples were annealed as described in section 5.2.1.2. Although there were some technical difficulties experienced during the annealing of sample 1, no technical issues were experienced during the annealing of sample 2. Sample 2 was analysed using EDS before and after the annealing process and SEM images were

obtained. Both samples were analysed using optical microscopy after having been annealed (as well as an unannealed sample deposited using the same parameters as sample 2 for comparison).

After the annealing process, the visual properties of sample 2 had changed little, whereas sample 1 had darkened slightly. When observed under a microscope, it became apparent that sample 1 was covered in small blisters of up to  $\sim 30\text{ }\mu\text{m}$  in diameter, with spacing of  $\sim 10\text{ }\mu\text{m}$  between them. Conversely, sample 2 had no blisters and exhibited more favourable surface morphology than the unannealed sample, with the slight pitting seen on the unannealed sample not being evident on sample 2. This can be seen in Figure 5-1. Although the cause of the blistering on sample 1 could not be identified with a high degree of certainty, it was considered probable that it was due to the technical difficulties experienced 14 minutes into the annealing process and the resulting temperature fluctuation. The favourable results seen on sample 2, however, were a useful indication that an electroplated stack can withstand the rapid temperature ramping of  $16\text{ }^{\circ}\text{C s}^{-1}$  and the relatively rapid cooling of  $\sim 1\text{ }^{\circ}\text{C s}^{-1}$  at the end of the annealing process.



**Figure 5-1 - Two samples annealed using the HDS at  $350\text{ }^{\circ}\text{C}$  for 30 minutes (samples 1 and 2), alongside an unannealed sample for comparison. The blistering seen on sample 1 is likely as a result of a technical problem. The scale bars represent  $20\text{ }\mu\text{m}$ .**

EDS was performed using a Hitachi Desktop SEM at an acceleration of 15 kV. The EDS results are presented in a bar chart in Figure 5-2. It is possible to see that the annealing treatment has caused an increase in the signal for copper and a decrease in the signal for tin. Although not included in the graph, it is worth noting that the abundance for molybdenum in both analysis was returned at a value of  $\sim 1\%$ , suggesting that the signal from the bottom of the electroplated stack is very weak due

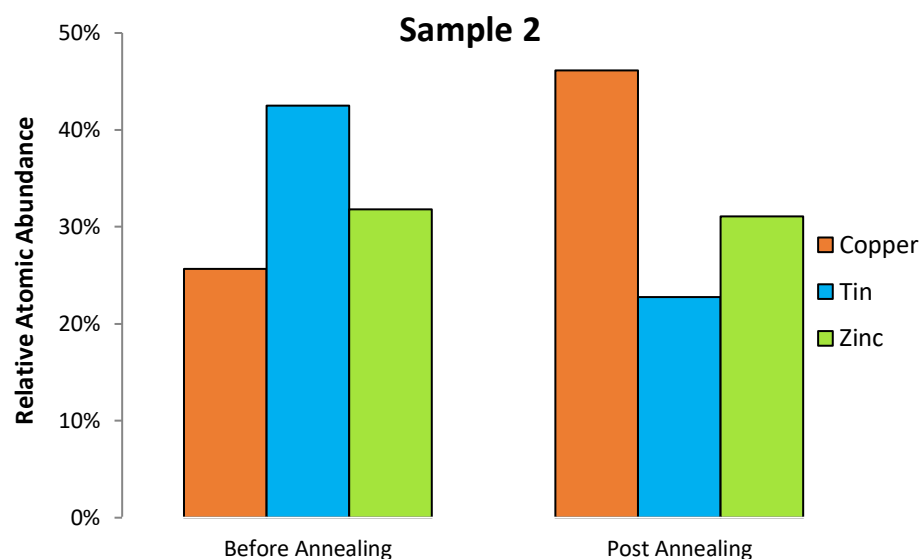


**Figure 5-2 - Comparative atomic abundancies of copper, tin and zinc on sample 2, obtained through EDS, before and after annealing using the HDS.**

to the limitations of the penetration depth. Given that copper is at the bottom of the electroplated stack, one would expect the copper signal to increase as a result of an alloying process as it diffuses upwards through the deposited material. Tin, on the other hand, sits in the central layer of the deposited stack, therefore a substantial variation in the abundance reading would not be expected. This significant drop in the detected signal suggests that some of the deposited tin was lost through evaporation during the annealing process. Some consideration was given to this in subsequent experiments, however, tin loss is more prone to occur during the sulphurisation stage as tin evaporates in the form of tin sulphide [6]. It may be the case that the relatively aggressive treatment received in the HDS caused this loss to occur during a pre-alloying experiment. The zinc abundance appeared to be of a similar value before and after annealing. As zinc sits at the top of the deposited stack, the expectation was that the abundance value would drop due to diffusion downwards through the deposited material causing a weakening of the EDS signal. However, if it is concluded that some tin has evaporated during the annealing process, the relative abundance of zinc would increase in value, assuming that the proportion of zinc lost through evaporation was smaller than the proportion of tin lost. This may be a reasonable assumption to make in the case of a sulphurisation experiment, but the boiling point of tin is significantly higher at 2856 °C [7] than it is for zinc at 907 °C [8]. However, when the melting points of the three metals are

considered, this may offer an explanation. Tin, which suffered the greatest material losses, has the lowest melting point at 232 °C [7], while copper, for which the EDS signal increased, has the highest melting point at 1085 °C [9]. The melting point for zinc, which maintained a similar apparent abundance after annealing to that of before, has a melting point between that of copper and tin at 420 °C [8]. This suggests that the melting point of a metal is more important when considering potential material losses during the pre-alloying stage.

The SEM images of sample 2 are presented in Figure 5-3. It can be seen that prior to annealing, the zinc deposit at the top of the electroplated stack exhibited island formation. There was some difficulty experienced in the focussing of the post-annealed image, however, it is possible to discern that there has been some change in the shape of the grains, in that they are flatter and slightly broader in their appearance, as if they have partially merged with adjacent grains (although this may not be obvious at first glance). This, combined with the EDS results, suggests that the HDS treatment, at least to some degree, was effective in achieving the desired result of dispersing and intermixing the metallic layers, although the extent of this was not measured. Although experimentation using the HDS was not pursued further due to practical (location related) reasons, the information gained regarding the dispersion of the elements and the ability of the sample to withstand the rapid heating and cooling (but not temperature fluctuation due to technical difficulties) was useful in subsequent experiments using the RTP furnace.

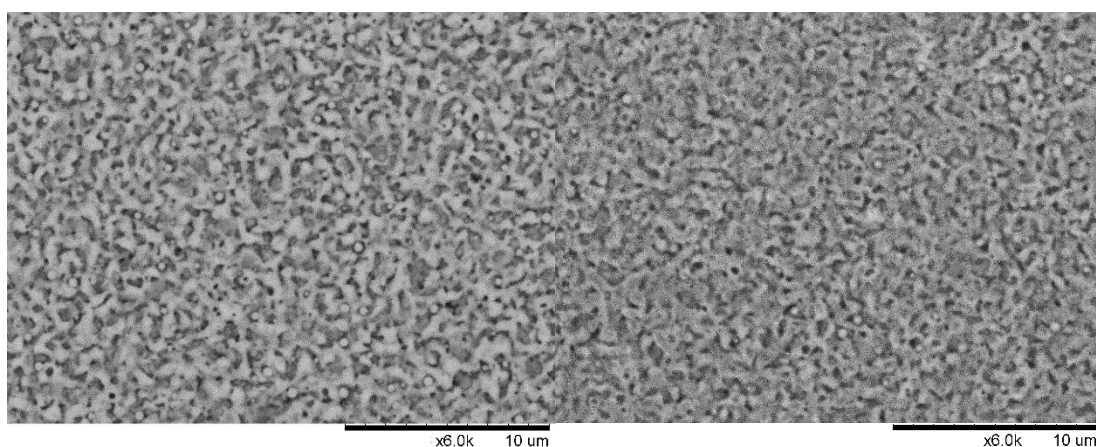


**Figure 5-3 - SEM images of sample 2 taken before (left) and after (right) annealing in the HDS. Images were obtained using a desktop SEM at an acceleration of 15 kV.**

### 5.3.1.2 *Pre-Alloying Using a Rapid Thermal Processing Furnace*

The RTP furnace was used for two sets of pre-alloying experiments – one in which the heating duration was kept constant and the temperature varied between each sample, and one in which the temperature was kept constant and the heating duration was varied between each sample. The samples used in the temperature varied experiments were three-layer electroplated stacks prepared as described in section 5.2.1.1. A description of how the RTP furnace was used in annealing these samples is given in section 5.2.1.2. A relatively large quantity of charge was passed during the deposition of zinc due to the fact that the deposition efficiency experiments were not completed by that stage in the project, and the SEM images and interpretation of the XPS data at that time suggested that a large quantity of charge may have been required to achieve the desired film properties. Having annealed five samples at a range of different temperatures, the first form of analysis undertaken was simple visual inspection. Photographs of the samples are presented in Figure 5-4. The initial feature to note is the blue colour seen on the sample annealed at 340 °C, which extends across the vast majority of the sample area. Despite the fact that, according to logbook entries, the pressure at the end of the annealing process was of a similar value to that of the other samples, it transpired that this colour change was due to the formation of oxides, as revealed by subsequent XPS analysis (see Figure 5-11).

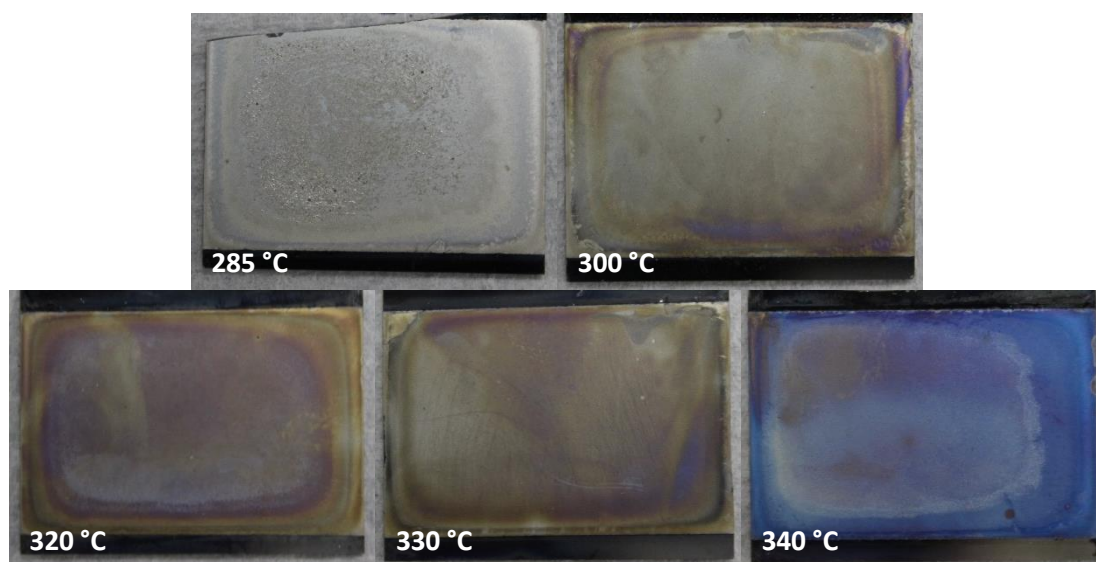


**Figure 5-4 – Photographs of the five samples annealed for 20 minutes at a range of temperatures. The lowest temperature led to blister formation, while the highest temperature led to discolouration that may be indicative of oxide formation.**



Another noteworthy observation is that the sample annealed at 285 °C suffered from the extensive formation of small blisters – a feature not seen on the other samples. This sample had the lowest annealing temperature, therefore the blisters may form as the metallic films are transitioning to an intermixed state, and disappear once the transition is complete, which would be expected to take longer at lower temperatures. The samples annealed at 300 °C, 320 °C and 330 °C were all similar in appearance, each of them exhibiting a slight copper-like tint (particularly the 320 °C sample) and some degree of inhomogeneity. There is also a “ring-effect” around the edges of the samples. This may be as a result of lateral flow of material across the surface of the substrate [10], or may relate the difference in film morphology seen near the edges of zinc deposits (see section 4.3.6.4). The copper-like tint was taken as a favourable observation, as it suggests that material from the film that is lowest in the deposited stack had diffused through both of the overlying layers to the top surface and that the desired intermixing had been achieved.

The next stage of analysis was to examine the samples using a FEG-SEM, and a selection of the obtained SEM images are presented in Figure 5-5. One image of

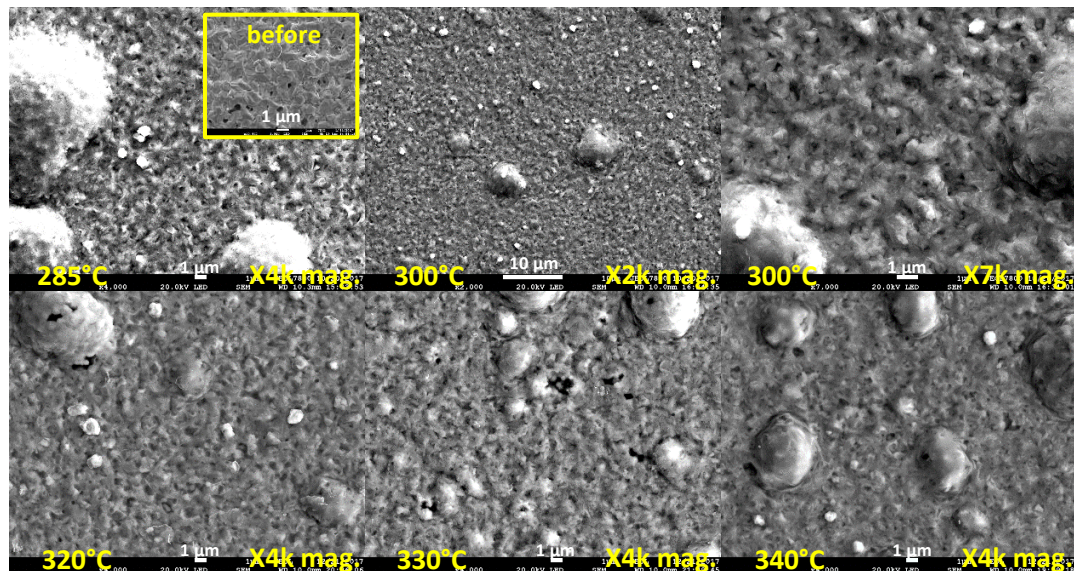


**Figure 5-5 – Images (taken using a FEG-SEM with an acceleration of 20 kV) of samples annealed for 20 minutes at a range of temperatures. All samples exhibit some blistering and a similar irregular grain structure, although the blisters are larger on the sample annealed at 285 °C than on the other samples. An example of a film prior to annealing is included inside the image for the 285 °C sample for comparison. Please note that scale bar represents 1 μm on all images except that for 300 °C, for which it represents 10 μm.**

4,000X magnification is presented for each of the samples annealed at 285 °C, 320 °C, 330 °C and 340 °C, whereas two images are presented for the sample annealed at 300 °C at magnifications of 2,000X and 7,000X (a 4,000X magnification image was not obtained for this sample). It is evident in these images that all of the samples experienced some blistering, however, once the level of magnification is taken into account, it can be discerned that the blisters seen on the sample annealed at 285 °C are approximately twice the diameter of those seen on other samples (~5-10 µm c.f. ~10-20 µm). All of the sample films exhibit a similar irregular grain structure with high levels of coverage and no evidence of dewetting, as well as some small individual grains of approximately 1-2 µm diameter that appear to sit on top of film (estimated number density of 3-5 per 100 µm<sup>2</sup>). The reason for the occurrence of the small individual grains was not ascertained, however, the key factor of note was that no temperature related trends in the film morphology were observed with the exception of the larger blisters being visible on the sample annealed at the lowest temperature (285 °C). In order to gain further insight, EDS colour maps and elemental quantification measurements were taken in addition to the SEM images.

Layered EDS colour map images were obtained for all five of the samples, and two examples are presented in Figure 5-6, one of the sample annealed at 285 °C and one of the sample annealed at 320 °C. It can be seen that there does not appear to be any one particular element that dominates the blisters or the small individual grains on either of the samples. It is also possible to see in both of these images that there are

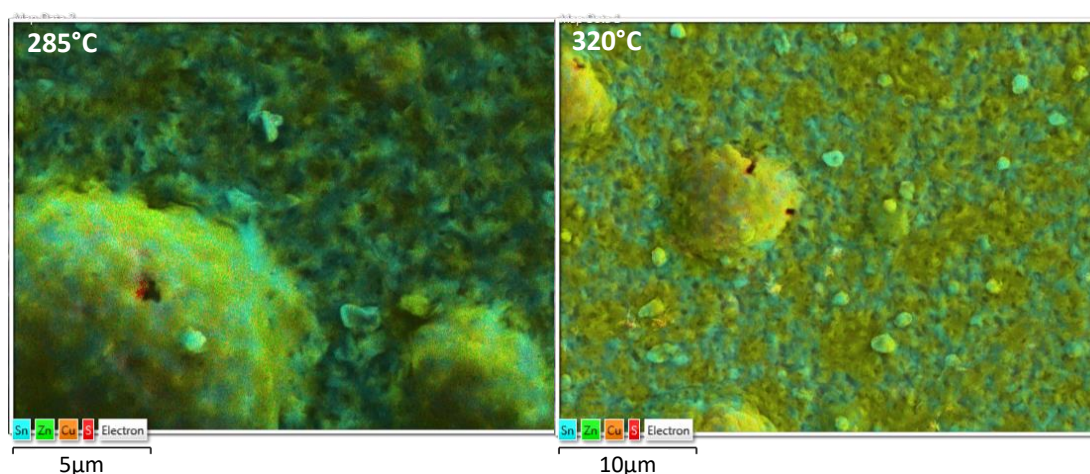


**Figure 5-6 – Layered EDS colour maps of two of the annealed samples showing some lateral separation of metallic elements.**

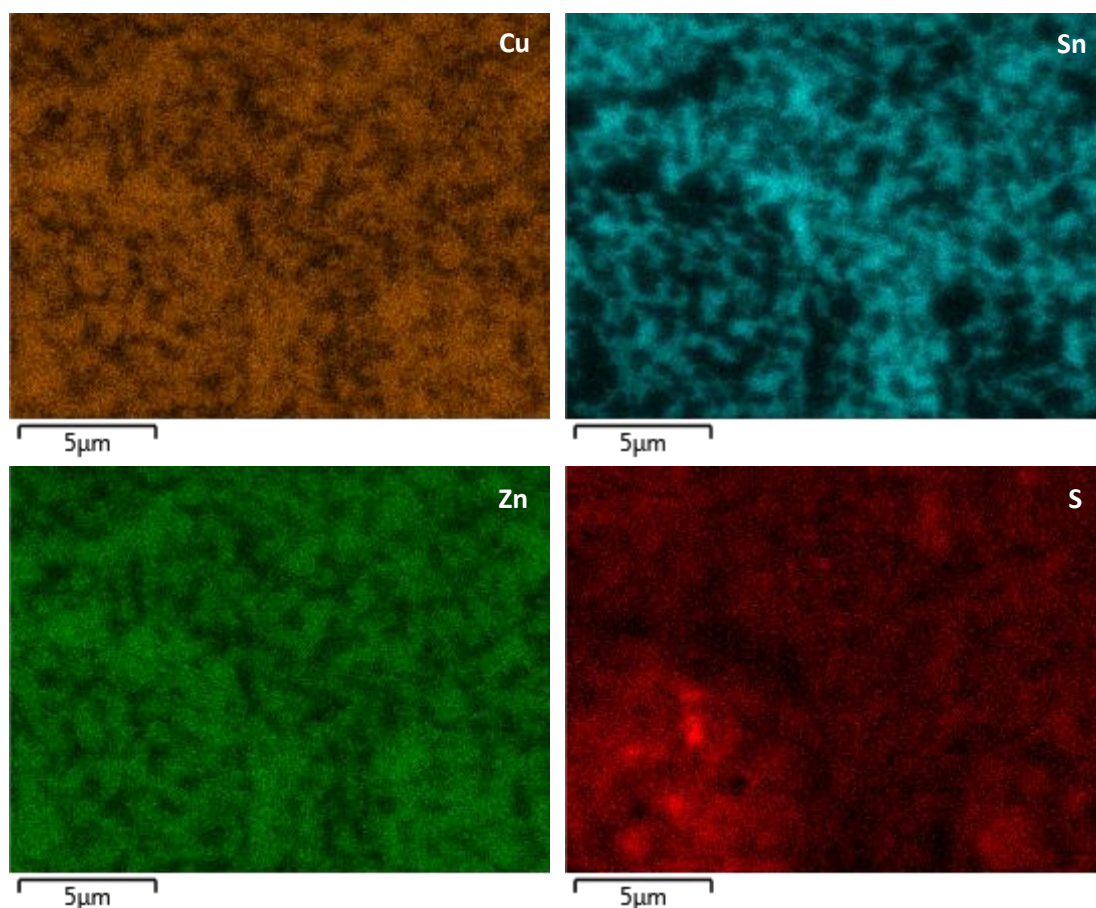


**Figure 5-7 – Individual elemental colour maps for the sample annealed at 285 °C. It is apparent that zinc and copper have alloyed together and are spatially separate from the tin.**

regions of distinct blue, the colour assigned to tin, where the other elements are not present. When the individual (non-layered) colour map images are observed (which are presented in Figure 5-7 and Figure 5-8), it is possible to see that there is a matrix of tin throughout the visible area, in which there are voids containing regions, or grains, that comprise of copper and zinc – it is almost as if the colour map image for tin is a photographic negative of that for copper or zinc. It is evident that these copper-zinc grains are larger in the sample annealed at 320 °C (Figure 5-8) than they are in the sample annealed at 285 °C (Figure 5-7), particularly when the difference in image magnification is taken into account. This feature was seen in the colour map sets for all of the samples annealed at 300 °C and above, there being no trend in the grain size past this point. The relatively thick layer of zinc deposited on these samples appears to have caused the situation where none of the copper is alloyed with tin, as the copper alloyed preferentially with the zinc, leaving none left available



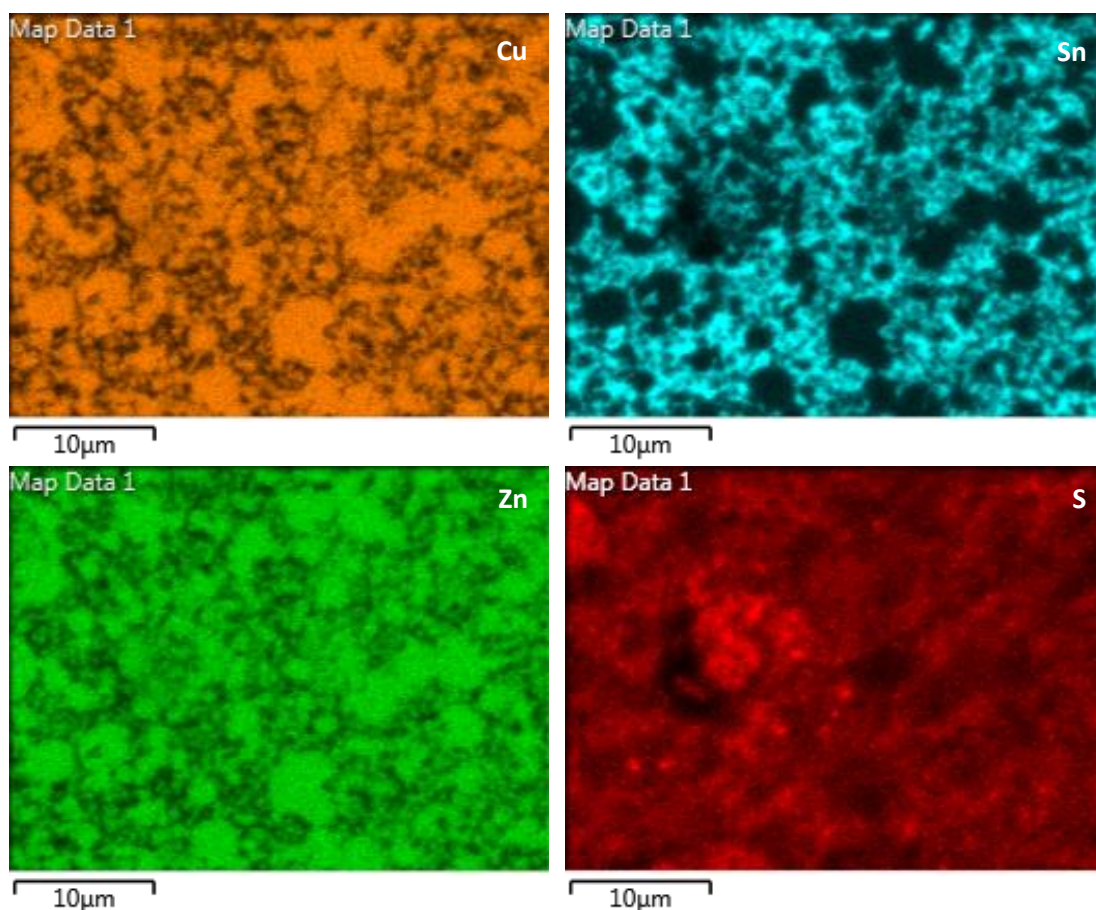


**Figure 5-8 – Individual elemental colour maps for the sample annealed at 320 °C. The alloyed Cu-Zn has agglomerated into larger regions than those seen on the sample annealed at 285 °C.**

to alloy with tin. The preferential alloying of copper with zinc is discussed by Scragg in [10] and therefore could not be considered to be an unexpected result. The smaller conglomerations of Cu-Zn seen on the sample annealed at 285 °C may be due to the mobility of the metals at that temperature. Higher temperatures are typically associated with higher rates of diffusion – it may be the case that 285 °C is sufficiently hot for the metals to diffuse over the short vertical thickness of the electroplated stack in the 20 minute annealing time, but no significant lateral diffusion is taking place. Metals annealed at higher temperatures will have experienced greater levels of mobility, allowing the opportunity for adjacent grains of Cu-Zn alloy to coalesce. Relatively large regions devoid of tin were not considered to be a favourable feature. The annealing temperature of 285 °C led to significant blistering, which was also an unfavourable result, therefore consideration had to be given to the quantity of zinc deposited on samples used for future annealing

experiments and the effect this may have on the elemental homogeneity of the samples post annealing.

As can be seen in the images, sulphur was also included in the elemental analysis, despite the fact that these were not sulphurised films. The reason for this was that, although no sulphur was placed in the annealing box when these samples were processed, the furnace that was used for these pre-alloying experiments was also used for sulphurisation experiments, meaning that there was always a small (but unquantifiable) amount of sulphur adhering to the inside furnace walls. Sulphur was therefore included in the elemental analysis as an approximate indicator for the extent to which sulphur was present in the film after pre-alloying. The sulphur signal was significantly weaker than the other three elements and the colour map images appeared feint. In order to enhance the visibility, a filter was applied to the sulphur colour maps to increase the brightness. Observing all four of the individual colour maps for the sample annealed at 285 °C does not reveal any particular affinity for copper to bond with any of the metallic elements preferentially, however, the colour maps for the 320 °C sample suggest that there could be a slight preference for copper to bond with tin. This result was also observed for the samples annealed at 330 °C and 340 °C, but not 300 °C. Although this apparent preference is only weak, it would not be considered favourable to have an uneven distribution of sulphur in the annealed samples.

In order to establish if there were any trends relating to elemental losses and sulphur diffusion with respect to annealing temperature, the elemental abundancies were plotted against temperature for all four of the elements and this graph is presented in Figure 5-9. Observing this graph, there does not appear to be a strong correlation between annealing temperature and atomic abundance for any of the elements. There may be a slight drop in the copper abundance accompanied by a slight increase in the tin abundance as temperature increases, but this is not a strong trend and would also seem unlikely, given the small difference in boiling point between copper and tin (2560 °C [9] c.f. 2586 °C [7]) when compared to that of zinc (907 °C [8]). The sulphur abundance had been expected to increase with respect to temperature as it had been assumed that greater diffusion into the film would take place, however, this did not seem to be evident. These results were seen as reassuring as they suggested

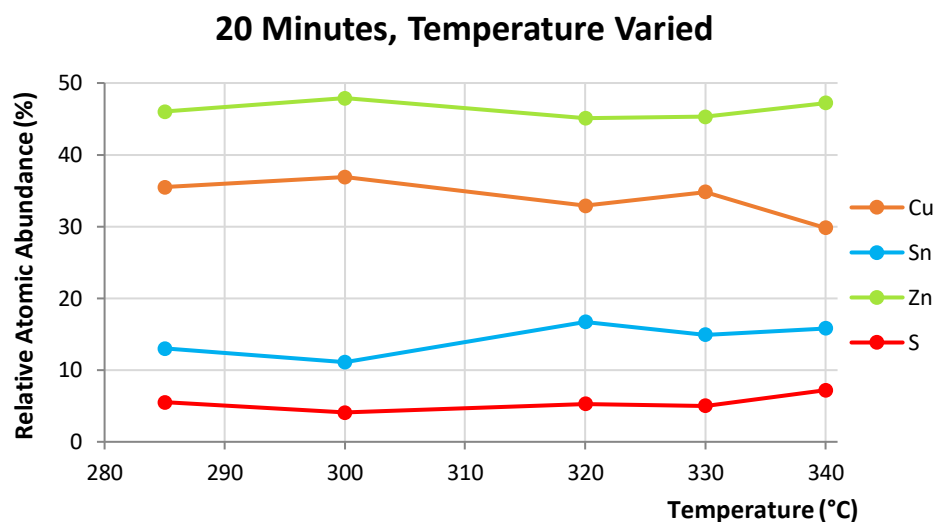


**Figure 5-9 – Elemental abundancies plotted against temperature for the five annealed samples. There are no strong temperature related trends.**

that the factor of elemental losses and sulphur diffusion did not need to be taken into consideration when selecting a pre-alloying annealing temperature, thus simplifying the decision. In order to verify the information gained using the FEG-SEM, further analysis was performed on the samples by means of XRD and XPS depth profiling.

XRD was carried out on all five annealed samples, as well as one unannealed sample electroplated under identical conditions, as described in section 5.2.2.2. As stated previously, the XRD peaks were identified using the Crystallographic Open Database (COD). All of the peak identifications in discussions relating to XRD should be taken to be referenced against this [11, 12, 13, 14, 15, 16, 17]. Six XRD patterns are plotted in Figure 5-10 transitioning from the unannealed sample at the bottom of the graph and gradually increasing in temperature, with the pattern plotted at the top of the graph being for the highest annealing temperature (340 °C). All of the marked peaks that are visible on the sample annealed at 340 °C are also visible for all of the other annealed samples. The unannealed sample appears to have undergone some room temperature alloying – there is one peak that is attributed to CuSn with a sorosite structure at 30.1°, and another at 43.2° that is attributable to a number of phases including sorosite CuSn. The presence of Cu<sub>0.8</sub>Zn<sub>0.2</sub> was also detected by the presence of peaks at 37.6°, 42.0°, 57.7°, and it also shares in the peak at 43.2°. Peaks associated with copper, tin and zinc were also detected and are marked on the pattern plot. For the annealed samples, the peaks relating to sorosite CuSn and Cu<sub>0.8</sub>Zn<sub>0.2</sub> are

### Alloying Anneal, 20 Minutes: XRD

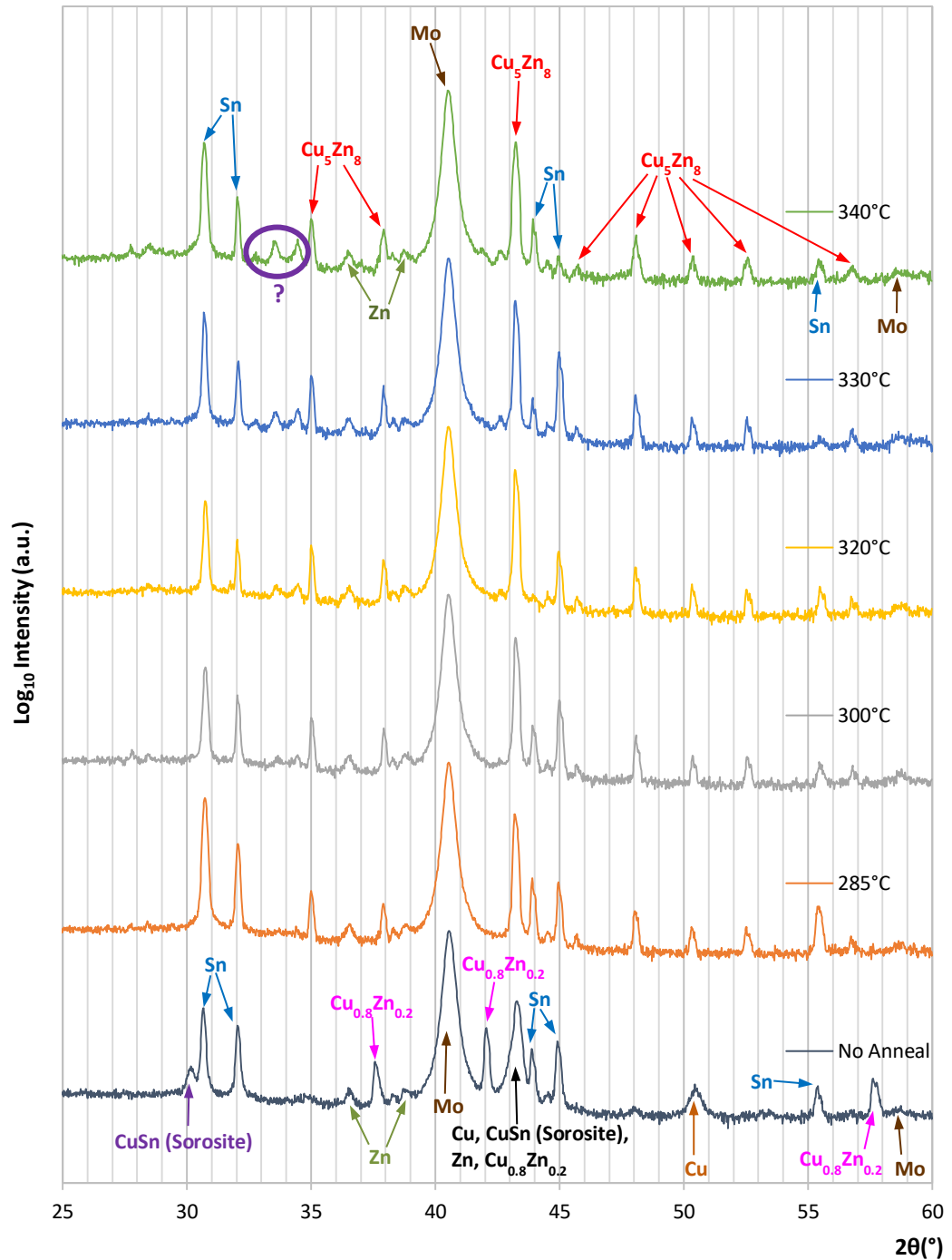


**Figure 5-10 – XRD patterns for the unannealed sample (bottom pattern) and the five annealed samples, the annealing temperature increasing with each pattern plot such that the highest temperature is at the top. Some unidentified peaks have been circled on the uppermost pattern.**

no longer apparent, with the exception of the peak at 43.2°, which has sharpened and has been reattributed to Cu<sub>5</sub>Zn<sub>8</sub> (although it may also be attributed to zinc). The

reason this peak is no longer attributed to sorosite  $\text{CuSn}$ , copper or  $\text{Cu}_{0.8}\text{Zn}_{0.2}$ , is that the other peaks that indicated the presence of these phases in the unannealed sample are no longer present in the diffraction patterns of the annealed samples. A number of additional peaks relating to  $\text{Cu}_5\text{Zn}_8$  are present for the annealed samples at  $35.0^\circ$ ,  $37.9^\circ$ ,  $45.8^\circ$ ,  $48.1^\circ$ ,  $50.3^\circ$ ,  $52.5^\circ$  and  $56.8^\circ$ . All five of the Sn peaks seen for the unannealed sample are also present for the annealed samples, as well as the relatively small peaks relating to zinc. The copper peak at  $50.5^\circ$  seen for the unannealed sample is not present for the annealed samples – although there is a peak present at  $50.3^\circ$  for the annealed samples, this is sharper than the one seen for copper and is attributable to  $\text{Cu}_5\text{Zn}_8$ . If both copper and  $\text{Cu}_5\text{Zn}_8$  were present, the two peaks at similar but slightly different angles would likely lead to the broadening of a peak, not the sharpening. The disappearance of the peaks associated with  $\text{CuSn}$ , copper, and the copper-rich  $\text{Cu}_{0.8}\text{Zn}_{0.2}$  phase suggests that the intermixing of the elements as a result of the annealing processes caused all of the copper to become alloyed with zinc, the zinc being in excess and having some peaks remaining post annealing. The tin present in the annealed samples was not in an alloyed phase due to the preferential alloying of copper with the zinc – the copper was effectively consumed in its entirety by the excess quantity of zinc.

When examining the XRD patterns for temperature related trends, it appears that the degree of alloying is not temperature dependent within the tested range, however, there are a small number of unidentified peaks that have been circled on the plot line for the  $340^\circ\text{C}$  sample. The intensity of these peaks roughly correlate with temperature, being least visible for  $285^\circ\text{C}$ . Attempts to identify them as metal alloys suggested that they may be attributable to  $\text{Cu}_3\text{Sn}$ , however, it would seem unlikely that this phase would be present given the discussion in the preceding paragraph relating to the consumption of copper by excess zinc, and the fact that the other peaks that would be associated with this phase were not seen. It was considered most likely that these peaks were as a result of the presence of oxide or sulphide phases, the identification of which would have been very time consuming given the sheer number of potentially attributable phases listed on the database. It was therefore inferred that a lower annealing temperature would be favourable for the avoidance of unwanted oxide or sulphide phases. More information regarding the diffusion of



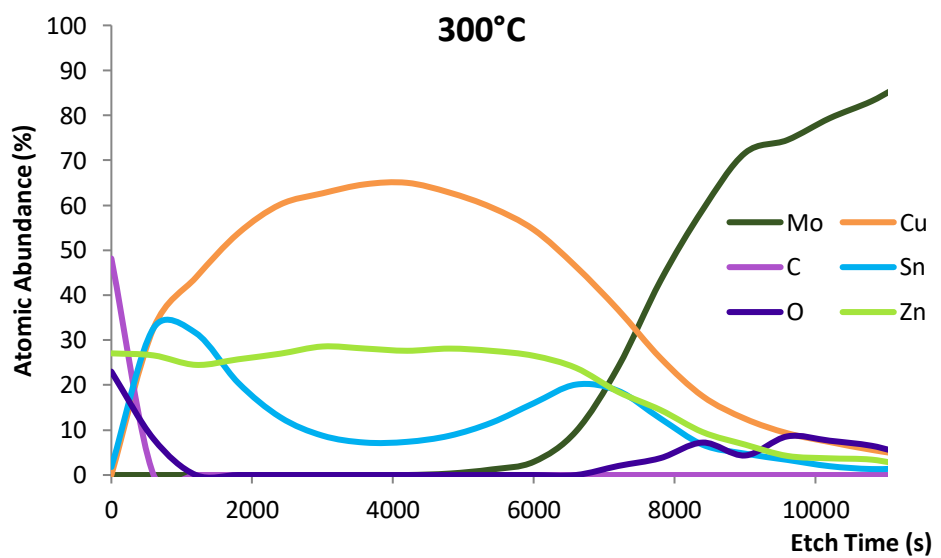
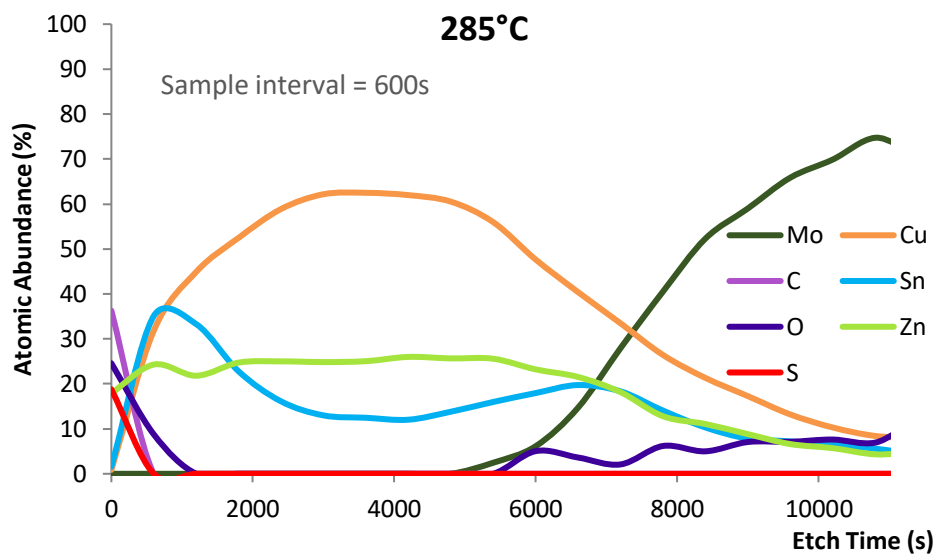
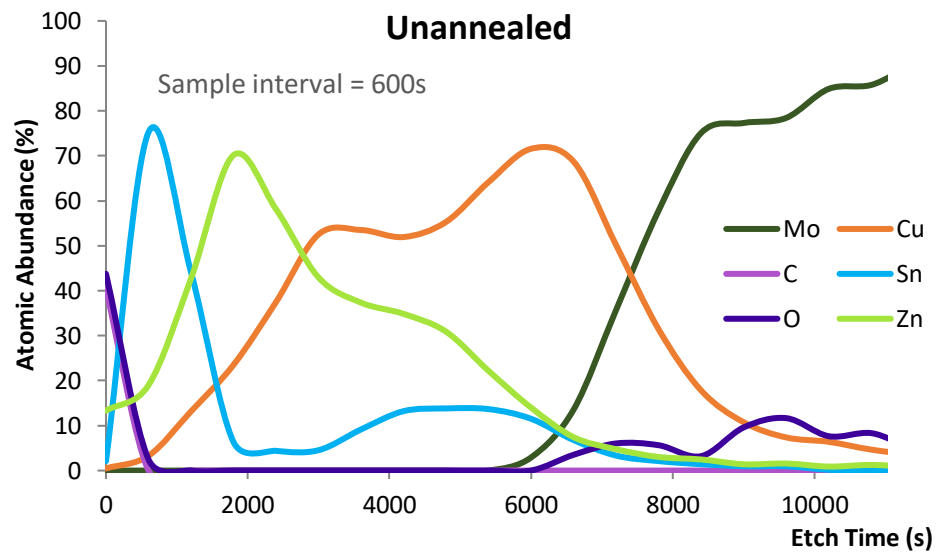


**Figure 5-11 (part 1)**

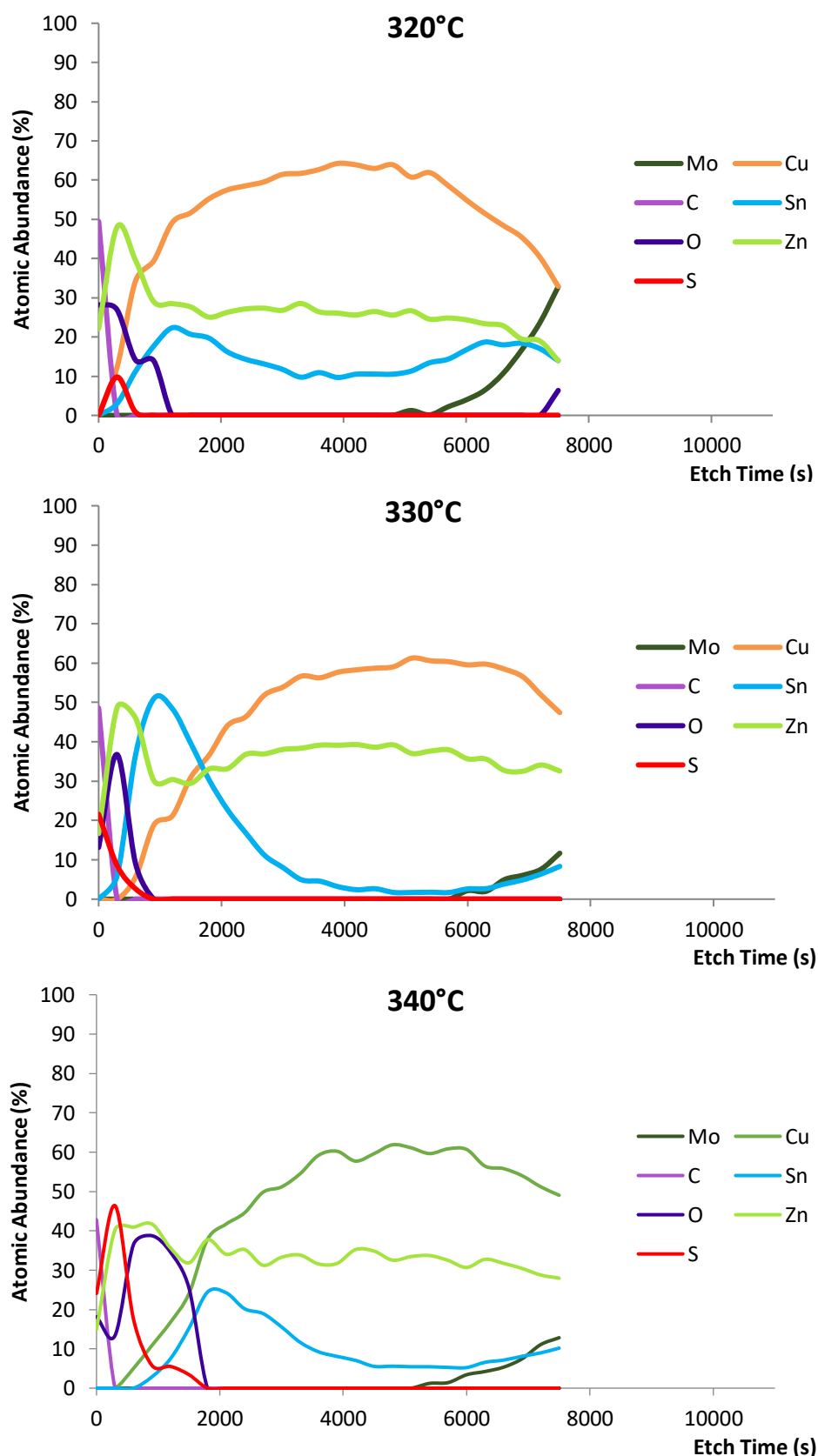


**Figure 5-11 – XPS depth profiles of an unannealed sample as well as the five annealed samples. There appears to be some vertical separation of copper and tin on the annealed samples. There also appears to be greater diffusion of oxygen and sulphur into the film at higher temperatures.**

oxygen and sulphur into the metals can be gained through the means of XPS depth profiles.

XPS depth profiles for each of the annealed samples and an unannealed sample electroplated under identical conditions are presented in Figure 5-11 (details of the XPS depth profiling settings are given in section 5.2.2.3). It appears that some technical issues were experienced during the execution of the XPS experiments as the depth profiles for the three latter samples were terminated after 7,500 s rather than the required 11,000s. In addition to this, the detection of sulphur was erroneously omitted from the profile performed on the sample annealed at 300 °C. Despite these problems, it is still possible to obtain useful information from the profile graphs. All of the annealed samples display a similar profile pattern for copper, tin and zinc, and are substantially different in appearance to that of the unannealed sample. A detailed discussion of possible reasons for obtaining the results seen in the profile of the unannealed sample is given in section 4.3.7.1, these reasons relating to the fact that there are three layers of different deposited metals and that they have a granular structure. These factors were considered likely to subside once the metals had intermixed, leading to a more accurate picture of the true elemental profile being obtained through the XPS depth profiles. It can be seen that on all of the annealed samples, the zinc has become dispersed with a relatively consistent abundance throughout the thickness of the deposited metal, with some deviation seen in the form of a modest peak present on the profiles of samples annealed at 320 °C and 330 °C at approximately 300 s etching time. This is very much in contrast to the strong peak seen at 1800 s on the unannealed sample. Similarly, the tin appears to have dispersed to an extent, with the tin abundance being greater near the interface with molybdenum on the annealed samples. Copper has also shown signs of dispersion, with a shift towards greater abundancies being seen earlier in the etching process than seen on the unannealed sample. There is, however, a significant difference between the profiles seen for each of the three deposited elements on the annealed samples. Copper appears to be most abundant in the centre of the deposited film, whereas tin displays two peaks which are positioned near the top and near the bottom of the film – the tin abundance is approximately inversely proportional to that of the copper. In contrast, the zinc abundance remains at a

similar value throughout the thickness of the film. It could be hypothesised that as copper diffuses upwards from the bottom of the deposit and tin diffuses downwards from the top, a Cu-Zn alloy starts to form in the area at which they meet in the centre. Due to the positive free energy of mixing of copper and zinc, and the negative free energy of mixing of zinc and tin [18], this region becomes rich in the Cu-Zn alloy, displacing the tin such that it diffuses away from the centre, creating tin-rich regions at the top and bottom of the film.

In addition to the observations made with regard to the electrodeposited elements, it is possible to see that the samples alloyed at 320 °C or above suffered increased oxygen diffusion into the films, and, in the case of the sample annealed at 340 °C, increased sulphur diffusion as well. Both of these are undesired effects, and these observations support the hypothesis that the circled peaks in Figure 5-10 correspond to oxides and/or sulphides. The XPS depth profiles suggest that 285 °C is sufficiently hot to cause the desired intermixing and alloying, as do the XRD patterns. The EDS colour maps also suggest that there may be some advantage in choosing this temperature rather than any of the higher temperatures as the lateral conglomeration of Cu-Zn rich grains was found to be less substantial on the corresponding sample. Conversely, the visual observations and the SEM images revealed that there was significantly more blistering occurring on the sample annealed at 285 °C. Film integrity is considered important in the further processing of the film, particularly in the deposition of subsequent layers – blisters could cause the buffer layer to come into contact with the molybdenum substrate, leading to electrical shunting in a finished device, for example. For these reasons, it was considered that 300 °C offered the best compromise – there was no increase in oxygen diffusion into the film, unlikely to be raised sulphur diffusion levels (from observing other XPS depth profiles of samples annealed at less than 340 °C), and no more substantial blistering than that seen on any of the other samples. The same degree of alloying and intermixing was seen at this temperature as for all of the other temperatures tested. It was therefore chosen as the temperature to be used in the next batch of pre-alloying experiments, which were focussed on optimising the annealing duration.

For the next set of experiments, which focussed on optimising the annealing duration, precursor samples were prepared by the electroplating of copper, tin and

zinc, as described in section 5.2.1.1. The copper and tin layers were deposited using the same parameters as the sample in the previous batch, however, a thinner zinc deposit was used because additional information on deposition efficiency had become available through MP-AES experiments in the meantime. Samples were annealed for time durations varying from 5 to 40 minutes at a temperature of 300 °C. Unfortunately, photographs were not obtained of these samples, however their appearance was most similar to that of the sample annealed at 300 °C in Figure 5-4, although slightly lighter in colour with less of a copper-like tint. There was no significant difference between the appearance of each of the samples in the time varied batch, and, although some blistering was evident, it was confined to the very edges of the films.

SEM images, as well as EDS colour maps were acquired using a FEG-SEM, and SEM images of three of the annealed samples (annealed at 5, 10 and 40 minutes respectively) are presented in Figure 5-12. When observing the higher magnification images (10,000X, top), it is possible to see that an irregular grain structure has been obtained. The films exhibit good coverage and no evidence of dewetting is seen.

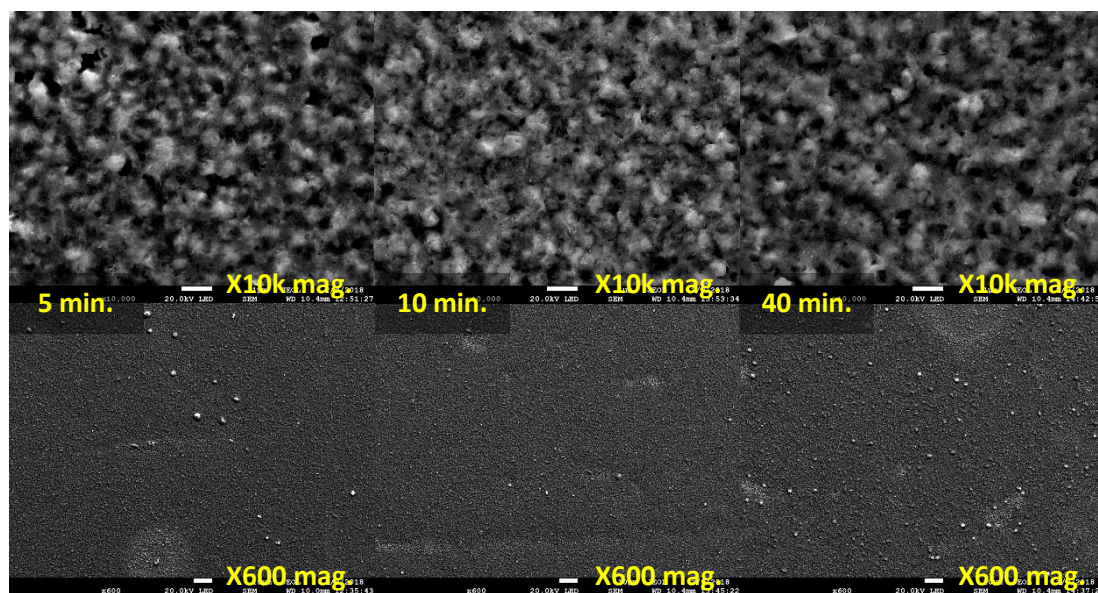


**Figure 5-12 – SEM images (obtained using a FEG-SEM with an acceleration of 20 kV) of three of the five samples annealed at 300 °C at a range of durations. Each sample has a similar grain structure, however, there are a greater number of blisters seen on the sample annealed for the longest duration. The scale bars represent 10 µm on the 600x magnification images and 1 µm on the 10,000x magnification images.**

There may be some slight cracking visible in the top left of the image corresponding to the sample annealed for 5 minutes, but in general there are no duration related trends observed. When the lower magnification images (600X, bottom) are observed, it can be seen that some blistering of the films has occurred. The film annealed for 40 minutes displays the greatest number density of blisters ( $\sim 10$  per  $900\ \mu\text{m}^2$ ), the blisters being  $\sim 4\ \mu\text{m}$  in diameter, whereas the film annealed for 5 minutes has the largest blisters ( $\sim 5\text{-}7\ \mu\text{m}$  in diameter) with a number density of  $\sim 5$  per  $900\ \mu\text{m}^2$ . The sample annealed for 10 minutes exhibits a desirable combination of a similarly low blister number density to that of the sample annealed for 5 minutes and the smaller blister size seen on the sample annealed for 40 minutes.

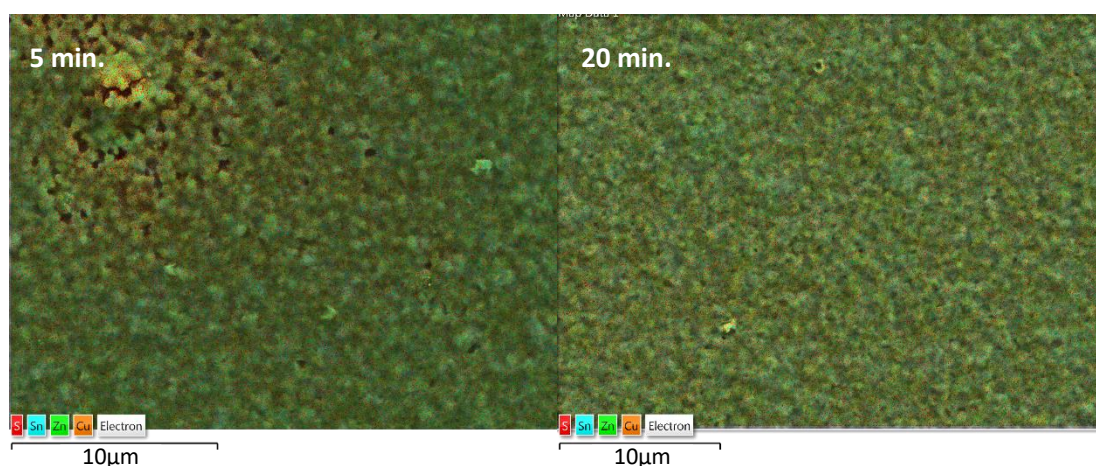


**Figure 5-13 – Layered EDS colour maps for the sample annealed for 5 minutes (left) and 20 minutes (right).**

When layered EDS colour maps were obtained (Figure 5-13), the separation of tin from the other two metals was not clearly visible for any of the samples (5 minute and 20 minute anneals are presented as an example), however, when the individual colour maps (Figure 5-14 and Figure 5-15) are examined it is possible to see that some separation has occurred. The degree of separation appeared less on the sample annealed for 5 minutes than on the samples with longer annealing times, as is evident when the individual colour maps for the samples annealed for 5 minutes (Figure 5-14) and 20 minutes (Figure 5-15) are compared. This suggests that intermixing and alloying of the elements has been achieved to a lesser extent on the sample annealed for 5 minutes than on the other samples. What is also evident when examining the



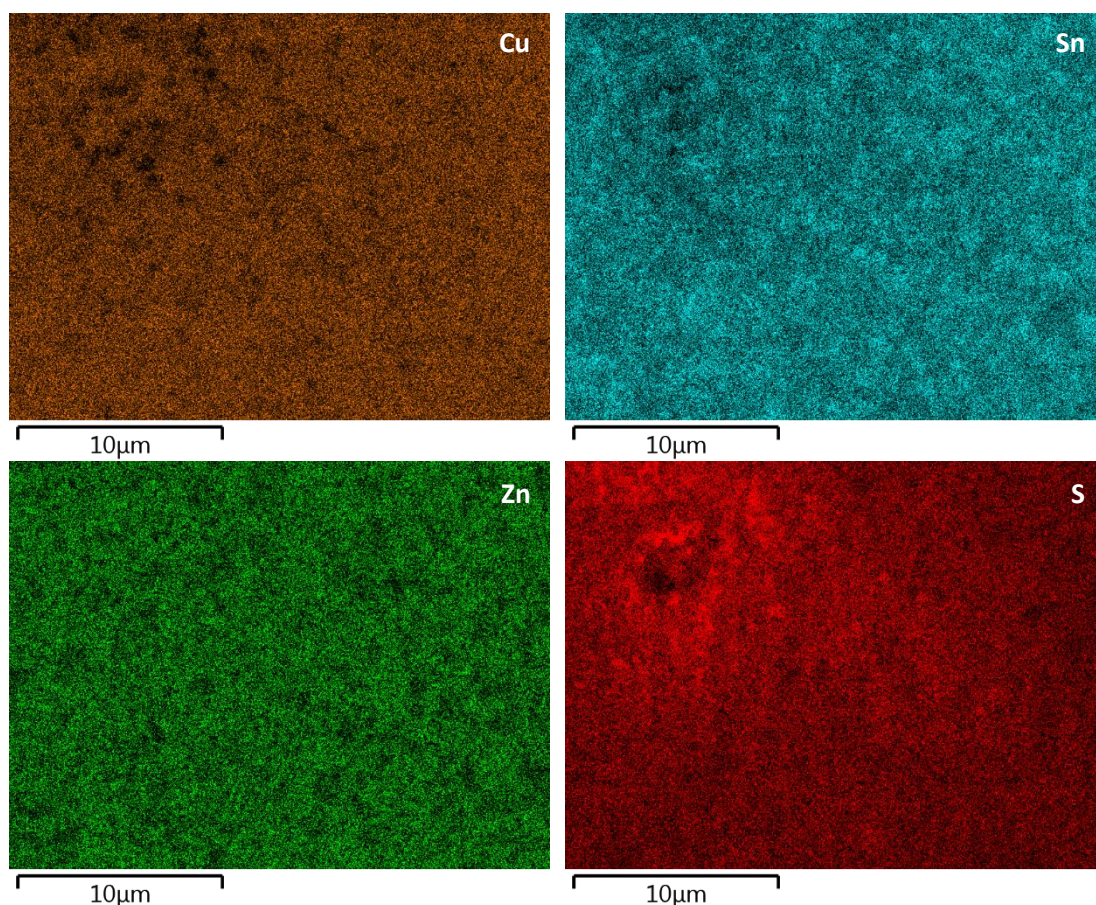


**Figure 5-14 – Individual elemental colour maps for the sample annealed for 5 minutes, showing a slight separation between the zinc and the tin.**

colour maps, is that the larger conglomerated regions of Cu-Zn alloys have not materialised in the way that is seen for the previous batch (temperature varied) samples, which were electrodeposited with a thicker zinc layer when originally prepared. When examining the colour maps in Figure 5-14 (5 minute anneal), the relatively weak separation effect that is visible for the zinc and tin makes it impossible to discern whether the copper is exhibiting a preferential co-siting with any of the other elements, however, for samples annealed for 10 or more minutes, it is possible to see that copper is not exhibiting preferential co-siting – it does not conform to either of the separation patterns exhibit by tin or zinc. The likely reasoning for this is as follows: Unlike the previous (temperature varied) batch of samples, there is no excess of zinc due to a thinner film of zinc being deposited during the precursor stack preparation. Copper will have alloyed with zinc preferentially, however, once the majority of zinc has alloyed with copper, there remains an excess of un-alloyed copper. This remaining copper is available to alloy



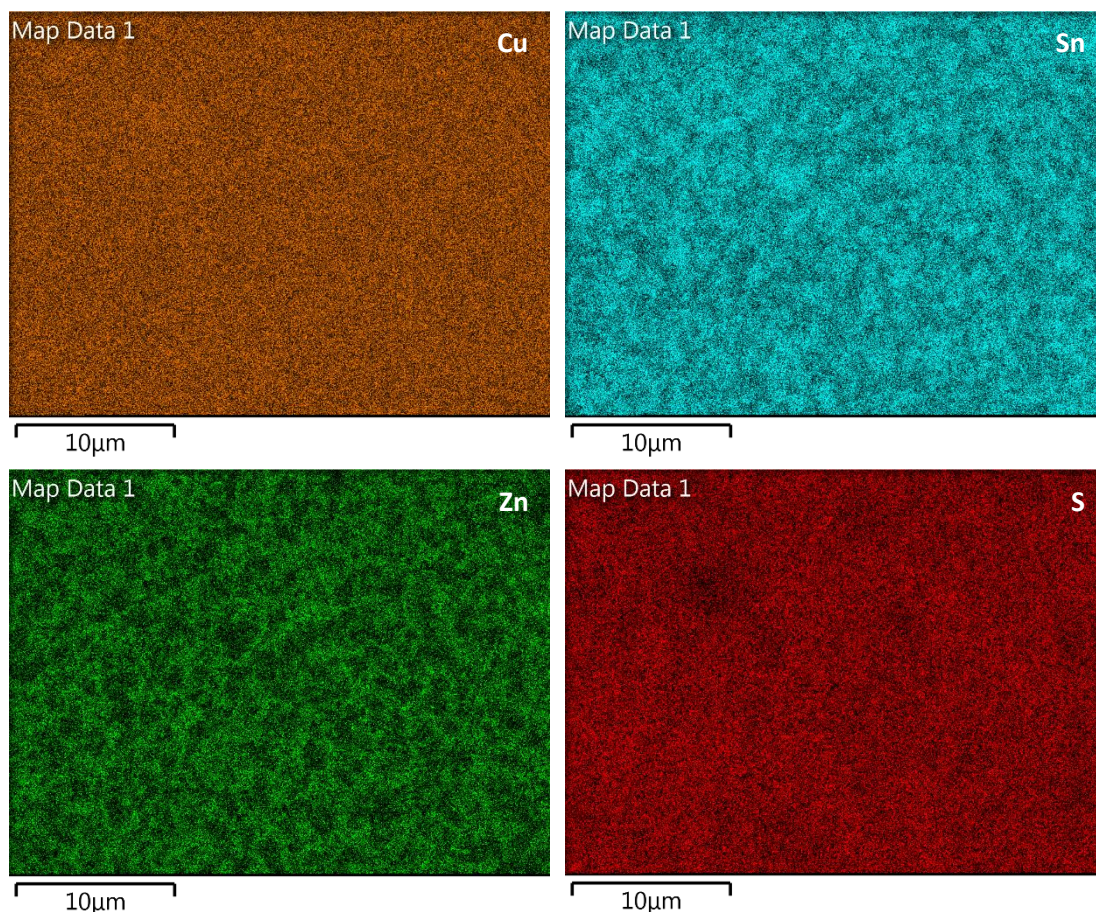


**Figure 5-15 – Individual elemental colour maps for the sample annealed for 20 minutes, showing an increase in separation between the zinc and the tin when compared to the sample annealed for 5 minutes. Copper appears to have an even dispersion.**

with tin. It can be predicted that when XRD patterns are analysed for the duration varied batch of samples, the annealed films will display some Cu-Sn phases that were not present in the previous (temperature varied) batch of samples. It is also noteworthy that the colour map for sulphur does not indicate any preferential co-siting of sulphur with any of the other elements.

EDS was used to obtain elemental abundancies on four of the five annealed samples and the abundancies are plotted against annealing duration for copper, zinc, tin and sulphur in Figure 5-16. There do not appear to be any trends in abundance that relate to the annealing duration – this is reassuring as it reinforces the hypothesis that no significant elemental losses are occurring at this temperature. There is a slightly raised abundance of copper on the sample annealed for 20 minutes, but this is not a



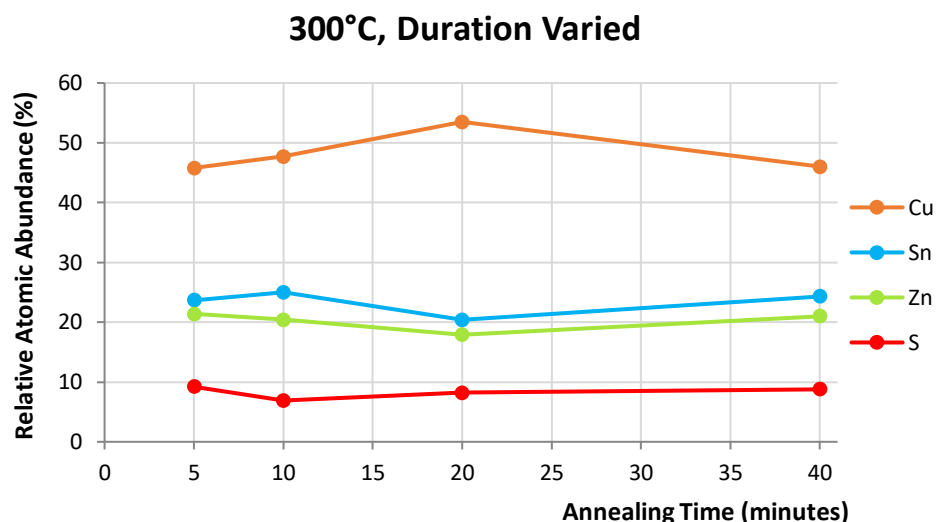


**Figure 5-16 - Elemental abundancies plotted against annealing duration for four of the annealed samples. There are no strong duration related trends.**

continuing trend and has been assumed to be an anomalous result. Further analysis was carried out on these samples by means of XRD and XPS depth profiles.

XRD was carried out on all five annealed samples, as well as one unannealed sample electroplated under identical conditions, as described in section 5.2.2.2. As a reminder to the reader, all of the peak identifications in discussions relating to XRD should be taken to be referenced against the COD [11, 12, 13, 14, 15, 16, 17]. Six XRD patterns are plotted in Figure 5-17 transitioning from the unannealed sample at the bottom of the graph and gradually increasing in annealing duration, with the pattern plotted at the top of the graph being for the longest annealing duration (40 minutes). All of the marked peaks that are visible on the sample annealed for 40 minutes are also visible for all of the other annealed samples. In common with the previous (temperature varied) batch of samples, the unannealed sample appears to have undergone some room temperature alloying – there is one small peak that is attributed to CuSn with a sorosite structure at 30.1°, and another peak at 43.2° that is attributable to a number of phases including sorosite CuSn. The presence of Cu<sub>0.8</sub>Zn<sub>0.2</sub> was also detected by the presence of peaks at 37.6°, 42.0°, 57.7°, and it also shares in the peak at 43.2°. As previously, peaks associated with copper, tin and zinc were also detected and are marked on the pattern plot. For the annealed samples, in common with the previous batch, the peaks relating to Cu<sub>0.8</sub>Zn<sub>0.2</sub> are no longer

### Alloying Anneal, 300°C: XRD

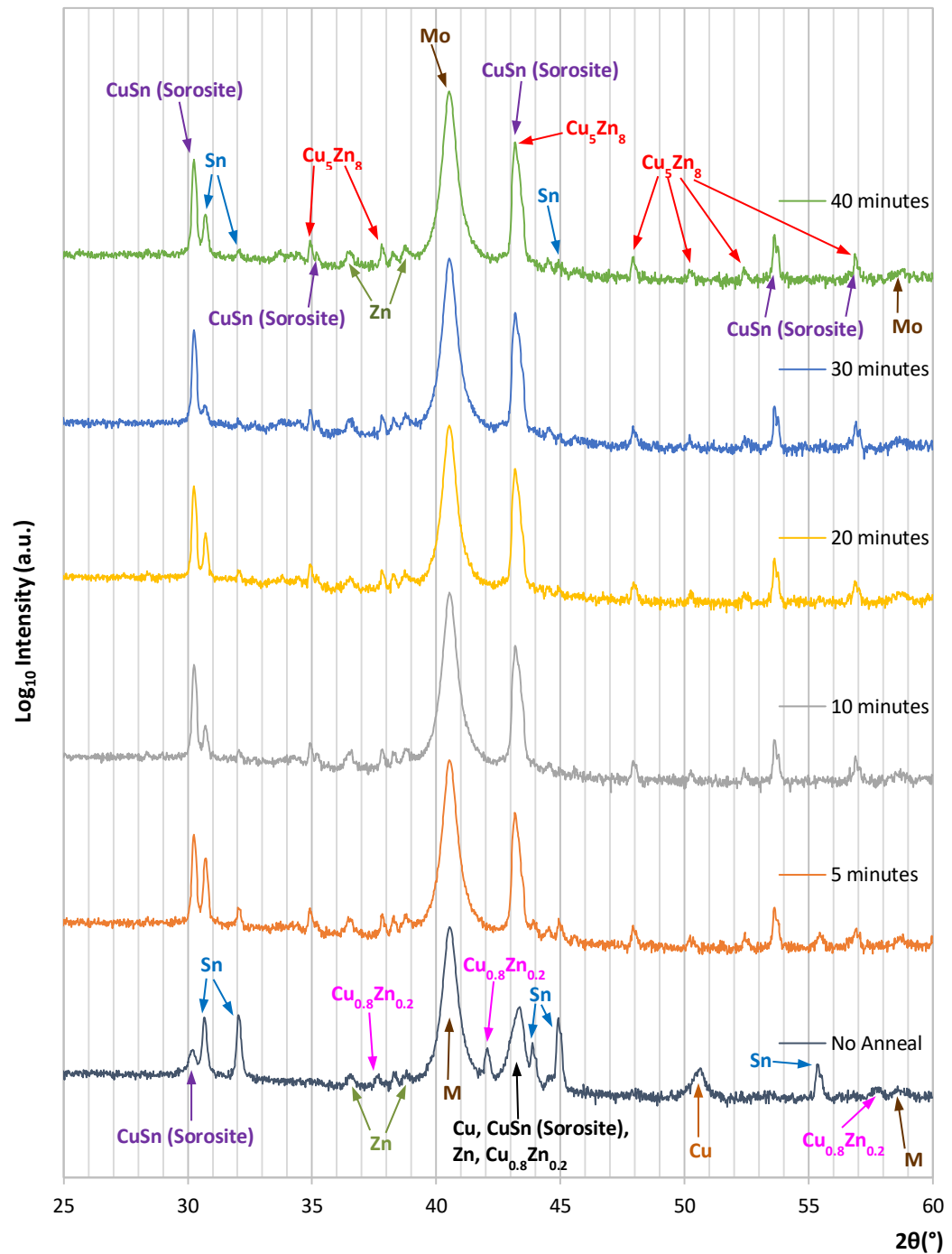


**Figure 5-17 – XRD patterns for the unannealed sample (bottom pattern) and the five annealed samples, the annealing duration increasing with each pattern plot such that the longest duration is at the top.**

apparent, with the exception of the peak at  $43.2^{\circ}$ , which has sharpened and has been reattributed to  $\text{Cu}_5\text{Zn}_8$  and sorosite  $\text{CuSn}$  (although it may also be attributed to zinc) as the other peaks that indicated the presence of copper and  $\text{Cu}_{0.8}\text{Zn}_{0.2}$  in the

unannealed sample are no longer present in the diffraction patterns of the annealed samples. Also in common with the previous sample batch are the additional peaks relating to  $\text{Cu}_5\text{Zn}_8$  present for the annealed samples ( $35.0^\circ$ ,  $37.9^\circ$ ,  $45.8^\circ$ ,  $48.1^\circ$ ,  $50.3^\circ$ ,  $52.5^\circ$  and  $56.8^\circ$ ). There are, however, several differences between this (time varied) set of samples and the previous (temperature varied) set. Firstly, the sample annealed for just 5 minutes exhibits some peaks in common with the unannealed sample that are not visible for the samples annealed for 10 minutes or more. These are peaks relating to tin at  $55.3^\circ$  and  $43.9^\circ$ . The other peaks relating to tin ( $30.8^\circ$ ,  $33.0^\circ$  and  $45.0^\circ$ ) have not subsided as much after 5 minutes of annealing as they have after 10 minutes or more. Secondly, sorosite  $\text{CuSn}$  peaks have become enhanced ( $30.1^\circ$ ) or apparent ( $35.1^\circ$  and  $53.6^\circ$ ) on the annealed samples, when in the previous batch they were eliminated upon annealing. Thirdly, the tin peaks have either subsided or been eliminated on the annealed samples, whereas in the previous batch the tin peaks were not substantially affected by the annealing process. The first of these three differences suggests that 5 minutes is insufficient time for the deposited metals to fully intermix and alloy at this temperature ( $300^\circ\text{C}$ ), hence the relatively weak elemental separation seen in the EDS colour maps for the corresponding sample. The second and third differences also support the findings of the analysis of the EDS colour maps in suggesting that the smaller quantity of deposited zinc has not led to the full “consumption” of copper into a Cu-Zn alloy, leaving some copper available to alloy with tin. This is considered a more favourable result as it leads to a more even dispersion of the elements in the annealed films.

XPS depth profiles for four of the five annealed samples, as well as one unannealed sample that was electroplated under identical conditions, are presented in Figure 5-18 (details of the XPS depth profiling settings are given in section 5.2.2.3). It is possible to see that significant dispersion has occurred on all of the annealed samples, with the peaks in abundance for copper, tin and zinc having subsided and broadened. For samples annealed for 10 minutes or longer, there is no increase in the degree of dispersion with respect to annealing duration, suggesting that full intermixing of the elements is achieved after 10 minutes of annealing at  $300^\circ\text{C}$ . The depth profile for the sample annealed for only 5 minutes is relatively rich in tin, and has a lower abundance of copper, for the first  $\sim 1000$  s of etching. This suggests that full

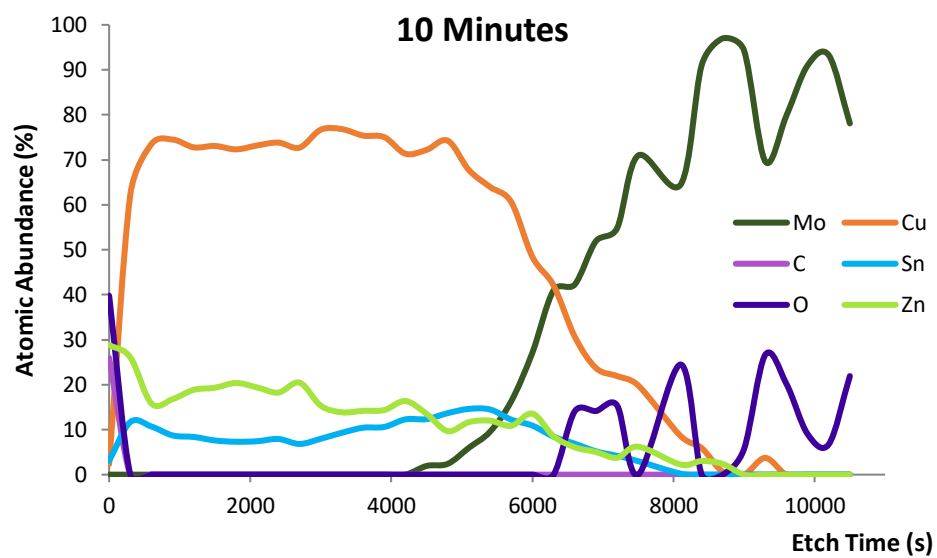
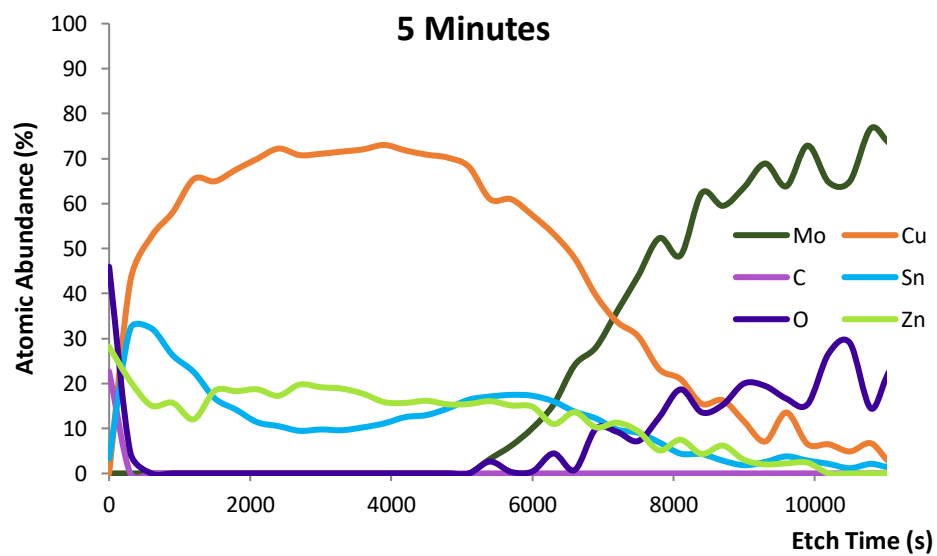
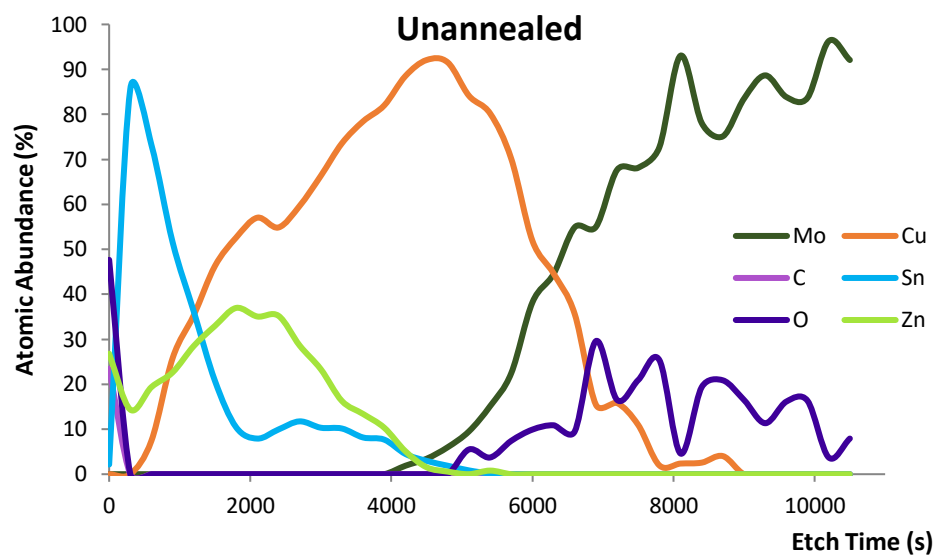
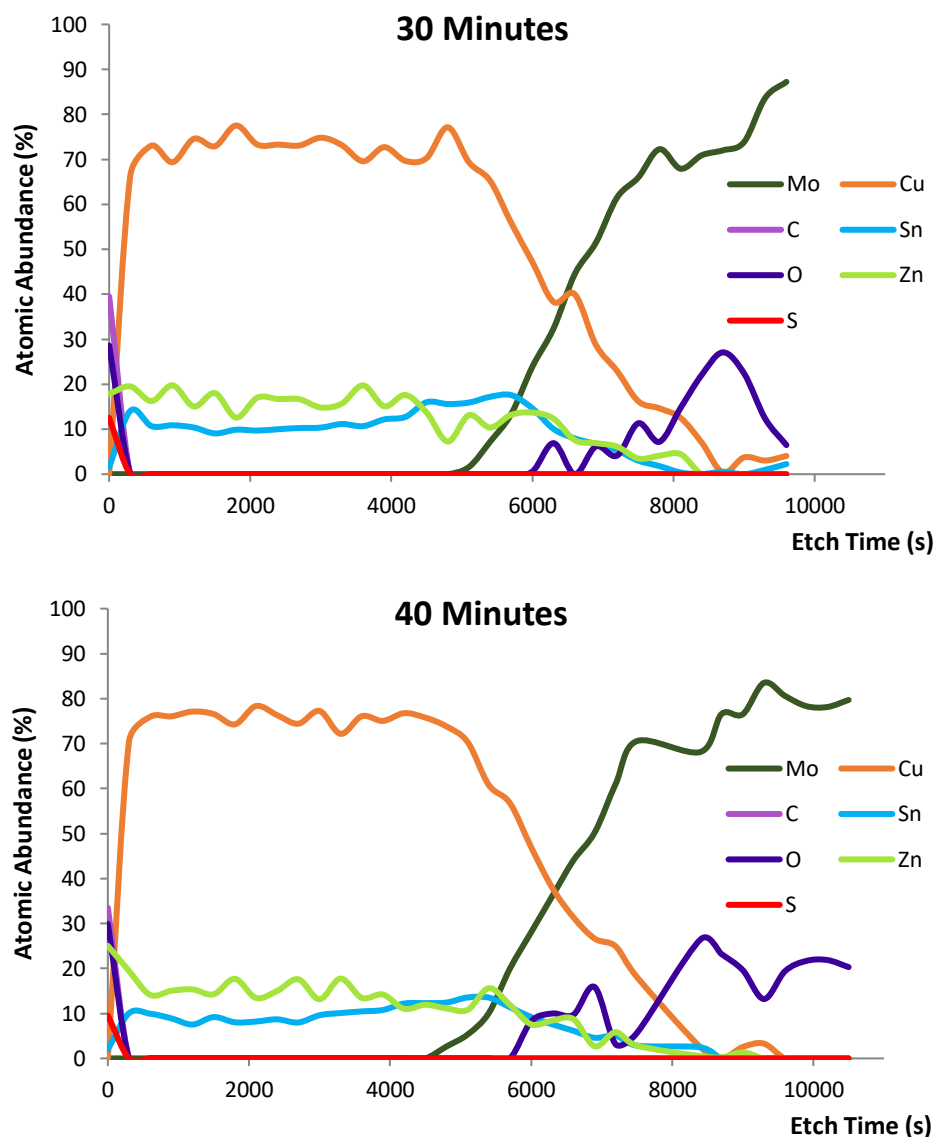


Figure 5-18 (part 1)



**Figure 5-18 – XPS depth profiles of an unannealed sample and four of the annealed samples. Full intermixing of the deposited elements appears to occur on samples annealed for 10 minutes or longer.**

intermixing and alloying has not occurred after this duration, in agreement with the XRD data. It is noted that all of the annealed samples indicate an increase in tin abundance at ~4000-6000 s of etching, although the explanation for this remains unknown. A favourable result seen in these depth profiles is that oxygen does not appear to have diffused into the films, and sulphur (where included in the analysis for longer annealing durations) has also not undergone significant diffusion into the films, the abundancies for oxygen and sulphur both reaching zero by the first sample point at 300 s into the etching process.

The decision was taken that 10 minutes at 300 °C was an appropriate time and temperature to be used for the pre-alloying process. The information available indicated that 5 minutes was insufficient to fully intermix the constituent elements, and that there were no additional benefits to annealing the samples for 20 minutes or more. What also became apparent from the data relating to the two sets of pre-alloying experiments was the importance of controlling the elemental ratios – in this case through the quantity of deposited zinc – as this has substantial effects on the ability of the elements to fully disperse throughout the annealed film without forming regions that are rich in copper and zinc but depleted of tin, or vice versa. Having optimised the conditions for the pre-alloying process, the focus was shifted to optimising conditions during the sulphurisation process, particularly as a preliminary experiment had indicated that blistering may be a problem. This was initially approached by adjusting the background pressure in the furnace, which will be discussed in the next section.

### **5.3.2 Reducing Blistering and Optimising Pressure During Sulphurisation**

Initial sulphurisation experiments were carried out in which conditions were used that had been optimised for the sulphurisation of spin-coated solution processed CZTS films. The reason these parameters were chosen was as part of a trial and error process and a familiarisation exercise in the use of the RTP furnace. They had already been established as successful in the sulphurisation of other CZTS films and served as a simple starting point. The furnace settings are given in Table 5-1 in section 5.2.1.2, and the other annealing parameters used were a background pressure of 300 Torr and a sulphur mass of 100 mg. All of the films discussed in this subsection had an area of 4 cm<sup>2</sup> and did not undergo a pre-alloy annealing treatment. The pre-alloying was omitted as there was a desire to optimise the two processes separately, and test the benefits of pre-alloying in a later set of experiments. The first film to undergo a sulphurisation process had been electrodeposited with copper, tin and zinc in a three-layer stack (as described in section 5.2.1.1), with a relatively thick zinc film being utilised as the deposition efficiency data had not yet been fully acquired and analysed at this stage in the experimentation. The results of this initial annealing process can be seen in Figure 5-19, in which a photograph of the annealed film is presented. It is evident that extensive blistering had occurred throughout the



**Figure 5-19 - A sulphurised film displaying extensive blistering and evidence of the rupturing of material from the central area of the sample. This film was prepared using a three-layer electroplated stack and was annealed at 550 °C with 100 mg of sulphur and a background pressure of 300 Torr.**

film, and there is also a substantial difference in colour that occurs across a distinct but jagged line near the perimeter, appearing as if material had ruptured out of the more central area of the deposit. Consulting relevant literature and conferring with collaborative colleagues led to the belief that this blistering may have been as a result of tin escaping from the sample during the sulphurisation process. The drop in tin content during sulphurisation of CZTS films is documented in literature [6, 19], as the tin escapes in the form of gaseous tin sulphide. It is reported in [20] that stacking configurations in which copper layers were deposited above tin layers minimised the tin losses for samples in which precursors were deposited through sputtering. For this

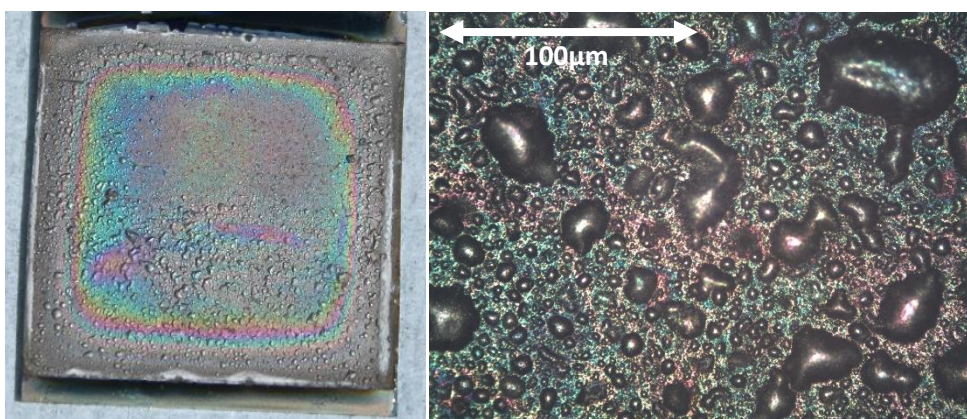
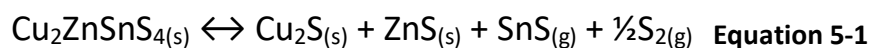


**Figure 5-20 - A sulphurised film prepared from a four-layer stack and annealed with 100 mg sulphur at a background pressure of 300 Torr. It can be seen that extensive blistering has occurred on this sample.**

reason, a trial was conducted in which a four-layer stack (Cu-Sn-Cu-Zn, deposited as described in section 5.2.1.1) was subjected to the same sulphurisation process as described for the previous sample. This film can be seen in Figure 5-20, where a photograph is presented alongside a microscope image. Although from examining the photograph it appears that the rupturing of material seen on the previous sample has not occurred in this instance, suggesting that tin loss may have been suppressed to an extent by the second copper layer, substantial blistering did still occur, as can be seen in the microscope image. The surface of the film is almost entirely covered in blisters of up to ~70 µm across. For this reason, further optimisation was required, and the decision was taken to place the initial focus on the background pressure in the furnace. In literature, it is more common for relatively low background pressures to be reportedly used when sulphurising metallic precursors for CZTS, for example 22.5 Torr (maintained under gas flow) [21] or 5 mTorr (sealed at commencement of annealing) [6]. A pressure as low as 5 mTorr would have been difficult to maintain using the furnace apparatus available during this project, however, pressures in the hundreds of mTorr were achievable. Collaborative researchers in another institution had found that using a background pressure of 3.75 Torr for the sulphurisation of metallic precursors deposited via sputtering in the manufacture of CZTS returned favourable results in comparison to higher pressures, which was also taken into consideration. It was therefore decided that a pressure range of 150 mTorr to 30.0 Torr would be appropriate for the optimisation trials. Some consideration also needed to be given to the mass of sulphur used as this also affects tin losses during sulphurisation. At temperatures above 500 °C, CZTS can break down according to the following equation [19]:



Sufficiently high pressures of the gaseous phases cause the equilibrium to shift to the left, such that CZTS is obtained and tin losses are reduced [19]. This suggests that increasing the quantity of sulphur placed into the graphite annealing box could suppress the loss of tin and the associated blistering. It is also reported in [21] that increasing the mass of sulphur reduced tin losses. The sulphur mass used by the aforementioned research collaborators, who were using a graphite annealing box of the same dimensions as that used in this project, was 250 mg. For these reasons, the



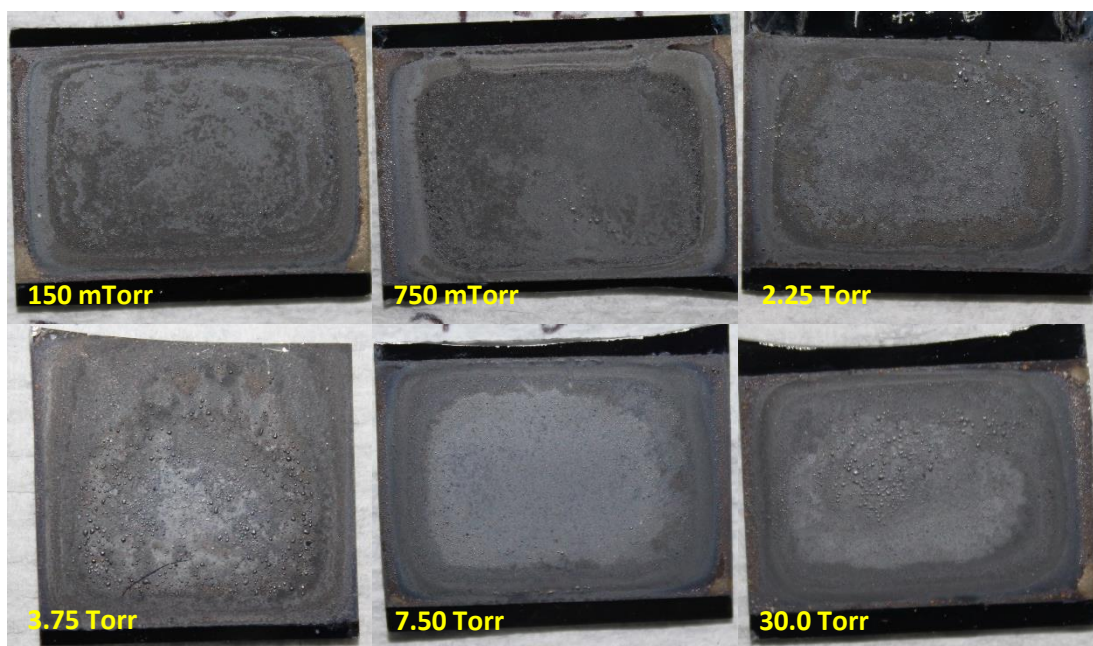


**Figure 5-21 - Six samples sulphurised at a range of background pressures, the pressures being no greater than one tenth of that used previously. It is possible to see that the blistering is greatly reduced compared to those sulphurised at 300 Torr, although it is not possible to see a trend within the selected range.**

mass of sulphur placed into the annealing box was increased from the 100 mg used previously to 250 mg during the set of experiments focussed on optimising the background pressure.

Six precursor stacks were prepared as described in section 5.2.1.1. A three-layer stack configuration was used as it was hoped that film blistering could be minimised without the need for a second copper layer, thus keeping to a simpler electrodeposition procedure. Relatively thick zinc films were deposited as the films were prepared prior to the completion of zinc deposition efficiency experiments. Having carried out sulphurisation of the samples using the heating settings given in Table 5-1 (see section 5.2.1.2), the samples were photographed, and these images are presented in Figure 5-21. It is possible to see that, although some blistering is evident on all of the samples, it is substantially less severe than that seen on the previous two sulphurised samples (presented in Figure 5-19 and Figure 5-20). Although the sample annealed at 7.50 Torr does appear to have fewer large blisters than the other samples, no correlation between the background pressure and the resultant extent of blistering can be seen. Further analysis of the samples was required in order to establish an optimum background annealing pressure.

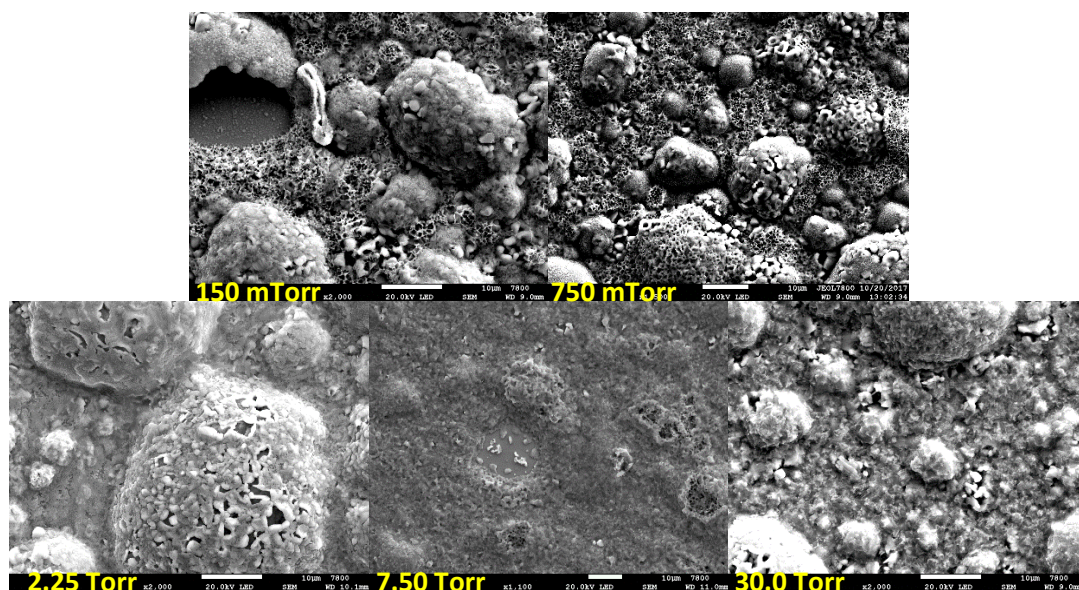


**Figure 5-22 - SEM images of five samples sulphurised at a range of background pressures. Samples sulphurised at lower pressures appear to exhibit more porous films, whereas higher pressures led to more granular appearance. The white scale bar on each image represents 10 µm and an acceleration of 20 kV was used.**

SEM images were obtained of five of the six sulphurised samples (using a FEG-SEM), the images being presented in Figure 5-22. Once the differences in magnification are taken into account, it can be seen that each sample experienced a similar degree of blistering, both in terms of blister size and blister coverage. It appears that films that were annealed at the two lowest background pressures had highly irregular structures, with some regions appearing granular (particularly on blisters) and other regions having a porous appearance. Higher pressures led to slightly more consistent films that were more granular, which may be considered more favourable.

To try and ascertain if there were any pressure related trends in the elemental abundancies, which could indicate trends in the quantity of unwanted phase formation, atomic abundance data was plotted on a suitable graph. A graph displaying atomic abundancies plotted against background pressure for four of the samples is presented in Figure 5-23. The initial impression given by this graph is that there could be a correlation between zinc abundance and pressure, suggesting that more zinc is lost at lower background pressures, while other elements remain

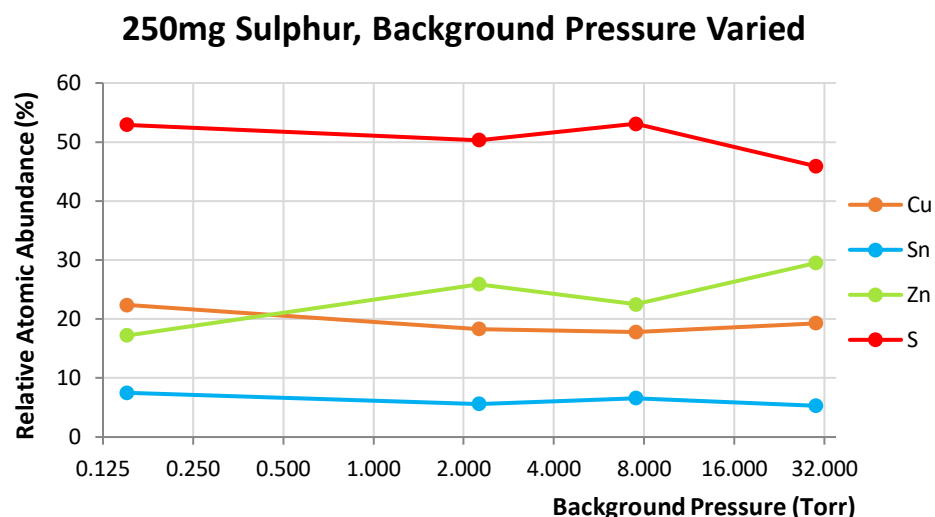


**Figure 5-23 - Elemental abundancies plotted against sulphurisation background pressure for four different pressures. Please note the logarithmic (base 2) scale for the pressure on the horizontal axis.**

unaffected. Closer inspection reveals that, not only does the zinc abundance not increase between every increase in pressure, but as the greatest increase is between the lowest and second-lowest pressure, it would only take one anomalous result at the lowest pressure to have caused this apparent trend. It was therefore considered that the data may not indicate a pressure related trend for any of the elements. It was of particular concern prior to obtaining this EDS data that there could have been a trend in the abundance of tin, as tin loss was the suspected cause of blistering on samples sulphurised previously, therefore the lack of pressure related trend was considered a useful piece of information. It is however, worth noting, that the abundance of zinc would be expected to be less than that of copper in a CZTS sample, the opposite of which is indicated for three of the four samples. This suggests that the quantity of zinc in the sulphurised samples was more than that required and supports the hypothesis that zinc sulphide could be present as a secondary phase (the surplus zinc being available to react with the sulphur vapour in the furnace). In order to gain further information about the phases from which the films were comprised, analysis was carried out using XRD and Raman spectroscopy.

XRD was carried out on the sulphurised samples as described in section 5.2.2.2. As a reminder to the reader, all of the peak identifications in discussions relating to XRD should be taken to be referenced against the COD [11, 12, 13, 14, 15, 16, 17]. XRD

## 250mg Sulphur, Background Pressure Varied: XRD

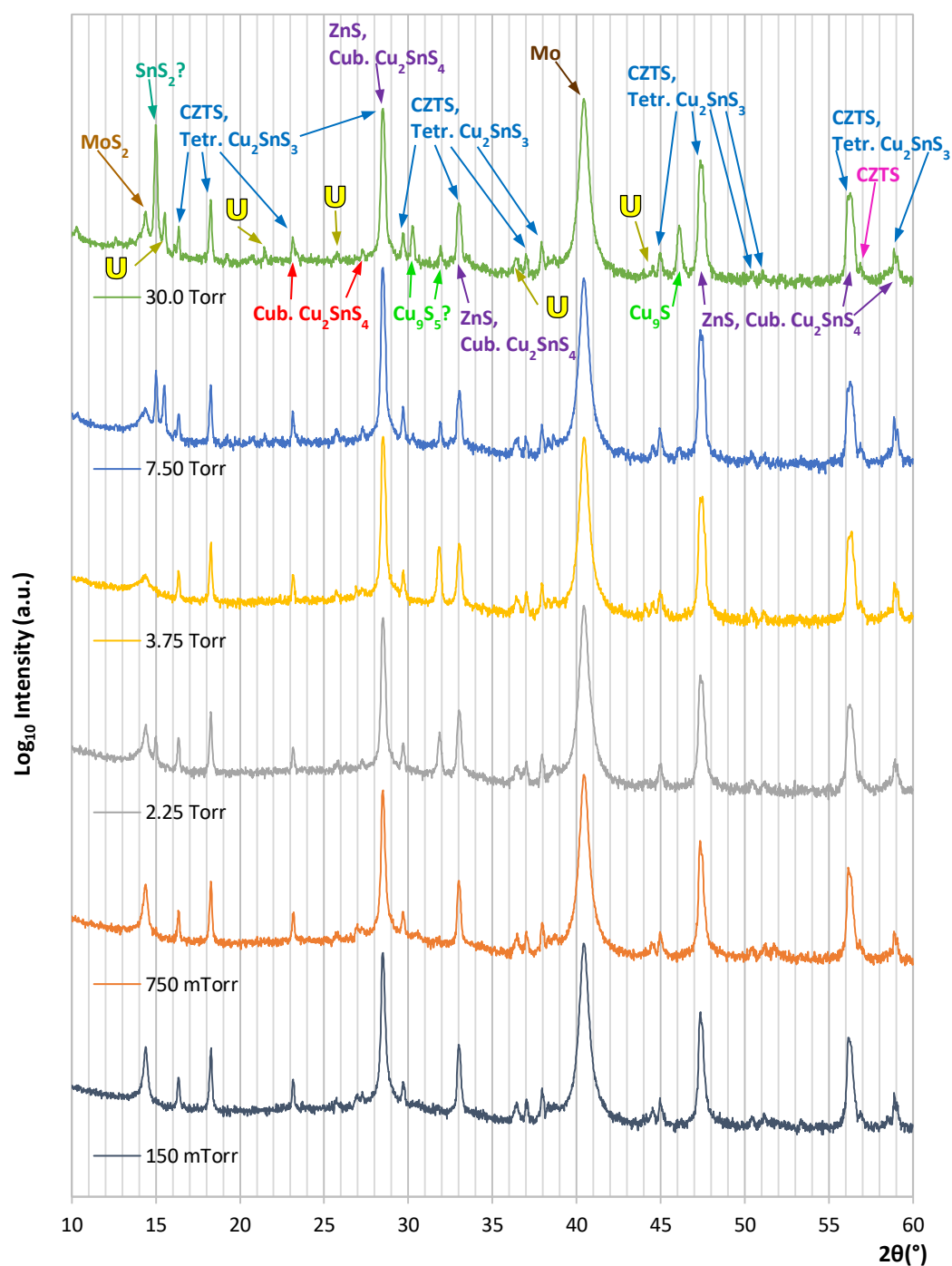


**Figure 5-24 - XRD patterns for samples sulphurised at six different background pressures. One small unique peak is visible for CZTS on all samples, while peaks that are unidentified or associated with unwanted phases are more prominent for higher pressures.**

patterns for the six sulphurised samples are presented in Figure 5-24 and have been plotted such that the highest background annealing pressure is represented at the top

and the lowest at the bottom. As can be seen, peaks have been identified using the COD and have been labelled on the uppermost (30.0 Torr) pattern plot on the graph. All of the peaks that occur on other patterns are also evident on the uppermost pattern, however there are peaks that are not present on all of the pattern plots. There are a number of unidentifiable peaks that are marked with a yellow 'U', the most prominent of which occurs at  $15.5^\circ$ . This peak is also visible on the pattern plot for 7.50 Torr, and at a smaller magnitude on the pattern plot for 2.25 Torr, but not for other pressures. Similarly, the unidentified peak at  $21.5^\circ$  is not visible for pressures of 3.75 Torr or less. There is a peak at  $30.0^\circ$  that is visible for 30.0 Torr, 7.50 Torr and 2.25 Torr, and is most prominent for 30.0 Torr. This peak has been attributed to hexagonal berndtite-2T  $\text{SnS}_2$ , which is an unwanted secondary phase. The label has been marked with a question mark as, although it corresponds with a peak associated with this phase, other associated peaks are not visible in the patterns. Another unwanted secondary phase that appears to have presented is hexagonal  $\text{Cu}_9\text{S}_5$ . For 30.0 Torr, peaks associated with this phase are visible at  $35.1^\circ$ ,  $37.0^\circ$  and  $46.0^\circ$ , although those at  $35.1^\circ$  and  $37.0^\circ$  are marked with a question mark as they are not an exact match. The peaks at  $35.1^\circ$  and  $46.0^\circ$  are also visible for 7.50 Torr at a reduced amplitude, while the peak at  $37.0^\circ$  is visible on all pattern plots for 2.25 Torr and above. A small unique peak is visible at  $27.2^\circ$  for cubic  $\text{Cu}_2\text{SnS}_4$  on all of the pattern plots, suggesting that it is present in a relatively small proportion on all of the samples in this batch. There are numerous other peaks present that are also associated with this phase, however these can all be associated with at least two other phases, including CZTS. Molybdenum and molybdenum disulphide ( $\text{MoS}_2$ ) are also indicated as present on all samples, which was to be expected. There are fifteen peaks visible on all samples that are associated with CZTS (in this instance, slightly off-stoichiometric  $\text{Cu}_{1.885}\text{Zn}_{1.058}\text{SnS}_4$  is the closest match on the COD), fourteen of which are also associated with tetragonal copper tin sulphide (kramite) and five of which are also associated with cubic ZnS (sphalerite). This makes it almost impossible to determine whether these unwanted phases are present, or to estimate their proportions. There is, however, one relatively small peak that is unique to CZTS and is visible on all of the pattern plots, confirming the presence of CZTS on all samples. This peak can be found at  $56.9^\circ$ . It is worth noting that the peaks seen here that are identified as potentially relating to CZTS, are a good match for those



seen in the diffraction pattern published in [22], and that none of the peaks that are characteristic of CZTS are lacking in the angle range analysed.

In summary, CZTS has been identified as present on all of the samples, as have small quantities of the unwanted phase, cubic  $\text{Cu}_2\text{SnS}_4$ . It is impossible to determine whether tetragonal kuramite or cubic sphalerite are present from the XRD patterns for any of the samples. In terms of trends, peaks that may be associated with the unwanted phases, hexagonal berndtite-2T ( $\text{SnS}_2$ ) and hexagonal  $\text{Cu}_9\text{S}_5$ , as well as several unidentifiable peaks, are more prominent on samples annealed with higher background pressures, and that the samples annealed at 750 mTorr and 150 mTorr returned the most favourable XRD results. The overlapping of most of the CZTS peaks with those of unwanted phases means that other information, such as that gained through Raman spectroscopy, will need to be considered before concluding which background pressure is most suitable.

Reference [22] presents Raman spectra for CZTS and eight secondary phases that commonly occur in the manufacture of CZTS, the spectra having been obtained using a laser with a wavelength of 488 nm (relatively close to the 532 nm used in this project). The secondary phases included were hexagonal  $\text{MoS}_2$ , cubic  $\text{ZnS}$ , tetragonal  $\text{Cu}_2\text{SnS}_3$ , cubic  $\text{Cu}_2\text{SnS}_3$ , orthorhombic  $\text{Cu}_3\text{SnS}_4$ , orthorhombic  $\text{SnS}$ , hexagonal  $\text{SnS}_2$  and hexagonal  $\text{Cu}_{2-x}\text{S}$ . The Raman spectrum for CZTS seen in [22] is presented in Figure 5-25 (presented previously as Figure 2-21 in section 2.4.3). Raman

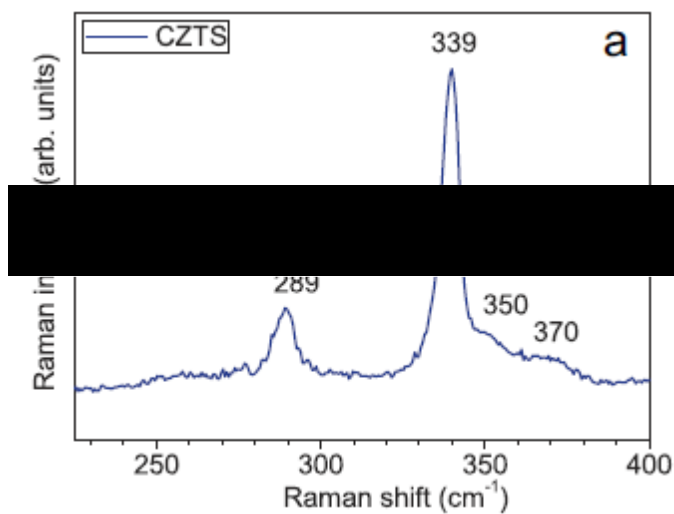


**Figure 5-25 - The Raman spectrum for CZTS when using a laser with a wavelength of 488 nm, as presented in [22].**

spectroscopy in this project was conducted as described in section 5.2.2.4. Raman spectra for the six annealed samples are presented in Figure 5-26, and as with the

### Sulphurised, Pressure Varied: Raman Spectra

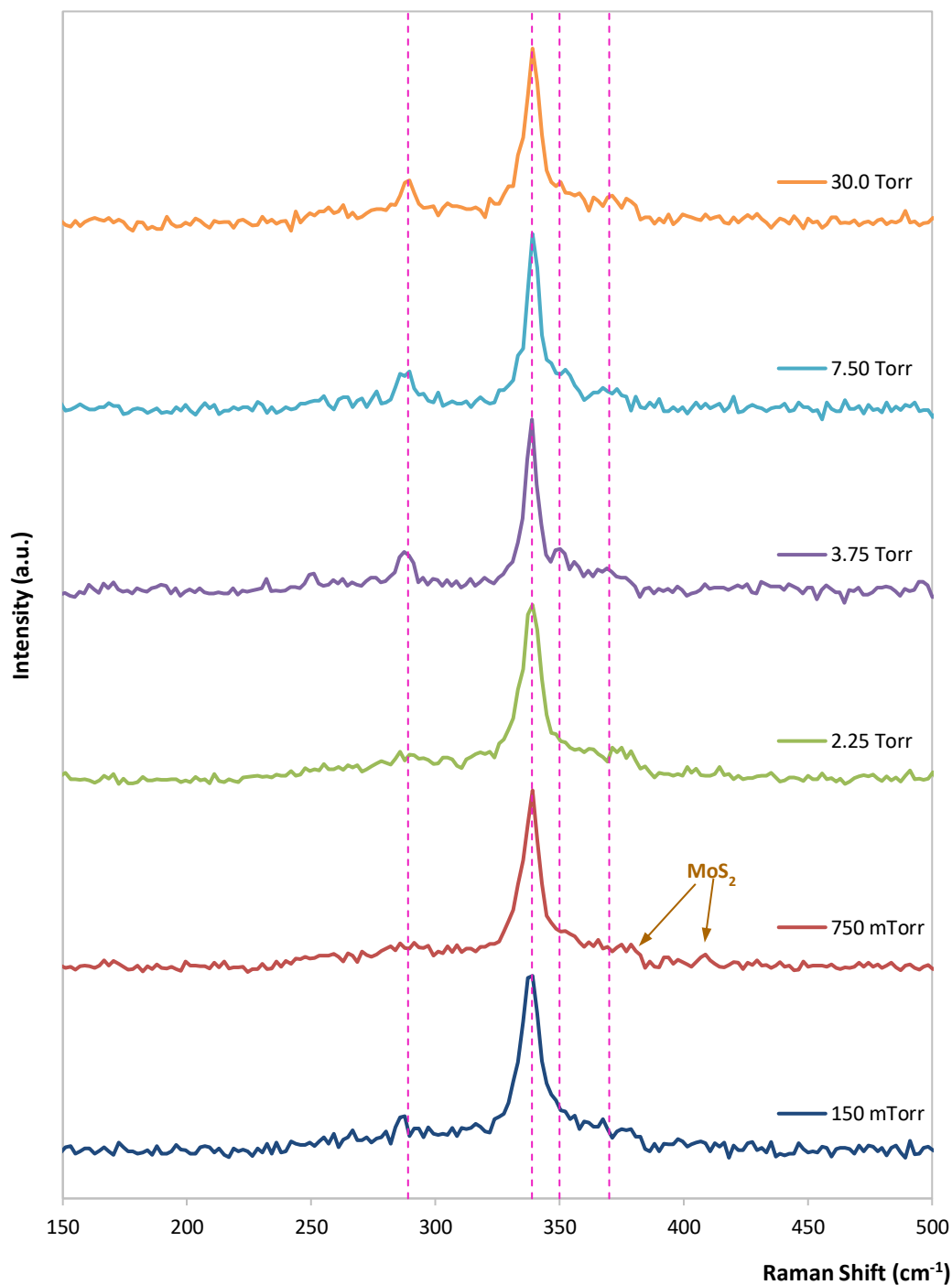


**Figure 5-26 - Raman spectra for the sulphurised samples showing a good match for CZTS, particularly at pressures of 3.75 Torr and above (the pink dotted vertical lines indicate where peaks associated with CZTS lie). Unfortunately, it was not possible to rule out the presence of tetragonal  $\text{Cu}_2\text{SnS}_3$  or cubic  $\text{ZnS}$ .**

XRD patterns, the highest background pressure is represented at the top of the graph area and the lowest at the bottom. The Raman spectra presented in Figure 5-26 were compared against those in [22] in order to identify peaks associated with CZTS and any of the aforementioned secondary phases. It was immediately possible to see that there were no peaks associated with orthorhombic SnS ( $160\text{ cm}^{-1}$ ,  $190\text{ cm}^{-1}$  and  $219\text{ cm}^{-1}$ ) or hexagonal  $\text{Cu}_{2-x}\text{S}$  ( $475\text{ cm}^{-1}$ ) as there were no coincident peaks on any of the spectra. It was considered unlikely that cubic  $\text{Cu}_2\text{SnS}_3$  or hexagonal  $\text{MoS}_2$  were present according to the Raman data. Although there may be a small peak attributable to cubic  $\text{Cu}_2\text{SnS}_3$  at  $356\text{ cm}^{-1}$ , this could also be attributed to the broad CZTS peaks seen at  $350\text{ cm}^{-1}$  and  $370\text{ cm}^{-1}$ , and the other peaks associated with cubic  $\text{Cu}_2\text{SnS}_3$  ( $267\text{ cm}^{-1}$  and  $303\text{ cm}^{-1}$ ) are not seen. Hexagonal  $\text{MoS}_2$  was considered unlikely to be represented in the majority of the Raman spectra because the two taller attributable peaks at  $384\text{ cm}^{-1}$  and  $410\text{ cm}^{-1}$  are not present in any of the spectra, with the possible exception of that for 750 mTorr, where the relevant peaks have been labelled. Although peaks are seen at a coincident  $288\text{ cm}^{-1}$  on spectra for samples annealed with background pressures of 150 mTorr, 3.75 Torr, 7.50 Torr and 30.0 Torr, this can be attributed to a nearby CZTS peak ( $289\text{ cm}^{-1}$ ). Hexagonal  $\text{MoS}_2$  was indicated as present by the XRD data, but this phase sits beneath the CZTS and is unlikely to be detected by Raman spectroscopy when the penetration depth is much shallower ( $\sim 140\text{ nm}$  for a  $488\text{ nm}$  laser [22]) than that of XRD. Two other phases that were considered to be relatively unlikely to be present in the data were hexagonal  $\text{SnS}_2$  and orthorhombic  $\text{Cu}_3\text{SnS}_4$ . Each phase only has one Raman peak at  $314\text{ cm}^{-1}$  and  $318\text{ cm}^{-1}$  respectively, neither of which appear to be present on the obtained spectra. Unfortunately, it is impossible to rule out the presence of ZnS as this has only one major peak, which is positioned at  $352\text{ cm}^{-1}$ , meaning that it could be masked by the broad CZTS peak at  $350\text{ cm}^{-1}$ . The other peak would be positioned at  $275\text{ cm}^{-1}$  and could be undetectable due to its very low magnitude. Similarly, tetragonal  $\text{Cu}_2\text{SnS}_3$  has peaks at  $352\text{ cm}^{-1}$  and  $337\text{ cm}^{-1}$ , which could be masked by the nearby CZTS peaks at  $339\text{ cm}^{-1}$  and  $350\text{ cm}^{-1}$ , and one other peak at  $297\text{ cm}^{-1}$ . Although peaks are not clearly seen at  $297\text{ cm}^{-1}$  on the spectra, it would be relatively small in magnitude and a proportionately small quantity may remain undetected. It is considered likely that CZTS is present on all samples – the main peak at  $339\text{ cm}^{-1}$  is present in all of the spectra, as is the characteristic CZTS



“shoulder” just to the right of the main peak. This is a close match to the CZTS Raman spectrum presented in Figure 5-25. It is noteworthy, however, that some of the obtained Raman spectra in Figure 5-26 are a closer match to the spectrum in Figure 5-25 than others, particularly with regards to the peak at  $289\text{ cm}^{-1}$ . This peak is not visible in the spectra for 750 mTorr and 2.25 Torr, and is relatively weak in the spectrum for 150 mTorr. It is more prominent in the spectra for samples annealed at 3.75 Torr and above (it is approximately equal in magnitude between these three spectra), and these appear to give the closest match to the CZTS spectrum. This is in contrast to the XRD patterns, in which higher background pressures led to an increase in peaks relating to unwanted secondary phases, some of which were unidentified. It was therefore decided that 3.75 Torr would be adopted for use as the background pressure in the next batch of sulphurisation experiments, which focussed on optimising the sulphur concentration. This pressure was considered to give the best compromise between a Raman spectrum that closely matches that of CZTS and an XRD pattern that displays fewer peaks associated with unidentified and unwanted phases than those for samples annealed at higher background pressures.

### **5.3.3 Optimisation of Sulphur Concentration for Sulphurisation**

Before carrying out a set of experiments to optimise the sulphur concentration, it was necessary to decide upon a range of sulphur masses with which to experiment with. It was reported in [6] that 50 mg of sulphur was added to a graphite annealing box that was placed in a sealed RTP furnace at a pressure of 5 mTorr. Both of these values are relatively low – the pressure selected for use in this project was 3.75 Torr, and the sulphur mass was only one fifth of that used by researchers collaborating with this project, as commented on in section 5.3.2. It was also reported in [21] that increasing the partial pressure of gaseous sulphur when annealing under argon flow, led to the reduction in tin loss during sulphurisation, tin loss being an undesirable effect. In order to achieve this partial pressure increase in a sealed furnace, it would be necessary to increase the mass of sulphur added to the graphite annealing box. The range of sulphur masses chosen for the sulphur concentration optimisation experiments in this project was 75 – 750 mg.

Six precursor samples were prepared as described in section 5.2.1.1 using a three-layer stacking configuration. The zinc layer was of a reduced thickness compared to

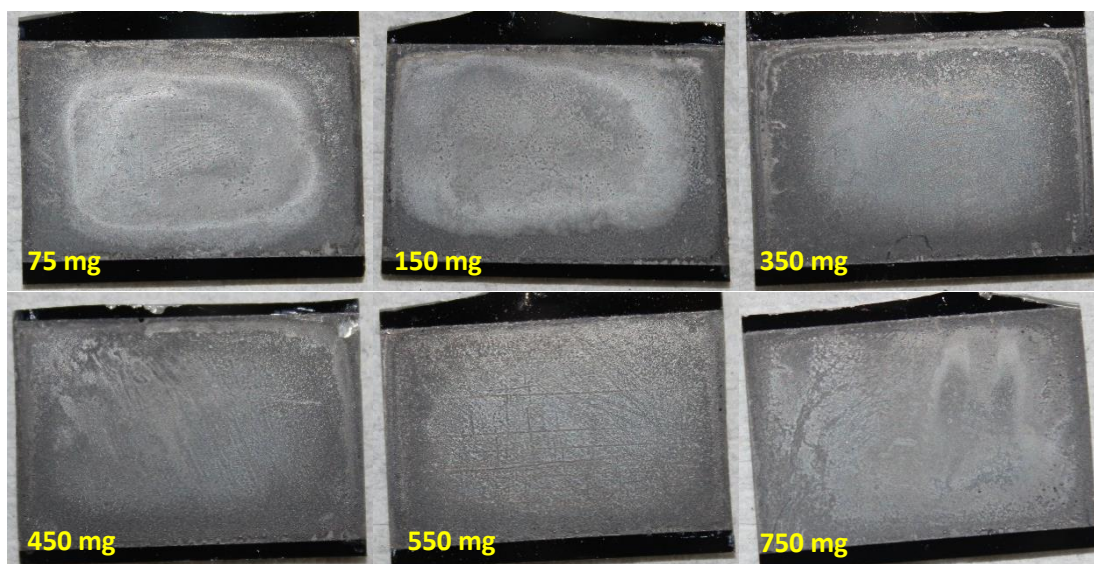


**Figure 5-27 – Photographs of six samples sulphurised with different sulphur masses. No blistering of the films is visible in these photographs.**

those used in the background pressure optimisation experiments due to the fact that zinc deposition efficiency data had since become available, and the indication was that the deposition efficiency was greater than had been previously assumed. The furnace heating settings were the same as those stated in Table 5-1 in section 5.2.1.2 and the background pressure was 3.75 Torr. Photographs were obtained of the six sulphurised samples and are presented in Figure 5-27. It is possible to see that less blistering has occurred on this batch of samples when compared to those in the previous batch (see Figure 5-21) as there are no blisters that are clearly visible in these photographs. It is also noticeable that films sulphurised with the lowest sulphur masses (75 mg and 150 mg) appear to have thinner films than the other samples. This suggest that greater material loss may have occurred on these samples, despite the lack of visible blistering.

In order to more closely examine the films, SEM images were taken on a FEG-SEM and can be seen in Figure 5-28. Two images of each sample are presented, one of a relatively low magnification and one of a relatively high magnification. Looking firstly at the lower magnification images, it is evident that films sulphurised with the two smallest sulphur quantities underwent less blistering than the other films, although there is a pinhole visible on the sample sulphurised with 150 mg sulphur. The largest blisters resulted for 550 mg, although there were fewer in number on this

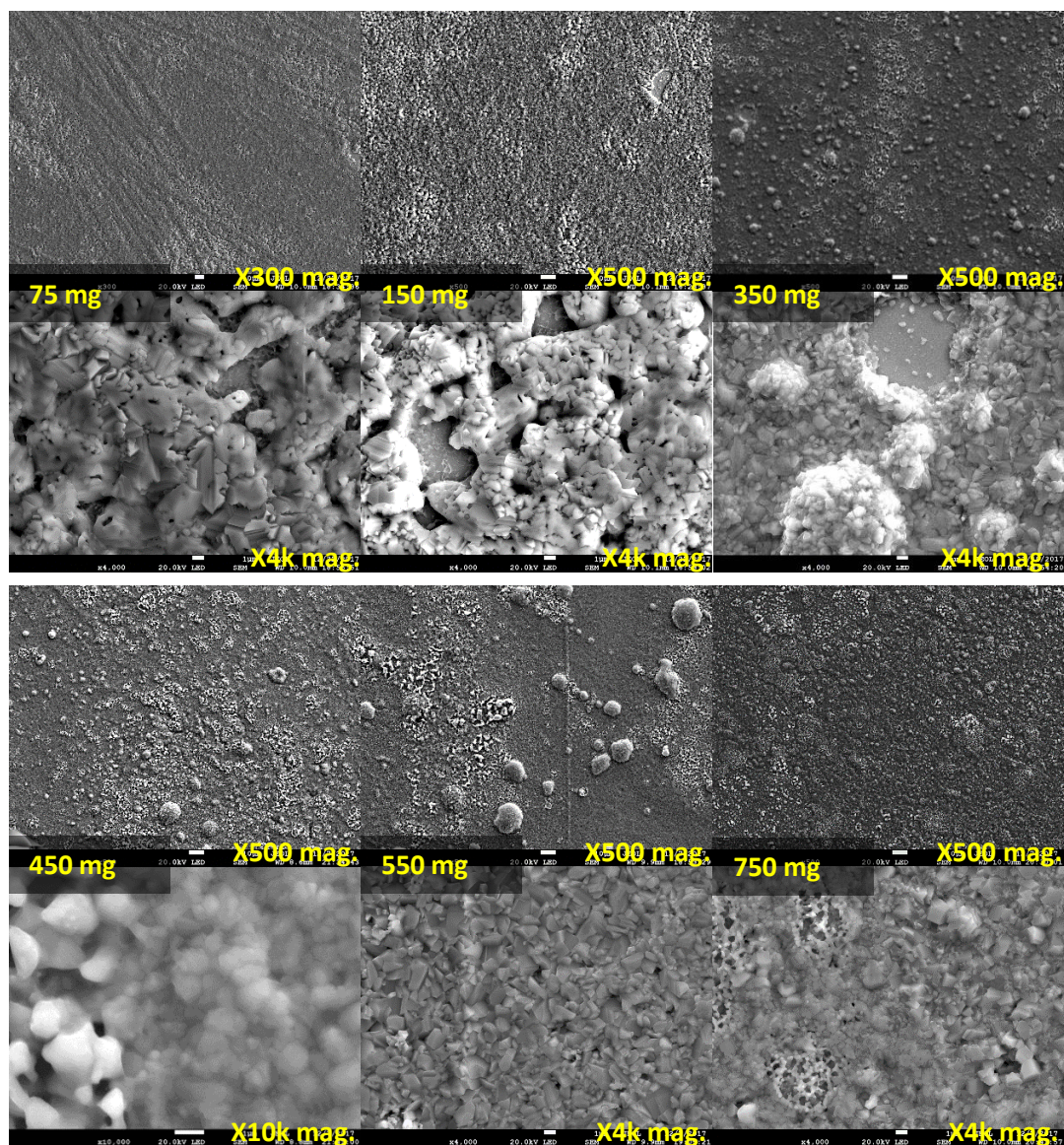


**Figure 5-28 – High and low magnification SEM images of the six samples sulphurised with different sulphur quantities. The images were taken with an acceleration voltage of 20 kV. The scale bars represent 10  $\mu$ m on the 300x and 500x magnification images, and 10  $\mu$ m on the 4,000x and 10,000x magnification images. Lower sulphur concentrations led to films with voids, whereas higher concentrations led to more blistering.**

sample than on those for 350 mg, 450 mg or 750 mg. For 750 mg, the blisters appear significantly shallower than for 350 mg, 450 mg or 550 mg, and may relate to areas of increased porosity rather than domed voids, with porosity also being evident for 450 mg and 550 mg. It is also noticeable that there are streak marks on the 75 mg sample and the 550 mg sample. Although the exact cause of this is not known, it was noticed during the electroplating experiments that thin zinc layers were not particularly well adhering and there was some concern that some zinc may have been



inadvertently removed as the sample substrates were trimmed prior to the annealing treatments. Friction against the lint-free paper on which they were placed during the glass breaking process may have resulted in the streaking that is seen on those two samples. Referring to the higher magnification images, the samples for 75 mg and 150 mg appear to exhibit irregularly shaped voids in the film in which the underlying substrate is exposed. These voids are not akin to pinholes or blisters – their appearance is as that of a material that has been spread thinly to the point that it can no longer cover its substrate, rather than a film that has been damaged or had some material removed. Some form of granular structure was visible on all films, good examples being those for 350 mg and 550 mg, and some porosity is seen in the images for 450 mg and 750 mg. Aside from the poor coverage seen on the samples for the two lowest sulphur concentrations, it is difficult to discern any clear trends among the remaining samples. All four of these films exhibit some blistering and film porosity, and although there is no clear trend, the sample for 750 mg appears to have suffered the least damage in terms of blistering. Before the reasons behind this could be speculated, it was necessary to perform further analysis using EDS.

Further analysis was carried out by means of plotting elemental abundancies against sulphur mass on the graph presented in Figure 5-29. As expected, it is possible to see that the zinc content is significantly reduced when compared to the previous batch of

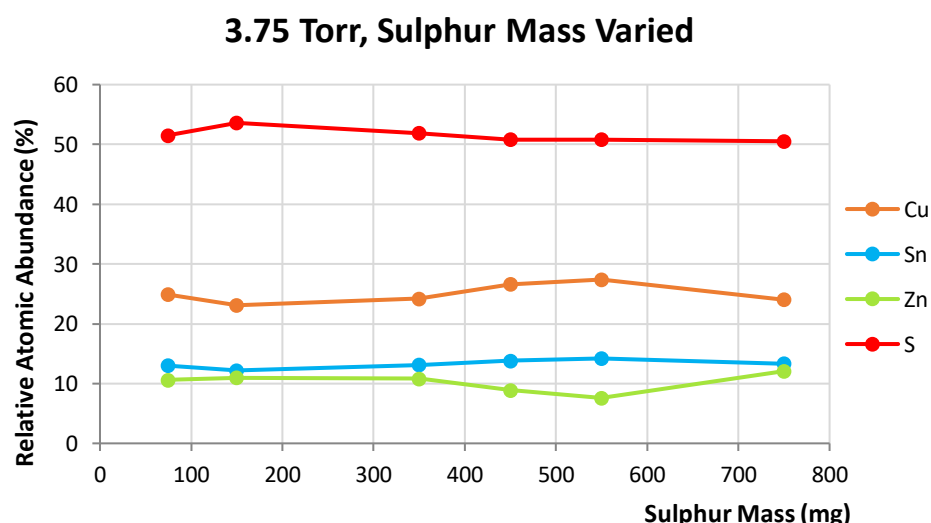


**Figure 5-29 – Atomic abundancies for all four elements plotted against the sulphur mass used in the sulphurisation process. There does not appear to be any correlation visible for any of the elements.**

samples, but there are no apparent trends relating to sulphur concentration and the abundancies of any of the elements. It is interesting to note that sulphur concentration during annealing did not affect the relative abundance of tin in the annealed films. It also indicates that apparent material losses resulting when 150 mg sulphur or less is used are not resulting due to the loss of just tin – if material is escaping, it is being shared in equal proportions amongst the three metallic elements. The equilibrium equation, Equation 5-1 stated previously in section 5.3.2, does not offer a full explanation for this – although it would seem logical that, as lower gas partial pressures shift the equation to the right, lower sulphur concentration would result in more material losses, these losses would primarily affect tin as it would escape in the form of gaseous  $\text{SnS}$  while  $\text{Cu}_2\text{S}$  and  $\text{ZnS}$  would remain on the substrate in solid form. This remains an unexplained result within this project, however XRD may yield some information as to the phases that comprise each film.

XRD patterns are presented for all six samples in Figure 5-30, with the pattern relating to the lowest sulphur mass being plotted at the bottom, transitioning to the highest sulphur mass at the top. As a reminder to the reader, all of the peak identifications in discussions relating to XRD should be taken to be referenced against the COD [11, 12, 13, 14, 15, 16, 17]. Compared to the previous batch of samples (see Figure 5-24), there are fewer unidentified peaks and some of the peaks associated with unwanted secondary phases that were apparent on some of the samples in the previous batch are not seen in this batch. More specifically, the unidentified peaks at  $15.5^\circ$  and  $21.5^\circ$  have disappeared, and peaks associated with hexagonal berndtite-2T  $\text{SnS}_2$  ( $15.0^\circ$ ) and hexagonal  $\text{Cu}_9\text{S}_5$  ( $30.1^\circ$ ,  $31.9^\circ$  and  $46.0^\circ$ ) are no longer visible, with the exception of a peak at  $31.9^\circ$  for 75 mg sulphur that may be associated with hexagonal  $\text{Cu}_9\text{S}_5$  but is not an exact match. It is still possible to see a small peak associated only with cubic  $\text{Cu}_2\text{SnS}_4$  ( $27.2^\circ$ ) for all samples in this batch. The fifteen peaks associated with CZTS are visible, with the unique peak at  $56.9^\circ$  being present for all sulphur masses. In terms of trends relating to sulphur mass, it is possible to see that the cubic  $\text{Cu}_2\text{SnS}_4$  ( $27.2^\circ$ ) peak is stronger on the 75 mg and 150 mg samples, as is the unidentified peak at  $25.7^\circ$ . With the possible hexagonal  $\text{Cu}_9\text{S}_5$  peak also being present for 75 mg sulphur, it can be stated that more favourable results in terms of avoiding unwanted phases appear to be achieved

### 3.75 Torr, Sulphur Mass Varied: XRD

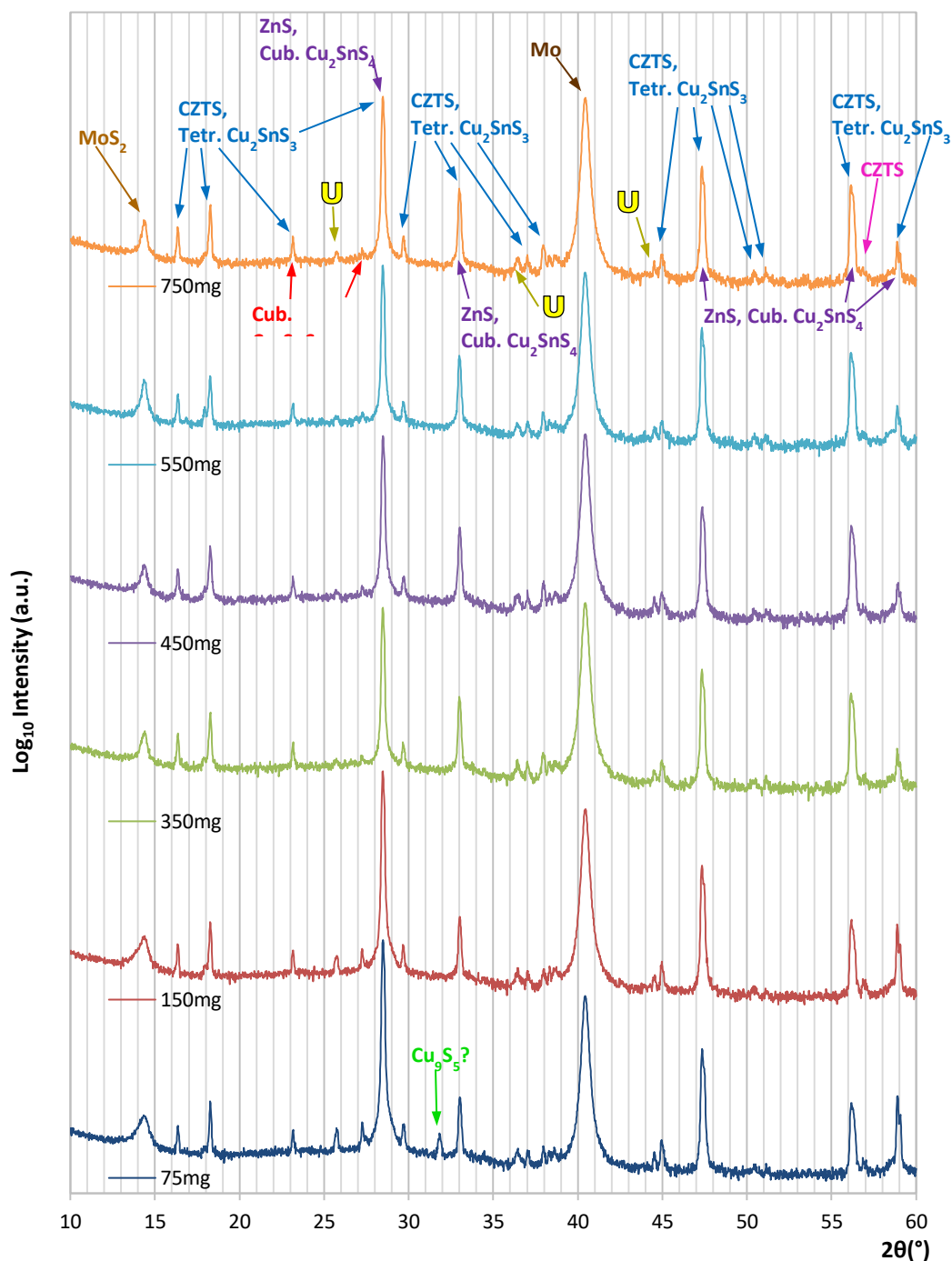


**Figure 5-30 – XRD patterns for six samples sulphurised with a range of sulphur quantities. Patterns relating to the two lowest sulphur masses show stronger peaks for unwanted phases than the other samples. A small peak unique to CZTS at 56.9° is visible for all samples.**

with sulphur masses of 350 mg or greater. Again, it is worth noting that, in common with the previous set of results, the peaks seen here that are identified as potentially

relating to CZTS, are a good match for those seen in the diffraction pattern published in [22], and that none of the peaks that are characteristic of CZTS are lacking in the angle range analysed. It is, unfortunately, still impossible to confirm or exclude the presence of tetragonal kuramite ( $\text{Cu}_2\text{SnS}_3$ ) or cubic sphalerite ( $\text{ZnS}$ ). This is in common with the diffraction pattern seen in [22], in which the coincidental peak positions for these compounds are also stated. Further information may be yielded in the analysis of the Raman spectroscopy data, Raman spectra having been obtained for all six samples.

Raman spectra are presented in Figure 5-31, the vertical pink dotted lines indicating the positions of peaks attributed to CZTS as given in [22]. As with the previous batch of samples (section 5.3.2, Figure 5-26), the spectra were cross matched against those presented in [22] for CZTS and eight unwanted phases, in order to identify or eliminate the phases present. As previously, it was not possible to eliminate the presence of cubic  $\text{ZnS}$  or tetragonal  $\text{Cu}_2\text{SnS}_3$  due to the close proximity of the main peaks to those of CZTS. Peaks relating to hexagonal  $\text{MoS}_2$ , orthorhombic  $\text{Cu}_3\text{SnS}_4$ , orthorhombic  $\text{SnS}$  and hexagonal  $\text{Cu}_{2-x}\text{S}$  were not seen in the spectra for any of the samples, however, some peaks of a relatively low magnitude were seen for other unwanted phases in some of the spectra. Small peaks attributed to cubic  $\text{Cu}_2\text{SnS}_3$  can be seen in the spectrum for 150 mg, and hexagonal  $\text{SnS}_2$  may be present on the 450 mg sample. Having carried out the analysis using [22] as a reference, it was found that an unidentified peak was visible at  $307\text{ cm}^{-1}$  on the 550 mg sample, as well as apparent broad, low magnitude peaks at  $374\text{ cm}^{-1}$  on several of the samples. Referring to [23] revealed that the peak at  $307\text{ cm}^{-1}$  could be attributed to  $\text{Sn}_2\text{S}_3$ , and, with a 532 nm laser, a broad peak for CZTS appears at  $374\text{ cm}^{-1}$  as well as the main peak shifting slightly to  $337\text{ cm}^{-1}$  when compared to the 488 nm laser used in [22]. A literature search for a Raman spectrum for cubic  $\text{Cu}_2\text{SnS}_4$  was conducted due to the fact that this compound is indicated as being present by the XRD data, however this search proved unsuccessful. In terms of general trends relating to the sulphur concentration, it is difficult to identify any in the Raman data. It is worth noting that the CZTS peaks in general do not appear as distinct in this set of spectra as they do in those in Figure 5-26.

### 3.75 Torr, Sulphur Mass Varied: Raman Spectra

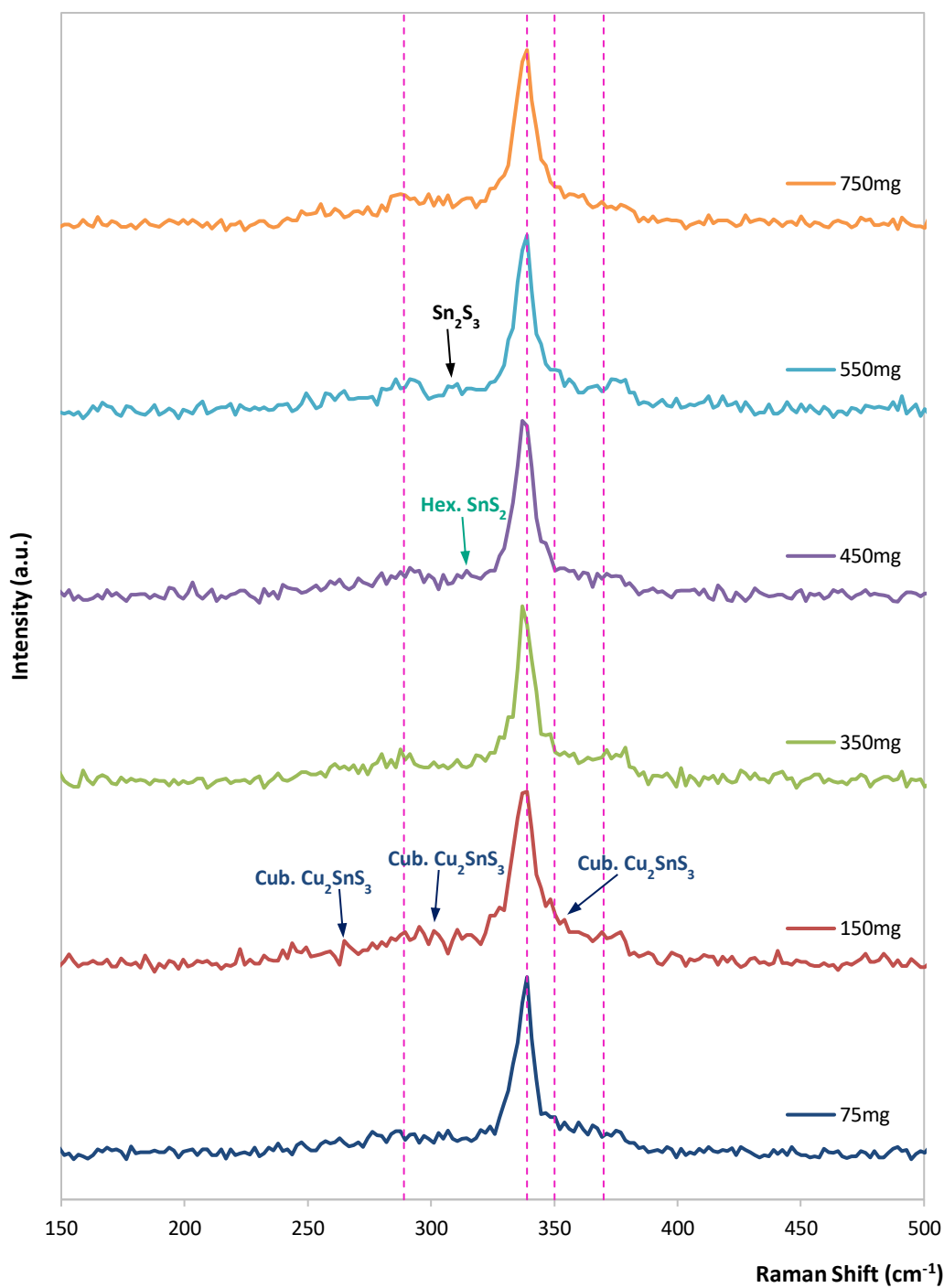


**Figure 5-31 – Raman spectra for six sulphurised samples with varied sulphur masses. The vertical pink dotted lines indicate the expected positions of CZTS peaks, and some small peaks relating to unwanted phases have been labelled. Unfortunately, it was not possible to rule out the presence of tetragonal  $\text{Cu}_2\text{SnS}_3$  or cubic  $\text{ZnS}$ .**



It was challenging to select an optimum sulphur mass from the data available – XRD patterns suggested that the lowest masses were best avoided due to the increase in magnitude of peaks relating to unwanted phases, while the Raman spectra and EDS elemental abundancies did not reveal any specific trends. SEM images showed that lesser sulphur masses led to voids forming in the films, while conversely, greater sulphur masses led to increased blistering and regions of apparent porosity. Ultimately, the decision was taken based on the SEM images suggesting that, although 350 mg of sulphur or greater did lead to increased blistering and porosity, these phenomena were least evident on the sample sulphurised with 750 mg sulphur, which was the mass selected for subsequent sulphurisation experiments.

#### **5.3.4 Combining the Elemental Alloying and Sulphurisation Processes**

Having conducted experiments to establish improved conditions for the pre-alloying and sulphurisation of precursors individually, the next step of the project was firstly to test whether the pre-alloying process was giving a significant benefit to the quality of the CZTS films, and secondly to ascertain whether these benefits could be retained if the pre-alloying and sulphurisation processes were combined into a single furnace operation. In order to establish this, nine precursor samples were prepared with three-layer electroplated stacks (see section 5.2.1.1) and three samples each were subjected to one of the following:

1. Pre-alloying followed by sulphurisation executed in separate furnace operations (samples were labelled “Alloying Separate 1”, “Alloying Separate 2” and “Alloying Separate 3”).
2. Pre-alloying and sulphurisation combined into a single furnace operation (samples were labelled “Alloying Integrated 1”, “Alloying Integrated 2” and “Alloying Integrated 3”).
3. Sulphurisation only – no pre-alloying step included (samples were labelled “No Alloying 1”, “No Alloying 2” and “No Alloying 3”).

The pre-alloying process was carried out at 300 °C for 10 minutes using a ramp rate of 2.5 °C s<sup>-1</sup> and a background pressure of 150 mTorr (this was the pressure used during the pre-alloy time and temperature optimisation experiments). The sulphurisation process was carried out using the heating settings given in Table 5-1

(section 5.2.1.2), a background pressure of 3.75 Torr and a sulphur mass of 750 mg. When the two processes were combined, the first heating stage was 300 °C for 10 minutes with a ramp rate of 2.5 °C s<sup>-1</sup>, followed by a 2.5 °C s<sup>-1</sup> ramp to 400 °C, the heating process following the sequence in Table 5-1 thereafter. The background pressure selected was 3.75 Torr – the pressure optimised for sulphurisation, as it was considered more likely that the sulphurisation would be negatively affected by a change in background pressure than the pre-alloying. After the sulphurisation process had been completed, each sample was photographed from multiple angles in order to capture and compare the visual features of the annealed film. Samples were also analysed using XRD and Raman spectroscopy and the results compared between each sample in order to gauge whether which, if any, of the three approaches to alloying and annealing were advantageous. Furthermore, all nine of the samples were processed further and completed into photovoltaic devices, which will be discussed in chapter 6. Finally, a single experiment was conducted in which 750 mg sulphur was placed into the graphite annealing box and heated in the furnace at 300 °C for 10 minutes (2.5 °C s<sup>-1</sup> ramp rate, 3.75 Torr background pressure) in order to test how much of the sulphur evaporated in this process and hence whether the integrated pre-alloying was being conducted in a sulphur-rich environment.

Photographs of the samples, all taken from a similar angle, are presented in Figure 5-32. It is possible to see that the overall homogeneity of the films is poor, with variations in the appearance of the films across each substrate. It is particularly noticeable that a “ring effect” is visible on all of the samples, with darker material tending to sit closer to the edge of the films. In terms of establishing differences in outcome relating to the different pre-alloying treatments, it is not possible to say with any degree of confidence that there is significant variation between the samples where the pre-alloying was carried out separately and the samples where the pre-alloying was integrated into the sulphurisation process. It is, however, evident that the samples that did not undergo a pre-alloying treatment have a greater number of small pinholes visible in their films. These pinholes may be caused by the loss of tin as tin sulphide vapour during the sulphurisation stage. Given that it has been established that the thinner zinc deposits from the chosen (acid-sulphate) electrolyte do not give full coverage of the underlying tin (see chapter 4, section 4.3.6.4), the

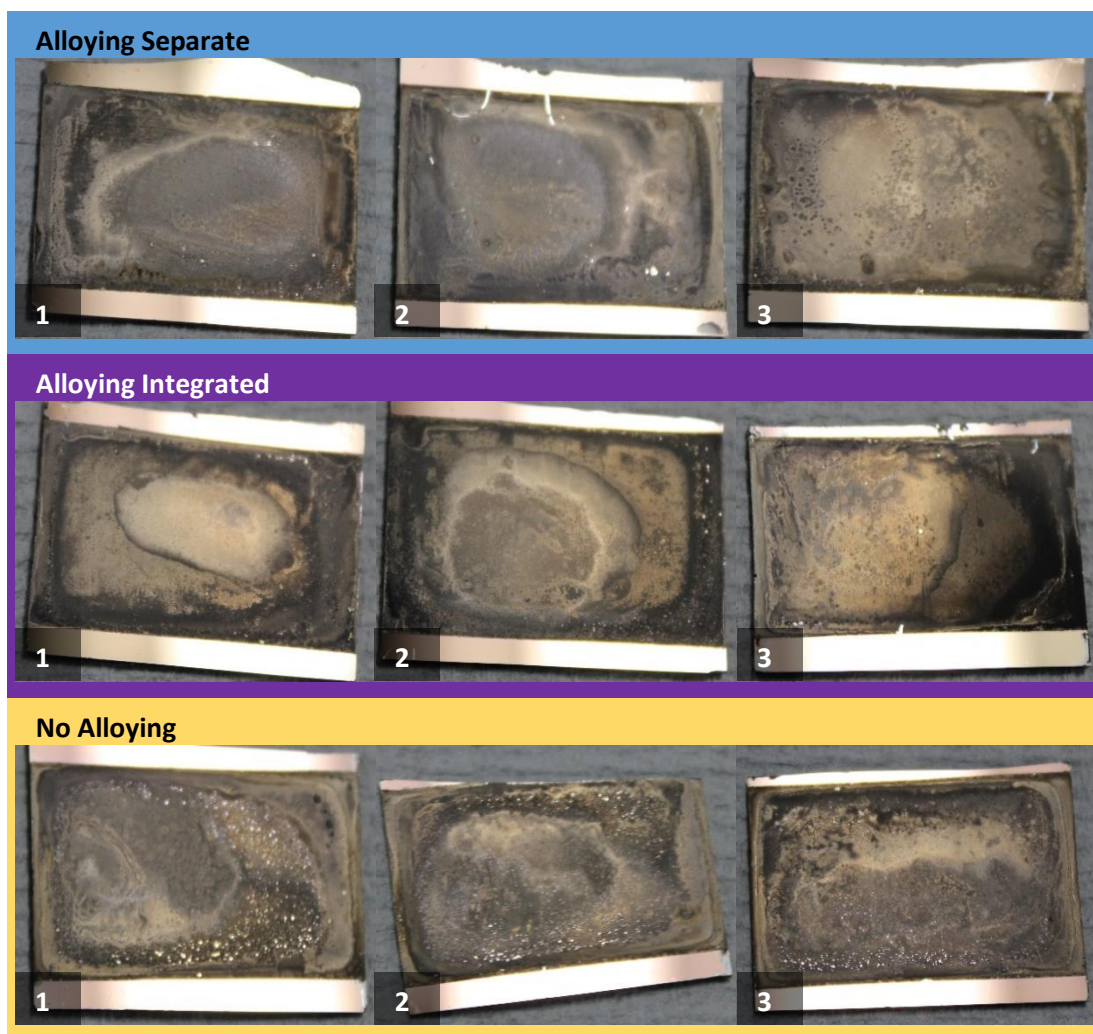


**Figure 5-32 - Photographs of the nine sulphurised samples taken without a flash at a slight offset angle. It is possible to see that the samples that were not pre-alloyed (bottom) have a greater number of small pinholes in their films.**

alloyed precursors will have a lower concentration of tin at the exposed surface of the film than the unalloyed ones (as evidenced by the XPS depth profiles seen in section 5.3.1). This may be a factor in reducing tin losses, which leads to fewer pinholes. Furthermore, the alloying of tin with copper may reduce its ability to form tin sulphide, rather than a ternary sulphide phase containing copper. The smaller number of pinholes observed on the six samples that underwent a pre-alloying treatment can be seen as a favourable result – not only is it evidence that the pre-alloying process is a beneficial treatment, it suggests that this treatment is still beneficial when combined into the same furnace operation as the sulphurisation process. Further information on the chemical composition of the samples can be revealed in the XRD and Raman spectroscopy measurements.

The resulting patterns from the XRD experiments are presented in Figure 5-33, with the peaks having been labelled in the same manner as seen previously. As a reminder

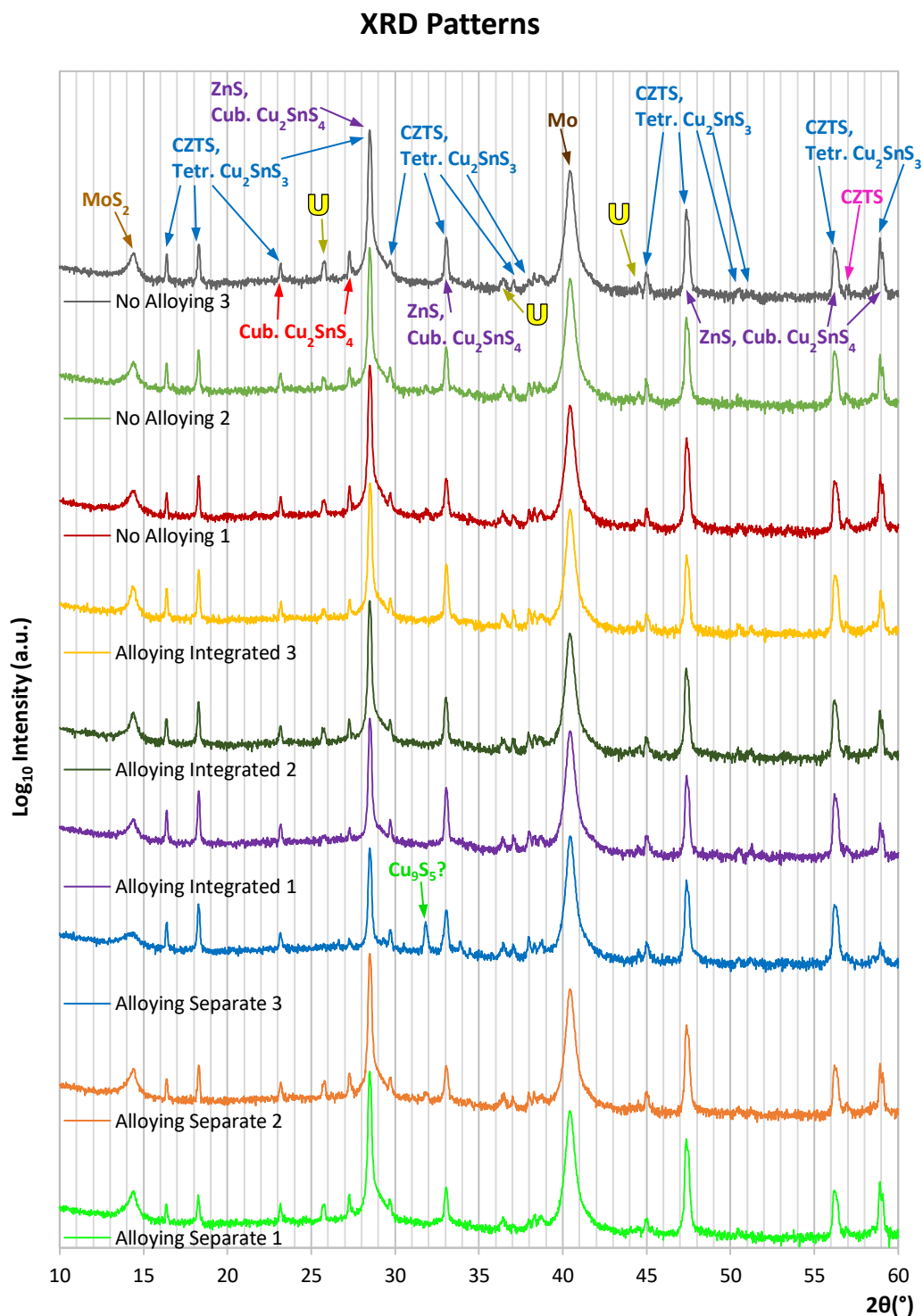


**Figure 5-33 - XRD patterns for the nine sulphurised samples. Unidentified peaks are indicated by a yellow "U". There does not appear to be a trend associated with the pre-alloying treatments.**

to the reader, all of the peak identifications in discussions relating to XRD should be taken to be referenced against the COD [11, 12, 13, 14, 15, 16, 17]. It is possible to see that all of the samples exhibit the fifteen peaks associated with CZTS, including the one small unique peak at  $56.9^\circ$ . It is less clear, however, if there are any trends relating to the furnace treatments that the samples received. Other than a peak that may be associated with hexagonal  $\text{Cu}_9\text{S}_5$  labelled on one of the sample named “Alloying Integrated 1” (although the main peak at  $46.1^\circ$  associated with this compound is not seen), and the diminished unique peak for cubic  $\text{Cu}_2\text{SnS}_4$  ( $27.2^\circ$ ) on this sample, there is little difference between the patterns. These data do not give any indication of significant differences in the chemical composition of the films relating to the difference in pre-alloying treatments or visual properties of the films (particularly when compared to the XRD patterns for samples without a pre-alloying step seen in Figure 5-30). It is worth noting at this stage that the XRD experiments were set up such that an area of  $0.6 \times 20 \text{ mm}^2$  was analysed on each sample, and that the analysis was carried out near to the centre of each sample. This means that the pattern obtained is effectively an overview of the analysed area, without specific information as to where each of the identified phases are present within that area. It also would not necessarily detect phases that are only present at the edges of the samples, given that the majority of the analysed area is not close to the sample edge. In contrast, that Raman spectrometer only analyses a spot of  $3 \text{ }\mu\text{m}$  diameter when set at 20x magnification (as was the case in the experiments in this project), meaning that the spectrum obtained is specific to the point analysed. This allows for the analysis of specific features, such as blisters, and comparison between specific points, such as the centre and a point close to the edge, which is not possible with the data obtained using the XRD in this project. When analysing the nine samples described here, Raman spectra were obtained for multiple points on each sample, focussing initially on parts of the films in the centre of the substrates, particularly that which appeared of good quality, and then on more distinct features in both the centre and at the edge, such as darker regions, blisters or craters in the films.

In Figure 5-34, one Raman spectrum from each sample is presented. Each spectrum was chosen on the basis that it returned the closest match for CZTS out of all the spectra obtained on the corresponding sample. The CZTS peaks have been marked

### Most Favourable Raman Spectrum from Each Sample

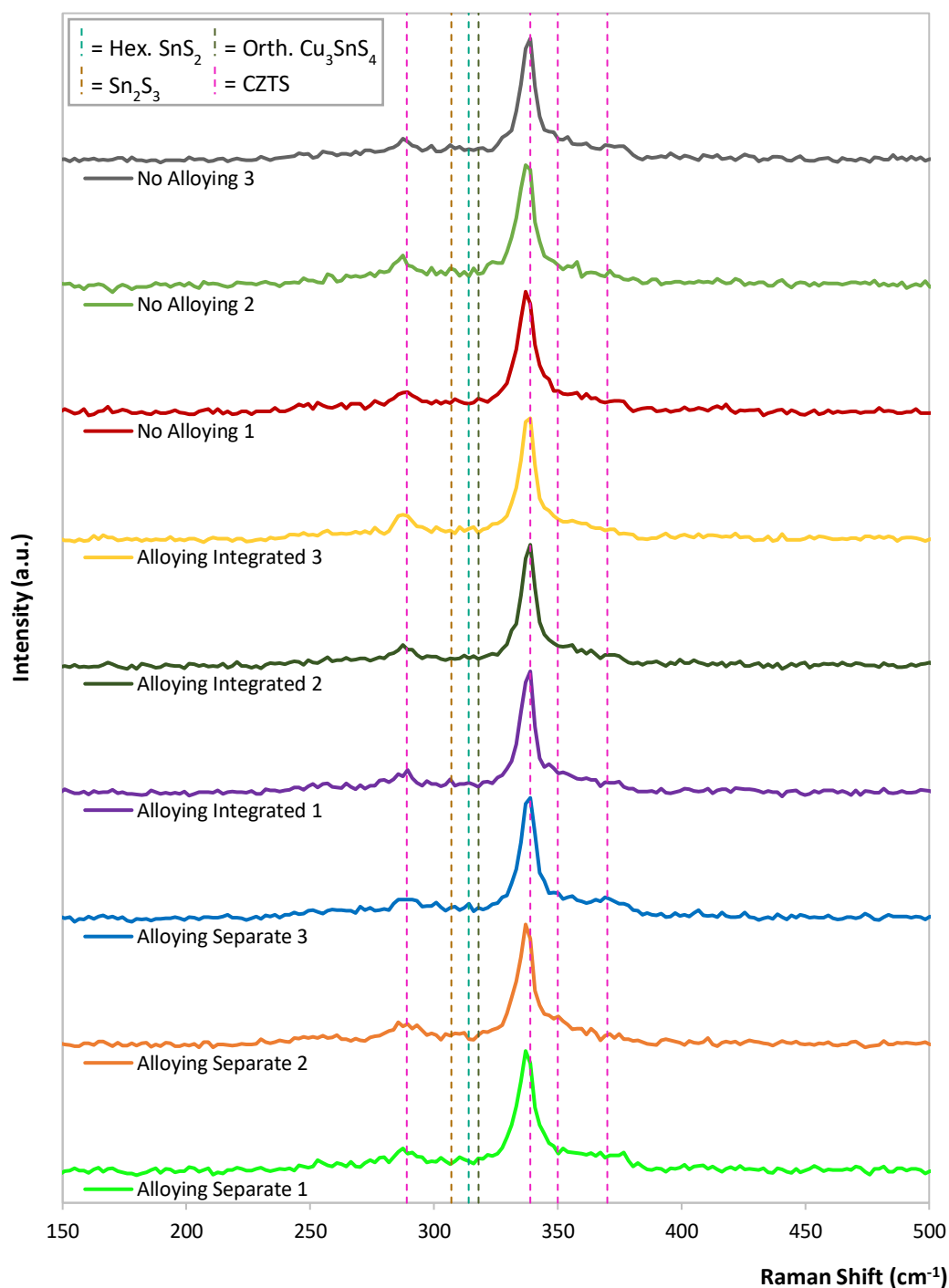


**Figure 5-34 - One Raman spectrum from each sample, chosen for having the closest match for CZTS and the least evidence of unwanted phases. The positions of CZTS peaks and three unwanted phases are indicated with vertical dotted lines, as per the key in the top left of the graph.**

### Selected Raman Spectra, One from Each Sample

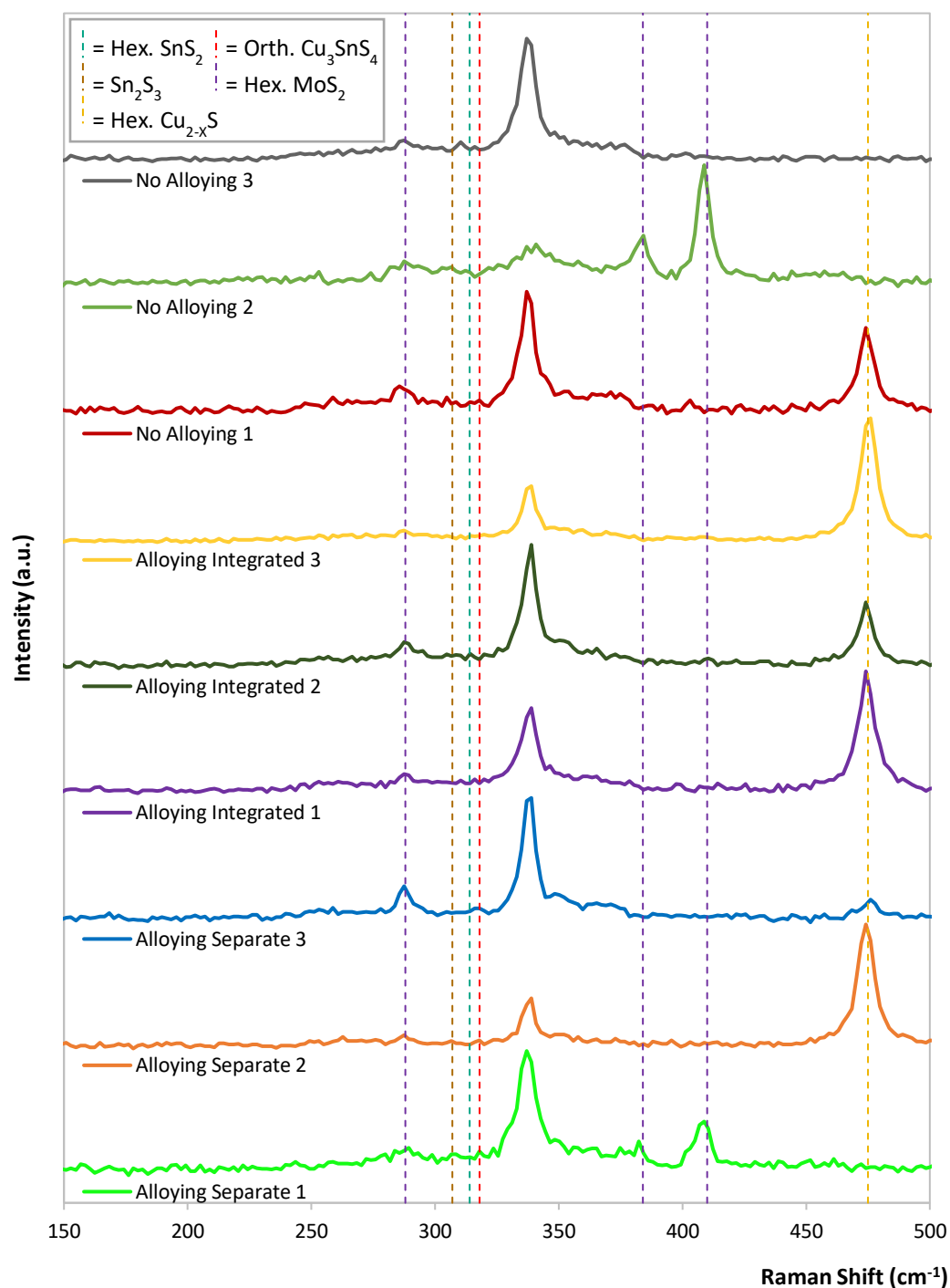


**Figure 5-35 - One Raman spectrum from each sample selected to show the greatest variety of unwanted phases. There are substantial variations between the samples, but no particular trends relating to the pre-alloying treatments are evident.**



by means of vertical pink dotted lines, although, as previously, it is not possible to completely rule out the presence of small quantities of ZnS and tetragonal  $\text{Cu}_2\text{SnS}_3$ . There are no strong peaks associated with unwanted phases, although there may be small peaks present for  $\text{Sn}_2\text{S}_3$ , hexagonal  $\text{SnS}_2$  and orthorhombic  $\text{Cu}_3\text{SnS}_4$  in some of the spectra, the positions of the peaks being indicated by light brown, turquoise and red vertical dotted lines respectively. In common with the XRD patterns, there does not appear to be any specific trend relating to the treatment received by the samples, suggesting that there may not be a significant difference in the chemical compositions of the films. In reality, Figure 5-34 does not reflect the true variation seen between the spectra obtained from different samples. Figure 5-35 also presents one Raman spectrum obtained from each sample, but these spectra were chosen to show the greatest variety of unwanted phases.

In addition to CZTS and the small peaks associated with  $\text{Sn}_2\text{S}_3$ , hexagonal  $\text{SnS}_2$  and orthorhombic  $\text{Cu}_3\text{SnS}_4$  seen previously, it is evident that there are substantial peaks associated with hexagonal  $\text{Cu}_{2-x}\text{S}$  and hexagonal  $\text{MoS}_2$  present on multiple samples. The positions of these peaks are indicated by vertical yellow and vertical purple dotted lines respectively. There are no specific trends relating to the treatments that the samples underwent, however, there is some correlation between the appearance of the region of the film and the compounds found to be present in the corresponding Raman spectrum. In particular, regions that appeared darker were more likely to contain  $\text{Cu}_{2-x}\text{S}$ , whereas regions that had the appearance of pinholes or craters were more likely to contain  $\text{MoS}_2$ . Examples of microscope images of darker material and a pinhole can be seen in Figure 5-36. Of the fifty-four Raman spectra obtained across

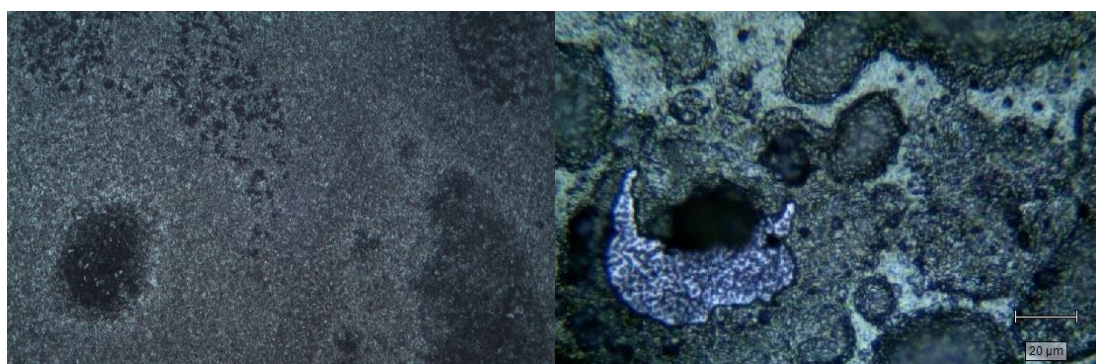


**Figure 5-36 - Microscope images taken at 20X magnification showing darker regions associated with  $\text{Cu}_{2-x}\text{S}$  (left) and a pinhole associated with  $\text{MoS}_2$  (right).**



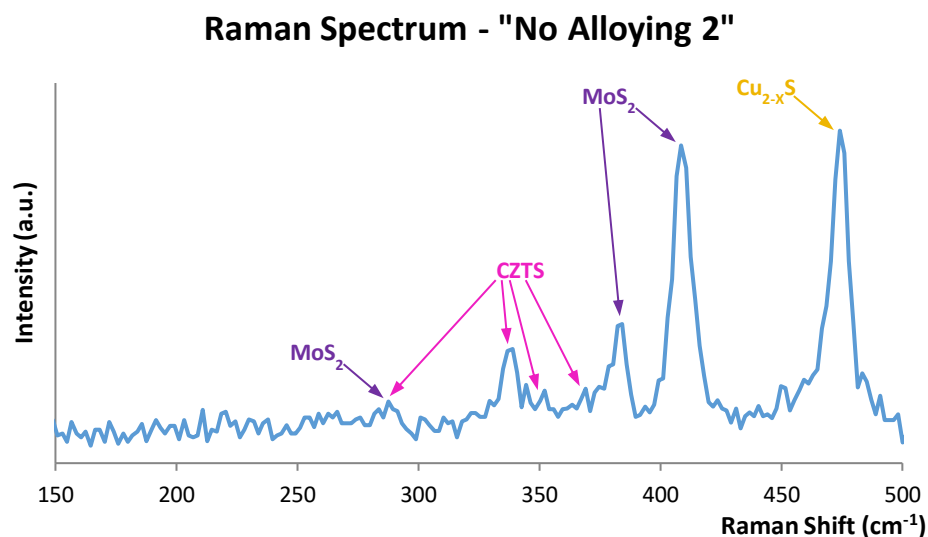


**Figure 5-37 - The only Raman spectrum obtained which exhibits peaks for both  $\text{MoS}_2$  and  $\text{Cu}_{2-x}\text{S}$ . The spectrum was obtained from a dark region bordering a crater.**

the nine samples, only one of them returned clear peaks for both  $\text{Cu}_{2-x}\text{S}$  and hexagonal  $\text{MoS}_2$ . This spectrum was obtained from a dark region of film near the edge of a crater on the sample labelled “No Alloying 2” and is presented in Figure 5-37. What is also noteworthy is the inconsistency between samples – for example, the sample labelled “No Alloying 3” returned spectra with a good match for CZTS without peaks associated with  $\text{Cu}_{2-x}\text{S}$  and  $\text{MoS}_2$  on all points sampled, including darker regions at both the edge and centre, whereas the sample labelled “No Alloying 2” only returned one spectrum without peaks associated with unwanted phases, which was obtained near the centre. Similarly, the sample labelled “Alloying Separate 2” returned peaks associated with  $\text{Cu}_{2-x}\text{S}$  near the edges of the sample, with this compound apparently absent from the film closer to the centre, while the sample labelled “Alloying Separate 3” showed the opposite, with  $\text{Cu}_{2-x}\text{S}$  being evident near the centre but absent near the edges, including on blistered and unblistered parts of the film. These variations, which were seen to an extent between all of the samples, are an indication that the chemical composition of each film is highly sensitive to an additional factor that is not related to the pre-alloying of the precursors, such that any effect the pre-alloying may be having is likely to be masked by these variations. The cause of the variations in the compounds obtained may relate to variations in the abundance ratios between the three deposited elements, both locally between

different points on each sample and more generally between samples. CZTS is sensitive to the stoichiometry of its composition, and sub-optimum elemental ratios will lead to the formation of unwanted phases, including  $\text{Cu}_{2-x}\text{S}$  [24]. The reason for the degree of variation seen in this set of samples may be that the electrodeposited precursor films were simply too thin, meaning that even relatively small variations in the mass or thickness of the deposited films would have led to proportionately large variations in the elemental ratios, causing the formation of unwanted phases, such as  $\text{Cu}_{2-x}\text{S}$ . The detection of  $\text{MoS}_2$  is indicative of an exposed substrate – although  $\text{MoS}_2$  is expected to form in any case due to the diffusion of sulphur through the deposited layer during the sulphurisation process, the shallow penetration depth of the laser used in the Raman spectrometer ( $\sim 140$  nm) would not detect the  $\text{MoS}_2$  beneath the CZTS film. It is noteworthy that this compound was most apparent on a sample that had not received a pre-alloying treatment, although this in itself is not sufficient to establish a trend. There would be scope for further work involving the study of the effect of the thickness of the deposited precursor stack if the project were to be extended. The overall thickness (the quantity of each element being adjusted by the same proportion) of deposited precursor films could be altered between samples and the uniformity of the obtained phases compared.

Having conducted an experiment in which the pre-alloying step was integrated into the sulphurisation process by means of a period at which the furnace temperature was held at  $300^\circ\text{C}$  for 10 minutes prior to the temperature increasing, it was decided that it would be useful to ascertain how much sulphur would have evaporated during this pre-alloying step. In order to do this, 750 mg sulphur was placed in the graphite annealing box, the box was weighed and then placed in the furnace, and then a heating cycle was run at  $300^\circ\text{C}$  for 10 minutes with a ramp rate of  $2.5^\circ\text{C s}^{-1}$ . The box was then weighed again once the system had cooled. It was found that the total mass at the end of the process was 744 mg less than that at the start, and no remaining sulphur was visible inside the box. This indicated that all of the sulphur would likely have evaporated during the pre-alloying step of the combined pre-alloying and sulphurisation process. This was not surprising, given that the melting point and boiling point of sulphur at atmospheric pressure are  $115^\circ\text{C}$  and  $445^\circ\text{C}$  respectively [25], with the boiling point falling to  $161^\circ\text{C}$  at the 3.75 Torr pressure

used in this experiment [26]. Nonetheless, this was considered an unfavourable result, as it was desired that the conditions during the pre-alloying stage of the combined process would be as near as possible to that when the process is carried out separately, i.e. not sulphur-rich. It would also affect the sulphur concentration during the sulphurisation (higher temperature) stages of the heating cycle as more sulphur vapour would have escaped from the annealing box by the point at which the sulphurisation temperatures were reached, although this may be compensated somewhat by the fact that the sulphur will have had a greater time period in which to diffuse into the metallic precursors prior to reaching the reaction temperature of 550 °C. In order to prevent this premature evaporation from occurring, it would be necessary to carry out the annealing processes in a dual zone furnace, in which the sulphur could be placed in a zone held at a lower temperature than the samples until the sulphurisation stage was reached. This would not normally involve a graphite box and an RTP system, and can be carried out using a multi-zone tube furnace under gas flow to carry the evaporated sulphur to the samples. Such a setup is described in [21].

Although the analytical experiments described in this section did not indicate any clear trends in the chemical compositions of the films relating to the pre-alloying treatments, it was observed that the inclusion of a pre-alloying treatment, whether separate or integrated into the sulphurisation process, was beneficial as it did reduce the number of pinholes in the sulphurised films. Although additional analytical techniques, such as EDS, may have revealed such trends, these were not carried out due to time constraints on the project. Despite this, the effect of the differences in film morphology on solar cell performance form part of the discussions to follow in chapter 6, as the films described in this section were processed into completed photovoltaic devices.

## **5.4 Conclusions**

Successful trials were conducted using a hot-dip simulator for initial experimentation in the pre-alloying of electroplated stacks. Although the level of analysis carried out on these samples was not as extensive as that on those pre-alloyed using the rapid thermal processing furnace, it was shown that the samples could withstand a rapid

temperature increase to 350 °C at 16 °C s<sup>-1</sup> and some evidence of intermixing and dispersion of the deposited elements was demonstrated. This indicated that the HDS may be suitable for this stage of the annealing process and proved useful in informing the subsequent stage of experimentation with the RTP furnace.

Conditions for the pre-alloying of the electroplated precursor stacks through the use of an RTP furnace were optimised. It was demonstrated through the use of XRD and XPS depth profiling that even the lowest temperature tested (285 °C) was sufficient to intermix and alloy the elements, but visual observations demonstrated that a slightly higher temperature of 300 °C was needed to avoid the formation of large blisters and allow the intermixed film to form a smoother surface. Higher temperatures led to some oxidation and premature diffusion of sulphur into the films. It was discovered that an annealing time of 10 or more minutes was sufficient to fully intermix and alloy the elements at a temperature of 300 °C. It also became apparent that the quantity of zinc deposited onto the precursor stack affected the ability of tin to alloy with the copper, with the preferential alloying of copper with zinc meaning that tin was left unalloyed when excess zinc was present.

There are numerous parameters by which the sulphurisation process would need to be optimised, and in this project it was taken upon to address two of them, these being the background pressure and the sulphur concentration. It was demonstrated that the pre-alloying stage of the annealing process was beneficial to the films in that there was a reduction in the number of pinholes observed, and the pre-alloying process was successfully integrated into the sulphurisation process. Unfortunately, it was not possible to directly link the pre-alloying process received to the variations seen in the film composition data obtained using XRD or Raman spectroscopy. It was considered most likely that these were most strongly affected by variations in the elemental ratios, which may be mitigated by the deposition of thicker precursor films – an investigation into this would be an opportunity for further work should the project be extended. It was also impossible to rule out the possibility of small quantities of cubic ZnS and tetragonal Cu<sub>2</sub>SnS<sub>3</sub> due to the close proximity of the main associated peaks with those of CZTS for both XRD and Raman spectroscopy. It would be necessary to study the CZTS films using lasers of a broad range of wavelengths in order to distinguish these compounds. It would also be useful to

analyse the films for elemental composition using EDS in order to establish whether there are significant differences in the elemental ratios between the samples receiving a pre-alloying treatment and those not. This may give some indication as to whether the pinholes seen on samples that did not undergo a pre-alloying treatment were caused by tin losses during sulphurisation. A full optimisation of the temperature/time for the sulphurisation heating profile would also further improve the chances of obtaining higher quality films and thus enabling a more effective comparison between sulphurised samples receiving pre-alloying treatments. This would also be an opportunity for further study. Although time constraints meant that the desired range of analysis was not carried out on the sulphurised films that had undergone differing pre-alloying treatments, these samples were used for further processing into photovoltaic devices, which did provide some additional information on the benefits of the pre-alloying process. These experiments and results will be described and discussed further in chapter 6.

## 5.5 References

- [1] Y. Ren, “Annealing of  $\text{Cu}_2\text{ZnSn}(\text{S},\text{Se})_4$  Thin Films,” Uppsala Universitet, Uppsala, Sweden, 2017.
- [2] H. Yoo, J. Kim and L. Zhang, “Sulfurization Temperature Effects on the Growth of  $\text{Cu}_2\text{ZnSnS}_4$  Thin Film,” *Current Applied Physics*, vol. 12, no. 4, pp. 1052-1057, July 2012.
- [3] S. Ahmed, K. B. Reuter, O. Gunawan, L. Guo, L. T. Romankiw and H. Deligianni, “A High Efficiency Electrodeposited  $\text{Cu}_2\text{ZnSnS}_4$  Solar Cell,” *Advanced Energy Materials*, vol. 2, no. 2, pp. 253-259, February 2012.
- [4] L. Guo, Y. Zhu, O. Gunawan, T. Gokmen, V. R. Deline, S. Ahmed, L. T. Romankiw and H. Deligianni, “Electrodeposited  $\text{Cu}_2\text{ZnSnSe}_4$  Thin Film Solar Cell with 7% Power Conversion Efficiency,” *Progress in Photovoltaics: Research and Applications*, vol. 22, no. 1, pp. 58-68, January 2014.

- [5] J. J. Scragg, "Section 3.11 - Conversion of Precursors into Compound Semiconductors: Annealing of Metal Stacks in the Absence of Sulfur," in *Copper Zinc Tin Sulfide Thin Films for Photovoltaics: Synthesis and Characterisation by Electrochemical Methods*, Berlin, Springer-Verlag, 2011, pp. 77-86.
- [6] S. M. Pawar, A. I. Inamdar, B. S. Pawar, K. V. Gurav, S. W. Shin, X. Yanjun, S. S. Kolekar, J.-H. Lee, J. H. Kim and H. Im, "Synthesis of Cu<sub>2</sub>ZnSnS<sub>4</sub> (CZTS) Absorber by Rapid Thermal Processing (RTP) Sulfurization of Stacked Metallic Precursor Films for Solar Cell Applications," *Materials Letters*, vol. 118, pp. 76-79, 2014.
- [7] Royal Society of Chemistry, "Tin - Element Information, Properties and Uses | Periodic Table," 2019. [Online]. Available: <http://www.rsc.org/periodic-table/element/50/tin>. [Accessed 23 April 2019].
- [8] Royal Society of Chemistry, "Zinc - Element Information, Properties and Uses | Periodic Table," 2019. [Online]. Available: <http://www.rsc.org/periodic-table/element/30/zinc>. [Accessed 23 April 2019].
- [9] Royal Society of Chemistry, "Copper - Element Information, Properties and Uses | Periodic Table," 2019. [Online]. Available: <http://www.rsc.org/periodic-table/element/29/Copper>. [Accessed 23 April 2019].
- [10] J. J. Scragg, "Section 3.1 - Conversion of Precursors into Compound Semiconductors: Alloying of Precursors," in *Copper Zinc Tin Sulfide Thin Films for Photovoltaics: Synthesis and Characterisation by Electrochemical Methods*, Berlin, Springer-Verlag, 2011, pp. 59-64.
- [11] A. Vaitkus, A. Merkys and S. Gražulis, "Validation of the Crystallography Open Database using the Crystallographic Information Framework," *Journal of Applied Crystallography*, vol. 54, no. 2, pp. 611-672, 2021.
- [12] M. Quirós, S. Gražulis, S. Girdzijauskaitė, A. Merkys and A. Vaitkus, "Using SMILES strings for the description of chemical connectivity in the Crystallography Open Database," *Journal of Cheminformatics*, vol. 10, no. 23, p. 23, 2018.
- [13] A. Merkys, A. Vaitkus, J. Butkus, M. Okulič-Kazarinas, V. Kairys and S. Gražulis, "COD::CIF::Parser: an error-correcting CIF parser for the Perl language," *Journal of Applied Crystallography*, vol. 49, no. 1, pp. 292-301, 2016.

- [14] S. Gražulis, A. Merkys, A. Vaitkus and M. Okulič-Kazarinas, “Computing stoichiometric molecular composition from crystal structures,” *Journal of Applied Crystallography*, vol. 48, no. 1, pp. 85-91, 2015.
- [15] S. Gražulis, A. Daškevič, A. Merkys, D. Chateigner, L. Lutterotti, M. Quirós, N. R. Serebryanaya, P. Moeck, R. T. Downs and A. LeBail, “Crystallography Open Database (COD): an open-access collection of crystal structures and platform for world-wide collaboration,” *Nucleic Acids Research*, vol. 40, no. D1, pp. D420-D427, 2012.
- [16] S. Gražulis, D. Chateigner, R. T. Downs, A. T. Yokochi, M. Quiros, L. Lutterotti, E. Manakova, J. Butkus, P. Moeck and A. Le Bail, “Crystallography Open Database – an open-access collection of crystal structures,” *Journal of Applied Crystallography*, vol. 42, no. 4, pp. 726-729, 2009.
- [17] R. T. Downs and M. Hall-Wallace, “The American Mineralogist Crystal Structure Database,” *American Mineralogist*, no. 88, pp. 247-250, 2003.
- [18] J. J. Scragg, “Section 2.8 - Electrodeposition of Metallic Precursors: Electrodeposition of Zn from an Acid Chloride Electrolyte,” in *Copper Zinc Tin Sulfide Thin Films for Photovoltaics: Synthesis and Characterisation by Electrochemical Methods*, Berlin, Springer-Verlag, 2011, pp. 42-47.
- [19] A. Redinger, D. M. Berg, P. J. Dale and S. Siebentritt, “The Consequences of Kesterite Equilibria for Efficient Solar Cells,” *Journal of the American Chemical Society*, vol. 133, no. 10, pp. 3320-3323, 2011.
- [20] M. Abusnina, M. Matin, H. Moutinho and M. Al-Jassim, “Impact of the Stack Order in Cu-Zn-Sn Metal Precursors on the Properties of Cu<sub>2</sub>ZnSnS<sub>4</sub> Thin Films,” in *IEEE 42nd Photovoltaic Specialist Conference, PVSC 2015*, New Orleans, 2015.
- [21] J. J. Scragg, T. Ericson, T. Kubart, M. Edoff and C. Platzer-Bjorkman, “Chemical Insights into the Instability of Cu<sub>2</sub>ZnSnS<sub>4</sub> Films during Annealing,” *Chemistry of Materials*, vol. 23, no. 20, pp. 4625-4633, 2011.
- [22] P. A. Fernandes, P. M. P. Salome and A. F. da Cunha, “Study of Polycrystalline Cu<sub>2</sub>ZnSnS<sub>4</sub> Films by Raman Scattering,” *Journal of Alloys and Compounds*, vol. 509, no. 28, pp. 7600-7606, 2011.
- [23] R. B. Ettlinger, “CTS and CZTS for Solar Cells made by Pulsed Laser Deposition and Pulsed Electron Deposition,” DTU Fotonik, Lyngby, 2016.

- [24] R. A. Wibowo, H. Yoo, A. Holzing, R. Lechner, S. Jost, J. Palm, M. Gowtham, B. Louis and R. Hock, "A Study of Kesterite  $\text{Cu}_2\text{ZnSn}(\text{Se},\text{S})_4$  Formation from Sputtered Cu–Zn–Sn Metal Precursors by Rapid Thermal Processing Sulfo-Selenization of the Metal Thin Films," *Thin Solid Films*, vol. 535, pp. 57-61, May 2013.
- [25] Royal Society of Chemistry, "Sulfur - Element information, properties and uses | Periodic Table," 2021. [Online]. Available: <https://www.rsc.org/periodic-table/element/16/sulfur>. [Accessed 4 May 2021].
- [26] TriMen Chemicals, "Boiling Point Calculator," 17 April 2013. [Online]. Available: <http://www.trimen.pl/witek/calculators/wrzenie.html>. [Accessed 4 May 2021].



## 6 Photovoltaic Device Fabrication and Measurement

### 6.1 Introduction

Having carried out optimisation of the deposition of metallic precursors, as well as some optimisation of the annealing and sulphurisation processes, it was deemed necessary to further process manufactured CZTS films into completed photovoltaic devices. This was in order to ascertain whether the optimisation carried out thus far translated into effective working devices. This chapter is, in effect, a continuation of the optimisation work carried out in chapter 5, in that it compares the results obtained using different annealing sequences, but rather than simply comparing film morphology and composition, it studies whether these previous observations can be correlated with solar cell performance. In particular, comparison is drawn between films that have received no pre-alloying process prior to sulphurisation, films that have received a separate pre-alloying process prior to sulphurisation, and films that received a pre-alloying treatment and sulphurisation within a single furnace operation. In addition to this, cell performances are correlated with their positioning on the sample substrate, and comparison drawn between morphological properties of the cell films and the J-V characteristics observed. It is possible to carry out some photoresponse measurements without the deposition of further layers after CZTS. This can be done through the immersion of CZTS samples in a suitable electroconductive solution, such as a europium nitrate electrolyte [1], with the sample being set up as the working electrode connected to a potentiostat/galvanostat. The electrolyte effectively acts as a substitute for the layers that would normally be subsequently deposited. This technique can be used to calculate the equivalent quantum efficiency (EQE) of a sample (a measurement of the flow of electrons extracted from a with respect to the photons incident upon a sample [2] at different wavelengths) and hence estimate the band gap of the CZTS under test [3]. Consideration was given to whether this technique would be useful in this project, however, after discussion with experienced colleagues and collaborators it was decided against. This was partly because the CZTS films had numerous blisters and visible pinholes, and advice was provided that the electrolyte would simply “soak through” the CZTS film and form direct contact with the Mo substrate, rather than

form the desired pseudo p-n junction with CZTS. Another reason for not deploying this technique was that it does not allow for the scoring of a film into a grid of multiple different cells, an approach that was used to analyse different regions of sample effectively in this project (see below). Characterisation of CZTS by use of electrochemical techniques is perhaps most suited to the analysis of single crystal CZTS, as carried out by Ng et al and Durant et al [3, 4].

## 6.2 Experimental Methods

Nine sulphurised CZTS films were completed into photovoltaic devices and electrical measurements were carried out in order to obtain power conversion efficiencies. These nine films were those discussed in section 5.3.4. The following paragraph reiterates how these films were prepared:

Three-layer electroplated stacks of copper, tin and zinc were deposited onto Mo-SLG with surface areas of 4 cm<sup>2</sup>. Each of the three elements were deposited using static electrodes and stagnant electrolytes under optimised conditions as discussed in chapters 3 and 4. Copper was deposited using an alkaline electrolyte to a charge-passed density of 572 mC cm<sup>-2</sup> and tin was deposited using a methanesulfonic acid electrolyte to a charge-passed density of 312 mC cm<sup>-2</sup>. The electrolyte formulae are stated in sections 2.1.5 and 2.1.8 respectively. Zinc was deposited using an acid-sulphate electrolyte (Electrolyte Zn 6, section 2.1.9) to a charge-passed density of 420mC/cm<sup>2</sup>. The nine samples were then divided evenly into three groups of three, each group being subjected to one of three annealing sequences using the RTP furnace. These sequences were either pre-alloying followed by sulphurisation executed in separate furnace operations (“Alloying Separate”), pre-alloying and sulphurisation combined into a single furnace operation (“Alloying Integrated”), or sulphurisation without a pre-alloying step included (“No Alloying”). Details of the annealing conditions and parameters are given in section 5.3.4, while an overview of the RTP furnace setup can be found in section 2.2.2.

The processing of the CZTS samples into completed photovoltaic devices is described in detail in section 2.3. The prepared CZTS films were deposited with ~70nm thick CdS films via chemical bath deposition (section 2.3.1), followed by the

sputtering of 50nm iZnO and 500nm AZO (section 2.3.2). Each sample was then divided into a grid of fifteen  $4 \times 4$  mm<sup>2</sup> individual cells and a reference system assigned, as detailed in section 2.3.3. Electrical measurements for the calculation of the power conversion efficiency were then carried out on each individual cell using a solar simulator under the illumination of the AM1.5 Global spectrum with an irradiance of 100 mW cm<sup>-2</sup> (also detailed in section 2.3.3).

### 6.3 Results and Discussion

In total, 135 individual cells were measured across nine substrates, and the efficiencies are plotted on the scatter graph presented in Figure 6-1. As there were three substrates designated to each annealing sequence, this equated to 45 individual cells per annealing sequence. Each annealing sequence is colour coded in order to identify the related data points, and vertical grid lines have been added to separate the results relating to each substrate. The mean efficiency values for each annealing

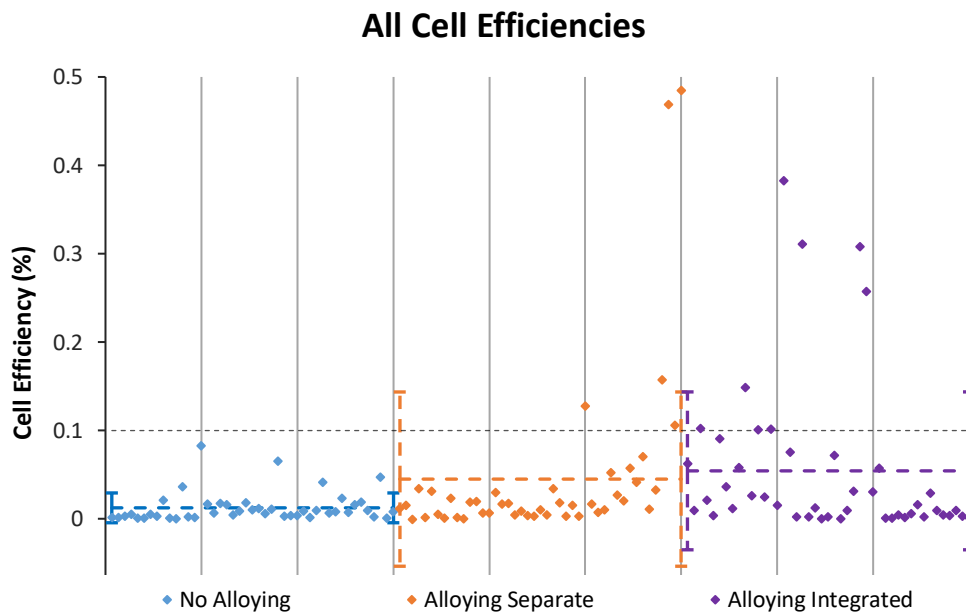


**Figure 6-1 – Cell efficiencies plotted for all annealing sequences. The vertical gridlines separate the results in terms of substrates, while the horizontal coloured dotted lines indicate the average efficiency for each annealing sequence. The vertical coloured dotted lines (error bars) indicate the standard deviation in results for each annealing sequence, and a horizontal dotted grey line has been added at 0.1%, as cells that obtained this efficiency or greater were considered in more detail.**

sequence are indicated by horizontal dotted lines, and the standard deviations are indicated by the error bars at the ends of each horizontal dotted line. It is possible to observe that the inclusion of a pre-alloying phase benefits the average cell efficiency. Furthermore, the highest average cell efficiency is achieved by the integrated alloying sequence. The integrated alloying process also returned a slightly lower value for the standard deviation – it more consistently returns higher efficiencies. Of all the cells tested, one hundred and twenty seven of them were found to have power conversion efficiencies of less than 0.1% and were considered non-functional, however, thirteen cells were found to have efficiencies of 0.1% or greater, six of which exceeded 0.2%. Although 0.1% could be viewed as an arbitrary value, it was considered reasonable that a cell should be able to register at least one decimal place when tested to be worth treating as a working device, and this equated to roughly 10% of all the cells measured here. The efficiencies of the thirteen functional cells are plotted in Figure 6-2, with the sample of origin being indicated by the colour and shape of the corresponding data plot. The dotted horizontal lines indicate the mean efficiency of the functional cells on each represented sample. It is possible to see that no functional cells were obtained on samples that did not undergo a pre-alloying process. This reaffirms the suggestion that the pre-alloying process is necessary in

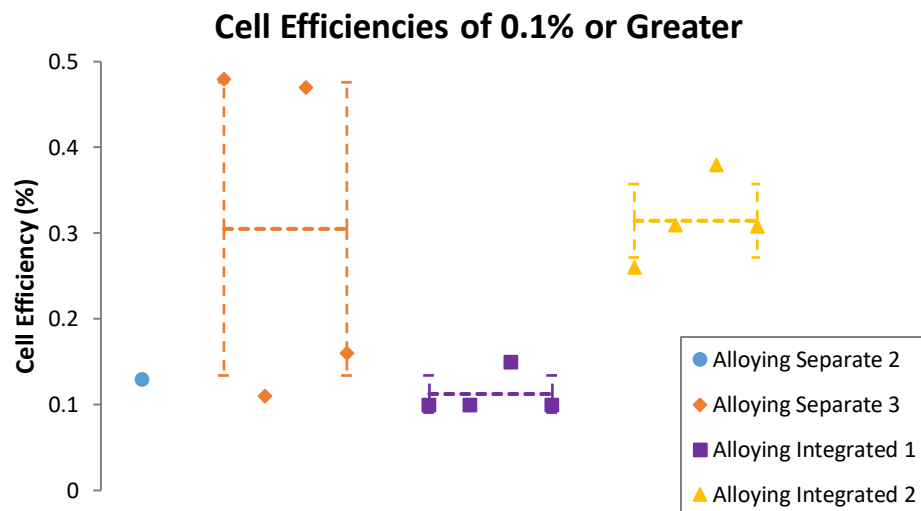


**Figure 6-2 - Power conversion efficiencies for the thirteen functional cells, separated by sample of origin. The horizontal dotted lines represent the average efficiency of the functioning cells on each sample and the error bars represent the standard deviation for that sample.**

order to obtain the most favourable results, and indicates that the improvements in morphological findings in section 5.3.4 – that the pre-alloying step reduces the number of pinholes in the CZTS films – translates into an increased probability of obtaining functional devices. Considering the data in Figure 6-2 in terms of each substrate, the best results were achieved on the substrate labelled Alloying Integrated 2 – the efficiencies of the three functional cells have the lowest standard deviation and the highest average value. Although the two most efficient cells were achieved on the substrate labelled Alloying Separate 3, the standard deviation is significantly greater and the average efficiency value slightly lower. It is also notable that the substrate labelled Alloying Integrated 1 also has a low standard deviation value, and achieved four functional cells. If the data is considered in terms of how the cells were processed, i.e. whether the alloying was integrated or performed separately, the calculated average functional cell efficiency for separate alloying was slightly higher at 0.27%, compared to 0.21% for integrated alloying. However, integrated alloying returned eight functional cells, while separate alloying only returned five. The standard deviation of the functional cell efficiencies was also lower for integrated alloying, in agreement with the results presented in Figure 6-1. This reinforces the suggestion that, not only is the integrated alloying process more convenient, it is also more consistent in producing functional cells. Although this is a positive finding, due to the relatively small number of functional cells, the experiment would need to be repeated multiple times with fresh samples to confidently conclude that integrating the alloying process is beneficial to cell performance, although these preliminary results would suggest that it is.

For the five cells with efficiencies greater than 0.2%, J-V curves have been plotted and are presented alongside photographs of the cells in Figure 6-3 – Figure 6-7. It is noteworthy that all of these cells sit near to the edge of the samples, either in column A or column E. Although the thickness variation across the CZTS films was not measured, it is possible to speculate based on the appearance of the films that CZTS is of insufficient thickness near the centre of the sample. This could lead to incomplete absorption of the incident radiation, thus reducing the power output of the cells in this region. The functional cells do not appear to have any large pinholes

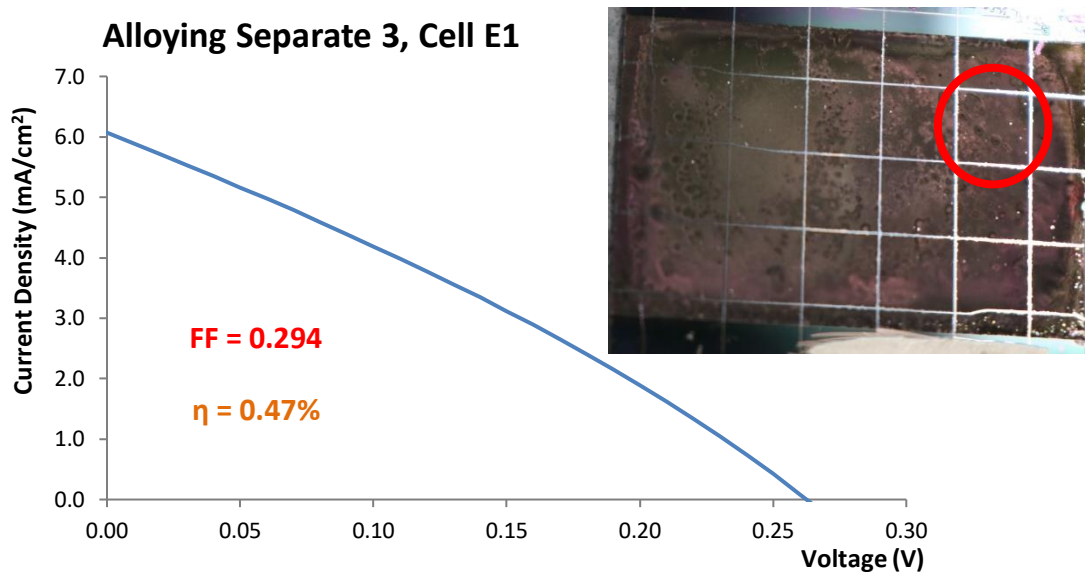


**Figure 6-3 - J-V curve and photograph of the cell with the highest fill factor.**

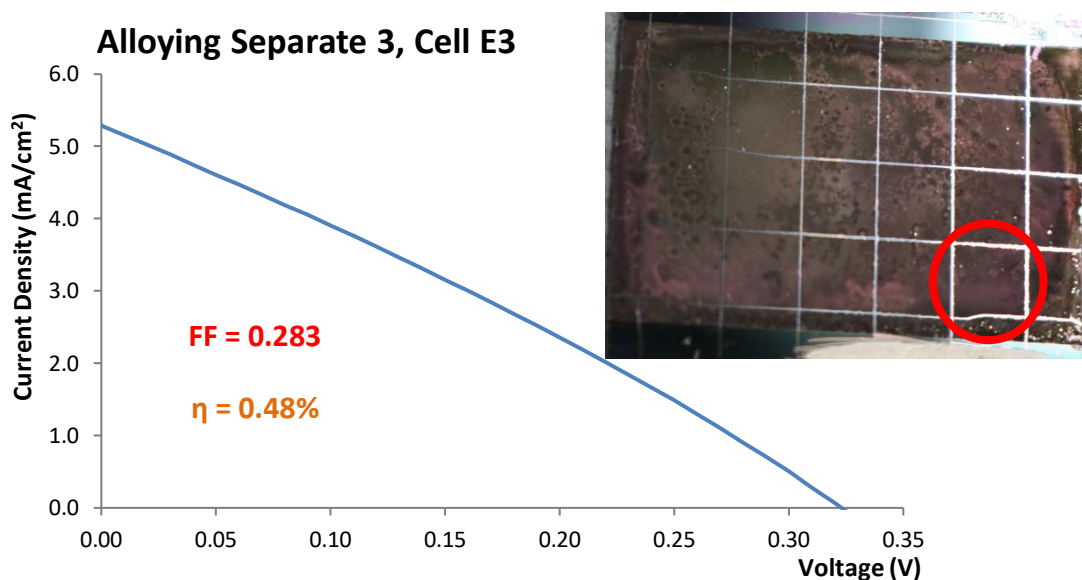


**Figure 6-4 - J-V curve and photograph of the film with the highest power conversion efficiency.**

present (although some small pinholes may be visible on the cells in Figure 6-3 and Figure 6-4, these could also be grains of dust), but some inhomogeneity is visible, particularly on the cells in Figure 6-5, Figure 6-6 and Figure 6-7. Visual inhomogeneity can be indicative of the presence of unwanted phases (see discussion regarding Raman spectroscopy results in section 5.3.4), which may give some

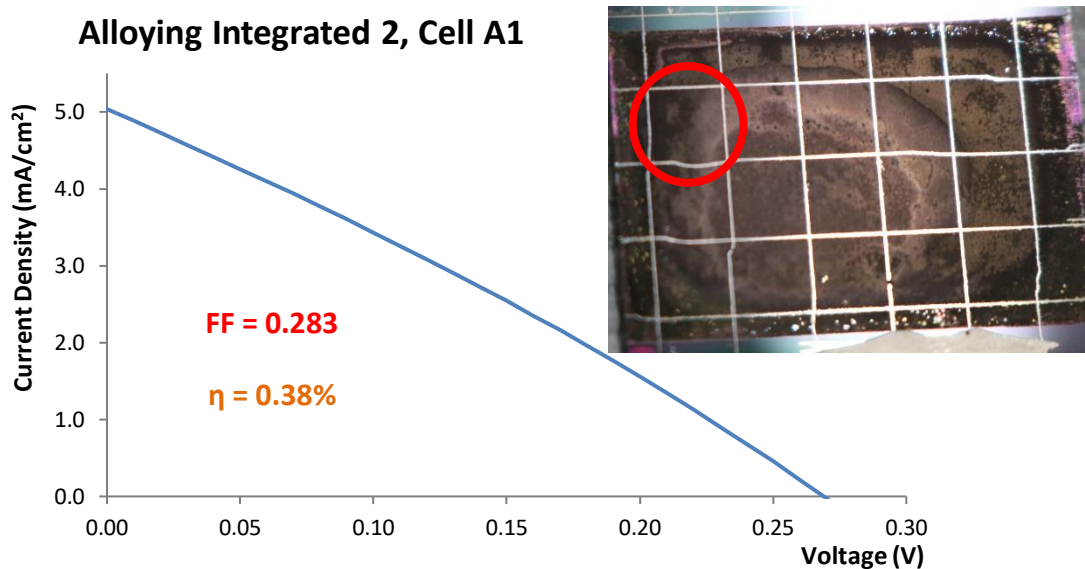


**Figure 6-5 - J-V curve and cell photograph of one of the highest performing cells, despite the visible inhomogeneity in the cell film.**

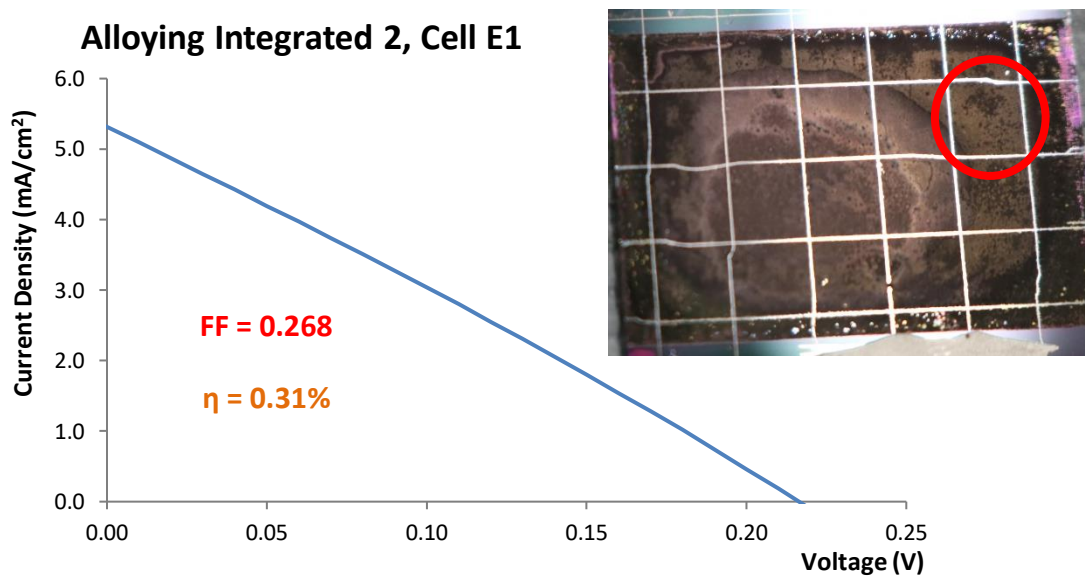


**Figure 6-6 - Another example of one of the higher performing cells. It is a notable trend that these cells sit near the edges of the samples.**

explanation as to the reasons for obtaining relatively low efficiencies in general. The presence of unwanted phases can cause the trapping of charges at the interfaces between grains of differing phases, which could have the result of increasing the series resistance of the device. Charge trapping can also facilitate the recombination

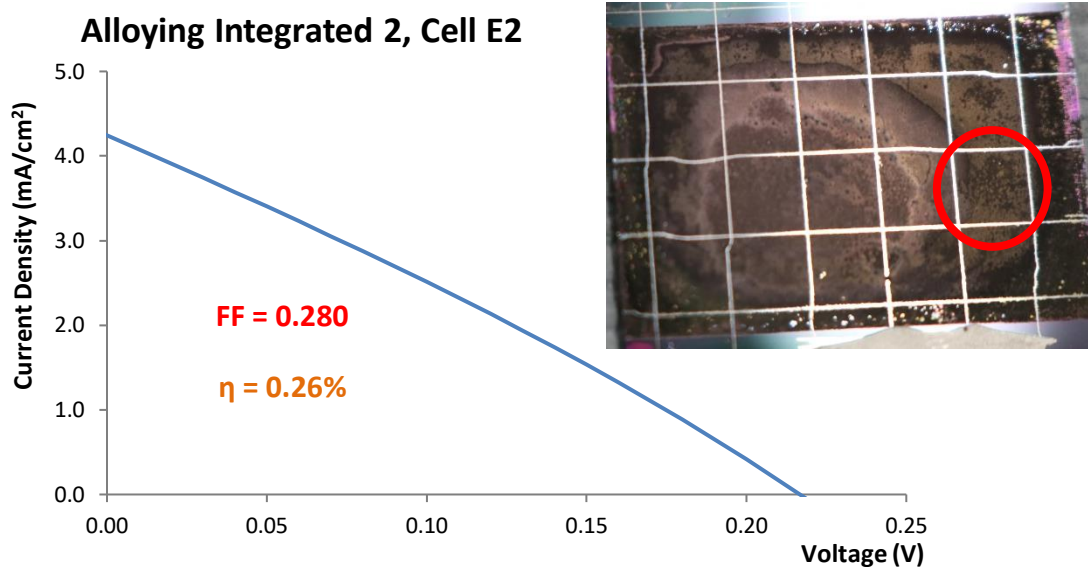


**Figure 6-7 - The fifth-best performing cell, also at the edge of its sample. It is suspected that CZTS film near the centre of samples is of insufficient thickness.**

of opposite charges, which would in turn reduce the value of  $J_{SC}$  and therefore the overall power conversion efficiency. The fill factors on the J-V curves of all of the devices were very poor, the highest value of 29.4% being achieved on the J-V curve in Figure 6-3, and the shapes of the J-V curves were far from that of a good quality solar cell, as seen in the example in Figure 2-16, section 2.3.3. When compared to the values obtained by Ahmed et al ( $J_{SC} = 22 \text{ mA cm}^{-2}$ ,  $V_{OC} = 567 \text{ mV}$ ,  $FF = 58.1\%$  and  $\eta = 7.3\%$ ) [5] on an electroplated device with a pre-alloying step, the values obtained from the highest performing device in this project ( $J_{SC} = 5.3 \text{ mA cm}^{-2}$ ,  $V_{OC} = 320 \text{ mV}$ ,  $FF = 28.3\%$  and  $\eta = 0.48\%$ ) could be considered to be somewhat deficient. However, Khalil et al reported in [6] an electrodeposited film on a molybdenum foil substrate with an efficiency of 0.55% achieved with a cell area of  $0.15 \text{ cm}^2$ , similar to the cells reported here. The fill factor was reported as 35.7%, the  $J_{SC}$  was  $7.60 \text{ mA cm}^{-2}$  and the  $V_{OC}$  was 204 mV (unfortunately, values for  $R_S$  and  $R_{SH}$  were not given). The work presented here, although achieving slightly lower  $J_{SC}$ ,  $FF$  and overall efficiency, did achieve a significantly higher  $V_{OC}$ , which is promising (a brief discussion about factors that affect the  $V_{OC}$  and  $J_{SC}$  is included within the following text). Now considering the fill factor, other than the possible high series resistance commented on previously, a factor that could negatively affect this is the



shunt resistance of the devices. Shunt resistance relates to leakage of current through the cell [7], i.e. charge that passes between the top and bottom contacts of the device without passing through the photoactive material (or the external circuit that the device is connected to), and pinholes can often act as a shunting path. In order to obtain a high fill factor, and a higher performing cell in general, it is necessary to achieve as high a shunt resistance as possible (as well as a low series resistance) [7]. One method of calculating the shunt resistance ( $R_{SH}$ ) and the series resistance ( $R_S$ ) is by taking the inverse of the gradient of a J-V curve at the  $J_{SC}$  and the  $V_{OC}$  respectively. This was performed automatically by the solar simulator data analysis software (written by Dr Justin Searle). For the cell with the highest fill factor, the  $R_{SH} = 55.3 \Omega \text{ cm}^2$  and the  $R_S = 28.4 \Omega \text{ cm}^2$ . For the cell with the highest performance efficiency, the  $R_{SH} = 74.3 \Omega \text{ cm}^2$  and the  $R_S = 43.4 \Omega \text{ cm}^2$ . The solar cell reported by Ahmed et al in [5] had an  $R_{SH}$  of  $368 \Omega \text{ cm}^2$  and an  $R_S$  of  $4.1 \Omega \text{ cm}^2$ , significantly more favourable values for both types of resistance. One of the reasons for the high series resistances seen here may be that no metallic evaporated grid was added to the top of the solar cell devices. A metallic grid can be added as the top contact to improve charge collection and therefore reduce series resistance, however, a grid can easily become damaged if a sample is scored and divided into multiple smaller cells, so it was not added to the samples in this project. Had such a grid been added, it may have led to a significant improvement in the device efficiencies: Electrodeposited devices are reported by Guo et al in [8] that have efficiencies of 3.5% and 4.9%, with  $R_S$  values of  $4.5 \Omega \text{ cm}^2$  and  $4.0 \Omega \text{ cm}^2$ , and  $R_{SH}$  values of just  $70 \Omega \text{ cm}^2$  and  $150 \Omega \text{ cm}^2$  respectively. Also, the  $V_{OC}$  values were 301 mV and 338 mV, not dissimilar to the values obtained for the best cells presented here. This demonstrates that it is still possible to obtain moderately respectable cell efficiencies with relatively poor shunt resistances, provided that the series resistances are low. As there is the potential to decrease the series resistances of the cells presented here by adding metallic grid contacts, these preliminary results could be considered promising.

Although the best performing cells in this project were found in locations where there were fewer visible pinholes, it is possible to see from SEM images of sulphurised films in chapter 5 that microscopic pinholes and regions of film porosity

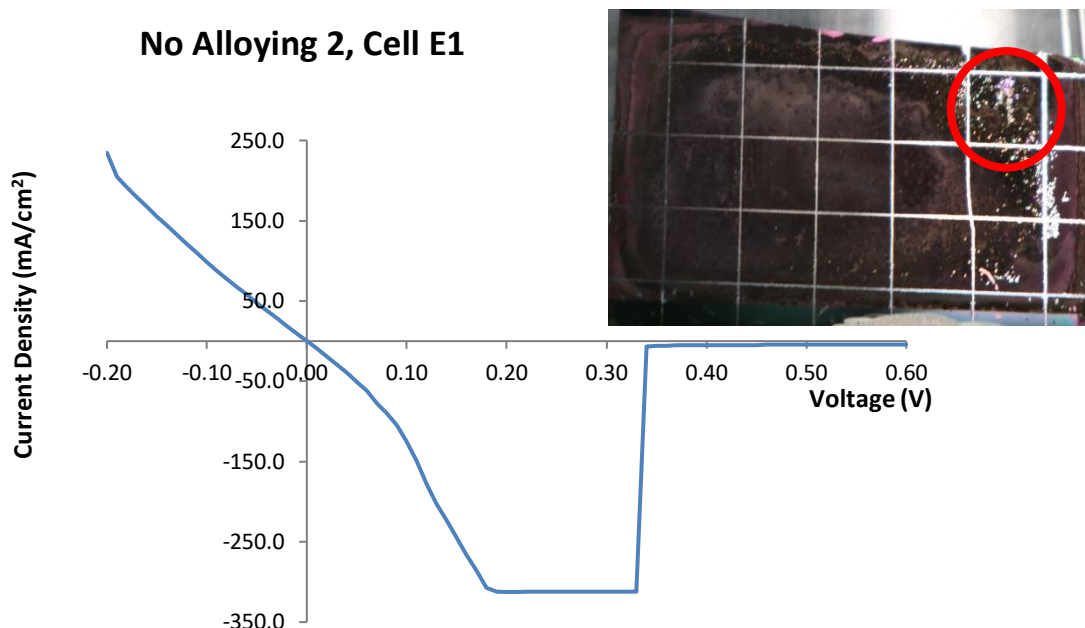


**Figure 6-8 - A non-functional solar cell displaying a large number of pinholes and an ohmic J-V characteristic. This is likely indicative of high levels of shunting through the device.**

can be present that are not necessarily detectable by simple visual inspection – see Figure 5-31, section 5.3.3, for example. These invisible features would likely lead to shunting paths through the CZTS films and may be responsible for the low shunt resistance of the devices, and, at least in part, the low overall cell performances in general. Further film optimisation experiments would be necessary to improve upon this, which could include the electrodeposition of thicker precursor films.

In addition to the J-V curves for the five highest performing cells, two J-V curves are presented for non-functional cells, along with corresponding photographs. It is possible to see in the photograph in Figure 6-8 that a significant proportion of the cell has been damaged by the presence of pinholes. It could be predicted that this would lead to a high degree of shunting, such that the dominant current flowing through the device when a voltage bias is applied would not pass through the photoactive material, leading to the ohmic characteristics that would be expected from a resistor. The J-V plot presented confirms this – the value range of the graph has been extended to cover the full voltage sweep from -0.2V to +0.6V, as the plot line does not pass into the positive quadrant. It can be seen that the device approximately

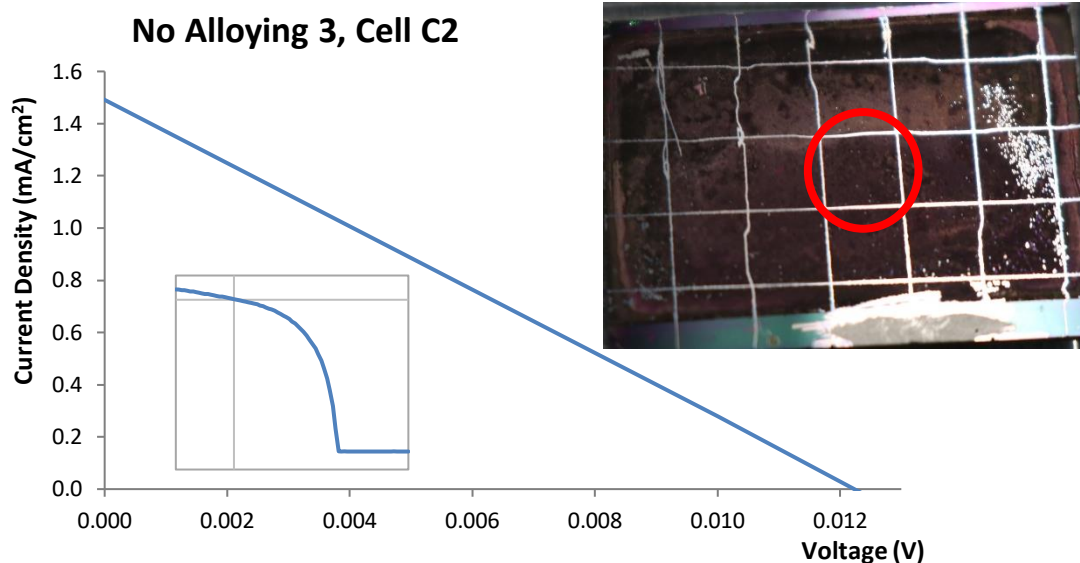


**Figure 6-9 - A non-functioning device in the centre of a sample with no large pinholes being evident. Unlike the cell in Figure 6-8, some rectifying behaviour is evident in the inset graph, which shows the full voltage sweep from -0.2V to +0.6V (the current density range being +50 mA cm<sup>-2</sup> to -350 mA cm<sup>-2</sup>).**

follows Ohm's law until the maximum current density amplitude is reached at a value of -310 mA cm<sup>-2</sup>, at which point it is automatically restricted by the solar simulator software. This is in contrast to the solar cell represented in Figure 6-9. This cell is near the centre of a sample and does not appear to suffer from any visible pinholes, however it is still non-functional as a photovoltaic device, with a low  $J_{SC}$  of 1.5 mA and a particularly low  $V_{OC}$  of 12 mV. Despite this, when the full voltage sweep is included in the graph plot (see inset of Figure 6-9), it is possible to see that it does not display the simple ohmic J-V characteristics seen in Figure 6-8, but it does exhibit some of the rectifying behaviour of a p-n junction. The shunt resistance was found to be 50.9  $\Omega$  cm<sup>2</sup> and the series resistance was 48.7  $\Omega$  cm<sup>2</sup>. Although these values are not good, they are also not substantially worse than some of the values quoted for functional cells in the commentary above. This suggests that there are other reasons for the cell's poor performance than simply the lack of a metallic grid contact and the existence of pinhole shunting paths. There are multiple factors that can lower the  $V_{OC}$  of a CZTS solar cell, which can include charge carrier trapping and recombination by deep defects and at interfaces between layers and secondary phases [9]. As discussed in section 1.2, some types of defect are beneficial or even

necessary for CZTS to obtain its p-type nature. However, other types of defect can be detrimental to cell performance as they can cause localised variations in the band gap and fermi level, reducing the optical absorption capabilities of the film [10]. A useful list of the types of defects that can form in CZTS and the effects that result from these defects has been published by Kumar et al in reference [10]. A poor  $J_{SC}$  can occur as a result of non-ohmic contact between the CZTS and Mo layers, where a Schottky potential barrier can form [11]. A poor  $J_{SC}$  can also be a result of the presence of high band-gap secondary phases ( $SnS_2$  or  $ZnS$ , for example) at the interface between CZTS and Mo, where these phases can act to impede the transport of holes between the two layers [11]. These factors would cause an increase in the series resistance. The exact reason for the lack of power output from the cell presented in Figure 6-9 is unknown, however it is likely to be as a result of a combination of the factors discussed here, such as charge carrier recombination and incomplete light absorption resulting from the presence of defects and secondary phases, which in turn have detrimental effects on the  $V_{OC}$  and  $J_{SC}$ . A broader range of characterisation techniques would be required in order to obtain a more accurate description of the causes.

From the observations made of the visual properties of the cell films and the corresponding electrical measurements, it would appear that the excessively thin films located near the substrate centres are not capable of outputting any significant power, while the thicker film regions close to the substrate edges are more prone to shunting due to pinholes in the light absorbing layer. In order to obtain a functional device, the film needs to be both sufficiently thick and free from pinholes. This is most likely to occur on samples that have received a pre-alloying treatment nearer to the edges of the substrates. In order to ascertain more detail of the reasons behind the cell performances obtained for individual cells, it would be useful to characterise the CZTS films with a grid reference system in place prior to completion into photovoltaic devices. This may be achievable if a plastic grid of  $4 \times 4 \text{ mm}^2$  squares were printed using a 3D printer, that could be placed on top of each sample as it underwent analysis via a range of non-destructive techniques. This could include Raman spectroscopy, SEM-EDS and XRD, the XRD requiring the fitment of a

collimator to narrow the beam to a 1 mm diameter spot. This would allow the study of unwanted phases, as well as detailed film morphology, while creating the capability of correlating the characterisation data with the electrical characteristics of the completed cells.

## **6.4 Conclusions**

The pre-alloying process has been shown to lead to superior results, not just in terms of the visible morphological differences between sulphurised films expressed in section 5.3.4, but also in terms of the power conversion efficiencies subsequently achieved by completed photovoltaic cells. There is significant evidence that the pre-alloying stage can be integrated into the sulphurisation process without detriment to cell performance, as demonstrated by the slight increase in the average cell efficiency (across all cells) when the alloying process was integrated. In addition to this, an integrated alloying process led to a lower standard deviation in the cell efficiencies and a greater number of cells obtaining 0.1% efficiency or above, suggesting that it could help in producing more consistent results. Although only thirteen of the 135 manufactured cells achieved 0.1% efficiency or more (the highest being 0.48%), some of these initial results could be considered promising given that the open circuit voltages and shunt resistances were comparable to some seen in literature [6, 8], with the high series resistance appearing to be the most significant limiting factor. Further studies to improve the yield of functional devices by limiting the pinhole shunting paths, and improving efficiencies by reducing series resistance through the use of a metallic grid top contact would likely improve the results significantly.

## **6.5 References**

- [1] P. K. Sarswat, *Alternative Methods to Fabricate and Evaluate Copper Zinc Tin Sulfide Based Absorber Layers on Transparent Conducting Electrodes*, Salt Lake City, Utah: University of Utah, 2012.
- [2] T. W. Schmidt and M. J. Y. Tayebjee, "Section 1.24 - Upconversion," in *Comprehensive Renewable Energy*, vol. 1, A. Sayigh, Ed., Amsterdam, Elsevier, 2012, pp. 533-548.

- [3] T. M. Ng, M. T. Weller, G. P. Kissling, L. M. Peter, P. Dale, F. Babbe, J. de Wild, B. Wenger, H. J. Snaith and D. Lane, "Optoelectronic and spectroscopic characterization of vapour-transport grown  $\text{Cu}_2\text{ZnSnS}_4$  single crystals," *Journal of Materials Chemistry A*, vol. 5, no. 3, pp. 1192-1200, 2017.
- [4] B. K. Durant and B. A. Parkinson, "Photovoltaic response of natural Kesterite crystals," *Solar Energy Materials and Solar Cells*, vol. 144, pp. 586-591, 2016.
- [5] S. Ahmed, K. B. Reuter, O. Gunawan, L. Guo, L. T. Romankiw and H. Deligianni, "A High Efficiency Electrodeposited  $\text{Cu}_2\text{ZnSnS}_4$  Solar Cell," *Advanced Energy Materials*, vol. 2, no. 2, pp. 253-259, February 2012.
- [6] M. I. Khalil, R. Bernasconi, A. Lucotti, A. Le Donne, R. A. Mereu, S. Binetti, J. L. Hart, M. L. Taheri, L. Nobili and L. Magagnin, "CZTS thin film solar cells on flexible Molybdenum foil by electrodeposition-annealing route," *Journal of Applied Electrochemistry*, vol. 51, no. 2, p. 209–218, 2021.
- [7] J. Nelson, "Section 1.4 - Introduction: Characteristics of the Photovoltaic Cell: A Summary," in *The Physics of Solar Cells*, London, Imperial College Press, 2004, pp. 7-15.
- [8] L. Guo, Y. Zhu, O. Gunawan, T. Gokmen, V. R. Deline, S. Ahmed, L. T. Romankiw and H. Deligianni, "Electrodeposited  $\text{Cu}_2\text{ZnSnSe}_4$  Thin Film Solar Cell with 7% Power Conversion Efficiency," *Progress in Photovoltaics: Research and Applications*, vol. 22, no. 1, pp. 58-68, January 2014.
- [9] Y. Gong, Y. Zhang, Q. Zhu, Y. Zhou, R. Qiu, C. Niu, W. Yan, W. Huang and X. Hao, "Identifying the origin of the Voc deficit of kesterite solar cells from the two grain growth mechanisms induced by  $\text{Sn}^{2+}$  and  $\text{Sn}^{4+}$  precursors in DMSO solution," *Energy and Environmental Science*, Online Publication, 15 February 2021.
- [10] M. Kumar, A. Dubey, N. Adhikari, S. Venkatesan and Q. Qiao, "Strategic review of secondary phases, defects and defect-complexes in kesterite CZTS–Se solar cells," *Energy & Environmental Science*, vol. 8, no. 11, pp. 3134-3159, 2015.
- [11] K. F. Tai, *Investigating the Open-Circuit Voltage Deficit in  $\text{Cu}_2\text{ZnSn}(\text{S},\text{Se})_4$  Solar Cells*, Singapore: Nanyang Technological University, 2015.

## 7 Conclusions and Further Work

### 7.1 Conclusions

The successful electrodeposition and characterisation of copper, tin and zinc films on molybdenum coated glass for the manufacture of CZTS films was completed, including the successful deposition of an optional second layer of copper upon the tin. A high standard of optimisation of the copper and tin films was achieved, although there is scope for further work in the optimisation of the microscopic coverage of zinc films when deposited onto tin. It was found that the microscopic properties of the films were highly sensitive to the deposition parameters, with copper being particularly sensitive to the deposition potential and tin being sensitive to the deposition current. The deposition potential for copper being deposited onto molybdenum was optimised at  $-0.98\text{ V}$  vs  $\text{Hg|HgO}$  from an alkaline electrolyte, while tin, which deposited successfully from a methanesulfonic acid based electrolyte, was optimised to an initial high current density period of  $-20\text{ mA cm}^{-2}$  for  $1.2\text{ s}$  to nucleate grains, falling to  $-5\text{ mA cm}^{-2}$  to minimise hydrogen evolution thereafter. The deposition of zinc onto tin proved more challenging than the deposition of zinc onto copper due to the lack of ability of tin and zinc to alloy with one another. Much of the experimentation regarding the deposition of zinc onto tin was focussed on adjustments to the electrolyte composition and attempts to limit hydrogen evolution. It was found that an acid-sulphate electrolyte designed for the deposition of zinc onto sheet steel gave an acceptable compromise between microscopic coverage, macroscopic uniformity and absence of damage due to hydrogen evolution, three factors that were found to be in competition, and that a galvanostatic deposition at  $-50\text{ mA cm}^{-2}$  returned acceptable results. When depositing a second copper layer onto tin, there was strong competition between the necessity to rapidly cover the tin substrate with copper in order to avoid tin dissolution, and the avoidance of hydrogen evolution caused by the use of more negative potentials. This was overcome through using a more concentrated electrolyte and pre-polarising the substrate at  $-1.18\text{ V}$  prior immersion in the deposition solution and then changing the potential to  $-1.14\text{ V}$  after  $20\text{ s}$ .

Much time was dedicated to attempting to gauge the deposition efficiency in order that the deposited elemental ratios could be known and tuned. It is almost impossible to quantify the quantity of metal being deposited in the electroplating process if the efficiency is not known, causing significant difficulty in adjusting the elemental ratios of the metallic stack. It was learned that it is necessary to adopt a critical approach to some of the efficiency data, particularly that obtained through MP-AES or XPS depth profiling. A more effective approach may be to compare films after they have been processed into CZTS, focussing on comparative EDS elemental data and the compounds obtained, and feeding that information back into tuning the quantity of each metal deposited, rather than focussing on the precise elemental ratios. It was considered likely that the unwanted phases found when CZTS films were analysed through Raman spectroscopy were as a result in variations between the elemental ratios across the deposition area, and some work may be required to address this. The quantity of zinc deposited had substantial effects on the ability of copper to alloy with tin in the pre-alloying stage and this is a key area for consideration. A cross-sectional SEM analysis with EDS colour mapping could help to gain insight into the distribution of elements across the thickness of un-annealed, pre-alloyed and sulphurised films, and would offer useful complementary information to that gained through XPS depth profiles. Alternatively, SIMS depth profiling could potentially be used in place of XPS, as (as discussed in section 4.3.7.1), it may offer a more accurate elemental profile.

The temperature and duration of the pre-alloying step were successfully optimised at 300 °C for 10 minutes, and the sulphur concentration and nitrogen background pressure for sulphurisation were optimised to 750 mg of sulphur and 3.75 Torr of nitrogen, using an RTP furnace. The pre-alloying step was shown to be beneficial to the morphology of the CZTS films, resulting in fewer blisters being formed. It was also shown that the benefits of the pre-alloying step can also be retained when it is integrated into the same furnace operation as the sulphurisation step. These benefits were translated into a greater number of functional solar cells when CZTS films were progressed into completed devices. More specifically, 8 out of 45 cells with an integrated pre-alloying process achieved 0.1% efficiency or greater, compared to 5



out of 45 for those that underwent a separate pre-alloying process, and 0 out of 45 for those that received no pre-alloying process.

The most efficient solar cell devices were found to have films that were both sufficiently thick and devoid of any large pinholes. As it was necessary to characterise the CZTS films prior to completion into devices, it was not possible to correlate the lack of unwanted phases with functioning CZTS devices. Ideally it would be necessary to devise a spatial referencing system that could be applied to the CZTS films prior to buffer and window layer deposition in order to achieve this.

This project started with the very basics of electrodeposition and progressed through multiple stages of characterisation and adjustment in order to finally achieve some working solar cells. Although much has been achieved in improving and optimising each stage of the CZTS film manufacturing process, further work would be required in order to obtain higher power conversion efficiencies and more reproducible functional solar cells.

## **7.2 Further Work**

Part of the purpose of this project was to investigate a deposition method for CZTS that is industrially scalable. Although this is true of electrodeposition, industrial electroplating is carried out galvanostatically rather than potentiostatically. Galvanostatic deposition was achieved for tin and zinc, but not copper. This would be scope for further investigation, and would likely require significant reformulation of the electrolyte composition, starting with an increase in the copper salt concentration. This would add flexibility to the deposition current range while lessening the risk of the potential being driven to a value that is negative enough to cause hydrogen evolution. Other improvements that could be made to the electroplating parameters could involve the adjustment of the zinc electrolyte composition in order to increase the microscopic coverage of the underlying tin. This could involve increasing the concentration of dextrin (a levelling agent) in the chosen acid-sulphate electrolyte, adding sodium dodecylbenzenesulfonate (a surfactant) to

increase throwing power, or trialling the addition of Zylite™ brightener that was used in the acid-chloride electrolyte designed for car restoration. Scope for further experimentation also remained with the acid-chloride electrolyte for car restoration. Although it did not produce consistently homogeneous zinc deposits, the more favourable of the deposits may have been suitable for advancement onto the sulphurisation and annealing stage for comparison with the films produced from the acid-sulphate electrolyte.

Another potential future area of work relating to the electrodeposition of the metallic layers is the tuning of the overall thickness of the electroplated stack. As discussed at the end of chapter 5, CZTS is very sensitive to precise stoichiometry, and variations across the area of the deposited film could be leading to the formation of the detected unwanted secondary phases. Depositing thicker layers overall could reduce the impact of slight localised variations in the film thickness on the localised elemental ratios. Rather than focussing on measuring the elemental ratios of the electrodeposited precursors, it could be more effective to examine the elemental ratios after sulphurisation, and correlate this with the Raman spectroscopy and XRD data to identify which particular elemental ratios are least likely to give rise to unwanted secondary phases. A useful exercise would be to calibrate the EDS system on the FEG-SEM in order to obtain data that is more quantitative. EDS would not be suitable for gathering accurate quantitative data on an electroplated stack even if it were calibrated due to the strength of signal for each element being effected by its position in the stack. Use of a calibrated EDS system for elemental quantification on sulphurised films would enable the obtainment of accurate information on the elemental ratios, without the need for a destructive technique like those used in attempts to quantify the deposition efficiencies, such as XPS depth profiling, MP-AES or deposition-stripping tests.

One area of work that would be of priority if this project were extended is the comprehensive optimisation of the sulphurisation process. As mentioned in chapter 5, although all the sulphurisation work presented in this thesis was carried out by the author, the sulphurisation heating settings used were those that had been optimised for spin coated CZTS by a post-doctoral research colleague, Dr. Zhengfei Wei. For

example, the 400°C was designed to ensure that all sulphur had evaporated prior to the reaction temperature being reached, however it was never established in the course of this project whether it was of benefit when sulphurising electroplated metallic precursors. Although the optimisation of the background pressure and sulphur concentration made significant improvements in reducing material losses and the associated blistering, it would be necessary to also optimise the heating profile for electrodeposited stack precursors in order to realise the full potential of this technique.

In addition to the optimisation of the sulphurisation process, it would be useful to more extensively characterise and compare the sulphurised films, particularly to analyse the differences in elemental ratios found on samples that received a pre-alloying process and those that did not. This may help to identify whether the pinholes found on samples that did not receive a pre-alloying treatment were due to one of the elements evaporating, particularly tin.

In order to further understand and relate the solar cell electrical measurements to the composition of the CZTS film, it would be useful to be able to characterise the CZTS films with a grid reference system in place prior to completion into photovoltaic devices. This may be achievable if a plastic grid of  $4 \times 4 \text{ mm}^2$  squares were printed using a 3D printer (which would take the form of a plastic mesh), that could be placed on top of each sample as it underwent analysis via a range of non-destructive techniques (the squares would be numbered in order to create a positional reference system). This would enable the cross matching of the film composition data with the electrical characteristics of the completed cells, and facilitate the optimisation of the cell performances. It is proposed that SEM-EDS could be used for the identification of microscopic pinholes, porous film regions and elemental ratios, and Raman spectroscopy and XRD could be used for the identification of unwanted phases. Raman spectroscopy could be particularly powerful if lasers of multiple wavelengths were used in order to obtain greater separation between peaks associated with CZTS and specific unwanted phases, such as  $\text{Cu}_2\text{SnS}_3$ .

If this project were to be extended and the proposed further work undertaken as detailed above, then significant improvements upon the cell efficiencies detailed in this thesis could be obtained with electrodeposited CZTS.